

UC San Diego

UC San Diego Electronic Theses and Dissertations

Title

Assessment of FRP composite strengthened reinforced concrete bridge structures at the component and systems level through progressive damage and Non-Destructive Evaluation (NDE)

Permalink

<https://escholarship.org/uc/item/7h5194qt>

Author

Ghosh, Kumar Kanti

Publication Date

2006

Peer reviewed|Thesis/dissertation

UNIVERSITY OF CALIFORNIA, SAN DIEGO

**ASSESSMENT OF FRP COMPOSITE STRENGTHENED REINFORCED
CONCRETE BRIDGE STRUCTURES AT THE COMPONENT AND SYSTEMS
LEVEL THROUGH PROGRESSIVE DAMAGE AND NON-DESTRUCTIVE
EVALUATION (NDE)**

A dissertation submitted in partial satisfaction of the requirements for the degree of

Doctor of Philosophy

in

Structural Engineering

By

Kumar Kanti Ghosh

Committee in charge:

Professor Vistasp M. Karbhari, Chair
Professor Carl H. Gibson
Professor Francesco Lanza di Scalea
Professor P. Benson Shing
Professor Mohan M. Trivedi

2006

Copyright

Kumar Kanti Ghosh, 2006

All rights reserved.

The dissertation of Kumar Kanti Ghosh is approved, and it is acceptable in quality and form for publication on microfilm:

Chair

University of California, San Diego

2006

TABLE OF CONTENTS

SIGNATURE PAGE	iii
TABLE OF CONTENTS	iv
LIST OF FIGURES	x
LIST OF TABLES	xxii
ACKNOWLEDGEMENTS	xxiv
VITA	xxv
ABSTRACT	xxvi
1 INTRODUCTION	1
1.1	Problem Statement	2
1.2	Scope of Current Research and Thesis Organization	3
2 OVERVIEW OF THE STATE OF THE ART IN SYSTEMS LEVEL STRENGTHENING WITH FRP COMPOSITES	6
2.1	Introduction	6
2.2	Strengthening of RC Components with FRP Composites	6
2.2.1	Flexural Strengthening of Beams and Slabs	6
2.2.2	Shear Strengthening of Beams	8
2.3	Effect of Strengthening of RC Bridge Components at Systems Level ...	8
2.3.1	Relevant Systems Level Tests Demonstrating Effect of Stress Re-Distribution and Damage Progression on Overall Structural Behavior	9
2.3.2	Existing Systems Level Research in FRP Composite Strengthening of Bridge Components	15
2.4	Conclusions	20

3	COMPONENT LEVEL STUDY OF FIELD SPECIMENS	22
3.1	Introduction	22
3.2	Research Objectives	23
3.3	Description of Test Specimens	24
3.4	Material Properties and Capacity Prediction	28
3.5	Test Setup and Instrumentation	40
3.6	Instrumentation and Data Acquisition	41
3.7	Test Results and Discussion	46
	3.7.1 Ultimate Load Capacities of Slabs	46
	3.7.2 Slab Deflections and Cracking	47
	3.7.3 Strain Development in the FRP Material	54
3.8	Progressive Damage Characterization	57
	3.8.1 Detection and characterization of pre-existing defect/damage ...	59
	3.8.2 Damage Detection/Progression from Thermography Data	67
	3.8.3 Correlation of Damage Progression to Strain Gage Data	76
3.9	Comparison of Predicted and Experimental Results	78
3.10	Correlating Test Specimen to Bridge Deck Capacity	81
3.11	Research Extension to the Systems Level	85
4	EXPERIMENTAL PROGRAM	87
4.1	Introduction	87
4.2	Research Objectives	88
4.3	Description of Test Specimen	90
4.4	General Test Plan	96

4.5	Initial Analytical Modeling and Design	97
4.5.1	Design of Unstrengthened Components for Phase 1 of Test	101
4.5.1.1	Design capacity of deck slabs	101
4.5.1.2	Design capacity of unstrengthened girders	103
4.5.2	Design of Strengthened Deck Slabs for Phase 2 of Test	105
4.5.3	Design of Strengthened Girder for Phase 3 of Test	116
4.6	Test Setup	125
4.7	CFRP Strengthening Procedures	129
4.7.1	Strengthening of the deck slabs	129
4.7.1.1	Strengthening procedure	129
4.7.1.2	Material properties of composite for slab strengthening	132
4.7.2	Strengthening of the girder	138
4.7.2.1	Strengthening procedure	138
4.7.2.2	Material properties of composite for girder strengthening	142
4.8	Instrumentation	145
4.8.1	Instrumentation details of linear potentiometers and load cells..	145
4.8.2	Instrumentation details of strain gages	146
4.8.3	Instrumentation details for IR Thermography inspections	151
4.8.4	Instrumentation details for forced excitation based modal testing	152
5	TEST RESULTS	156
5.1	Results from Phase 1 of Testing – Introduction	157

5.1.1	Load Capacity and Stiffness Results	158
5.1.2	Deflection Profiles and Crack Patterns	168
5.1.3	Strain Profiles	178
5.1.4	Comparison of Test Results with Design	183
5.2	Results from Phase 2 of Testing – Introduction	187
5.2.1	Load Capacity and Stiffness Results	187
5.2.2	Deflection Profiles and Crack Patterns	198
5.2.3	Strain Profiles	208
5.2.4	Comparison of Test Results with Design	221
5.3	Results from Phase 3 of Testing – Introduction	222
5.3.1	Load Capacity and Stiffness Results	222
5.3.2	Deflection Profiles and Crack Patterns	231
5.3.3	Strain Profiles	248
5.3.4	Comparison of Test Results with Design Basis in Phase 3	259
6	NON DESTRUCTIVE EVALUATION (NDE) 1 – THERMOGRAPHY	261
6.1	IR Thermography Inspection – Objectives	261
6.2	Inspection Details and Post-Processing of Data	262
6.3	Inspection Results from Pultruded Strips in Slab 1	268
6.4	Comparison of Thermography Results with Crack Patterns in Slab 1 ...	286
6.5	Inspection Results from Fabric Laminates in Slab 2	295
6.6	Comparison of Thermography Results with Crack Patterns in Slab 2 ...	302
6.7	Conclusions	304

7	NON DESTRUCTIVE EVALUATION (NDE) 2 – MODAL TESTING	306
7.1	Introduction	306
7.2	Current Modal Test Objectives	307
7.3	Theoretical Basis of Modal Analysis	310
7.4	Test Setup and Input-Output Data	313
7.5	Modal Test Results	319
7.6	Finite Element Modeling and Initial Parameter Estimation	328
7.7	Model Updating Results	333
	7.7.1 Segmentation of FE Model for Model Updating	333
	7.7.2 Model Updating	335
	7.7.3 Model Updating Results	338
7.8	Comparison of Model Updating With Experimental Load-Deflection Results	350
8	FINITE ELEMENT MODELING AND ANALYSIS	359
8.1	Introduction	359
8.2	Description of the FE Model	
	8.2.1 Geometry and Element Types	360
	8.2.2 Material Properties	360
	8.2.2.1 Reinforced Concrete	363
	8.2.2.2 FRP Composite	368
	8.2.2.3 Connectors	369
	8.2.3 Loading and Solution Control	370
8.3	Analysis Results	371

8.3.1	Phase 1 of Test	371
8.3.1.1	Load-Deflection Response	371
8.3.1.2	Damage Progression and Strain Profiles	374
8.3.2	Phase 2 of Test	381
8.3.2.1	Load-Deflection Response	381
8.3.2.2	Damage Progression and Strain Profiles	384
8.3.3	Phase 3 of Test	390
8.3.3.1	Load-Deflection Response	391
8.3.3.2	Damage Progression and Strain Profiles	394
8.4	Summary	402
9	DESIGN IMPLICATIONS, CONCLUSIONS AND RECOMMENDATIONS	403
9.1	Limitations of the Current Design Methodology	403
9.2	Proposed Design Methodology for CFRP Composite Strengthening ...	406
9.3	Primary Findings	416
9.4	Conclusions	425
9.5	Recommendations for Future Research	426
	APPENDIX A	428
	REFERENCES	447

LIST OF FIGURES

1.1	Overview of scope of research	3
3.1	Onsite rehabilitation of bridge deck slabs	26
	(a) Prefabricated pultruded strips	
	(b) Site-impregnated fabric laminates	
3.2	Location of FRP strengthening on test slabs	27
	(a) Specimen S2 with wet layup fabric	
	(b) Specimen S3 with adhesively bonded prefabricated strips	
3.3	Test specimens	29
	(a) Specimen S1	
	(b) Specimen S2	
	(c) Specimen S3	
3.4	FE Modeling of the test components	29
	(a) Finite element model of the bridge frame	
	(b) Location of test component in the bridge	
	(c) Finite element model of test component	
3.5	Comparison of experimental and analytical mode shapes	32
	(a) Experimental mode shape ($f = 205$ Hz)	
	(b) Analytical mode shape ($f = 205$ Hz) from FEM	
3.6	Test setup	41
3.7	Locations of linear potentiometers	42
3.8	Locations of accelerometers for vibration tests	44
	(a) Setup 1	
	(b) Setup 2	
3.9	Locations of strain gages on composite strips/laminates	45
	(a) Specimen S2	
	(b) Specimen S3	
3.10	Load-displacement plots for test specimens	47
3.11	Progression of deflection in the slabs	
	(a) With loading at 89 kN and 267 kN	49
	(b) With loading at 445 kN and 623 kN	50
	(c) With loading at 791 kN and 862 kN	51

3.12	Crack pattern in Specimen 1	52
3.13	Crack patterns in strengthened specimens 2 and 3	54
3.14	(a) Development of axial strains in specimen S2 along transverse laminate 3	55
	(b) Development of axial strains in specimen S2 along longitudinal laminate	56
3.15	(a) Development of axial strains in specimen S3 along transverse laminate 3	56
	(b) Development of axial strains in specimen S3 along longitudinal laminate	57
3.16	Initial thermography inspection of specimens	58
	(a) Data acquisition unit	
	(b) Setup for inspection	
3.17	Representative detection of pre-existing defects in composite laminates ..	60
3.18	Representative thermal signatures from baseline inspection	63
	(a) Regions used for plotting thermal intensity profiles	
	(b) Thermal intensity profile in x-direction in Zone 1	
	(c) Thermal intensity profile in x-direction in Zone 2	
	(d) Thermal intensity profile in y-direction in Zone 2	
3.19	Thermal signature over air voids of varying damage severity	63
	(a) Thermal intensity over minor defect	
	(b) Thermal intensity over major defect	
3.20	Thermal signature over fabric undulations	64
3.21	Thermal signature at locations of substrate cracks	65
3.22	Visual and baseline thermography inspection of slab 3 before testing	66
	(a) Visual inspection before test	
	(b) Baseline thermography data before test	
3.23	Regions of thermography inspection in slab 3 with damage areas	67
3.24	Progression of damage in Zone 1 of longitudinal strip 2 of Slab 3	68
3.25	Appearance of debond areas in Zone 2 of longitudinal strip 2 of slab 3 ...	68
3.26	Appearance of debond areas in zone 4 of longitudinal strip 1 of slab 3 ...	69
3.27	Appearance of debond areas in zone 3 of longitudinal strip 1 of slab 3 ...	69
3.28	Crack pattern in Slab 3 and correspondence with thermography inspection	72

3.29	Visual observation of debonded area in composite strip	73
3.30	Comparison between strain and thermography intensity profiles	75
	(a) Trend of strain profile along length of composite with increase in loading	
	(b) Damage progression detected from thermography data with increase in loading	
3.31	Thermal profiles along length of fabric laminate with loading	76
3.32	Theoretical punching shear failure perimeter in slab S1	82
4.1	Overall dimensions of the test specimen	92
4.2	Reinforcement details (Cross-section and plan) of the test specimen	93
4.3	Internal steel stirrup details in middle longitudinal girder	94
4.4	Construction of test specimen	95
	(a) Construction of specimen formwork	
	(b) Pouring of concrete and finishing of specimen surface	
4.5	Strength development plot for concrete	95
4.6	Finite element model	99
4.7	Transverse strain contours in model under simulated wheel loads	100
4.8	Parameters in sectional analysis for determination of flexural capacity ...	101
4.9	Shear demand on middle girder for phase 2 limit load	103
4.10	Shear demand vs. capacity on middle girder for phase 2 limit load	105
4.11	Manufacturing of composite panels for preliminary material tests	106
4.12	Pull-off test specimens	108
	(a) Preparation of pull-off specimens	
	(b) Pull-off failures after tests	
4.13	Theoretical punching shear failure perimeter	110
4.14	Schematic of the strengthening of deck slabs	114
4.15	Shear demand on center girder for phase 3 limit load	116
4.16	Schematic of FRP contribution parameters	118
4.17	Schematic of shear strengthening of girder with composite stirrups	122
4.18	Schematic of cross-sectional view of strengthened girder	123
4.19	Shear demand vs. capacity of strengthened girder for phase 3 limit load ..	124
4.20	Cross-sectional schematic of test setup	125
4.21	Schematic of load cell assembly	126

4.22	Test setup details	128
4.23	Preparation of the concrete surface before strengthening the slabs	130
	(a) Application of primer coat	
	(b) Primed surface for composite installation	
4.24	Installation of pultruded strips in slab 1	131
4.25	Installation of fabric laminates in slab 2	132
4.26	Manufacturing composite and resin test panels	133
4.27	Surface preparation and drilling of anchor holes	139
4.28	Installation of composite stirrup and anchor in girder	141
4.29	Comparison of shear capacities with preliminary and test batch properties	145
4.30	Locations of vertical linear potentiometers	146
4.31	Locations of strain gages on deck slabs	147
4.32	Gage locations on longitudinal and shear reinforcement of girders	149
4.33	Locations of gages on composite after slab strengthening	150
4.34	Locations of gages on composite stirrup after girder strengthening	150
4.35	Non-destructive inspections using IR Thermography	152
	(a) Thermography data acquisition unit	
	(b) Thermography setup	
4.36	Locations of accelerometers for the three setups	154
4.37	Forced excitation with three different excitation sources	155
5.1	Schematic of test plan	157
5.2	Load-deflection plots for slab 1 in phase 1	161
5.3	Comparison of load-deflection plots between deck slabs	161
5.4	(a) Actuator load 1 vs. mid-span deflection plots for middle girder	163
	(b) Actuator load 1 vs. mid-span deflection plots for edge girder	
	(c) Comparison of load-deflection plots between edge girders	
5.5	Schematic of deflection of specimen under load	166
5.6	(a) Deflection along length of middle girder	169
	(b) Deflection along length of edge girder 1	
	(c) Deflection along length of edge girder	
5.7	Deflection contour over deck slabs at 400 kN (90 kips)	172
5.8	Deflection profile along Row 2 of linear potentiometers	173

5.9	Deflection profile along Row M of linear potentiometers	173
5.10	Progression of cracks in the deck slabs below load area	174
	(a) Crack pattern in Slab 1 during Phase 1 loading	
	(b) Crack pattern in Slab 2 during Phase 1 loading	
5.11	Propagation of cracks from slabs into girders during Phase 1 loading	176
	(a) Propagation of cracks from slabs into Center girder	
	(b) Propagation of cracks from slabs into Edge girder	
5.12	Flexural cracks in the center girder at the end of Phase 1 of test	177
5.13	Shear cracks in the center girder at the end of Phase 1 of test	177
5.14	Strain profile in slab reinforcement at mid-span	179
5.15	Strain profile in slab reinforcement at 508 mm (20") from mid-span	180
5.16	Strain profile in center girder stirrups	182
5.17	Maximum recorded strains in the instrumented steel stirrups along the length of the center girder during phase 1 loading	183
5.18	Parameters in sectional analysis for determination of flexural capacity ...	185
5.19	Deflections at support locations	186
5.20	Location of maximum recorded strain in steel stirrups	188
5.21	Strain profile extrapolation for girder stirrup	189
5.22	Load-deflection plots for slab 1	191
5.23	Effect of strengthening of slabs on load-deflection plot for slab 1	192
5.24	Comparison of load-deflection plots between deck slabs in phase 2	192
5.25	(a) Actuator load 1 vs. mid-span deflection plots for middle girder	194
	(b) Actuator load 2 vs. mid-span deflection plots for edge girder	
	(c) Comparison of load-deflection plots between edge girders	
5.26	(a) Deflection along length of middle girder	199
	(b) Deflection along length of edge girder 1	
	(c) Deflection along length of edge girder 2	
5.27	contour over deck slabs at 666 kN (150 kips)	202
5.28	Deflection profile along Row 2 of linear potentiometers	203
5.29	Deflection profile along Row M of linear potentiometers	203
5.30	Progression of cracks in the strengthened deck slabs	205
5.31	Crack pattern in the center girder at the end of phase 2 of test	207
5.32	Crack pattern in the edge girder at the end of phase 2 of test	208
5.33	Strain profile in slab reinforcement at mid-span	210

5.34	Strain profile in slab reinforcement at 508 mm (20") from mid-span	211
5.35	Strain profile in center girder steel stirrups	213
5.36	Maximum recorded strains in the instrumented steel stirrups along the length of the center girder during phase 2 loading	214
5.37	(a) Strain profile in transverse composite strips (T3 and T4) of strengthened Slab 1 for phase 2 loading	215
	(b) Strain profile in transverse composite strips (T5 and T6) of strengthened Slab 1 for phase 2 loading	216
5.38	(a) Strain profile in transverse composite laminates (T8 and T9) of strengthened Slab 2 for phase 2 loading	217
	(b) Strain profile in transverse composite laminate T10 of strengthened Slab 2 for phase 2 loading	218
5.39	Strain profile in longitudinal strip/laminate of strengthened slabs	220
5.40	Strain profile extrapolation for ultimate load demand prediction	223
5.41	Load-deflection plots for slab 1	226
5.42	Comparison of load-deflection plots between deck slabs in phase 3	227
5.43	(a) Actuator load 1 vs. mid-span deflection plots for middle girder	228
	(b) Actuator load 2 vs. mid-span deflection plots for edge girder	
	(c) Comparison of mid-span load-deflection plots between edge girders	
5.44	(a) Deflection along length of middle girder	232
	(b) Deflection along length of edge girder 1	
	(c) Deflection along length of edge girder 1	
5.45	Deflection contour over deck slabs at 666 kN (150 kips)	235
5.46	Deflection profile along Row 2 of linear potentiometers	236
5.47	Deflection profile along Row M of linear potentiometers	236
5.48	Typical visual inspection of cracks at 846 kN (190 kips)	238
5.49	Visual inspection of cracks at 846 kN (190 kips) in slab over center girder	239
5.50	Visual inspection of cracks at 846 kN (190 kips) at slab girder joint	239
5.51	Schematic of punching shear failure perimeters in slabs	240
5.52	Schematic of intersection of the punching shear cracks with composite ...	241
5.53	Representative damage areas in slab 2	242
5.54	Representative damage areas in slab 1	243
5.55	Punch-through of the load through concrete at top of slabs	244

5.56	Failure planes along transverse cross section of specimen	245
5.57	Failure planes along longitudinal cross section of specimen	246
5.58	Center girder segment at the end of phase 3 loading	247
5.59	Damaged area in composite stirrup at end of test	248
5.60	Strain profile in slab reinforcement at mid-span	249
5.61	Strain profile in slab reinforcement at 508 mm (20") from mid-span	250
5.62	(a) Strain profile in center girder stirrups along bottom line of gages	251
	(b) Strain profile in center girder stirrups along top line of gages	
5.63	(a) Strain profile in transverse composite strips (T3 and T4) of strengthened Slab 1 for phase 3 loading	254
	(b) Strain profile in transverse composite strips (T5 and T6) of strengthened Slab 1 for phase 3 loading	255
5.64	(a) Strain profile in transverse composite laminates (T8 and T9) of strengthened Slab 2 for phase 3 loading	256
	(b) Strain profile in transverse composite laminate T10 of strengthened Slab 2	257
5.65	(a) Strain profile in longitudinal composite strip of strengthened slab 1 ...	257
	(b) Strain profile in longitudinal composite laminates of strengthened slab 2	258
5.66	Strain profile in composite stirrup of center girder	259
6.1	Details related to thermography data acquisition	263
6.2	Thermal intensity profiles for pultruded strips between locations with and without defects	264
	(a) Thermal decay curve	
	(b) Thermal intensity differential	
6.3	Representative damage area in pultruded strip	265
6.4	Representative defect/damage areas in fabric laminate	267
	(a) Interlaminar air void defects	
	(b) Debonded area at composite-concrete interface	
6.5	Thermal decay laminates at locations with and without defects	267
6.6	Thermal intensity differentials between areas with and without defects ...	268
6.7	Typical post-installation sub-surface defects detected by visual inspection	269

	(a) Unbonded area	
	(b) Defect area in strip	
6.8	Typical sub-surface defects detected by thermography inspection	270
6.9	(a) Overall schematic of slab 1 strengthened with pultruded strips	271
	(b) Locations of thermography inspections in Slab 1	272
6.10	Distinction between modes of debonding as observed visually and from thermography results (935-0 kN stands for thermography inspection carried out on unloading the specimen after reaching load of 935 kN)	274
	(a) Debonding at composite-concrete interface	
	(b) Interlaminar debonding occurring in the composite strip due to separation between the fibers and matrix of the strip	
6.11	Locations of defect type 1 (No progression of defects)	276
6.12	Locations of defect type 2 (With pre-existing and new defects)	277
6.13	Damage at transverse-longitudinal strip overlap area (Defect type 3)	279
6.14	Damage at concrete-longitudinal strip interface	280
6.15	Visual observation of damage at the edges of the transverse pultruded strips on unloading specimen after reaching failure load	282
6.16	Damage at edges of transverse strips (Defect type 3)	283
6.17	Damage at concrete-transverse strip interface (Damage after failure)	284
6.18	Debonded area at concrete-transverse strip interface (Damage after failure)	285
6.19	Damage areas identified through thermography inspections	286
6.20	Damage regions in slab 1 after removal of cracked concrete	288
6.21	(a) Correspondence of thermography inspections with crack pattern (Strip 5)	289
	(b) Correspondence of thermography inspections with crack pattern (Strip 1)	290
	(c) Correspondence of thermography with crack in longitudinal direction	291
6.22	(a) Locations of thermography inspections in Slab 1 used in Figure 6.22 to show correspondence between thermography and visual observations..	292
	(b) Comparisons between thermography and visual inspections in slab 1	293
6.23	Typical post-installation sub-surface defects detected by visual inspections	296
6.24	Typical shallow defects detected by baseline thermography inspections ..	297

6.25	Typical debonds / deeper defects detected by baseline inspections	298
6.26	Locations of thermography inspections in Slab 2	299
6.27	Damage area observed after failure at location L10	300
6.28	Comparison of inspection results at baseline and after failure	301
6.29	Comparison of failure perimeter with thermography inspection	302
6.30	Visual inspections of damage regions in slab 2	304
6.31	Visual inspection of damage at location L10 of thermography inspection.	304
7.1	Test setup with locations of accelerometers and excitation source	314
7.2	Typical force input by the three excitation sources	315
	(a) Force input by shaker excitation	
	(b) Force input by impact hammer	
	(c) Force input by drop hammer	
7.3	Typical acceleration time histories for the three excitation sources	316
	(a) Acceleration history for shaker excitation	
	(b) Acceleration history for impact hammer	
	(c) Acceleration history for drop hammer	
7.4	Typical force spectrum for the three excitation sources	318
	(a) Force spectrum for shaker excitation	
	(b) Force spectrum for impact hammer	
	(c) Force spectrum for drop hammer	
7.5	FRF magnitude plots for Phase 1 of testing	320
7.6	FRF magnitude plots for Phase 2 of testing	320
7.7	FRF magnitude plots for Phase 3 of testing	321
7.8	Trend of frequency ratio over the load stages	322
7.9	FRF comparisons from baseline 1 modal test for shaker and hammers ...	324
7.10	FRF comparisons from baseline 2 modal test for shaker and hammers ...	324
7.11	FRF comparisons from baseline 3 modal test for shaker and hammers ...	325
7.12	Mode shapes and complexity plots from baseline 1 modal test results	327
7.13	Finite element model of the test specimen	328
7.14	(a) Comparison of deflections below actuator load 1 between test and model	332
	(b) Comparison of deflections below actuator load 2 between test and model	

	(c) Comparison of deflection at center-girder midspan between test and model	
7.15	Plan view showing regions in the specimen with parameters to be updated in the FE model	335
7.16	(a) Locations of regions in the deck slabs used for model updating	345
	(b) Ratio of updated effective modulus in the 5 regions of Slab 1	346
	(c) Ratio of updated effective modulus in the 5 regions of Slab 2	346
	(d) Locations of regions in the girders used for model updating	347
	(e) Ratio of updated effective modulus in the 5 regions of center girder ...	348
	(f) Ratio of updated effective modulus in the 5 regions of edge girder 1 ..	348
	(g) Ratio of updated effective modulus in the 5 regions of edge girder 2 ..	349
	(h) Ratio of updated effective stiffness of the 6 springs simulating supports	349
7.17	Comparison of stiffness ratio below load area of slab 1	354
7.18	Comparison of stiffness ratio below load area of slab 2	354
7.19	Comparison of stiffness ratio at mid-span of center girder	355
7.20	Comparison of stiffness ratio at mid-span of edge girder 1	355
7.21	Comparison of stiffness ratio at mid-span of edge girder 2	356
7.22	Initial load-deflection responses at S-5 over load stages	357
7.23	Initial load-deflection responses at S-4 over load stages	358
7.24	Initial load-deflection responses at S-6 over load stages	358
8.1	Geometry of the baseline model (Phase 1)	361
8.2	Location of multi-point constraints at locations of supports	361
8.3	Geometry of the model with strengthening of the slabs (Phase 2)	362
8.4	Geometry of model with strengthening of the center girder (Phase 3)	362
8.5	Typical stress-strain curve for concrete	363
8.6	Compressive stress-strain curve of concrete used for model	365
8.7	Tensile stress-strain curve of concrete used for model	366
8.8	(a) Stress-strain curve of # 3 rebars used for girder stirrups	367
	(b) Stress-strain curve of # 9 rebars used for girder flexural reinforcement	368
	(c) Stress-strain curve of # 5 rebars used for slab flexural reinforcement .	368
8.9	Verification of load-deflection response of slab 1 – Phase 1	372

8.10	Verification of load-deflection response of slab 2 – Phase 1	372
8.11	Verification of load-deflection response of center girder – Phase 1	373
8.12	Verification of load-deflection response of edge girder 1 – Phase 1	373
8.13	Verification of load-deflection response of edge girder 2 – Phase 1	373
8.14	Maximum principal strain vectors in slabs at 214 kN (48 kips) – Phase 1.	374
8.15	Maximum principal strain vectors in slabs at 289 kN (65 kips) – Phase 1.	375
8.16	Maximum principal strain vectors in slabs at 356 kN (80 kips) – Phase 1.	375
8.17	Maximum principal strain vectors in slabs at 400 kN (90 kips) – Phase 1.	375
8.18	(a) Comparison of crack patterns in slab 1 below load area from numerical model and test observations at 400 kN (90 kips) - End of Phase 1	376
	(b) Comparison of crack patterns in slab 2 below load area from numerical model and test observations at 400 kN (90 kips) - End of Phase 1	377
8.19	(a) Comparison of strain profile in slab 1 transverse reinforcement below load	378
	(b) Comparison of strain profile in slab 2 transverse reinforcement below load	378
8.20	Maximum principal strain vectors in center girder – Phase 1	380
8.21	Comparison of crack patterns in center girder from numerical model and test observations at 400 kN (90 kips) - Final load cycle of Phase 1	380
8.22	Verification of load-deflection response of slab 1 – Phase 2	382
8.23	Verification of load-deflection response of slab 2 – Phase 2	382
8.24	Verification of load-deflection response of center girder – Phase 2	383
8.25	Verification of load-deflection response of edge girder 1 – Phase 2	383
8.26	Verification of load-deflection response of edge girder 2 – Phase 2	384
8.27	Maximum principal strain vectors (NE >0.0001) in center girder – Phase 2	385
8.28	Comparison of crack patterns in center girder from numerical model and test observations at 667 kN (150 kips) – Final load cycle of Phase 2	386
8.29	Nominal strain (N11) contours in center girder stirrups at 667 kN	387
8.30	Comparison of highest strain vs. load response in center girder stirrup from analytical model and strain gage data during Phase 2	388
8.31	Strain profile comparison in slab transverse reinforcement – Phase 2	389

8.32	Comparison of strain profile in slab composite reinforcement – Phase 2 ..	390
8.33	Verification of load-deflection response of slab 1 – Phase 2	392
8.34	Verification of load-deflection response of slab 2 – Phase 2	392
8.35	Verification of load-deflection response of center girder – Phase 2	393
8.36	Verification of load-deflection response of edge girder 1 – Phase 2	393
8.37	Verification of load-deflection response of edge girder 2 – Phase 2	394
8.38	Principal strain contours in the composite systems at 930 kN – Phase 3 ..	395
8.39	Comparison of strain profile in slab composite reinforcement – Phase 3 ..	395
8.40	Maximum principal strain contours at slab bottom at 930 kN – Phase 3 ..	397
8.41	Crack pattern at bottom of slabs below load areas from test observations.	398
8.42	Minimum principal strain contours on slab top at 930 kN – Phase 3	399
8.43	Crushing of concrete on slab top below load at 930 kN – Phase 3	399
8.44	Comparison of highest strain vs. load response in center girder steel stirrup from analytical model and test data for 667 kN load cycle during Phase 2 and Phase 3	400
8.45	Comparison of highest strain vs. load response in center girder steel stirrup from analytical model and test data for 667 kN load cycle during Phase 2 and Phase 3	401
A.1	Mode shape and complexity plot after unloading from 214 kN – Phase 1	429
A.2	Mode shape and complexity plot after unloading from 289 kN – Phase 1	430
A.3	Mode shape and complexity plot after unloading from 400 kN – Phase 1	431
A.4	Mode shape and complexity plot from Baseline 2 modal test – Phase 2 ...	432
A.5	Mode shape and complexity plot after unloading from 400 kN -Phase 2...	433
A.6	Mode shape and complexity plot after unloading from 578 kN -Phase 2...	434
A.7	Mode shape and complexity plot after unloading from 668 kN -Phase 2..	435
A.8	Mode shape and complexity plot from baseline 3 modal tests – Phase 3..	436
A.9	Mode shape and complexity plot after unloading from 668 kN -Phase 3..	437
A.10	Mode shape and complexity plot after unloading from 756 kN -Phase 3..	438
A.11	Mode shape and complexity plot after unloading from 846 kN -Phase 3..	439

LIST OF TABLES

3.1	Failure Loads and Mode for Test Specimens	40
3.2	Predicted and experimental failure Loads for test specimens and bridge slabs	85
4.1	Performance characteristics for reinforcing steel	94
4.2	Test phases	97
4.3	Preliminary material properties of FRP composite	107
4.4	Preliminary bond properties of composite	108
4.5	Tensile test properties of composite from slab strengthening	134
4.6	test properties of pure resin from slab strengthening	134
4.7	Pull-off test results from slab strengthening	135
4.8	Batch ratios of properties between preliminary and test panels	136
4.9	Recalculated ultimate moment capacities of the strengthened slabs	138
4.10	Tensile test properties of composite	143
4.11	Pull-off test results from girder strengthening	143
4.12	Batch ratios of properties between test and preliminary design panels	144
4.13	Performance details of the capacitive accelerometers	153
5.1	Test phases	156
5.2	Loading protocol for phase 1	160
5.3	(a) Effective stiffness ratio in slabs in phase 1 from linear potentiometer data	167
	(b) Effective stiffness ratio in girders in phase 1 from potentiometer data	
5.4	Loading protocol for phase 2	190
5.5	(a) Effective stiffness ratio in slabs in phase 2 from linear potentiometer data	197
	(b) Effective stiffness ratio in girders in phase 2 from potentiometer data.	198
5.6	Loading protocol for phase 3	224
5.7	(a) Effective stiffness ratio in slabs in phase 3 from linear potentiometer data	230
	(b) Effective stiffness ratio in girders in phase 3 from potentiometer data	

6.1	Defect types and locations as identified from thermography inspections ..	275
6.2	Summary of thermal signatures for defect types	294
7.1	Load stages at which modal testing was carried out	309
7.2	Natural frequencies of the test specimen over the load stages	321
7.3	Estimated reinforced concrete properties for slab and beam elements	329
7.4	Initial stiffness estimates of support spring elements	331
7.5	Comparison of frequencies and MAC between the test specimen and the model	340
7.6	Deflections and stiffness ratios obtained for Slabs under 2.25 kN load ...	352
7.7	Deflections and stiffness ratios for Girders under 2.25 kN load	353
8.1	Tensile test properties of composites	369
8.2	Stiffness estimates of grounded connectors at the supports	370
9.1	Proposed FRP composite strengthening methodology for slab-girder systems	407
9.2	Symbols and notations used in Table 9.1	414
A.1	(a) Mode 1 normalized modal amplitudes over the load stages	440
	(b) Mode 2 normalized modal amplitudes over the load stages	441
	(c) Mode 4 normalized modal amplitudes over the load stages	442
	(d) Mode 6 normalized modal amplitudes over the load stages	443
A.2	(a) Updated parameters for Phase 1 of testing	444
	(b) Updated parameters for Phase 2 of testing	445
	(c) Updated parameters for Phase 3 of testing	446

ACKNOWLEDGEMENTS

I will like to express sincere appreciation to Professor Vistasp M. Karbhari for his support, guidance and interest throughout this project. The financial support from the California Department of Transportation (Caltrans) is gratefully acknowledged. I will also like to thank Dr. Charles Sikorsky for his important inputs in this project. Additional contributions in the form of materials were provided by Fyfe Co. LLC. with Peter Milligan and Scott Arnold making contributions of time and effort during the systems level test. Thanks are also extended to all the lab personnel, especially, Alex, Charly, Chris, Bob and Larry and to all the undergraduate assistants, particularly, John, Matthew, Jared and Steve for their help during construction of the specimens. I will also like to thank the graduate students at UCSD for their valuable suggestions and help.

I will like to express my gratitude to my parents for their inspiration and for having faith in me. Finally this work would not have been possible without the love and encouragement from my wife, Madhurima, who always supported me even in the worst of times.

The following papers were based entirely on work reported in this thesis and the co-authorship of my advisor is acknowledged:

- i) Evaluation of Strengthening through Laboratory Testing of Rehabilitated Bridge Decks after In-Service Loading, In Press, Journal of Composite Structures
- ii) A Critical Review of Infrared Thermography as a Method for Non-Destructive Evaluation of FRP Rehabilitated Structures, International Journal of Materials and Product Technology, Vol. 25, No. 4, 2006, pp. 241-266.

VITA

- 1999 B.E., Department of Civil Engineering, Jadavpur University, India
- 2002 M.A.Sc., Department of Civil Engineering, University of Toronto
- 2002-2006 Graduate Student Researcher, Department of Structural
Engineering, University of California, San Diego
- 2006 Ph.D., Department of Structural Engineering, University of
California, San Diego

ABSTRACT OF THE DISSERTATION

Assessment of FRP Composite Strengthened Reinforced Concrete Bridge Structures at
the Component and Systems Level through Progressive Damage and Non-Destructive
Evaluation (NDE)

by

Kumar Kanti Ghosh

Doctor of Philosophy in Structural Engineering

University of California, San Diego, 2006

Professor Vistasp M. Karbhari, Chair

There is growing use of FRP composite materials in the civil infrastructure for rehabilitation of deficient bridge components including deck slabs and girders. However assessment of the effectiveness of rehabilitation over time and monitoring the progression of damage or change in load paths between the structural components, caused by sequential strengthening of the components, has not been undertaken to date. Investigation was first carried out at “component level” on both unstrengthened and field-rehabilitated slab specimens cut out from a major highway bridge. The slabs were tested to failure and the progression of damage was characterized through instrumentation and

NDE. The test data on the failure modes and capacity loads were correlated to the available analytical models and design guidelines. The test capacity was also correlated to the bridge deck capacity based on local-global modeling. Research at the “systems level” was then undertaken, in which a three-girder two-span bridge deck system was tested to simulate behavior under field loading in which the deck slabs are found to be susceptible to punching shear type failures and the longitudinal girders are usually found to be deficient in terms of shear demand. The objective of the study was to evaluate damage progression in the deck slabs and the longitudinal girders under simulated truck load and to detect changes in the overall response of structure at systems level caused by strengthening of individual components that might cause other components to reach their critical limit states under the higher load demands which can be resisted by the strengthened components. NDE techniques, including IR thermography and forced vibration based dynamic modal tests, were evaluated as means to quantify the damage localization and progression under simulated field loading as well as to quantitatively monitor changes in the response of the components, caused by subsequent modifications of the structure, at systems level. The test data on the failure modes, capacity loads and specimen behavior were correlated to the both analytical and numerical models. Based on the limitations of the available design guideline for FRP strengthening, a modified design methodology was proposed for FRP strengthening of slab-girder systems.

1 INTRODUCTION

A considerable number of the existing reinforced concrete bridge inventory in the United States is classified as structurally deficient or in serious need of repair and strengthening. Data from the US National Bridge Inventory indicates that in the federal aid system, which includes about 276,200 federally maintained bridges, 40% of all bridges are 15-35 years old [1]. Thus most of these bridges have been subjected to significant periods of loading over their life span complemented by the increase in the number of the load bearing trucks and the weight carried by them. Moreover, over the life-span of the bridges there have been modifications in the design standards and thus components such as the deck slabs and the longitudinal girders are often found to be deficient in satisfying the truck load demands per the new design codes. The situation is made worse by the deterioration of the existing infrastructure due to environmental exposure, (which includes extensive use of deicing salts, variations in temperature, etc.). All of these have caused extensive cracking and strength degradations to occur in a large number of these bridges. It is estimated that out of about 575,000 highway bridges in the United States, 230,000 are rated as structurally deficient or functionally obsolete and are thus in need of replacement or serious rehabilitation work [1].

The rapid deterioration of the infrastructure and the limited funding available for infrastructure maintenance has promoted the use of newer materials such as Fiber Reinforced Polymer (FRP) composites as an optimized repair and strengthening technique. In this method, the FRP material (glass or carbon) is externally bonded to the concrete surface of the deficient structural component using epoxy adhesives. The high

strength/stiffness-to-weight ratio, tailorable mechanical properties, corrosion resistance and ease of installation with limited disruption of traffic are some of the well recognized advantages of the composite materials in bridge rehabilitation applications. All the above benefits have projected FRP repair and strengthening as a very promising technique for the rehabilitation/strengthening of deficient reinforced concrete structural components in bridges. A state-of-the art survey of FRP composites for construction applications in civil engineering can be found in [2] and is hence not repeated herein.

1.1 Problem Statement

While a significant amount of research has been conducted on the use of externally bonded FRP composites on individual components there has been almost no research at the systems level. There is also lack of information on the long-term in-field performance of FRP strengthened composite structures. As with all strengthening techniques which modify structural response there is a concern that changes made to a single component could cause inadvertent damage to the other components of the system either as a result of stress redistribution or through the failure of a “weak link” in the unstrengthened portions of the structural system. This research is aimed at investigating systems level response resulting from sequential rehabilitation of components, and developing guidelines for design, which would complement the existing composite strengthening guideline [3], from the study relevant to slab on girder bridge systems. In addition the effectiveness of IR thermography and vibration based modal analysis as non-destructive techniques to infer damage initiation and progression is also an aim of the study.

1.2 Scope of Current Research and Thesis Organization

The current research was divided into two phases. A flowchart outlining the overall scope of the research is shown in Figure 1.1.

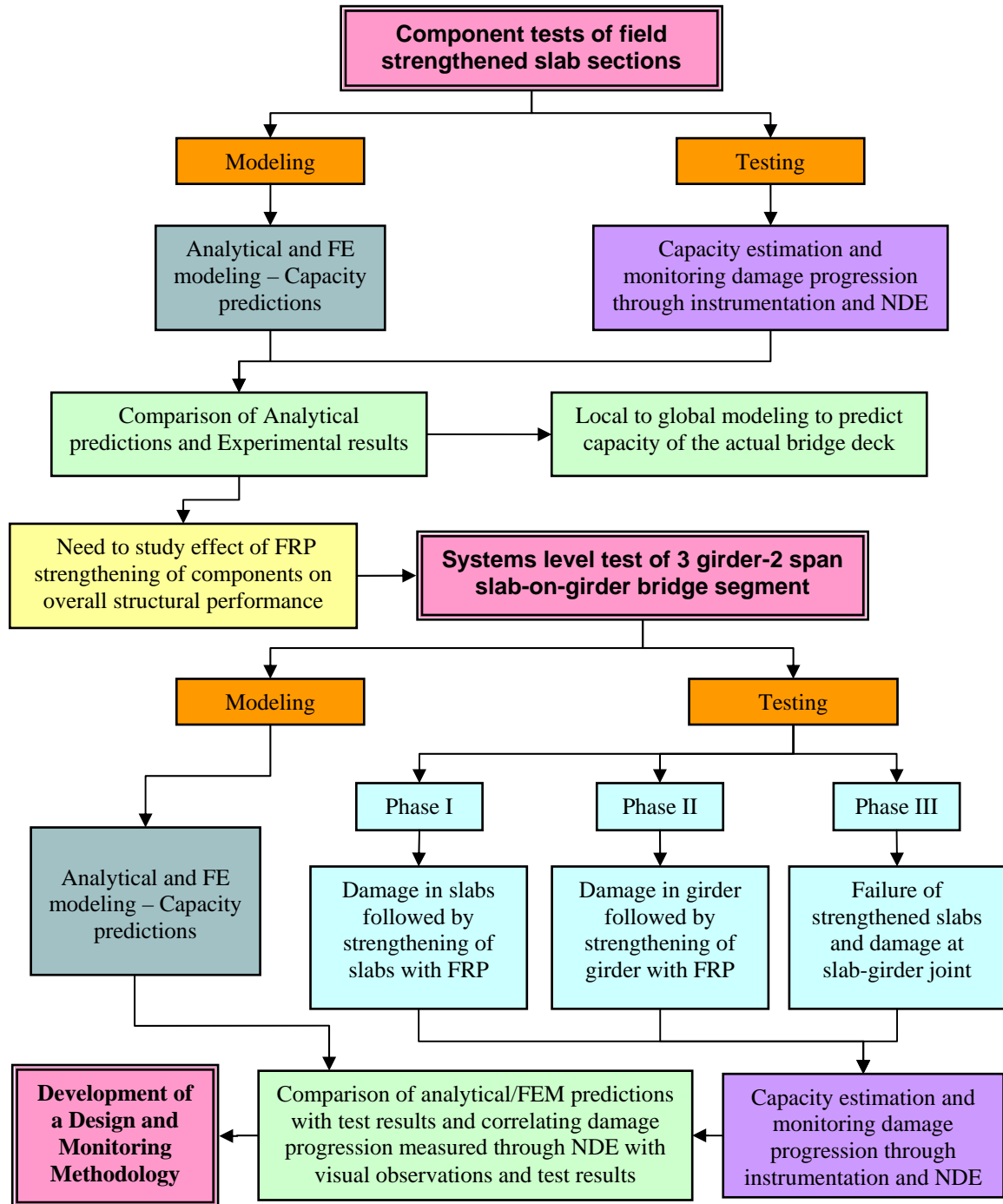


Figure 1.1 Overview of scope of research

Phase 1 involved component level study of field specimens through testing of slab sections cut-out from a bridge, both with externally bonded FRP, and without strengthening, after being in service for a period of time, thereby enabling assessment of the effectiveness of strengthening after being subjected to field representative loading and environmental exposures. The primary test objective was to determine the behavior and failure capacity of the deck slabs, representative of bridge deck components subjected to realistic deterioration and damage over time, to evaluate long-term performance of FRP composite strengthening. Available analytical models were used to predict the ultimate capacity of the test specimens and were compared with the test results. Local to global modeling was also used to predict the ultimate capacity of the actual bridge deck slabs from that of the test components. The failure mechanisms and progression of damage was monitored and characterized using experimental results and NDE inspections by thermography and modal testing. Further details of the component level study and the research findings have been presented in Chapter 3.

Phase 2 of the research involved assessment of FRP composite strengthening at the systems level through testing of a three-girder two bay reinforced concrete bridge deck segment under field representative loading conditions, with sequential strengthening of the slab and the girder with FRP composites. This phase of study ensued from the research review and the findings from the component level study, that there is a need for a large scale systems level testing through which the effects of progression of damage and changes in the load distribution/failure mechanism caused by the strengthening of individual components could be assessed in terms of overall system performance. The test specimen details, preliminary design predictions and composite strengthening details

are presented in Chapter 4. The test protocol and the test results are presented in Chapter 5. Two NDE methods, Thermography and Modal Testing were used to quantitatively monitor the progression of damage and effects of the sequential strengthening of components on the structural performance through inspections at regular load intervals. The thermography results were used to monitor the appearance and progression of damage at the local level at the composite-concrete interface in the deck slabs with an increase in loading. The modal tests were used to determine the dynamic characteristics of the structure which were then used for subsequent model calibration and updating to predict the structural response in terms of degradation/enhancement of the stiffness at discrete locations of the test specimen by taking into account the effect of damage progression and sequential strengthening of the specimen with FRP composites. The NDE results were correlated to the visual observations of crack patterns and failure mechanisms as well as to strain and displacement data measured during the test. The results of the thermography and modal testing inspections are presented in Chapters 6 and 7, respectively. Analytical modeling of the test specimen behavior and sequential strengthening of components over the load stages was carried out for capacity and response prediction and subsequent comparisons with the test results and this is presented in Chapter 8. A design methodology taking into account the overall structural response in the FRP strengthening design and incorporating the results of NDE methodologies for periodic structural condition monitoring are then be presented in Chapter 9.

While the specific thrust of this research is aimed at bridge structures with an emphasis on slab-on-girder systems it should be noted that the approach is general enough to allow appropriate extension to other systems, including in buildings.

2 OVERVIEW OF THE STATE OF THE ART IN SYSTEMS LEVEL STRENGTHENING WITH FRP COMPOSITES

2.1 Introduction

The rapid deterioration of the bridge infrastructure and the limited funding available for their maintenance has promoted the use of Fiber Reinforced Polymer (FRP) composites as one of a range of optimized repair and strengthening techniques. Some of the benefits associated with the use of these materials in civil infrastructure renewal were discussed in the previous chapter. Considerable research has been carried out at the components level to successfully demonstrate through laboratory tests of externally bonded FRP overlays or strips, the effectiveness of these materials for flexural/shear strengthening of beams and slabs as well as wrapping of columns for seismic retrofitting [2]. However research at the systems level is sparse and thus will be the primary focus of this review, as the basis of the current research. Some examples of component level applications are first summarized next in this chapter.

2.2 Strengthening of RC Components with FRP Composites

2.2.1 Flexural Strengthening of Beams and Slabs

Extensive research and field implementation has been carried out on RC beams and slabs strengthened with externally bonded-FRP reinforcement. This involves bonding the composite laminates to sections of the structural components in tension, with fibers in the composite parallel to the principal stress direction [2]. The early works on the strengthening of RC beams with composite plates externally bonded to the tension

flanges [4] indicated that such strengthening can result in significant enhancements in strength and stiffness of the beam. This increase is due to the resistance of the externally bonded composite laminate to the opening of flexural cracks or the formation of new cracks. Reviews on the topic have been published recently [5, 6, 7, 8] and will thus not be repeated herein. The gain in flexural strength of FRP strengthened beams depends on a number of factors such as the type of FRP used, the fiber volume fraction, the fiber orientation, concrete strength, proper anchorage of the composite reinforcement [9, 10] and mode of failure. Models [11, 12] and design guidelines [3] have also been developed to better predict the debonding strain levels at the composite-concrete interface based on the experimental data of FRP strengthened beams.

The promising applications of externally bonded composites for flexural strengthening of RC beams led to the extension of this application towards the strengthening of RC slabs. A large number of the medium and short span bridges in North America are constructed with slab-on-girder decks in which the reinforced concrete deck slabs are supported by several steel or concrete girders [13]. Since the distance between the girders is typically less than the span of the bridge, the slabs are subjected to one-way load transfer mechanisms in which the load on the deck slabs is transferred directly in the transverse direction to the supporting girders resulting in a positive bending moment between the beams and negative bending moment over the beams. Research on the flexural strengthening of one-way slabs with externally bonded FRP in the positive moment regions have been carried out at the component level on representative deck slabs [14, 15, 16, 17]. For flexural strengthening of the slabs in the negative moment regions, use of near surface mounted reinforcement in the form of

CFRP bars installed into grooves cut into the concrete surface have been reported [14]. Slabs with low or medium reinforcement ratios are usually found to fail in flexure rather than in punching shear [18]. Failure modes for slabs with reinforcement ratios of 1% or higher are usually found to be governed by a punching shear type mode of failure [19]. Thus design of the FRP composite needs to take this into account to realize the full effectiveness of the strengthening scheme.

2.2.2 Shear Strengthening of Beams

The use of externally bonded FRP at locations of high shear stresses has been demonstrated to contribute to increasing the shear capacity of RC beam components. Results of research on the shear strengthening of beams with FRP have been reported in [20, 21, 22, 23]. The strength gain depends on the type of FRP used, fiber volume fraction, the fiber orientation, FRP reinforcement ratio and use of mechanical anchors to prevent premature debonding of the composite [24, 25]. A detailed review of research on the shear strengthening of RC beams with externally bonded FRP composites can be found in [26] and hence is not repeated here.

2.3 Effect of Strengthening of RC Bridge Components at Systems Level

Most research on FRP composite strengthening conducted to date has been directed at the component level. Thus the focus of study has been the local response of components in terms of crack patterns, failure mechanisms and enhancement in strength and ductility. All these test results give a good understanding of the component response and help in building the confidence level in the user/owner community to accept the use

of this new construction material. However, in a bridge system the strengthening of only a single component can cause significant stress re-distribution and can result in changes in overall structural performance. There is also a concern that a change to a component can result in unintended consequences to adjoining components. In addition, the failure mechanisms and structural response of a component at the systems level might be different than that if it was to be treated on its own since it will be affected by the global load distribution rather than by local load application. This necessitates further study of the effectiveness of FRP strengthening and progression of damage at the systems level through large scale systems tests and focused demonstration studies through actual in-field application and monitoring of the rehabilitated systems.

2.3.1 Relevant Systems Level Tests Demonstrating Effect of Stress Re-Distribution and Damage Progression on Overall Structural Behavior

The interaction between the different structural components of a slab-on-girder bridge towards the overall structural performance at the systems level has been reported by researchers based on systems tests. It has been recognized that in a slab-on-girder system, both the slabs and girders are equally susceptible to damage under traffic load and these damages are interlinked. The damage in a girder will increase the residual deformations which in turn can cause damage in the slabs, particularly if there are large deformation differentials between the adjacent girders [27]. In general the actual load demands on the deck slabs depend not only on the magnitude of the wheel load and the girder spacing but also on the stiffness of the girders and the span length of the bridge

[13]. Also in the slab-on-girder system the failure mechanism will be greatly influenced by the relative strengths of the slab and beam components.

Oh et al. [28] evaluated the ultimate load behavior of an existing prestressed concrete slab-I-girder bridge through an in-place failure test. The load was applied to the actual bridge at the site using hydraulic jacks and the load pattern simulated a single truck. The first occurrence of flexural cracking occurred at the bottom of the girders in the mid-span region at a load of 313 kN and thereafter the girders experienced gradual stiffness degradation due to crack development. With further loading, at 1176 kN, major shear cracks were observed to develop at quarter point regions of the girders. At a load of 1960 kN, cracks were found to develop at the interface between the slab and the median strip which was cast monolithically with the slab at construction. At 2350 kN, the concrete median strip on the deck slab was detached and this resulted in redistribution of stresses due to reduction of stiffness of the slab component. This was followed by the compressive crushing failure of the slab in the loaded area at 4312 kN. The test results indicated that progression of damage can occur between the components of the bridge system depending on the relative strength/stiffness of the components.

The behavior of multi-span slab bridges before, during and after repair was investigated by Shahrooz et al. [29] through study of the level of moment distribution during the various stages of repair. The study was carried out on in-service bridges in the field with varying amounts of deterioration over the pier lines in the form of spalling of concrete and loss of top steel in the negative moment regions of the deck slabs resulting in loss of continuity between the adjacent spans and thus increasing the positive moment demand and overstressing the slab bottom reinforcement. The repair method used

involved removal and replacement of the damaged concrete and top steel. However this repair method was seen to often result in further overstressing of the bottom steel and thus the purpose of the study was to monitor the response of the bridge both during and after repair through truckload tests. The removal of the concrete and damaged steel in the negative moment area during the repair was found to cause redistribution of moment resulting in an increase of the positive moment resisted by the slabs by about 38%. The repair method was found to enhance the participation of the top reinforcement, thereby increasing their contribution towards resisting applied negative moments by 36% as compared to before repair. However in the positive moment regions there was a permanent redistribution of live load moment and the bottom reinforcement resisted 22% more moment as compared to that before repair. The test results indicated that although the repair methodology was able to improve the stiffness and participation of the negative reinforcement it resulted in a moment redistribution increasing the moment demand on the positive reinforcement. It was suggested that shoring of the deck slabs should have been carried out during the repair to prevent such moment redistribution.

Issa et al. [30] studied the behavior of full-depth precast concrete panels for bridge rehabilitation. In this rehabilitation method, the damaged deck slabs are replaced by precast concrete panels that can be installed on the existing concrete or steel girders and connected by steel studs through shear pockets for composite action. The deck panels are then post-tensioned in the longitudinal (traffic) direction of the bridge to provide continuity and secure tightness of the joints between the adjacent precast elements. The test system represented a single lane scaled down model of a two-span continuous prototype bridge with two lines of supporting beams. Three such models were tested, the

first being constructed without any post-tensioning in the deck system, the second being post-tensioned with a prestress level of 1.43 MPa (208 psi) in the deck system and the third had a larger prestress level of 2.62 MPa (380 psi). The presence of the pre-stressing in the second and third models were effective in delaying the initiation of cracks in the concrete deck panels as compared to the first model and increased the load capacity from 390 kN to 480 kN. The cracks in the deck panels of the first two models were found to initiate at the vicinity of the central supports and with an increase in loading gradually developed away from the supports with ultimate failure in the deck systems. However for the third specimen with the higher level of prestressing force, the initiation of cracking and damage in the deck slabs was delayed and ultimate failure at the systems level was shifted from the slabs onto the supporting steel girder with the development of a crack in the web of the girder between the top and bottom flanges. Thus even though at the component level, the deck slabs of the third specimen had higher resistance imparted by the higher level of prestressing, at the systems level no strength enhancement was achieved as compared to the second specimen since the damage progression and subsequent failure at the girder prevented the slab component from reaching full capacity.

It has also long been recognized in seismic design that by increasing the strength and ductility of critical components in a system their brittle and catastrophic failure can be prevented and the occurrence of more desirable failure mechanisms can be promoted in other components of the system [31]. Considerable research has been carried out in this regard on beam-column connections of RC building frame structures. However results from these tests can also be extended to bridge systems with the beam-column joints in buildings being analogous to pier column-cap beam joints in bridges. These

results also help to give an understanding of the progression of damage between components of a system caused by the sequential strengthening of the components. Most such existing building frame structures with non-seismic detailing are found to be dominated by weak column-strong beam behavior [32]. In such a structural system, the moment capacity of the beams strengthened by the participation of the slabs places high moment demands on the columns. Due to inadequate ductility of such existing columns, premature structural failure can result under lateral loads. Thus a retrofit strategy for such a structural system involves strengthening and adding ductility to the columns through the use of steel or composite jackets in the potential plastic hinge regions. However such a local strengthening of the structural system by enhancing the strength and ductility of the columns will move the failure to occur in the beam-column joint. In the presence of proper detailing of the joints, moving the failure from the column to the joint can improve the global system behavior [33]. However in the absence of proper detailing, shear failure in the joint can be brittle and catastrophic and thus subsequently requires the joint to be strengthened. Combined use of FRP laminates and near surface mounted FRP bars have been proposed to be used in the joint region to enhance its strength and ductility [34] and thus moving the failure from the beam-column joint to the beam. Thus the driving criterion behind such sequential strengthening of components is the hierarchy of strength such that by strength enhancement of those members whose failure is not desirable, it is possible to attain a ductile global performance of the system.

The above methodology of hierarchy of strength governing the seismic design of building frames has also been extended to bridge systems. However the one significant difference between the seismic retrofit of building frames and bridge systems is that for

the bridge systems, the desired failure mode is through formation of plastic hinges at the top of lower columns in an area that can be well confined for ductile response and can be inspected and repaired following a major earthquake [35]. In existing bridge systems designed before the development of stringent seismic design standards, the column-cap beam joints are usually found to have insufficient shear detailing. Thus retrofits of the joints are often suggested in the form of fiber reinforced concrete jacketing [36], casting of post-tensioned reinforced concrete bolsters in the joint regions [37], removal of existing columns and beam column joints and replacing them with well-confined circular columns and properly detailed joint region and post-tensioning of the cap beam [35]. Such retrofit strategies transfer the brittle failure at the joints to the columns of the bridge systems and these columns can then be retrofitted with steel, concrete or composite jackets to result in a ductile mode of failure in the well confined plastic hinge regions of the columns [31].

Based on the above discussion it is evident that once a component of the system is strengthened or retrofitted the failure will move or “progress” along this hierarchy to the next weak component until ultimate failure in one of the components is achieved. A similar analogy can be applied to FRP composite strengthening of slab-on-girder system subjected to traffic loading. Based on the relative strength of the slab and girder, the initial failure will occur in the weakest component. However it is necessary to recognize that if only that component of the bridge superstructure-system (e.g. the deck slabs or the supporting girders or other structural components such as diaphragms or slab-girder joints) is strengthened with FRP without understanding and considering the limiting capacity of the adjoining un-strengthened components, then there will be a possibility of

damage progression following the “hierarchy of strength” approach to the next weak link of the system that will prevent the strengthened component from reaching its ultimate design capacity. The strengthening of a component with FRP composite also has the potential to result in changes in load-distribution and failure mechanism at the systems level as was discussed earlier since it can be treated as a structural modification. All the above emphasizes the need for an assessment of effectiveness of FRP composite strengthening of slab-girder components at the systems level to evaluate the progression of damage and change in load distribution produced by such strengthening and finally to determine the ultimate global load capacity of the system.

2.3.2 Existing Systems Level Research in FRP Composite Strengthening of Bridge Components

Of particular interest to the current research is the slab-on-girder segment of bridge superstructure which is most prone to degradation under traffic loading and environmental exposure and is also rendered strength deficient under increasing demands of truck loads and design standard requirements. Thus the deck slabs or the longitudinal supporting girders of typical existing RC bridges are often found to be in need of strength enhancement. The general trend in the field strengthening projects with externally bonded FRP composites is to strengthen only that component of the structure that shows the more imminent signs of damage and deterioration through visual inspections or non-destructive evaluation (NDE) tests.

Some of the field applications, at the systems level, of externally bonded FRP composite in strengthening of bridge girders have been reported in [38, 39, 40, 41 and

42]. Miller et al. [38] reported the application of CFRP plates for the flexural strengthening of a steel girder of a slab-on-girder bridge on I-704 in Delaware. One layer of CFRP plate was bonded to the tension flange of a steel girder. To demonstrate the effect of the retrofit on the global flexural stiffness, load tests were performed before and after application of the CFRP plate. The test measured strains in the girder as a three-axle truck was driven over the slab-on-girder bridge before and after the girder strengthening. Comparison of the load test data indicated that the addition of the CFRP plates resulted in an 11.6% increase in the global flexural stiffness of the slab-girder system.

Cardinale and Orlando [39] described the rehabilitation of a deficient RC bridge in Italy through application of a concrete overlay on the deck slabs, external prestressing with tendons for flexural strengthening of longitudinal girders and installation of woven CFRP composite fabric for shear strengthening of the girders. The bridge was load tested before and after the rehabilitation. Based on measurements of deflections, the static tests indicated that the stiffness of the strengthened bridge was increased by about 20% after the rehabilitation work. Vibration tests were also carried out to dynamically obtain measurement of the global stiffness. The first natural eigenfrequency was found to increase from 2.46 Hz to 2.7 Hz and based on FE modal analysis this also corresponded to about 20% increase in the global stiffness.

Hag-Elsafi et al. [40] conducted in-service evaluation of a FRP strengthening system in a RC T-beam bridge in New York. CFRP laminate systems were used to improve the flexural and shear capacities of the bridge system and restrain freeze-thaw cracking through strengthening of the girders with U-jackets and strengthening of the bottom soffit of the slabs between the girders with laminates in the transverse direction.

The bridge was instrumented and load tested before and after installation of the FRP laminates as well as after a period of 2 years after the rehabilitation to evaluate effectiveness of the strengthening systems. For a truckload of 196 kN, the strains in the girder rebars below the load area were reduced by about 5%. Also the live load distribution factors of the girders were found to improve by about 12% after installation of the composite systems indicating better load distribution between the slabs and the girders. It was commented that the benefits of the laminate systems used in the project were not fully realized because of the relatively small service loading range from the truckload application. Also the strain measurements obtained after the composite system was in service for two years showed no changes from those obtained after the rehabilitation, indicating that the composite systems did not undergo any degradation during the studied period of in-field service.

Hutchinson [41] reported shear strengthening of I-shaped prestressed concrete girders with CFRP sheets for the Maryland Bridge in Winnipeg, Manitoba and John Hart Bridge in British Columbia. A single CFRP layer was applied over a 4 m length near the ends of each girder of the John Hart Bridge. The shear capacity of the beams was reported to be increased by 15-20%. However no results were presented on the effect of the strengthening on the overall stiffness of the slab-girder system.

An evaluation of the field performance of FRP bridge repairs was also reported by Stallings et al. [42]. The seven span bridge studied under the investigation was located in Alabama and the girders exhibited a well developed system of flexural cracks with minor spalling. These cracks extended from the bottom of the girders up to the underside of the deck slabs. One span of the bridge was repaired through installation of CFRP plates on

the bottom surface of the girders with the objective of mitigating the deterioration of the bridge resulting from the flexural cracks in the girders as well as to increase the load capacity of the bridge. Static load tests were performed before and after the repair using trucks with a gross weight of 346 kN and deflection and strain measurements were recorded. The application of the FRP systems was found to reduce the rebar stresses in the girders by an average of 8% and the maximum girder deflection by an average of 7%. Based on these measurements, the effective girder moment of inertia was calculated to have increased by 5% after the FRP repair.

Field applications of externally bonded FRP composite in strengthening of deck slabs in slab-on-girder bridges, though fewer than the applications on girders, have been reported by [27, 43, 44]. Schuman et al. [43] reported the strengthening of the deck slabs of a cast-in-place concrete T-girder bridge in California. The deck slabs were found to be susceptible to punching shear type failure due to the formation of evenly spaced longitudinal and transverse cracks at the slab soffit. The strengthening was designed based on the calculated internal steel reinforcement deficiency in the deck slabs. Two rehabilitation systems, namely CFRP fabric laminates and pultruded strips were bonded to the bottom soffit of the deck slabs in 5 spans of the bridge for comparative evaluation of the two systems. Forced vibration tests were performed on the bridge immediately before and after the completion of the rehabilitation of the deck slabs. The structural stiffness was computed through model updating based on the measured eigenvalues. The addition of the composite systems was found to result in stiffness enhancement of the bridge system, with the increase being a function of the amount of degradation in the

slabs. A maximum stiffness increase in the range of 32% was recorded in a slab span with the highest level of degradation.

Similar application of composite materials for strengthening deck slabs was reported by Lee et al [44]. The application was in the deck slabs of a RC T-girder bridge in which extensive longitudinal and transverse cracks in the deck slabs indicated potential for punching shear failures. Several bays of the bridge were strengthened with carbon fabric laminates and pultruded strips. The strengthening of the deck slabs resulted in stiffness enhancements with the greatest increase recorded being 29%. All the estimates of stiffness enhancements were based on global measurements through dynamic modal tests and thus reflected the effect of strengthening of the deck slabs on the slab-girder system as a whole.

Oh et al. [27] reported the assessment of bridge deck panels with the deck slabs strengthened with CFRP sheets. The deck slabs were found to be deficient in biaxial flexure with cracks developing in the longitudinal and transverse direction. Prototype deck panels supported on two edge girders simulating the actual bridge decks were constructed and tested. Two strengthening variables were studied in the research, namely the strengthening ratio and direction of the composite laminates. The strengthening of the deck panels by FRP was found to restrain the opening of the cracks and resulted in enhancement of flexural strength and stiffness. The deck panels strengthened in both the longitudinal and transverse directions had the best overall performance and displayed ductile failure modes in biaxial bending with the formation of numerous small cracks. A maximum flexural strength enhancement of 37% was recorded for these deck panels.

However no information was provided on the effect of the strengthening on the overall structural stiffness or performance.

2.4 Conclusions

Based on the review of existing research on applications of composite strengthening at the systems level it was found that no comprehensive study has been carried out on the effect of such strengthening of components on other components of the system. Even though the applications were at the systems level, the focus of study was essentially the performance of the component that showed the most degradation and damage in the system. No observations were made in any of the reported research on whether such strengthening of a component caused the other components to prematurely reach critical limit states under the higher load demands. The primary drawback seems to be that once the effectiveness of the externally bonded FRP composites in enhancing the flexural or shear strength/stiffness of the slab or girder components was established through laboratory testing and research, the applications were extended directly to the field without exhaustive laboratory research and testing on the performance of such strengthening at the systems level. Even though valuable data on the effectiveness of FRP composite strengthening of slab or girder components at the systems level were obtained through the field applications as described previously [38 - 44], such assessment of global performance was limited to computations of global stiffness and changes produced by the application of composites. The true load capacity can not be obtained realistically from such condition assessments in service because the safety assessment and load tests in such field applications were conducted under service load so as not to produce any

substantial damage to the structure. Thus it was not possible to conclude conclusively based on the existing research on whether such strengthening of individual components had the potential to cause unintended consequences on the un-strengthened components of the system through changes in load distribution or under the higher load demands imposed by the strengthened components.

A review of existing research and the state of the art on strengthening of slab-on-girder bridge components with FRP composites emphasizes the need for a large scale systems level test of slab-on-girder segment through which the effects of progression of damage and changes in the load distribution/failure mechanism in the components on the overall system performance could be studied under application of field-representative loading conditions and with sequential strengthening of individual components.

3 COMPONENT LEVEL STUDY OF FIELD SPECIMENS

3.1 Introduction

The efficacy of externally bonded composites in strength enhancement of reinforced concrete components has been well established through previous research, as was discussed in the literature review. This included evaluation of strengthening of RC slabs [15, 45] as well as shear strengthening of longitudinal girders [26, 20] with externally bonded FRP composites. However there are still unanswered questions related to time and traffic load related response specially when combined with changes in environmental conditions, including exposure to high levels of temperature and humidity. Thus there is a need to assess the response of FRP rehabilitated specimens after long-term deterioration and damage representative of field conditions. The use of analytical models to predict the behavior and ultimate capacity of such specimens also needs to be validated. In order to have a realistic prediction of the in-service response/capacity of such bridge decks that would be representative of the in-field damage/deterioration over time, it is necessary to first identify the “effective” material properties of the structure to be incorporated in the appropriate parameters of the analytical model. A system identification technique had been used by Stubbs et. al. [46] to identify “effective” properties based on time data obtained from dynamic modals tests on the actual structure. In addition, to increase the confidence level for widespread use of these new construction materials in field conditions, it is necessary to identify material and installation process level defects and the determination of their criticality over the service life of these materials. While some defects can be readily identified by visual means others are not as

easily identified, and there is a critical need for the development of methods of non-destructive testing (NDT) that can be used effectively in the field as a means of inspection. A review of methods of NDT and their comparison in terms of potential effectiveness of use as related to FRP rehabilitated concrete was presented by Kaiser et. al. [47, 48]. Of the methods considered, infrared thermography was identified as being a useful tool for the detection of debonding and cracking and its use had been investigated earlier [49, 50, 51]. However these studies were carried out more at the materials level for characterization of defects in composites rather than evaluating the technique for monitoring damage progression in composite strengthened reinforced-concrete structures.

3.2 Research Objectives

The objectives of the component level study of field specimens were to evaluate the behavior of bridge deck slabs, with field-representative damage and deterioration, prior to and after being strengthened with externally bonded FRP composite laminates and strips. Tests were conducted on slab sections cut from a bridge, both with externally bonded FRP, and without strengthening, after being in service for a period of time, thereby enabling assessment of effectiveness. This was possible since the bridge was rehabilitated previously with externally bonded FRP [52] in order to both strengthen deficient regions and to provide service-life extension till a new structure could be planned. The primary objective of this test program was to evaluate the behavior and failure capacity of the RC deck slabs, both with externally bonded FRP composite and without strengthening, representative of bridge deck components subjected to realistic deterioration and damage over time to evaluate long-term performance of FRP composite

strengthening. Dynamic modal tests were carried out to match the analytical model parameters to the behavior of the test specimens. Cyclic load tests were used to identify the response and failure capacity of the specimens and non-destructive thermography inspections were performed at regular intervals to monitor the progression of damage in the composite rehabilitated specimens. Available analytical models were used to predict the ultimate capacity of the test specimens and were compared with the test results. A local to global modeling technique was also used to predict the ultimate capacity of the actual bridge deck slabs from that of the test components. Thus the research provided data related to both destructive, non-destructive, post-use and analytical response evaluation of field specimens after service.

3.3 Description of Test Specimens

The test specimens were cut-out from deck slab segments of the Watson Wash bridge. This was a reinforced concrete T-girder bridge, built in 1970, consisting of 18 spans each of 12.8 m (42 feet) length and having 5 bays with the main longitudinal girders at 2.13 m (7 feet) spacing. Over time the bridge had shown significant distress in the form of transverse and longitudinal cracking of the decks, efflorescence in cracks, presence of alkali silica reaction (ASR), and local punching shear failure. Also the bridge had been designed in accordance with the 1969 California Department of Transportation (Caltrans) Bridge Design Specification (BDS) [53] and hence the reinforcement was inadequate to meet some current load requirements related to punching loads. Punching shear failure had occurred previously in a bay and although it was repaired through conventional methods of patching and filling, distress in other bays indicated the

potential for further occurrences. In order to strengthen the decks to meet current requirements and to avoid further occurrence of punching shear, selected bays were rehabilitated with externally bonded FRP [54]. The rehabilitation was also conducted to extend the service life of the structure to the point when planned demolition and replacement of the bridge could take place [55]. Both prefabricated carbon pultruded strips, which were adhesively bonded to the concrete substrate, and unidirectional carbon fabric laminates impregnated using wet layup were used as external rehabilitation schemes as shown in Figure 3.1.

Just prior to demolition of the bridge three test specimens of the bridge deck, each of size 3.05 m (10') in length x 1.37 m (4.5') in width and of 156 mm (6¼") full slab thickness were cut from the bridge and removed. The sizes were determined both by logistics of removal and the desire to have sections of the slab independent of girder reinforcement. Each was cut from a midspan region, with the first being an unrehabilitated section (from an area that did not show significant deterioration), the second being from a section rehabilitated for permit truck loading, i.e. 1.5 times the current design load, using the wet layup process and the third being from a section rehabilitated to resist punching shear, i.e. to control opening of the preexisting crack widths under current design load, through adhesive bonding of pultruded strips. Details of initial slab capacity and of strengthening were presented by Lee et. al. [56]. Figures 3.2(a) and (b) show schematically the locations of the FRP on the two test sections cut from rehabilitated slabs of the bridge.



a) Prefabricated pultruded strips

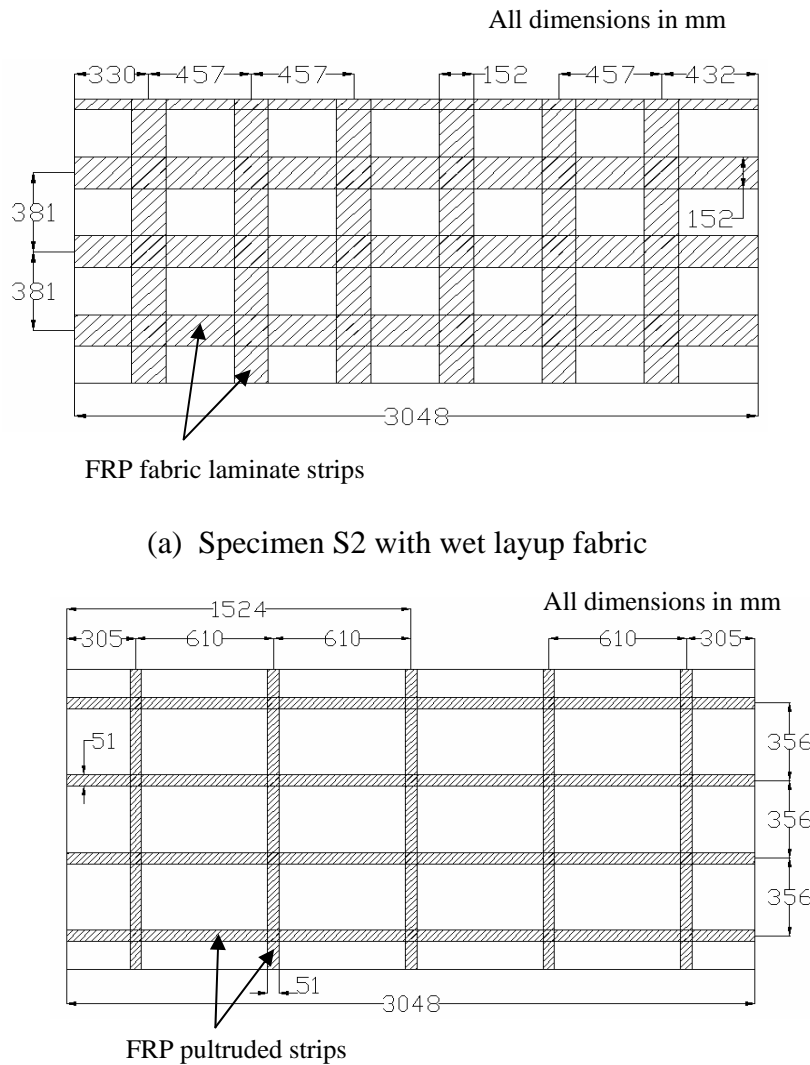
b) Site-impregnated fabric laminates

Figure 3.1 Onsite rehabilitation of bridge deck slabs

Specimen S1 was an unstrengthened control component of the bridge deck cut-off from mid-span section of the bridge. The specimens consisted of #5 rebars (15.9 mm or 0.625 inch diameter) spaced at approximately 140 mm (5.5 inches) center-to-center in the transverse direction and #5 rebars (15.9 mm or 0.625 inch diameter) spaced at 244 mm (9.6 inches) center-to-center in the longitudinal direction. The specimen had longitudinal and transverse cracks which had made the deck slab deficient in punching shear.

Specimen S2 was a component of the bridge deck strengthened with unidirectional carbon fiber impregnated on site with epoxy resin using the wet layup process. The 2 layer thick laminate strips were spaced at 457 mm (18") center-to-center in transverse direction and single layer laminates were spaced at 380 mm (15") centers in the longitudinal direction. All laminate strips were 150 mm (6") wide. Specimen S3 was cut out from the segment of the bridge deck strengthened with pultruded carbon/epoxy composite strips spaced at 610 mm (24") centers in the transverse direction and at 356 mm (14") center-to-center in the longitudinal direction. All the pultruded strips were 50

mm (2") wide and consisted of only a single layer in both the longitudinal and the transverse directions. The external composite reinforcement ratio was 1.33 times higher in S2 since it was designed to carry permit truck load while specimen S3 was cut out from an area of the bridge deck where the rehabilitation scheme was designed only to prevent local punching shear failures through control of the crack width opening.



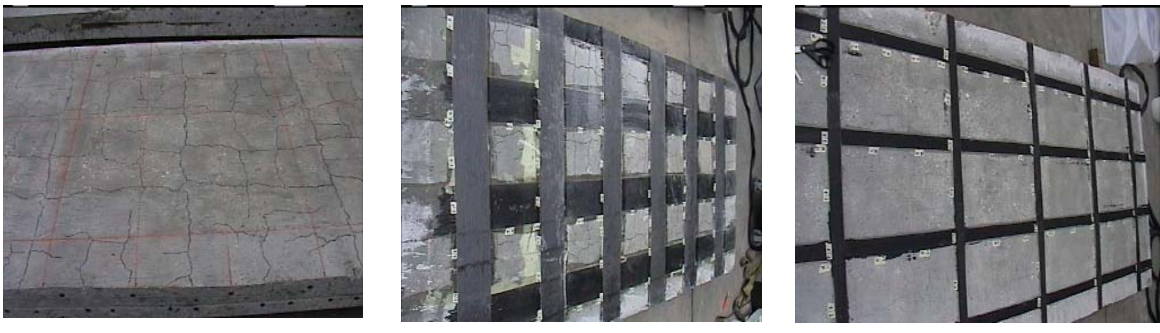
(b) Specimen S3 with adhesively bonded prefabricated strips

Figure 3.2 Location of FRP strengthening on test slabs

All the test specimens had a considerable number of existing cracks in both the transverse and longitudinal directions resulting from over 30 years of traffic loading as well as from the effects of severe environmental exposure. The transverse cracks were noted to be usually spaced at 140 mm (5.5”) and correspond to the spacing of the internal transverse steel reinforcement. Secondary cracks were also observed in both the transverse and the longitudinal directions in between the main cracks. The test specimens as obtained from the Watson Wash Bridge are presented in Figure 3.3.

3.4 Material Properties and Capacity Prediction

The boundary and loading conditions used for the component test specimens were designed to simulate one-way load transfer mechanism of the actual bridge decks where the load on the decks was transferred primarily to the longitudinal girders. In order to determine the proper boundary conditions for the test specimens, a detailed finite element model of the actual bridge was constructed and analyzed. The analysis was carried out under the application of a concentrated wheel load representative of the actual HS20 wheel load configuration acting on the bridge deck [53]. The finite element model used for the analysis of one of the frames (consisting of 4 spans between hinge points) of the actual bridge deck is presented in Figure 3.4 (a).

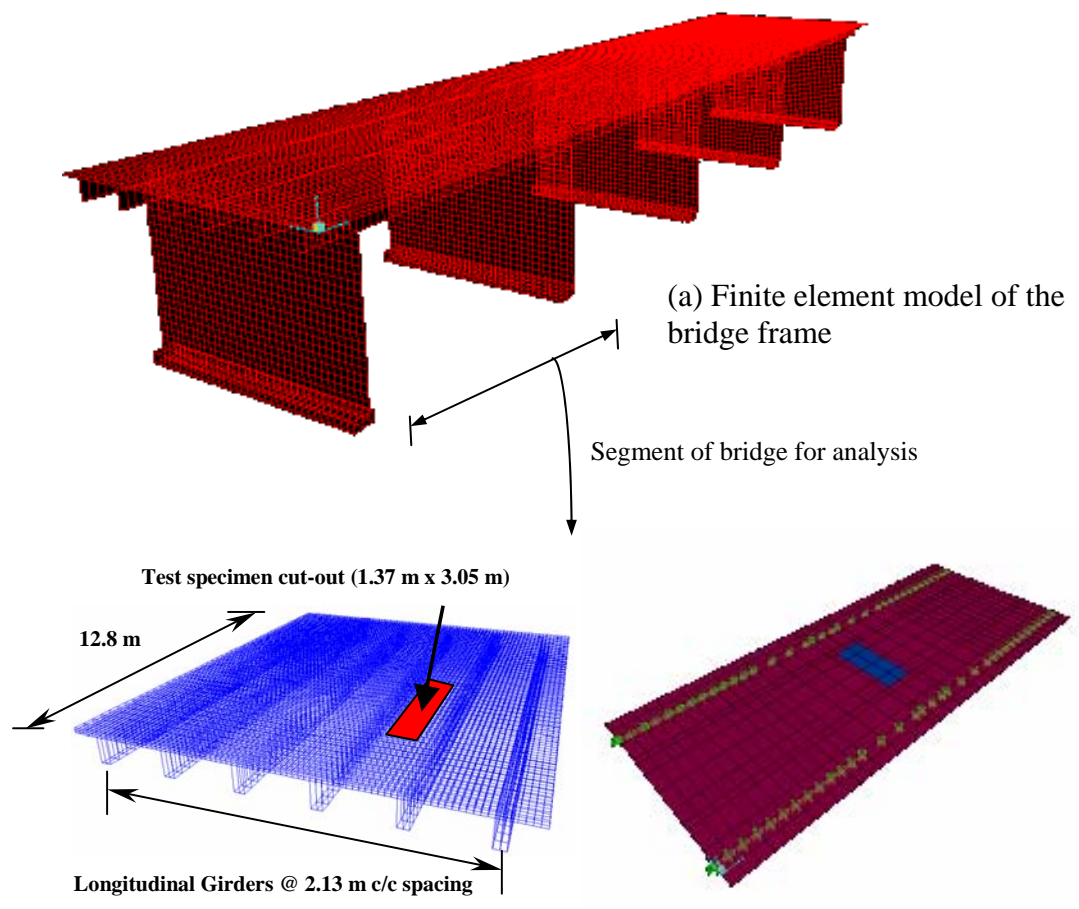


a) Specimen S1

b) Specimen S2

c) Specimen S3

Figure 3.3 Test specimens



(a) Finite element model of the bridge frame

Segment of bridge for analysis

Test specimen cut-out (1.37 m x 3.05 m)

12.8 m

Longitudinal Girders @ 2.13 m c/c spacing

(b) Location of test component in the bridge

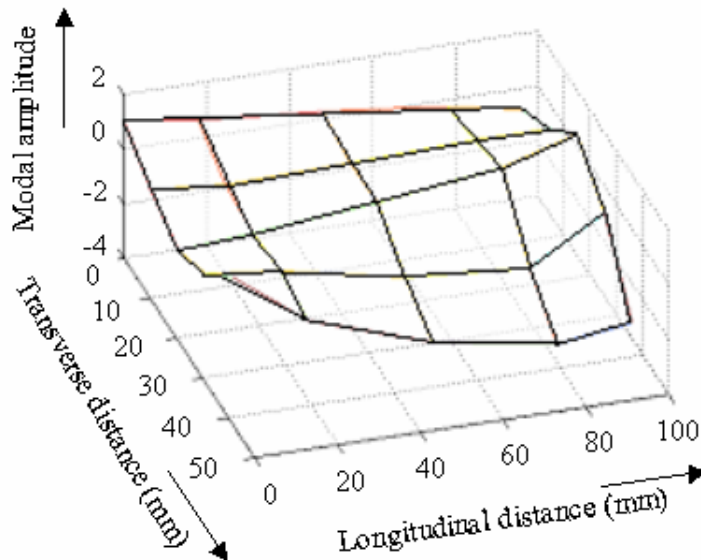
(c) Finite element model of test component

Figure 3.4 FE Modeling of the test components

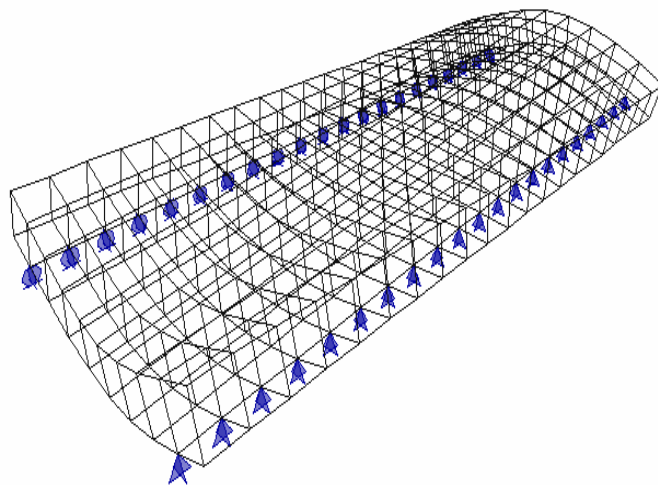
Shell elements were used to model the deck slabs, longitudinal and transverse girders and the abutments. 3-D solid elements were used to model the footing while the footing restraints were modeled using spring elements. The location of the test component when it was cut-out from the bridge deck slab is shown in Figure 3.4 (b). Global-local modeling was then conducted, with the FE model of the test component as shown in Figure 3.4 (c), to develop the necessary test boundary conditions for the specimens such that they mimicked the stress conditions at global level. Under the selected test conditions (described in the next section) contours of the transverse membrane forces from the finite element models of the full bridge deck and the component test specimens were found to match closely indicating that the test specimens would have a behavior similar to the corresponding portion of the actual bridge deck.

The edges of the test specimens were simply supported on steel rollers in the longitudinal direction to simulate the one-way load transfer mechanism. However it was not possible to simulate the vertical deflections along the longitudinal supports representative of girder deflection in the actual bridge. Also because of size limitation, the transverse span-length of the test specimens was smaller than that of the bridge deck. The combination of these two factors resulted in higher stiffness of the test specimens and this had to be taken into account while predicting their true capacities. In order to identify the effective baseline material stiffness to be incorporated into the finite element model for capacity prediction, forced vibration based dynamic modal tests were performed on the test specimens. The time data collected from the tests was used to determine the frequencies and mode shapes. From the power spectral response, the predominant natural frequency of the control specimen (S1) was identified to be 205 Hz

and from the mode shape this frequency was found to correspond to the second longitudinal bending mode. A finite element model of the test specimen was developed with 4-noded solid elements to define a baseline model, with the mass density and Poisson's ratio of reinforced concrete assumed to be 2400 kg/m^3 (150 lb/ft^3) and 0.15, respectively. Since the bridge was constructed in the 1970s, no information on the concrete material property of the deck slabs was available. Thus in order to identify the concrete property in terms of its elastic modulus, an iterative process with different elastic modulus (E) of concrete was used until the frequency corresponding to the second longitudinal bending mode from the model matched 205 Hz and the resulting "effective" modulus was found to be 28.6 GPa (4150 ksi). A comparison of the mode shapes, corresponding to natural frequency of 205 Hz, obtained from the experimental vibration tests and analytical model is presented in Figure 3.5. The term "effective" modulus will be used herein to refer to the modulus value assigned to the model for true prediction of specimen capacity. From the vibration tests of the slab components only one modal frequency could be identified to the desired level of accuracy (because of high stiffness of the test specimen) and thus only the specimen modulus was adjusted in the model.



(a) Experimental mode shape ($f = 205$ Hz)



(b) Analytical mode shape ($f = 205$ Hz) from FEM

Figure 3.5 Comparison of experimental and analytical mode shapes

The results were compared to the “effective” modulus identified from modal tests and system identification performed on the actual bridge decks, both prior to and after rehabilitation [52]. The unrehabilitated bridge decks had an effective modulus of 17.8 GPa (2582 ksi) and the rehabilitation of the decks with site-impregnated carbon fabric laminates and adhesively bonded prefabricated pultruded strips resulted in enhancements

in the effective stiffness by 20% and 13.9%, respectively [52]. Thus the test specimens had a higher effective stiffness, as obtained by the product of the effective modulus and the moment of inertia of the cross-section, which would result in a higher capacity as compared to the actual bridge decks, and this has to be considered while correlating the capacities of the test specimens to the actual field capacities. Corresponding to the “effective” modulus, the “effective” concrete strength to be used for capacity prediction was computed to be 36.56 MPa (5300 psi). It is to be noted that the effective concrete compressive strength might not be the true concrete strength and has been used as a parametric value to be incorporated into the capacity prediction models to take into account the model stiffness and boundary conditions.

The steel reinforcement had yield strength, f_Y , of 414 MPa (60 ksi) and a tensile modulus, E_S , of 200 GPa (29000 ksi). The unidirectional two-layer carbon fabric was used in widths of 152 mm (6 in.), running in the transverse direction of the specimen, with a cured composite thickness of 1.88 mm (0.0739 in.) having a composite modulus and strength in the fiber direction of 78.96 GPa (11452 ksi) and 1.1 GPa (160 ksi), respectively. The unidirectional one-layer carbon fabric was also used in widths of 152 mm (6”), running in the longitudinal direction of the specimen, with a cured composite thickness of 1.1 mm (0.0434 in.) having a composite modulus and strength in the fiber direction of 76.27 GPa (11062 ksi) and 1.13 GPa (164 ksi), respectively. The prefabricated carbon/epoxy strips were 51 mm (2 in.) wide and 1.3 mm (0.05”) thick with tensile modulus and strength in the fiber direction of 173.9 GPa (25222 ksi) and 2.51 GPa (364 ksi), respectively. The material properties of the composite strips and laminates

were obtained from tensile tests of the composite samples used for strengthening the bridge decks [52].

The general punching shear capacity of the slab, V_n , was determined from the equilibrium of forces as:

$$V_n = 2 \left(b_1 + b_2 + \frac{2d}{\tan \theta} \right) \frac{d}{\tan \theta} f_t \quad \dots\dots\dots(3.1)$$

where, f_t = diagonal concrete tensile strength = $\left(0.17 + \frac{0.33}{\beta_c} \right) \sqrt{f'_c} \leq 0.33 \sqrt{f'_c}$ (in MPa)

and f'_c is the compressive strength of concrete (36.56 MPa in this case), b_1 is the short side of the concentrated load area (203 mm or 8" in this case), b_2 is the long side of the concentrated load area (508 mm or 20" in this case), d is the average effective depth of the section (122 mm or 4.8125" in this case) and θ is the angle between the horizontal and assumed failure plane. The theoretical formulation for punching shear (equation 3.1) is equivalent to the AASHTO [57] prescribed equation for an angle of the failure plane, θ , being 45° . However experimental results such as those reported by Graddy et al. [58] suggested a value of 38° as being more representative.

The punching shear capacities corresponding to θ values of 45° and 38° , respectively, were determined as:

$$\text{For } \theta = 45^\circ, V_n = 2(203 + 508 + 2 \times 122) \times 122 \times \left(0.17 + \frac{0.33}{508/203} \right) \sqrt{36.56} = 425 \text{ kN}$$

$$\text{For } \theta = 38^\circ, V_n = 2 \left(203 + 508 + \frac{2 \times 122}{\tan 38} \right) \times \frac{122}{\tan 38} \times \left(0.17 + \frac{0.33}{508/203} \right) \sqrt{36.56} = 583 \text{ kN}$$

The punching shear capacity of the test specimen was thus predicted to be between 425 kN (96 kips) and 583 kN (131 kips). As is evident from these formulations, the actual punching shear capacity will be governed by the angle of shear failure plane, which can be influenced by locations of the preexisting cracks. Moreover the punching shear capacity would depend on the properties of concrete in the local region of the applied concentrated wheel load as well as the amount of aggregate interlock available.

The flexural capacities of the test specimens were then computed using design oriented sectional capacity analysis using the “effective” modulus of reinforced concrete to be 28.6 GPa (4150 ksi). The flexural capacity at steel yield for the unrehabilitated control specimen, corresponding to bottom steel strain of 0.002, was computed to be 63.61 kN-m/m (14.3 kip-ft/ft). From the finite element model this capacity was found to correspond to a concentrated load demand of 512 kN (115 kips).

For the two test specimens strengthened with FRP composite strips and laminates, it was expected that the strengthening scheme would change the mode of failure from punching shear to flexural failure, culminating in the debonding of the laminates or strips at failure of the specimens. This was based on the assumption that the strengthening of the specimens with the composite strips or laminates would limit the opening of the cracks and ensure sufficient aggregate interlock so that punching shear failure mode would be avoided. It is to be noted that the debonding strain and not the rupture strain was used as the operative limiting strain in the composite and this was estimated using an energy based procedure proposed by Niu and Wu [11], in which the maximum axial force in the composite at debonding is obtained as,

$$P_{\max} = b_2 \sqrt{2G_f E_2 t_2} \dots\dots\dots(3.2)$$

where, E_2 , t_2 and b_2 are the elastic modulus, thickness and width of FRP, respectively. G_f is the interfacial fracture energy given by the area of the $\tau - \delta$ curve obtained from shear peel tests of the composite samples and were computed to be 0.976 N/mm (5.6 lb/in) for the site-impregnated 2-layer carbon composite laminates [59] and 1.2 N/mm (6.85 lb/in) for the 1-layer pultruded carbon composite strips [60].

For the site-impregnated 2-layer carbon composite laminates, with E_2 , t_2 , b_2 and G_f being 78.96 GPa (11452 ksi), 1.88 mm (0.074"), 152.4 mm (6") and 0.976 N/mm (5.6 lb/in), respectively, the maximum axial force in the composite at debonding was obtained using equation 3.2 as,

$$P_{\max} = b_2 \sqrt{2G_f E_2 t_2} = 152.4 \sqrt{2 \times 0.976 \times 78960 \times 1.88} = 82.04 \text{ kN (18.4 kips)}. \dots\dots(3.3)$$

The corresponding maximum debonding strain in the composite was obtained as,

$$\varepsilon_{\max} = \frac{P_{\max}}{t_2 b_2 E_2} = \frac{82040}{1.88 \times 152.4 \times 78960} = 3626 \text{ micro-strains} \dots\dots\dots(3.4)$$

For the site-impregnated 1-layer carbon composite laminates, with E_2 , t_2 , b_2 and G_f being 76.27 GPa (11062 ksi), 1.1 mm (0.043"), 152.4 mm (6") and 0.976 N/mm (5.6 lb/in), respectively, the maximum axial force in the composite at debonding was obtained as,

$$P_{\max} = b_2 \sqrt{2G_f E_2 t_2} = 152.4 \sqrt{2 \times 0.976 \times 76270 \times 1.1} = 61.67 \text{ kN (13.9 kips)}. \dots\dots\dots(3.5)$$

The corresponding maximum debonding strain in the composite was obtained as,

$$\varepsilon_{\max} = \frac{P_{\max}}{t_2 b_2 E_2} = \frac{81670}{1.1 \times 152.4 \times 76270} = 4823 \text{ micro-strains} \dots\dots\dots(3.6)$$

Similarly, for prefabricated 1-layer pultruded carbon composite strips, with E_2 , t_2 , b_2 and G_f being 173.9 GPa (25222 ksi), 1.3 mm (0.05”), 50.8 mm (2”) and 1.2 N/mm (6.85 lb/in), respectively, the maximum axial force in the composite at debonding was obtained as,

$$P_{\max} = b_2 \sqrt{2G_f E_2 t_2} = 50.8 \sqrt{2 \times 1.2 \times 173900 \times 1.3} = 37.42 \text{ kN (8.4 kips)} \quad \dots\dots\dots(3.7)$$

The corresponding maximum debonding strain in the composite was obtained as,

$$\varepsilon_{\max} = \frac{P_{\max}}{t_2 b_2 E_2} = \frac{37420}{1.3 \times 50.8 \times 173900} = 3260 \text{ micro-strains} \quad \dots\dots\dots(3.8)$$

ACI-440 [3] also gives an estimate of debonding strains in composites and was used to compare with the predicted debonding strains obtained from Niu and Wu’s [11] model. For the site-impregnated 2-layer carbon composite laminates, with ε_u , E_2 , and nt_f being 1.4%, 78.96 MPa and 1.88 mm, respectively, the debonding strain as per ACI-440 [3] was obtained as:

$$\varepsilon_{fu} = \text{design rupture strain} = 0.95 \times 1.4\% = 1.33\%$$

For $E_f nt_f = 78960 \times 1.88 = 148,445 < 180,000$, the bond co-efficient was obtained as:

$$\kappa_m = \frac{1}{60\varepsilon_{fu}} \left(1 - \frac{nE_f t_f}{360,000} \right) = \frac{1}{60 \times 0.0133} \left(1 - \frac{148,445}{360,000} \right) = 0.74 \quad \dots\dots\dots(3.9)$$

and thus, the ultimate debonding strain = $\kappa_m \varepsilon_{fu} = 0.74 \times 0.0133 = 9842$ micro-strains.

For the prefabricated 1-layer pultruded carbon composite strips, with ε_u , E_2 and nt_f being 1.4%, 173.9 MPa and 1.3 mm, respectively, the debonding strain as per ACI-440 [3] was obtained as:

$$\varepsilon_{fu} = \text{design rupture strain} = 0.95 \times 1.4\% = 1.33\% \quad \dots\dots\dots(3.10)$$

For $E_f n t_f = 173900 \times 1.3 = 226,070 > 180,000$,

$$\text{the bond co-efficient, } \kappa_m = \frac{1}{60 \varepsilon_{fu}} \left(\frac{90,000}{n E_f t_f} \right) = \frac{1}{60 \times 0.0133} \left(\frac{90,000}{226,070} \right) = 0.5 \quad \dots\dots(3.11)$$

and thus, the ultimate debonding strain = $\kappa_m \varepsilon_{fu} = 0.5 \times 0.0133 = 6650$ micro-strains.

$$\dots\dots\dots(3.12)$$

The debonding strains predicted by ACI-440 [3] were thus found to be much higher as compared to those predicted by the theoretical model [11]. To have a conservative estimate of flexural capacity the lower debonding strain predictions were used. It is also to be noted that the strain prediction equation in ACI-440 [3] only takes into account the rupture strain, elastic modulus and the thickness of the composite. The theoretical model [11] also takes into consideration the interfacial fracture energy, G_f , and is thus more representative of the bond characteristics of the composite. Thus in the presence of representative interfacial fracture energy information, it is expected to predict the debonding strain level more accurately than ACI-440 [3].

The flexural capacities of the strengthened specimens were computed through sectional capacity analysis corresponding to the ultimate limit state at which the top concrete reached the crushing strain of 0.003 and the fabric laminate and pultruded strip at the bottom of the section reached the predicted debonding strains of 3626 and 3260 micro-strains, respectively. Also, as determined through field modal tests, there were 20% and 13.9% enhancements in the effective modulus for the decks rehabilitated with the fabric laminates and pultruded strips, respectively. Thus as compared to the effective modulus of 28.6 GPa (4150 ksi) for specimen S1, the effective modulus of concrete for specimens S2 and S3 were taken as 34.3 GPa (4975 ksi) and 32.6 GPa (4728 ksi),

respectively. The ultimate moment capacity of the specimen rehabilitated with the carbon fabric laminates, S2, was computed to be 99.42 kN-m/m (22.4 kip-ft/ft), which was found to correspond to a concentrated load demand of 827 kN (186 kips) from the finite element model. The ultimate moment capacity of the specimen rehabilitated with the carbon pultruded strips, S3, was computed to be 81.7 kN-m/m (18.4 kip-ft/ft), which was found to correspond to a concentrated load demand of 680 kN (153 kips) from the finite element model. It should be noted that the slab with the carbon fabric rehabilitation scheme was designed for permit load and thus had a higher composite reinforcement ratio as compared to the specimen strengthened with the pultruded strips which was designed only to prevent punching shear failure. Thus the specimen with the carbon fiber laminate rehabilitation scheme had a higher flexural strength. Table 3.1 summarizes the predicted capacities and failure modes of the test specimens.

Table 3.1 Failure Loads and Mode for Test Specimens

Specimen Description	Predicted Failure Load (kN)	Predicted Mode of Failure
S1, unstrengthened control	425 ¹ to 583 ²	Punching shear
S2, strengthened for permit load, using carbon fabric	827 ³	Flexural failure with debonding of the FRP composite
S3, strengthened for punching shear, using prefabricated carbon/epoxy strips	680 ⁴	Flexural failure with debonding of pultruded strips

¹ Shear failure plane angle, $\theta = 45^\circ$

² Shear failure plane angle, $\theta = 38^\circ$

³ Capacity prediction corresponding to $\varepsilon_C = 0.003$ and $\varepsilon_{FRP} = 3626 \mu S$

⁴ Capacity prediction corresponding to $\varepsilon_C = 0.003$ and $\varepsilon_{FRP} = 3660 \mu S$

Note: The theoretical failure loads have to be reduced by a strength factor, $\phi = 0.9$, live load factor of 1.7 and load impact factor of 1.3 to get design failure loads.

3.5 Test Setup and Instrumentation

The test specimens were placed on roller supports, simulating simply supported conditions, running continuously along the two 3.05 m (10') long edges and at a distance of 152 mm (6'') from the outer edge of the specimens, giving a center-to-center distance between supports of 1.07 m (42''). The two shorter outer edges of the slab were free edges. Two 3.05 m (10') long, 152 mm (6'') wide and 25.4 mm (1'') thick steel bearing plates, with 6.4 mm (¼'') thick neoprene bearing strips on top of it, were mounted between the roller supports and the underside of the slab to ensure uniform bearing of the

test specimens on the supports. The roller supports were welded to steel plates, which were tied down to concrete support blocks by post tensioned steel rods.

Load was applied, through a 76 mm (3") thick elastomeric pad, under displacement control, over a contact area of 508 mm x 203 mm (20" x 8") centered on the specimen, simulating a HS20 wheel load configuration [12.16]. At increments of 44.5 kN (10 kips) the load was cycled back to zero and then reloaded to the initial level to enable assessment of cracking and stability. The test setup is shown in Figure 3.6.

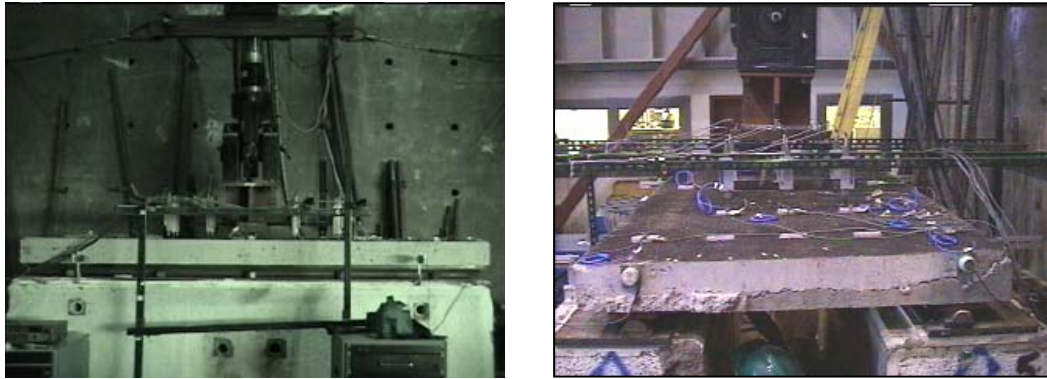


Figure 3.6 Test setup

3.6 Instrumentation and Data Acquisition

Vertical deflections in the area around load application were measured using 15, $\pm 76\text{mm}$ (± 3 inch) linear potentiometers. Three of these potentiometers along the centerline of the specimens were used to measure deflections from the underside of the specimens so as not to interfere with the load actuator. The remaining 12 potentiometers were used to measure deflections from the top of the specimens. The locations of the potentiometers with respect to the specimen are presented in Figure 3.7.

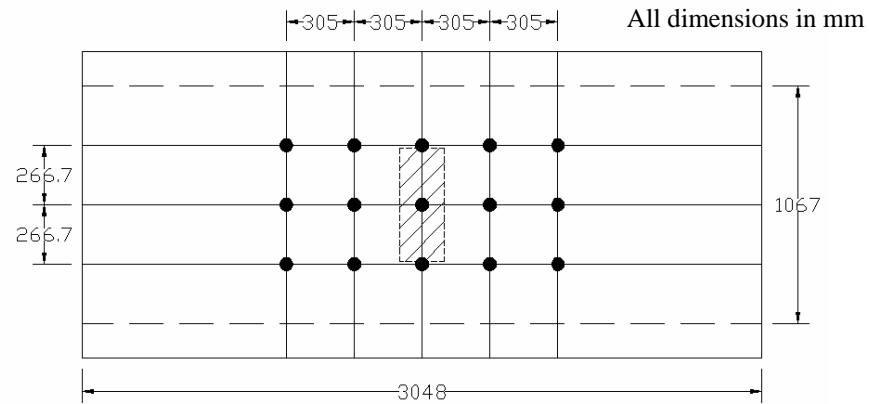


Figure 3.7 Locations of linear potentiometers

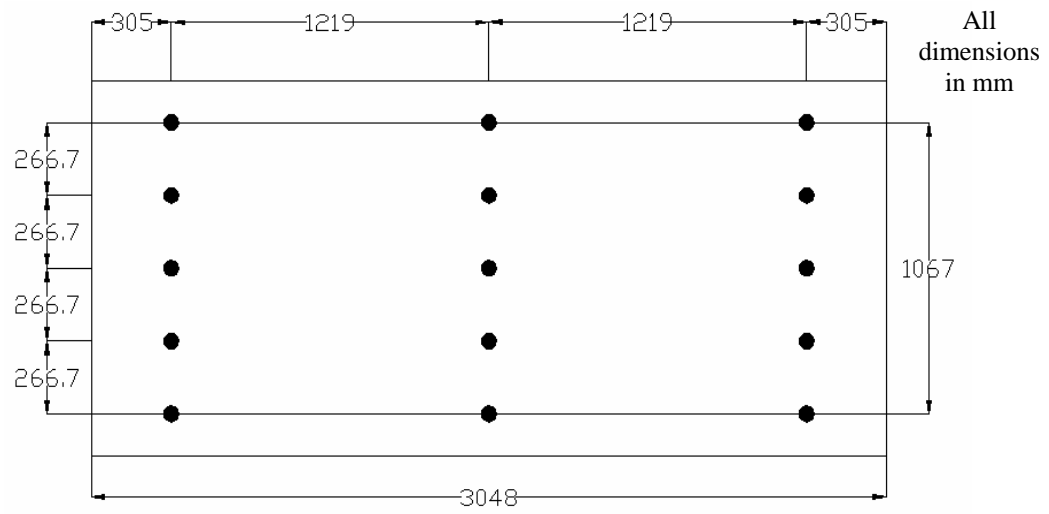
In addition to the vertical linear potentiometers, four horizontal potentiometers were used along the long edge of the specimens two on each side of the long edges, each placed at a distance of 457 mm (1.5 feet) from the outside edge of the specimens. These potentiometers were used to measure any horizontal movement of the test specimens during the test. Moreover four rotation sensors were used, two on each outer unsupported shorter edge and were placed right over the supports to measure any rotations of the test specimens at the outer edges.

A data acquisition system was used to record the loads from the actuator, the deflection readings from the linear potentiometers and strain readings from the electrical resistance strain gages. Values were recorded at intervals of 4.45 kN (1 kip) load increments through a complete load cycle. Fatigue deterioration and crack progression as well as the appearance of any new cracks were documented at the end of each load cycle.

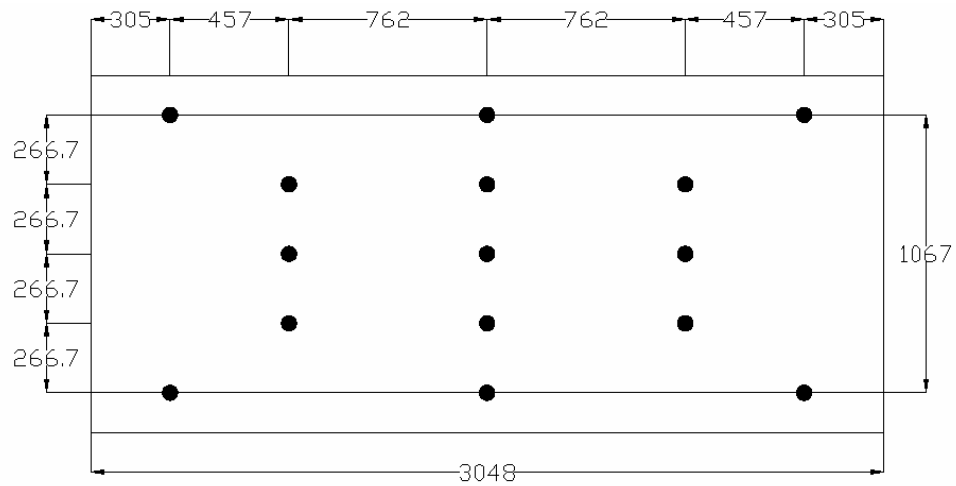
Forced excitation based dynamic testing was carried out for purposes of system identification to determine the “effective” modulus of the test specimens for capacity

prediction of the field deteriorated specimens. A total of 15 piezoelectric accelerometers were used at two location setups in order to capture the major natural frequencies of the test specimens. The locations of the accelerometers with respect to the test specimens are presented in Figure 3.8. The dynamic tests were carried out at intervals of 178 kN (40 kips) at the end of the loading cycle i.e. after returning to zero load. During the dynamic tests the actuator was retracted for the purpose of placing accelerometers along the centerline of the test specimens. A small hammer with a load cell attached at the tip was used to impart the external excitation. A frequency domain transformation was used to obtain the natural frequencies of the test specimens from the accelerometer data.

Electrical resistance strain gages with a gage length of 20 mm (0.8”) were also used on the carbon composite laminates and strips in specimens S2 and S3 respectively, to monitor the increase in strains in the composite material with the progression of damage. A total of 27 strain gages were used in specimen S2 and 22 gages were used in specimen S3. The locations of the strain gages are presented in Figure 3.9. Since most of the deflections and load transfer in the specimens were expected to occur in the transverse direction, the laminates/strips running in the transverse direction were more extensively instrumented as compared to the longitudinal strips/laminates. However at least one longitudinal strip/laminate was instrumented with strain gages in each of the specimens.

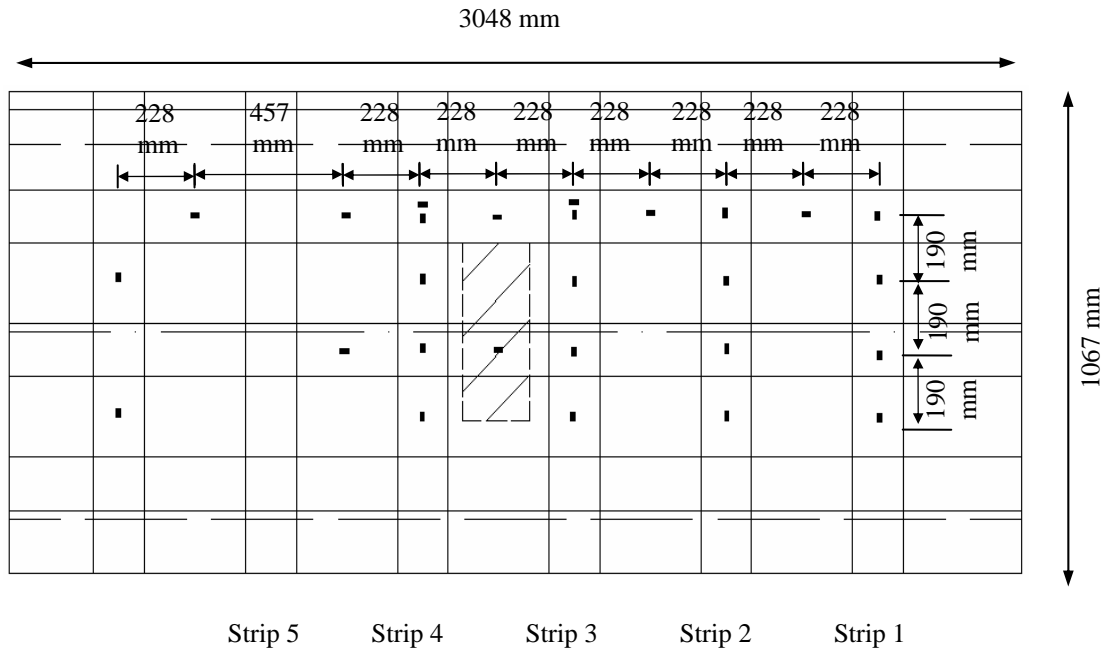


(a) Setup 1

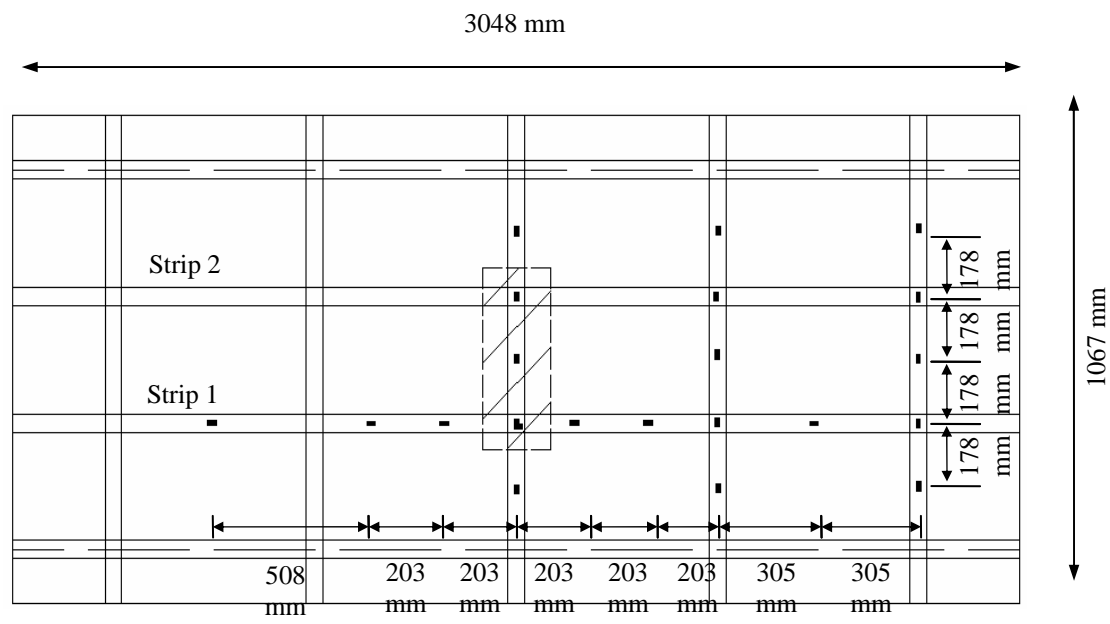


(b) Setup 2

Figure 3.8 Locations of accelerometers for vibration tests



(a) Specimen S2



(b) Specimen S3

Figure 3.9 Locations of strain gages on composite strips/laminates

3.7 Test Results and Discussion

3.7.1 Ultimate Load Capacities of Slabs

Overall load-midspan displacement response envelope curves for the 3 slabs are shown in Figure 3.10. The unstrengthened slab, S1, failed in punching shear at a load of 501 kN (112.6 kips). Punching shear failure was followed by yielding of the internal steel reinforcement resulting in the plateau in load-deflection response as seen in Figure 3.10. The load was retained up to a maximum center deflection of approximately 12.2 mm (0.48) inches, beyond which there was a rapid reduction in the specimen capacity. Final failure was caused by opening of preexisting cracks at the bottom of the specimen, with the load pad punching through at the top of the slab.

Specimen S2 was cutout from the bridge deck segment strengthened with unidirectional carbon fabric field impregnated with epoxy. The specimen failed at a load of 862 kN (193.7 kips) with a corresponding mid-span deflection of 13.5 mm (0.53 inches). Slab failure was initiated in flexure by debonding of the composite strips and was followed by punching of the load pad through the concrete at the top of the slab. Thus the rehabilitation scheme resulted in enhancement in the capacity of the specimen as compared to the control specimen while at the same time changing the failure mode from punching shear to flexural failure.

Specimen S3 was cutout from the bridge deck segment strengthened with prefabricated carbon/epoxy pultruded composite strips. The specimen failed at a load of 791 kN (177.76 kips) with a corresponding mid-span deflection of 11.7 mm (0.46 inches). The primary purpose of this rehabilitation scheme was only to prevent punching shear failure through control of the crack widths as opposed to the objective of strength

enhancement in specimen S2. Consequently, specimen S3 had a lower level of strength enhancement as compared to specimen S2 and also failed at a lower level of mid-span deflection. Slab failure was initiated in flexure by debonding of the prefabricated strips. This was followed by punching of the load pad through the concrete at the top of the slab, since the punching shear could not be resisted without the FRP composite.

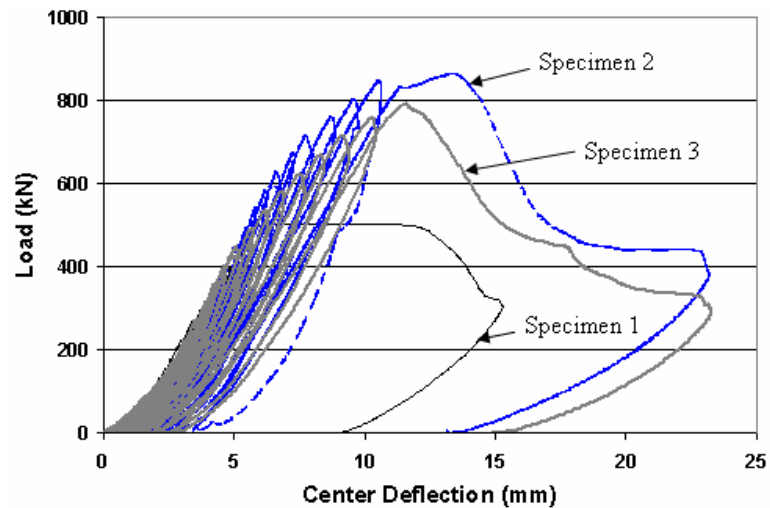
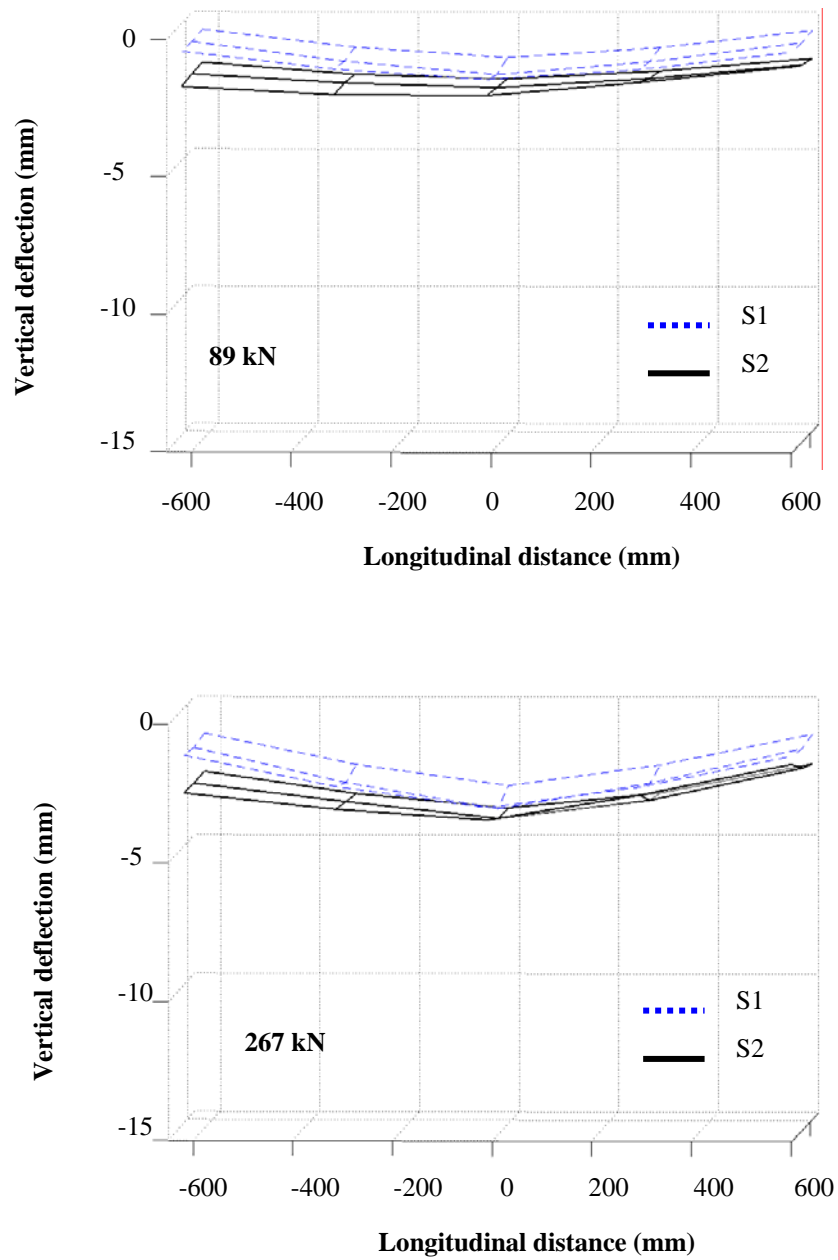


Figure 3.10 Load-displacement plots for test specimens

3.7.2 Slab Deflections and Cracking

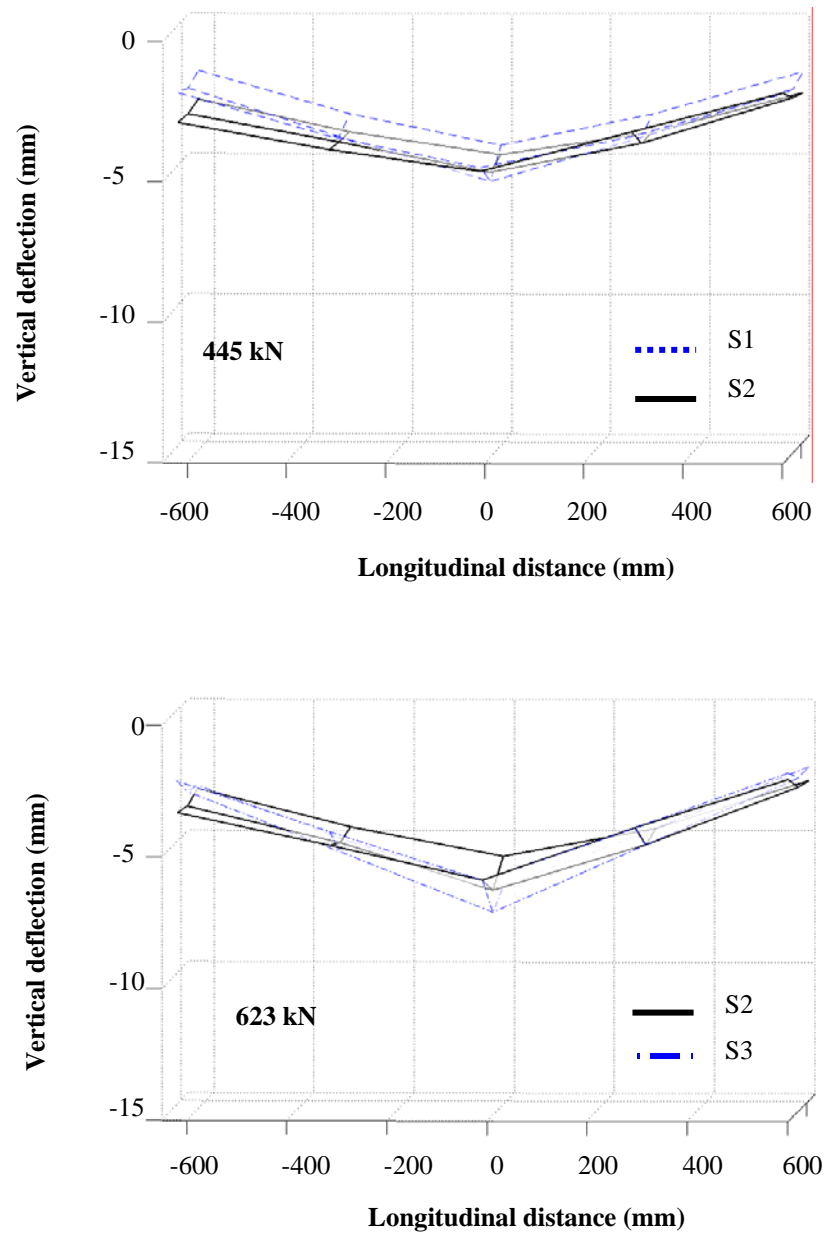
15 linear potentiometers were used for each specimen around the loading area in order to obtain the displacement profile of the specimens with the application of the load. The primary purpose of getting the displacement profile was to identify whether the composite strengthening schemes were able to distribute the wheel load over a larger area thus preventing localized punching shear failure. The characteristic displacement profiles of the test specimens are presented in Figure 3.11. From Figure 3.11 it is evident that specimens S2 and S3 were able to resist higher deflections (and hence show greater

ductility) prior to failure as compared to specimen S1. For the strengthened specimens the failure zone was also spread over a larger area, thus implying that the rehabilitation scheme was successful in redistributing the load, as compared to the control specimens where failure was extremely localized around the loading area. Moreover since in these specimens the failure mode was transformed to flexure, there were considerable deflections in the longitudinal direction away from the load area. Specimen S2 with a higher external composite reinforcement and higher flexural capacity than specimen S3, had higher longitudinal deflections in regions away from the load area.



Deflection profiles of S2 and S3 were similar upto 445 kN (100 kips)

Figure 3.11(a) Progression of deflection in the slabs with loading at 89 kN and 267 kN



Deflection profiles of S2 and S3 were similar upto 445 kN (100 kips)

Figure 3.11(b) Progression of deflection in the slabs with loading at 445 kN and 623 kN

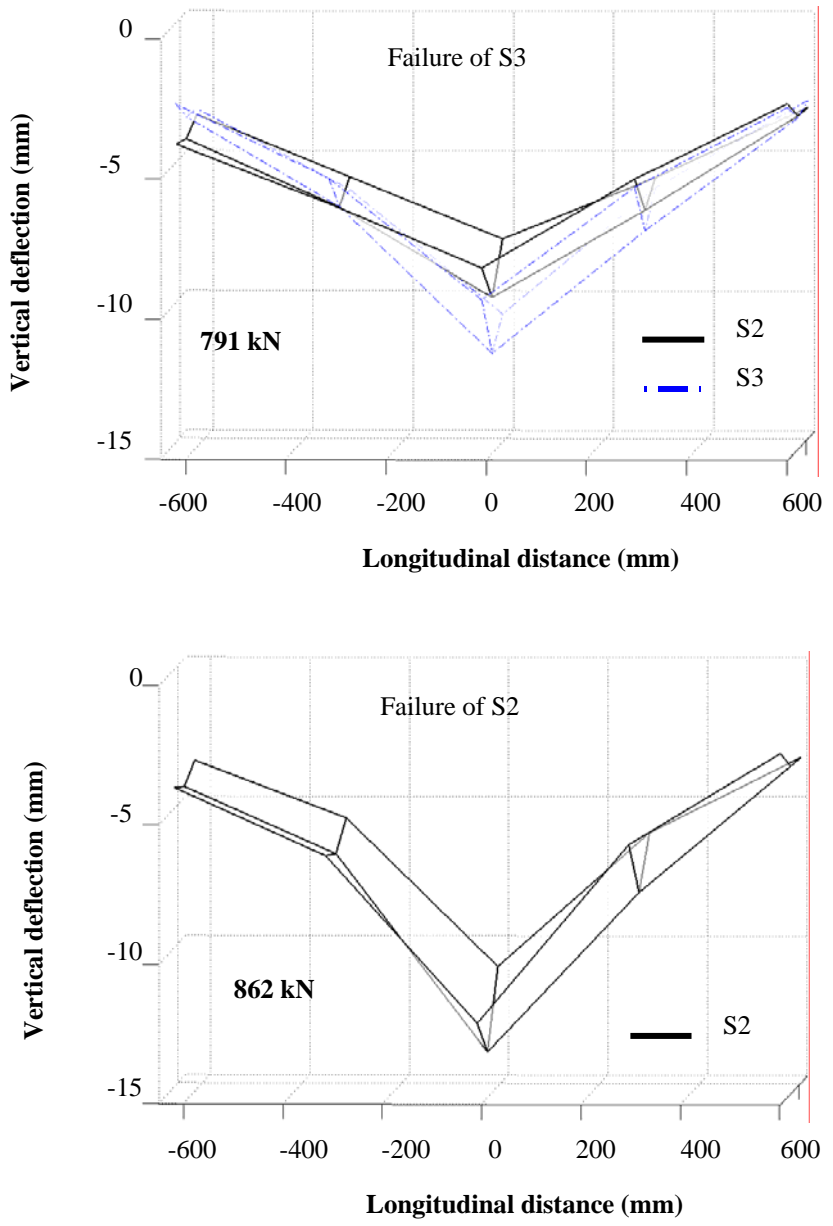


Figure 3.11(c) Progression of deflection in the slabs with loading at 791 kN and 862 kN

For the control specimen S1, the failure was mostly localized around the loading area with the main transverse cracks at the bottom forming at 178 mm (7") and 406 mm (16") on either side of the centerline of the slab. The main longitudinal cracks were

formed at about 457 mm (18") on either side of the slab centerline. Fatigue deterioration due to in-service loading of the slabs, prior to their removal from the bridge, had resulted in preexisting cracks spaced at about 17 mm (7") in the longitudinal direction and at about 203 mm (8") in the transverse direction. During the test the cracks opened up more and small pieces of concrete would drop near the peak load at every cycle. However, the most noticeable opening of cracks was observed at the locations of the main cracks where the shear failure plane originating from the top of the slab around the loading contact area intersected the bottom of the slab. The crack patterns noted at the bottom and over the cross-section in specimen, S1 are schematically presented in Figure 3.12.

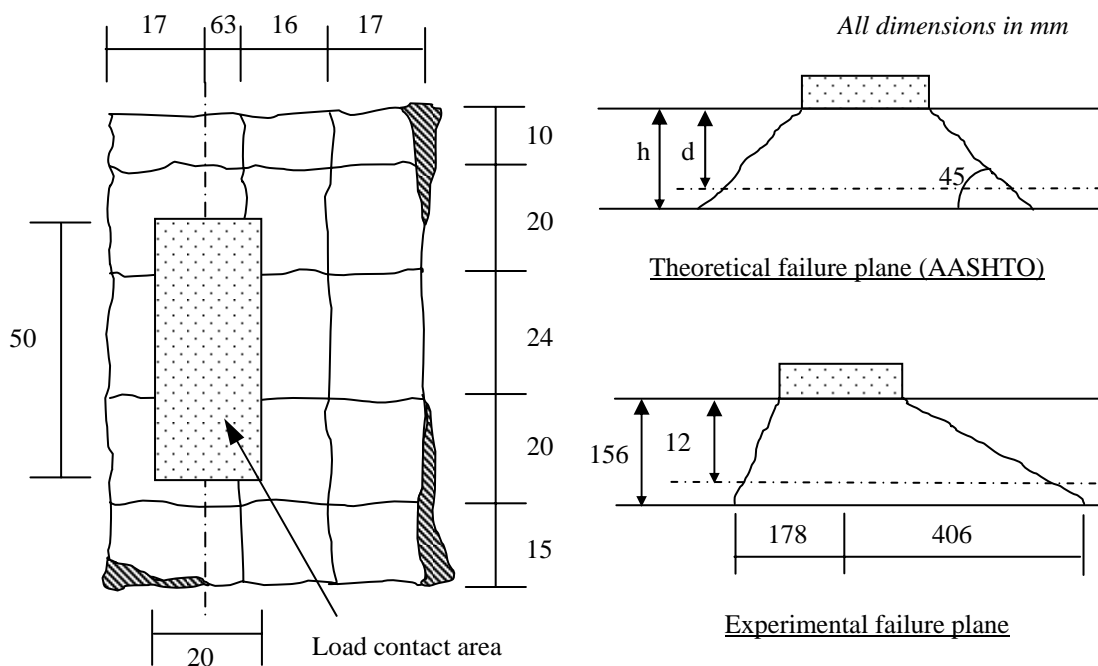


Figure 3.12 Crack pattern in Specimen 1

The opening of the cracks was significantly less in the FRP strengthened specimens before the delamination of the composite strips since the strips were able to effectively hold together the cracks. In S2, strengthened with the carbon composite fabric laminates, the failure zone was spread over a larger area with the main transverse cracks forming at around 533 mm (21") from the centerline of the slab. For S3, strengthened with prefabricated pultruded carbon composite strips, the main transverse cracks formed at around 533 mm (21") on the right and at 356 mm (14") on the left from the centerline of the slab. Although cracking was primarily restricted to pre-existing cracks, for specimen S3, a number of new minor cracks started to appear between the major pre-existing transverse and longitudinal cracks at a load level of 623 kN (140 kips). For both the specimens the main longitudinal cracks were formed at about 457 mm (18") from the centerline of the specimens. The failure zones defined by the primary crack patterns at the bottom of the specimens, S2 and S3, are presented in Figure 3.13.

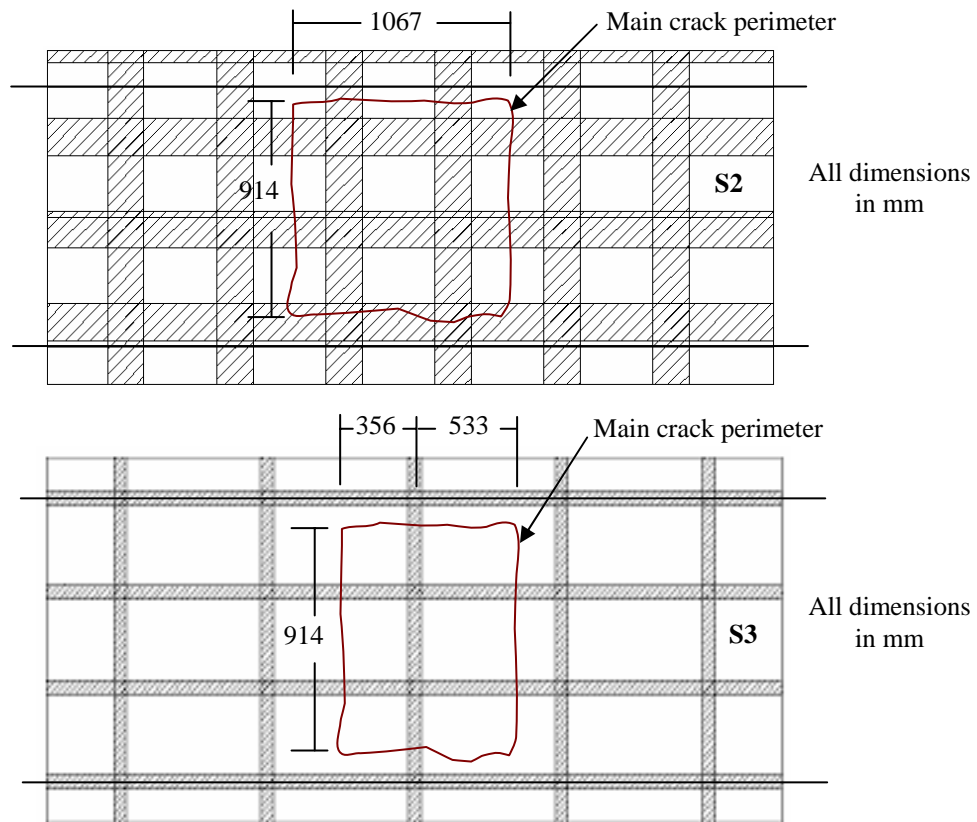


Figure 3.13 Crack patterns in strengthened specimens 2 and 3

3.7.3 Strain Development in the FRP Material

For specimen S2, strengthened with carbon fabric composite laminates, the axial strain profiles in transverse strip 3 (as in Figure 3.9) and along the length of longitudinal strip, as a function of load are presented in Figure 3.14 (a) and Figure 3.14 (b), respectively. The maximum axial strain recorded in the transverse strip was 3227 microstrains. The longitudinal composite strip, made up of one layer of carbon fabric laminate as compared to two layers for the transverse strips, reached a higher axial strain level of 4672 microstrains. Considerable segments of strips 3 and 4 (as shown in Figure 3.9),

were found to be debonded at failure along with some segments of strips 2 and 5 at the intersection regions with the longitudinal strips.

For specimen S3, strengthened with prefabricated carbon composite pultruded strips, the axial strain profiles in transverse strip 3 (Figure 3.9) and along the length of longitudinal strip, as a function of load are presented in Figure 3.15 (a) and Figure 3.15 (b), respectively. The maximum axial strain recorded in the transverse strip was 4274 micro-strain. Strip 3 being located at the middle of the specimen and also running in the transverse direction was subjected to maximum deflections and thus to highest axial strains. Strip3 (Figure 3.9) was debonded along its entire length while considerable portions of strips 2 and 4 were also debonded at failure. Moreover the two central longitudinal strips were also debonded under the load area.

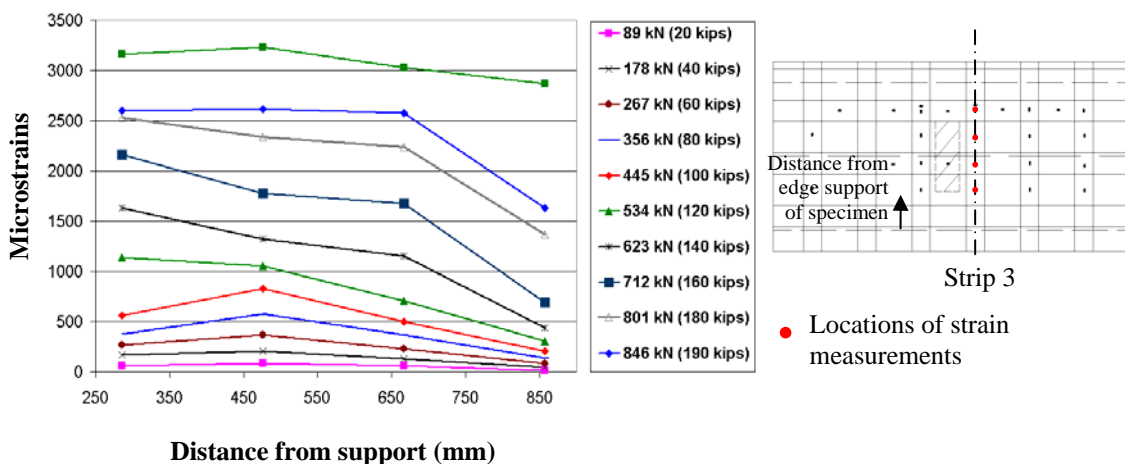


Figure 3.14a Development of axial strains in specimen S2 along transverse laminate 3

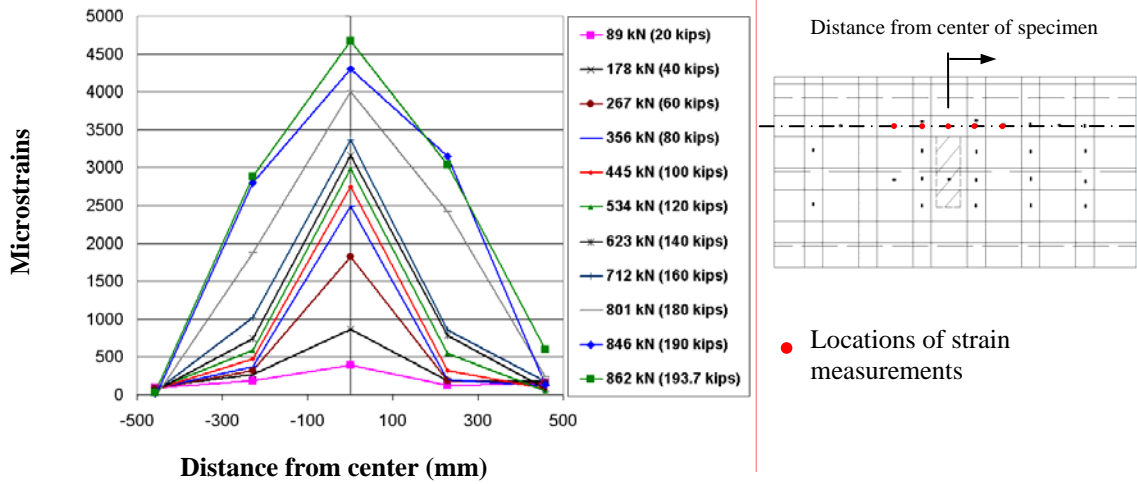


Figure 3.14b Development of axial strains in specimen S2 along longitudinal laminate

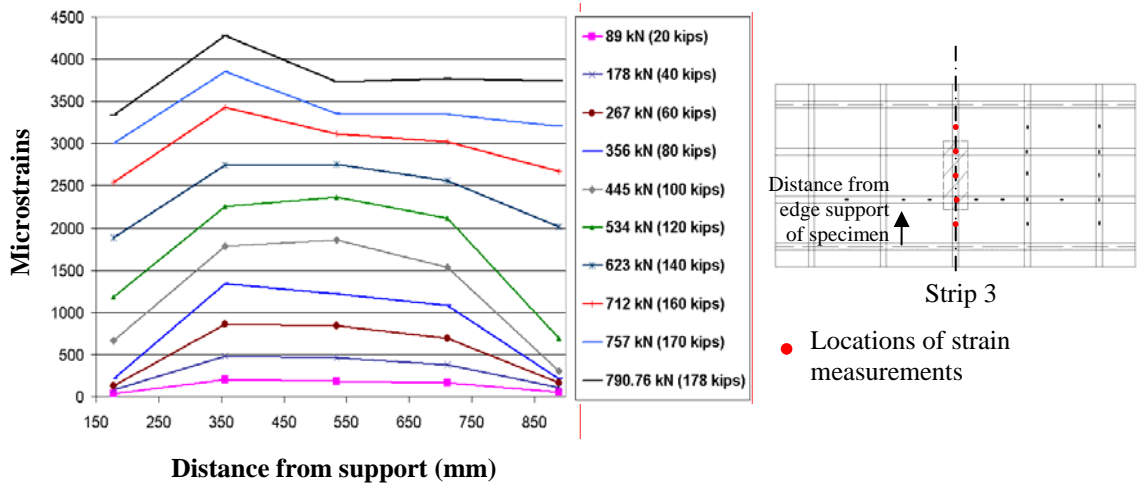


Figure 3.15a Development of axial strains in specimen S3 along transverse laminate 3

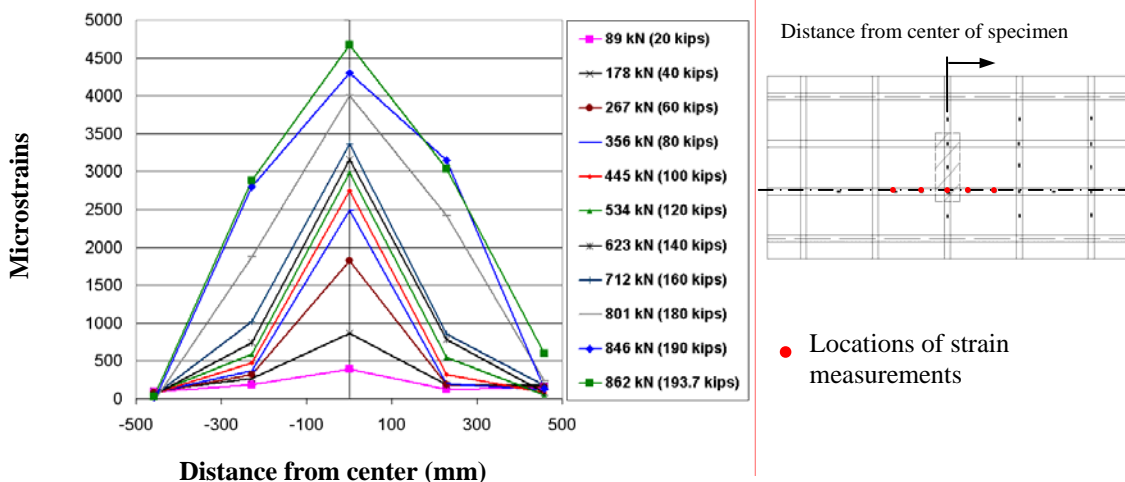


Figure 3.15b Development of axial strains in specimen S3 along longitudinal laminate

3.8 Progressive Damage Characterization

Non-destructive evaluation of the FRP composite strengthened test specimens was carried out using the IR thermography technique. The objective of using IR Thermography for the component tests was two-fold, the first being the detection of any pre-existing defect/damage areas in the composite strips themselves and the second being the characterization of damage progression in strip locations with increase in loading. Inspection was carried out before the test for both the rehabilitated specimens, S2 and S3, to provide a baseline for subsequent inspection.

The data was acquired using a commercial thermographic non-destructive testing (NDT) system. Flash heating provided by 2 xenon flashtubes with 5 ms flash duration, each powered by a 6.4 kJ capacitor bank was used to stimulate the temperature differential between the composite and any potential areas of debond/delamination and the thermal emissivity of the test surface over time was acquired using a commercial

thermographic NDT system (Figure 3.16). An infrared camera operating in the 2–5 μm spectral range was used and continuous data was acquired at a 60 Hz frame rate for 10 seconds after flash heating for each shot. The field of view of the Thermography system used was 305 mm x 229 mm (12" x 9") and thus the region of inspection of each of the test specimens was divided into a number of small elements each of which was imaged independently. An overlap of about 51 mm (2") was maintained between adjacent shots so that the adjacent thermal profiles could be brought together and superimposed during processing of the thermography data. Once the base-line was established, data was obtained at 178 kN (40 kip) intervals, first at the intended load level and then after reducing the load to zero. The thermal intensity data from the IR camera was recorded for 10 seconds after application of thermal input. The principles of the pulsed thermography technique in detection and characterization of defects/damage areas in composite bonded to concrete surface can be found in [61].



(a) Data acquisition unit



(b) Setup for inspection

Figure 3.16 Initial thermography inspection of specimens

3.8.1 Detection and characterization of pre-existing defect/damage

The thermal intensity at a defect location from the thermography data is a function of the defect depth and the properties of the composite. Thus linear profiles and 2-D mapping of the thermal intensities over the composite surface was carried out to determine the time frame within each shot of thermography inspection (which consisted of acquiring 10 seconds of continuous data at that location), at which pre-existing or any new damage/defects become detectable from the thermography data because of the difference in thermal intensities at locations with and without defects. In Slab 2, strengthened with site-impregnated carbon composite fabric laminates, a number of pre-existing defect locations in the composite were indicated by high thermal intensity (hot spot) regions observed in the 2-D thermal intensity plots (Figures 3.17 and 3.18a). A majority of the defects in the fabric laminates were located at the overlap regions of the longitudinal and transverse laminates (Figure 3.17), indicating the potential of presence of defects in the form of voids, fiber undulations and resin rich areas in such locations. The presence of majority of defects at the overlap regions of the longitudinal and transverse laminates was attributed to the difficulty associated with attaining proper bond during installation of the composite laminates at such overlap regions. This is because when a layer of fabric laminate is laid out over another layer at different orientation in the form of a grid, the thickness of the bottom layer causes the top layer to go up and down at the overlap region resulting in poor bond of the top layer with concrete at the intersection areas. This is shown in Figure 3.17.

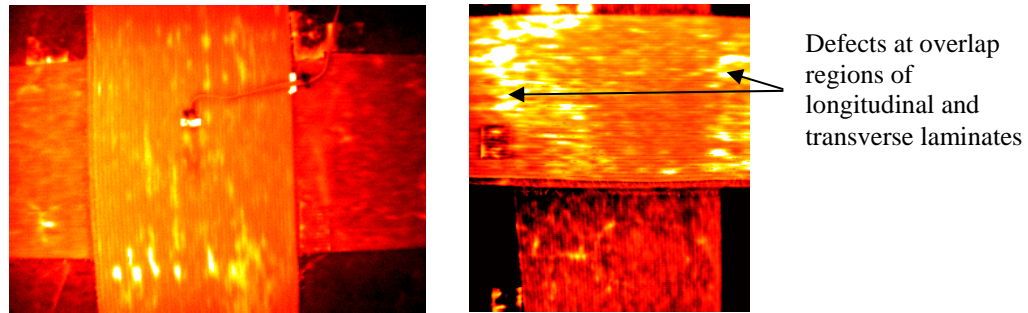


Figure 3.17 Representative detection of pre-existing defects in composite laminates

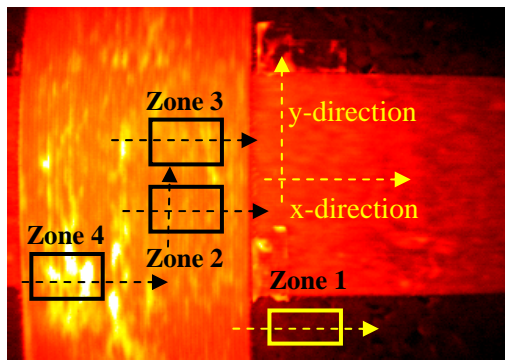
The thermal intensity at a location obtained from the thermography data is a function of the thermal emissivity of the material at that location. Figure 3.18a shows a representative 2-D thermal image obtained from the thermography inspection at the overlap region of a longitudinal and transverse fabric laminate bonded to concrete in slab 2. Four zones in this thermal image were chosen for further quantitative analysis in terms of the absolute thermal intensity values. Zone 1 is in concrete; zone 2 is a defect free area of the composite laminate; zones 3 and 4 are areas in the composite laminate with defects of different severity magnitudes. The linear thermal intensity profiles in these selected zones were then obtained along the x or y directions of the thermal image and the direction of plotting the linear thermal profiles is also shown in Figure 3.18a. The linear thermal profile obtained in Zone 1 (concrete) in the x-direction is shown in Figure 3.18b. The corresponding linear thermal profile in Zone 2 (defect free composite) in the x-direction is shown in Figure 3.18 c. The average thermal intensity magnitude in Zone 1 (concrete) was 125 as compared to 450 in zone 2 (defect free composite) because of the difference in the thermal emissivities of the two materials.

The linear thermal intensity profile in zone 2 in the y-direction is plotted in Figure 3.18d. The y-direction in Zone 2 was in the fiber direction of the fabric laminate while the x-direction was perpendicular to the fiber orientation, as shown in Figure 3.18a. On comparing Figures 3.18c and 3.18d, it is seen that the thermal intensity profile in the x-direction in Figure 3.18c (representative of the thermal intensity profile perpendicular to the orientation of the fibers in the fabric laminate) is much more irregular along the length of the profile with the thermal intensity varying between 400 and 550. In contrast to this, in Figure 3.18d the thermal intensity profile in the y-direction (i.e. in the direction of the fiber orientation of the fabric laminate) was uniform with average thermal intensity magnitude of 450.

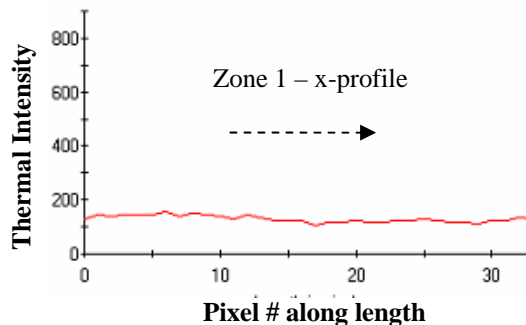
Zones 3 and 4 in Figure 3.18a represent regions in the composite with air void defects of varying severity which can be attributed to the defect size. From the thermography inspection data a defect can be detected based on identification of locations of high thermal intensities (hot spots) and the relative magnitude of the intensity will be an indication of the severity of the defect. The linear profiles of thermal intensities over zones 3 and 4 in Figure 3.18a in the x-direction are plotted in Figure 3.19. The maximum thermal intensity in zone 3 with the minor defects was 600. Compared to this the maximum thermal intensity magnitude in zone 4 with major defects was 825 with the higher thermal intensity in this zone being characteristic of a more severe defect.

The second objective of the defect characterization was to identify different types of defects in a composite fabric laminate based on their characteristic thermal intensity profiles. The defects in Figures 3.17 to 3.19 are representative of air voids in the

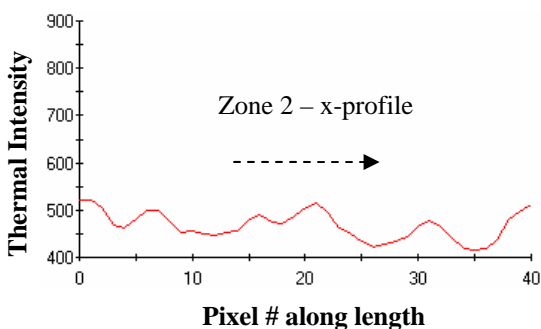
composite produced during installation of the composite strips. From the thermal profiles in Figures 3.17 to 3.19 it is seen that the change in thermal intensity along the length of the profile was irregular, with sudden increase in the thermal intensities at the locations of the air voids. As compared to the air voids, Figure 3.20 shows the thermography data at a location of fabric undulation in the laminate. Fabric undulations produced during installation of the composite also resulted in the formation of unbonded areas with similar thermal intensity magnitudes (around 800) as an area with major air void defects (Figure 3.19b). However the thermal intensity profile at such unbonded areas shown in Figure 3.20 was much smoother, with characteristic peaks and troughs in the thermal intensity profile being representative of the fabric undulation.



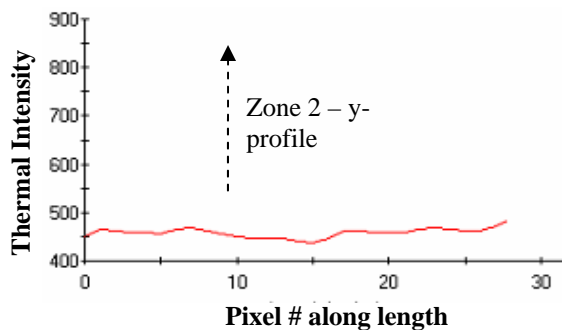
a) Regions used for plotting thermal intensity profiles



b) Thermal intensity profile in x-direction in Zone 1



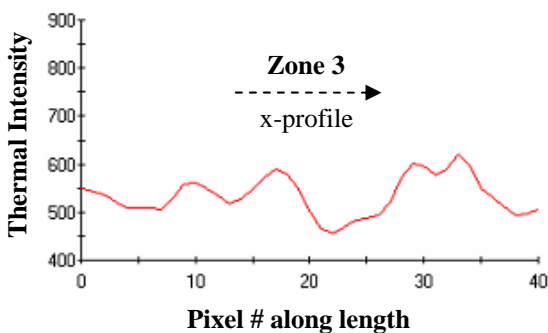
c) Thermal intensity profile in x-direction in Zone 2



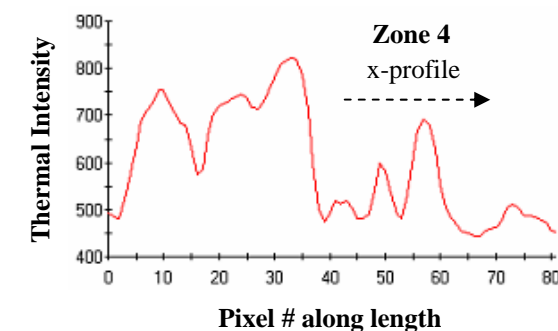
d) Thermal intensity profile in y-direction in Zone 2

-----> Direction of thermal profile

Figure 3.18 Representative thermal signatures from baseline inspection



(a) Thermal intensity over minor defect



(b) Thermal intensity over major defect

-----> Direction of thermal profile

Figure 3.19 Thermal signature over air voids of varying damage severity

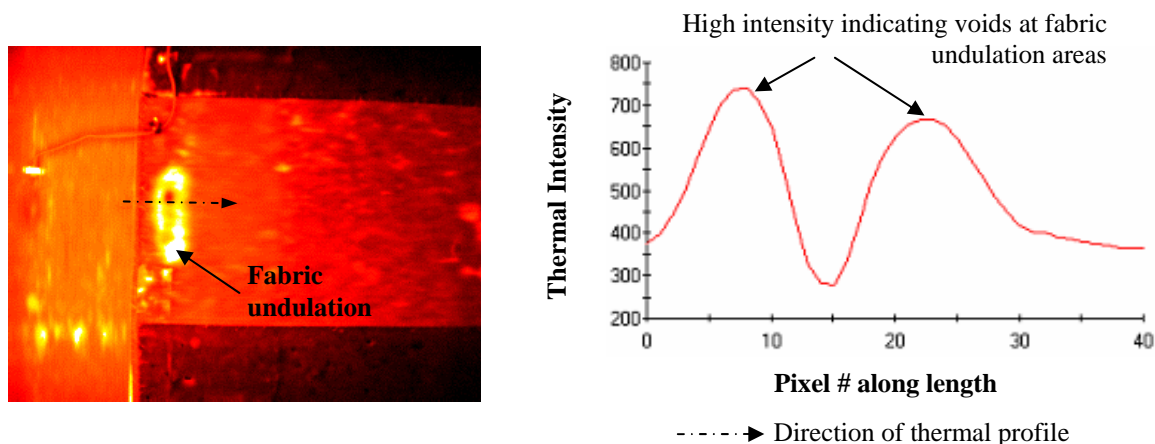


Figure 3.20 Thermal signature over fabric undulations

The test specimen S2 was cut out from a segment of a bridge deck which was strengthened with the fabric laminates in the field and this strengthening scheme was in service for about two years before demolition of the bridge. The composite laminates in the strengthened deck slab was thus subjected to field loading and environmental exposure conditions. As was previously mentioned, the deck slabs showed extensive cracking in the longitudinal and transverse direction before they were strengthened with the composite laminates. The fatigue loading of the deck slabs in the field under daily traffic loads was expected to cause opening/closing of these pre-existing cracks or could result in the appearance of new cracks, which would produce damage in the composite laminates traversing across these cracks at the composite-concrete bondline. Such damage areas at locations of pre-existing longitudinal and transverse cracks traversing a composite laminate were detected in the baseline thermography inspections and are shown in Figure 3.21. From the thermal intensity profile these damage areas could be distinguished by the sharp and sudden increase in the thermal intensity at the locations of

the cracks representative of localized damage of the composite at the crack locations. Also from the 2-D thermal image in Figure 3.21, it was seen that the damage instead of being confined in a circular or elliptical area (as in the case of air voids or unbonded areas), propagated along the length of the crack.

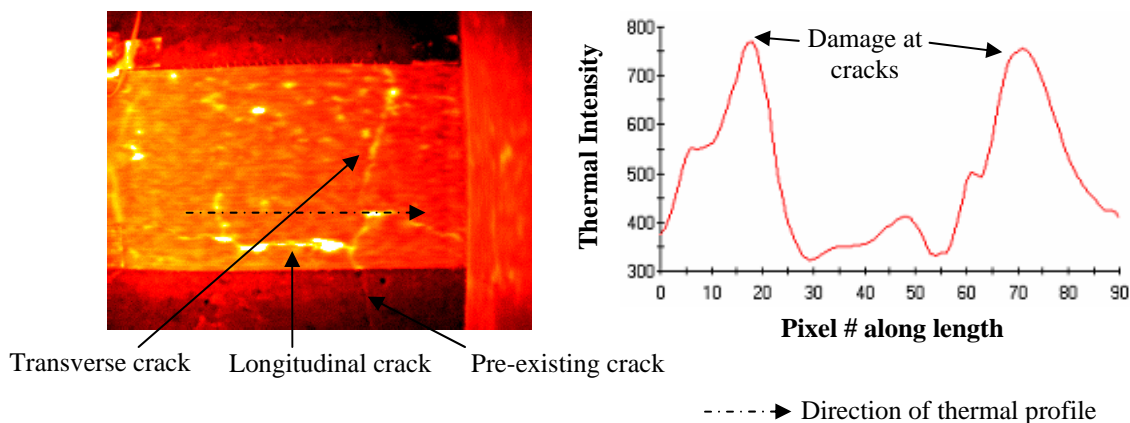
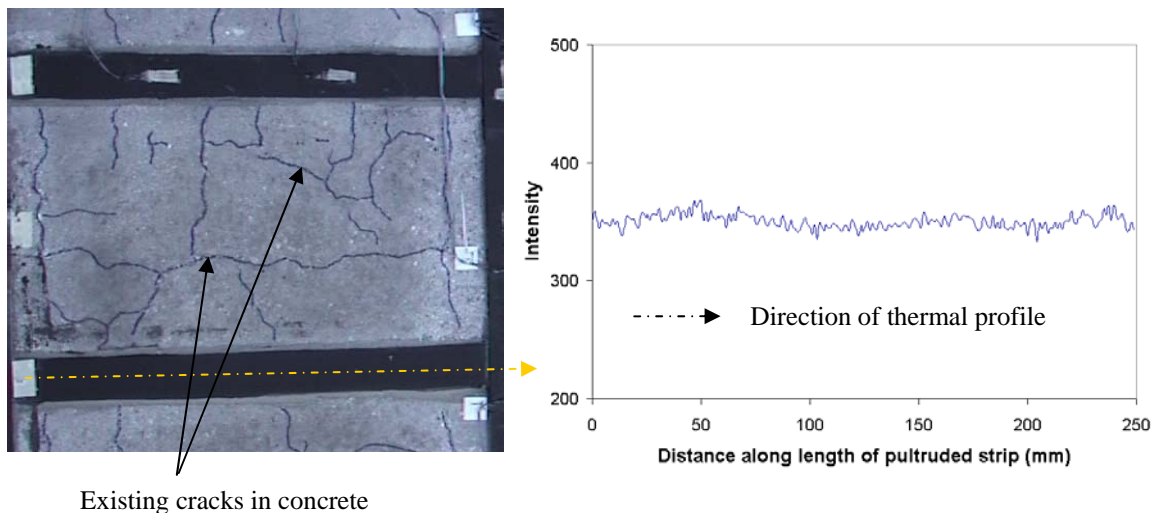


Figure 3.21 Thermal signature at locations of substrate cracks

In Slab 3, which was rehabilitated with prefabricated pultruded strips, no major pre-existing defects were detected in the composite strips from the thermography inspections. The baseline thermal profiles were uniform along the length of the strips with few peaks and valleys in the thermal profile indicating the absence of substrate defects. A representative thermal profile along the length of the pultruded strips is shown in Figure 3.22b. The uniformity in the thermal profile magnitudes in the pultruded strips can be explained by the better quality control that can be achieved both in the manufacturing of the pultruded composite strips as well as during bonding these strips to the concrete surface with the epoxy adhesive, as compared to the wet lay-up installation

process used for the fabric laminates. Representative visual inspection of Slab 3 is presented in Figure 3.22a and shows the presence of longitudinal and transverse cracks in the unstrengthened sections of concrete. The objective of the rehabilitation of slab 3 with the pultruded strips was to restrain the opening of these existing cracks so as to prevent the occurrence of punching shear failure. Since no substrate damage areas were detected in the pultruded strips from the baseline thermography inspection data (as shown in Figure 3.22b) at the intersection areas of the composite strips with the existing cracks, this indicated that the pultruded strips were effective in restraining the opening of the existing cracks.



(a) Visual inspection before test

(b) Baseline thermography data before test

Figure 3.22 Visual and baseline thermography inspection of slab 3 before testing

3.8.2 Damage Detection/Progression from Thermography Data

In slab 3, rehabilitated with prefabricated carbon composite pultruded strips, appearance of damage areas (indicated by changes in the thermal intensity when compared to previous load stages) at some locations of the longitudinal composite strips were observed during the inspection at 623 kN (140 kips). At the inspection carried out at 712 kN (160 kips) these damage areas were found to grow along with the appearance of new ones. The locations of thermography inspections in slab 3 showing damage areas are illustrated in Figure 3.23. Figure 3.24 shows the progression of damage in longitudinal strip 2 as indicated by the linear profiles as well as 2-D and 3-D mapping of the thermal intensities over the surface of the composite strips acquired at unloading after reaching the desired load level so as to compare with the baseline intensity at zero load. The appearance of damage areas at other locations of the strip at 712 kN is illustrated in Figure 3.25. The appearance of damage/debond areas in longitudinal strip 1 is illustrated in Figures 3.26 and Figure 3.27.

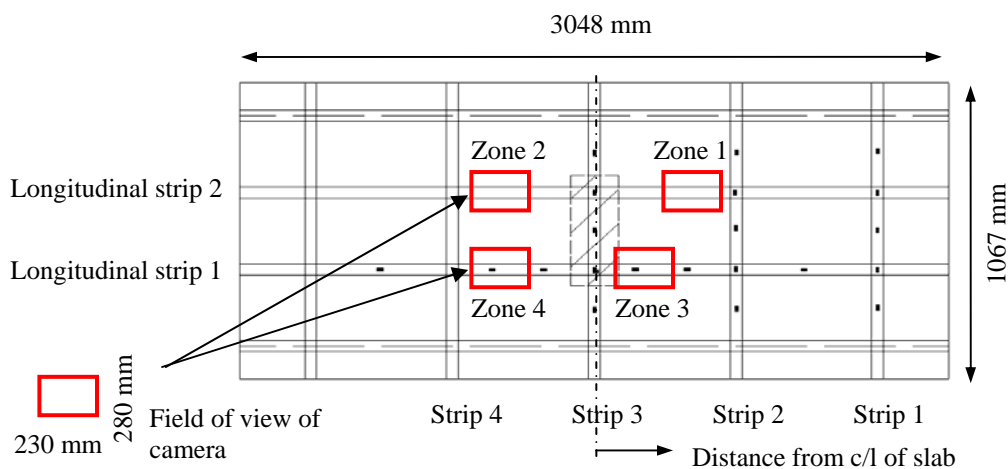


Figure 3.23 Regions of thermography inspection in slab 3 with damage areas

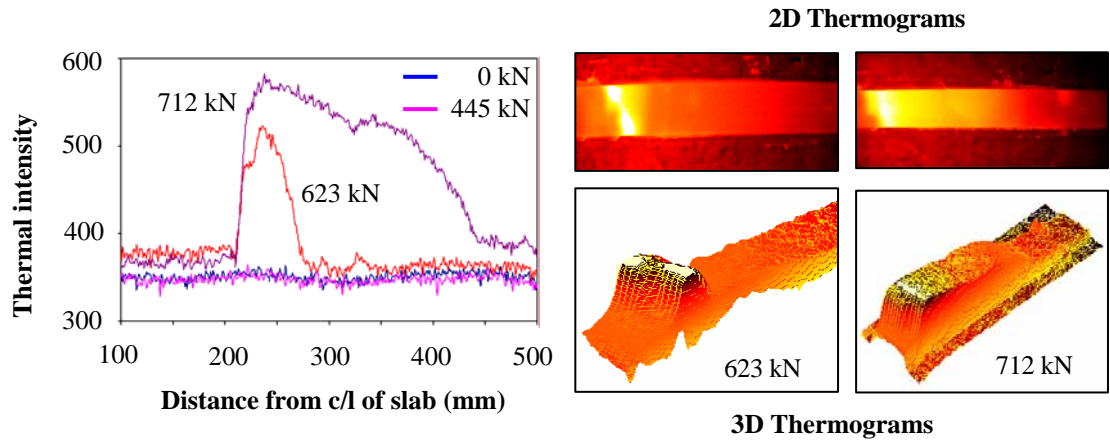


Figure 3.24 Progression of damage in Zone 1 of longitudinal strip 2 of Slab 3

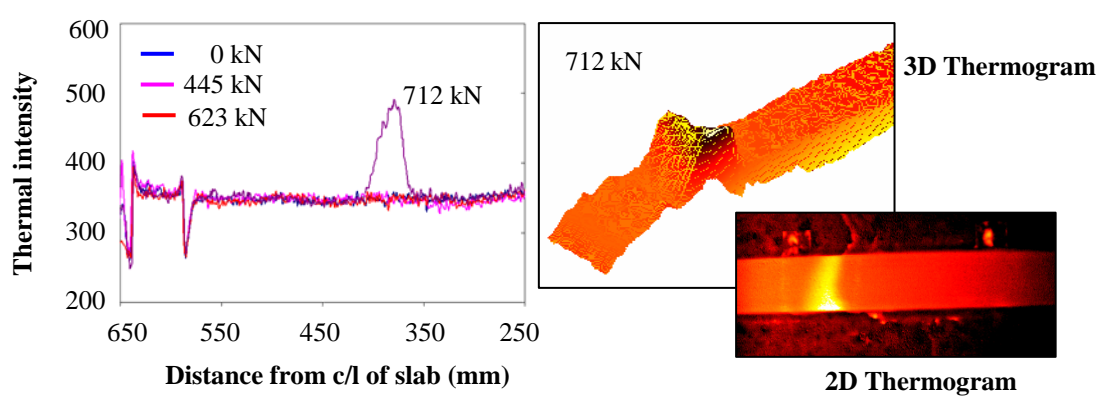


Figure 3.25 Appearance of debond areas in Zone 2 of longitudinal strip 2 of slab 3

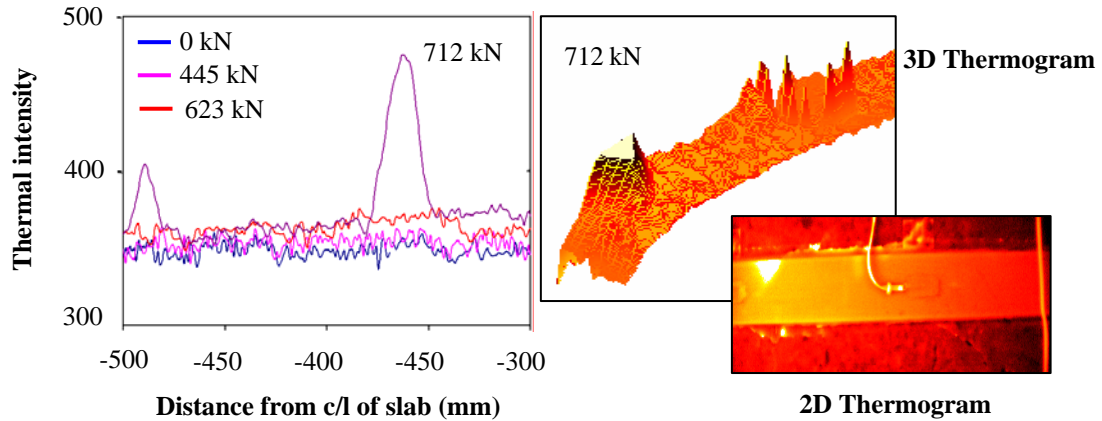


Figure 3.26 Appearance of debond areas in zone 4 of longitudinal strip 1 of slab 3

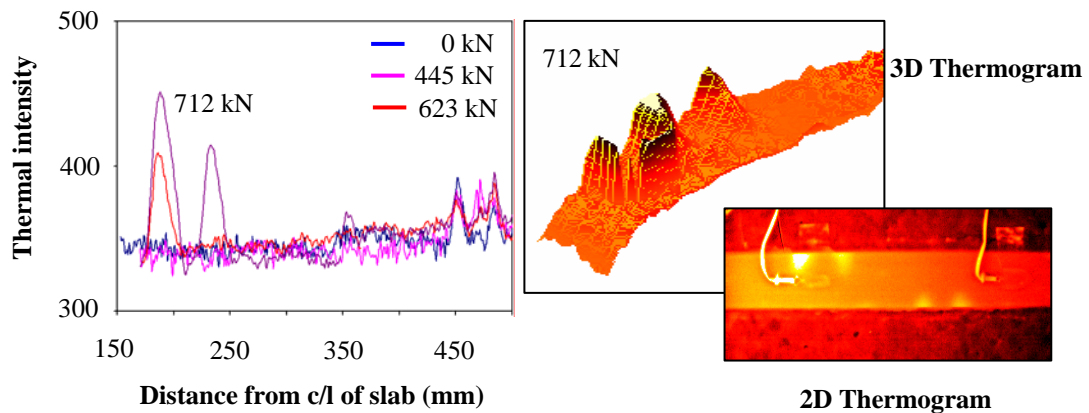


Figure 3.27 Appearance of debond areas in zone 3 of longitudinal strip 1 of slab 3

It is evident from Figures 3.24 to 3.27 that damage in the FRP composite strip strengthened regions started out as a localized phenomenon resulting in the sharp changes in the thermal intensity with peaks at the location of the defects. In order to verify the validity of these defects, the thermography profiles were compared to the crack patterns observed in the slabs illustrated in Figure 3.28. The opening up of pre-existing cracks caused failures in all the test specimens. In slab 3, the cracks widths were kept under

control by the rehabilitation scheme up to 623 kN (140 kips), beyond which the opening up of the cracks was observed visually through the falling of fine sand and small pieces of concrete. This corresponds well with the thermography data where significant changes in the thermal intensity were observed only beyond 623 kN (140 kips) shown in Figures 3.24 to 3.27. The falling of debris accelerated beyond 757 kN (170 kips) and failure occurred at 791 kN (177.76 kips) with the opening up of punching shear cracks at the bottom surface of the slab. On close inspection, the primary cracks (as shown in Figure 3.28) were found to intersect longitudinal strip 1 at approximately 550 mm, 190 mm and -355 mm (longitudinal distances measured with respect to the center-line of the slab) and intersected longitudinal strip 2 at 555 mm, 130 mm and -360 mm, as shown in Figure 3.28. The locations of the cracks were found to coincide with the locations of the thermal intensity peaks obtained from the thermography data indicating that debonding of the strips was initiated by the high stress concentration at these cracks. The correspondence between the locations of cracks from visual observation and the locations of damage indicated by the thermal intensity peaks in the thermal profiles along the length of the composite strips is shown in Figure 3.28. At 712 kN (160 kips) the strain in the longitudinal composite strip was lower than the debonding strain as was shown earlier in Figure 3.15b. Therefore most of the measured intensity peaks were localized over a region of only 30 to 50 mm around the crack. The only exception was in composite strip 2, where thermographic inspection at 623 kN (140 kips) showed intensity changes indicating debonding over a region of about 70 mm. At 712 kN (160 kips) significant change in thermal intensity with respect to the baseline was observed over a region of 232 mm. On close inspection a horizontal crack was observed to propagate along the

longitudinal strip (shown in Figure 3.29) between the main transverse cracks at 130 mm and 555 mm resulting in debonding of the strip. It should be noted that the thermal intensity change gradually decreased towards the overlap area between the transverse and longitudinal strips (as seen in Figure 3.24 and also in Figure 3.28) because the restraint offered by the transverse composite strips checked the growth of debonding in the longitudinal strip. A thermal intensity peak of magnitude lower than the other peaks was also observed at 488 mm to the left of the centerline in longitudinal strip 1 and the location of this thermal intensity peak coincided with the location of a secondary crack at approximately 490 mm to the left of the centerline of the specimen. All comparisons between visual inspections of crack patterns and damage areas detected from thermography data are shown in Figure 3.28.

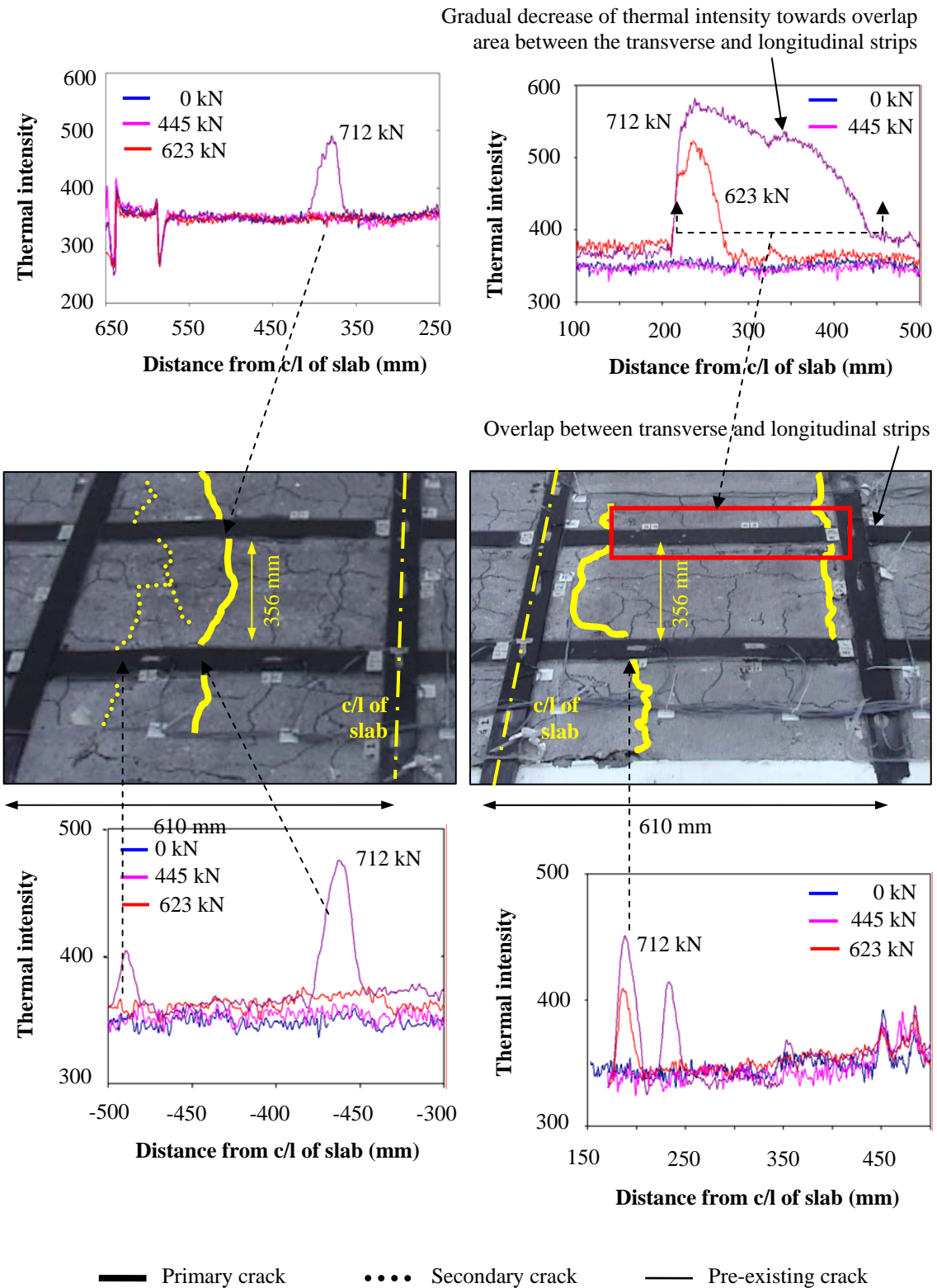


Figure 3.28 Crack pattern in Slab 3 and correspondence with thermography inspection

The correspondence of the locations of the major cracks with the locations of high thermal intensities indicate that damage in the composite was initiated due to cracking of the adhesive between the composite strip and the concrete due to high stress concentrations at the locations of the cracks. The damage severity at these locations indicated by the magnitude of the thermal intensity increased with increased loading due to increase in the crack widths. Finally, as the composite strips approached the debonding strain levels at 712 kN (160 kips) damage started to propagate out from these locations and along the length of the strip, as shown in Figure 3.24, resulting in subsequent drop in capacity and failure of the rehabilitated deck slab. A comparison of the damage progression obtained from the thermography data to the strain gage data is presented in Figure 3.30. The strain profile along the length of the pultruded strip with increase of loading is shown in Figure 3.30a. Localized increase in the strain levels was seen at 712 kN (160 kips) from the strain profile. Localized damage areas indicated by the thermal intensity peaks were also detected by thermography inspections at this load level as shown in Figure 3.30b.

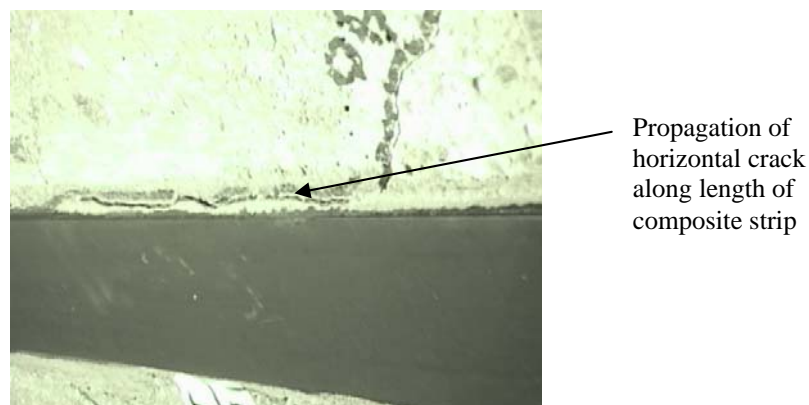
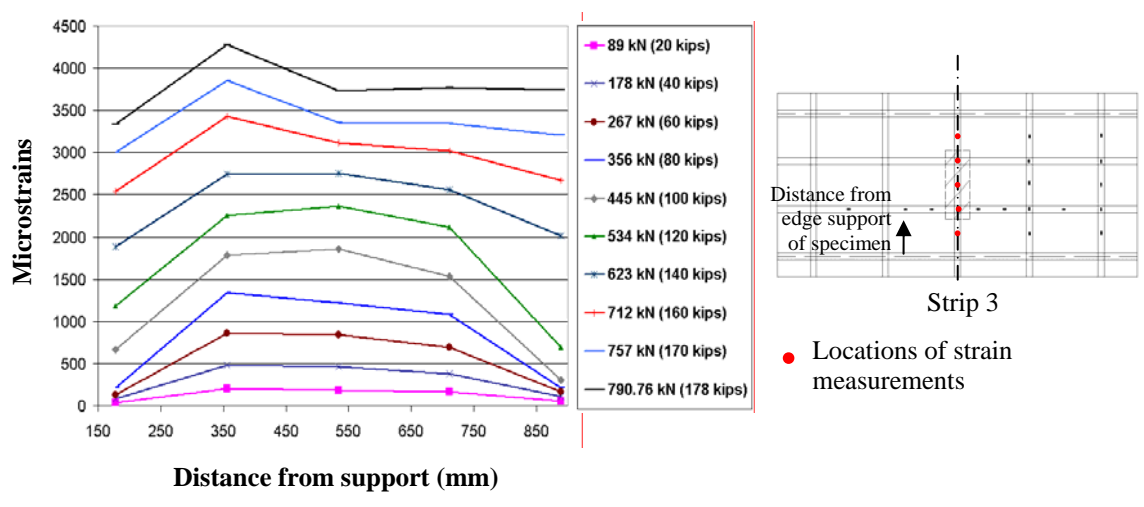
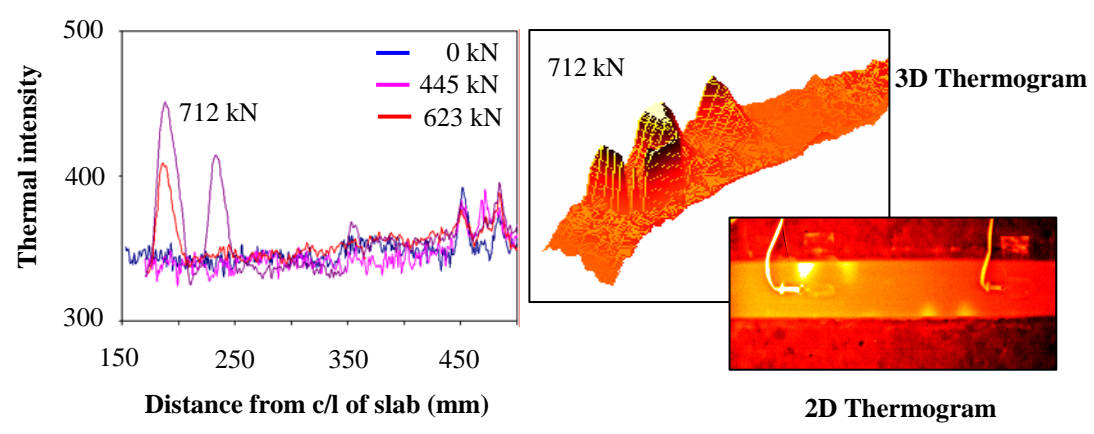


Figure 3.29 Visual observation of debonded area in composite strip

Thermographic inspections were also carried out in specimen S2 at intervals of 178 kN (40 kips) during the test, up to 801 kN (180 kips), beyond which inspection was deemed to be unsafe. No significant changes in thermal intensity along the length of the fabric laminates were obtained from the data at the subsequent load stages of inspection as compared to the baseline intensity. A comparison of thermal intensity profiles obtained along the length of a fabric laminate at three load levels is shown in Figure 3.31. The difference in the thermal intensities at the different load levels was negligible indicating that no major appearance of damage areas took place in the composite laminates at the load levels up to which thermographic inspection was carried out. This was also confirmed from the strain gage profiles (presented earlier in Figure 3.14) where the strains in the composite laminates were observed to remain below the debonding strains at the load stages of inspection. Because of safety issues no thermography inspection could be carried out between 801 kN (180 kips) and failure load of 862 kN (194 kips) and thus no thermography data was available at the load stages at which the composite laminates reached debonding strain levels.



(a) Trend of strain profile along length of composite with increase in loading



(b) Damage progression detected from thermography data with increase in loading

Figure 3.30 Comparison between strain and thermography intensity profiles

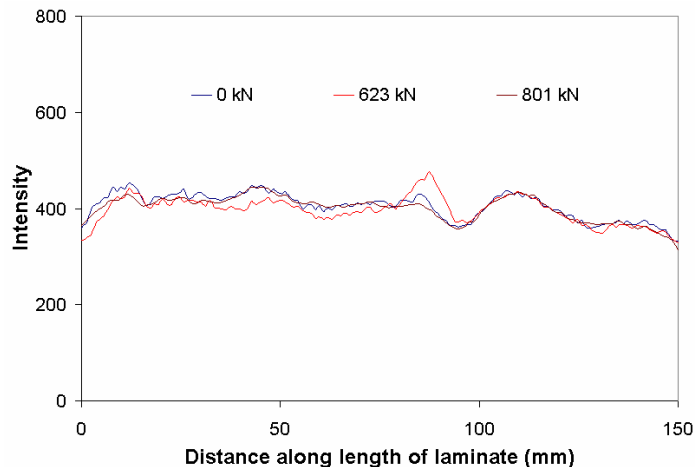


Figure 3.31 Thermal profiles along length of fabric laminate with loading

3.8.3 Correlation of Damage Progression to Strain Gage Data

Test specimens S2 and S3 were instrumented with 20 mm gage electrical resistance strain gages in order to monitor the strains in the composite laminates and strips, respectively, with the progression of loading. The axial strain profiles along the lengths of the longitudinal composite laminates/strips in specimens S2 and S3 are presented in Figures 3.14b and 3.15b, respectively. In slab 3, a significant increase in the axial strain in longitudinal composite strip 1 could be observed to occur at a load of 801 kN (180 kips) at the strain gage location at -205 mm (-8 ") from the centerline of the slab. The strain at this location increased from 1000 to 1800 micro-strains between 712 kN and 801 kN. This matched the 712 kN (160 kips) load stage at which the appearance of damage area in the composite was detected through thermographic inspection. Also the increase in strain measured by the gage located on longitudinal composite strip at 205 mm from the slab centerline at 801 kN was substantiated by the appearance of a major transverse crack at 190 mm (7.5") from the slab centerline and the detection of damage

areas through thermographic inspection at 712 kN in Zone 4 of longitudinal composite strip 1 (as shown in Figure 3.26). The debonding strain of the pultruded strips was estimated to be around 3200 microstrains from fracture energy based analysis. It is observed from the thermal profiles that the axial strain reached the debonding strain only at 712 kN thus explaining the appearance of major damage areas in the thermographic inspections at this load level. Since the composite strip 2 was not instrumented with strain gages no direct co-relation between the strain gage data and the thermography data could be obtained. However the thermal intensity profiles in this strip followed the general trend in terms of appearance of intensity peaks, as that of strip 1. Also the progression of the damage in terms of growth of debonded areas was evident in strip 2 (as illustrated in Figure 3.24). It is to be noted that thermography inspection data indicated the initiation of damage areas, which were found to correspond well with the locations of the main cracks. However, apart from the one location in strip 2, progression of these damage areas were not too evident since even at the final load levels of inspection, the strains in the composite strips were below the debonding strains, as are indicated by the strain profiles in Figure 3.14 and 3.15. The debonding strain was exceeded only at the localized areas near the cracks, resulting in the initiation of damage/debonds that was detected by the thermographic inspections as areas with higher thermal intensities than the surrounding. Also the damage areas were found to appear in the inspections between 623 kN and 712 kN.

The debonding strains of the 1-layer and 2-layers carbon fabric laminates in slab 2 were predicted to be around 4800 and 3200 microstrains, respectively, through fracture energy analysis. From the strain gage data of S2, the strains in the composite were found

to be below this level at 801 kN (180 kips), as shown in Figure 3.14. This, along with the effective control of crack widths in specimen S2, due to higher composite reinforcement ratio as compared to S3, explains why no major damage areas were observed in the composite laminates from the thermography inspections at these load levels.

3.9 Comparison of Predicted and Experimental Results

The unstrengthened specimen, S1, was predicted to have a punching shear capacity between 425 kN (96 kips) and 583 kN (131 kips), depending on the angle of the failure plane varying between 38° [58] to 45° [57]. The flexural capacity at steel yield was also predicted to be 512 kN (115 kips) from theoretical sectional capacity analysis. The design predictions for the capacities of the test specimens were presented earlier in section 3.4 of this chapter. All the capacity predictions were based on the use of an “effective” modulus of concrete of 28.6 GPa (4150 ksi) and corresponding “effective” concrete compressive strength of 36.56 MPa (5300 psi), as described in section 3.4. The specimen was found to fail in punching shear failure mode at a load of 501 kN (112.6 kips), which was within the range of predicted shear capacity values and indicated the occurrence of a failure plane at an angle between 38° and 45° . Moreover, the plateau in the load deflection response (Figure 3.10) of the specimen following shear failure indicated yielding of the internal steel reinforcement as predicted to occur at 512 kN (115 kips). The crack pattern noted at the bottom and over the cross-section of the specimen around the loading contact area was presented in Figure 3.12. It was observed that in contrast to the constant failure plane angle around the load contact area, assumed in the AASHTO [57] and theoretical shear capacity formulations of un-cracked reinforced

concrete sections [58], the failure plane formed in an actual bridge deck slab might be governed by the locations of pre-existing cracks. In specimen, S1, the failure planes along the four edges of the load contact area were formed at approximate angles of 64° , 38° , 27° and 38° respectively, with the horizontal plane and all the failure planes after originating from the edges of the load contact area joined pre-existing cracks at the bottom of the slab. Equation 3.1 for determining shear capacity, as presented earlier, can be rewritten as follows:

$$V_n = 2 \left(b_1 + b_2 + \frac{2d}{\tan \theta} \right) \frac{d}{\tan \theta} f_t = A_{eff} f_t \quad \dots\dots\dots (3.13)$$

where, A_{eff} = Area described by intersection of the shear failure surfaces on the horizontal plane at distance d minus area of the load contact area. Thus for specimen, S1, with experimental shear capacity, $V_n = 501$ kN and the concrete tensile strength, f_t ,

$$\text{determined as, } f_t = \left(0.17 + \frac{0.33}{\beta_c} \right) \sqrt{f'_c} = \left(0.17 + \frac{0.33}{508/203} \right) \sqrt{36.56} = 1.825 \text{ MPa,}$$

$$A_{eff} = \frac{V_n}{f_t} = 0.27 \text{ m}^2 \text{ (3 sq. ft).}$$

From the crack pattern at the bottom of the specimen of thickness 156 mm ($6\frac{1}{4}$ " (Figure 3.12), the shear failure plane was found to enclose an area of 901 mm x 584 mm (36 " x 23 "), which corresponds to 817 mm x 502 mm (32.2 " x 19.8 ") at a distance d of 122 mm (4.8125 "). For the load contact area of 508 mm x 203 mm (20 " x 8 "), the effective area was obtained as,

$$A_{eff} = (0.817 \times 0.502 - 0.508 \times 0.203) = 0.3 \text{ m}^2 \text{ (3.2 sq. ft), which matched closely with the effective area of } 0.27 \text{ m}^2 \text{ (3 sq. ft), predicted from the experimental shear capacity.}$$

Thus, the validity of the shear failure surfaces and the use of an “effective” concrete modulus to predict the capacity of the specimen, which took into account the stiffness and boundary conditions, were justified.

For specimen S2, rehabilitated with site-impregnated carbon fabric laminate strips, the ultimate capacity was predicted to be 99.42 kN-m/m (22.4 kip-ft/ft), which was found to correspond to a concentrated load demand of 827 kN (186 kips) from the finite element model. This capacity was predicted for a top concrete strain of 0.003 and composite debonding strain of 3626 micro-strain. The experimental failure load was 862 kN (193.8 kips) with the maximum strain in the transverse composite strip of 3227 micro-strains. Thus both the capacity and debonding strain predictions were within reasonable levels of accuracy. The maximum strain in the 1-layer longitudinal composite strips was also predicted to be 4823 micro-strains, which corresponds well with the experimentally observed value of 4672 micro-strains.

The ultimate moment capacity of specimen S3, rehabilitated with the carbon fiber pultruded strips, was estimated to be 81.7 kN-m/m (18.4 kip-ft/ft), which was found to correspond to a concentrated load demand of 680 kN (153 kips) from the finite element model. This capacity was predicted for a top concrete strain of 0.003 and composite debonding strain of 3260 micro-strain. The experimental failure load was 791 kN (177.8 kips) with the maximum strain in the transverse composite strip of 4274 micro-strains. The capacity prediction for this specimen was off by about 15% and this was because of use of a lower debonding strain in capacity prediction than was actually observed during the test. The debonding strain predictions using Niu and Wu’s model [18] were obtained for interfacial fracture energy, G_f , values from independent tests of similar composite

samples and thus might not be fully representative of the bond conditions of the composite in the test specimens. However the model was found to give a good initial estimate of the debonding strain in the absence of other experimental data. These predictions were also found to be closer to experimental strain levels than the debonding strain estimates by ACI-440 [3].

3.10 Correlating Test Specimen to Bridge Deck Capacity

The final objective of the component level study was to predict the capacity of the actual bridge deck from the test capacities of the components. As discussed previously in this chapter, the test specimens mimicked the behavior of the bridge decks in terms of load transfer mechanism and the moment contours matched closely around the loading contact area. However, the longitudinal edges of the test specimens being supported all along its length on steel rollers, could not simulate the flexible behavior of the longitudinal girders to which the load was transferred to from the actual bridge decks. Moreover the smaller clear span length of 1.07 m (42") in the component test specimens, as compared to 1.85 m (73") for the bridge decks, resulted in higher stiffness for the test specimens. As a result the test specimen was able to carry a higher load as compared to the bridge deck. Thus it became necessary to determine the equivalent capacities of the bridge decks based on local-to-global modeling by taking into account the effects of the boundary conditions. It is to be recognized that since the behavior of both the test specimens and the bridge decks were governed by similar failure modes, an equivalent capacity could be achieved based on attaining equivalent failure modes.

For the unstrengthened test specimen, S1, failure was governed by localized punching shear, which was caused by the opening of cracks defined by the shear failure plane when the stress exceeded the tensile strength of concrete. Thus the equivalent capacities between the test specimen and the bridge deck was determined based on the load demands necessary to cause equivalent stress profiles in the potential failure zone. The failure perimeter for typical punching shear was assumed to be defined by the failure plane formed at an angle of 38° [17] initiating from the perimeter of the load contact area of 203 mm x 508 mm (8" x 20"). The corresponding shear cracks, as illustrated in Figure 3.32, were formed at 453 mm (18") and 301 mm (12") from the centerline of the slab in the transverse and longitudinal directions, respectively.

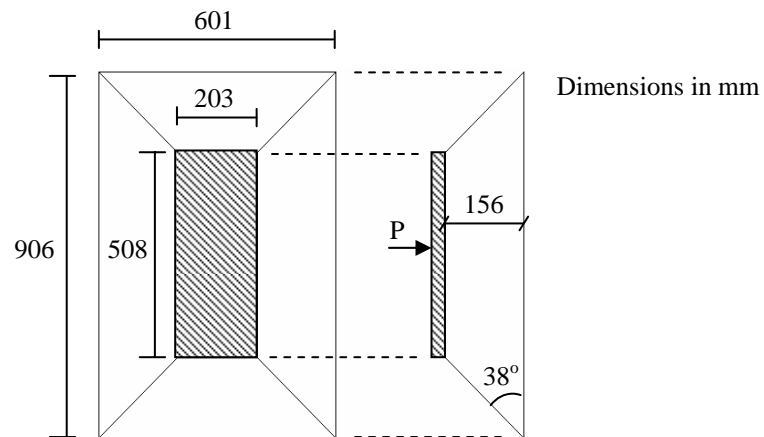


Figure 3.32 Theoretical punching shear failure perimeter in slab S1

The stress profiles along this perimeter for the ultimate test punching load of 501 kN (113 kips), applied over the load footprint area, were obtained from the finite element model of the test specimen. The load necessary to cause equivalent stresses along a similar perimeter area in the bridge deck, with the footprint wheel load being applied at

the center of the deck, was obtained as 222 kN (50 kips) from the finite element model of the bridge deck frame. Thus, the un-rehabilitated bridge deck was predicted to have a theoretical load capacity of 222 kN (50 kips), which when complemented with the strength reduction factor of 0.9, live load factor of 1.7 and impact factor of 1.3, resulted in a design capacity of 90 kN (20 kips). Thus the deck slab capacity failed to satisfy the permit truck-load demand of 107 kN (24 kips), as specified by California BDS [53]. This justified the rehabilitation of the bridge decks with externally bonded FRP composite strips to satisfy the current load demand criterion.

A similar approach was adopted to determine the equivalent capacity of the rehabilitated bridge decks. The governing failure mode in these specimens was determined from the load-deflection history (Figure 3.10) and strain profiles (Figures 3.14 to 3.15) in the composite strips. The axial strain profiles in the longitudinal strips were found to remain below the predicted debond strain levels since the primary load transfer in the slab is in the transverse direction. The transverse composite strips in the middle of the test specimens, S2 and S3, were found to reach the debond strain levels. The interesting feature noted from the strain profile was that in the initial stages of loading the strain in the middle of the strip was higher than at other locations along the length of the strip. This is an indication of flexural behavior of the rehabilitated specimens with better distribution of load over a large area as indicated also by the load-deflection plots (Figure 3.11). However beyond 534 kN (120 kips) the axial strains at the end of the strip start to pick up and gradually the strains all along the strip even out. From the crack pattern (Figure 3.13) the perimeter of the main crack was observed to be at 457 mm (18") from the slab centerline in the transverse direction. It was concluded that at the

higher stages of loading as these cracks started to open up, the high stress concentrations at locations of the composite strips overlapping these cracks cause localized debonding of the strips. The debond areas then progressed along the length of the composite strips with increase of loading. This explains the pickup of strains at the end of the strip close to the primary cracks and was corroborated by the thermography inspections. Thus the areas in the transverse composite strips traversing the primary cracks defined the potential failure zone in the rehabilitated specimens. The equivalent capacity of the rehabilitated bridge decks were thus obtained from the load required to produce equivalent stress profiles in the potential failure zones of the composite strips. Specimen S2, a component from the deck rehabilitated with site-impregnated carbon fabric laminate strips, had a test failure capacity of 862 kN (194 kips). Specimen S3, a component from the deck rehabilitated with prefabricated pultruded carbon composite strips with a lower strengthening ratio as compared to S2, had a failure capacity of 791 kN (177 kips). The stress profiles produced by these failure loads in the intersection regions of the composite strips with the primary cracks were determined from the FEM and on matching them with those obtained from the FEM of the bridge deck resulted in equivalent capacities of 404 kN (91 kips) and 370 kN (83 kips) for bridge decks rehabilitated with carbon fabric laminate and prefabricated pultruded strips, respectively. Using the strength, live load and impact reduction factors of 0.9, 1.7 and 1.3, this corresponded to design wheel load capacities of 165 kN (37 kips) and 150 kN (33 kips), respectively and thus satisfied the permit wheel load demands. The capacities of the test specimens and predicted capacities of the actual bridge deck slabs are presented in Table 3.2.

Table 3.2 Predicted and experimental failure Loads for test specimens and bridge slabs

Specimen Description	Predicted failure load (kN)	Experimental failure load (kN)	Predicted design failure load of the bridge deck slabs (kN)
S1, unstrengthened control	425 ¹ to 583 ²	501	90
S2, strengthened for permit load, using carbon fabric	827 ³	862	165
S3, strengthened for punching shear, using prefabricated carbon/epoxy strips	680 ⁴	791	150

¹ Shear failure plane angle, $\theta = 45^\circ$

² Shear failure plane angle, $\theta = 38^\circ$

³ Capacity prediction corresponding to $\varepsilon_C = 0.003$ and $\varepsilon_{FRP} = 3626 \mu\text{s}$

⁴ Capacity prediction corresponding to $\varepsilon_C = 0.003$ and $\varepsilon_{FRP} = 3660 \mu\text{s}$

Note: The theoretical failure loads were reduced by a strength factor, $\phi = 0.9$, live load factor of 1.7 and load impact factor of 1.3 to get design failure loads.

3.11 Research Extension to the Systems Level

This study was conducted only at the component level in that it studied the effectiveness of FRP composites in strengthening RC structural components, namely deficient deck slabs. As was discussed in the literature review in chapter 2, the strengthening of only a component can change load distribution and result in changes in the overall structural performance at the system level. There is always a concern that a change to an isolated structural component can result in unintended consequences to

adjoining components. At the component level tests, the boundary conditions and specimen geometry were found to play a significant role. Thus it is necessary to isolate these effects by conducting a system level test so that the actual field performance of the component slabs and girders in a slab-girder bridge system could be studied. Also it was of interest to see if NDE techniques could be used to identify the shifts in damage localization, overall response and quantification of damage progression caused by these subsequent modifications to the structure, so that the true structural response could be modeled based on the current state of damage. This necessitated the extension of the research at the component level to the systems level so that the effectiveness of FRP strengthening on the overall structural performance and the progression of damage at the systems level due to the strengthening of individual components could be studied. The findings of the research at the systems level are presented in the subsequent chapters.

Portions of this chapter are reprints or has been submitted for publication of the material as it appears in the following publications:

- i) Evaluation of Strengthening through Laboratory Testing of Rehabilitated Bridge Decks after In-Service Loading, In Press, Journal of Composite Structures
- ii) A Critical Review of Infrared Thermography as a Method for Non-Destructive Evaluation of FRP Rehabilitated Structures, International Journal of Materials and Product Technology, Vol. 25, No. 4, 2006, pp. 241-266.

The dissertation author was the primary investigator of these papers.

4 EXPERIMENTAL PROGRAM

4.1 Introduction

Most of the research and in-field applications of FRP composites for the rehabilitation/strengthening of reinforced concrete structures have looked at the effectiveness of such strengthening at the component level. This includes evaluation of the strengthening of reinforced concrete slabs [15, 45, 52, 56] as well as shear strengthening of longitudinal girders [20, 21, 26] with externally bonded FRP composites. However very little of the research to date has focused on the effect of strengthening of a component on the overall structural performance at the systems level and changes in load distribution and load paths caused by such structural modifications. After review of the reinforcement details used in some typical RC slab and girder bridge deck systems, it was observed that the longitudinal girders of the deck system have reinforcement details such that they will have sufficient reserve capacity at the load level where the deck slabs would reach their critical limit state, usually in terms of punching shear capacity. Hence most of the damage at the initial load levels will be concentrated in the deck slabs with the longitudinal girders having little or no damage. Thus the general trend will be to strengthen only the deck slabs with FRP composite strips bonded to the bottom surface of the slabs often resulting in a configuration wherein a thin stiffened slab is supported between more flexible girders and diaphragms. However after the slabs are strengthened, the bridge deck will be able to withstand higher loads and this will increase the load demands on the longitudinal girders. An effective punching-shear strengthening scheme in the slabs will reduce the opening of cracks and very little damage will occur in the slabs at these load levels until the composite

strips reach debonding strain levels. Thus most of the damage will be localized in the un-strengthened longitudinal girders and depending on the section and reinforcement details will push them towards flexural or shear criticality before the full capacity of the strengthened deck slabs can be reached. The girders would thus require strengthening to result in full utilization of the enhanced capacity of the deck slabs.

In addition most of the current research looks at the short-term effectiveness of the composite materials. The widespread application of these materials for strengthening of RC structures is contingent to some extent on a more reliable and comprehensive knowledge of the long-term behavior of these materials under realistic field conditions simulating the effects of cyclic loading and environmental exposures and prediction of the debonding failure mode based on the quality and integrity of the bond to concrete. Periodic Non-Destructive Evaluation (NDE) of rehabilitated structures can not only help to ensure public safety through assessment of installation quality and monitoring the performance of the structure through detecting the appearance or growth of damage/defect areas but also help to gather long-term information on the performance and behavior of these new construction materials in realistic field conditions. Thus it is of interest to see if NDE techniques can be used to identify the shifts in damage localization, overall response and quantification of damage progression caused by these subsequent modifications to the structure, so that the true structural response can be modeled based on the current state of damage.

4.2 Research Objectives

Evaluation of in-field performance of FRP composites and assessment of effectiveness of specific NDE techniques of IR Thermography and Modal testing were

carried out at the component level as part of initial field study and was described in the previous chapter. The component level study indicated the need for assessment of FRP strengthening at the systems level and this led to the development of the test program in which a three-girder two span reinforced concrete bridge deck segment was constructed and tested under field representative loading conditions. The objectives of the research were as follows:

- i) To evaluate the systems level effect of FRP composite strengthening of structural components through sequential and systematic strengthening of the components of the test specimen and to determine if this results in any unintended consequences on other components of the system.
- ii) To monitor the progression of damage within the components (namely the deck slabs and longitudinal girders) and then between the components of the system with their sequential strengthening with FRP composite. The monitoring of damage progression was carried out through instrumentation of the test specimen with linear potentiometers and strain gages as well as non-destructive evaluation (NDE) using Modal Testing and Infrared Thermography.
- iii) To evaluate the effectiveness of Modal Testing and IR Thermography as global and local NDE techniques, respectively, for quantitatively monitoring the progression of damage in and between the components of the system. These NDE results are correlated to the structural performance as obtained from the load capacity and strain/displacement profiles.

- iv) To develop a methodology for composite strengthening design at the systems levels such that rather than treating composite strengthening as a patch repair technique the design should take into account the overall structural response.

4.3 Description of Test Specimen

The test specimen was a three-girder two span bridge deck segment with center-to-center distance between the longitudinal girders of 1.68 m (5.5 feet) and total longitudinal span length of 3.6m (12'4"). An overhang of 607 mm (24") was also constructed on either side of the longitudinal edge girders to simulate the flange region of the external girders and to simulate continuity of the deck slabs over the girders. The slab thickness was 152 mm (6") which was representative of deck slab depths in the field. The girders had a total depth (including the slab flange) of 559 mm (22") and a width of 203 mm (8"). The main transverse reinforcement in the slabs consisted of #5 bars spaced at 203 mm (8") center-to-center and the main longitudinal reinforcement consisted of #5 bars spaced at 406 mm (16"), which resulted in a longitudinal to transverse reinforcement ratio of 2. This design simulated pre-1970 designs of slab-girder bridges in which typically a transverse to longitudinal reinforcement ratio of 2 was also used. This was observed in the slab sections cut-off from the Watson Wash Bridge [56, 62] in which, as described in the previous chapter, the transverse reinforcement consisted of #5 rebars spaced at 140 mm (5.5") and the longitudinal reinforcement consisted of #5 rebars spaced at 280 mm (11"). However the spacing of the main transverse reinforcement in the test specimen was chosen to be about 1.5 times larger than the spacing of pre-1970 representative bridge deck [203 mm (8") as compared to 140 mm (5.5")] to cause a

reduction of the maximum positive moment capacity of the slabs in the test specimen with respect to a typical pre-1970 bridge deck slab at construction by about 30%. This was done to take into account the lower concrete strengths used in pre-1970 design and construction of bridges as well as to take into account the degradation of such existing deck slabs over time caused by environmental exposure and continued traffic loading. It should be noted that a transverse to longitudinal reinforcement ratio of 2 along with ratio of longitudinal span length to distance between the longitudinal girders greater than 2 in typical existing slab-girder bridge decks would result in one-way load transfer mechanism, in which the load from the slabs would be transferred directly to the longitudinal girders and thereby to the abutments. For the girders, #9 and #11 bars were used for the longitudinal reinforcement and #3 bars were used for the stirrups. The overall dimensions of the test specimen are presented in Figure 4.1 and the reinforcement details are presented in Figure 4.2. The specific stirrup spacing, as presented in Figure 4.3 and high longitudinal reinforcement ratio were used in the girders to simulate shear deficiency in the middle girder. The design for the stirrup spacing will be discussed later in this chapter. A closer stirrup spacing of 76 mm (3") was used near the support regions of the middle longitudinal girder to avoid an undesirable premature local failure in this region. This was because the test specimen was supported on load cells placed at each end of the girders and the shear demand was highest at these locations. However in the case of shear strengthening of the middle longitudinal girder with externally bonded U-shaped FRP composite stirrups, the presence of the load cell below the girder at the support makes it impossible to use a continuous U-stirrup to wrap around the web of the beam at the support locations. Thus the closer internal steel stirrup spacing of 76 mm (3")

was used at the support so that the shear capacity at the support even without the composite strengthening was higher than the maximum design shear demand. The longitudinal reinforcement was kept similar in all the three girders to ensure that none of the girders would fail in flexure. However on account of lower shear demand on the edge girders a uniform stirrup spacing of 305 mm (12") was used. Grade 60 steel was used for all the reinforcing bars. The stress-strain data of the reinforcing steel used for the test specimen is presented in Table 4.1.

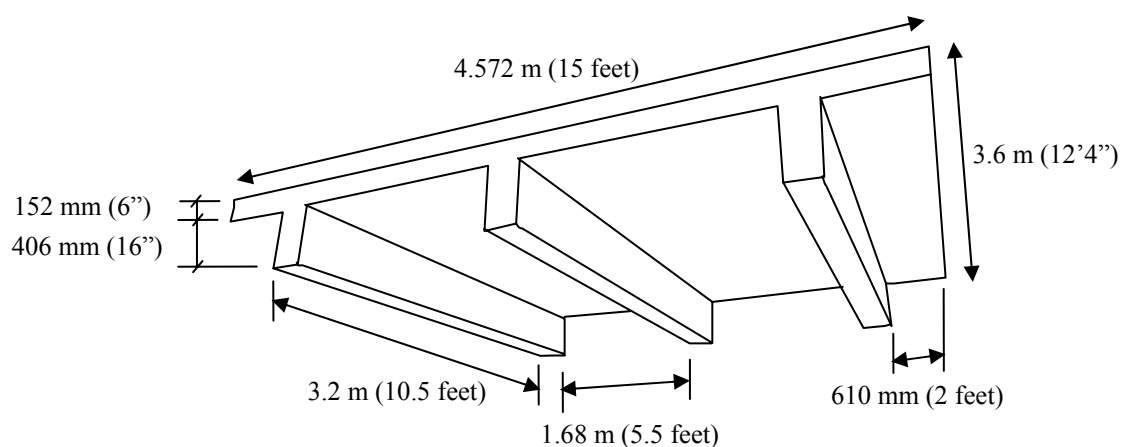


Figure 4.1 Overall dimensions of the test specimen

The form for the specimen was built on the floor and the reinforcement with the details discussed was laid out such that a clear cover of 25 mm (1") was maintained (Figure 4.4a). The specimen was then cast in place with a designed concrete strength of 28 MPa (4000 psi) and the construction procedure was kept as close to field practices as possible (Figure 4.4b). However the concrete batch provided by the supplier resulted in ultimate strength around 44 MPa (6390 psi) as measured at the end of test phase. The strength development plot of concrete, as obtained from periodic testing of cylinders made during construction of the specimen, is presented in Figure 4.5.

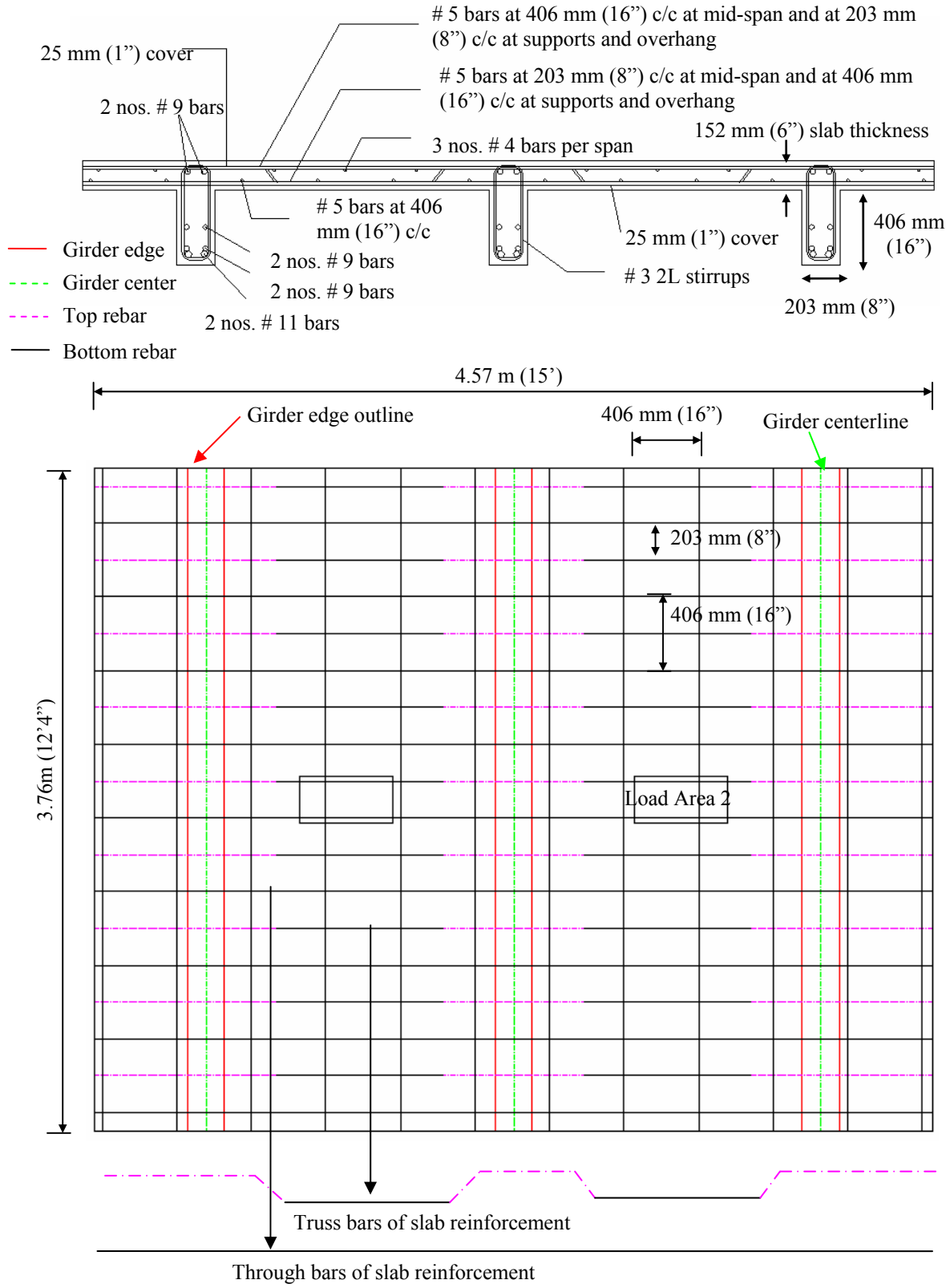


Figure 4.2 Reinforcement details (Cross-section and plan view) of the test specimen

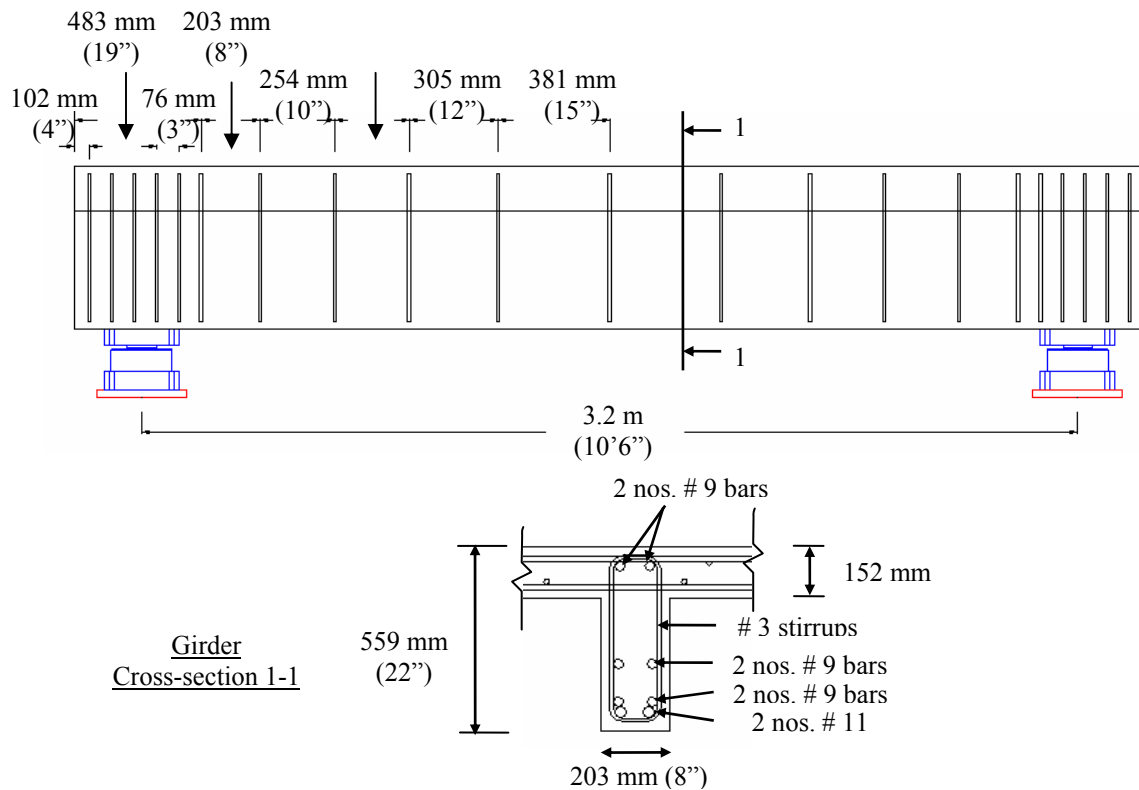


Figure 4.3 Internal steel stirrup details in middle longitudinal girder

Table 4.1 Performance characteristics for reinforcing steel

Rebar Type	Avg. Yield stress, f_y	Avg. Yield Strain, ϵ_y	Avg. rupture stress, f_u	Avg. rupture Strain, ϵ_u
# 3	474 MPa (68.70 ksi)	0.002714	741 MPa (107.51 ksi)	0.178891
# 4	452 MPa (65.53 ksi)	0.002406	725 MPa (105.10 ksi)	0.192918
# 5	458 MPa (66.50 ksi)	0.002568	748 MPa (108.47 ksi)	0.187311
# 9	490 MPa (70.98 ksi)	0.003042	696 MPa (100.90 ksi)	0.175413
# 11	460 MPa (66.73 ksi)	0.002484	772 MPa (112.03 ksi)	0.104539



(a) Construction of specimen formwork



(b) Pouring of concrete and finishing of specimen surface

Figure 4.4 Construction of test specimen

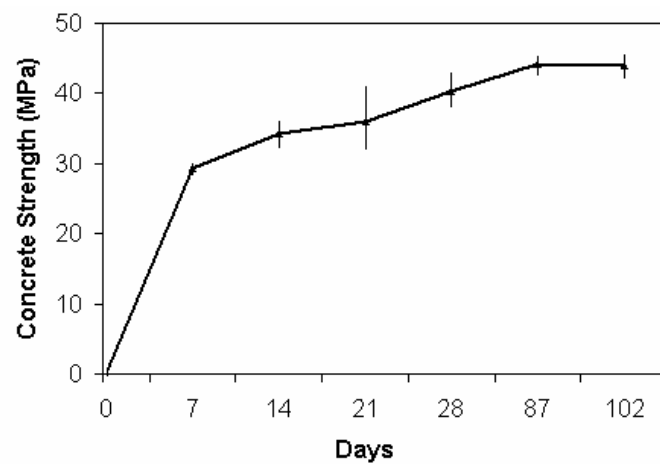


Figure 4.5 Strength development plot for concrete

4.4 General Test Plan

The test was planned to be carried out in three phases. Phase 1 involved loading to initiate cracking in the slabs and to cause them to reach a predetermined level of damage. This level was chosen as 75% of yield strain in the transverse steel reinforcement in the slab below the load area predicted to occur at 339 kN (76.2 kips) (the design prediction will be presented in the next section) or 75% of the punching shear capacity of the slabs predicted to occur at 415 kN (93 kips) (the design prediction will be presented in the next section), whichever was reached first. Such a load level was deemed to be representative of deterioration in the deck slab that would warrant rehabilitation/strengthening of the slabs with externally bonded FRP composites to prevent further degradation and premature failure. However, at this level of loading, the girders would not reach critical capacities in flexure or shear and thus would not need any strengthening (the middle longitudinal girder with the specified internal steel stirrup spacing was predicted to reach shear criticality when the strain in the stirrups exceeded 75% of yield strain, which was estimated to occur at 490 kN or 110 kips). It was anticipated that the deck slabs would be strengthened with two different composite strengthening schemes, namely prefabricated carbon pultruded strips and site-impregnated carbon fabric laminates, to check the relative effectiveness of the two systems.

Phase 2 involved loading the specimen to initiate shear criticality in the center longitudinal girder, which as defined earlier, was predicted to be reached at 75% of yield in the internal steel stirrups estimated to occur at 490 kN (110 kips). The girder was then designed to be strengthened with externally bonded CFRP composite U-wrap stirrups with fiber composite anchors. The shear strengthening of the girder would allow the deck system

to resist higher load levels and Phase 3 involved further loading of the test specimen until the strengthened slabs reached their enhanced flexural capacity governed by debonding of the composite strips and ultimate failure of the test specimen due to punching shear failure of the deck slabs. The progression and localization of damage in the deck slabs and the girder was assessed using NDE techniques at beginning and end of each phase as well as at intermediate load levels. The general test plan with the critical limit states governing each phase of testing is presented in Table 4.2.

Table 4.2 Test phases

Test phase	Purpose	Limit state
1	Reached flexural/punching shear criticality in deck slabs and strengthened only the slabs in flexure with FRP composite	75% of yield strain in the transverse steel reinforcement in the slab below the load area or 75% of the punching shear capacity of the slabs, whichever was reached first
2	Reached shear criticality in center girder and strengthened girder in shear with FRP composite stirrups	75% of yield strain in the internal steel stirrups of center girder
3	Ultimate failure of strengthened deck slabs	Debonding of composite in the strengthened slabs followed by punching shear failure

4.5 Initial Analytical Modeling and Design

The slab reinforcement was chosen to be representative of typical existing pre-1970 slab-girder bridge decks with approximately 25% reduction in the area of steel reinforcement to take into account the expected degradation over time of the deck slab under traffic loading and environmental exposure. The general geometry of the test specimen was also guided by the geometry of the Watson Wash bridge deck system [56, 62]. The flexural and punching shear capacity of the deck slabs were computed using available analytical models and end of stage 1 loading was defined based on the limit

state presented in Table 4.2. The internal steel stirrup spacing of the center girder was designed such that it would have sufficient reserve shear capacity at the end of stage 1 of loading but would become susceptible to shear criticality under the higher load demands imposed by the strengthened slabs. The strengthening schemes of the deck slabs with the two composite systems were designed based on the criteria of having a strength enhancement ratio of 2. It has been indicated in literature [5, 63, 64] that externally bonded FRP composite reinforcement can increase the overall flexural strength of a RC member from 10 to 160%. Thus for the test specimen, as an initial design parameter, the strength enhancement was chosen to be 100% which would also allow a sufficient design window for the girder to reach shear criticality before failure of the strengthened deck slabs. The flexural strength of the strengthened slabs was defined by the limit state corresponding to reaching debonding strain in the composite strips and/or crushing strain in concrete. The design of the strengthening scheme was also based on the second criteria of having the strain in the externally bonded FRP composite within reasonable bounds to restrain the opening of the cracks in the deck slabs to avoid premature punching shear failure. The end of stage 2 loading was defined to be achieved when the internal steel stirrups in the middle girder reached 75% of yield strain indicating shear criticality. The shear strengthening of the girder with externally bonded FRP composite U-stirrups was designed so that the shear capacity of the strengthened girder would be higher than the shear demand under the wheel load at which the strengthened deck slabs would reach their ultimate capacity at the end of stage 3 loading. The details of the design steps will be discussed in subsequent sections of this chapter.

The capacity estimates were based on design oriented sectional analysis, taking into account the non-linear material properties, corresponding to achieving pre-defined limit states [65]. The load demands necessary to make the member in the test specimen reach the corresponding capacity were determined using a simplistic linear-elastic finite element model, since the moment demand is primarily a function of the specimen geometry. 8-noded 3-D solid elements were used to generate the model as presented in Figure 4.6. The girders were supported at the ends with center-to-center distance in the longitudinal direction of 3.2 m (10.5 feet). At the supports roller conditions were used in the vertical and longitudinal directions simulating a simply supported boundary condition. However to restrict movement in the transverse direction to simulate the effect of diaphragms between girders, hinge conditions were used that allowed rotation but no transverse movement.

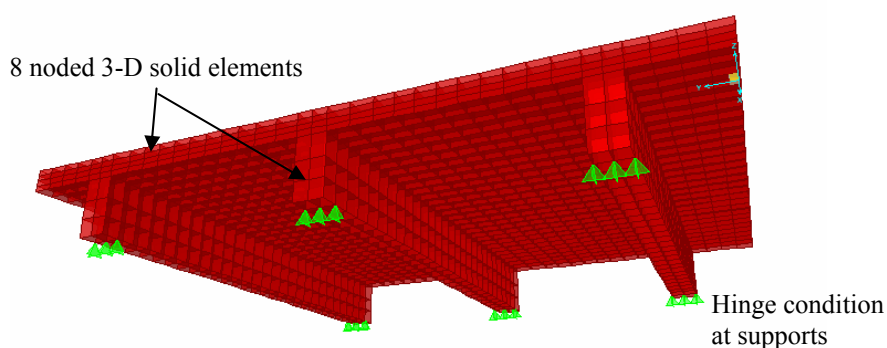


Figure 4.6 Finite element model

Truck wheel loads over a tire contact area of 508 mm x 254 mm (20" x 10"), as is specified by AASHTO [57], was simulated by pressure loads applied on the deck slabs as illustrated in Figure 4.7. The loads were applied at the longitudinal mid-span of the

specimen with center-to-center distance in the transverse direction of 1.83 m (6 feet). This simulated the axle distance specified by AASHTO [57] for a truck wheel load. The moment contours over the test specimen model could thus be obtained for iterative pressure loads (Figure 4.7) and were compared to the corresponding moment capacities predicted for the test specimen through analytical models at specific load stages. The pressure load at which the moment demand matched the moment capacity was taken as the predicted wheel load demand on the test specimen to reach the desired limit state at each stage of loading.

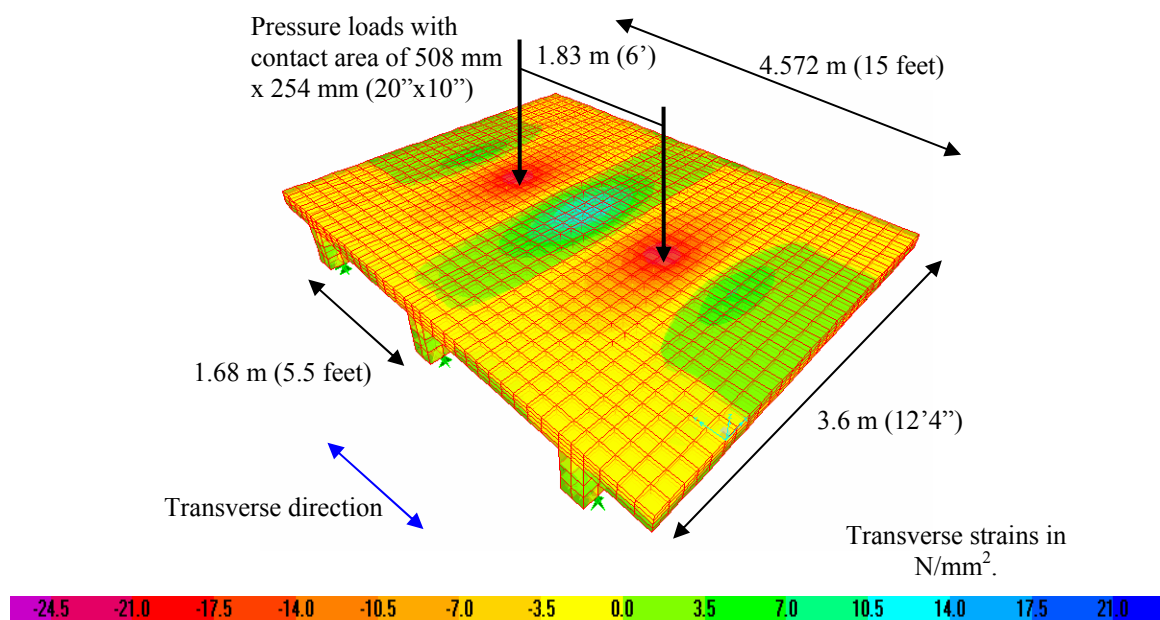


Figure 4.7 Transverse strain contours in model under simulated wheel loads

4.5.1 Design of Unstrengthened Components for Phase 1 of Test

4.5.1.1 Design capacity of deck slabs

The flexural and punching shear capacities of the deck slabs were computed to define phase 1 of loading. The flexural capacity of the deck slab was obtained through sectional analysis corresponding to the limit state at which the bottom transverse steel in the slab reached 75% of yield strain. For #5 rebars used for slab reinforcement, the yield strain as obtained through preliminary material tests was 2380 micro-strain. Thus for the limit state corresponding to reaching 1790 micro-strains (75% of yield strain) in the steel reinforcement and for the concrete compressive strength, f_c' , steel yield strength, f_y and effective depth, d (Figure 4.8), the transverse flexural capacity was computed as 38.4 kN-m/m (8.63 k-ft/ft). From the finite element model (Figure 4.7), the wheel load producing the stress contour for which the moment demand matched the computed moment capacity of 38.4 kN-m/m (8.63 k-ft/ft) was found to be 339 kN (76.2 kips).

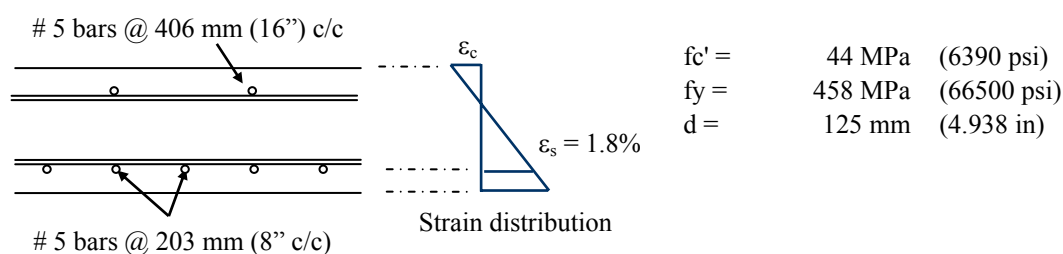


Figure 4.8 Parameters in sectional analysis for determination of flexural capacity

The punching shear capacity of the slabs, V_n , was determined from the equilibrium of forces given by:

$$V_n = 2 \left(b_1 + b_2 + \frac{2d}{\tan \theta} \right) \frac{d}{\tan \theta} f_t \quad \dots\dots\dots(4.1)$$

where, f_t = diagonal concrete tensile strength, (in MPa) = $\left(0.17 + \frac{0.33}{\beta_c} \right) \sqrt{f'_c} \leq 0.33 \sqrt{f'_c}$

and f'_c is the compressive strength of concrete (44 MPa or 6390 psi), b_1 is the short side of the concentrated load area (254 mm or 10”), b_2 is the long side of the concentrated load area (508 mm or 20” in this case), d is the average effective depth of the section (125 mm or 4.938” in this case) and θ is the angle between the horizontal and assumed failure plane.

The theoretical formulation for punching shear (equation 4.1) is equivalent to the AASHTO [57] prescribed equation for an angle of the failure plane, θ , being 45° . The corresponding punching shear capacity was determined using equation 4.1 as:

$$V_n = 2(254 + 508 + 2 \times 125) \times 125 \times \left(0.17 + \frac{0.33}{508/254} \right) \sqrt{44} = 554 \text{ kN (124 kips)}$$

The limiting wheel load for phase 1 from punching shear criteria, defined as 75% of punching shear capacity was 415 kN (93 kips). Thus the load limit for phase 1 was defined as 75% of yield strain in the slab transverse reinforcement predicted to be produced by wheel load of 339 kN (76.2 kips) or 75% of punching shear capacity predicted to be produced by wheel load of 415 kN (93 kips). Since these predicted loads were based only on initial simplistic estimate, close monitoring of the yield strains in the slab reinforcement and opening of punching shear cracks was carried out during the testing at every load cycle to ensure that the slabs did not go beyond these damage states.

4.5.1.2 Design capacity of unstrengthened girders

The internal steel stirrups of the girders were designed such that in the shear critical area near the supports they would reach 75% of their yield strain under application of 490 kN (110 kips) of wheel load. This load of 490 kN (110 kips) was in between the bounds of the predicted punching shear capacity of the unstrengthened deck slabs at 415 kN (93 kips) and the ultimate capacity of the FRP composite strengthened deck slabs predicted to be reached at 645 kN (145 kips) (as shown in the design estimates presented in the next section). Such a design isolated the primary failure modes in the three phases, namely damage in the deck slabs in phase 1, damage in the center girder in phase 2 and damage in the strengthened deck slabs in phase 3 of loading. The shear demand in the middle girder was computed for this wheel load demand of 490 kN (110 kips) from the FE model and is presented in Figure 4.9.

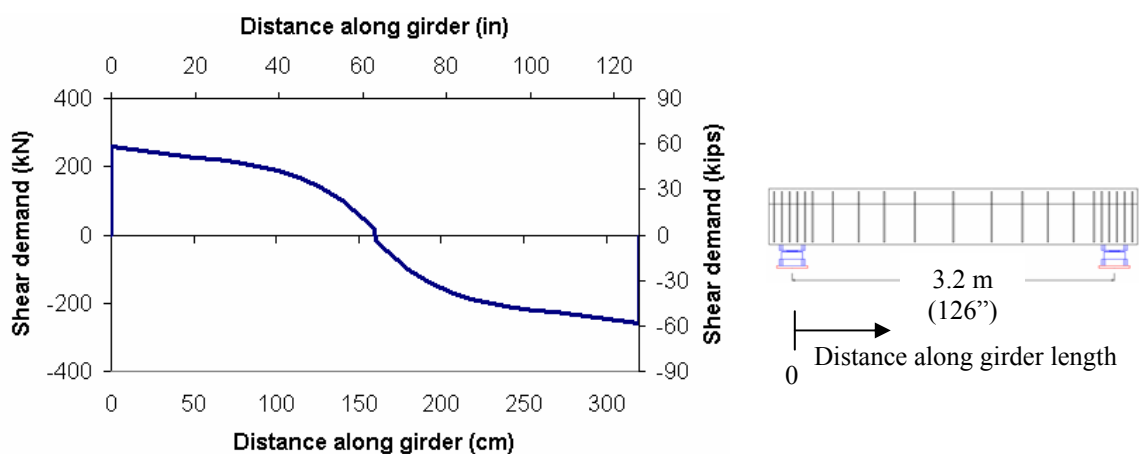


Figure 4.9 Shear demand on middle girder for phase 2 limit load

The shear capacity for different spacing of steel stirrups was obtained using design oriented analytical models [53, 57]. The shear resistance, V_n was calculated as:

$$V_n = V_c + V_s = 0.083\beta\sqrt{f'_c}bd + \frac{A_v f_y d (\cot \theta + \cot \alpha) \sin \alpha}{s} \quad (\text{In SI units}) \quad \dots\dots\dots (4.2)$$

V_c and V_s are the shear resistance contributions from concrete and steel, respectively.

b = effective web width (203 mm or 8")

d = effective depth of girder (489 mm or 19.25")

f'_c = compressive strength of concrete (44 MPa or 6390 psi)

A_v = area of shear reinforcement (2 legged #3 stirrups, 142 mm² or 0.22in²)

f_y = yield strength of steel shear stirrups (474 MPa or 68700 psi)

β = factor indicating ability of diagonally cracked concrete to transmit tension = 2

θ = angle of inclination of diagonal compressive stresses = 45°

α = angle of inclination of transverse reinforcement to longitudinal axis = 90°

To attain shear criticality in the center girder, a stirrup arrangement was chosen (Figure 4.3) so that the shear demand at 490 kN (110 kips) was bounded by the shear capacities at 75% yield and at full yield of the stirrups. This is presented in Figure 4.10. The stirrups were spaced closely near the support region to prevent any local failures and this is reflected in Figure 4.9 with high shear capacity for about 203 mm (8") from the support. From about 203 mm (8") to about 1.07 m (42") from the support, the shear demand was found to lie between the capacities at 75% and full yield of the stirrups and thus this represented the region on either side of the girder which was deficient in shear.

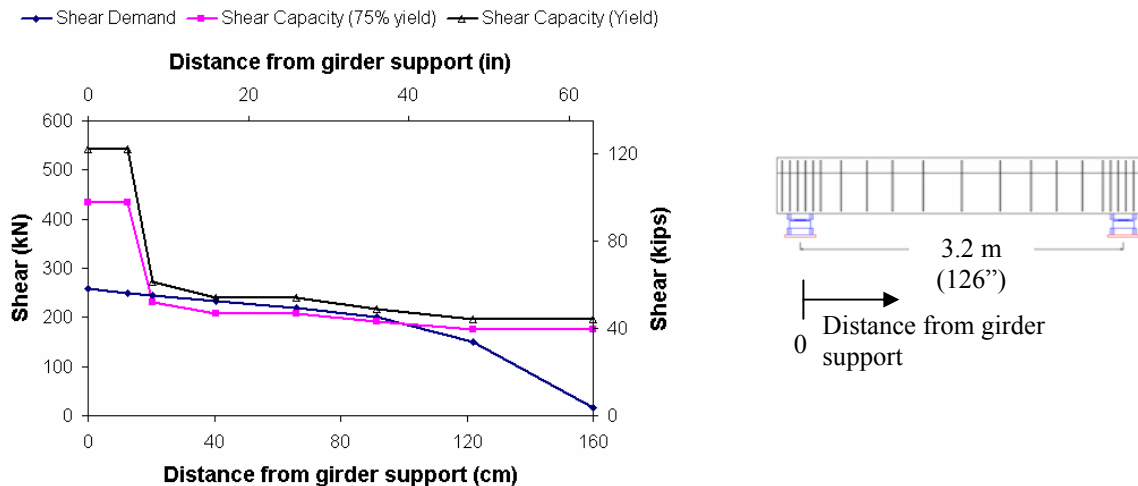


Figure 4.10 Shear demand vs. capacity on middle girder for phase 2 limit load

The shear demand on the external girders was much lower than that on the middle girder. For phase 2 limit load of 490 kN (110 kips), the maximum shear demand on the edge girder was 110 kN (24.7 kips) as compared to 258 kN (58.1 kips) on the center girder. A steel stirrup spacing of 305 mm (12") was found to be sufficient to meet the shear demand corresponding to the wheel load at which the capacity of the strengthened deck slabs was reached.

4.5.2 Design of Strengthened Deck Slabs for Phase 2 of Test

When the slabs reached the pre-defined damage state (Table 4.2) at the end of phase 1 of loading, they were strengthened with FRP composite. Two different strengthening schemes were used for the two deck slabs, namely, prefabricated carbon pultruded strips and site-impregnated carbon fabric laminates, to test for the comparative effectiveness of the two systems. Preliminary tension tests were conducted using test coupons cut-out from representative composite panels to determine the material

properties, such as strength, modulus and thickness, based on which the design of the strengthening schemes was done. The composite test panels were manufactured following the same procedure that was adopted later for installation of the composite systems onto the test specimen. A typical wet-layup process, as specified by the manufacturer, was followed for manufacturing the site-impregnated carbon fabric composite panels consisting of 1 layer, 2 layers and 3 layers of CFRP fabric. The manufacturing of these test panels is presented in Figure 4.11. The manufacturers also supplied 102 mm (4”) wide prefabricated carbon pultruded strips for preliminary material testing. The preliminary material properties of the fabric laminate and the pultruded strip systems, as obtained from the tension tests, are presented in Table 4.3. These properties were used for initial design estimates of the strengthened slabs. Separate test panels were also manufactured during the actual installation of the composite and those properties were used while comparing the test predictions to the experimental results.



Figure 4.11 Manufacturing of composite panels for preliminary material tests

Table 4.3 Preliminary material properties of FRP composite

Composite Type		1 layer fabric	2 layers fabric	3 layers fabric	Pultruded strip
Thickness Properties mm (inches)	Mean	1.67 (0.07)	3.13 (0.12)	4.20 (0.17)	1.37 (0.05)
	Std. Dev.	0.15 (0.01)	0.29 (0.01)	0.18 (0.01)	0 (0)
	COV	0.09	0.09	0.04	0
	Min	1.52 (0.06)	2.72 (0.11)	3.95 (0.16)	1.35 (0.05)
	Max	2.02 (0.08)	3.53 (0.14)	4.56 (0.18)	1.38 (0.05)
Strength Properties MPa (ksi)	Mean	717.40 (104.02)	692.50 (100.41)	588.86 (85.38)	2142.62 (310.68)
	Std. Dev.	88.70 (12.86)	112.01 (16.24)	43.87 (6.36)	221.50 (32.12)
	COV	0.12	0.16	0.07	0.10
	Min	515.24 (74.71)	535.91 (77.71)	527.73 (76.52)	1803.48 (261.5)
	Max	855.53 (124.05)	895.79 (129.89)	672.05 (97.45)	2672.34 (387.49)
Modulus Properties GPa (ksi)	Mean	46.01 (6671.84)	50.77 (7362.24)	53.14 (7705.35)	137.64 (19957.3)
	Std. Dev.	7.77 (1126.95)	7.88 (1142.63)	6.44 (933.26)	11.87 (1720.85)
	COV	0.17	0.16	0.12	0.09
	Min	35.00 (5074.57)	40.04 (5805.8)	43.45 (6299.67)	119.84 (17377.1)
	Max	59.36 (8607.35)	66.63 (9661.5)	62.05 (8996.96)	159.50 (23127.8)

Pull-off tests were also carried out to determine the bond performance of the composite systems. The FRP composite systems were bonded to concrete blocks, 305 mm x 178 mm x 76 mm (12" x 7" x 3") in size, using the corresponding manufacturer specified epoxy system (Figure 4.12a). Three 50 mm (2") diameter aluminum disks were bonded to the composite systems for each concrete block using a two-component epoxy adhesive. A drill-press operated hole-saw was used to core around the disks through the composite and into the concrete for a few millimeters to isolate the circular patch of composite to be tested. The disk was then pulled out using a pull-off tester and the average strength of the three pull-off tests from each concrete block was used to evaluate the bond performance. All the failures (Figure 4.12b) were in the concrete through and around aggregates indicating that the bond strength between composite and concrete was higher than the tensile strength of concrete and this was deemed to be acceptable bond

performance in terms of preliminary evaluation [66]. The pull-off strengths of the composite systems are presented in Table 4.4.



(a) Preparation of pull-off specimens

(b) Pull-off failures after tests

Figure 4.12 Pull-off test specimens

Table 4.4 Preliminary bond properties of composite

Composite Type	Pull-off Strength – MPa (psi)				
	Mean	Std. Dev.	COV	Min	Max
1 layer fabric	2.664 (386.36)	0.687 (99.60)	0.258	2.105 (305.32)	3.431 (497.56)
2 layers fabric	2.599 (376.94)	0.081 (11.77)	0.031	2.534 (367.51)	2.690 (390.13)
3 layers fabric	2.242 (325.11)	0.466 (67.55)	0.208	1.832 (265.74)	2.748 (398.61)
Pultruded strip	3.067 (444.78)	0.260 (37.64)	0.085	2.768 (401.44)	3.236 (469.29)

As presented in Table 4.4, the pull-off strengths for all tests were higher than 1.4 MPa (200 psi), which is the bare minimum pull-off strength specified by ACI-440 [3]. Also ACI-440 [3] specifies that for a strengthening scheme to be effective, the concrete substrate should have a minimum compressive strength, f_c' , of 17 MPa (2500 psi) and this requirement was also satisfied by the concrete that was used for the test specimen.

Based on all these preliminary evaluations, the composite systems were deemed to be suitable for strengthening the test specimen.

For both composite systems, fabric laminate and pultruded strip, the limit state defining the ultimate failure of the strengthened deck slabs was governed by debonding of the laminates/strips, since the computed debonding strain of the composite systems (presented later in this section) was lower than the rupture strain. Also in order for the composites to be effective in holding together the punching shear cracks before reaching the debonding strain level, the maximum spacing of the composite strips/laminates was defined by the punching shear crack spacing. Based on AASHTO [57] specifications, the theoretical punching shear failure plane was assumed to diverge away from the load contact area towards the bottom of the slab at an angle of 45° , as illustrated in Figure 4.12. Previous research [58] as well as results from component level tests as described in the previous chapter had shown that the punching shear failure planes would follow a shallower angle which would result in larger crack spacing and thus the predictions as per [57] were treated as a conservative assumption for determining maximum spacing for the composite strips/laminates. The primary punching shear cracks were predicted to trace out a theoretical punching shear failure perimeter of 559 mm (22") x 813 mm (32") as shown in Figure 4.13. Thus for the strengthening to be effective in preventing the punching shear failure, the maximum spacing of the transverse strips/laminates was defined as 559 mm (22") and that for the longitudinal strips/laminates was defined as 813 mm (32").

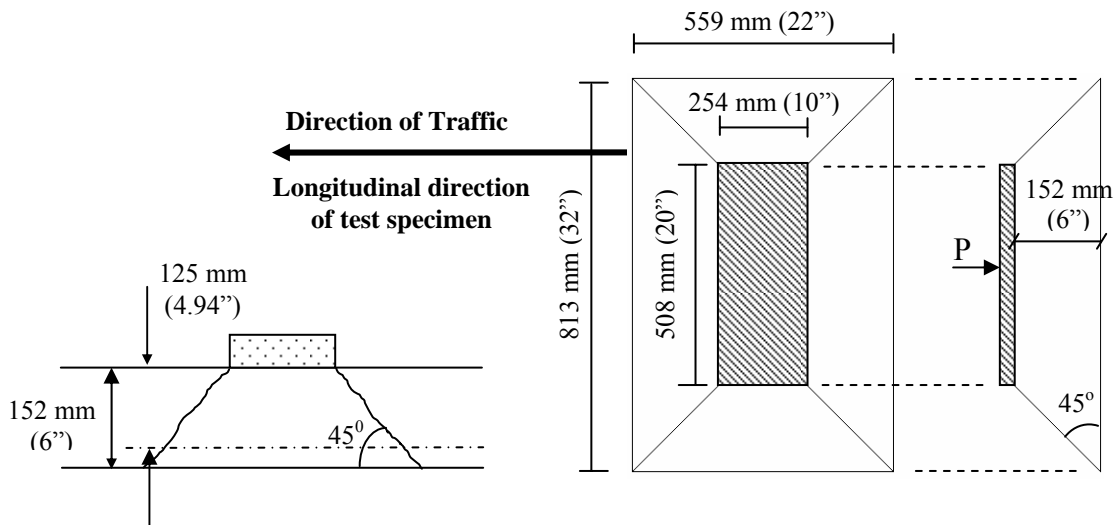


Figure 4.13 Theoretical punching shear failure perimeter

The flexural capacity of the strengthened slabs was computed by sectional analysis for different combinations of spacing, width and number of layers of composite. The internal steel and composite properties used were defined in Tables 4.1 and 4.3. The limit state used for the analysis was reaching debonding strain of the composite which was estimated using an energy based procedure [11], in which the maximum axial force in the composite at debonding was obtained as,

$$P_{max} = b_1 \sqrt{2G_f E_1 t_1} \dots\dots\dots(4.3)$$

where, E_1 , t_1 and b_1 are the elastic modulus, thickness and width of FRP, respectively.

The corresponding maximum debonding strain in the composite was obtained as,

$$\epsilon_{max} = \frac{P_{max}}{t_1 b_1 E_1} \dots\dots\dots(4.4)$$

The material properties were obtained from the tension tests, the results of which were presented in Table 4.3. G_f is the interfacial fracture energy given by the area of the

$\tau - \delta$ curve obtained from shear peel tests of the composite samples and were computed to be 0.976 N/mm (5.6 lb/in) for the site-impregnated 2-layer carbon composite laminates [59] and 1.2 N/mm (6.85 lb/in) for the 1-layer pultruded carbon composite strips [60].

For the site-impregnated 2-layer carbon composite laminates, with E_l , t_l , b_l and G_f being 50.77 GPa (7362.24 ksi), 3.13 mm (0.12"), 152.4 mm (6") and 0.976 N/mm (5.6 lb/in), respectively, the maximum axial force in the composite at debonding was obtained using Equation 4.3 as,

$$P_{\max} = b_l \sqrt{2G_f E_l t_l} = 84 \text{ kN (18.87 kips)}.$$

The corresponding maximum debonding strain in the composite was obtained using Equation 4.4 as,

$$\varepsilon_{\max} = \frac{P_{\max}}{t_l b_l E_l} = 3561 \text{ micro-strains}$$

Similarly, for prefabricated 1-layer pultruded carbon composite strips, with E_l , t_l , b_l and G_f being 137.6 GPa (19957 ksi), 1.37 mm (0.05"), 50.8 mm (2") and 1.2 N/mm (6.85 lb/in), respectively, the maximum axial force in the composite at debonding was obtained using Equation 4.3 as,

$$P_{\max} = b_l \sqrt{2G_f E_l t_l} = 32.9 \text{ kN (7.4 kips)}.$$

The corresponding maximum debonding strain in the composite was obtained using Equation 4.4 as,

$$\varepsilon_{\max} = \frac{P_{\max}}{t_l b_l E_l} = 3705 \text{ micro-strains}$$

The flexural capacity of the strengthened decks was then obtained using sectional capacity analysis corresponding to the limit state of reaching the debonding strain in the

composite. In order to evaluate comparative effectiveness of the two composite systems, the spacing of the two systems was designed to obtain equivalent transverse flexural capacity. Based on maximum spacing criterion of the transverse strips of 559 mm (22") as discussed previously in this section, the flexural capacity for 2 layers of 152 mm (6") wide site-impregnated fabric laminates, spaced at 533 mm (21") was computed as 72.1 kN-m/m (16.2 kip-ft/ft). Compared to the flexural capacity of the un-strengthened slab of 38.4 kN-m/m (8.63 k-ft/ft) at 75% of steel yield as computed for design phase 1, this resulted in a flexural capacity enhancement of approximately 90% which is in line with the strength enhancements observed in previous research [5, 63, 64] for FRP composite strengthening applications. This strength enhancement of the slab was also deemed to allow sufficient design window to achieve shear criticality of the girder. Based on this strength enhancement ratio, 1 layer of 102 mm (4") wide prefabricated-pultruded strips spaced at 381 mm (15") was predicted to have a flexural capacity of 73 kN-m/m (16.5 kip-ft/ft) that matched the capacity of the slab strengthened with the fabric laminates. The strengthening scheme for the transverse composite strips/laminates on the two slabs is presented in Figure 4.14.

Based on this strengthening scheme shown in Figure 4.14, the gross area of the 2 layers of 152 mm (6") wide and 1473 mm (58") long fabric laminates, spaced at 533 mm (21") resulting in a total of 7 numbers of such laminates in slab 2, was computed as 3.14 sq.m. (33.8 sq.ft.). Using manufacturer specified weight of the dry carbon fibers, in the carbon fabric system used, of 644 gm/m², the total weight of the carbon fibers used in slab 1 for transverse strengthening was 2022 gm (4.46 lbs).

Similarly for the pultruded strip system used in slab 1 with 1 layer of 102 mm (4") wide and 1473 mm (58") long prefabricated-pultruded strips, spaced at 381 mm (15") resulting in a total of 9 numbers of such strips, was computed as 1.35 sq.m. (14.53 sq.ft.). The strips were measured to be 1.34 mm (0.05") thick, resulting in gross volume of the strips of 1805 cm³ (0.06 ft³) and with fiber volume fraction of 68%, the total volume of the carbon fibers used in slab 1 was 1227.5 cm³ (0.04 ft³). Using a manufacturer specified density of the carbon fibers of 1.81 gm/cm³ (0.065 lb/in³), the total weight of the carbon fiber used in the pultruded strip system of slab 1 was 2221 gms (4.9 lbs).

Both the slabs were designed to reach the same ultimate capacity and this was also observed in the test, as will be presented in Chapter 5, when both the slabs reached ultimate load of 935 kN (210 kips). Thus for equivalent capacity of the slabs, the weight of the carbon fibers in the pultruded strip system was approximately 10% higher as compared to the weight of the carbon fibers in the fabric laminate system.

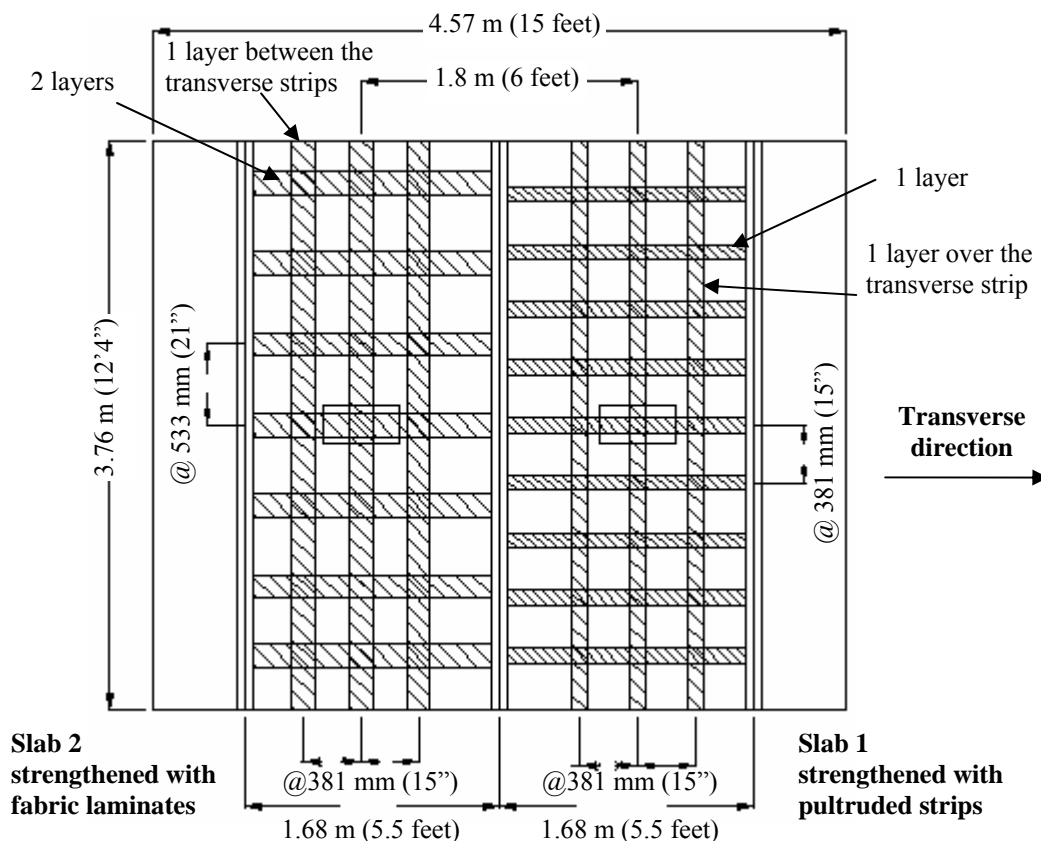


Figure 4.14 Schematic of the strengthening of deck slabs

Since the slabs were primarily designed for one way load transfer the reinforcement in the longitudinal direction was only necessary as distribution reinforcement and for holding together the punching shear cracks. The general design recommendation for longitudinal reinforcement in one-way deck slabs is to use a transverse to longitudinal reinforcement ratio of 2 [53]. However this is only a general recommendation and so the simplistic FEA model was used to compare the longitudinal and transverse moment contours for the test specimen. The ratio between transverse and longitudinal moment demands for a given loading under the load contact area was found to be around 1.4. However the longitudinal moment decreased rapidly beyond the load

area. This was attributed to the fact that in the FE model, because of the mesh attributes, high stress concentrations at the load areas resulted in larger force components than would be witnessed in the actual test specimen. Thus as a conservative and simplistic estimate to design the longitudinal composite reinforcement, a transverse to longitudinal moment demand ratio of 1.7 was used, resulting in a longitudinal moment demand of 42.4 kN-m/m (9.5 kip-ft/ft). Using the preliminary composite properties as presented in Table 4.3a, 1 layer of 152 mm (6") wide fabric laminate spaced at 381 mm (15") resulted in a moment capacity of 41.5 kN-m/m (9.3 kip-ft/ft).

1 layer of 102 mm (4") wide pultruded strip spaced at 559 mm (22") was computed to have equivalent longitudinal moment capacity as that of the fabric laminates. However from Figure 4.12, the punching shear cracks in the longitudinal direction were predicted to form at 813 mm (32") and thus with the strips spaced at 559 mm (22") and with one strip running below the load area, only one strip would be effective in restraining the opening of punching shear cracks. Thus based on the damage area in punching shear, the longitudinal pultruded strips were also designed to be spaced at 381 mm (15"). The strengthening for the deck slabs is presented in Figure 4.14.

From the FE model the load required to make the moment demand match the transverse moment capacity of 73 kN-m/m (16.5 kip-ft/ft) at failure of the strengthened slabs was computed as 645 kN (145 kips). Since this was only an estimate based on a simplistic model, the data from the strain gages on the steel reinforcement and the composite on the slabs were monitored throughout test phases 2 and 3 at all the load levels to predict the ultimate failure load of the slabs by debonding of the composite.

4.5.3 Design of Strengthened Girder for Phase 3 of Test

The design of the composite strengthening for the girders was based on the criteria that the strengthened girder would have a shear capacity higher than the shear demand produced by the wheel load at which the ultimate capacity of the strengthened deck slabs was reached. This wheel load demand was predicted in section 4.5.2 as 645 kN (145 kips) and the corresponding shear demand on the middle girder at this load level is presented in Figure 4.15.

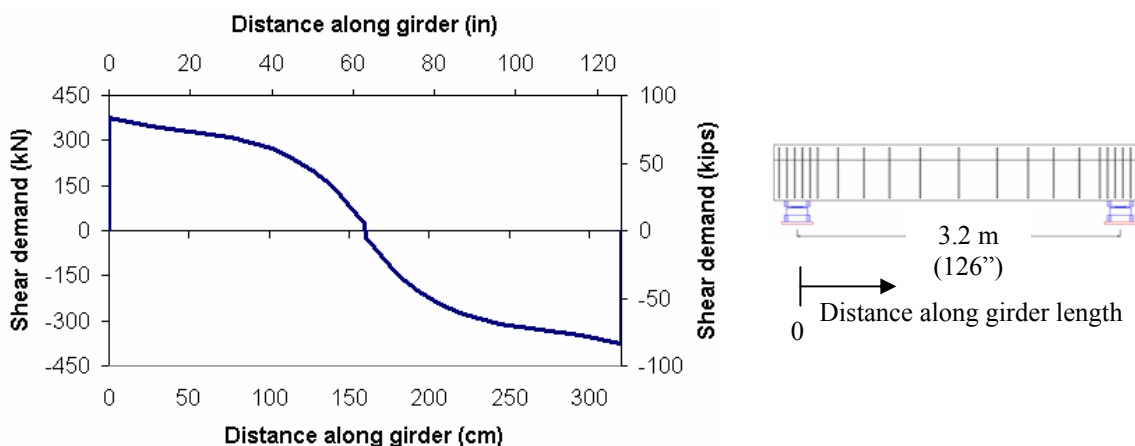


Figure 4.15 Shear demand on center girder for phase 3 limit load

The shear capacity of strengthened girder was obtained using the analytical formulations as proposed in composite design guideline [26], as follows:

$$\begin{aligned} \phi V_n &= \phi(V_c + V_s + \psi_f V_f) \\ &= 0.083\beta\sqrt{f'_c}bd + \frac{A_v f_y d (\cot \theta + \cot \alpha) \sin \alpha}{s} + \frac{A_{fv} f_{fe} d_f (\sin \alpha + \cos \alpha)}{s_f} \dots\dots\dots(4.5) \end{aligned}$$

where, the concrete and steel contributions, V_c and V_s were defined in equation 4.3. The components to obtain the contribution of the composite V_f are defined as follows:

The effective area of the composite stirrup was obtained as, $A_{fv} = 2nt_f w_f$, where the number of composite layers (n), the thickness of the composite (t_f) and the width of composite (w_f) is schematically presented in Figure 4.15.

The effective composite stress, f_{fe} was obtained as: $f_{fe} = \varepsilon_{fe} E_f$

where, E_f is the tensile modulus of the composite. The effective composite strain, ε_{fe} was obtained as, $\varepsilon_{fe} = k_v \varepsilon_{fu} \leq 0.004$, where ε_{fu} is the ultimate tensile strain of the composite. An environment correction factor is applied to this strain for field applications. However since the specimen was tested under controlled laboratory conditions without any environmental degradation, this factor was neglected. Also the design guide [3] specifies a limit of the effective composite strain of 0.004 to take into account the delamination of the composite from the concrete.

The bond reduction co-efficient, k_v [3] for computation of effective strain was defined as:

$$k_v = \frac{k_1 k_2 L_e}{11900 \varepsilon_{fu}} \leq 0.75 \quad \text{where,} \quad \left\{ \begin{array}{l} L_e = \frac{23300}{(nt_f E_f)^{0.58}} \\ k_1 = \left(\frac{f'_c}{27} \right)^{2/3} \\ k_2 = \frac{d_f - L_e}{d_f} \end{array} \right. \quad \text{in SI units} \quad \dots\dots (4.6)$$

where, L_e is defined as the active bond length over which the majority of the bond stress is maintained. k_1 and k_2 are modification factors that take into account the concrete strength and the type of wrapping scheme used. d_f is defined as the effective depth of the composite and is schematically represented in Figure 4.16. It is to be noted that the above

design equations are for unanchored shear strengthening. The effect of using anchors for the composite shear stirrup is discussed next in this section.

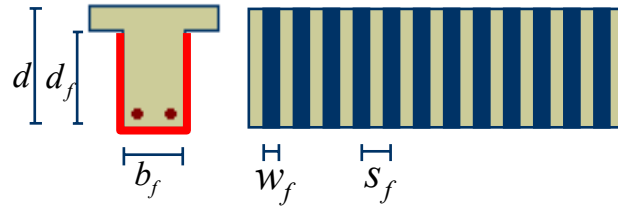


Figure 4.16 Schematic of FRP contribution parameters

Based on the design equations as presented above and for composite properties as obtained from preliminary tests (Table 4.3), the shear capacity of the strengthened girder was computed for different arrangements of number of plies, width and spacing of the composite stirrups. The final arrangement of the composite stirrups is presented in Figure 4.16. 3-layers of 152 mm (6") wide site-impregnated carbon fabric laminate strips were designed to be bonded to the web of the girder in the form of U-wraps at the spacing shown in Figure 4.17, such that the centerline of each composite stirrup was at mid-distance between the internal steel stirrups of the girder. The composite stirrups were designed to extend into the flange of the girder or the deck slabs by 102 mm (4"). The cross-section of the strengthened girder is schematically presented in Figure 4.18. Previous research [26] had shown that only composite stirrups bonded to the concrete surface would not be fully effective for shear strength enhancement since some stirrups might reach debonding strains earlier and result in drop in effective strain in the composite across the shear crack. Thus the use of a debonding design ultimate stress for all the composite stirrups traversing a shear crack may not be conservative. Also un-

anchored composite shear stirrups can cause a structure to fail in a more brittle manner with little to no increase in load and a decrease in ductility [67]. Locally, anchorages are required to transfer forces across a crack after debonding. From a global standpoint, anchorage is required to provide an out-of plane resistance to the assumed concrete compression strut in a similar manner as anchoring internal stirrups. Anchorage systems in the form of fiber or steel anchors can limit the drop in strains and allow the composite stirrups to carry the original debonding capacity for a more ductile failure [67]. Based on these test results on girder components, GFRP anchors were used in the current test with the composite shear stirrups. The schematic of the anchorage system is presented in Figure 4.18. The fibre anchors were taken through V-shaped holes drilled in the flange of the girder and splayed onto the fabric U-wrap between the second and third layers. The anchorage schemes and installation procedures will be presented in subsequent sections of this chapter. Though it has been shown that the anchors can result in some enhancement in the shear capacity [67] of the composite stirrups, this was not accounted for in the design, in order to obtain a conservative estimate of the shear capacity. The use of the anchors ensured that for estimate of the shear capacity of the composite strengthened girder it could be assumed that all the composite stirrups traversing a shear crack would be able to sustain the design ultimate debonding strains simultaneously. Consequently it would not be required to determine the non-uniform strain distribution in the composite stirrups in unanchored composite stirrup scenario. The GFRP anchors were designed based on a capacity based anchorage design concept proposed by [26]. According to this methodology, the anchors were designed based on two requirements, the first being the local requirement that each composite stirrup could meet or exceed the

design debonding limit state. The second requirement was to ensure that the anchorage system could resist the worst case out-of-plane loading condition from the assumed global load path to transfer the design stresses through truss action. The design of the anchorage system is outlined as follows:

i) Local criteria: The local requirement for anchorage design was to ensure that the strain capacity of the composite stirrups at anchorage pullout was larger than 0.004 [26]. Thus the maximum permissible FRP tensile force was calculated as:

$$T_{FRP}^{Ult} = A_{FRP} E_{FRP} (0.004) \quad \dots\dots\dots(4.7)$$

Using the material properties (Table 4.3) of the 152 mm (6") wide, 3 layer FRP composite laminates used for shear strengthening,

$$T_{FRP}^{Ult} = (0.17)(6)(7705.35)(0.004) = 140 \text{ kN (31.4 kips)}$$

Assuming that both legs of the composite U-stirrup could carry equal loads at anchor failure, the required capacity of the GFRP anchors [26] was computed as:

$$T_A^{Ult} = \frac{T_{FRP}^{Ult}}{1 + \mu} \quad \dots\dots\dots(4.8)$$

where μ is the coefficient of kinetic friction between the composite and concrete taking into account the frictional sliding of the debonded failure surfaces. Using $\mu = 0.7$ [26],

$$T_A^{Ult} = \frac{T_{FRP}^{Ult}}{1 + \mu} = 41.1 \text{ kN (9.23 kips)}$$

For the current research 12.7 mm (0.5") diameter GFRP anchors were used with a development length of 152 mm (6"), as shown in Figure 4.18, sandwiched between the second and third layers of composite stirrups. The axial capacity of the anchors was obtained as:

$$T_A^{Cap} = \tau_{Epoxy}^{Ult} \times (2L_{Dev}^{GFRP} + D_{GFRP}) (t_{CFRP} + t_{Anchor}) \quad \dots\dots\dots(4.9)$$

where,

τ_{Epoxy}^{Ult} = Ultimate shear strength of the epoxy, taken as 42 MPa (6.12 ksi) for epoxy used

L_{Dev}^{GFRP} = Development length of the GFRP anchors

D_{GFRP} = GFRP fiber anchor diameter

t_{CFRP} = Thickness of the CFRP composite stirrup layers underneath the GFRP anchor

t_{Anchor} = Thickness of GFRP anchor within the CFRP calculated by using equal area of round portion of the anchor with rectangular portion of width equal to the CFRP

Thus the axial capacity of the GFRP anchors used, was computed as:

$$T_A^{Cap} = 6.12 \times (2 \times 6 + 0.5) (0.12 + 0.0327) = 52 \text{ kN (11.68 kips)}$$

This satisfied the required capacity of the GFRP anchors of 41.1 kN (9.23 kips).

ii) Global criteria: The global requirement for anchorage design was to provide resistance of the global demands placed on the CFRP stirrups in the chamfer region of the strengthened girder. Thus the primary focus of the requirement was to provide the necessary resistance to the outward thrust of the assumed compression strut [26]. Further details of the design formulation can be found in [26], based on which the required capacity of the GFRP stirrups could be computed as:

$$T_A^{Ult} = \frac{T_{FRP}^{Ult} \times \tan \left(\frac{4 \left(\frac{b}{2} \right)}{\sqrt{(h)^2 + (\eta s)^2}} \right)}{2 \sin \theta} \quad \dots\dots\dots(4.10)$$

where,

b = beam web width, 203 mm (8")

h = beam height, 559 mm (22")

s = stirrup spacing, 229 mm (9") in the shear critical zones

η = number of effective shear stirrups bridging a shear crack (2 for current configuration with the shear cracks being assumed to be formed at an angle, $\theta = 45^\circ$)

Thus for $T_{FRP}^{Ult} = 140$ kN (31.4 kips), as computed earlier, the required capacity of the GFRP anchors was calculated using Equation 4.10 as 48.9 kN (10.98 kips). Thus the axial capacity of the GFRP anchors of 52 kN (11.68 kips) satisfied the required capacity from global criteria.

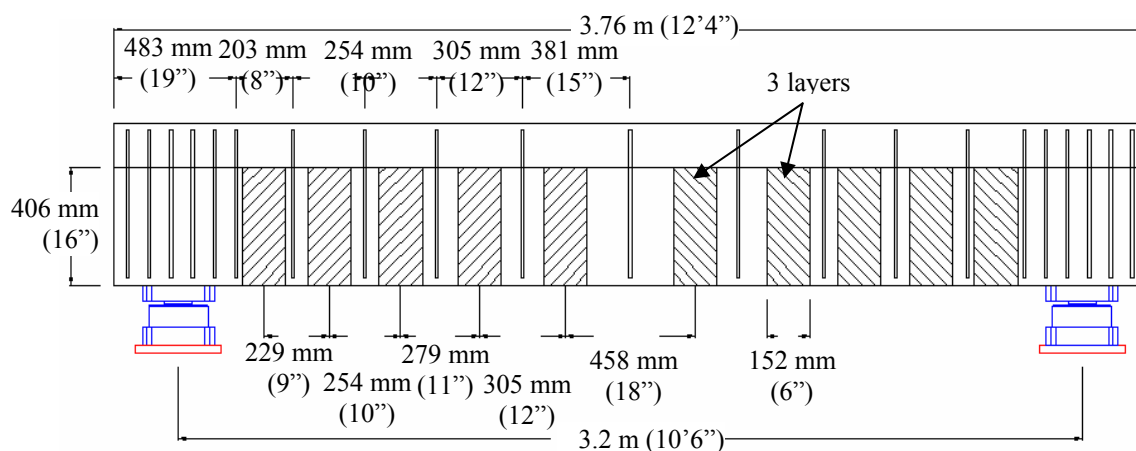


Figure 4.17 Schematic of shear strengthening of girder with composite stirrups

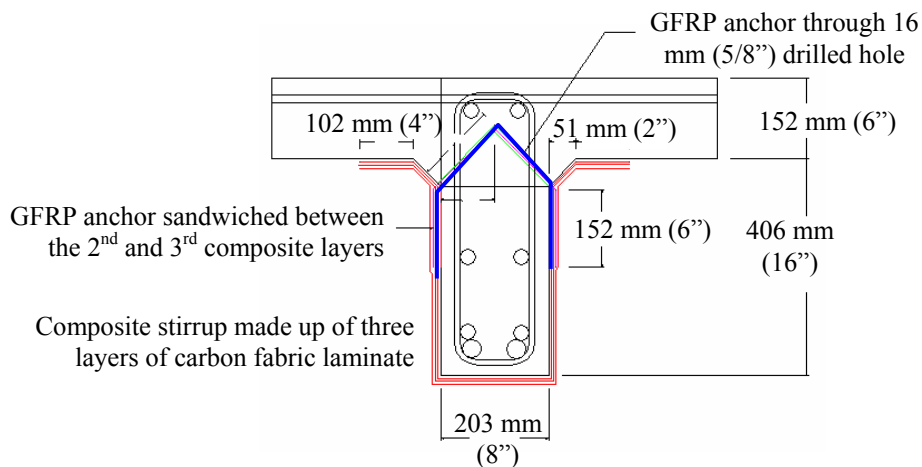


Figure 4.18 Schematic of cross-sectional view of strengthened girder

The comparison of the shear demand on the middle girder, at ultimate failure of the strengthened slabs, to the shear capacity of the strengthened girder, as obtained from the design equations of [3], is presented in Figure 4.19. It is to be recognized that equation 4.4 involves two reduction factors, ψ_f , which reduces the contribution of the composite stirrups, and ϕ , which is an overall strength reduction factor. Recommended value of ψ_f by [3] for three sided U-wraps is 0.85 while that for ϕ for shear capacity is 0.85. Thus the actual shear capacity of the strengthened girder was predicted to be higher than the shear demand which would ensure that the ultimate failure of the test specimen would be in the strengthened slabs rather than in the girder.

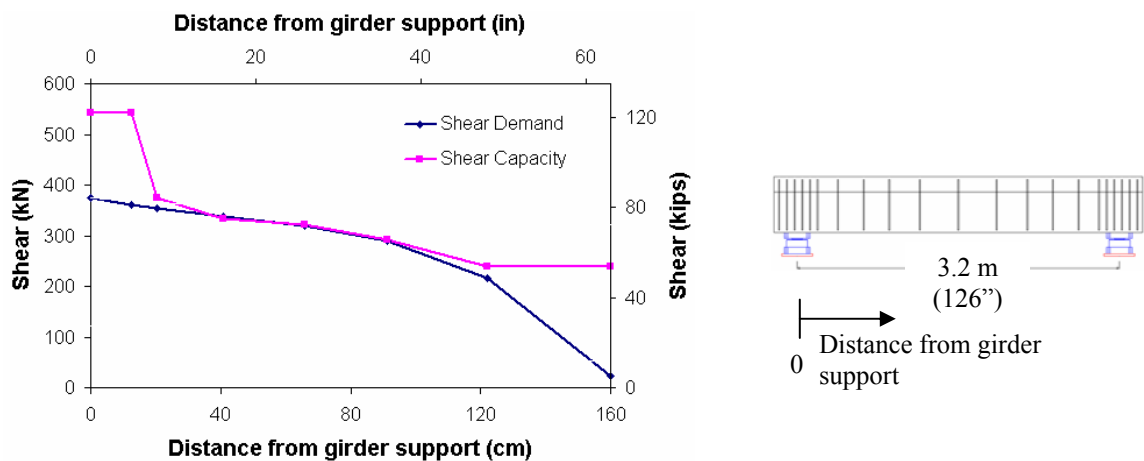


Figure 4.19 Shear demand vs. capacity of strengthened girder for phase 3 limit load

4.6 Test Setup

After construction, the specimen was left to cure for 21 days after which it was lifted up and placed on two rectangular concrete support blocks. The blocks ran in the transverse direction of the test specimen below the ends of the girders and were secured to the laboratory floor with post-tensioned rods (Figure 4.20). The test specimen was supported on six 980 kN (220 kips) load cells, one under each girder end at the girder centerline, such that the center-to-center longitudinal distance between the load cells at the two ends of each girder was 3.2 m (10'6"). A schematic of the test setup is presented in Figure 4.20. The load cells were constructed individually in two parts. The top consisted of a metal contact surface that was anchored into the bottom of the girder by two threaded bolts and was attached to a spherical surface at the bottom. This top portion of the support would then rest on the bottom part which consisted of a flat contact surface on top of the load cell itself. Such an assembly would enable the two parts to be in contact only at a point and to slide relative to each other. The entire assembly was then

placed on a two 25 mm (1") thick metal plates that rested on the concrete support blocks. Two 6.4 mm (1/4") thick Teflon sheets were bonded at the bottom of the load cell assembly and on top of the metal plate so as to allow sliding of the load cell assembly. This was done because it was found in a previous test [68] that without the Teflon sheets the friction present between the two parts of the load cell was considerable. The schematic of the load cell is presented in Figure 4.21.

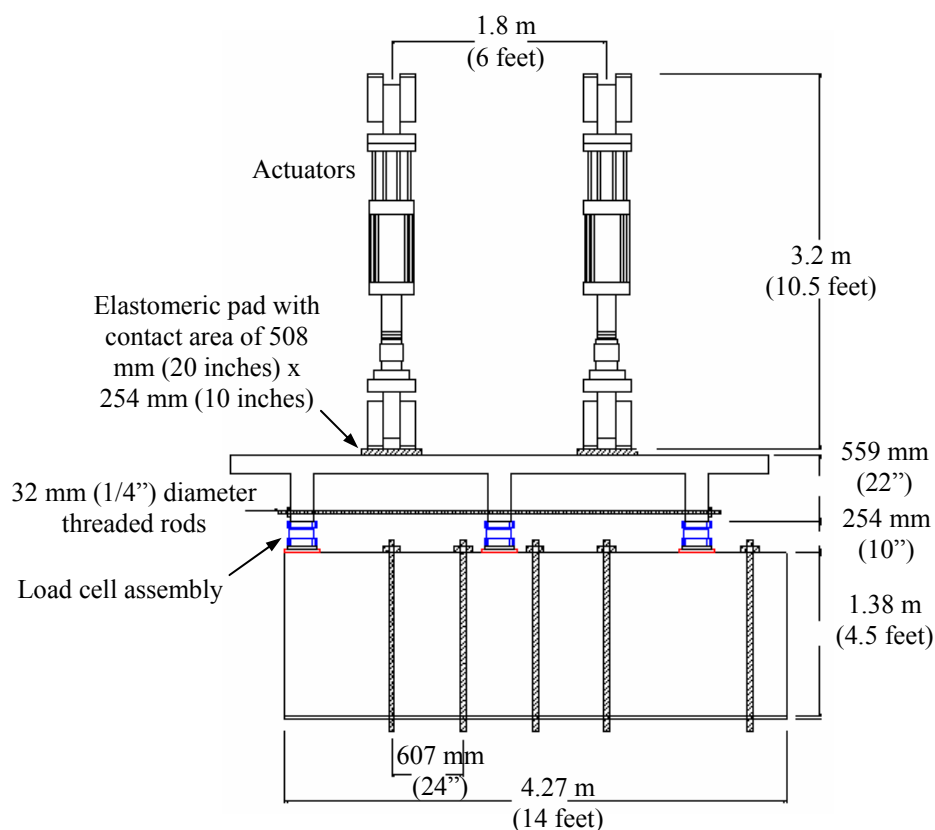


Figure 4.20 Cross-sectional schematic of test setup

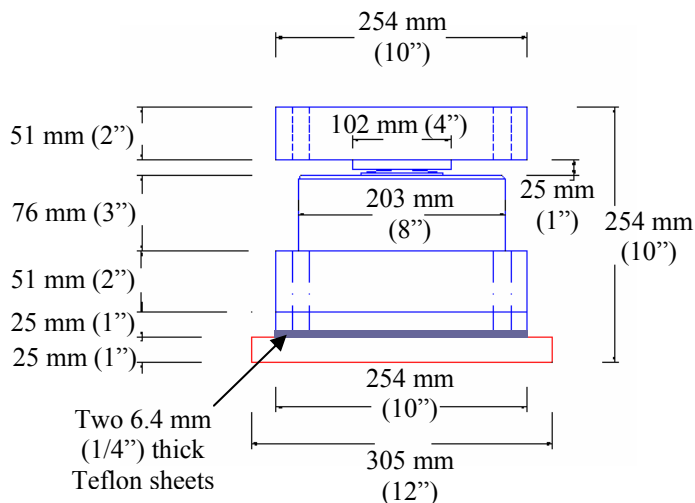


Figure 4.21 Schematic of load cell assembly

The load cell assembly thus simulated simply supported conditions in the vertical and longitudinal directions of the test specimen. However in order to restrict movement in the transverse direction to simulate the effect of diaphragm girders in a bridge deck system, two threaded rods, one at each end of the longitudinal span, were run across the entire transverse length through holes at the ends of the girders and were secured through hand tightened nuts at the ends outside the edge girder surface. This ensured that the outer girders could not deflect outwards at the support locations and were representative of the boundary conditions in a typical existing bridge deck segment. This is shown in Figure 4.22.

The specimen was tested under monotonically increasing load applied by two 979 kN (220 kips) capacity hydraulic actuators and the load was cycled at predetermined levels, to be discussed in chapter 5, to check for structural stability and to perform non destructive evaluations. The actuators were mounted to the strong wall of the laboratory.

The load from the actuators was transferred to the test specimens through load bearing plates having a loading footprint area of 508 mm (20 inches) x 254 mm (10 inches) that represented typical design wheel load contact areas of a truck load [57]. The center-to-center distance between the load contact areas was 1.83 m (6 feet) and simulated typical design axle distance of a truck [57]. A 76.2 mm (3-inch) thick elastomeric bearing pad was placed between the load bearing plates and the concrete surface to obtain a uniformly distributed constant pressure on the slab. The test setup is presented in Figure 14.22.



Through rod restraining transverse movement of edge girders

Load cells as support at ends of each girder

Figure 4.22 Test setup details

4.7 CFRP Strengthening Procedures

The strengthening of the test specimen was carried out in two phases. The first phase involved strengthening of the deck slabs in flexure after initiating punching shear criticality in the slabs at the end of stage 1 of testing. The second phase involved strengthening of the center girder in shear after reaching shear limit state in the girder at the end of stage 2 of loading.

4.7.1 Strengthening of the deck slabs

Two composite strengthening systems, site-impregnated carbon fabric laminates (Tyfo SCH-41[®]) and prefabricated carbon pultruded strips (Tyfo UC[®]), were used for the two deck slabs. The design of the systems was described in section 4.5.2. The installation procedure and the material properties of the composite used for the strengthening will be presented in the following sections.

4.7.1.1 Strengthening procedure

Since the surface condition of the substrate is an important parameter for ensuring proper bond between the substrate and the composite, the concrete surface of the test specimen was sandblasted, so as to take off the flaky cement layer on the surface of the specimen and to have a rough surface, before installation of the composite systems. Pressurized air was then used to remove all dust and loose particles and an epoxy paste was used to fill voids in the concrete. The application of the composite systems was a two step process. Since the composite was to be bonded to the soffit of the slabs it was necessary that the surface be tacky to hold the weight of the composite during curing of

the epoxy. Thus a primer coating of a two component saturant epoxy, Tyfo S[®], was applied on the concrete at the locations of the composite strips. The primed surface (Figure 4.23) was allowed to cure overnight so that it would be tacky the next morning for installation of the composite systems. Two different polymer systems were used for bonding the two composite systems. A two component tack-coat epoxy, Tyfo-TC[®], was used for bonding the pultruded strips to the soffit of slab 1. The saturant epoxy Tyfo-S[®] was first used for saturating the fabric laminates. However since this saturant epoxy had a low viscosity it was not suitable for overhead applications. Thus a filler material in powdered aerosol form was added to the saturant epoxy to get higher viscosity and tackiness for bonding the fabric laminates to the soffit of slab 2. This thickened epoxy will be referred to as Tyfo WS[®].



a) Application of primer coat



b) Primed surface for composite installation

Figure 4.23 Preparation of the concrete surface before strengthening the slabs

For strengthening slab 1 with pultruded strips, a layer of Tyfo TC[®] was applied on the soffit of the slab at the locations of composite bonding (Figure 4.24a) and adhesive was then applied on the transverse pultruded strips with a serrated spatula (Figure 4.24b). The strip was then bonded to the concrete and a hard rubber roller was used to drive out

any excess adhesive or air voids (Figure 4.24c). Adhesive squeezing out from the side of the strips would indicate that a proper bond was achieved between the concrete and the strips (Figure 4.24d). After all the transverse strips were bonded to the slab, a layer of adhesive was applied in the longitudinal direction (Figure 4.24e) and the longitudinal strip was bonded to the slab surface (Figure 4.24f).

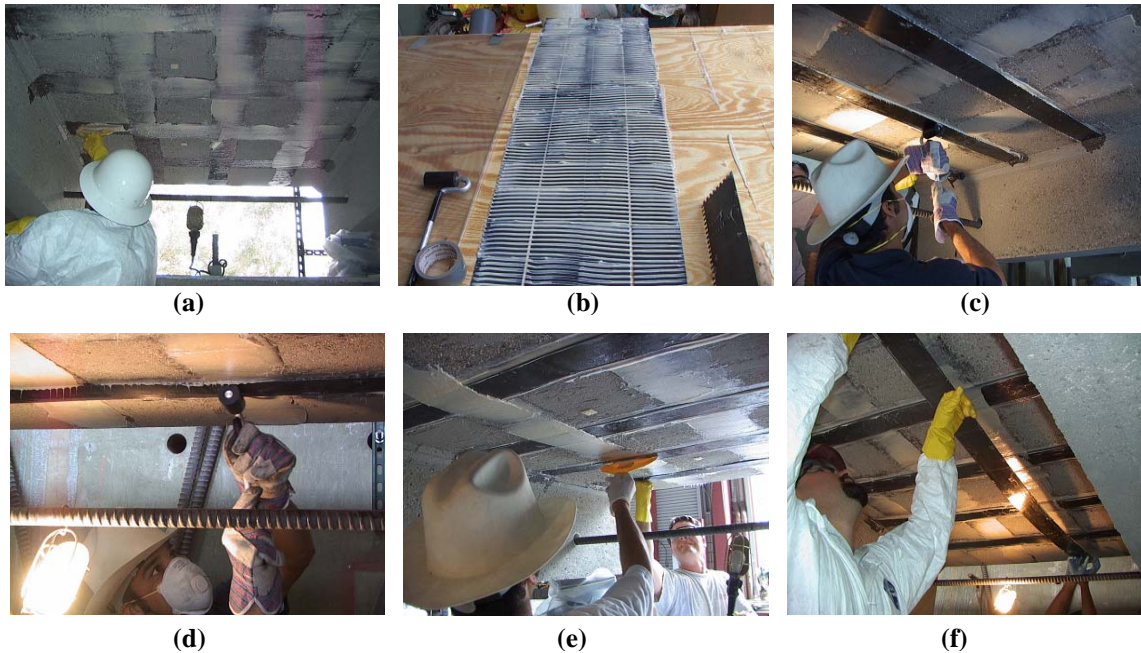


Figure 4.24 a) Adhesive application on concrete; b) Epoxy application on strips; c) Bonding transverse strip; d) Compaction of composite; e) Epoxy application for longitudinal strips; f) Bonding longitudinal strips

For strengthening slab 2 with carbon fabric laminates, a layer of Tyfo WS[®] was applied on the soffit of the slab at the locations of composite bonding, in both the longitudinal and transverse direction (Figure 4.25a). The fabric laminates were saturated with Tyfo S[®] epoxy (Figure 4.25b) and bonded to the concrete in the transverse direction. Tyfo WS[®] was applied over the fabric to ensure that it was tacky enough and did not fall

down by its weight. The longitudinal fabric laminates were then bonded to the slab (Figure 4.25c) over the transverse laminates and any excess epoxy was driven off from the composite with a spatula (Figure 4.25d). The second layer of transverse laminate was then bonded to the slab (Figure 4.25e) and a thin layer of epoxy was applied over the laminates to resemble the surface finish that is applied in the field as a protective coating (Figure 4.25f).

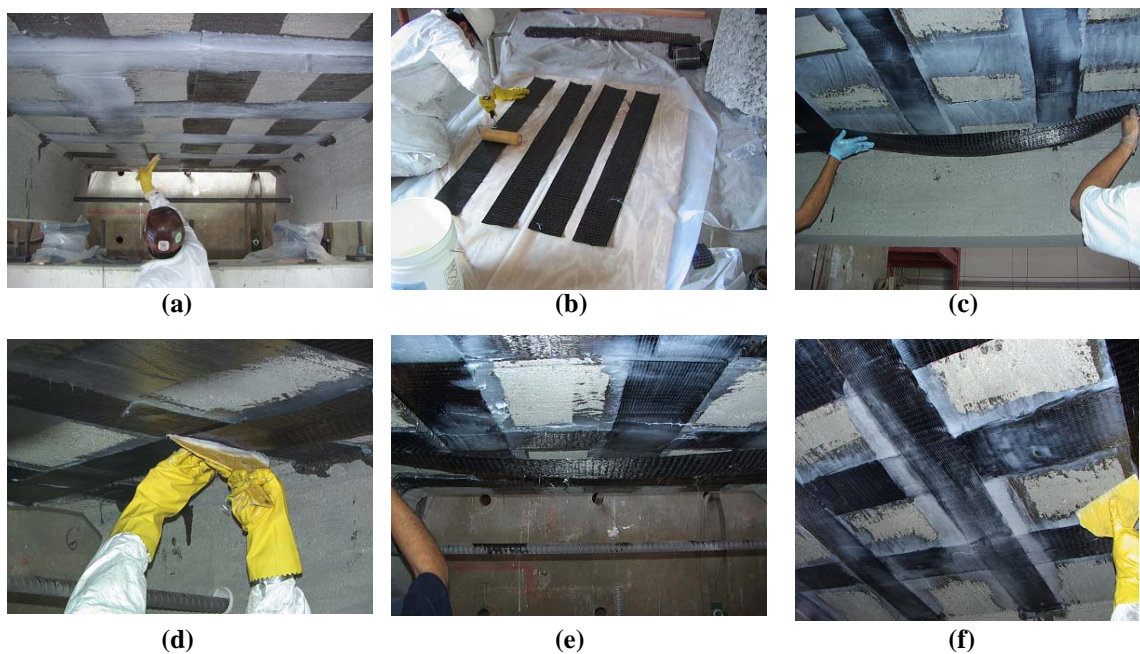


Figure 4.25 a) Application of epoxy on concrete; b) Saturating fabric with epoxy; c) Bonding first transverse and longitudinal layers of fabric laminates; d) Compaction of composite; e) Bonding second transverse layer; f) Finishing

4.7.1.2 Material properties of composite for slab strengthening

Test panels were made during installation of the composite systems to determine the material properties. For tension tests the manufacturer supplied pultruded strips of the same batch as that used for strengthening slab 1. For the fabric laminates test panels were

made with the same fabric and epoxy used in the test specimen. Both 1 layered and 2 layered panels were made to check for the properties of the transverse and longitudinal laminates. Three such panels for each type, 305 mm (12") square, were made of which a total of 21 tension test samples, 254 mm (10") long and 25.4 mm (1") wide, were cut. 21 tension test samples, 254 mm (10") long and 12.7 mm (0.5") wide, were also cut from the pultruded strips. This followed the specifications of design guide [3], in which a minimum of 20 test specimens is specified to determine the tensile properties of composite. Test panels were also made for the resin systems, namely Tyfo TC[®] and Tyfo WS[®] (Figure 4.26). The tensile test properties of the composite and the resin obtained after allowing a week of cure are presented in Table 4.5 and Table 4.6. The composite systems, 1 layer pultruded strip, 1 layer fabric laminate and 2 layers fabric laminate, were also bonded to two concrete blocks, 305 mm x 178 mm x 76 mm (12" x 7" x 3") in size, for each system. Pull-off tests were carried out, the results of which are presented in Table 4.7. All failures were in the concrete and above a minimum strength of 1.16 MPa (167.69 psi) indicating acceptable performance of the composite systems in terms of bond performance.



Figure 4.26 Manufacturing composite and resin test panels

Table 4.5 Tensile test properties of composite from slab strengthening

Composite Type		1 layer fabric	2 layers fabric	Pultruded strip
Thickness Properties mm (inches)	Mean	3.229 (0.127)	5.12 (0.202)	1.34 (0.05)
	Std. Dev.	0.338(0.013)	0.37 (0.015)	0.009 (0.0004)
	COV	0.105	0.07	0.0065
	Min	2.630 (0.104)	4.65 (0.183)	1.33 (0.052)
	Max	3.738 (0.147)	5.79 (0.23)	1.36 (0.054)
Strength Properties MPa (ksi)	Mean	261.5 (37.92)	322.03 (46.69)	1944.44 (281.94)
	Std. Dev.	52.9 (7.68)	38.92 (5.64)	236.98 (34.36)
	COV	0.203	0.121	0.122
	Min	171.5 (24.87)	268.11 (38.88)	1562.34 (226.54)
	Max	366.1 (53.1)	399.55 (57.94)	2337.61 (338.95)
Modulus Properties GPa (ksi)	Mean	26.5 (3835.8)	35.94 (5211.77)	140.0 (20300.1)
	Std. Dev.	5.3 (764.6)	8.36 (1211.64)	12.53 (1816.77)
	COV	0.2	0.23	0.09
	Min	17.6 (2551.7)	23.01 (3337.32)	126.1 (18283.78)
	Max	36.4 (5279.02)	56.12 (8137.11)	160.91 (23332.5)

Table 4.6 Tensile test properties of pure resin from slab strengthening

Composite Type		Tyfo TC [®]	TYFO WS [®]
Thickness Properties mm (inches)	Mean	4.13 (0.16)	3.13 (0.12)
	Std. Dev.	0.19 (0.008)	0.43 (0.02)
	COV	0.046	0.139
	Min	3.82 (0.15)	2.27 (0.09)
	Max	4.62 (0.18)	3.6 (0.14)
Strength Properties MPa (ksi)	Mean	19.02 (2.76)	13.05 (1.89)
	Std. Dev.	4.67 (0.68)	4.72 (0.69)
	COV	0.245	0.362
	Min	3.6 (0.52)	3.65 (0.53)
	Max	23.39 (3.39)	20.94 (3.04)
Modulus Properties GPa (ksi)	Mean	1.75 (254.08)	3.06 (444.17)
	Std. Dev.	0.28 (40.09)	1.06 (152.95)
	COV	0.158	0.344
	Min	1.38 (199.8)	1.04 (151.09)
	Max	2.25 (325.67)	5.74 (832.59)

Table 4.7 Pull-off test results from slab strengthening

Composite Type	Pull-off Strength – MPa (psi)				
	Mean	Std. Dev.	COV	Min	Max
1 layer fabric	1.21 (175.23)	0.24 (35.3)	0.20	1.01 (146.97)	1.48 (214.8)
2 layers fabric	1.16 (167.69)	0.14 (19.85)	0.12	1.01 (146.97)	1.29 (186.53)
Pultruded strip	1.36 (197.84)	0.21 (29.91)	0.15	1.21 (175.23)	1.60 (231.76)

On comparing the material properties of the composites obtained from the preliminary design test batch panels (Table 4.3) and those obtained from the test panels manufactured during installation of the composite on the test specimen (Table 4.5), variations in the properties were observed. The major difference was in terms of the thickness of the composite panels. The thickness of the 1 layer and 2 layer fabric laminates manufactured during installation of the composites on the test specimen were found to be significantly higher than the thickness of the laminates manufactured for estimation of initial design properties [93% and 64% higher mean thickness for the 1 layer and 2 layer laminates, respectively]. This was contributed to differences in workmanship (resulting in differences in the fiber volume fractions) and the addition of an aerosol based filler material in the epoxy system during manufacturing of the test panels, for better adhesion and tackiness of the composite to the soffit of the slabs as was discussed previously, representative of the laminates which were installed on the test specimen. Thus to compare the properties between the two batches of test panels these properties were normalized with respect to the thickness of the sample.

The ratio of the material properties of the two batches of test samples was computed as:

$$\text{Batch ratio for a property (strength or modulus)} = \frac{P_1 \times t_1 \times w_1}{P_2 \times t_2 \times w_2} \quad \dots\dots\dots(4.11)$$

where, P_1 , t_1 and w_1 were the measured mean properties (strength and modulus) of samples from the test batch and P_2 , t_2 and w_2 were the corresponding measured mean properties from the preliminary design batch. The batch ratios for the strength and modulus properties of the 1 and 2 layer laminates and the pultruded strips are presented in Table 4.8.

Table 4.8 Batch ratios of properties between preliminary and test panels

Property	1 layer laminate	2 layers laminate	Pultruded strip
Rupture stress	0.71	0.77	0.88
Modulus	1.12	1.17	1.02

It is seen from Table 4.8 that the ultimate strength of the composites from the test batch were lower than the strengths of the composites from the preliminary design batch (the 1 layer and 2 layer laminates and the pultruded strips from the test batch had 29%, 23% and 12% lower strengths, respectively, as compared to those from the preliminary design batch). However the modulus of the 1 layer and the 2 layer fabric laminate composites from the test batch were higher than the modulus of the corresponding preliminary design batch composites by 12% and 17% respectively. The modulus of the pultruded strips from both the batches was comparable with the difference being less than 2%. Because of uniformity in the properties of the pultruded strips achieved by better

quality control during manufacturing, the difference between the properties of the two batches of pultruded strips were less as compared to that of the 1 layer and 2 layer fabric laminates. It is to be noted that the design methodology of the strengthened deck slabs, as was outlined in section 4.5.2 of this chapter earlier, involved limiting the ultimate strain and consequently the ultimate design stress of the laminates by the debonding limit state of the composite. Since the debonding stress was always lower than the ultimate rupture stress, the limiting stress in the composite was governed by debonding and was obtained as, $\sigma_{debonding} = E \times \varepsilon_{debonding}$. Thus the design was governed more by the modulus (E) rather than the ultimate stress of the composite. Consequently the difference between the ultimate strengths of the composites from the two batches (as high as 29% for the 1 layer laminates) would not significantly affect the design predictions made using the properties of the composites from the preliminary design batch. Also since the design will be governed by the modulus, with the modulus of the test batch being higher than that of the design batch, the design based on the preliminary properties would be conservative. The design ultimate capacity of the strengthened slab components was recalculated based on the new composite properties from the test batch panels using the same analytical design procedure as was outlined in section 4.5.2 and is presented in Table 4.9. The design capacities of the two strengthening systems were found to remain unaffected.

Table 4.9 Recalculated ultimate moment capacities of the strengthened slabs

	Design with preliminary properties		Design with test batch properties	
	Moment capacity kN-m/m (kip-ft/ft)	Load capacity kN (kips)	Moment capacity kN-m/m (kip-ft/ft)	Load capacity kN (kips)
Slab 1 strengthened with pultruded strip	73 (16.5)	653 (147)	73.4 (16.49)	656 (148)
Slab 2 strengthened with fabric laminate	72.1 (16.2)	645 (145)	74.2 (16.68)	663 (149)

4.7.2 Strengthening of the girder

The specimen was tested after strengthening of the slabs until shear criticality was attained in the middle girder. The girder was then strengthened in shear with composite U-wraps following the design details described in section 4.5.3. The schematics of composite installation details were presented in Figures 4.17 and 4.18.

4.7.2.1 Strengthening procedure

The girder was sandblasted at the same time as the sandblasting of the slabs. All voids in the concrete were filled with a high strength epoxy paste. The bottom corners of the web in the girder were rounded to an approximate radius of 25.4 mm (1") with grinding stone and mechanical wheel grinder (Figure 4.27a). All uneven areas at the locations of composite stirrups were also ground to prevent development of any stress concentrations (Figure 4.27b). The edges of the pultruded strips and fabric laminates from the slab strengthening which would be overlapped by the U-composite stirrup from the girder were roughened with a belt sander to ensure development of a proper bond between the composite systems (Figure 4.27c). Anchor holes were then drilled at the intersection of the web and chamfer area of the girder following the details in Figure

4.17. Two anchor holes were drilled at the location of every composite stirrup, one from each side of the girder, at an angle of 45° . A drill rig was created to ensure that the holes were drilled at the right locations and angle so that the holes from either side would match up and meet at the center of the girder for each stirrup location. A total of 20 holes (2 each for the 10 composite stirrups), 15.8 mm (5/8") in diameter were drilled at the intersection of the web and chamfer with good accuracy (Figure 4.27d). A rat tail file and a small chisel were used to round off the ends of the holes (Figure 4.27e). Also thin belt sandpaper was pulled in through one end of the hole and out through another using a vacuum machine and was used to round off the inner radius where the two holes met. Pressurized air was then blown through the holes to clean any fine particles inside the hole. A string was then inserted through one end of the hole and taken out through the other end (Figure 4.27f) to be used later for pulling in the fiber anchors.

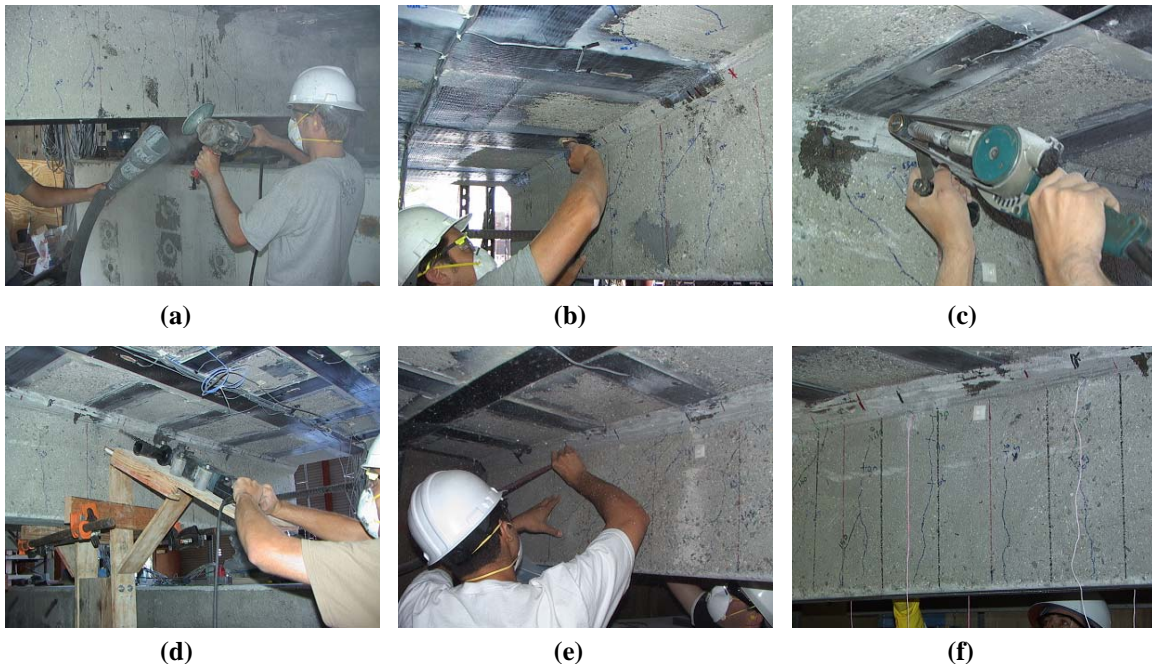


Figure 4.27 Surface preparation and drilling of anchor holes

The same type of carbon fabric (TYFO SCH-41[®]) and epoxy systems, as was used for strengthening slab2, was used for strengthening the girder. A layer of primer coat, with Tyfo S[®] saturant epoxy, was first applied on the concrete at the locations of the composite stirrups (Figure 4.28a) and was let to tack for about three hours. The fabric was saturated with the Tyfo S[®] epoxy in a resin bath (Figure 4.28b). A layer of thick epoxy, Tyfo WS[®] was applied on the primer coat and the areas near the overlap with the composite from the slab or at sharp corners near the flange-chamfer intersection of the girder were made smooth with the epoxy paste (Figure 4.28c). The first two layers of fabric laminate were bonded to the girder in the form of U wraps. As specified in the design details (Figure 4.18), the bonding of the laminate was started on one side from the flange of the girder, 102 mm (4") from the flange chamfer intersection, and was wrapped around the web to the girder flange on the other side. The fabric was bonded by one person while another person would hold the fabric from underneath the beam and keep it in tension so that fiber crimps could be avoided (Figure 4.28d). A spatula was used to apply the thick epoxy over the fabric between the composite layers while any excess epoxy would also be squeezed out. The compaction was always started from one end of the stirrup and was worked around the web of the girder to the other side.

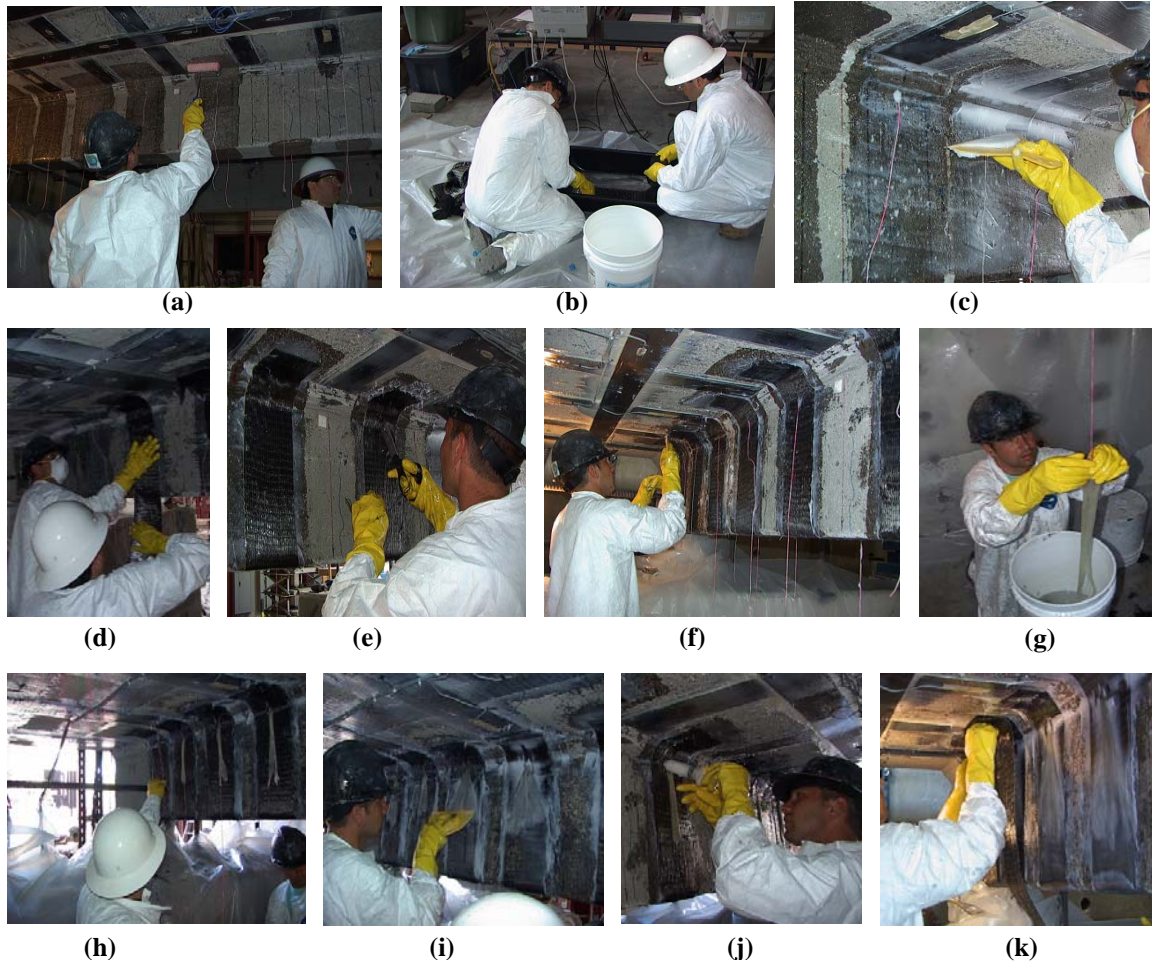


Figure 4.28 Installation of composite stirrup and anchor in girder

While bonding the first two layers of fabric, a slit was made between fibers with a scissor at the locations of the anchor holes (Figure 4.28e) and the string passing through the hole was pulled out through the slit (Figure 4.28f). The GFRP anchors (Tyfo SEH[®]) supplied by the manufacturer came as glass fiber bundles of 12.7 mm (1/2") diameter. The fibers were immersed in a bucket of Tyfo S[®] epoxy and then excess epoxy was squeezed out of the fibers (Figure 4.28g). The fiber anchors were then connected to one end of the string hanging out of the anchor holes and were pulled out through the other

end of the hole through the slit in the fabric (Figure 4.28h). The fibers were splayed along the web over the fabric for 152 mm (6") forming a V-shaped fan out from the hole (Figure 4.28i). All the holes were filled with the Tyfo WS[®] thick epoxy (Figure 4.28j) that was injected through one side of the hole until it flowed out from the other side. The third layer of carbon fabric U-wrap was then installed over the fibers (Figure 4.28k) and a thin layer of epoxy was applied as a surface finish coating.

4.7.2.2 Material properties of composite for girder strengthening

Three composite panels, 305 mm (12") square, were made with 3 layers of Tyfo SCH-41[®] fabric and Tyfo WS[®] epoxy during installation of the composite stirrups on the girder. A total of 21 tension test samples were cut from the panels and tested in tension. The tensile properties are presented in Table 4.10. The properties of the 2 layer and 3 layer composite laminates used for strengthening the deck slabs are also provided in Table 4.10 for comparison with the properties obtained for the 3 layer laminates. The mean strength and modulus of the 3 layer samples were found to be 25% and 37% higher than the strength and modulus of the 2 layer samples. 3 layers of fabric were also bonded to two concrete blocks and pull-off tests were carried out the results of which are presented in Table 4.11. All failures were into concrete indicating acceptable performance of the composite systems in terms of bond performance.

Table 4.10 Tensile test properties of composite

Composite Type		1 layer fabric	2 layers fabric	3 layers fabric
Thickness Properties mm (inches)	Mean	3.229 (0.127)	5.12 (0.202)	4.56 (0.18)
	Std. Dev.	0.338(0.013)	0.37 (0.015)	0.21 (0.01)
	COV	0.105	0.07	0.046
	Min	2.630 (0.104)	4.65 (0.183)	4.10 (0.16)
	Max	3.738 (0.147)	5.79 (0.23)	4.85 (0.19)
Strength Properties MPa (ksi)	Mean	261.5 (37.92)	322.03 (46.69)	431.31 (62.54)
	Std. Dev.	52.9 (7.68)	38.92 (5.64)	72.63 (10.53)
	COV	0.203	0.121	0.168
	Min	171.5 (24.87)	268.11 (38.88)	293.99 (42.63)
	Max	366.1 (53.1)	399.55 (57.94)	578.20 (83.84)
Modulus Properties GPa (ksi)	Mean	26.5 (3835.8)	35.94 (5211.77)	57.48 (8335.14)
	Std. Dev.	5.3 (764.6)	8.36 (1211.64)	11.40 (1653.48)
	COV	0.2	0.23	0.198
	Min	17.6 (2551.7)	23.01 (3337.32)	40.13 (5819.14)
	Max	36.4 (5279.02)	56.12 (8137.11)	83.61 (12123.74)

Note: The properties of the 1 layer and 2 layer laminates are from slab strengthening (table 4.5) and are shown here for comparison with the properties of the 3 layer laminates

Table 4.11 Pull-off test results from girder strengthening

Composite Type	Pull-off Strength – MPa (psi)				
	Mean	Std. Dev.	COV	Min	Max
3 layers fabric	1.42 (206.32)	0.552 (80)	0.388	0.7 (101.75)	2.03 (293.93)

A similar trend as was observed for the 1 and 2 layered laminates between the preliminary and test batch properties was also observed for the 3-layered composite panels. The thickness of the test batch 3 layer composite panels was about 9% higher than the corresponding thickness obtained from the preliminary design batch. Thus in order to compare the properties from the two batches, the batch ratio of the strength and modulus was computed using equation 4.11 presented in the previous section. As seen in Table

4.12, the ultimate normalized mean strength of the 3 layer panels from the test batch was 20% lower while the normalized mean modulus was 14% higher as compared to the normalized mean strength and modulus of the preliminary batch. As explained earlier in section 4.7.1.1 the design of the composite strengthening was governed by the limiting debonding stress and thus difference in the ultimate strengths of the two batches did not affect the design calculations. The comparison between the two capacities based on the material properties from the preliminary and the test batch of composites is presented in Figure 4.29. The difference was found to be negligible and thus the design calculation and strength/load demand predictions made with the properties of the preliminary composite panels would hold true for the strengthened girder in the test specimen.

Table 4.12 Batch ratios of properties between test and preliminary design panels

	Rupture stress	Modulus
3 layer laminate	0.803	1.14

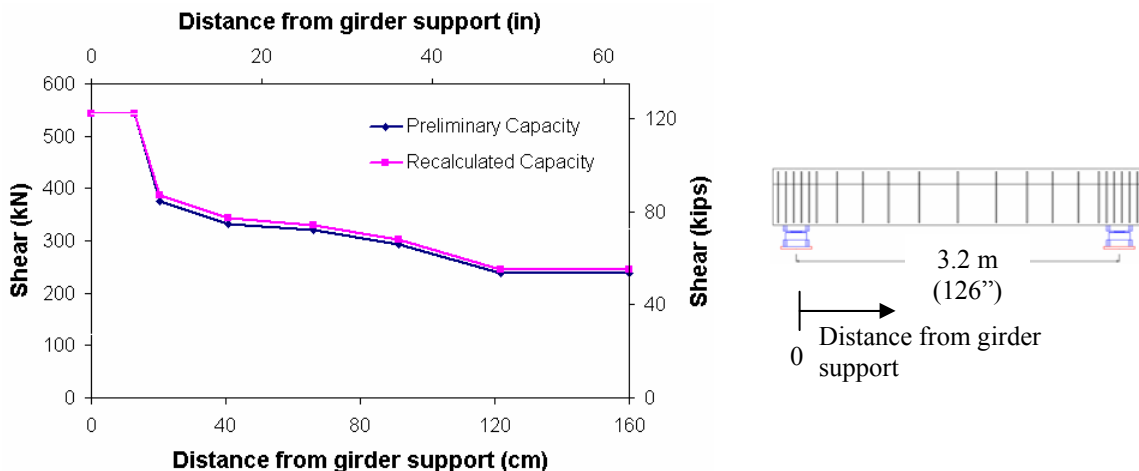


Figure 4.29 Comparison of shear capacities with preliminary and test batch properties

4.8 Instrumentation

4.8.1 Instrumentation details of linear potentiometers and load cells

Extensive instrumentation, in the form of linear potentiometers and strain gages, was used to characterize the strain and deflection profiles of the test specimen under loading. The instrumentation was designed to capture the changes in load distribution and load paths caused by subsequent stages of loading. Vertical deflections were measured by 47 linear potentiometers distributed around the test specimen with higher numbers at areas of high stress concentrations such as around the load contact area, mid and quarter spans of the components and at supports. The locations of the vertical linear potentiometers are presented in Figure 4.30. The linear potentiometers will be referred later by their row numbers which are also indicated in Figure 4.30. 3 horizontal linear potentiometers and 6 rotation sensors were also used at the outside edge of the girders, placed at their centerlines, to measure relative horizontal movements at the support locations and also to measure the rotations of the girders if any. The loads at the supports were measured by six 980 kN (220 kips) load

cells, the details of which were presented in Figure 4.21. The 980 kN (220 kips) capacity hydraulic actuators were also connected to the data acquisition system to obtain the actuator loads and deflections during loading of the test specimen.

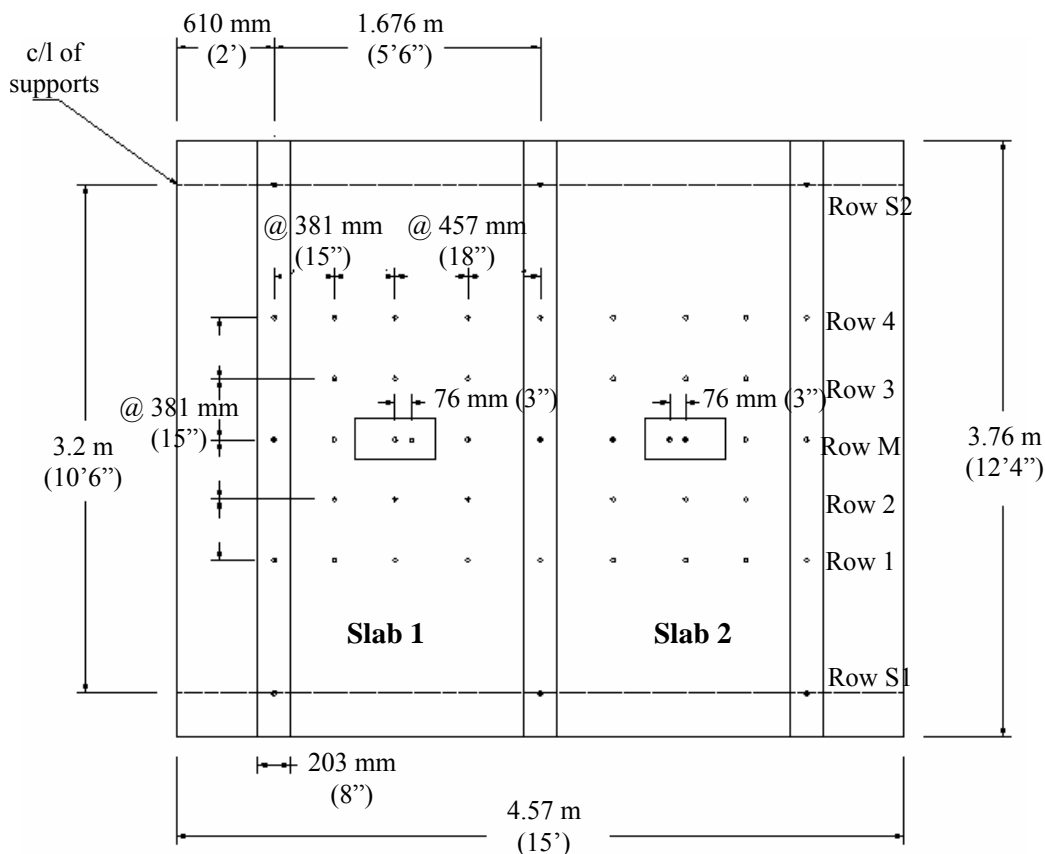


Figure 4.30 Locations of vertical linear potentiometers

4.8.2 Instrumentation details of strain gages

A total of 22 electrical resistance strain gages with a gage length of 5 mm were used on the steel reinforcement inside the slab to get the strains and thereby the corresponding moment/shear demand distribution profiles caused by the loading. The locations of these gages are presented in Figure 4.31. The gages with notation starting with 'T' were aligned in the transverse direction and gages with notation starting with 'L' were aligned in the

longitudinal direction of the specimen. Also gages with notations ending with numbers '1' or '4' were located on top reinforcement near girder supports while the ones ending with numbers '2' and '3' were located on the bottom reinforcement of the slabs near the load area. In figure 4.31, the through slab reinforcements are colored black and the truss bar slab reinforcements are colored black at bottom of slab and dashed magenta at top of slab.

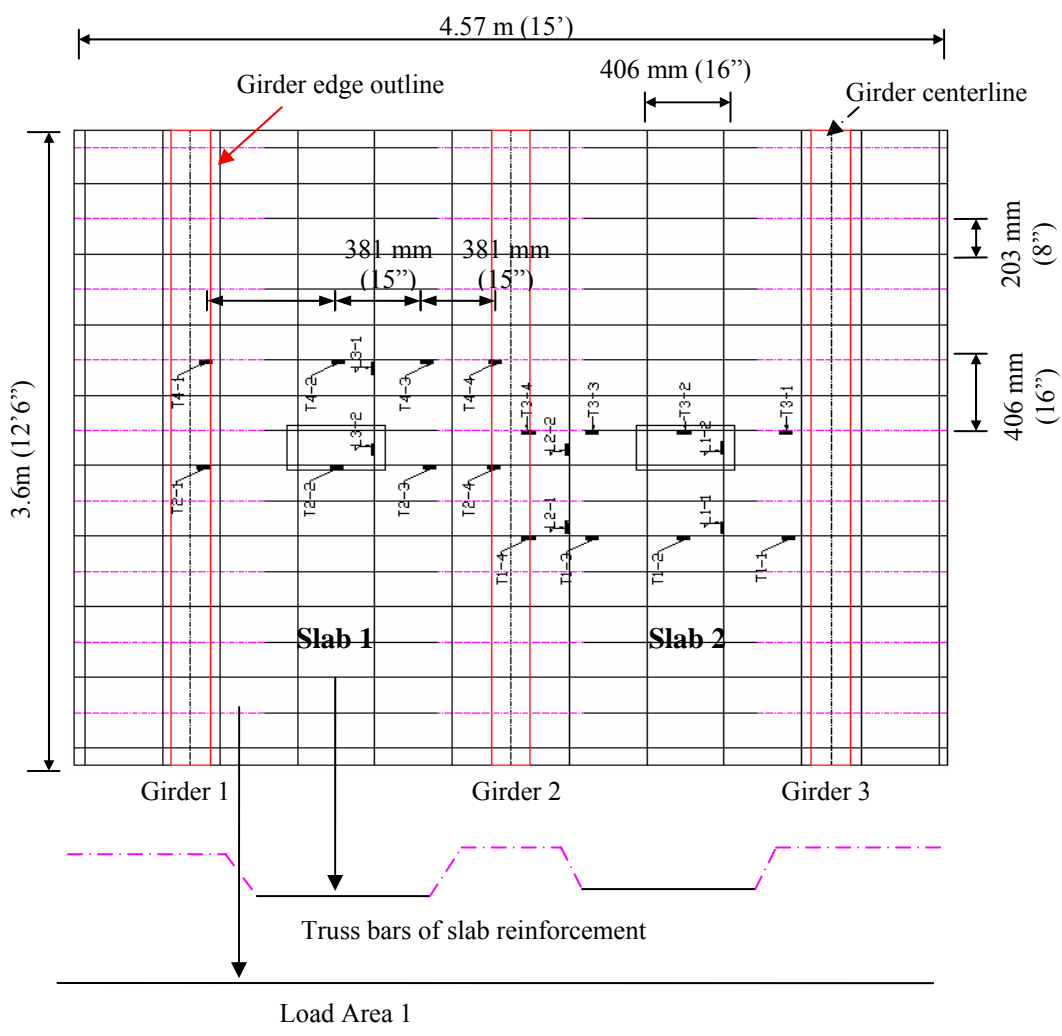
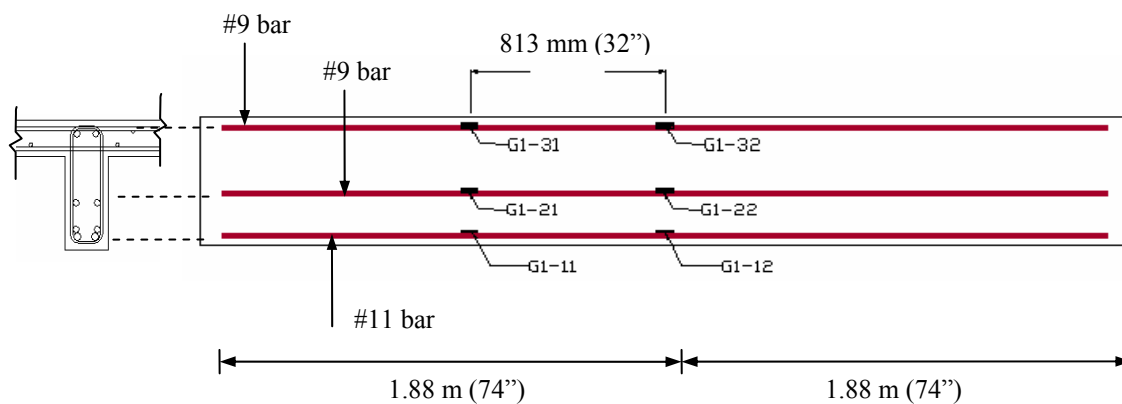


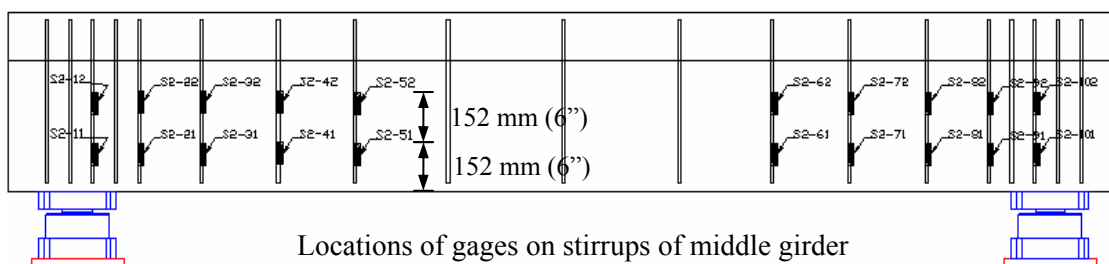
Figure 4.31 Locations of strain gages on deck slabs

6 electrical resistance strain gages with a gage length of 5 mm were installed on the longitudinal reinforcement of each girder at mid-span and quarter-span locations. These gages were installed such that the strain profile along the depth of the girder would assist in determining the moment levels at mid and quarter-span sections at any given load stage. 20 strain gages were installed on the stirrups of the center girder and 4 strain gages each were installed on the stirrups of the edge girders. The gages on the stirrups were located in the shear critical areas. The locations of the strain gages are presented in Figure 4.32. The locations of the internal steel stirrups in Figure 4.31 can be found in Figure 4.3.

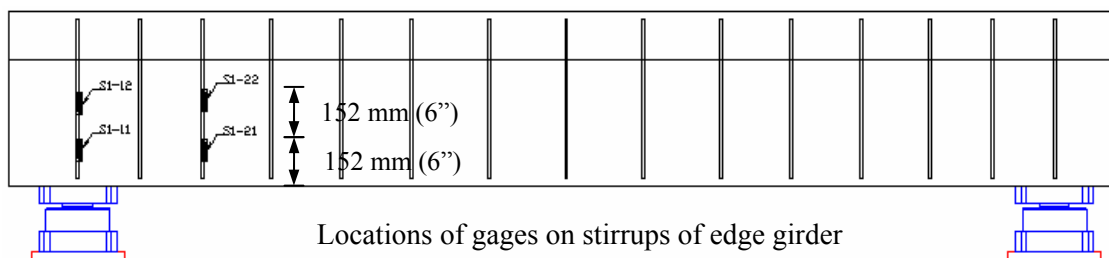
63 strain gages with 30 mm gage length were installed on the composite strips and laminates in the two slabs after the strengthening of the slabs at the end of phase 1 of loading. The locations of the strain gages are presented in Figure 4.33. The notation ‘T’ stands for transverse strip/laminate and notation ‘L’ stands for longitudinal strip/laminate. 32 strain gages with 30 mm gage length were also installed on the composite stirrups after the strengthening of the middle girder at the end of phase 2 of loading. The locations of the strain gages on each side of the girder are presented in Figure 4.34. The locations of the strain gages on the composite stirrups are shown in Figure 4.34 on one side of the girder only and are symmetric on the other side.



Locations of gages on longitudinal reinforcement of girder



Locations of gages on stirrups of middle girder



Locations of gages on stirrups of edge girder

Figure 4.32 Gage locations on longitudinal and shear reinforcement of girders

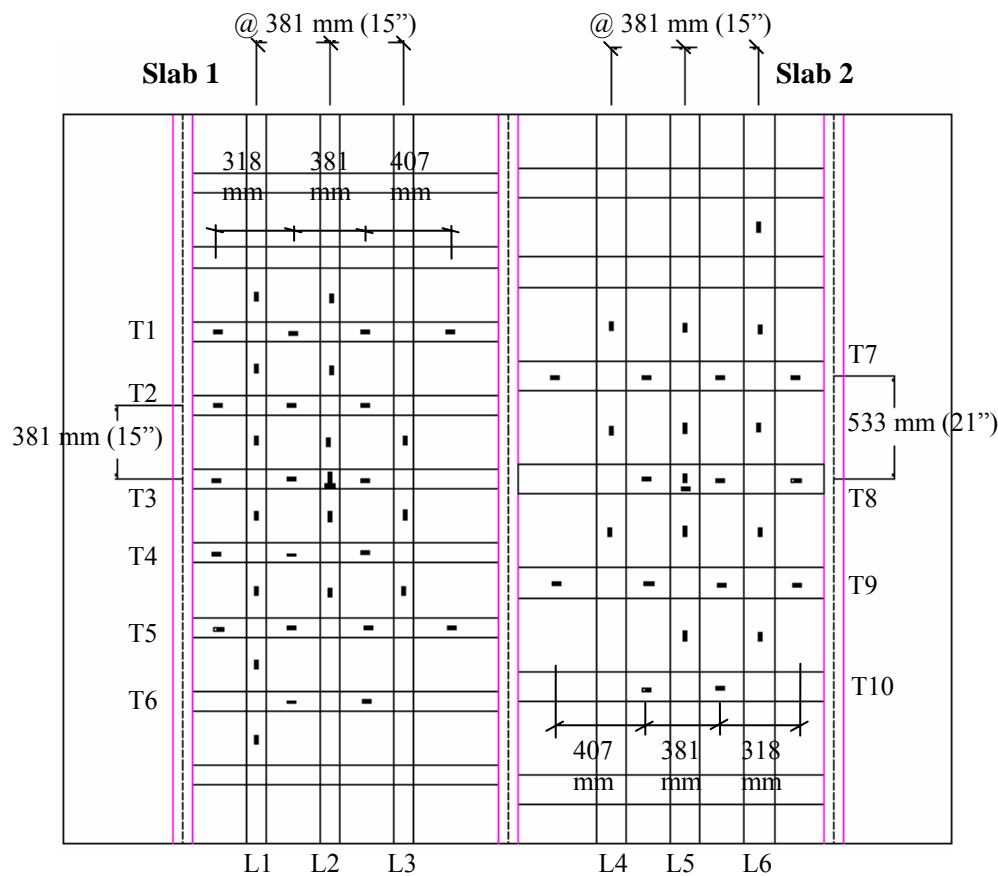


Figure 4.33 Locations of gages on composite after slab strengthening

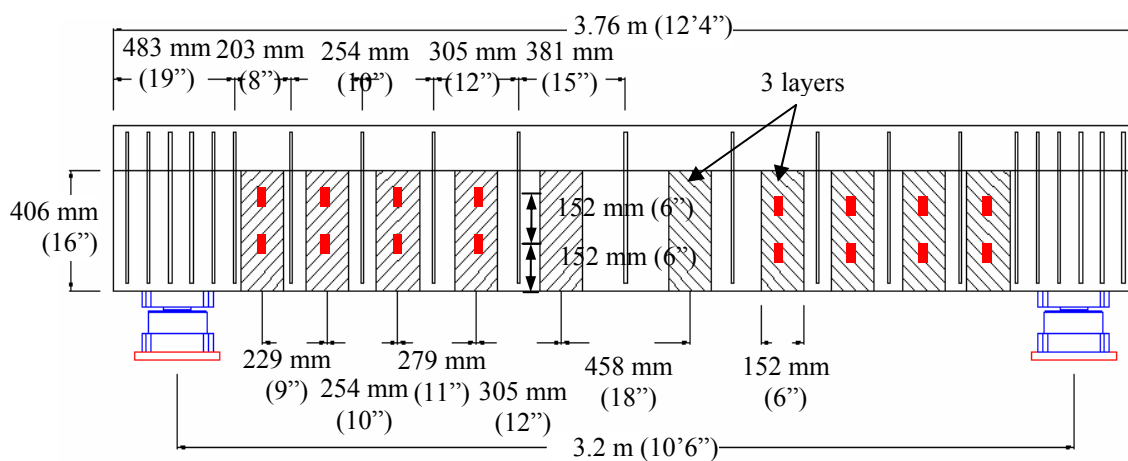


Figure 4.34 Locations of gages on composite stirrup after girder strengthening

4.8.3 Instrumentation details for IR Thermography inspections

The objective of using IR Thermography in the current test program was two-fold, the first being the detection of any pre-existing defect/damage areas in the composites those were produced during their installation on the soffit of the deck slabs. The second objective was the characterization of damage progression in the strips/laminates with loading. Inspection was carried out before the start of phase 2 of loading after strengthening of the deck slabs to form the baseline for subsequent inspections. The data was acquired using a commercial thermographic NDT system (Figure 4.35a). Flash heating, provided by 2 xenon flashtubes with 5 ms flash duration, was used to simulate a temperature differential between the composite and any potential defect. An infrared camera with a 256 x 256 pixel focal plane array, operating in the 2 – 5 μm spectral range was used. Continuous data was acquired at a 60 Hz frame rate for 20 sec after flash heating for each shot. The field of view of the Thermography system used was 305 mm x 230 mm (12" x 9") and thus the surface of the test specimens was divided into a number of grids and each grid was imaged independently. An overlap of about 51 mm (2") was maintained between the adjacent shots so that during the processing of the thermography data the adjacent thermal profiles could be brought together and superimposed. Further details of the inspection process will be presented in Chapter 6. The setup for thermography inspection of the composite in the strengthened deck slabs is presented in Figure 4.35b.



a) Thermography data acquisition unit



b) Thermography setup

Figure 4.35 Non-destructive inspections using IR Thermography

4.8.4 Instrumentation details for forced excitation based modal testing

The objective of the vibration tests was three-fold, i) To use system identification techniques to calibrate the baseline FE model based on dynamic characteristics like natural frequencies (and mode shapes); ii) To use system ID and model updating to calibrate subsequent FE models corresponding to various damage states and identify the impact of damage or rehabilitation on the structure and iii) To detect the appearance and progression of damage and evaluate how this affects the overall response of the structure in terms of dynamic characteristics.

In order to confidently determine the mode shape of the structure from vibration testing, an accurate measurement of mode shape with acceptable spatial resolution is needed. For 2nd order bending modes the minimum spatial resolution is $L/4$, where L is the length along which the mode shape will be determined. Thus to get an accurate mode shape for the 2nd transverse/longitudinal bending modes it was necessary to use at least 5 accelerometers per line. With sensor locations along the 3 girders and along the mid-span

of the 2 bays of the slab it was thus necessary to have a minimum of $5 \times 5 = 25$ accelerometers. The details of the capacitive accelerometers as presented by the manufacturer are provided in Table 4.13. The data from the accelerometers was collected through a National Instruments data acquisition system (DAQPAD-6052E).

Table 4.13 Performance details of the capacitive accelerometers

	ENGLISH	SI
Sensitivity ($\pm 5\%$)	100 mV/g	10.2 mV/(m/s ²)
Measurement Range	± 20 g pk	± 196 m/s ² pk
Frequency Range ($\pm 5\%$)	0 to 300 Hz	0 to 300 Hz
Frequency Range ($\pm 10\%$)	0 to 500 Hz	0 to 500 Hz
Resonant Frequency	>900 Hz	>900 Hz
Phase Response (100 Hz)	<10 °	<10 °
Damping Ratio	70 % Critical	70 % Critical
Broadband Resolution (0.5 to 100 Hz)	110 μ g rms	1080 μ m/s ² rms
Non-Linearity	$\leq 1\%$	$\leq 1\%$
Transverse Sensitivity	$\leq 3\%$	$\leq 3\%$

Three setups of accelerometers were used for the vibration tests. The first setup included 25 accelerometers evenly distributed over the test specimen in 5 rows of 5 each and was used to get the global modal characteristics of the test specimen. The second setup included 27 accelerometers distributed over slab 1 and the third setup of accelerometers included 27 accelerometers distributed over slab 2. These two setups were used to get local modal characteristics in the slab components indicating relative damage in the two slabs. Combination of setups 2 and 3 would also be used to obtain a better spatial resolution in obtaining the mode shapes of the test specimen. The setup locations are presented in Figure 4.36.

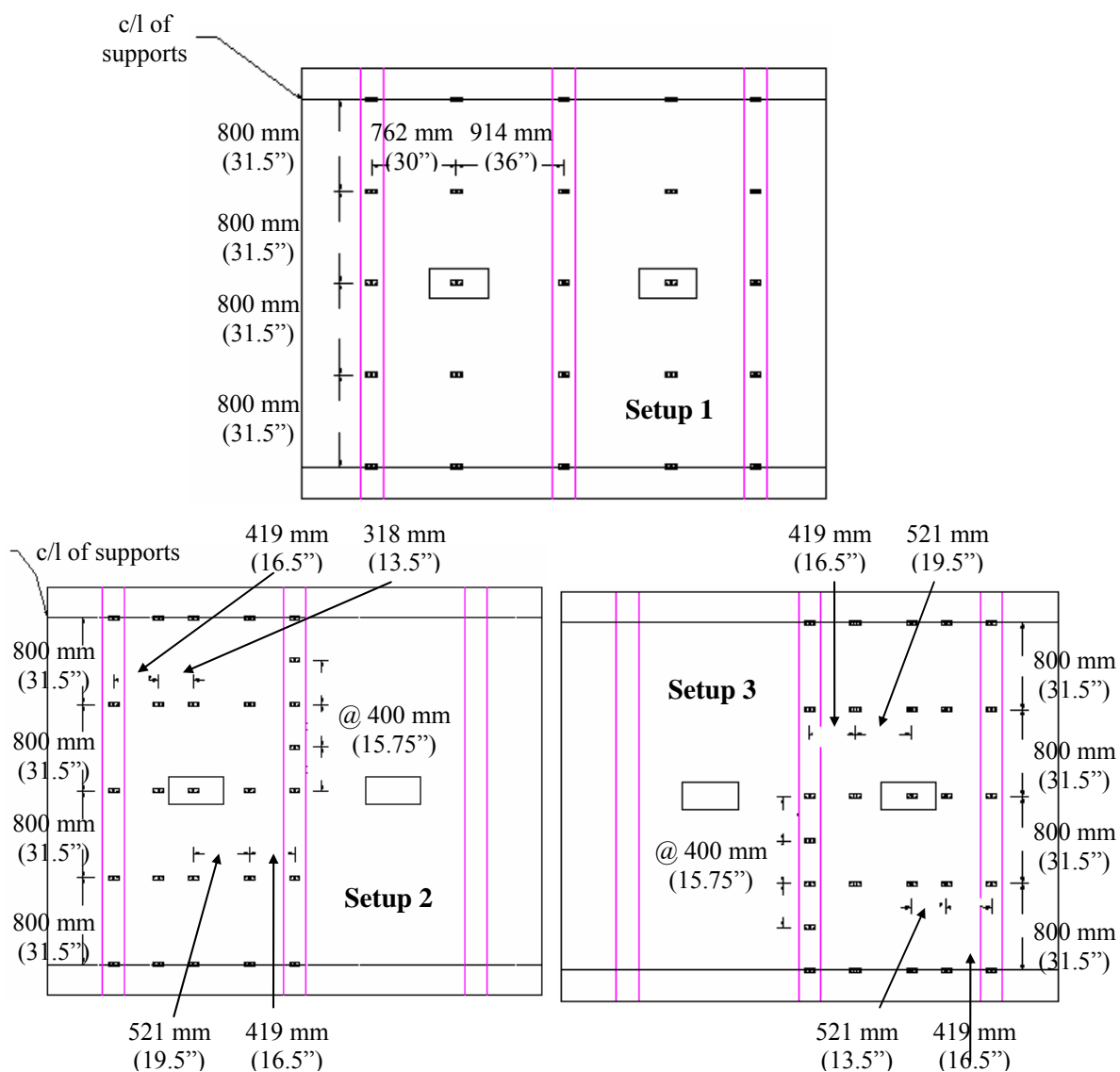


Figure 4.36 Locations of accelerometers for the three setups

Since a forced excitation based modal test procedure was followed, three different excitation sources were used for comparative evaluation of the modal characteristics obtained from these sources. The three sources used were: i) A drop hammer with a mass of 22.2 kg (60 lbs) dropped from a height of 640 mm (25.5 inches) producing an average

impact force of 7.6 kN (1.7 kips); ii) A small impact hammer with maximum impact force of 2.2 kN (500 lbs) and iii) A shaker with maximum impact force of 0.2 kN (50 lbs). The drop hammer was found to result in higher modal amplitudes but could excite only a few lower modes. The small hammer could excite more natural frequencies of the structure but had smaller modal amplitude as compared to the drop hammer. The shaker was used to get better frequency resolution for the purpose of system identification since the shaker could provide a longer time period excitation. Comparison between the three sources of excitation will be discussed later in chapter 6. The excitation sources are illustrated in Figure 4.37. The data was collected at zero load as well as at 107 kN (24 kips), which represented the permit truck load [57], after cycling back from each load step. The results from the vibration tests will be presented in Chapter 7.



Figure 4.37 Forced excitation with three different excitation sources

5 TEST RESULTS

The test was carried out in three stages following the test plan presented earlier in Section 4.4 and summarized in Figure 5.1. In stage 1 the specimen was loaded until the deck slabs reached their punching shear critical limit state and were then strengthened using externally bonded FRP composites. The specimen was further loaded in stage 2 until the girder reached shear critical limit state and was strengthened. The specimen was then loaded to failure in Stage 3. Non-destructive evaluations (NDE) were carried at regular load intervals throughout the test. The general test plan with the critical limit states governing each phase of testing is also presented here in Table 5.1 for reference.

Table 5.1 Test phases

Test phase	Purpose	Definition of Limit state
1	Reach flexural/punching shear criticality in deck slabs and strengthen only the slabs in flexure with FRP composite	75% of yield strain in the transverse steel reinforcement in the slab below the load area or 75% of the punching shear capacity of the slabs, whichever was reached first
2	Reach shear criticality in center girder and strengthen girder in shear with FRP composite stirrups	75% of yield strain in the internal steel stirrups of center girder
3	Ultimate failure of strengthened deck slabs	Debonding of composite in the strengthened slabs followed by punching shear failure

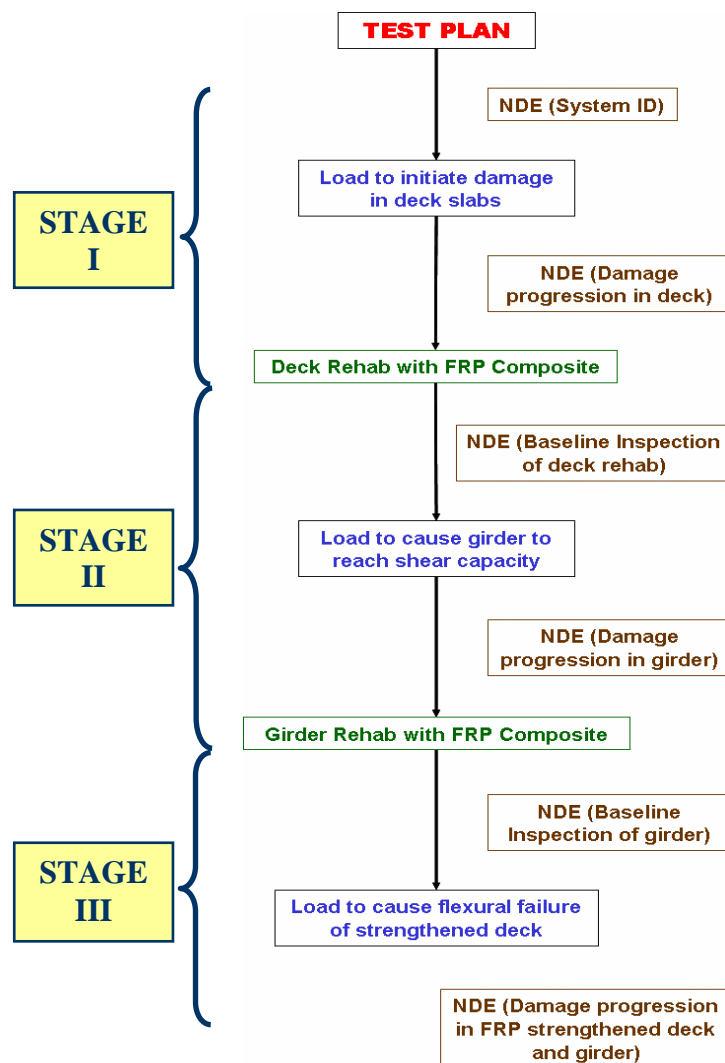


Figure 5.1 Schematic of test plan

5.1 Results from Phase 1 of Testing - Introduction

In phase 1 the test specimen was loaded to cause a predetermined level of damage in the deck slabs. This level was chosen as 75% of transverse steel yield (1926 microstrains) in the deck slab reinforcement or 75% of the punching shear capacity of the slabs (415 kN), whichever was reached first. Such a load level was deemed to be representative of deterioration in the deck slab that would warrant

rehabilitation/strengthening of the slabs with externally bonded FRP composites to prevent further degradation and failure. The theoretical predictions of the wheel loads at which this damage would be achieved were estimated and presented in Chapter 4.

5.1.1 Load Capacity and Stiffness Results

The loading protocol for phase 1 of test was designed by taking into account the theoretical loading states in terms of flexural and punching shear capacity of the deck slabs, as obtained from the initial estimates as presented in Chapter 4. The limit states, defined as 75% of yield strain in the slab transverse reinforcement was predicted to be produced by wheel load of 339 kN (76.2 kips) and the limit of 75% of punching shear capacity was predicted to be caused by wheel load of 415 kN (93 kips). The first cracks were predicted to occur around 156 kN (35 kips) for a cracking strain in the bottom concrete of 0.0132% corresponding to a cracking stress of 4.14 MPa (599.5 psi) which was predicted from Clause 9.5.2.3 of ACI 318 [69] as follows:

$$\text{Cracking stress, } \sigma_{cr} = 7.5 \sqrt{f'_c} = 7.5 \sqrt{6390} = 4.14 \text{ MPa (599.5 psi)} \quad \dots\dots\dots(5.1)$$

$$\text{Elastic modulus of concrete, } E_c = 57000 \sqrt{f'_c} = 57000 \sqrt{6390} = 31.46 \text{ GPa (4556 ksi)} \quad \dots\dots\dots(5.2)$$

Thus, the cracking strain was obtained as,

$$\varepsilon_{cr} = \frac{\sigma_{cr}}{E_c} = 0.132\% \quad \dots\dots\dots(5.3)$$

The specimen was first loaded upto 107 kN (24 kips) for each actuator corresponding to permit truck wheel load as specified by bridge design specifications

[53]. The specimen was then loaded upto 156 kN (35 kips) but no cracks were observed at this load level. The specimen was further loaded upto 214 kN (48 kips), at which stage cracks were observed at the bottom of the slabs. These cracks were primarily located below the load area and ran in the transverse direction between the girders. Further details of the crack pattern with the progression of cracks in the slabs will be presented later in section 5.1.2 of the chapter. The load was then first cycled back to 107 kN (24 kips) for NDE inspections and then brought down to zero. The next load cycle corresponded to 259 kN (65 kips). This was done to ensure, through inspection of the strain readings in the slab reinforcement, that the slabs did not reach their flexural criticality that was predicted at 339 kN (76 kips). As will be discussed in section 5.1.3 of this chapter, the strains in the slab reinforcement were found to be well below 75% of yield strain (1926 microstrains) at this load level, with maximum measured strain of 950 micro-strains. Thus after reaching 259 kN (65 kips) the load was cycled back to 107 kN (24 kips) for NDE inspections and then brought down to zero. The specimen was then loaded first to 356 kN (80 kips) to mark cracks and then loading continued to 400 kN (90 kips), at which stage punching shear cracks were found to be well developed and will be discussed later. The load was brought down to 107 kN (24 kips) for NDE inspections and then to zero. The loading protocol for phase 1 is presented in Table 5.2.

The load-deflection plot for slab 1 as obtained by plotting the actuator load on slab 1 against the deflection measured below the load obtained from the linear potentiometer LPM3, is presented in Figure 5.2. An estimate of the stiffness of the deck slab can be obtained based on the slope of the load-deflection plot. The effect of damage on the stiffness of the test specimen components will be presented in Chapter 7. No

change in slope of the load-deflection response was observed between the 107 kN (24 kips) and 214 kN (48 kips) load cycles indicating that insignificant damage occurred in the slab upto this load level. However degradation of the initial tangent stiffness at subsequent load stages was observed and represented damage due to the appearance of cracks at the bottom of the deck slabs that will be discussed in section 5.1.2. The load-deflection results of the two deck slabs are compared in Figure 5.3. For slab 2 the deflection at LPM9 was plotted against the load from actuator 2. It was seen that both the slabs had very similar behavior, with the initial tangent stiffness of slab 2 being slightly higher than that of slab 1.

Table 5.2 Loading protocol for phase 1

Load cycle #	Peak load kN (kips)	Load cycle remarks
1	107 (24)	NDE carried out under permit truck load [53] and used as baseline for subsequent inspections at other load cycles
2	214 (48)	Loading was stopped at 156 kN (35 kips), which was the theoretical load to cause cracking in slabs. However since no cracks were noticed, loading was continued to 214 kN (48 kips) which was halfway between baseline load of 107 kN (24 kips) and theoretical load to cause slab reinforcement to reach 75% yield at 320 kN (72 kips)
3	289 (65)	Loading to ensure that the slab reinforcement had not reached 75% of yield strain, which was predicted at 320 kN (72 kips)
4	400 (90)	Predicted 75% of punching shear capacity of deck slabs

* Note: For each load cycle after reaching peak load, the load was first brought down to 107 kN (24 kips) for NDE inspections and then the specimen was unloaded by retracting the actuators away from the specimen before starting the next load cycle

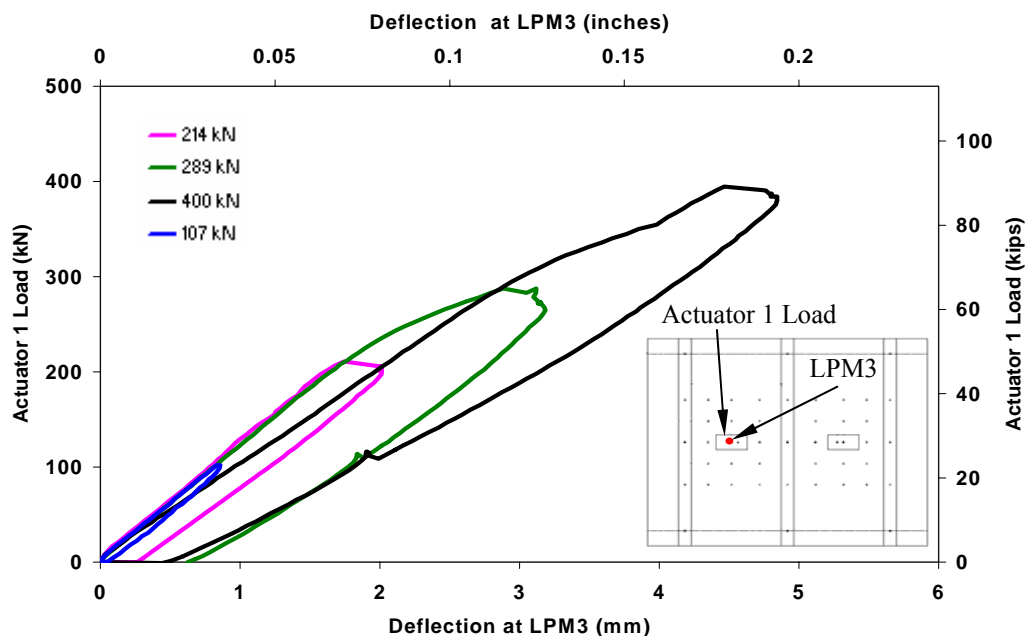
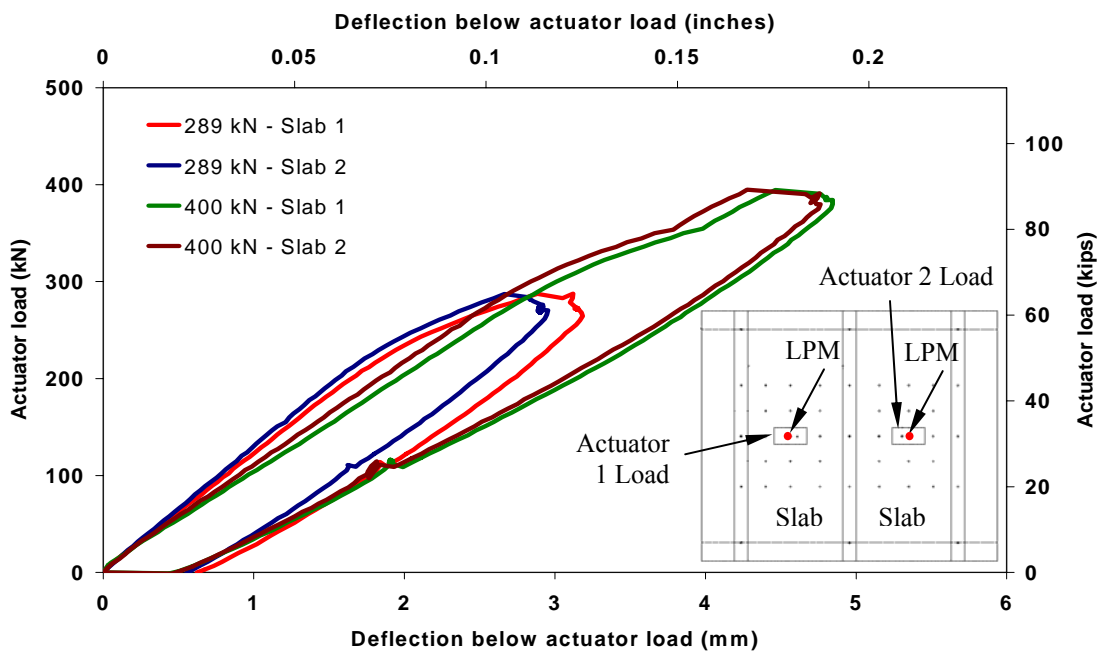


Figure 5.2 Load-deflection plots for slab 1 in phase 1



Note: For slab 1 Actuator load 1 was plotted against deflection at LPM3

For slab 2 Actuator load 2 was plotted against deflection at LPM9

Figure 5.3 Comparison of load-deflection plots between deck slabs

The deflections at the center of the middle and edge girders as measured by the linear potentiometers, LPM6, LPM1 and LPM11 respectively, were plotted against actuator load in Figures 5.4a and 5.4b. For the center girder some degradation in stiffness was seen between the 289 kN (65 kips) and 400 kN (90 kips) load cycles. However for the edge girders there was very little change in the slope of the load-deflection plots over the load cycles indicating that there was insignificant degradation. This was substantiated by visual observations of crack patterns, from which it could be seen that most of the damage for phase 1 was concentrated in the deck slabs. The only damage observed in the center girder was in the form of flexural cracks in the middle region of the girder and some cracks in the support region propagating from the slabs onto the center girder. The crack pattern observed in the girder with loading will be presented later in section 5.1.2. No significant cracks were observed in the edge girders. The deflections at the center of the edge girders, E1 and E2 (as shown in Figure 5.4c) were compared and the girder E1 was found to have comparatively larger deflection than that of E2 [1.41 mm at center of E1 as compared to 1.25 mm at center of E2 at peak load of 400 kN load cycle].

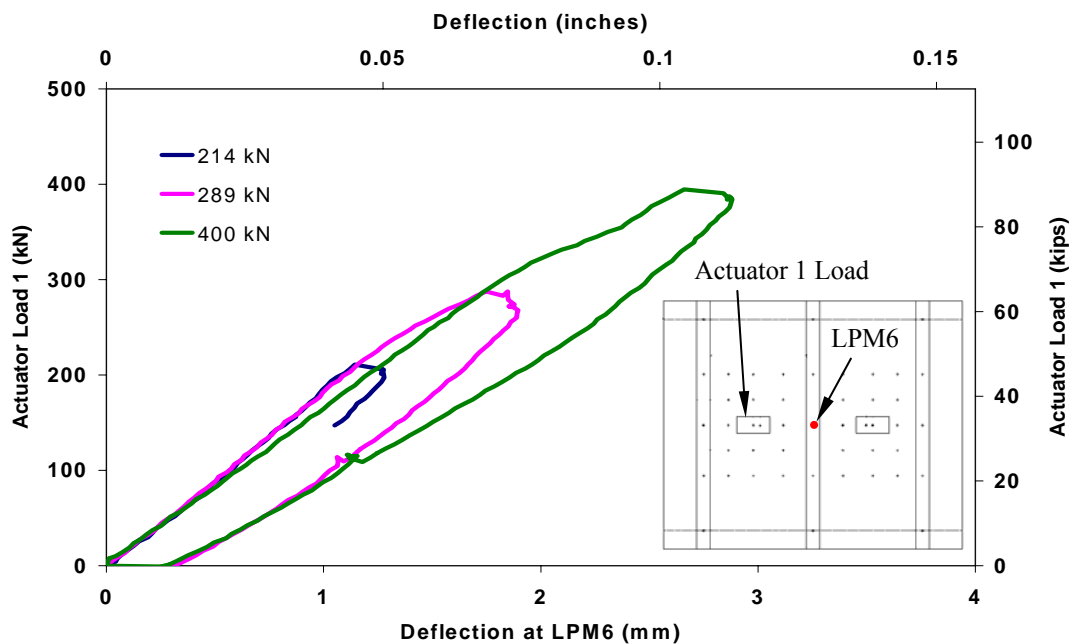


Figure 5.4a Actuator load 1 vs. mid-span deflection plots for middle girder

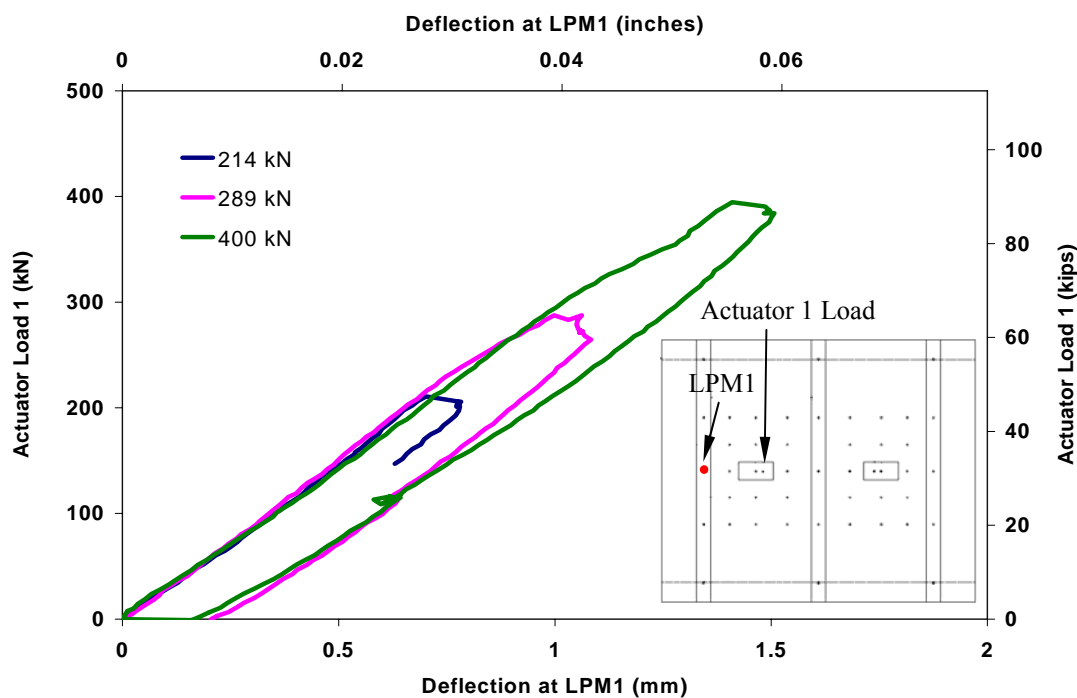
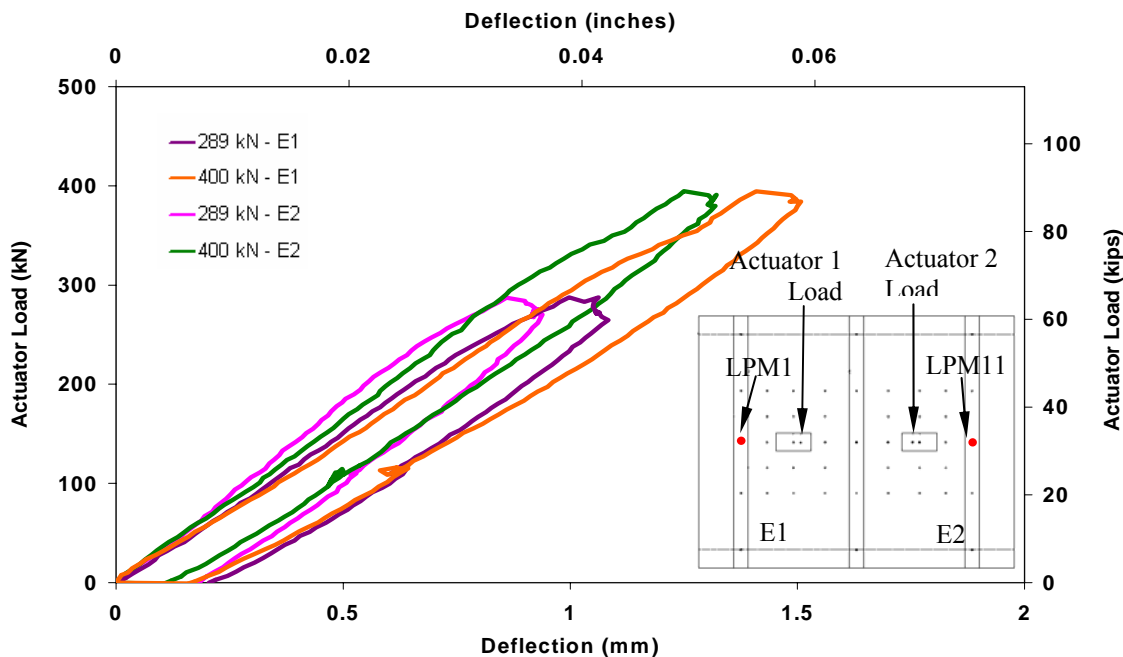


Figure 5.4b Actuator load 1 vs. mid-span deflection plots for edge girder



*Note: For edge beam 1 (E1) Actuator load 1 was plotted against deflection at LPM1
For edge beam 2(E2) Actuator load 2 was plotted against deflection at LPM11*

Figure 5.4c Comparison of load-deflection plots between edge girders

For comparative evaluation of the degradation of the slope of load-deflection response of the slabs and the girder over the load cycles, which was representative of the trend in damage progression, a parameter, “effective” stiffness, was defined as follows:

$$\text{Effective stiffness} = \frac{\text{Peak actuator load of a load cycle}}{\text{Deflection at that load at location under consideration}} \quad \dots (5.4)$$

It should be noted that this “effective” stiffness obtained from the linear potentiometer data can only be treated as a representative of the relative progression of change in response over the load cycles. The calculation of actual bending stiffness of the

slab/girder has to take into account the moment-curvature response rather than load-deflection response. These calculations will be presented later in Chapter 7. Thus since absolute values of the “effective” stiffness had no significance, “effective” stiffness ratios were computed as defined below:

$$\text{Effective stiffness ratio} = \frac{\text{Effective stiffness at a Load Cycle}}{\text{Effective stiffness at baseline (108 kN)}} \quad \dots(5.5)$$

The load of 108 kN (24 kips), which was also the first loading cycle of phase 1, was chosen as the baseline load and the effective stiffness ratios were calculated by comparing the effective stiffness at a load cycle with respect to the effective stiffness at this baseline load (Eqn. 5.5). This load represented a permit truck load of 107 kN (24 kips) [53] with the test specimen being in the linear elastic range at this load level without any degradation, so that the effective stiffness ratio at this load level is taken to be 1.0.

The effective stiffness ratios in the deck slabs and girders are presented in Tables 5.3a and 5.3b, respectively. It is to be noted that the total deflection measured at the deck slab is the sum of the deflection of the slab itself along with the deflection of the supporting girders. This is schematically presented in Figure 5.5. Thus the true deflection of the deck slab was obtained by subtracting the contribution of the girder deflection from the total deflection of the deck slabs, as given by equation 5.6.

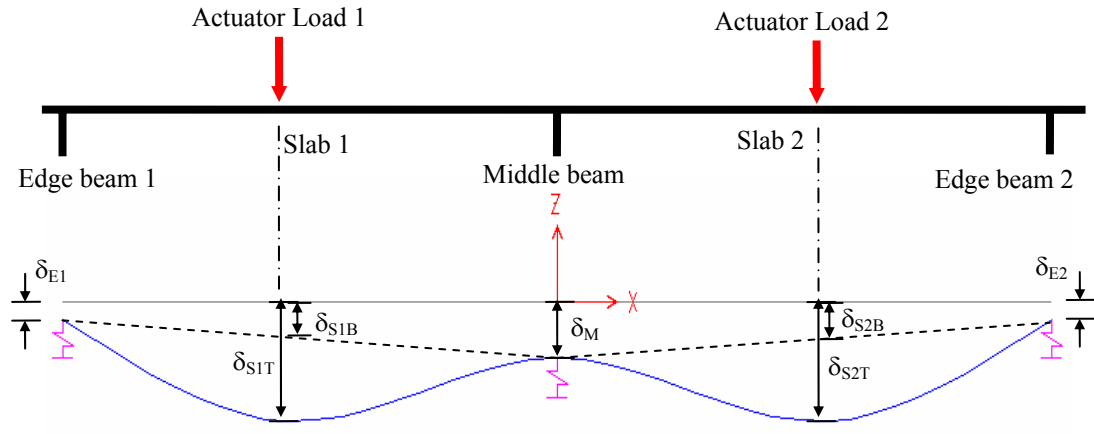


Figure 5.5 Schematic of deflection of specimen under load

In figure 5.5, the notations used represent the following:

- δ_{E1} Deflection of edge beam 1
- δ_{E2} Deflection of edge beam 2
- δ_M Deflection of middle beam
- δ_{S1T} Total deflection of slab 1 below actuator load 1
- δ_{S2T} Total deflection of slab 2 below actuator load 2
- δ_{S1B} Contribution of the deflections of edge beam 1 and middle beam to the deflection of slab 1
- δ_{S2B} Contribution of the deflections of edge beam 2 and middle beam to the deflection of slab 2

Thus the true deflections of slabs 1 and 2 can be expressed as:

$$\delta_{S1Actual} = \delta_{S1T} - \delta_{S1B} \dots\dots\dots(5.6a)$$

$$\delta_{S2Actual} = \delta_{S2T} - \delta_{S2B} \dots\dots\dots(5.6b)$$

Thus the deflections of the slabs presented in Table 5.3a were computed from the total deflections of the slabs and the girders (using equation 5.6) at the peak load of each load cycle and thereafter the effective stiffness ratios of the slabs were determined.

Table 5.3a Effective stiffness ratio in slabs in phase 1 from linear potentiometer data

Slab 1 (Deflections below actuator load)			Slab 2 (Deflections below actuator load)		
Actuator load kN (kips)	Actual deflection mm (inches)	Effective stiffness ratio	Actuator load kN (kips)	Actual deflection mm (inches)	Effective stiffness ratio
102.3 (23)	0.38 (0.015)	1.00	101.66 (22.8)	0.38 (0.015)	1.00
211.16 (47.5)	0.84 (0.033)	0.95	210.85 (47.4)	0.83 (0.033)	0.96
288.01 (64.7)	1.55 (0.061)	0.70	287.73 (64.6)	1.40 (0.055)	0.77
395.21 (88.8)	2.49 (0.098)	0.60	395.55 (88.9)	2.39 (0.094)	0.63

Table 5.3b Effective stiffness ratio in girders in phase 1 from potentiometer data

Center girder			Edge girder		
Actuator load kN (kips)	Mid-span deflection mm (inches)	Effective stiffness ratio	Actuator load kN (kips)	Mid-span deflection mm (inches)	Effective stiffness ratio
102.3 (23)	0.57 (0.023)	1.00	102.3 (23)	0.35 (0.014)	1.00
211.16 (47.5)	1.31 (0.051)	0.91	211.16 (47.5)	0.73 (0.029)	0.98
288.01 (64.7)	1.75 (0.069)	0.92	288.01 (64.7)	1.0 (0.039)	0.98
395.21 (88.8)	2.66 (0.105)	0.83	395.21 (88.8)	1.41 (0.056)	0.95

From Table 5.3a it is seen that for the deck slabs there was significant degradation of “effective” stiffness ratios between the 288 kN and 395 kN load cycles in phase 1. The load of 211.16 kN (47.5 kips) corresponds to the load cycle resulting in cracking in the slabs and the load of 395.2 kN (88.8 kips) corresponds to damage in deck slabs due to punching shear criticality. The effective stiffness ratios of slabs 1 and 2 were found to

drop to 0.6 and 0.63, respectively at the end of phase 1 loading in the 395 kN load cycle. This is hypothesized to be due to the punching shear cracking in the deck slabs which resulted in degradation of slab stiffness. The effective stiffness ratios of both slabs 1 and 2 were comparable with the effective stiffness ratios of slab 1 being slightly lower than that of slab 2, as seen in Table 5.3a, thus indicating that slab 1 had a slightly higher damage than slab 2. The reduction of “effective” stiffness in the center girder (as presented in Table 5.3b) was less drastic as compared to the slabs, with significant change being observed only at the 395 kN (88.8 kips) load cycle. This corresponds well with the visual inspection of formation of flexural and shear cracks in the center girder at 356 kN (80 kips), as will be discussed in the next section. The degradation of the effective stiffness ratio in the edge girders was insignificant during phase 1 loading.

5.1.2 Deflection Profiles and Crack Patterns

The deflection profiles over the test specimen were obtained from the linear potentiometers. The deflection profiles along the lengths of the middle and edge girders at the peak loads in each of the load cycles of phase 1 are presented in Figure 5.6. The deflections were measured at mid and quarter span and at supports of the girders. As expected, since the load on the middle girder was contributed by the influence areas of both the slabs, the center deflection of the middle girder (Figure 5.6a) was about 1.9 times the center deflection of the edge girders. The deflections of the two edge girders are shown in Figures 5.5b and 5.5c. The maximum deflection in edge girder 1 was slightly higher than that in edge girder 2 [1.41 mm in edge girder 1 as compared to 1.25 mm in edge girder 2] at peak load of 400 kN load cycle.

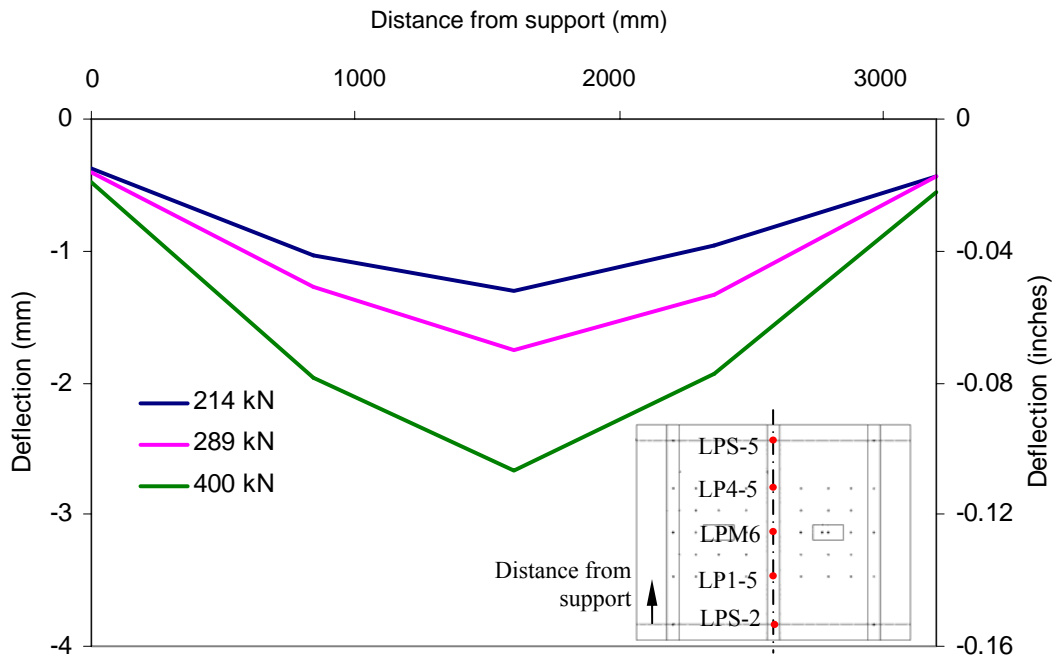


Figure 5.6a Deflection along length of middle girder

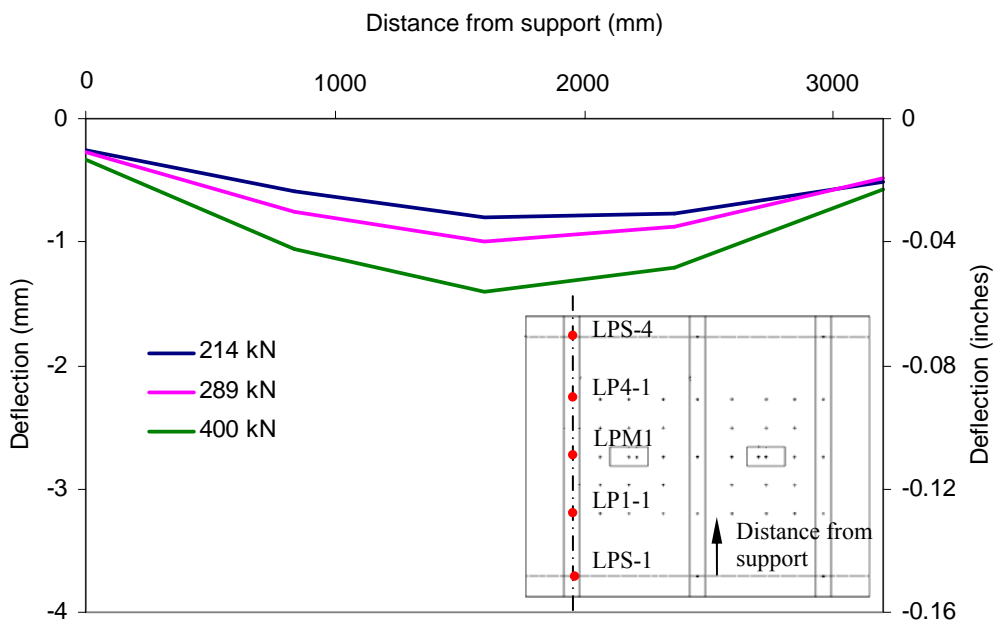


Figure 5.6b Deflection along length of edge girder 1

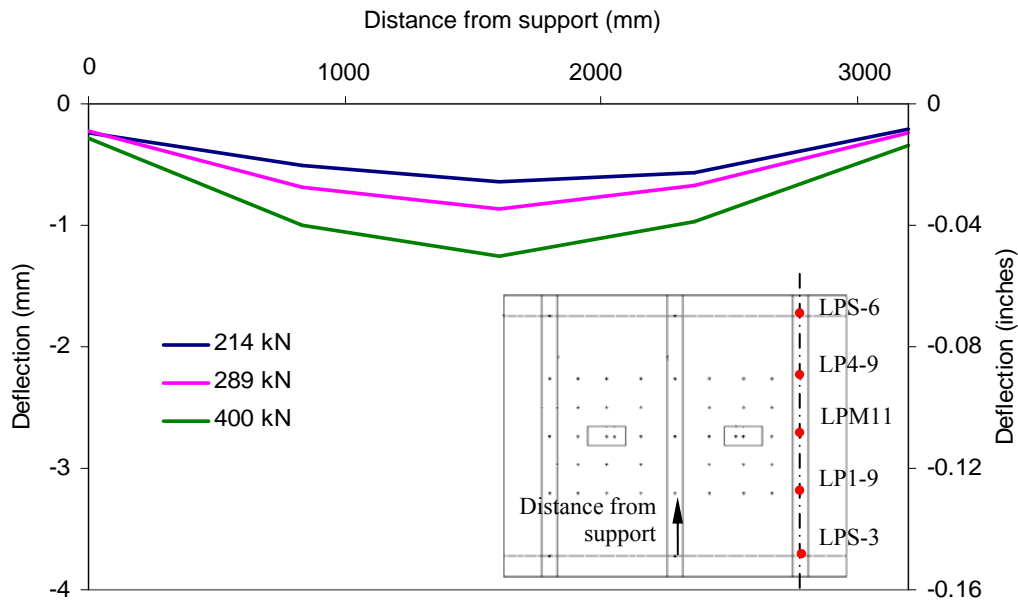


Figure 5.6c Deflection along length of edge girder 2

The deflection contour profile over the surface of the deck slabs at the end of phase 1 loading at 400 kN (90 kips) is presented in Figure 5.7. This plot gives a representation of the deflection profile trend over the surface of the slabs. It was observed that the highest deflections of the slabs were concentrated in the regions under the load contact areas of the actuators. Representative deflection measurements recorded by the rows of linear potentiometers at the peak loads at the end of each load cycle for phase 1 are presented in Figures 5.8 and 5.9. Row 2 of linear potentiometers was located 381 mm (15") away from mid-span of the specimen, at which the vertical deflections were measured by row M of potentiometers. Since row M of linear potentiometers was located along the line of loading, the deflections recorded along this line were higher than the corresponding deflections recorded at other locations. The highest deflections were recorded directly below the load areas. Also the highest deflection in slab 2 was slightly

lower than that in slab 1 [4.28 mm in slab 2 against 4.46 mm in slab 1] at the 400 kN (90 kips) load cycle. However, in general the behavior of the two slabs was similar.

As observed from the deflection profiles, the areas of the deck slabs under the load contact areas were subjected to the highest levels of stress concentrations and this was also corroborated by the visual inspections of crack patterns. The crack patterns observed are presented in Figure 5.10. The primary transverse and longitudinal cracks in the deck slabs were formed around 178 kN (40 kips) under the load contact areas. The transverse cracks were spaced at approximately 203 mm (8") which corresponded to the spacing of the transverse steel reinforcement in the deck slabs. However these cracks were few and were only observed below the load area. With further loading, in the 289 kN (65 kips) load cycle, a number of cracks were found to originate from the load area under the slabs and propagated diagonally across towards the ends of the girders as is shown in Figure 10. Similar trend in crack patterns was observed in the 356 kN (80 kips) load cycle. Finally in the 400 kN (90 kips) load cycle most of these cracks were well formed with the crack width below the load areas being about 0.8-1.2 mm (0.03-0.05") as shown in Figure 5.10. A number of minor diagonal cracks were formed at this load level along with the progression of the already existing diagonal cracks towards the ends of the girders. The damage and the crack pattern were representative of local punching shear failure deficiency in the deck slabs. This was corroborated by the strain profiles in the slab reinforcement, which will be presented in the next section of this chapter, from which the strains in the transverse slab reinforcement were found to be well below the yield strain indicating that the slabs had not reach flexural deficiency at the 400 kN (90 kips) load level.

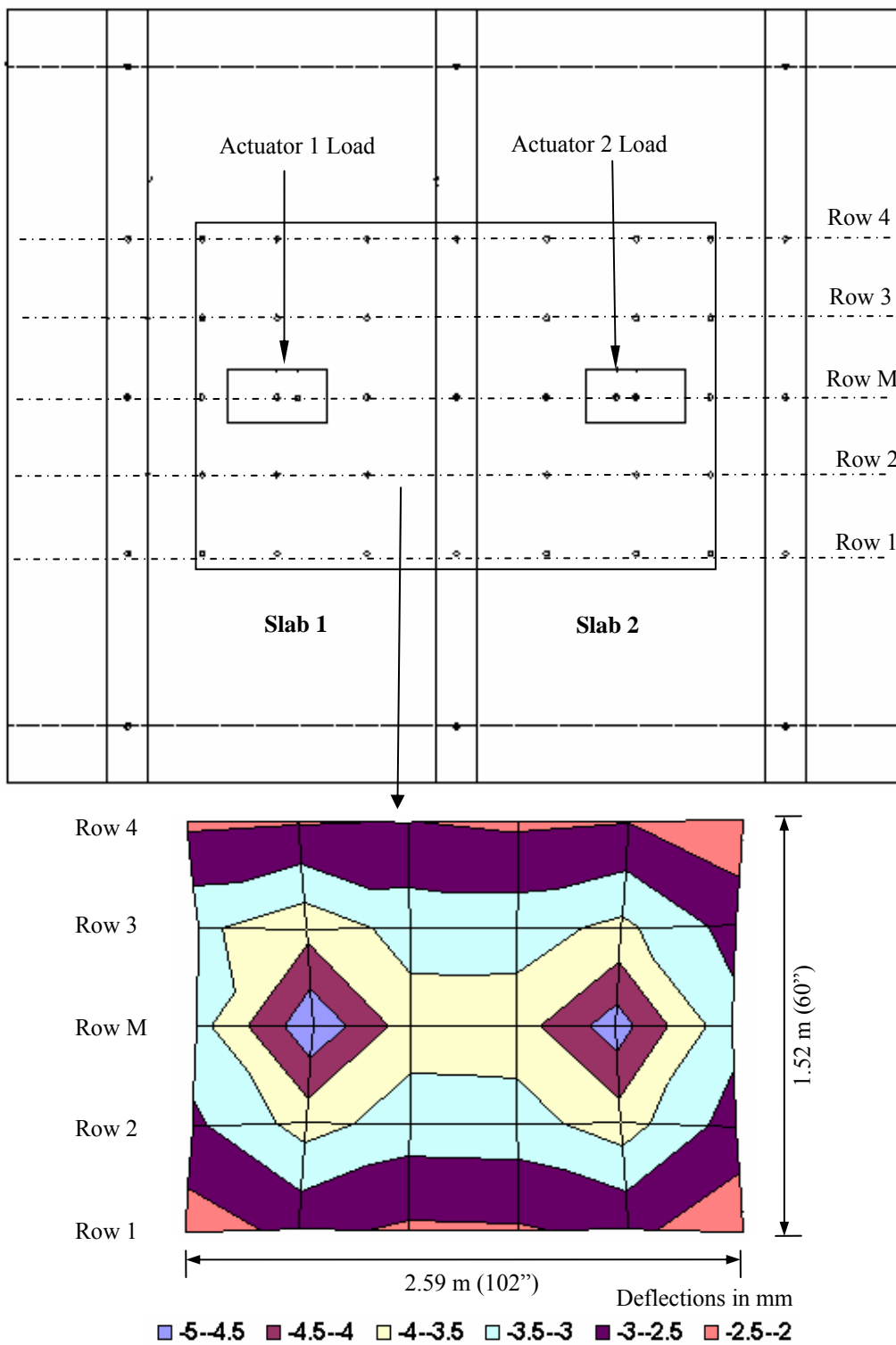


Figure 5.7 Deflection contour over deck slabs at 400 kN (90 kips)

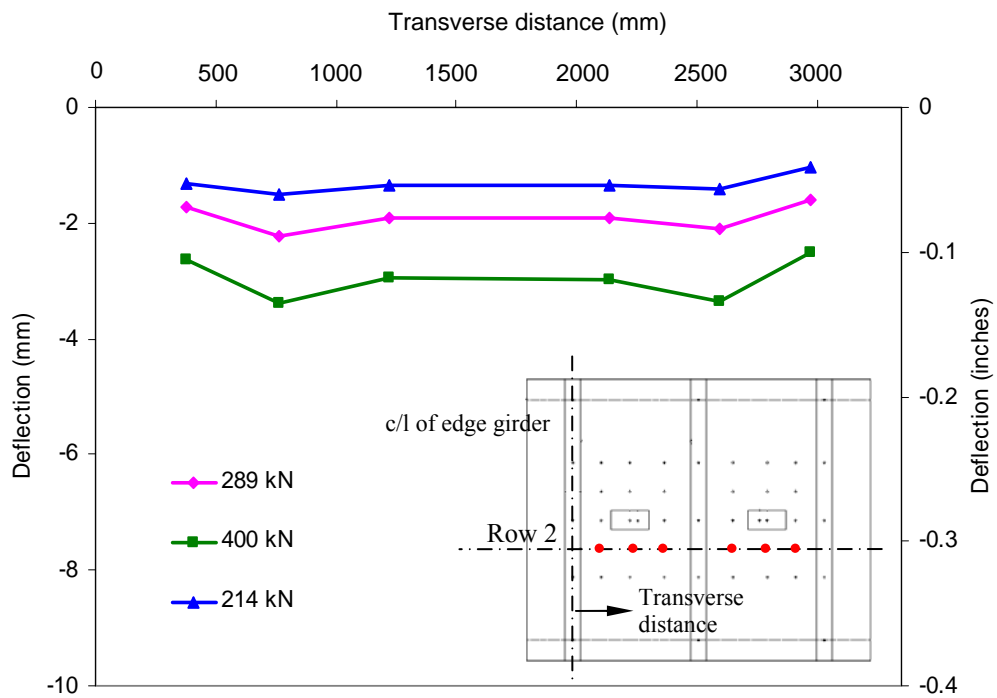


Figure 5.8 Deflection profile along Row 2 of linear potentiometers

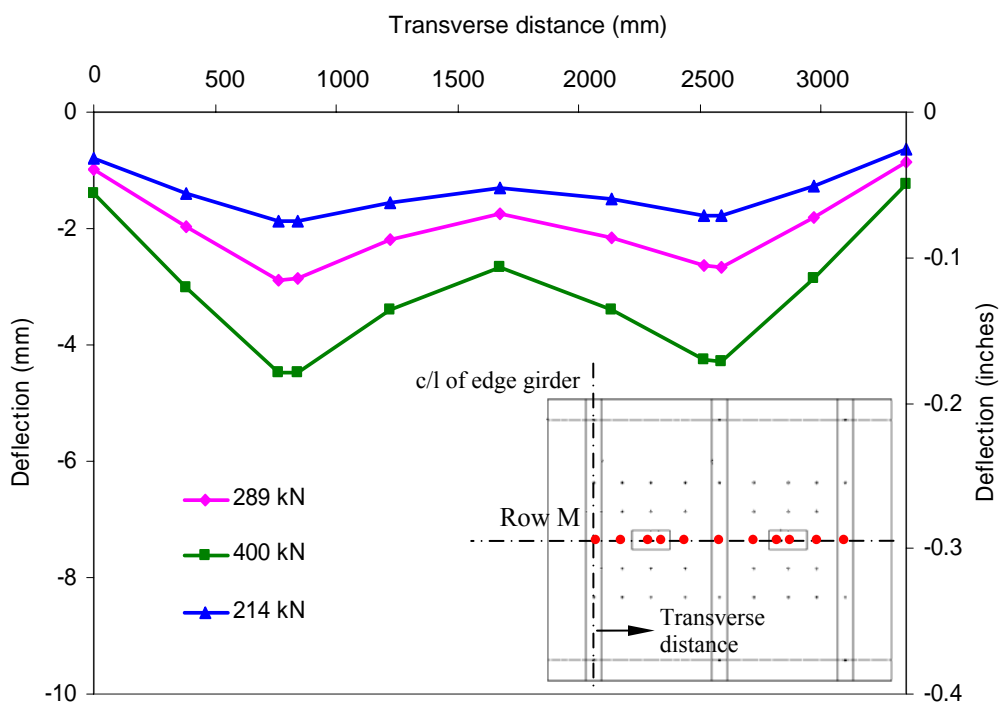
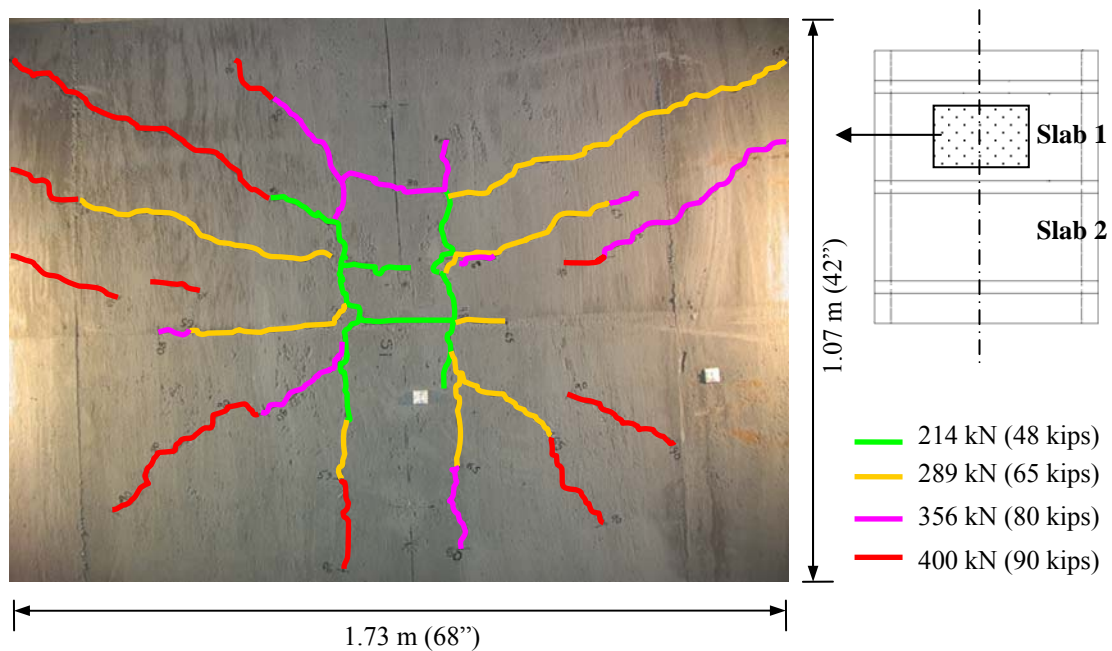
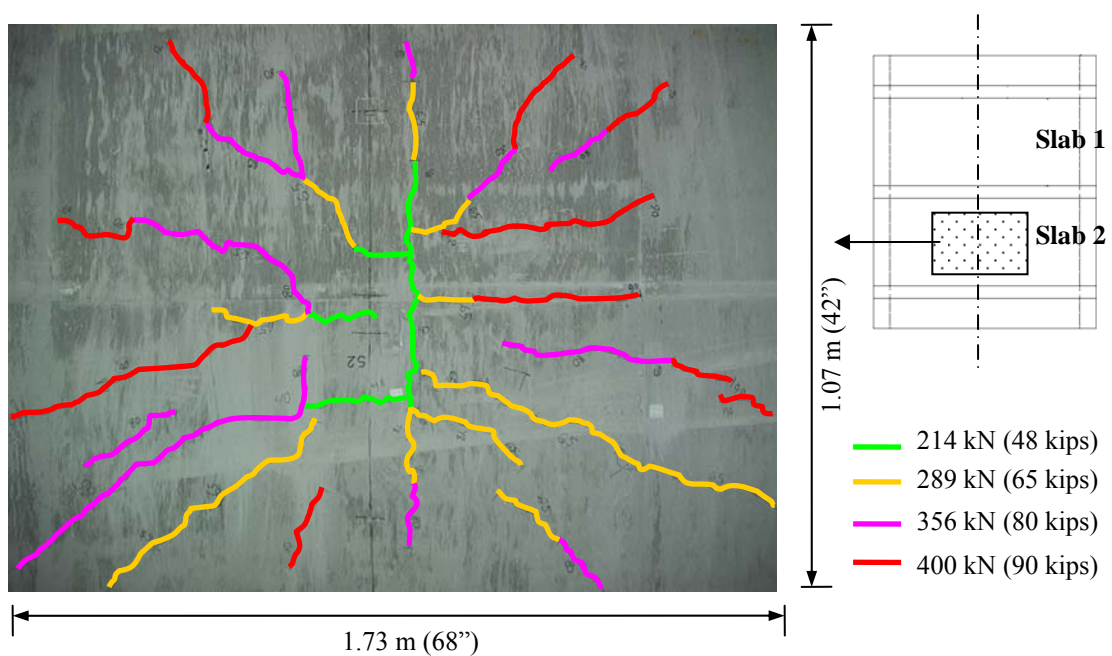


Figure 5.9 Deflection profile along Row M of linear potentiometers



(a) Crack pattern in Slab 1 during Phase 1 loading

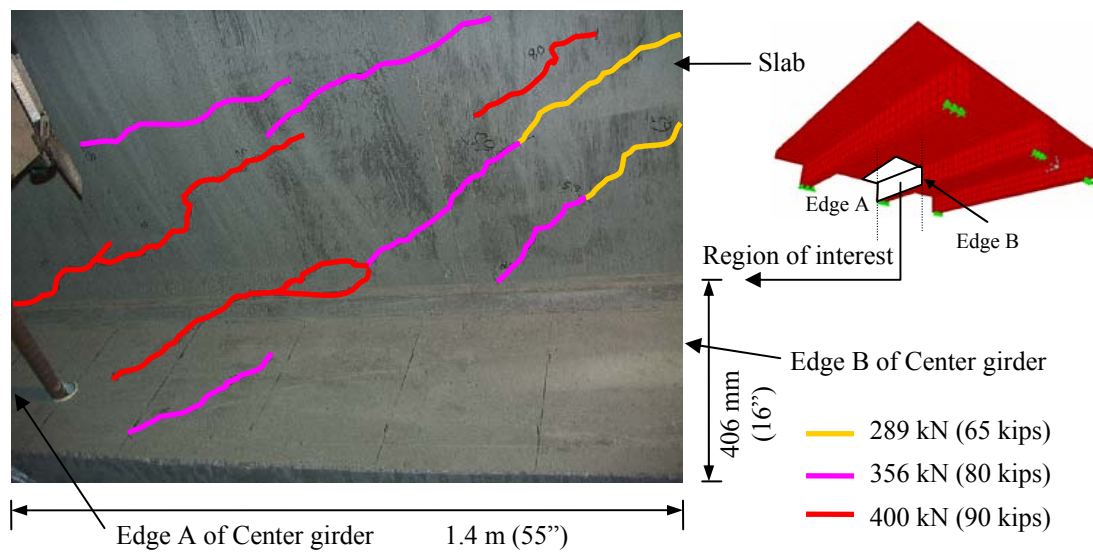


(b) Crack pattern in Slab 2 during Phase 1 loading

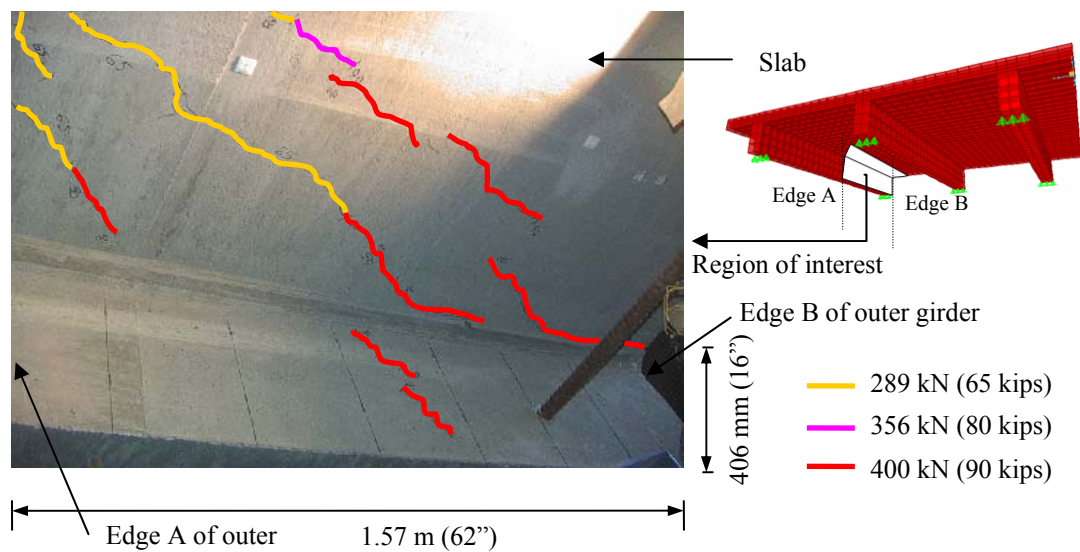
Figure 5.10 Progression of cracks in the deck slabs below load area

The major diagonal cracks in the slabs that propagated from the load area towards the middle longitudinal girder were found to either run along the girder chamfer at the slab-girder interface towards the outer edges of the specimen or joined the shear cracks and ran across the web of the girder. The cracks from the slab that propagated towards the edge girders were always found to run along the girder chamfer towards the outer edge of the specimen. This is presented in Figure 5.11.

No major damage was observed in the girders in phase 1 of loading. The first flexural cracks (Figure 5.12) were observed at the mid-span region of the center girder around 355 kN (80 kips). The cracks were spaced at approximately 178 mm (7") and propagated further up the web to about 305 mm (12 inches) of the girder at 400 kN (90 kips). A few shear cracks (Figure 5.13) also developed near the support areas of the center girder at 355 kN (80 kips) and were found to grow at 400 kN (90 kips). However, as will be discussed in the next section, the strains in the shear stirrups of the girder were well below yield strain (652 micro-strains, which was about 27% of predicted yield strain in the steel stirrups of 2414 micro-strains) indicating that the girder had not reached shear criticality at the end of phase 1 of test. Only a few hairline flexural cracks were formed in the edge girders at the end of phase 1 loading.



(a) Propagation of cracks from slabs into Center girder



(b) Propagation of cracks from slabs into Edge girder

Figure 5.11 Propagation of cracks from slabs into girders during Phase 1 loading

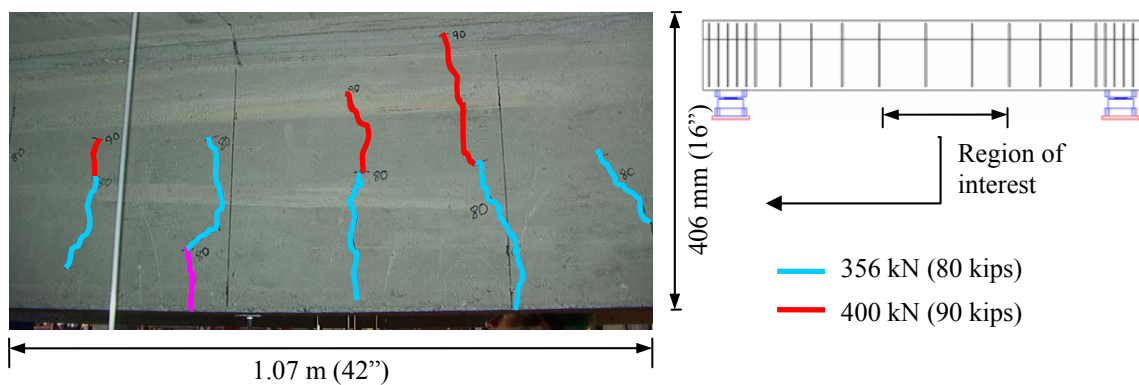


Figure 5.12 Flexural cracks in the center girder at the end of Phase 1 of test

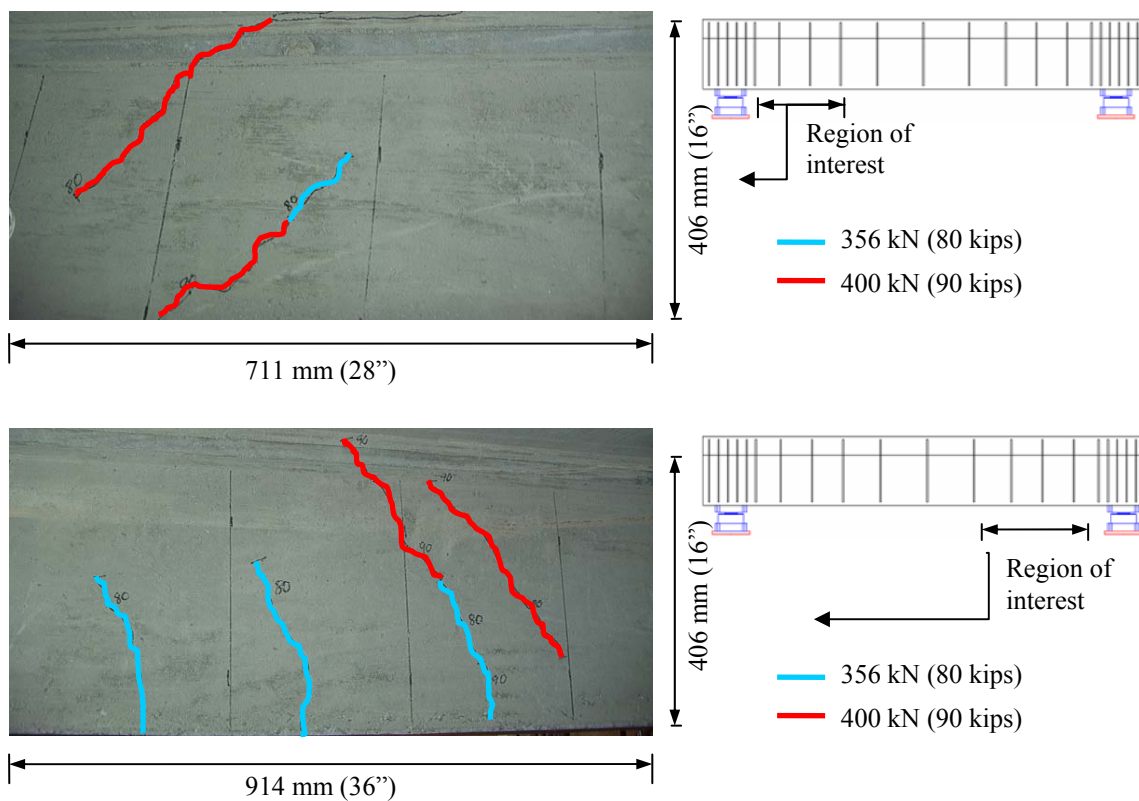


Figure 5.13 Shear cracks in the center girder at the end of Phase 1 of test

5.1.3 Strain Profiles

The strain profiles in the reinforcement of the deck slabs and the girders were obtained from the strain gage data. The development of strain in the transverse slab reinforcement along mid-span of the specimen is presented in Figure 5.14. The strains were highest below the load areas. The strain profile in the transverse slab reinforcement 508 mm (20") from mid-span is presented in Figure 5.15. The maximum strain at this location was 35% of maximum strain along mid-span [348 micro-strains compared to 950 micro-strains at the 400 kN (90 kips) load cycle] indicating that in the deck slabs, the load distribution was localized primarily around the load contact area. The predicted yield strain of the slab transverse steel from the material tests was 2568 micro-strains and thus the strains in the slab reinforcement were below yield strain for phase 1 loading. Also the transverse strain in the steel reinforcement of Slab 1 near the middle girder support location was high (1050 micro-strains) and was indicative of high stress areas along the intersection of the slab and girder.

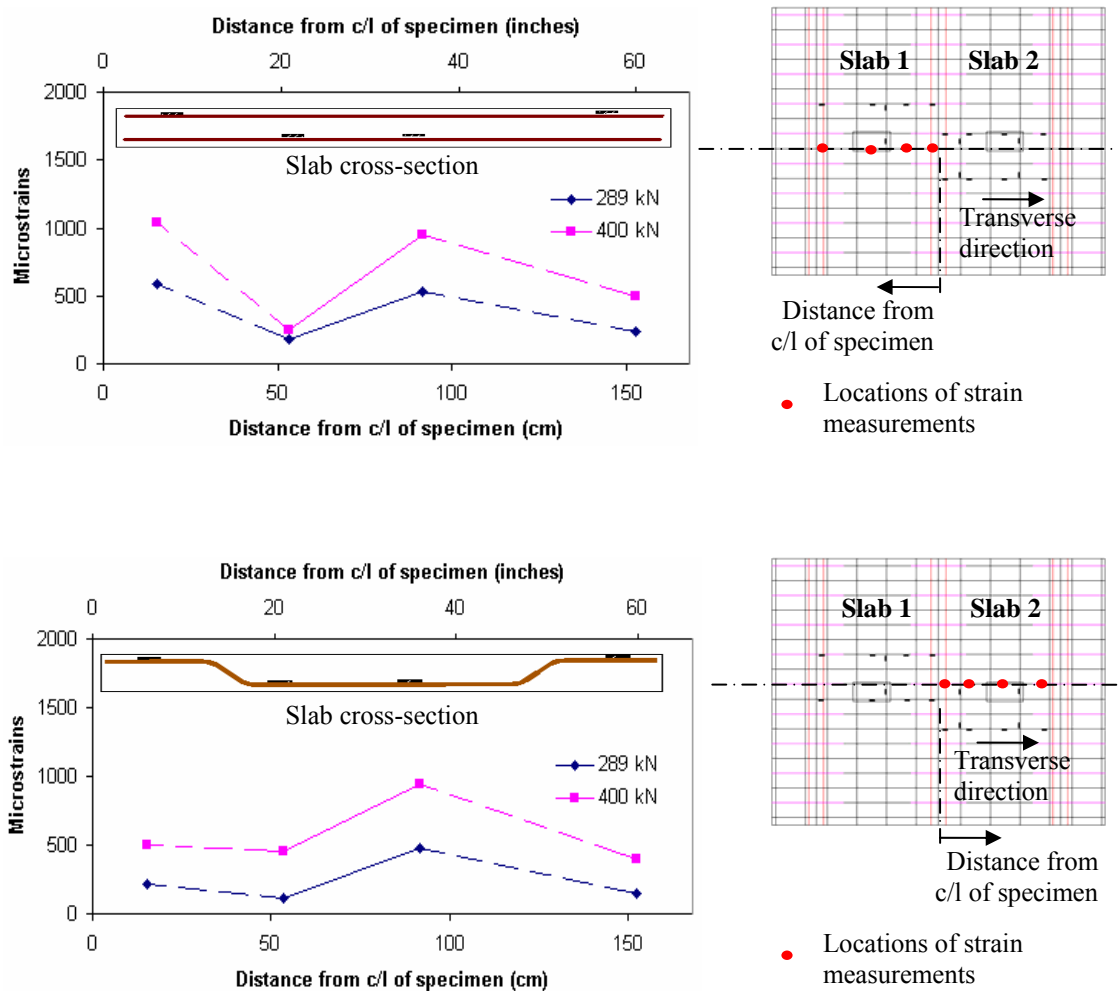


Figure 5.14 Strain profile in slab reinforcement at mid-span

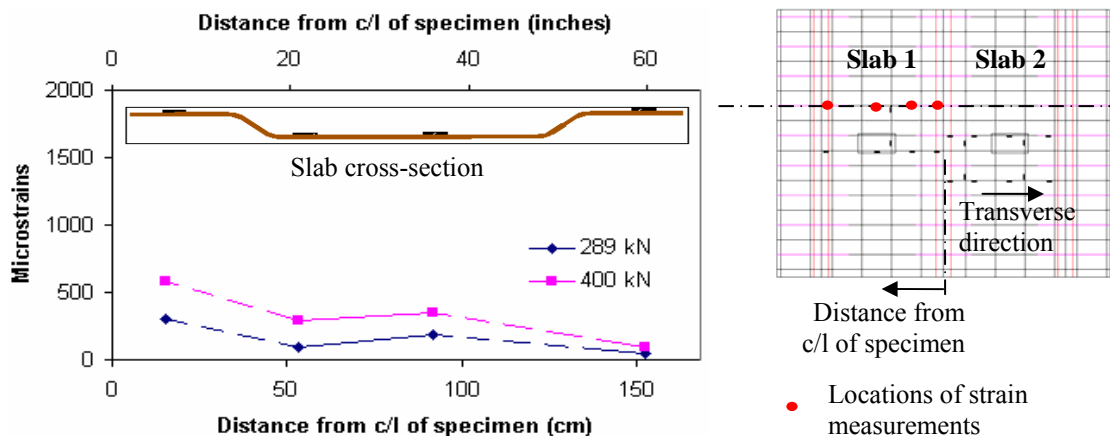


Figure 5.15 Strain profile in slab reinforcement at 508 mm (20") from mid-span

The strain profiles in both the slabs were similar indicating similar behavior of the deck slabs. The strains in the transverse steel reinforcement below the load area recorded in slabs 1 and 2 were 954 and 947 micro-strains, respectively. The strains in the center girder stirrups along the length of the girder are presented in Figure 5.16. The strains in the steel stirrups at the 289 kN (65 kips) load cycle were very low and almost uniform along the length of the girder. The maximum recorded strain at this load level was 125 micro-strains which was only about 5% of predicted yield strain in the steel stirrups of 2414 micro-strains. This was indicative of the shear resistance of the girder at this load level being contributed mainly by the concrete. No shear cracks were observed at this load level from visual inspections, as was presented in the earlier section. The strains in the steel stirrups, particularly at the shear critical areas near the girder supports were found to increase in the 400 kN (90 kips) load cycle. However the strains even at this load level were significantly below yield strain, indicating that the girders were not subjected to much degradation in phase 1 of loading. The maximum recorded strain at

this load level was 652 micro-strains, which was about 27% of predicted yield strain in the steel stirrups of 2414 micro-strains. This corroborated the visual observations that showed very little damage in the girders. The highest strain recorded in each instrumented stirrup along the length of the center girder is presented in Figure 5.17. The stirrups with higher strains towards the girder supports corresponded well with the areas at which the shear cracks were observed. The crack pattern in the center girder was shown earlier in Figure 5.13.

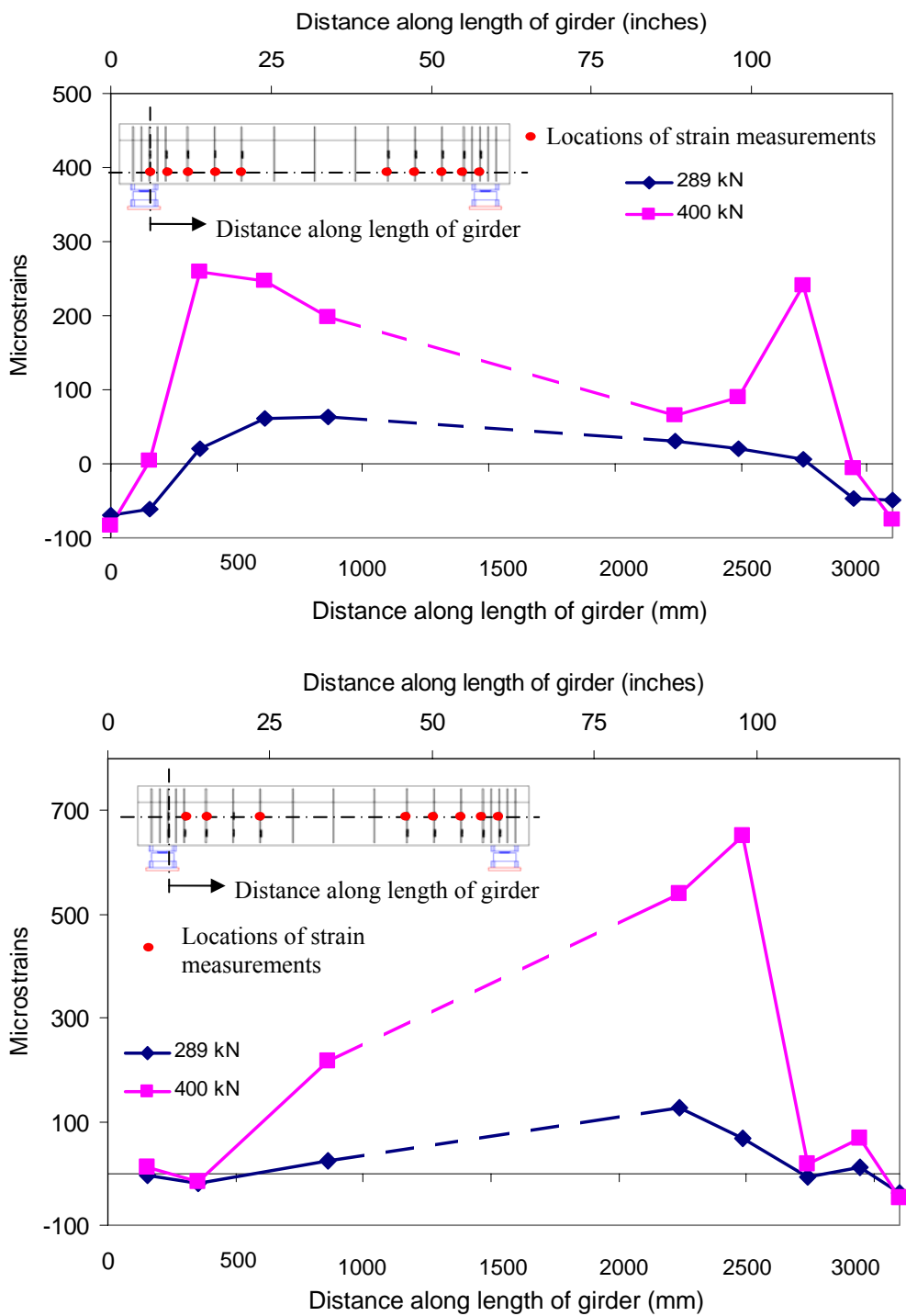


Figure 5.16 Strain profile in center girder stirrups

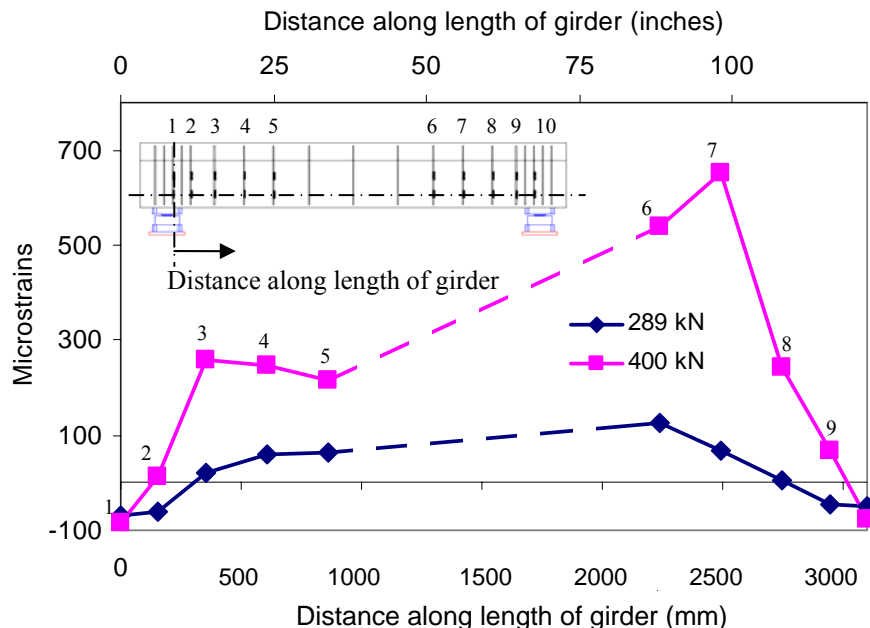


Figure 5.17 Maximum recorded strains in the instrumented steel stirrups along the length of the center girder during phase 1 loading

5.1.4 Comparison of Test Results with Design

The overall behavior of the test specimen matched the design limit state of reaching punching shear criticality in the deck slabs at 400 kN (90 kips) during phase 1 loading. The theoretical design estimates for the deck slabs were presented in section 4.5.1.1 of chapter 4. The slabs were found to develop punching shear deficiency at the end of phase 1 loading at the predicted load of 400 kN (90 kips), which corresponded to 75% of the theoretical punching shear capacity. At this load level the cracks in the slabs were well formed with the crack width below the load areas being about 0.8-1.2 mm (0.03-0.05"). This could be used as a criterion for defining the punching shear limit state that would warrant strengthening of the deck slabs [70]. Also most of the significant

damage was concentrated in the slabs with the girders going through very little damage, as indicated by the strains in the girder stirrups and the crack pattern. The theoretical flexural capacity did not match well with the experimental results. The transverse slab reinforcement was predicted to reach 75% of yield strain (1790 microstrains) at 339 kN (76 kips). However from the experimental strain measurements, the slab reinforcement reached 950 microstrains at 400 kN (90 kips). The analytical capacity estimate was performed for a representative 305 mm (1') section of slab, so that the effective area of the transverse steel reinforcement consisting of #5 bars (area of 198 mm² or 0.31 in²) spaced at 203 mm (8") in that section was calculated as:

$$A_{eff} = A_{rebar} \times \frac{SectionLength}{RebarSpacing} = 297 \text{ mm}^2 \text{ or } 0.46 \text{ in}^2 \text{ over a } 305 \text{ mm (1 foot) section.}$$

However, based on the construction details, in the 305 mm (1') section below the load area, two #5 rebars were located resulting in a total area of transverse steel reinforcement in the deck slabs of 396 mm² (0.62 in²). Thus a local sectional analysis performed with the area of slab reinforcement as 297 mm² or 0.46 in² over a 305 mm (1 foot) section would result in reduction of steel strain corresponding to a given load. Thus for the limit state corresponding to reaching 1790 micro-strains (75% of yield strain) in the steel reinforcement and for the concrete compressive strength, f_c' , steel yield strength, f_y and effective depth, d as specified in Figure 5.18, the transverse flexural moment capacities of the deck slab for the two steel area ratios were computed as:

$$M_n \text{ for slab reinforcement of } 0.46 \text{ in}^2 \text{ per foot width} = 38.4 \text{ kN-m/m (8.63 k-ft/ft)}$$

$$M_n \text{ for slab reinforcement of } 0.62 \text{ in}^2 \text{ per foot width} = 51.1 \text{ kN-m/m (11.48 k-ft/ft)}$$

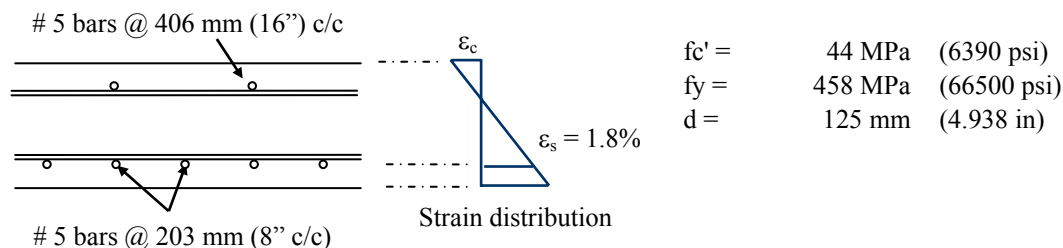


Figure 5.18 Parameters in sectional analysis for determination of flexural capacity

This for a linear elastic model, as was used for initial design estimates and was presented in Chapter 4, the corresponding reduced strain for the slab reinforcement of 0.62 in^2 per foot width as compared to reaching predicted strain of 1790 microstrains for slab reinforcement of 0.46 in^2 per foot width under the same load was computed as:

$$\epsilon_{\text{Reduced}} = 1790 \times \frac{38.4}{51.1} = 1345 \text{ microstrains}$$

However, even though the design estimate as presented above is valid for stationary wheel loads on the deck slabs in the test that resulted in localized response of the slabs around the load area, in the actual bridge deck, since the response of the slabs would be governed by a moving wheel load, it would be more realistic to calculate the sectional response based on effective area of slab reinforcement.

The difference between the initial estimate of the load demand required to reach the flexural capacity of the deck slabs and the experimental results could also be linked to the use of a simplistic linear elastic finite element model with homogeneous material properties (which was used to predict the load demand to reach the required flexural capacity and thus did not simulate the non-linear material behavior in the final stages of

loading in phase 1). Also the load-cells, acting as supports at the ends of the girders, were modeled as rigid supports in the initial FE model. However, as was recorded by the linear potentiometers mounted over the support locations, the load cells themselves had some settlement as is presented in Figure 5.19. The support settlements under loading and the non-linear material behavior were taken into account in the updated FE model, as will be presented in Chapter 8 and hence are not discussed further in this chapter.

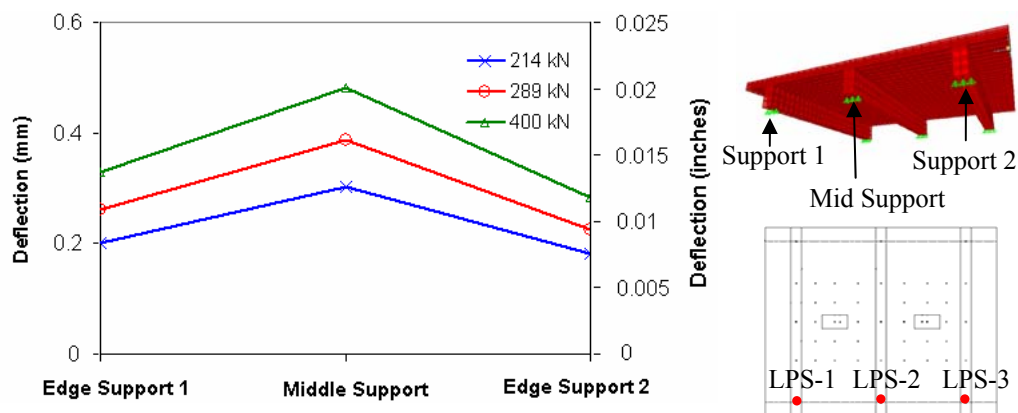


Figure 5.19 Deflections at support locations

Based on the results obtained from the updated model, it was found that the transverse slab reinforcement in the deck slabs below the load area would reach 945 and 938 microstrains in slabs 1 and 2, respectively at peak load of 400 kN (90 kips) load cycle as compared to 954 and 947 microstrains recorded experimentally in the transverse reinforcement of slabs 1 and 2, respectively. This indicated that at 400 kN the slab reinforcement was significantly below the yield strain of 2400 microstrains and thus punching shear rather than flexural failure would be the governing limit state in the slabs. The test results from phase 1 indicated that for typical reinforcement details used in

existing slab and girder bridges, there is a possibility that the initial damage in the slab-girder system will only be concentrated in the deck slabs with little damage in the girders that might prompt the designer to only strengthen the deck slabs with FRP composite.

5.2 Results from Phase 2 of Testing - Introduction

Phase 2 loading was carried out after strengthening of the deck slabs with FRP composites. The objective of this phase of testing was to study the behavior and damage progression in a slab-girder system after strengthening of only the slab components for flexural strength enhancement and resisting premature punching shear failures. Based on the reinforcement details it was predicted that shear criticality would be reached in the center girder, defined as achieving 75% of yield strain in the steel stirrups of the girder, before the full capacity of the strengthened deck slabs could be achieved. Thus most of the damage in this phase of testing was predicted to occur in the center longitudinal girder of the test specimen.

5.2.1 Load Capacity and Stiffness Results

Using an average yield strain of 2000 micro-strains for the steel stirrups, the shear criticality in the center girder was defined to be achieved at 1500 micro-strains (75% yield). From the initial simplistic analysis this strain was predicted to be reached at 490kN (110 kips) of wheel load. However it was found from phase 1 of testing that the simple linear elastic FE model under predicted the load demand as was discussed in section 5.1.4. Based on the updated FE model taking into account material non-linearity,

as will be presented in Chapter 8, maximum strain of 1513 microstrains was predicted to be reached at peak load of 667 kN.

A simplistic prediction of the ultimate load for phase 2 of loading was also obtained through extrapolation of the strain profile in the steel stirrups based on the experimental results obtained from phase 1 loading cycles. From the 400 kN (90 kips) load cycle, the strain measured by gage S2-72, located on a stirrup 660 mm (26") from the center of the support (Figure 5.20), was the highest since this stirrup traversed across a shear crack and was located at the shear critical area near the girder support. The strain increment profile at this location with loading from the 400 kN (90 kips) load cycle is presented in Figure 5.21 and was extrapolated to determine the load required to reach the 1500 micro-strains limit using a best-fit polynomial curve. Comparison of the extrapolated strain data with the true strains recorded in the steel stirrup at location S2-72 at the 666 kN (150 kips) load cycle is also shown in Figure 5.21. The required load demand was found to be 666 kN (150 kips). The peak loads used for phase 2 load cycles were 400 kN (90 kips), 578 kN (130 kips) and 666 kN (150 kips), in which the 578 kN (130 kips) load cycle was chosen as an intermediate load level to check for design predictions and to perform NDE inspections before reaching the 666 kN (150 kips) ultimate load level. The load cycles to which the specimen was subjected to during phase 2 loading are summarized in Table 5.4.

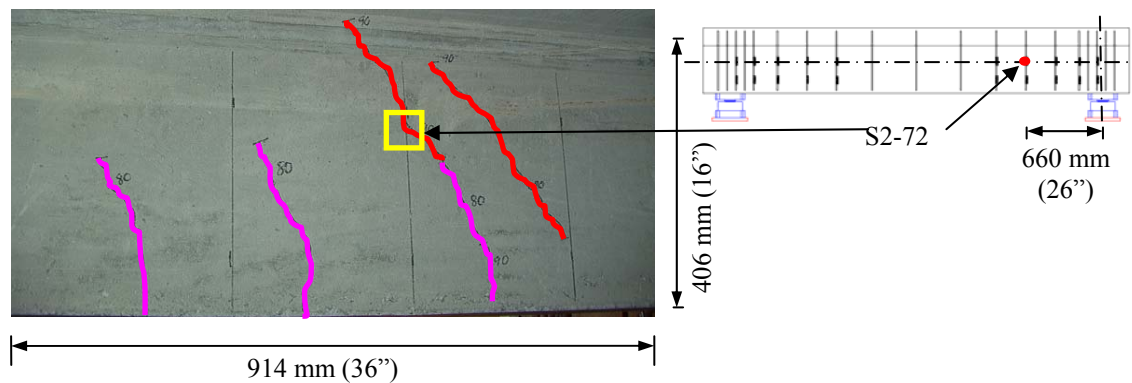


Figure 5.20 Location of maximum recorded strain in steel stirrups

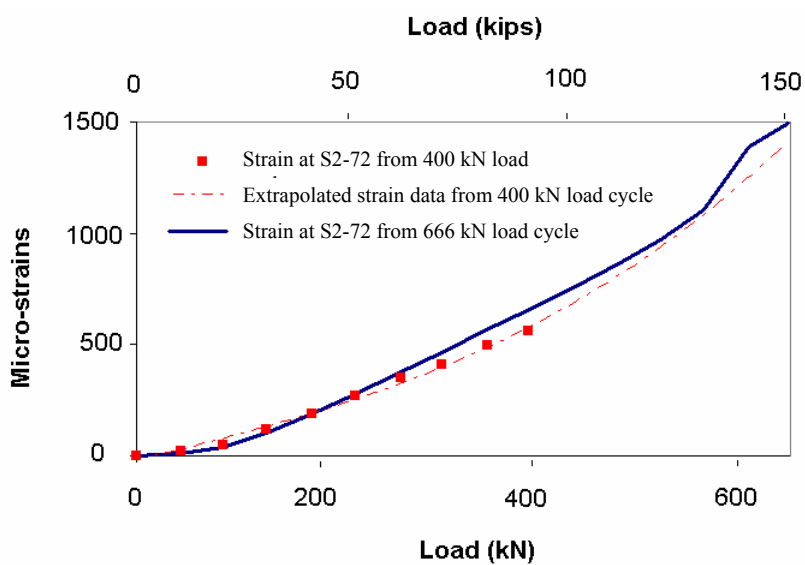


Figure 5.21 Strain profile extrapolation for girder stirrup

Table 5.4 Loading protocol for phase 2

Load cycle #	Peak load kN (kips)	Load cycle remarks
1	400 (90)	Comparison with ultimate load level of Phase 1 to evaluate changes in slab-girder system produced by strengthening of the slabs with FRP
2	578 (130)	Loading stopped at 489 kN (110 kips) to mark cracks and then loading continued to 578 kN (130 kips), which was the intermediate load level to check for design predictions, mark cracks and perform NDE inspections before reaching predicted Phase 2 ultimate load
3	666 (150)	Loading stopped at 623 kN (140 kips) to mark cracks and then loading continued to 666 kN (150 kips), which was the predicted Phase 2 ultimate load required to reach shear criticality of the center girder (75% of yield strain in the steel stirrups in critical areas)

* Note: For each load cycle after reaching peak load, the load was first brought down to 107 kN (24 kips) for NDE inspections and then the specimen was unloaded by retracting the actuators away from the specimen before starting the next load cycle

The load-deflection plot for Slab 1 over the Phase 2 load cycles was obtained by plotting the actuator load on slab 1 against the deflection measured below the load by linear potentiometer LPM3 and is presented in Figure 5.22. The effect of strengthening of the slabs with FRP composite at the end of phase 1 loading can be observed in Figure 5.23 which contains only the load-deflection plots of slab 1 for the 400 kN (90 kips) load cycle before and after strengthening the slabs with FRP composite. It was observed that before strengthening of the deck slabs with composite, for the 400 kN (90 kips) load cycle considerable degradation of stiffness occurred in Slab 1 after the 270 kN (60 kips)

level as the slab approached punching shear criticality. However after strengthening of the slabs with FRP composite when the specimen was loaded through the 400 kN (90 kips) load cycle, there was no change in the slope of the load-deflection plot throughout the load cycle indicating that the FRP composite was effective in restraining the opening of punching shear cracks, thereby preventing any loss of stiffness. The effect of FRP strengthening of the deck slabs on the performance of the test specimen will also be presented later in this chapter in terms of the strain profiles and crack patterns. Further from Figure 5.22 it can be observed that about 12% degradation of load-deflection slope with respect to the initial load-deflection slope of the strengthened slab occurred in the 578 kN (130 kips) load cycle. The degradation in the load-deflection slope of about 20% occurred in the 666 kN (150 kips) load cycle which corresponded to the predicted phase 2 ultimate load. As will be discussed in the subsequent sections, this load level corresponded to attaining shear criticality in the center girder with considerable cracking and high deflections/strains being recorded in the girder. This was reflected at the systems level in the load-deflection response of the slabs. The load-deflection responses of the two strengthened slabs are compared in Figure 5.24. The responses were found to be similar indicating that equivalent strengthening was achieved by the two composite systems in the two slabs. The stiffness of slab 2 was slightly higher than that of slab 1 [8.32mm maximum deflection in Slab 1 as compared to 8.08mm maximum deflection in Slab 2 at the 666 kN load cycle), but this was consistent with the observations from phase 1 of testing in which slab 1 was found to have slightly higher deflections than that of slab 2 (Figure 5.3).

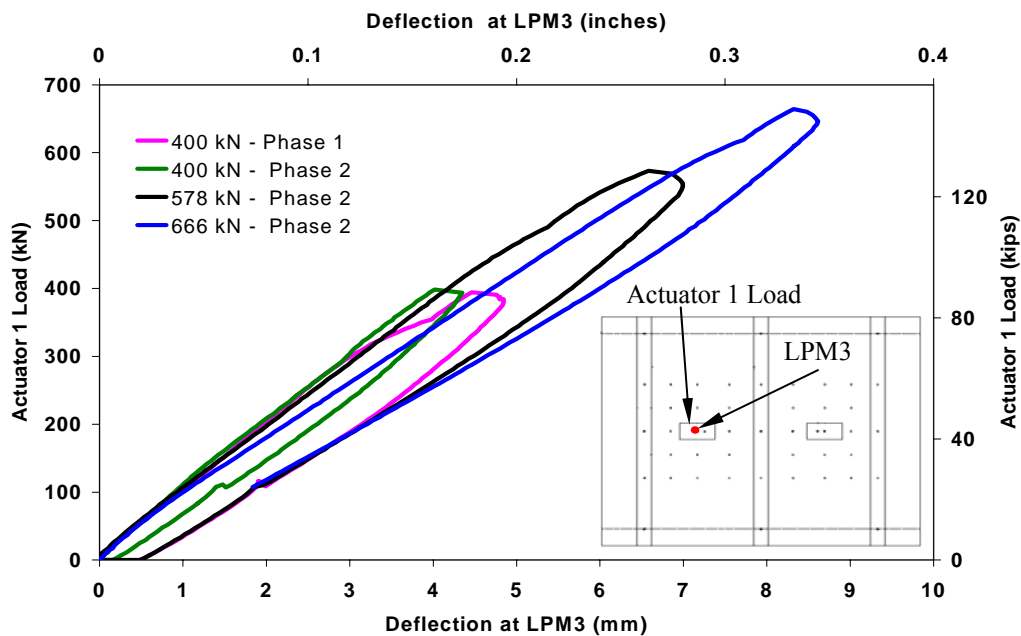


Figure 5.22 Load-deflection plots for slab 1

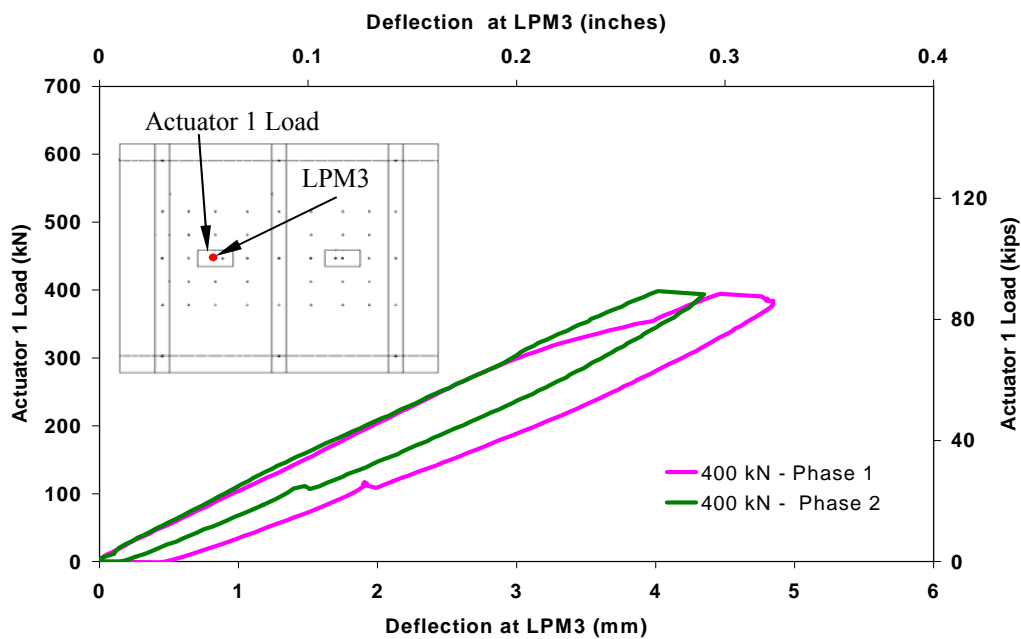
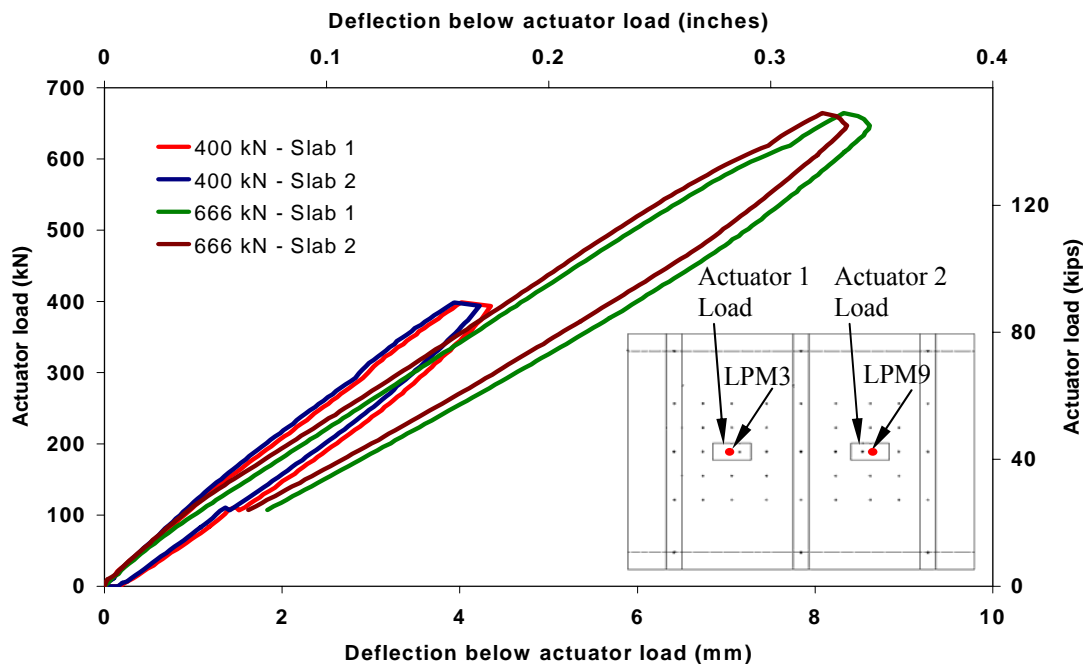


Figure 5.23 Effect of strengthening of slabs on load-deflection plot for slab 1



Note: For slab 1 Actuator load 1 was plotted against deflection at LPM3

For slab 2 Actuator load 2 was plotted against deflection at LPM9

Figure 5.24 Comparison of load-deflection plots between deck slabs in phase 2

The deflections at the center of the middle and edge girders as measured by the linear potentiometers, LPM6 and LPM11, respectively, are plotted against actuator loads in Figures 5.25a and 5.25b. As compared to the load-deflection plots in the girders from phase 1 of testing (Figure 5.4), where no significant degradation in response was observed, a decrease in the slope of load-deflection response for the girders was observed in phase 2 of test. This indicated that the girders were undergoing damage at this phase of test. Also relative to the initial Phase 2 load-deflection slope in the 400 kN (90 kips) load cycle, the degradation of the load-deflection slope of the center girder at the end of Phase 2 loading in the 666 kN (150 kips) load cycle was about 25% as compared to about 13%

in the edge girder at the same stage of loading. This indicated that the stiffness degradation of the center girder was more than that of the edge girders because of the shear criticality in the center girder at this stage of loading. Also comparison between the load-deflection plots of the two edge girders is presented in Figure 5.25c. Edge girder 1 was found to have slightly higher deflection than that of edge girder 2 at comparable load stages [2.81 mm deflection in edge girder 1 as compared to 2.53 mm deflection in edge girder 2 at peak load in the 666 kN (150 kips) load cycle.

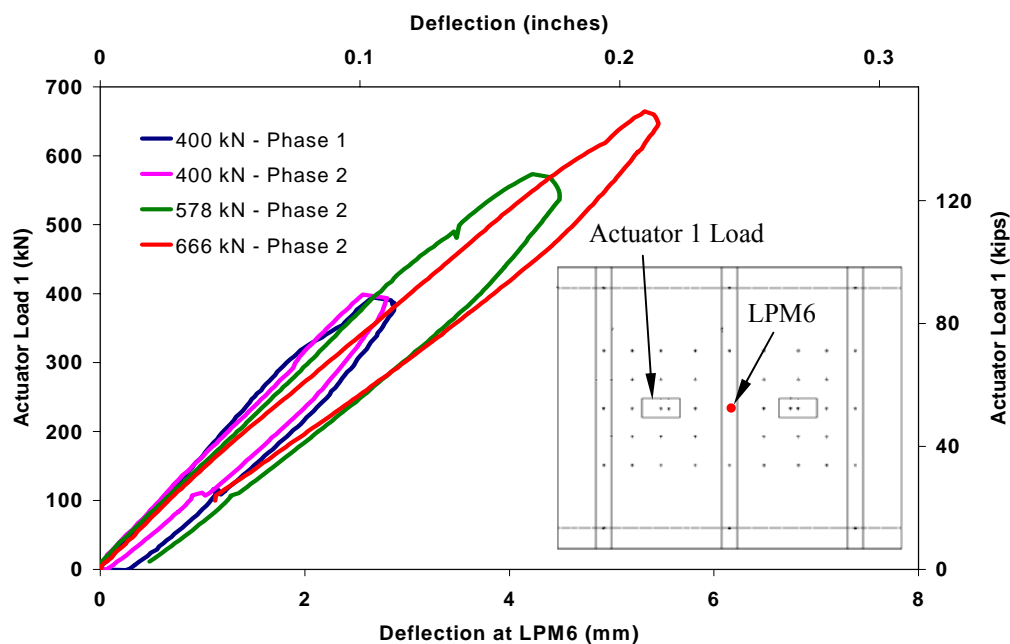


Figure 5.25a Actuator load 1 vs. mid-span deflection plots for middle girder

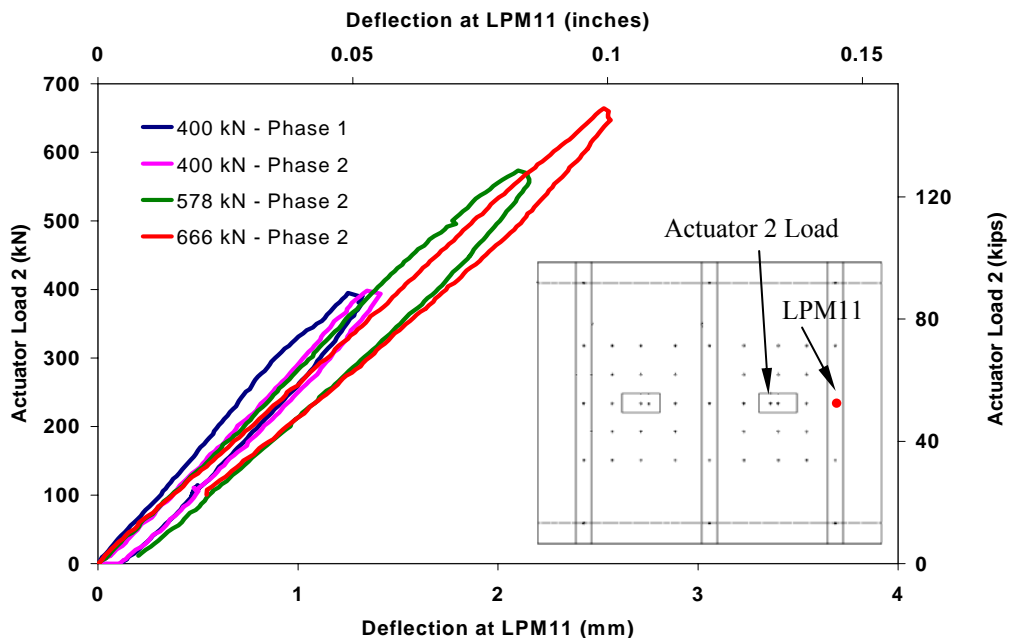
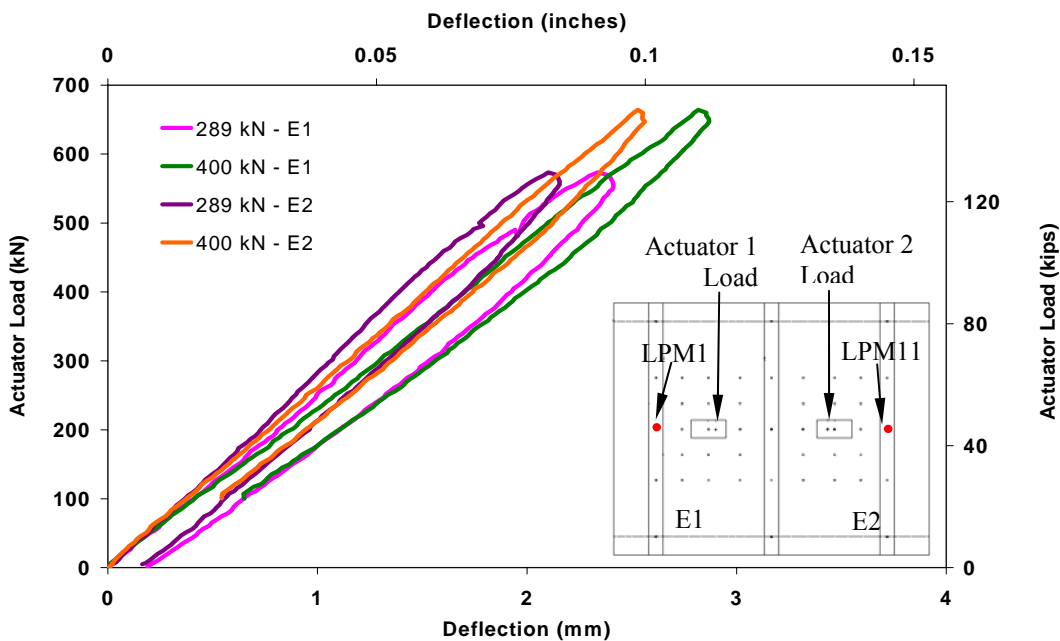


Figure 5.25b Actuator load 2 vs. mid-span deflection plots for edge girder



Note: For edge beam 1 (E1) Actuator load 1 was plotted against deflection at LPM1

For edge beam 2(E2) Actuator load 2 was plotted against deflection at LPM11

Figure 5.25c Comparison of load-deflection plots between edge girders

A comparative evaluation of the degradation of the slope of the load-deflection response of the slabs and the girder over the load cycles in phase 2 was obtained using the “effective” stiffness ratio, which was defined earlier in equation 5.5 and is repeated here for convenience:

$$\text{Effective stiffness ratio} = \frac{\text{Effective stiffness at a Load Cycle}}{\text{Effective stiffness at baseline (108 kN)}} \quad \dots(5.5)$$

The effective stiffness ratios in the deck slabs and girders during Phase 2 loading are presented in Tables 5.5a and 5.5b, respectively. The true deflections of the deck slabs were obtained by subtracting the contribution of the girder deflection from the total deflection of the slabs, as was discussed earlier in section 5.1.1 of this chapter and was given by equation 5.6. In slab 1 increase in the “effective” stiffness ratio from 0.6 to 0.72 was observed between the 395 kN (89 kips) and 399 kN (89.7 kips) load cycles, before and after strengthening of the deck slab with FRP composite, respectively. The corresponding increase in the effective stiffness ratio for slab 2 produced by strengthening with FRP composite was from 0.62 to 0.75. Also the decrease in the effective stiffness ratios in the deck slabs in the phase 2 load cycles were gradual, with the effective stiffness ratio in slab 1 decreasing from 0.72 to 0.57 through Phase 2 load cycles, indicating that the composite strengthening was effective in restraining damage progression in the slabs. The strengthening of the deck slabs had an insignificant effect on the effective stiffness of the girders, with the effective stiffness ratio of the center and edge girders increasing imperceptibly from 0.83 to 0.85 and from 0.95 to 0.96, respectively, before and after strengthening of the slabs. The reduction in the “effective”

stiffness ratio in the center girder was from 0.83 to 0.67 between the 400 kN (kips) and 666 kN (150 kips) load cycles. Through visual observations of shear cracking and high strains recorded in the steel stirrups of the center girder in phase 2 of test, which will be discussed in the next sections, the center girder was found to reach shear criticality during the 666 kN (150 kips) load cycle. The change in the effective stiffness ratio of the center girder from 0.93 to 0.67 during phase 2 loading was not as drastic as in the slabs (from 1.0 to 0.6) during phase 1 loading. The reason for this is that the “effective” stiffness ratio is more representative of flexural degradation since the deflections from the linear potentiometers used to calculate this ratio were mainly governed by flexural deformations. Most of the damage in the girder in phase 2 of test was produced by shear deficiency and thus the effective stiffness ratio was not representative of such damage. It was thus necessary to look at the crack pattern and the strain data from the steel stirrups of the girder to determine the damage progression in the girder. However the general trend in the degradation of the effective stiffness ratio in the center girder was followed during phase 2 load stage. The effective stiffness ratio of the edge girders during phase 2 loading degraded from 0.95 to 0.8 as shown in Table 5.5b. Thus the stiffness degradation of the edge girders was less than that of the center girder because of the lower load demand on the edge girders as compared to the center girder.

Table 5.5a Effective stiffness ratio in slabs in phase 2 from linear potentiometer data

Slab 1 (Deflections below actuator load)			Slab 2 (Deflections below actuator load)		
Actuator load kN (kips)	Actual deflection mm (inches)	Effective stiffness ratio	Actuator load kN (kips)	Actual deflection mm (inches)	Effective stiffness ratio
102.3 (23)*	0.38 (0.015)*	1.00*	101.66 (22.8)*	0.38 (0.015)*	1.00*
395.2 (88.8)*	2.49 (0.098)*	0.60*	395.55 (88.9)*	2.39 (0.094)*	0.62*
399.3 (89.7)	2.08 (0.082)	0.72	399.03 (89.67)	2.04 (0.08)	0.75
574.5 (129.1)	3.39 (0.133)	0.63	574.6 (129.12)	3.35 (0.132)	0.65
665.6 (149.6)	4.37 (0.172)	0.57	665.5 (149.55)	4.28 (0.169)	0.59

* From Phase 1 of test before strengthening of the deck slabs with composite

Note: The enhancement in the effective stiffness ratio in the 400 kN (90 kips) load cycle before and after strengthening the slabs with composite show the effect of the composite on the stiffness of the slabs

Table 5.5b Effective stiffness ratio in girders in phase 2 from potentiometer data

Center girder			Edge girder		
Actuator load kN (kips)	Mid-span deflection mm (inches)	Effective stiffness ratio	Actuator load kN (kips)	Mid-span deflection mm (inches)	Effective stiffness ratio
102.3 (23)*	0.57 (0.023)*	1.00*	101.66 (22.8)*	0.35 (0.014)*	1.00*
395.2 (88.8)*	1.31 (0.051)*	0.83*	395.55 (88.9)*	1.41 (0.056)*	0.95*
399.3 (89.7)	2.57 (0.101)	0.85	399.03 (89.67)	1.40 (0.055)	0.96
574.5 (129.1)	4.22 (0.166)	0.76	574.6 (129.12)	2.34 (0.092)	0.84
665.6 (149.6)	5.58 (0.219)	0.67	665.5 (149.55)	2.82 (0.111)	0.80

* From Phase 1 of test before strengthening of the deck slabs with composite

5.2.2 Deflection Profiles and Crack Patterns

The deflection profiles along the lengths of the center and edge girders at the peak loads of phase 2 load cycles are presented in Figures 5.26a, 5.26b and 5.26c. The deflections were measured at mid and quarter span and at supports of the girders. At the

666 kN (150 kips) load cycle the mid-span deflection of the center girder was 1.98 times the mid-span deflection of the edge girder. Also at the 400 kN (90 kips) load cycle before and after strengthening of the deck slabs with composite, there was no significant difference in the deflections recorded along the girder lengths. This indicated that strengthening of the slab components of the slab-girder system had insignificant effect on the response of the girder components.

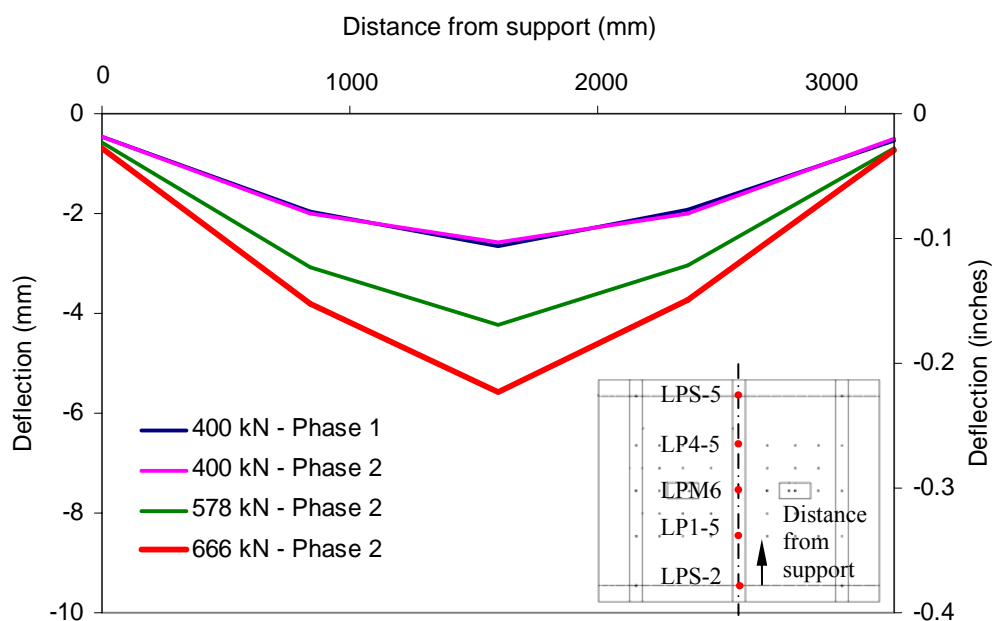


Figure 5.26a Deflection along length of middle girder

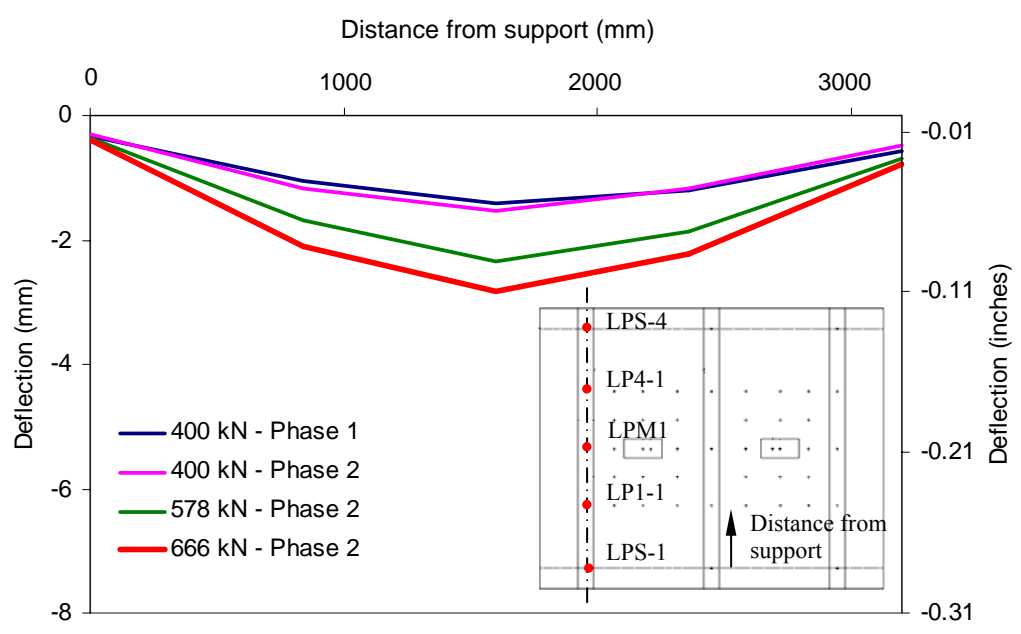


Figure 5.26b Deflection along length of edge girder 1

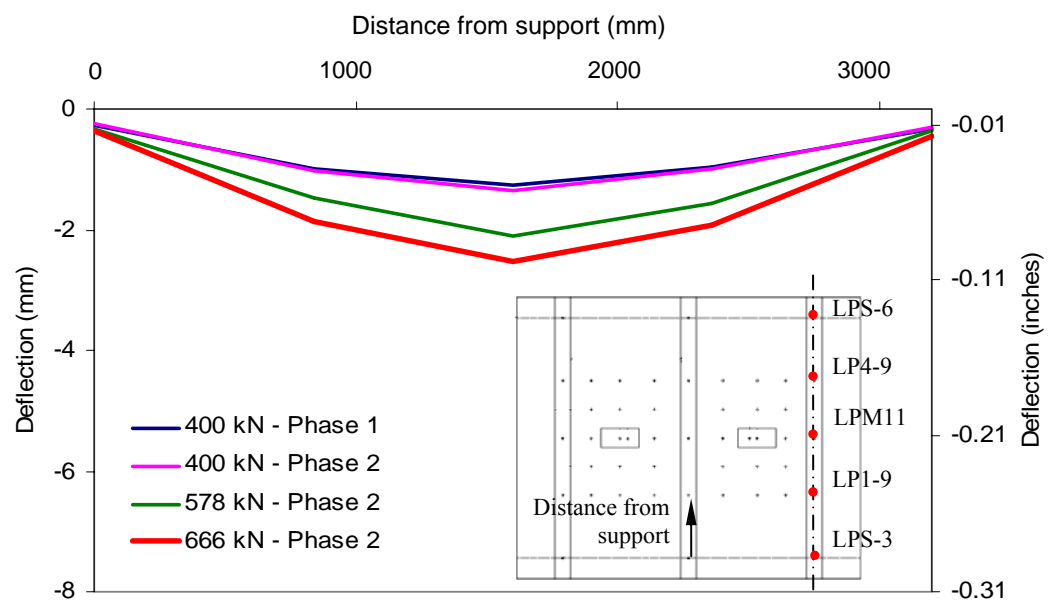


Figure 5.26c Deflection along length of edge girder 2

The deflection contour profile over the surface of the strengthened deck slabs at the end of phase 2 loading at 666 kN (150 kips) is presented in Figure 5.27. The highest deflections of the strengthened slabs were found to be concentrated in the areas under the load contact areas of the actuators. Representative deflection measurements recorded by the rows of linear potentiometers at the peak loads at the end of each load cycle for phase 2 are presented in Figures 5.28 and 5.29. Row 2 of linear potentiometers was located 381 mm (15") away from mid-span of the specimen, at which the vertical deflections were measured by row M of potentiometers. Since the row M of linear potentiometers was located along the line of loading of the test specimen, they showed higher deflections than potentiometers in Row 2, with the highest deflections being recorded below the load areas. It was also observed that the highest deflection in strengthened slab 2 was slightly lower than that in strengthened slab 1 [8.77 mm in slab 2 against 8.99 mm in slab 1] at the 666 kN (150 kips) load cycle. However, in general the behavior of the two strengthened slabs was similar indicating that equivalent strength enhancement was achieved by both the composite systems. The effectiveness of the composite systems in strengthening and increasing the stiffness of the deck slabs was also indicated by the reduction of deflections in the deck slabs after installation of the composite systems. This can be observed by comparing the deflections at the peak loads of the 400 kN (90 kips) load cycles before and after strengthening of the slabs with composite. The maximum deflection in the 400 kN (90 kips) load cycle, before and after strengthening of the slabs with FRP composite, decreased from 4.91 mm to 4.21 mm in slab 1 and from 4.76 mm to 4.1 mm in slab 2.

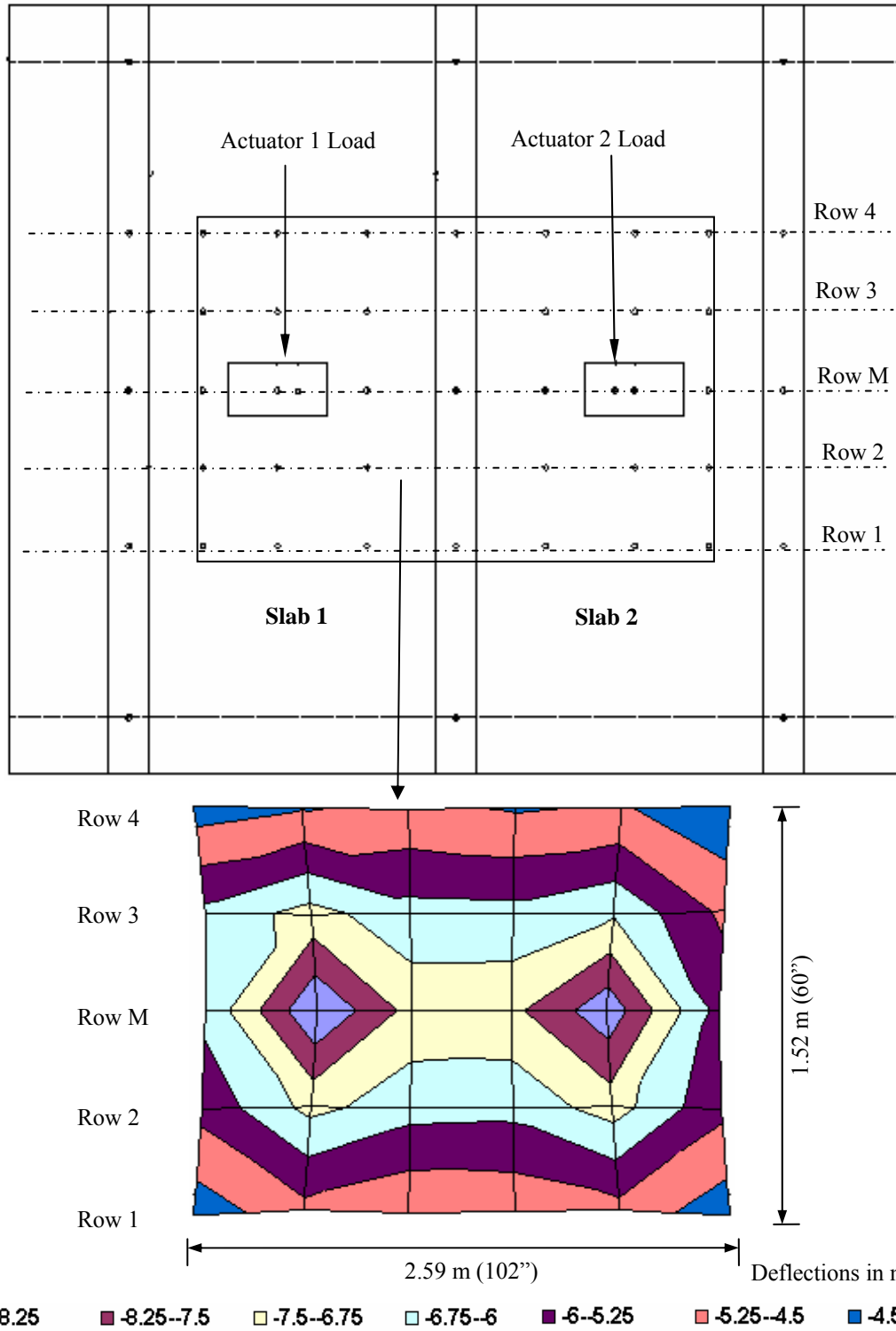


Figure 5.27 Deflection contour over deck slabs at 666 kN (150 kips)

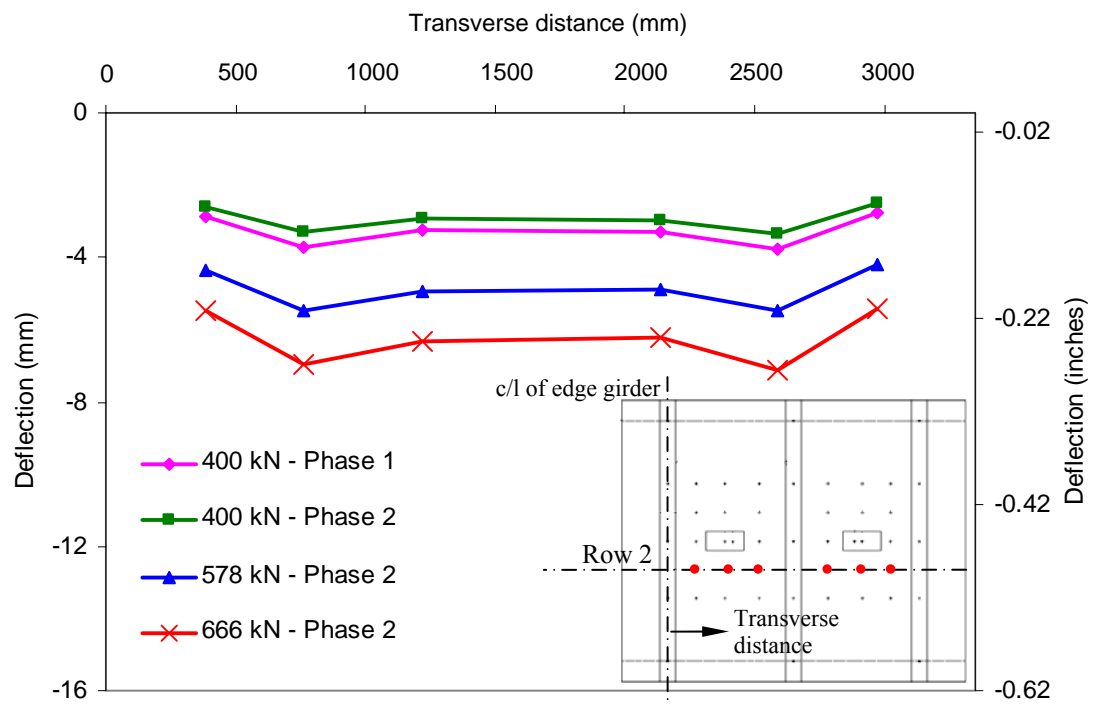


Figure 5.28 Deflection profile along Row 2 of linear potentiometers

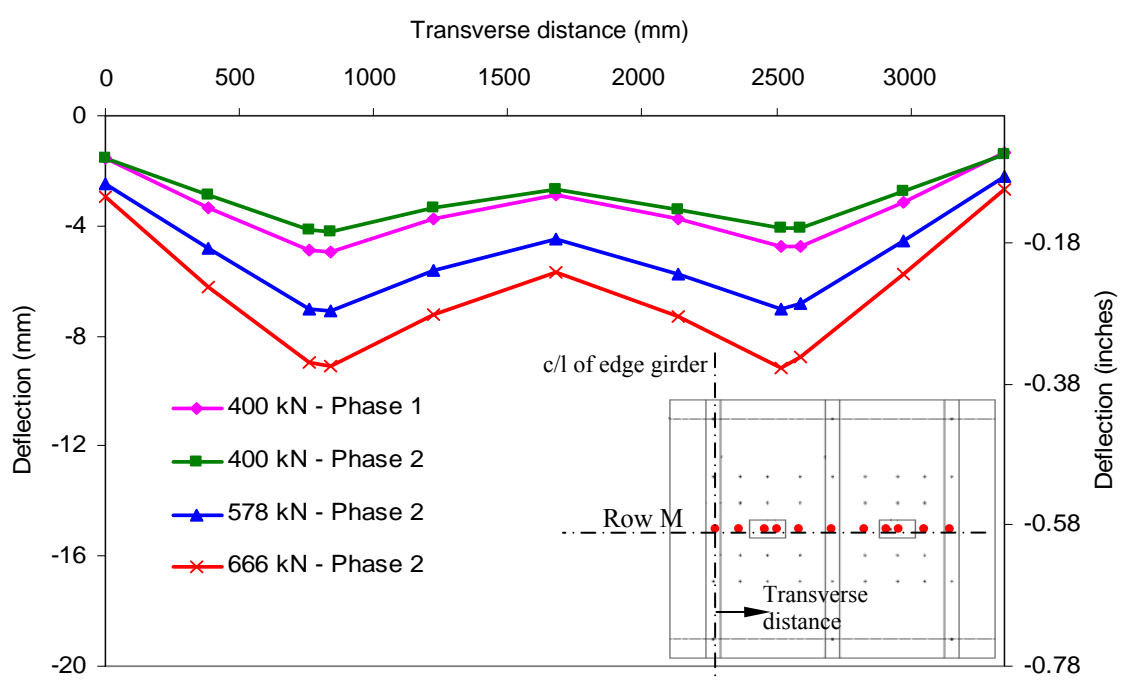


Figure 5.29 Deflection profile along Row M of linear potentiometers

It was discussed in section 5.1.2, that at the end of phase 1 both the deck slabs had considerable damage in the form of punching shear cracks of widths approximately 0.8-1.2 mm (0.03-0.05"). The cracks started as flexural cracks below the load area and then diverged away from the load area forming a pattern characteristic of punching shear deficiency. The strengthening of the slabs with the two composite systems was designed for strength enhancement of the slabs and also to prevent the opening of the punching shear cracks. The visual inspections of cracks formed in phase 2 of loading showed that the strengthening design was effective in restraining the opening of cracks. At 489 kN (110 kips) the pre-existing cracks in the slab near the load area were found to open slightly in the areas of the slab without the composite strip/laminate as shown in Figure 5.30. Most of these cracks diverged away from the load area. However even at the end of phase 2 loading of 666 kN (150 kips) none of these cracks opened significantly and the slabs were able to withstand the higher wheel-load demands. The crack patterns in the strengthened slabs under phase 2 load cycles are presented in Figure 5.30. The crack patterns were similar in both the slabs. However in slab 1, which was strengthened with 1 layer of 102 mm (4") wide pultruded strips, a number of short minor cracks developed under the load area at 579 kN (130 kips) as is shown in Figure 5.30. This was not observed in slab 2 which was strengthened with 2 layers of 152 mm (6") fabric laminates. The reason for this seems to be that the wider laminates in slab 2 resulted in better distribution of stress away from the load area in slab 2 while the stiffer and thinner pultruded strips attracted more stress and this resulted in localized cracking below the load area in slab 1.

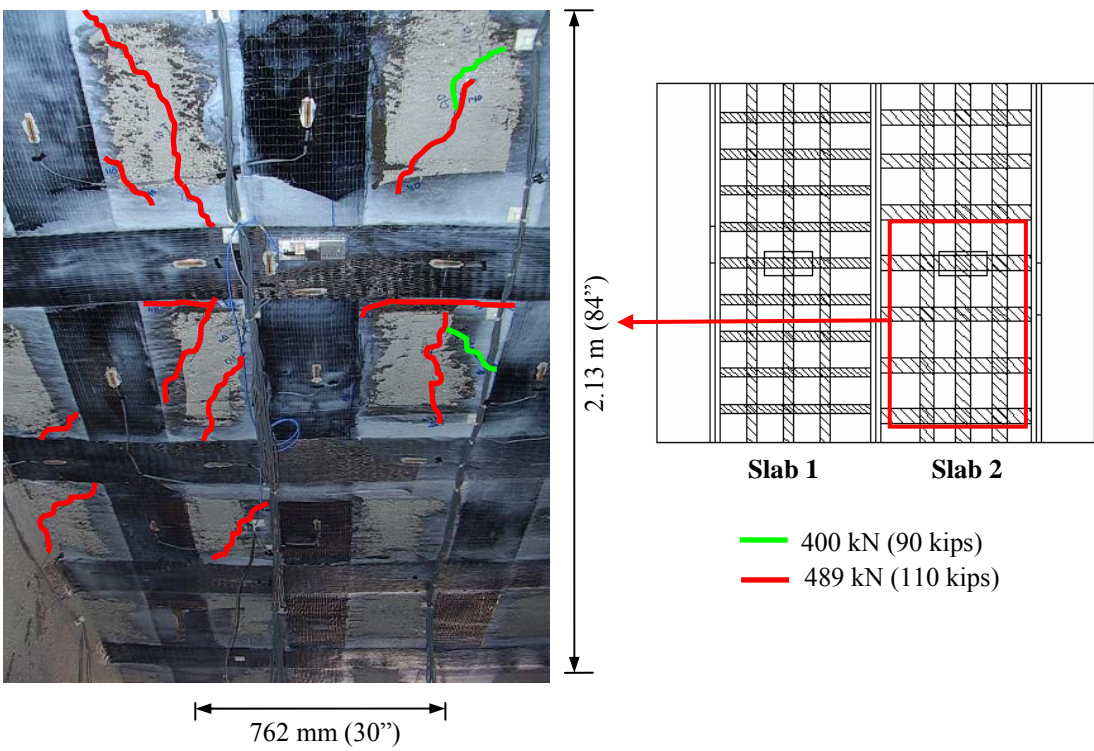
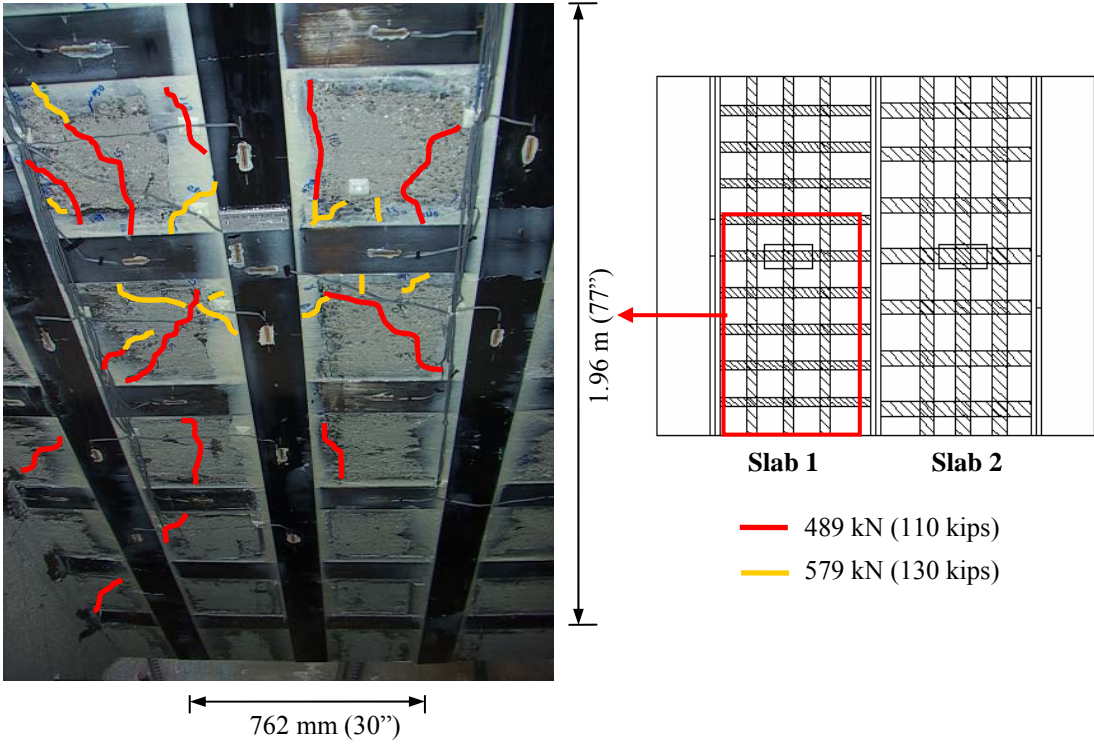


Figure 5.30 Progression of cracks in the strengthened deck slabs

Most of the damage and cracking in phase 2 of test was found to be localized in the shear critical areas of the center girder. The appearance of shear cracks in the center girder were observed in phase 1 at 400 kN (90 kips), as was discussed in section 5.1.2 of this chapter. These cracks were found to grow with loading in phase 2 along with the appearance of new shear cracks in the shear critical area of the girder near the support. The progression of shear cracking on either side of the center girder with increase of loading in phase 2 is presented in Figure 5.31. Most of the shear cracks were found to grow at 578 kN (130 kips) and new shear cracks were also found to appear close to the support at 666 kN (150 kips) as shown in Figure 5.31. Also at this load level most of the shear cracks were prominent and had a crack width of about 1 to 1.5 mm (0.04-0.06"). The data from the strain gages located on the steel stirrups were checked all through phase 2 and at 666 kN (150 kips) the strains in the stirrups near the support area around the locations of the shear cracks were found to be around 1800 micro-strains. This satisfied the limit state of exceeding 75% of steel yield strain and thus the girder was deemed to be shear critical at this load level. The strain gage data will be presented in the next section. For the edge girders, only a few widely spaced shear cracks of small crack width were observed in phase 2 of test (Figure 5.32). This was because the edge girders were subjected to lower shear demand than the center girder and were designed with closely spaced stirrups to prevent shear criticality. The flexural cracks in the center girder were first observed at 356 kN (80 kips) in phase 1 of test. No new flexural cracks appeared in the center girder in phase 2 of test indicating that the damage in the girder was primarily due to shear.

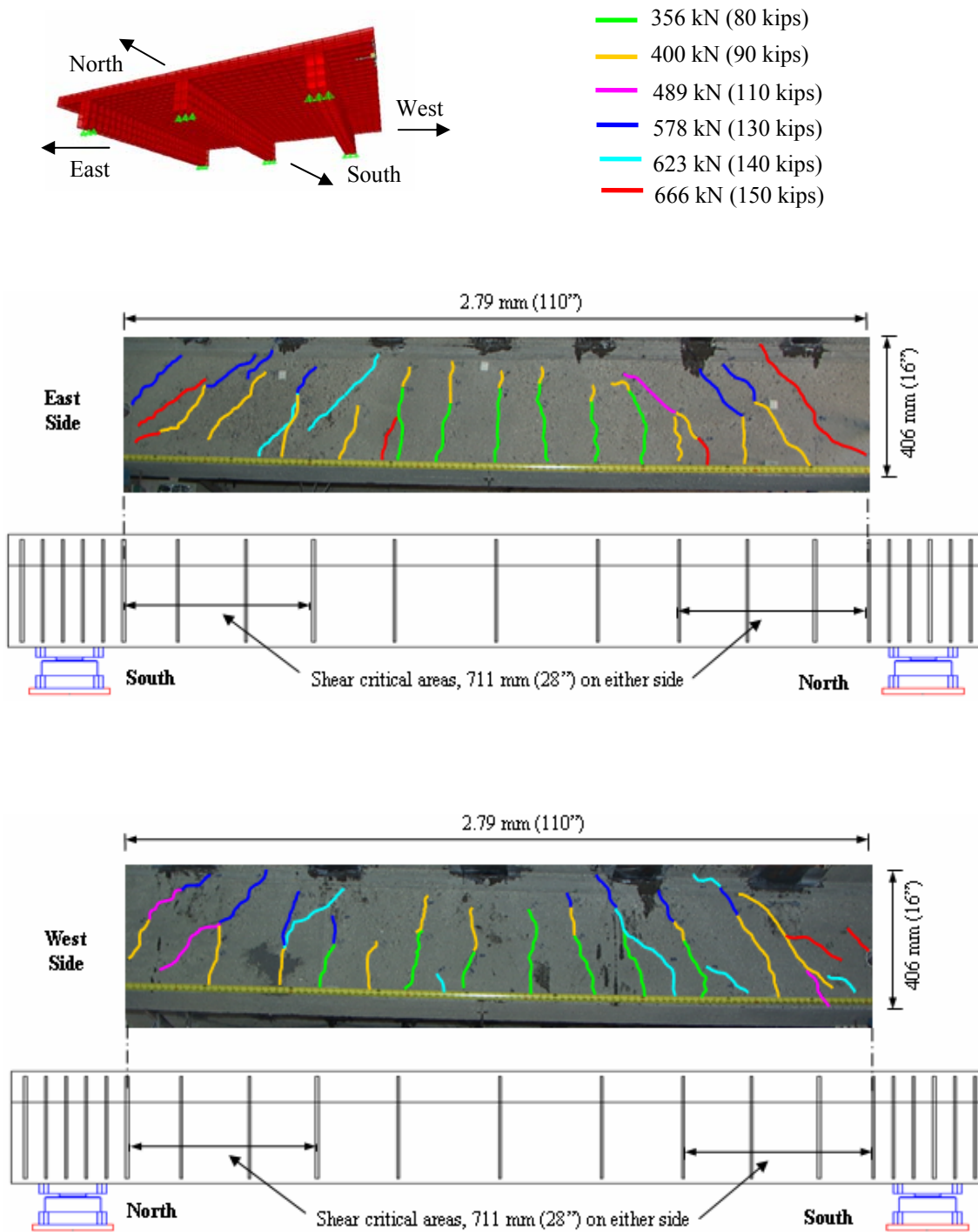


Figure 5.31 Crack pattern in the center girder at the end of phase 2 of test

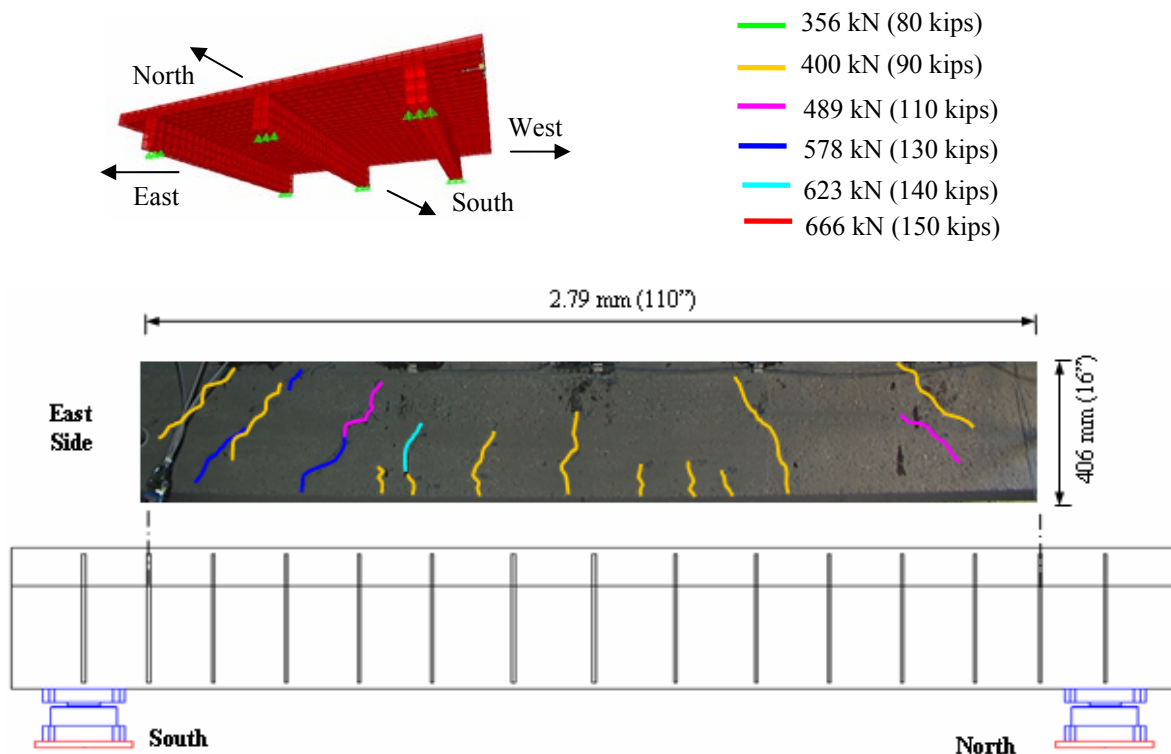


Figure 5.32 Crack pattern in the edge girder at the end of phase 2 of test

5.2.3 Strain Profiles

The development of strain in the transverse slab reinforcement along mid-span of the specimen is presented in Figure 5.33. The strains in the steel reinforcement below the load areas were identical in both the slabs indicating that equivalent strengthening was achieved in the two slabs by the two composite systems. Also on comparing the strain profiles in the slab reinforcement at 400 kN (90 kips) load cycle, before and after strengthening of the slabs, it was seen that the strains in the slab steel reinforcement were reduced after strengthening. Below the load area, the strains in the

slab reinforcement were reduced from 954 to 784 micro-strains in slab 1 and from 947 to 716 micro-strains in slab 2 at 400 kN (90 kips) load level, before and after strengthening of the slabs with the composite systems. The maximum strain in the slab steel reinforcement at 666 kN (150 kips) below the load areas were 1518 and 1547 micro-strains in slab 1 and slab 2, respectively indicating that at this load level the steel reinforcement in the slabs were still below yield strain levels and thus had reserve capacity which could not be utilized since the center girder had reached shear criticality. Also the transverse strain in the steel reinforcement of Slab 1 near the middle girder support location was high and was indicative of high stress areas along the intersection of the slab and girder.

The strain profile in the transverse slab reinforcement 508 mm (20") from mid-span is presented in Figure 5.34. The reduction in strain in the steel reinforcement at the 400 kN (90 kips) load cycle was observed from the strain profiles before and after strengthening by composite. Also it was noted that the strain near the slab-center girder intersection area was the highest [1018 micro-strains at the 666 kN load cycle] indicating high stresses in the negative moment area at these locations. However all the strains in the slab reinforcement were below the reinforcement yield strain of 2417 microstrains.

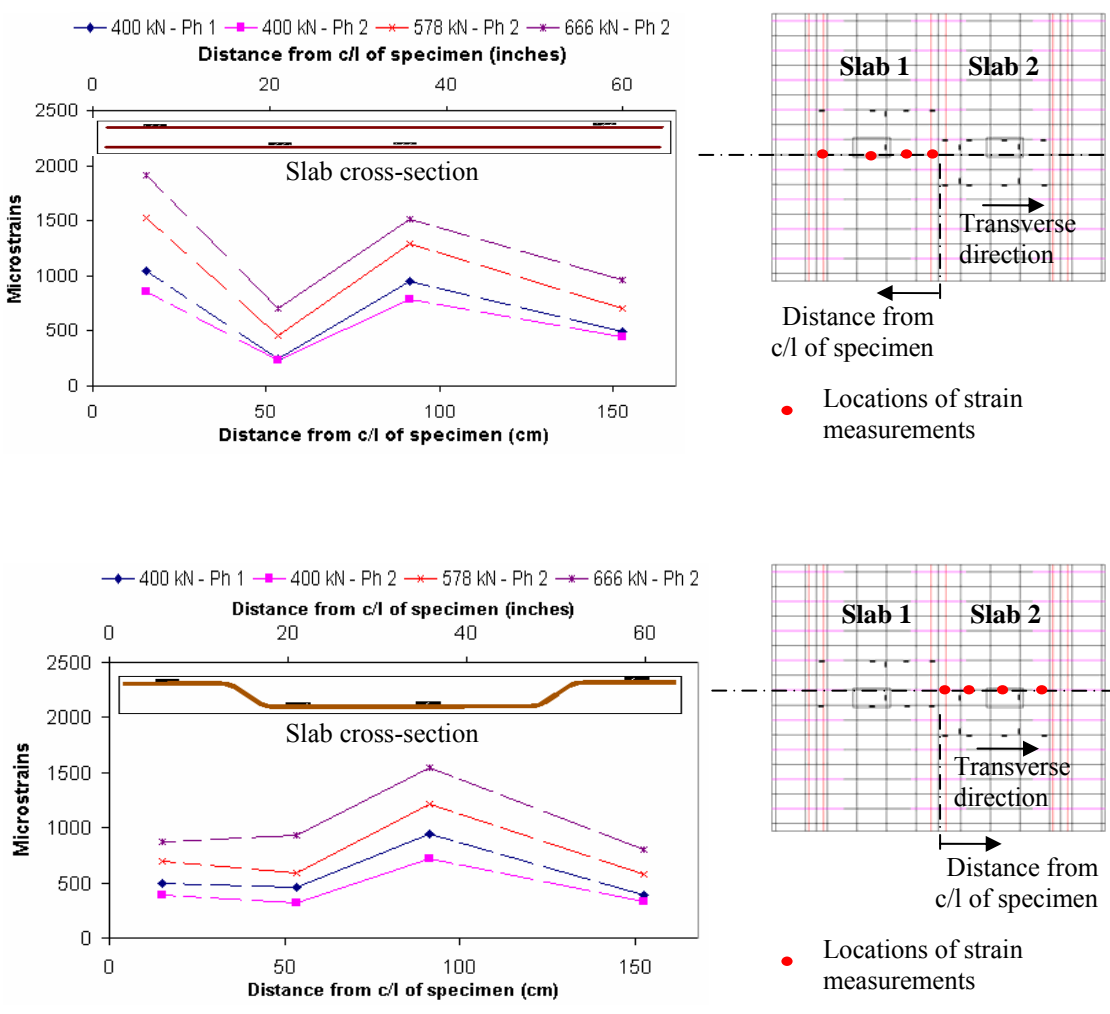


Figure 5.33 Strain profile in slab reinforcement at mid-span

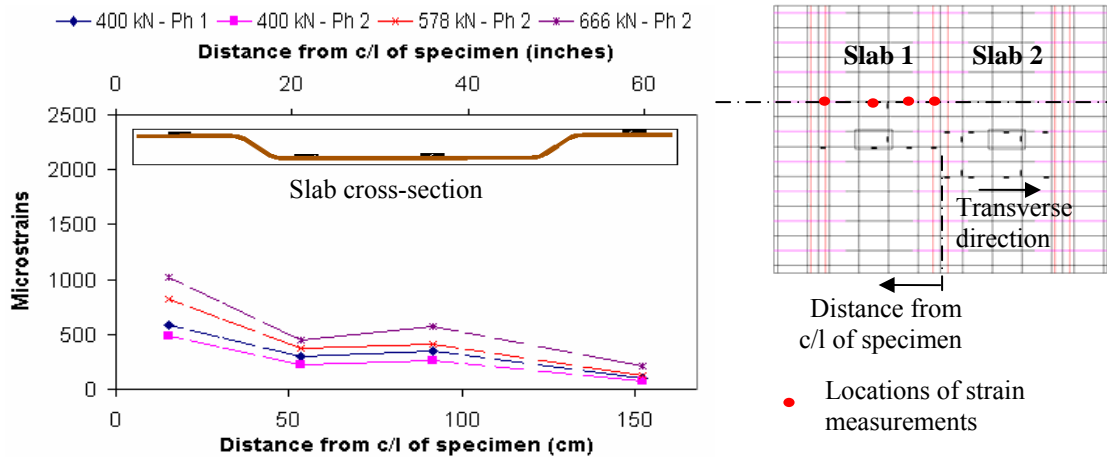


Figure 5.34 Strain profile in slab reinforcement at 508 mm (20") from mid-span

The strains in the center girder steel stirrups along the length of the girder are presented in Figure 5.35. The two sets of plots in Figure 5.35 represent the strains at the top and bottom of the leg of each stirrup along the length of the girder. Thus the higher strain in the stirrup at the top or bottom of the leg was dependent on where the stirrup was intersected by a shear crack. No significant change in the strains in the steel stirrups were observed from the strain profiles at the 400 kN (90 kips) load cycles before and after strengthening of the deck slabs with composite. This was expected and indicated that flexural strengthening of the slabs with composite had insignificant effect on the shear capacity of the center girder. The strains in the stirrups near the girder support were found to increase at the 578 kN (130 kips) load cycle and reached a maximum strain of 1660 micro-strains at the 666 kN (150 kips) load cycle, which was about 70% of the predicted yield strain in the steel stirrups of 2414 microstrains. The highest strain recorded in each instrumented stirrup along the length of the center girder is presented in Figure 5.36. The locations with the high strains corresponded with the locations of the shear cracks in the

center girder near the girder support region, as was discussed in the previous section. Since this strain level was almost 75% of yield strain (1500 micro-strains) which was the limiting criteria for shear criticality in the girder, loading was stopped. Based on the strain values in the stirrups and the significant damage through visual inspections of the crack pattern, the center girder was deemed to have reached shear criticality at the predicted load of 666 kN (150 kips).

The strains recorded on some of the representative composite pultruded strips on the slab 1 after strengthening are presented in Figure 5.37. The highest strain of 2576 micro-strains was recorded at 666 kN (150 kips) in the transverse strip below the load area (Strip T3). This was lower than the predicted ultimate debonding strain of 3568 micro-strains indicating that slab 1 had reserve capacity at the load of 666 kN (150 kips) at which the girder reached shear criticality. The strains in the strips away from the load area (Strips T4, T5 and T6) were found to decrease and are shown in Figure 5.37. The strains in the composite laminates of slab 2 followed similar trends of the strips in slab 1 with the highest strains recorded in the laminate below the load area and decreased progressively with distance (Figure 5.38). The highest strain recorded in the transverse laminates (T8) at 666 kN (150 kips) was 2228 micro-strains below the load area. This was lower than the predicted ultimate debonding strain of 3262 micro-strains indicating that slab 2 too had reserve capacity at the load of 666 kN (150 kips) at which the girder reached shear criticality. The strain in the transverse composite laminates away from the load area (Laminates T9 and T10) is also shown in Figure 5.38.

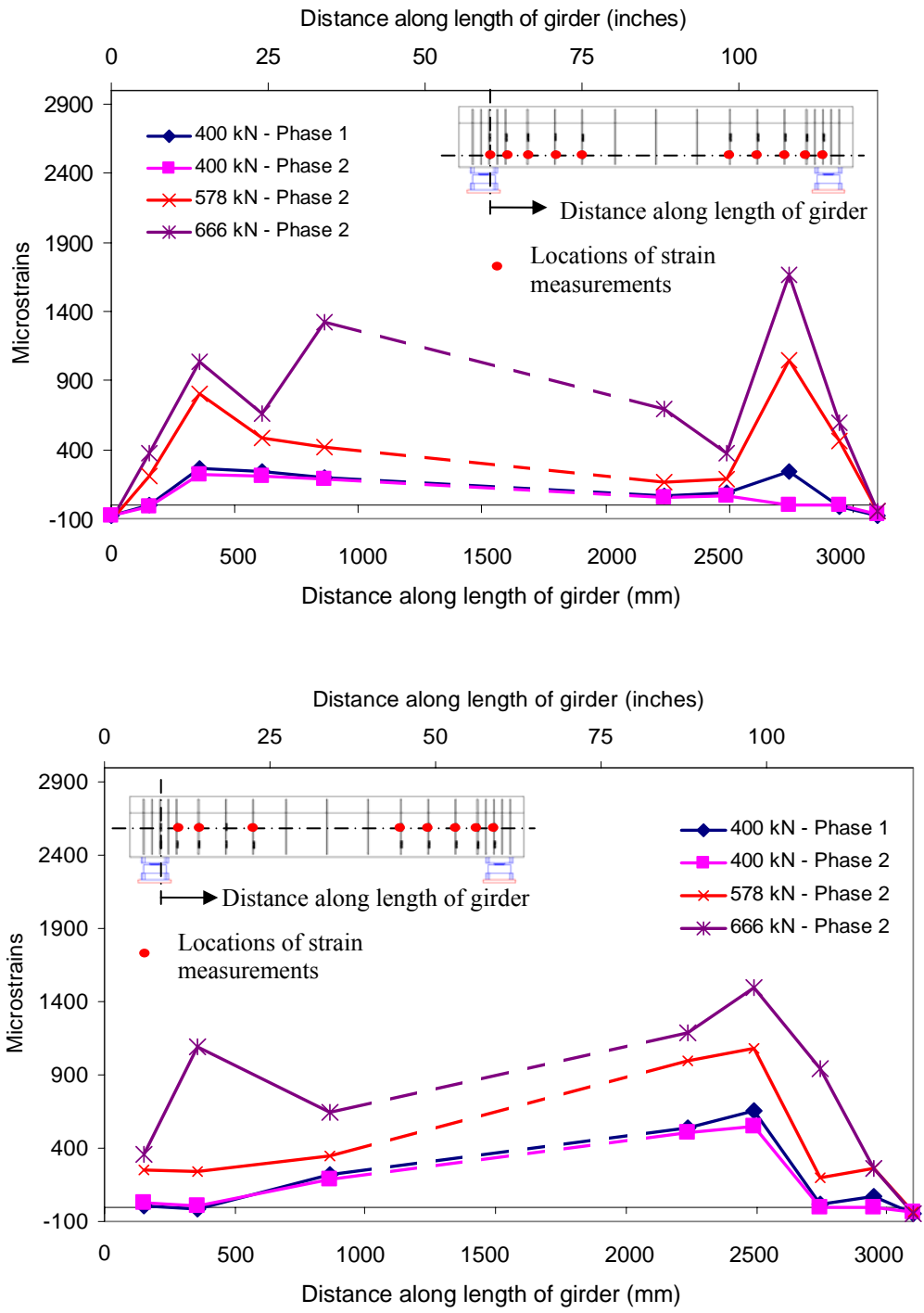


Figure 5.35 Strain profile in center girder steel stirrups

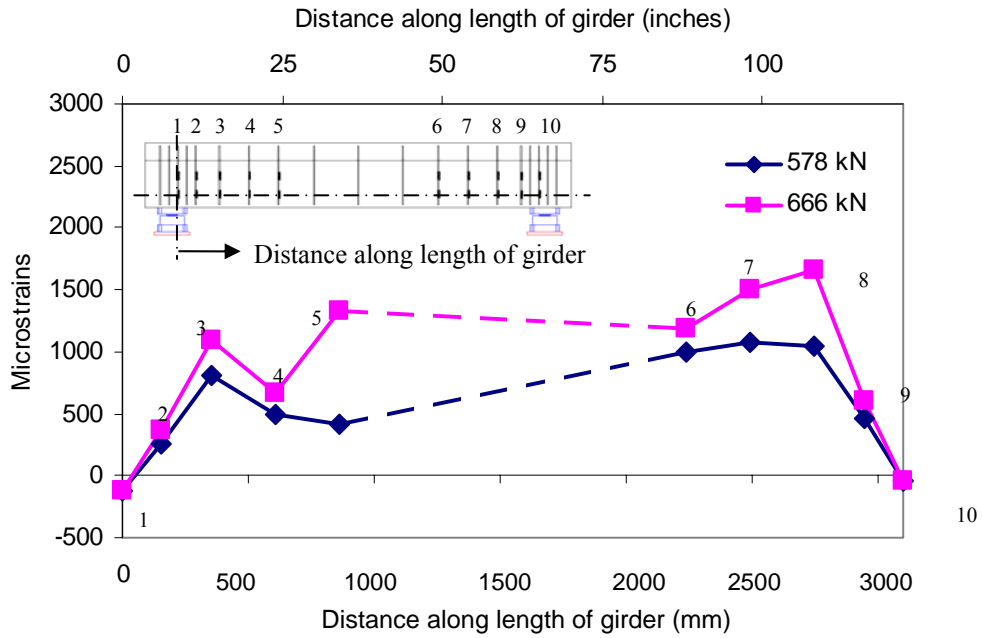


Figure 5.36 Maximum recorded strains in the instrumented steel stirrups along the length of the center girder during phase 2 loading

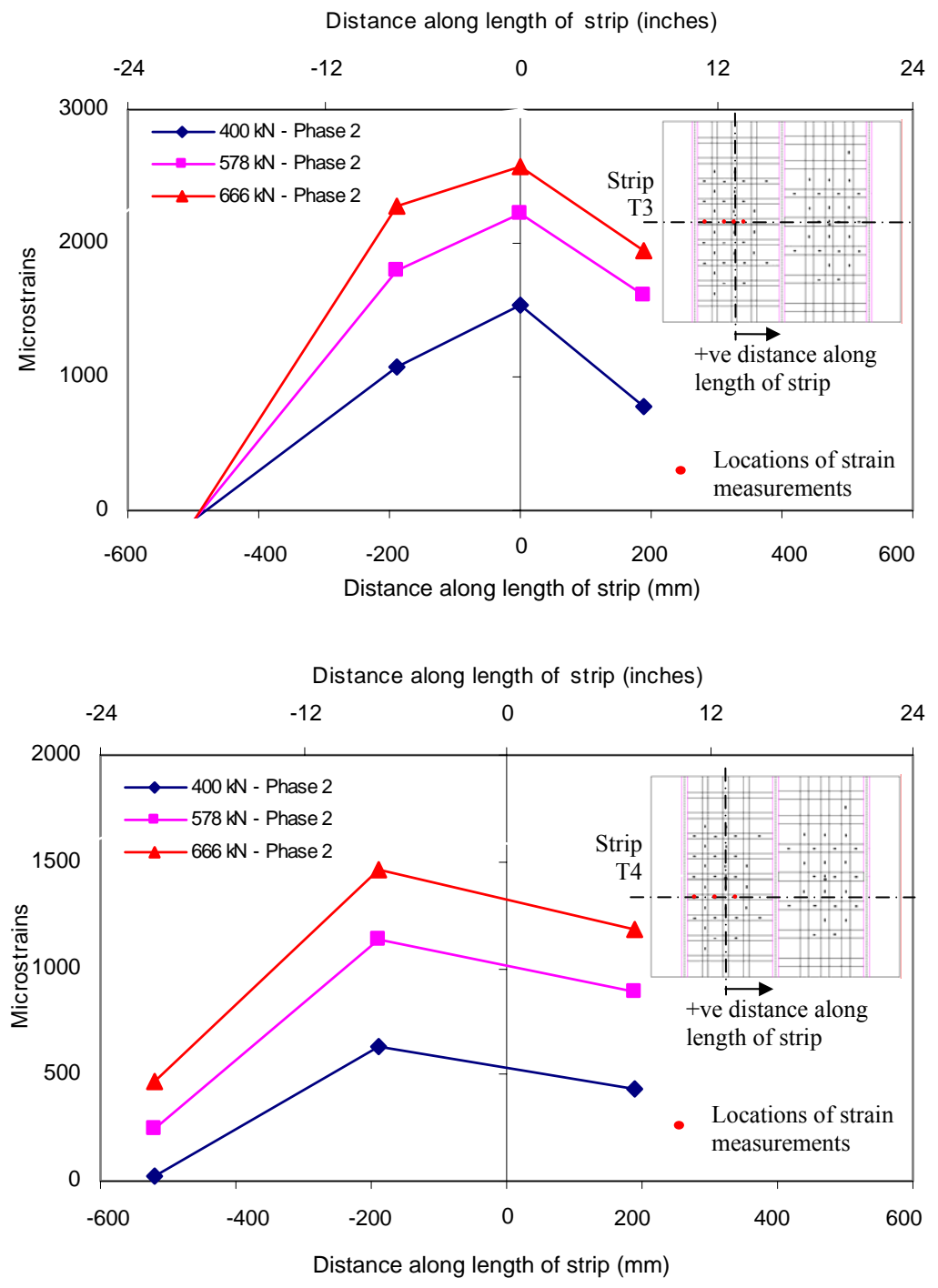


Figure 5.37a Strain profile in transverse composite strips (T3 and T4) of strengthened Slab 1 for phase 2 loading

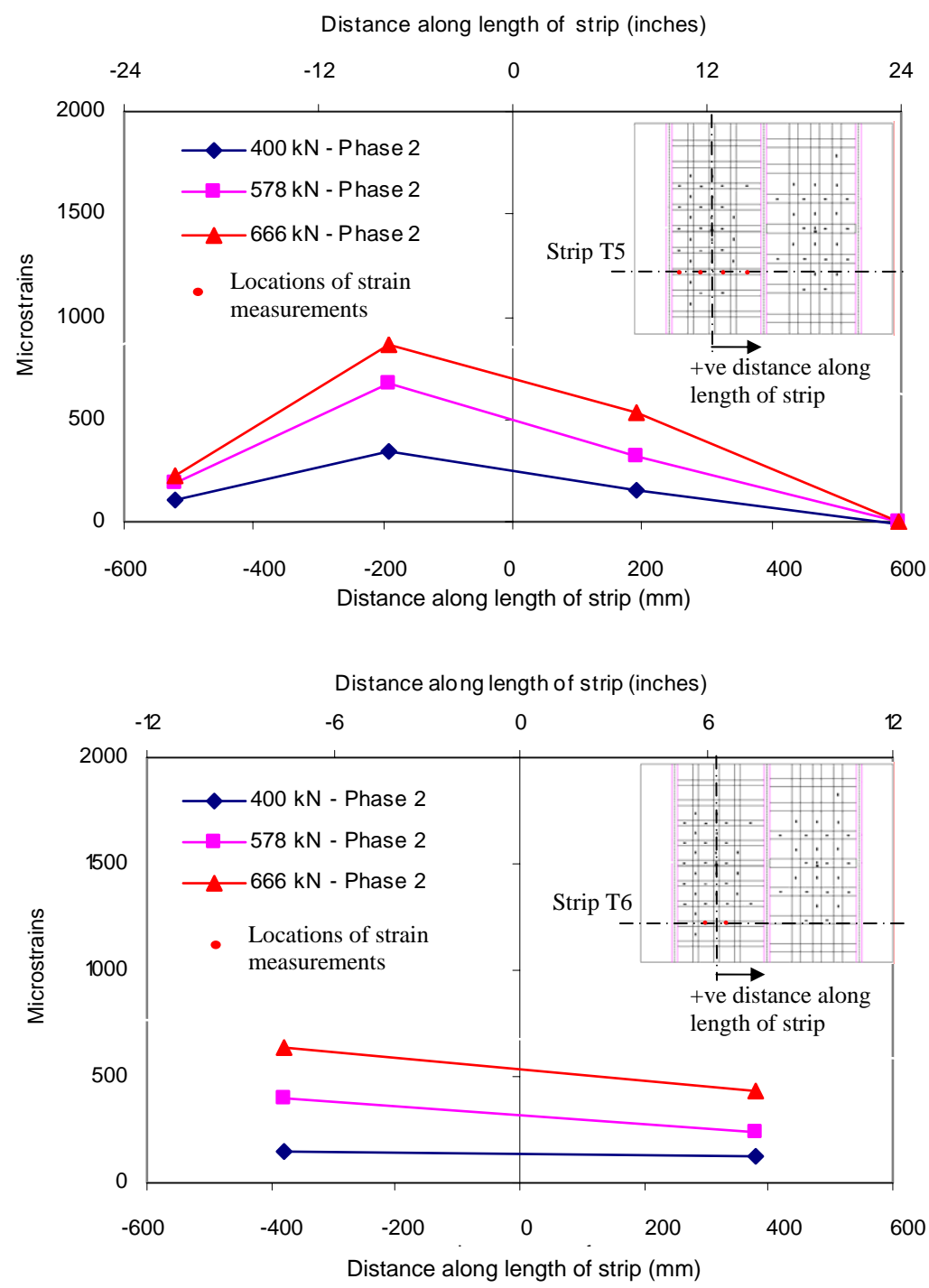


Figure 5.37b Strain profile in transverse composite strips (T5 and T6) of strengthened Slab 1 for phase 2 loading

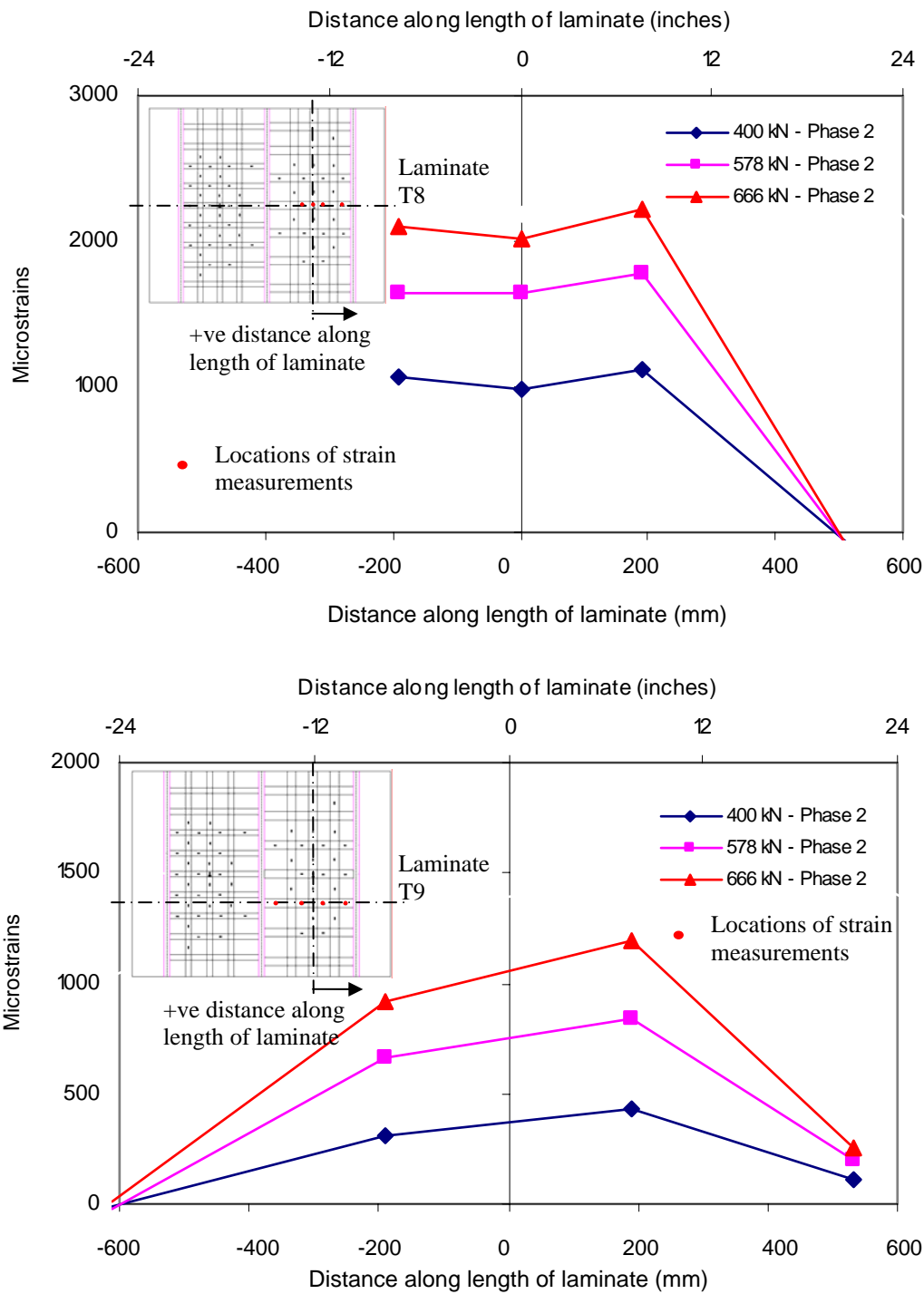


Figure 5.38a Strain profile in transverse composite laminates (T8 and T9) of strengthened Slab 2 for phase 2 loading

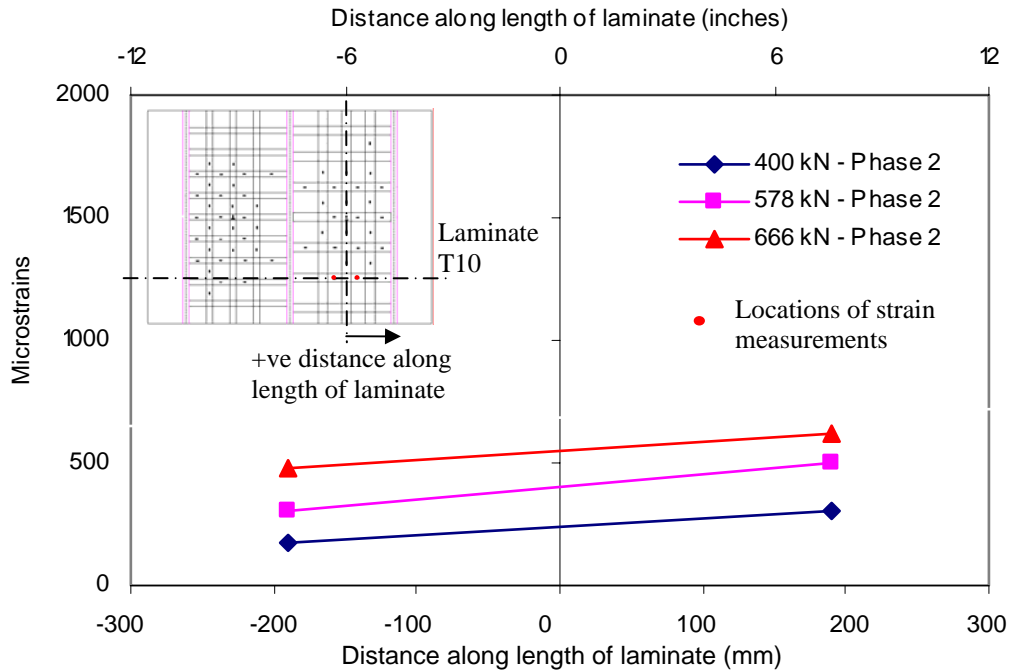


Figure 5.38b Strain profile in transverse composite laminate T10 of strengthened Slab 2 for phase 2 loading

At similar locations of the slab relative to the loading area, the strains in the laminates were lower than that in the pultruded strips. As mentioned earlier, the maximum recorded strain at peak load of 666 kN load cycle in transverse strip T3 was 2576 microstrains as compared to maximum recorded strain of 2228 microstrains in laminate T8. This was because the 2 layers of 152 mm (6") wide laminates had a larger cross-sectional area than that of the 1 layer of 102 mm (4") wide pultruded strips and thus for the same stress produced by the wheel load, the strains in the laminates were lower. However it is to be remembered that the laminates were spaced at 533 mm (21") while the pultruded strips were spaced at 381 mm (15") to take into account the difference in cross-section to achieve equivalent capacity. Also it is to be remembered that the amount

of carbon fibers in each type of composite (strip and fabric) was different and this was reflected in the different properties of the two systems (as was presented in Chapter 4) and the actual properties of the composite systems obtained through material tests were used to arrive at equivalent capacity for the two slabs. This resulted in overall similar behavior of the two strengthened slabs.

The strain profiles along the longitudinal composite strip (Strip L2) and laminate (Laminate L5) below the load area are presented in Figure 5.39. The highest strains recorded in the longitudinal strips and laminates at the end of phase 2 test at 666 kN (150 kips) were 2195 and 1887 micro-strains respectively.

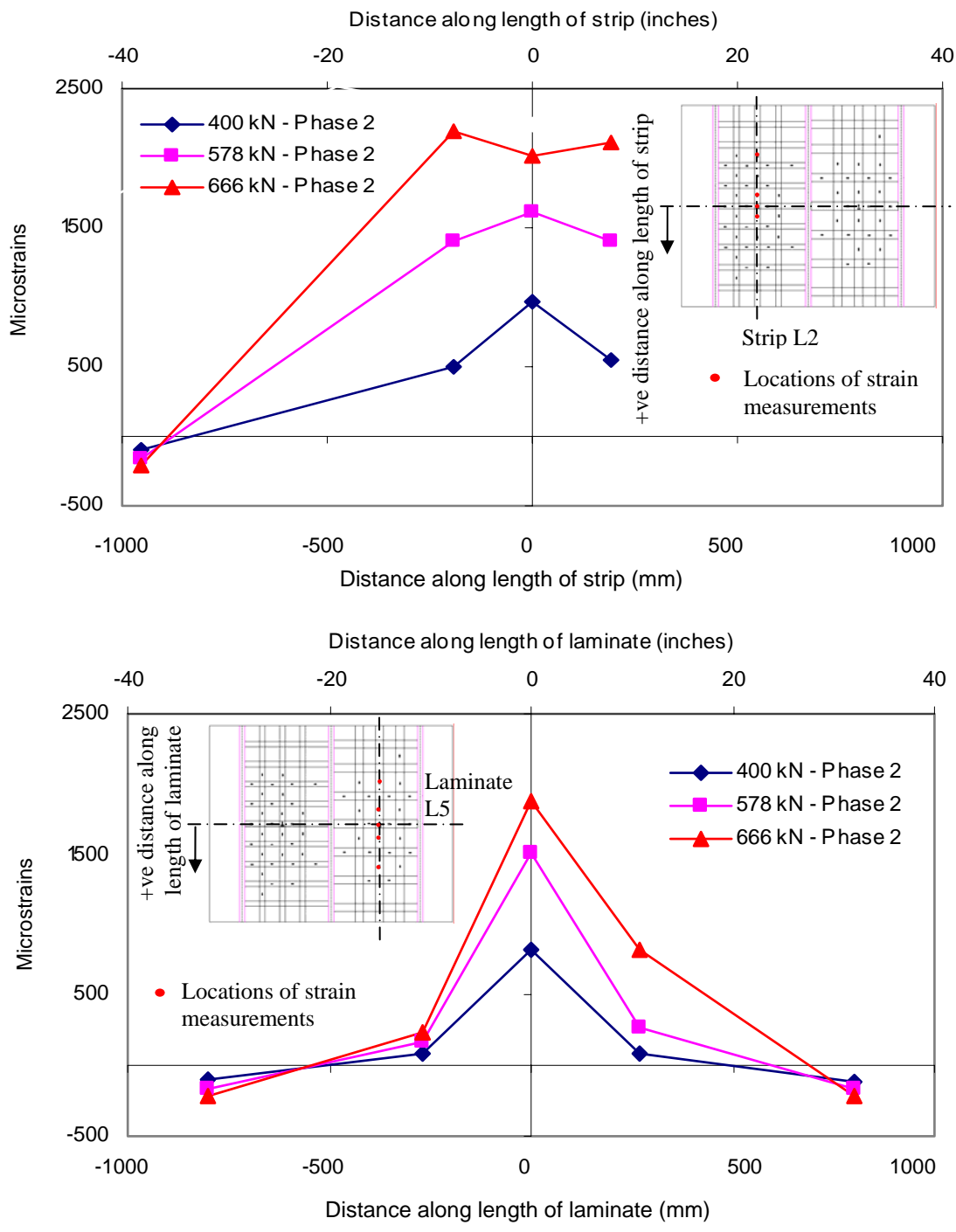


Figure 5.39 Strain profile in longitudinal strip/laminate of strengthened slabs

5.2.4 Comparison of Test Results with Design

The center girder was found to reach shear criticality at the predicted load of 666 kN (150 kips) indicated by the crack pattern that showed significant damage near the support locations of the center girder. This was corroborated by the high strain levels in the steel stirrups of the center girder near the support regions which reached the predicted strains above 1500 micro-strains. All the damage at this phase of test was localized in the center girder with the strengthened slabs undergoing very little damage. The effectiveness of the composite systems in strengthening the slabs was recognized by the decrease in the deflections (from 4.91 mm to 4.21 mm in slab 1 and from 4.76 mm to 4.1 mm in slab 2 at comparable actuator load of 400 kN) and strains (954 to 784 micro-strains in slab 1 and from 947 to 716 micro-strains in slab 2 at 400 kN load level) in the slab reinforcement at comparable load levels before and after strengthening. Also similar deflection and strain profiles in the two slabs indicated that equivalent capacities, as was designed for the slabs with the two composite systems, were achieved. The strains in the composite laminates/strips were below the debonding strain level indicating that the strengthened slabs had not reached ultimate capacity at the load level at which the girder reached shear criticality. This substantiated the primary concern of this research, that strengthening of individual components can push other components towards their limit state under the high load demands so that at the system level the strengthened component will not be able to reach its design capacity due to deficiency in other components of the system.

5.3 Results from Phase 3 of Testing - Introduction

Phase 3 loading was started after shear strengthening of the center girder with FRP composite stirrups. The objective of this phase was to study behavior and damage progression in a slab-girder system after strengthening of both the slab and the girder components with composite. The shear strengthening of the girder was designed such that the shear capacity of the strengthened girder was higher than the shear demand at the load level at which the deck slabs were predicted to reach their flexural limit state. Thus the damage in this phase of testing was predicted to occur in the strengthened deck slabs culminating in debonding of the composite strips/laminates and ultimate failure of the slabs.

5.3.1 Load Capacity and Stiffness Results

The debonding strains in the composite strips/laminates corresponding to the predefined failure limit state of the strengthened slabs were estimated as 3568 and 3262 micro-strains, respectively. From the updated FE model, the details of which will be presented later in Chapter 8, the maximum predicted strains in the composite systems at 930 kN (209 kips) were 3767 microstrains in the pultruded strips and 3386 microstrains in the fabric laminates.

A simplistic estimate of the design load at which this strain level would be reached was also determined based on the strain development in the composite with loading of the test specimen. This was based on the assumption that since both the steel and composite would be in the linear elastic range all through phase 3 loading, the trend of strain increment in the composite laminates/strips upto 666 kN (150 kips) in phase 2

would be followed over the load cycles of phase 3 as well. Since the areas below the load were the most highly stressed, the strain gages located below the actuator loads, namely CTM-1 in slab 1 and CTM-2 in slab 2 were used for extrapolated prediction of the failure load demand. The strain increment profile at these locations with loading from the 666 kN (150 kips) load cycle is presented in Figure 5.40 and was extrapolated using a best-fit curve to determine the load required, assuming continued self similar behavior, to reach the 3568 and 3262 micro-strains debonding limit. The required load demand was found to be 935 kN (210 kips) at which the predicted strains in the composite at locations CTM-1 and CTM-2 were 3578 and 3172 micro-strains respectively. Based on this ultimate failure load estimate, the peak loads used for phase 3 load cycles were 757 kN (170 kips), 846 kN (190 kips) and 935 kN (210 kips). The summary of the load cycles during phase 3 is presented in Table 5.6.

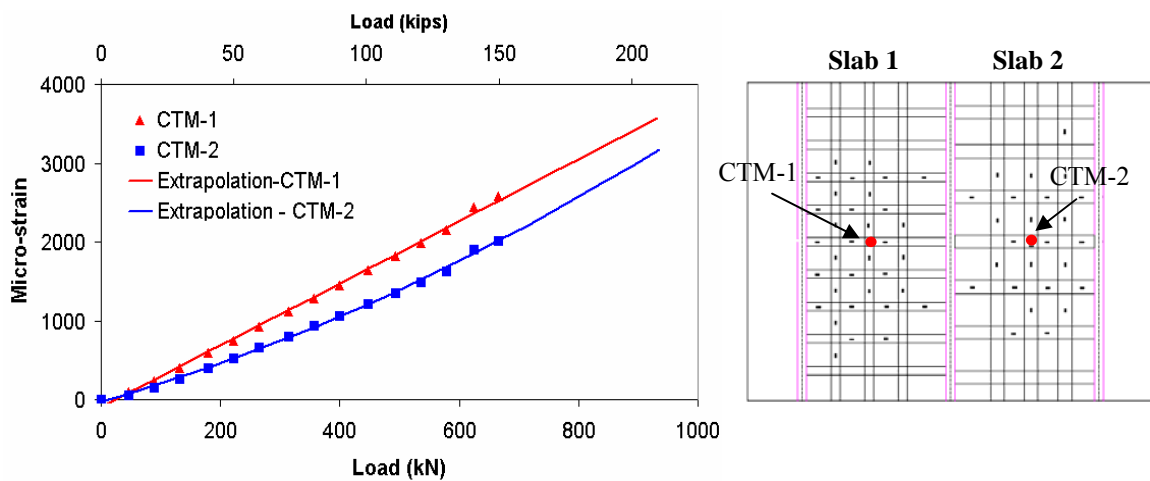


Figure 5.40 Strain profile extrapolation for ultimate load demand prediction

Table 5.6 Loading protocol for phase 3

Load cycle #	Peak load kN (kips)	Load cycle remarks
1	666 (150)	Comparison with ultimate load level of Phase 2 to evaluate changes in slab-girder system produced by shear strengthening of the center girder with FRP composite stirrups
2	757 (170)	Intermediate load level [1/3 of the loading between ultimate phase 2 (666 kN) and phase 3 (935) predicted loads] to check for design predictions, mark cracks and perform NDE inspections
3	846 (190)	Intermediate load level [2/3 of the loading between ultimate phase 2 (666 kN) and phase 3 (935) predicted loads] to check for design predictions, mark cracks and perform NDE inspections
4	935 (210)	Phase 3 ultimate failure load required to cause flexural failure of the strengthened slabs due to debonding of the composite laminates/strips followed by punch through of wheel load through concrete

* Note: For each load cycle after reaching peak load, the load was first brought down to 107 kN (24 kips) for NDE inspections and then the specimen was unloaded by retracting the actuators away from the specimen before starting the next load cycle

The load-deflection plot for Slab 1 over the Phase 3 load cycles was obtained by plotting the actuator load on slab 1 against the deflection below the load obtained from the linear potentiometer LPM3 and is presented in Figure 5.41. A gradual degradation of the load-deflection response slope was observed for the deck slabs over the load cycles. However no abrupt changes were observed indicating that the composite systems were effective in converting the punching shear failure mode of the deck slabs into more gradual flexural failure mode by restraining the opening of the punching shear cracks. The same was indicated from the calculations of “effective” stiffness for the deck slabs

which will be discussed later in this section. Also no changes in the load-deflection response of the slabs were observed on comparing the 666 kN (150 kips) load stages before and after shear strengthening of the center girder with composite indicating that shear strengthening of the center girder had insignificant effect on the stiffness of the slabs. The comparison of the load-deflection response of the two strengthened slabs in phase 3 is presented in Figure 5.42. The response was very similar in both the slabs indicating that the composite systems, pultruded strips and fabric laminates, produced equivalent flexural capacities for the slabs. Both the slabs failed at 933 kN (209.6 kips) which compared well with the 935 kN (210 kips) predicted for ultimate failure. However the maximum deflection below load in strengthened slab 1 was slightly higher than that in slab 2 at failure load [14.37 mm in slab 1 compared to 13.8 mm in slab 2]. Both the slabs failed due to debonding of the composite and this was followed by simultaneous punching through of the loadpad, representing the wheel load, through concrete. The failure modes of the two slabs will be discussed in more details in the next section of this chapter.

The deflections at the center of the middle and edge girder as measured by the linear potentiometers, LPM6 and LPM11 respectively, were plotted against actuator loads in Figures 5.43a and 5.43b. Very little difference was observed on comparing the slopes of the load deflection responses of the center girder (Figure 5.43a) at the 666 kN (150 kips) load stage before and after strengthening of the girder with composite stirrups. This was because the measured deflection was primarily governed by flexure while the girder was strengthened in shear. The strengthening of the center girder with externally bonded composite stirrups also had no effect on the load-deflection response of the edge girders

as shown in Figure 5.43b. With the progression of loading in phase 3 of testing, a slight decrease of the slope of the load-deflection response was observed in the center girder (by about 10% at the peak load of 935 kN load cycle as compared to the initial slope of the strengthened girder). This change of slope was much smaller as compared to the change in phase 2, where as much as 25% degradation of load-deflection response slope was observed, indicating that the shear strengthening with composite was effective in restraining the further damage in the girder during phase 3 loading. This was also verified from the “effective” stiffness results presented in Table 5.6, as will be discussed next. The load-deflection responses of the two edge girders were also compared and are shown in Figure 5.43c. Edge girder 1 was found to have slightly higher deflection than that of edge girder 2 at comparable load stages [4.21 mm deflection in edge girder 1 as compared to 3.68 mm deflection in edge girder 2 at peak load in the 935 kN (210 kips) load cycle.

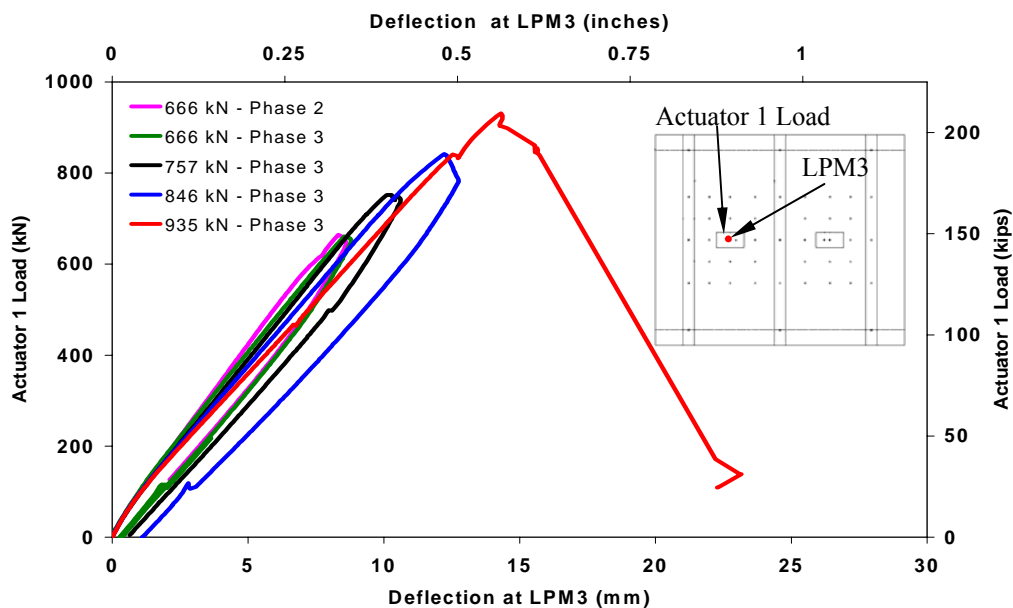
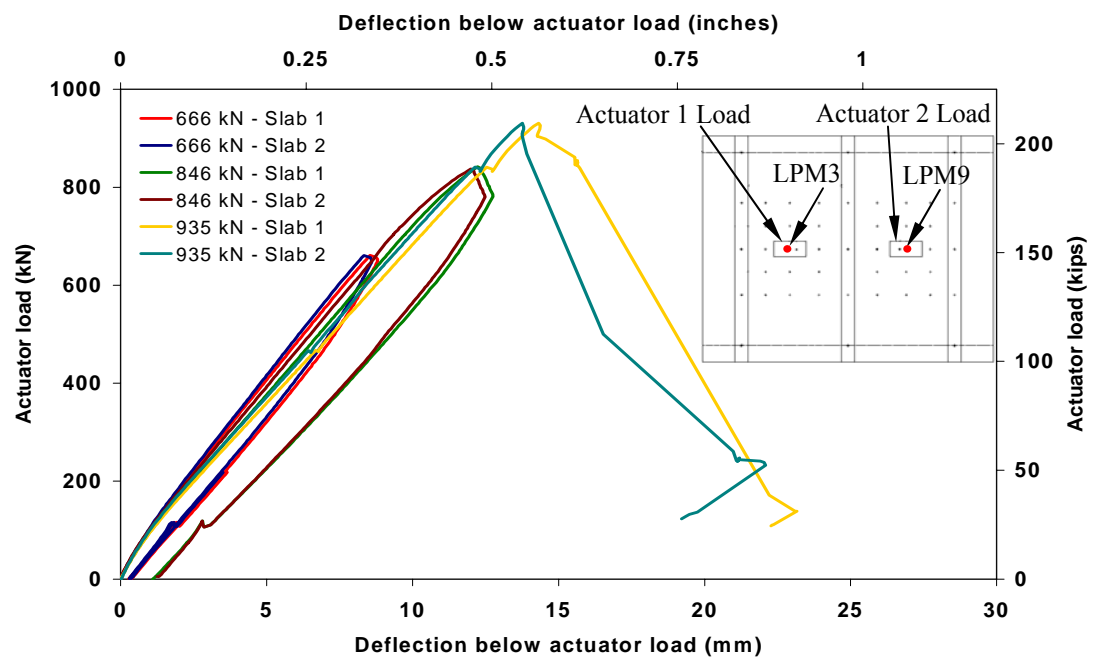


Figure 5.41 Load-deflection plots for slab 1



Note: For slab 1 Actuator load 1 was plotted against deflection at LPM3
For slab 2 Actuator load 2 was plotted against deflection at LPM9

Figure 5.42 Comparison of load-deflection plots between deck slabs in phase 3

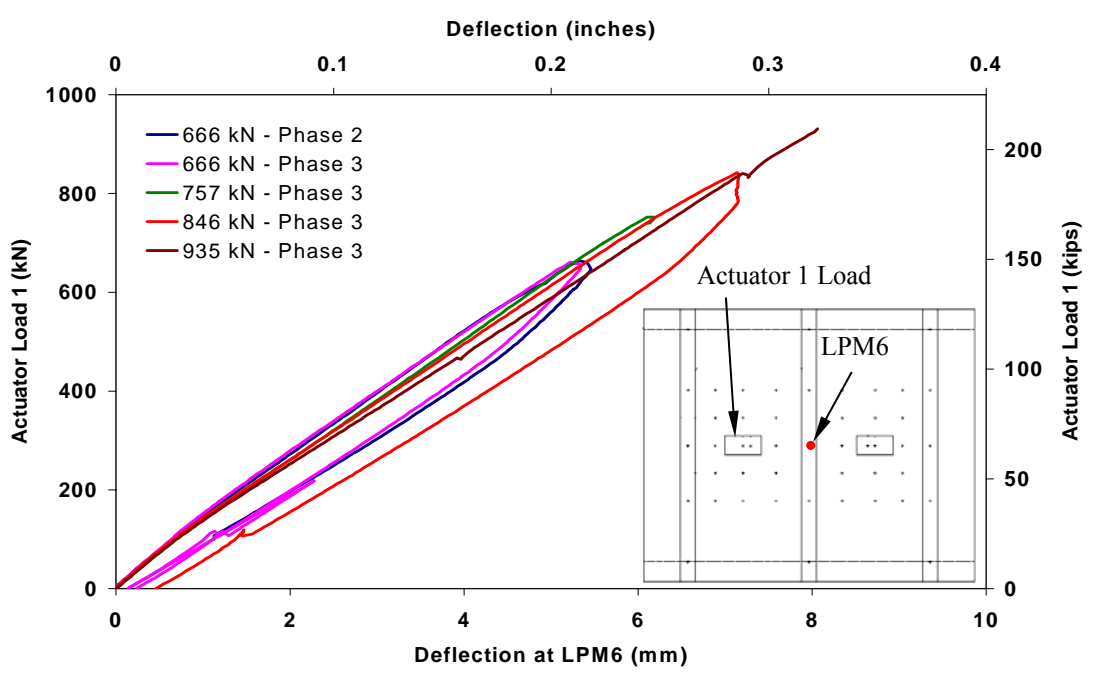


Figure 5.43a Actuator load 1 vs. mid-span deflection plots for middle girder

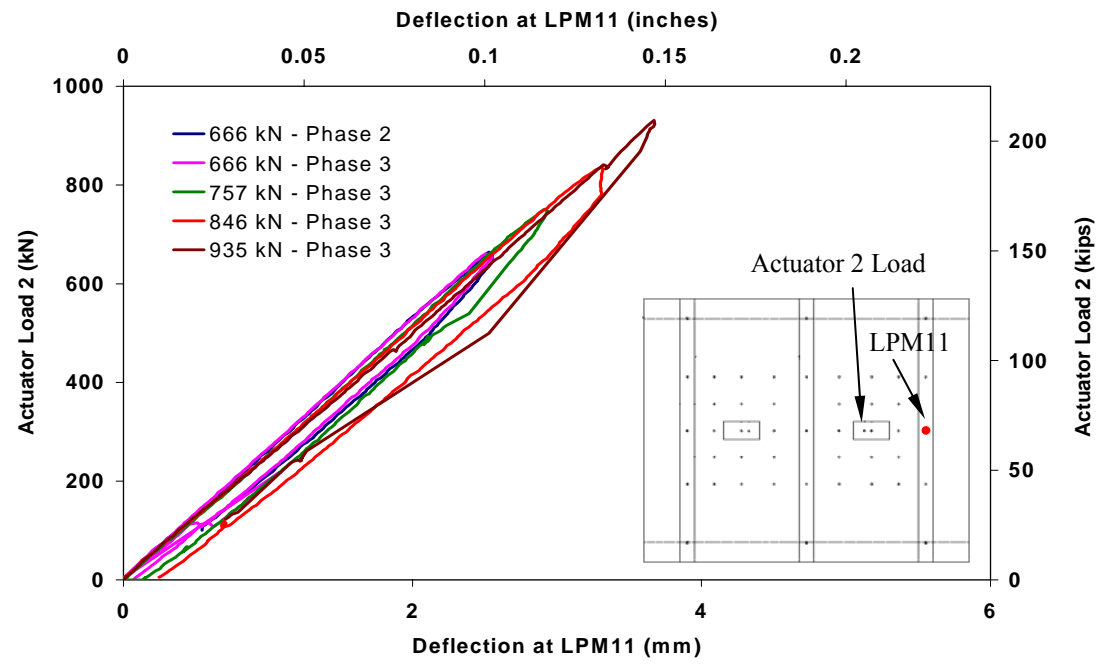
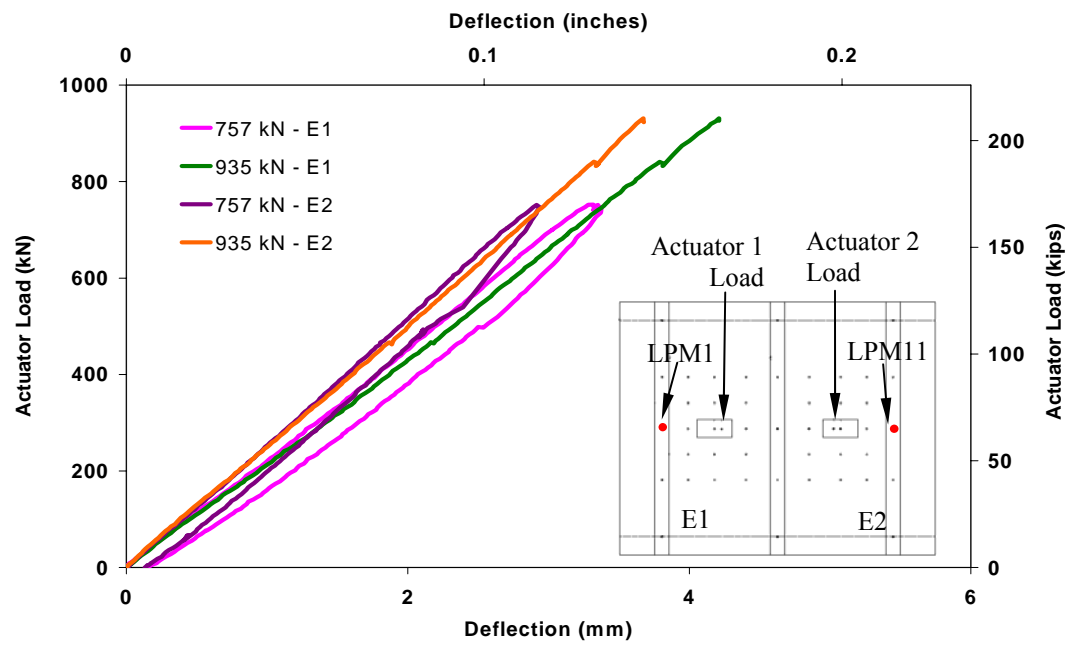


Figure 5.43b Actuator load 2 vs. mid-span deflection plots for edge girder



Note: For edge beam 1 (E1) Actuator load 1 was plotted against deflection at LPM1
For edge beam 2(E2) Actuator load 2 was plotted against deflection at LPM11

Figure 5.43c Comparison of mid-span load-deflection plots between edge girders

A comparative evaluation of the degradation of the slope of load-deflection response of the slabs and the girders over the load cycles in phase 3 was obtained using the “effective” stiffness, which was defined earlier in equation 5.4. The “effective” stiffness ratio was then computed as was defined earlier in equation 5.5 and are presented in Table 5.7. The true deflections of the deck slabs were obtained by subtracting the contribution of the girder deflection from the total deflection of the slabs, as was discussed earlier in section 5.1.1 of this chapter and was given by equation 5.6. The decrease of “effective” stiffness ratio in the slabs (Table 5.7a) was gradual in phase 3 and was consistent with that in phase 2 indicative of a flexural behavior rather than punching shear deficiency, which would result in significant change in the effective stiffness ratio as was observed in Phase 1. No increase in the effective stiffness ratio of the slabs was observed at the 666 kN (150 kips) load stage before and after strengthening of the center girder with composite stirrups indicating that strengthening of the center girder did not affect the stiffness of the strengthened slabs.

Table 5.7a Effective stiffness ratio in slabs in phase 3 from linear potentiometer data

Slab 1 (Deflections below actuator load)			Slab 2 (Deflections below actuator load)		
Actuator load kN (kips)	Actual deflection mm (inches)	Effective stiffness ratio	Actuator load kN (kips)	Actual deflection mm (inches)	Effective stiffness ratio
102.3 (23)*	0.38 (0.015)*	1.00*	101.66 (22.8)*	0.38 (0.015)*	1.00*
395.2 (88.8)*	2.49 (0.098)*	0.60*	395.55 (88.9)*	2.39 (0.094)*	0.63*
399.3 (89.7) [#]	2.08 (0.082) [#]	0.72 [#]	399.03 (89.67) [#]	2.04 (0.08) [#]	0.74 [#]
665.6 (149.6) [#]	4.37 (0.172) [#]	0.57 [#]	665.5 (149.55) [#]	4.28 (0.169) [#]	0.59 [#]
662.42 (148.9)	4.63 (0.182)	0.54	662.08 (148.8)	4.59 (0.181)	0.54
753.34 (169.3)	5.54 (0.218)	0.51	752.7 (169.1)	5.45 (0.215)	0.52
843.65 (189.6)	6.92 (0.272)	0.46	838.85 (188.5)	6.95 (0.273)	0.46
932.77 (209.6)	8.35 (0.329)	0.42	927.54 (208.4)	8.12 (0.320)	0.43

* From Phase 1 of test before strengthening of the deck slabs with composite

From Phase 2 of test after strengthening of the deck slabs with composite but before strengthening of the center girder with composite stirrups

Table 5.7b Effective stiffness ratio in girders in phase 3 from potentiometer data

Center girder			Edge girder		
Actuator load kN (kips)	Mid-span deflection mm (inches)	Effective stiffness ratio	Actuator load kN (kips)	Mid-span deflection mm (inches)	Effective stiffness ratio
102.3 (23)*	0.57 (0.023)*	1.00*	101.66 (22.8)*	0.35 (0.014)*	1.00*
395.2 (88.8)*	1.31 (0.051)*	0.83*	395.55 (88.9)*	1.41 (0.056)*	0.95*
399.3 (89.7) [#]	2.57 (0.101) [#]	0.85 [#]	399.03 (89.67) [#]	1.40 (0.055) [#]	0.96 [#]
665.6 (149.6) [#]	5.58 (0.219) [#]	0.67 [#]	665.5 (149.55) [#]	2.82 (0.111) [#]	0.80 [#]
662.42 (148.9)	5.22 (0.206)	0.71	662.08 (148.8)	2.82 (0.111)	0.80
753.34 (169.3)	6.10 (0.240)	0.69	752.7 (169.1)	3.28 (0.129)	0.78
843.65 (189.6)	7.13 (0.281)	0.66	838.85 (188.5)	3.77 (0.149)	0.76
932.77 (209.6)	8.06 (0.317)	0.65	927.54 (208.4)	4.21 (0.166)	0.75

* From Phase 1 of test before strengthening of the deck slabs with composite

From Phase 2 of test after strengthening of the deck slabs with composite but before strengthening of the center girder with composite stirrups

For the center girder the “effective” stiffness ratio increased from 0.67 to 0.71 after shear strengthening of the girder (Table 5.7b). The change was not significant since the “effective” stiffness ratio is more representative of the flexural stiffness and the center girder was strengthened in shear. Also after strengthening, the degradation of the stiffness ratio over the phase 3 load cycles was very small in the center girder [from 0.71 to 0.65 as compared to 0.85 to 0.67 in phase 2] indicating that the shear strengthening was effective in restraining damage in the girder. Thus with the strengthening of the girder component in phase 3 of test, the damage was transferred back into the deck slabs, which were predicted to reach ultimate failure at the end of phase 3. The strengthening of the center girder had no effect on the stiffness of the edge girder and also the effective stiffness ratio in the edge girders changed from 0.8 to 0.75 (as compared to 0.71 to 0.65 in the center girder) over Phase 3 loading indicating that the edge girders did not reach any critical limit states over this stage of loading.

5.3.2 Deflection Profiles and Crack Patterns

The deflection profiles along the lengths of the center and edge girders at the peak loads of phase 3 load cycles are presented in Figure 5.44. The deflections were measured at mid and quarter span and at supports of the girders. A slight reduction of deflection [5.58 mm to 5.22 mm] was observed in the center girder at 666 kN (150 kips) before and after shear strengthening of the girder with composite stirrups. However no such changes were observed in the edge girder since the shear strengthening of the center girder had no effect on the edge girder.

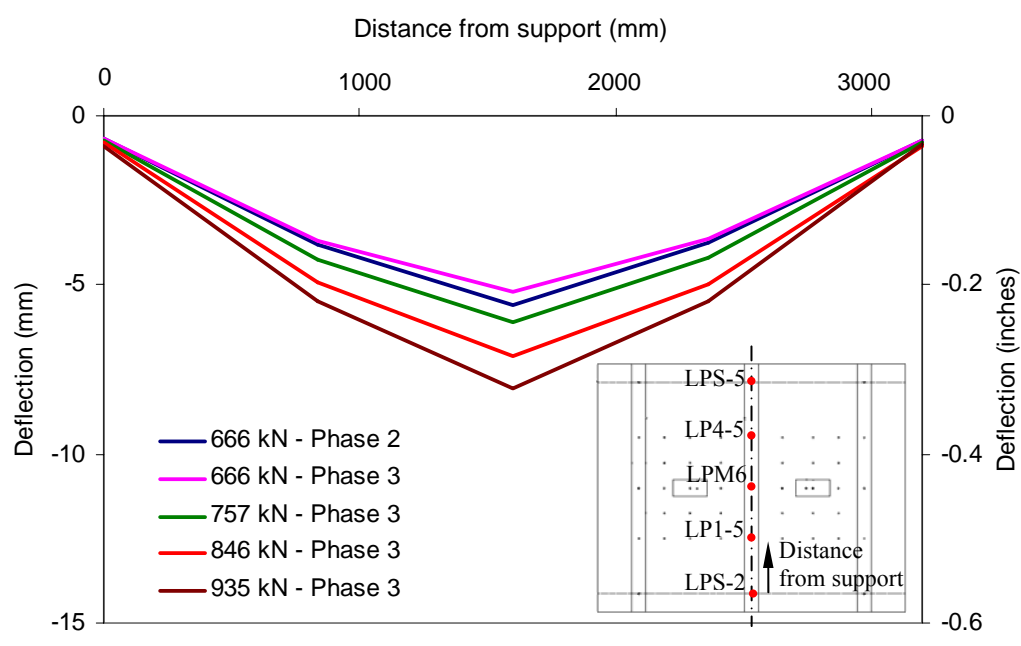


Figure 5.44a Deflection along length of middle girder

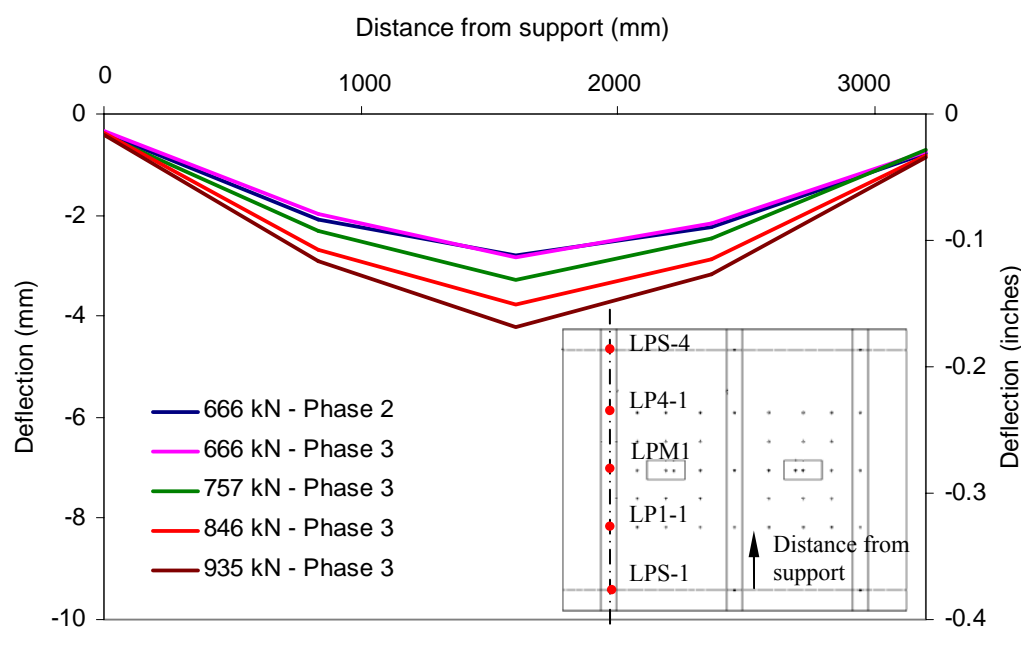


Figure 5.44b Deflection along length of edge girder 1

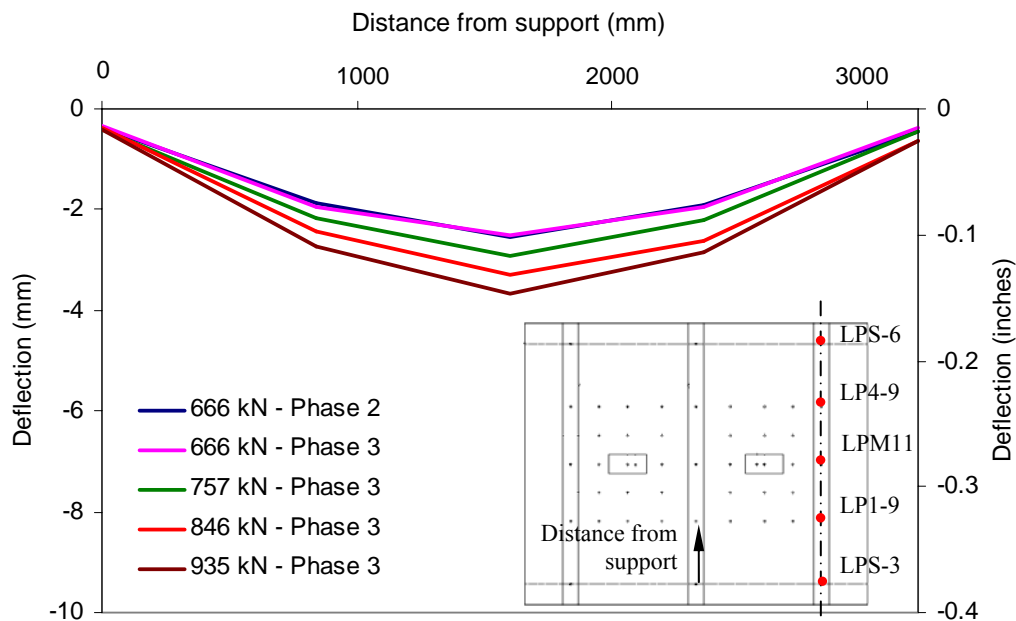


Figure 5.44c Deflection along length of edge girder 1

The contour profile of the deflections obtained from the linear potentiometer data over the surface of the strengthened deck slabs ultimate failure of the strengthened slabs at 933 kN (209.6 kips) is presented in Figure 5.45. The highest deflections of the strengthened slabs were found to be concentrated in the areas under the load contact areas of the actuators. Representative deflection measurements recorded by the rows of linear potentiometers at the peak loads at the end of each load cycle for phase 3 are presented in Figures 5.46 and 5.47. The row 2 of linear potentiometers was located 381 mm (15") away from mid-span of the specimen, at which the vertical deflections were measured by row M of potentiometers. The maximum deflections in the two strengthened slabs were almost identical over the load cycles of phase 3. However at the failure load of 935 kN (which occurred simultaneously in both slabs), the maximum deflection below the load

area in slab 1 was slightly higher as compared to that of slab 2 [14.31 mm in slab 1 as compared to 13.78 mm in slab 2]. Also it was seen from the deflection contour in Figure 5.45 that the damage region indicated by the high deflection areas was slightly larger in slab 1 than in slab 2. The comparative failure patterns of the two slabs will be discussed further in terms of the crack pattern and failure planes. Both the slabs reached the same failure load simultaneously and thus it was possible to compare the responses of the two slabs in order to evaluate comparative effectiveness of the two composite systems used to strengthen the two deck slabs.

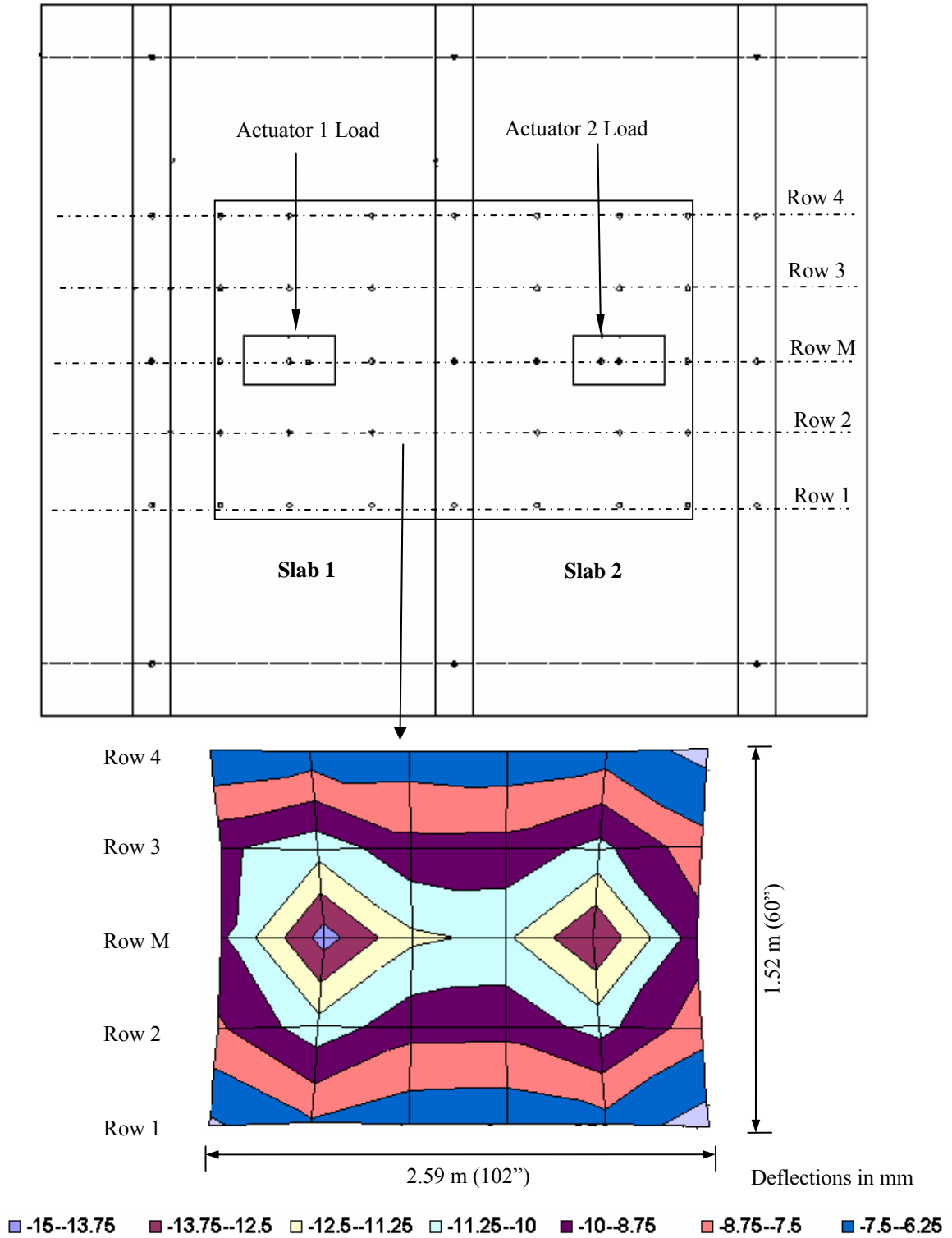


Figure 5.45 Deflection contour over deck slabs at 666 kN (150 kips)

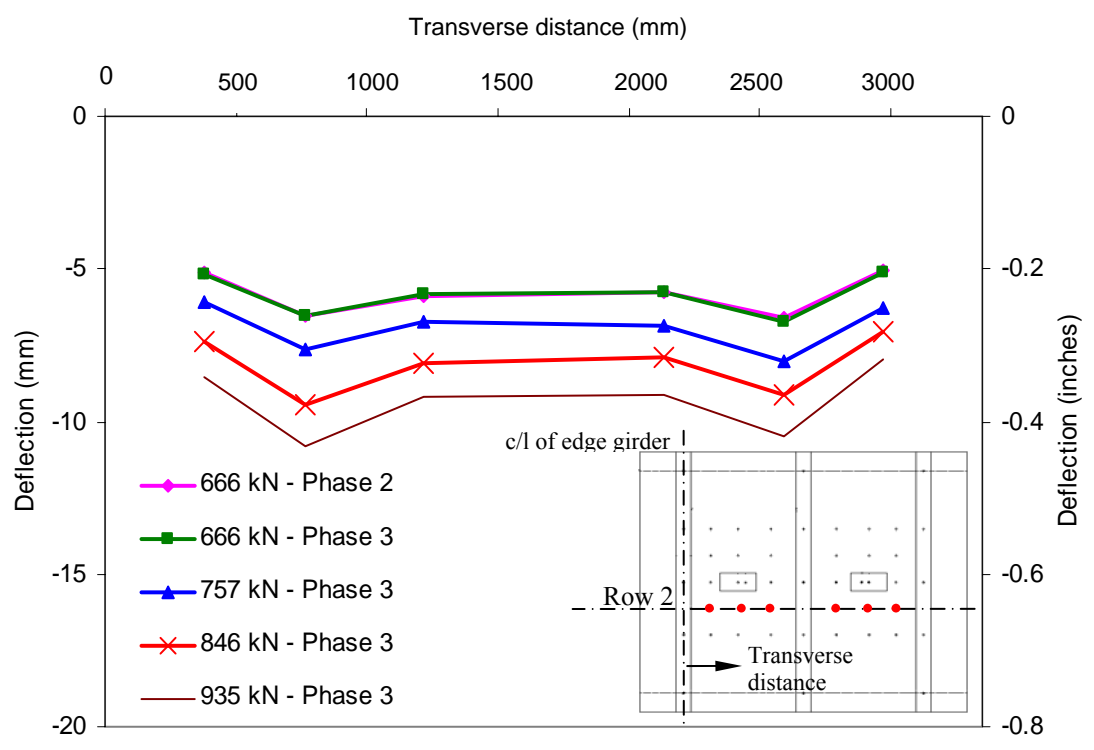


Figure 5.46 Deflection profile along Row 2 of linear potentiometers

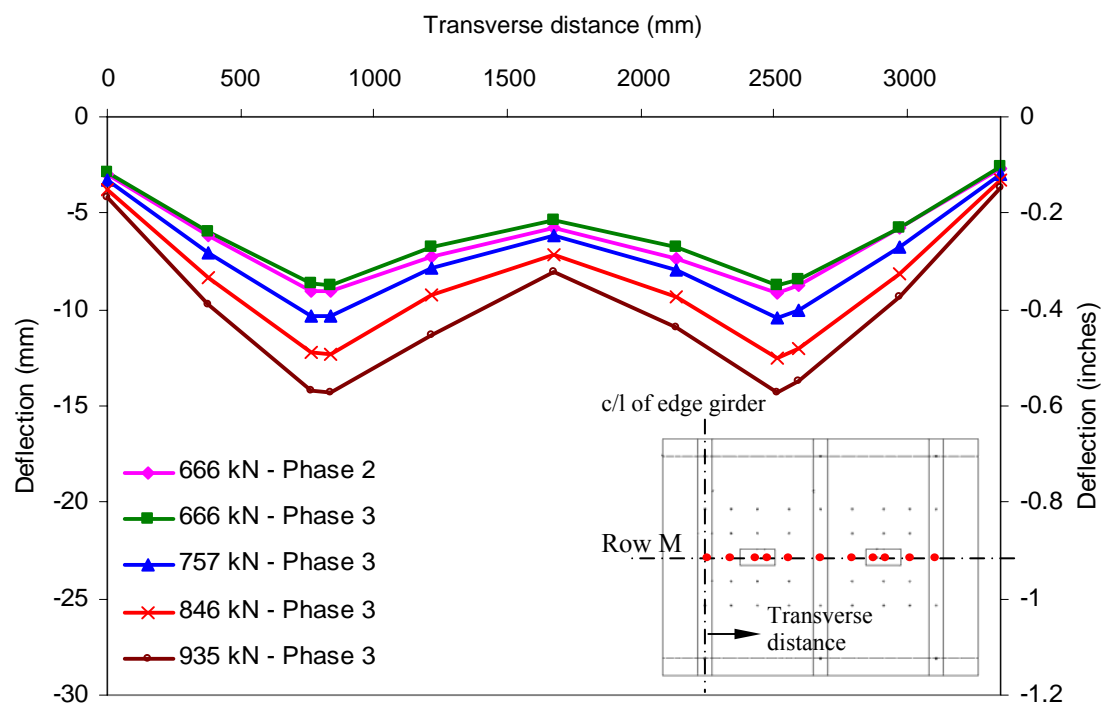


Figure 5.47 Deflection profile along Row M of linear potentiometers

No new cracks appeared in the deck slabs over the load cycles of phase 3. Both the composite systems were effective in restraining the opening of the existing cracks and thus prevented the occurrence of punching shear failure. Typical visual inspections of the deck slabs are presented in Figure 5.48. The cracks were visible only in the unstrengthened area of the slabs and no visual damage was evident in the composite at the areas where they intersected the cracks. Continuous popping sounds were heard throughout the load cycles of phase 3 as the epoxy at the borders of the composite strips/laminates cracked at the locations of the cracks. Also at 846 kN (190 kips) cracks were observed on the top surface of the specimen in the negative moment area of the slabs along the center girder, as shown in Figure 5.49. Cracks were also found to develop at this load level at the intersections of the slabs and the edge girders as shown in Figure 5.50. The measured crack widths on the top surface of the specimen over the center girder and at the slab-girder intersection regions were approximately 1 mm (0.04") and 0.6 mm (0.02"), respectively and thus the damage was not considerable. However the cracks were indicative of the initiation of damage in the slab-girder system with further loading. This was because since the slab and girder components of the slab-girder system were strengthened, the damage was localized in the next weak link of the slab-girder system at the slab and girder joints.

The debonding of the composite strips/laminates in the two slabs occurred simultaneously at 933 kN (209.6 kips). Since the debonding of the composite resulted in loss of the strength enhancement of the slabs produced by the composite, the slabs could not resist the high wheel load demands. Since the ultimate punching shear capacity of the unstrengthened deck slabs was predicted to be 534 kN (120 kips) (through design

calculations shown in Chapter 4), as soon as debonding of the composite occurred at a load of 935 kN, which was 1.75 times higher than the unstrengthened punching shear capacity, the debonding was followed by simultaneous punch through of the load pad, representing the wheel load, through the concrete. The punching shear failure perimeter is presented schematically in Figure 5.51.

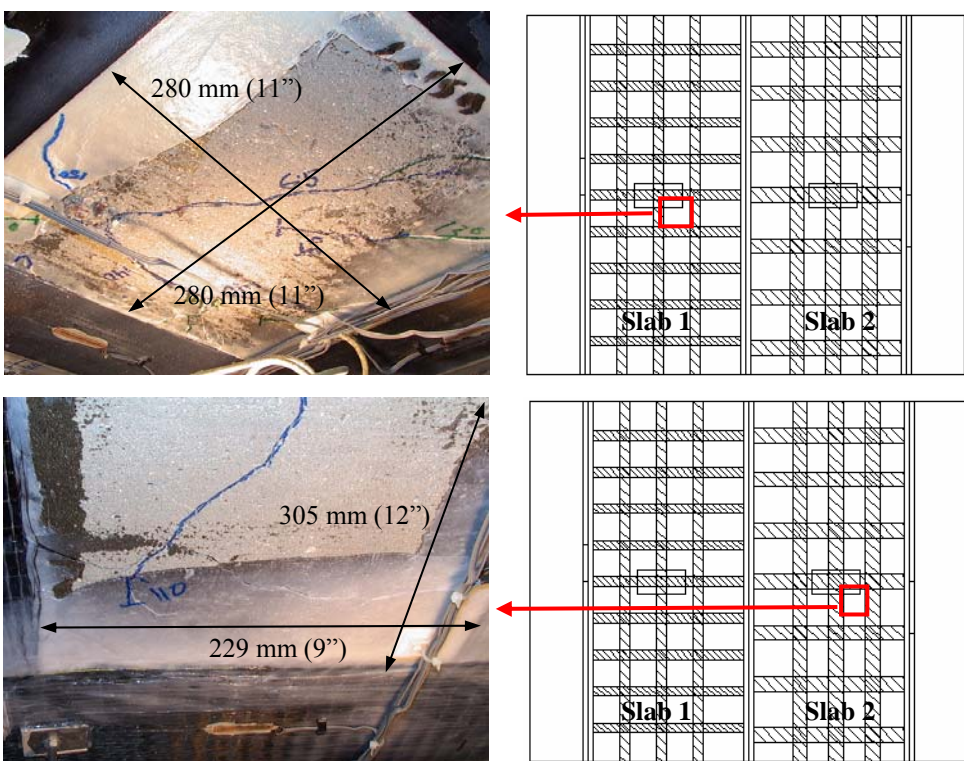


Figure 5.48 Typical visual inspection of cracks at 846 kN (190 kips)

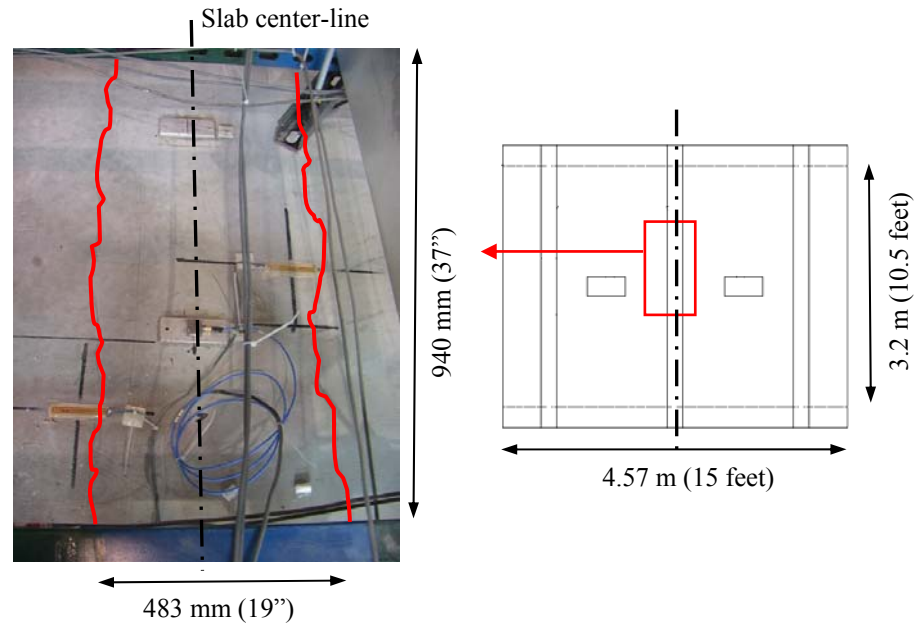


Figure 5.49 Visual inspection of cracks at 846 kN (190 kips) in slab over center girder

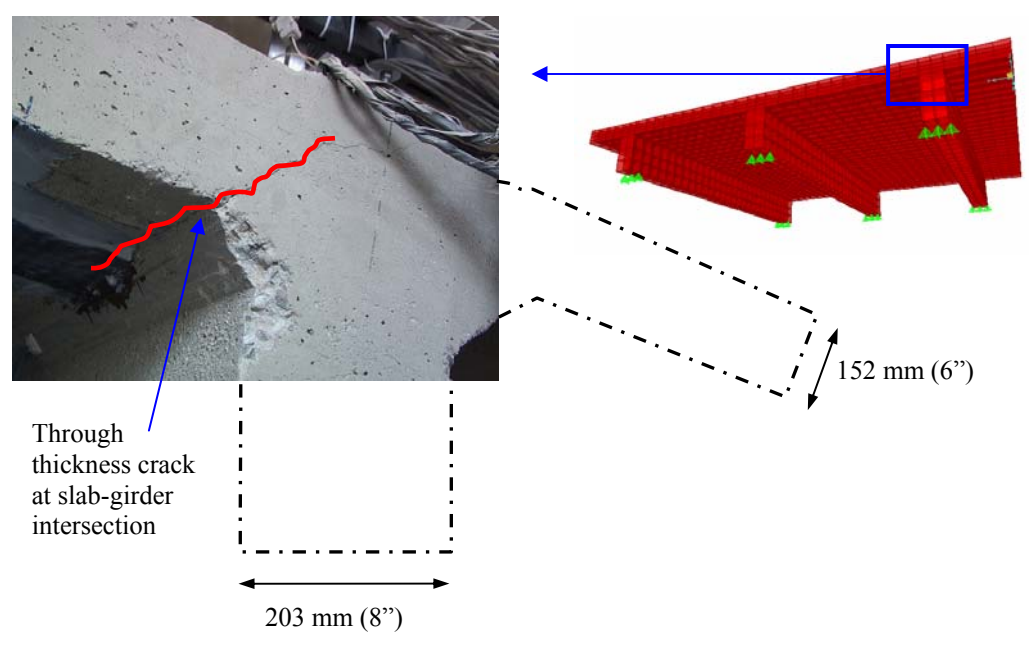


Figure 5.50 Visual inspection of cracks at 846 kN (190 kips) at slab-edge girder joint

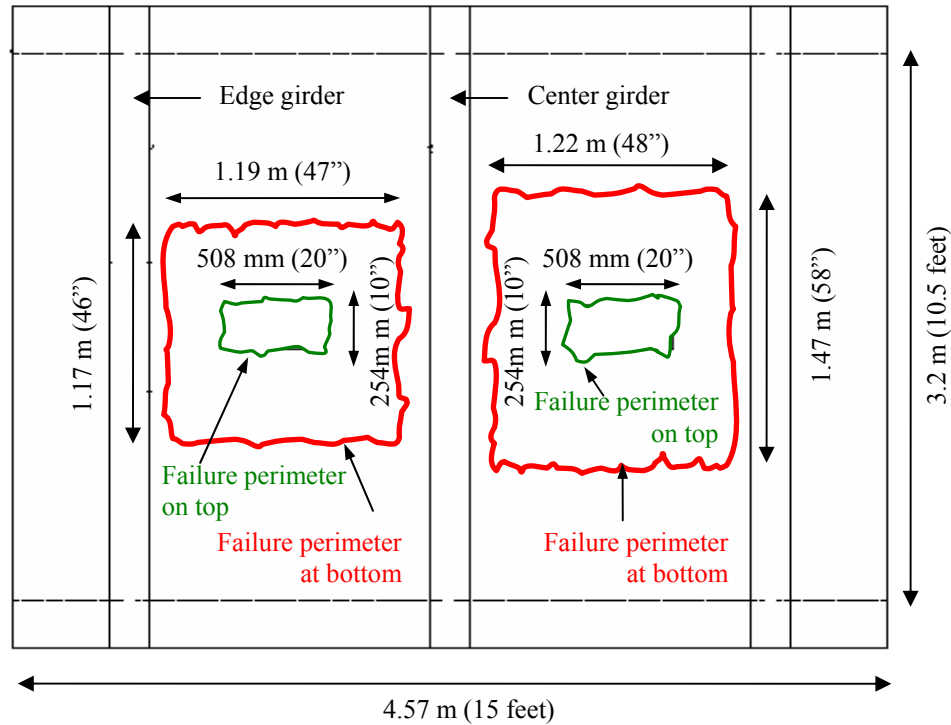


Figure 5.51 Schematic of punching shear failure perimeters in slabs

Comparison of the punching shear failure perimeters of the two slabs indicated that slab 1 strengthened with the pultruded strips, had a smaller damage area of 1.39 sq.m (15 sq.ft) as compared to damage area of 1.79 sq.m (19.3 sq.ft) in slab 2 which was strengthened with the fabric laminates. This indicated that the fabric laminates in slab 2 were able to distribute the load over a larger area as compared to the pultruded strips in slab 1. Thus even though till failure both the slabs had identical behavior, the extent and types of damage at ultimate failure of the two slabs were different. The locations of the punching shear failure perimeters at the bottom of the slabs with respect to the composite strips/laminates are presented in Figure 5.52.

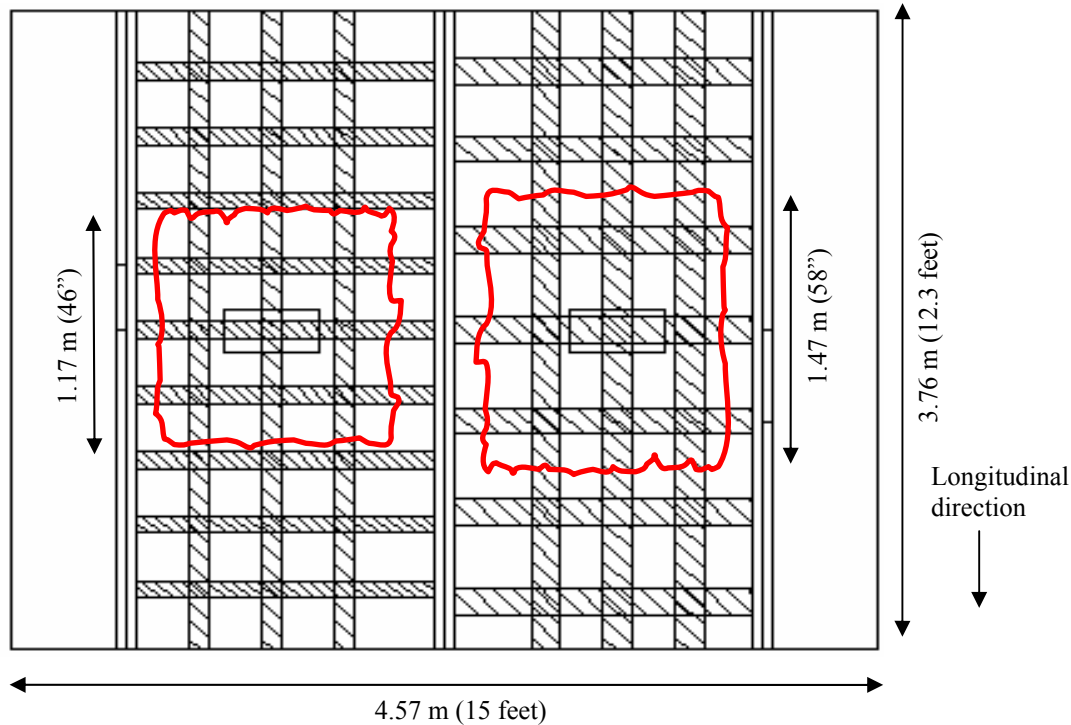


Figure 5.52 Schematic of intersection of the punching shear cracks with composite

All the composite areas at the intersection with the punching shear cracks were debonded at failure load. This included the areas in the longitudinal strips/laminates intersected by the cracks propagating in the transverse directions. The cracks propagating in the longitudinal direction intersected the transverse strips/laminates at the edges and caused debonding of the composite at these locations. Representative regions of failure in the two strengthened slabs are presented in Figures 5.53 to 5.55. However the mode of debonding was different in the two composite systems. The larger width of the fabric laminates resulted in gradual and smaller opening of the punching shear cracks. There were very few severely debonded areas and most of the debonding was localized at intersections with the punching shear cracks. In contrast, for the pultruded strips, large

areas of the strip in the vicinity of the punching shear cracks were debonded. Also at many locations of the debonded composite, the failure was interlaminar inside the composite strip itself rather than at the composite-concrete interface (shown in Figure 5.54). This indicated that the interlaminar bond strength of the pultruded strip was lower than the bond strength between the composite and the concrete. This resulted in a more abrupt mode of debonding with large opening of the punching shear cracks as compared to the fabric laminates.

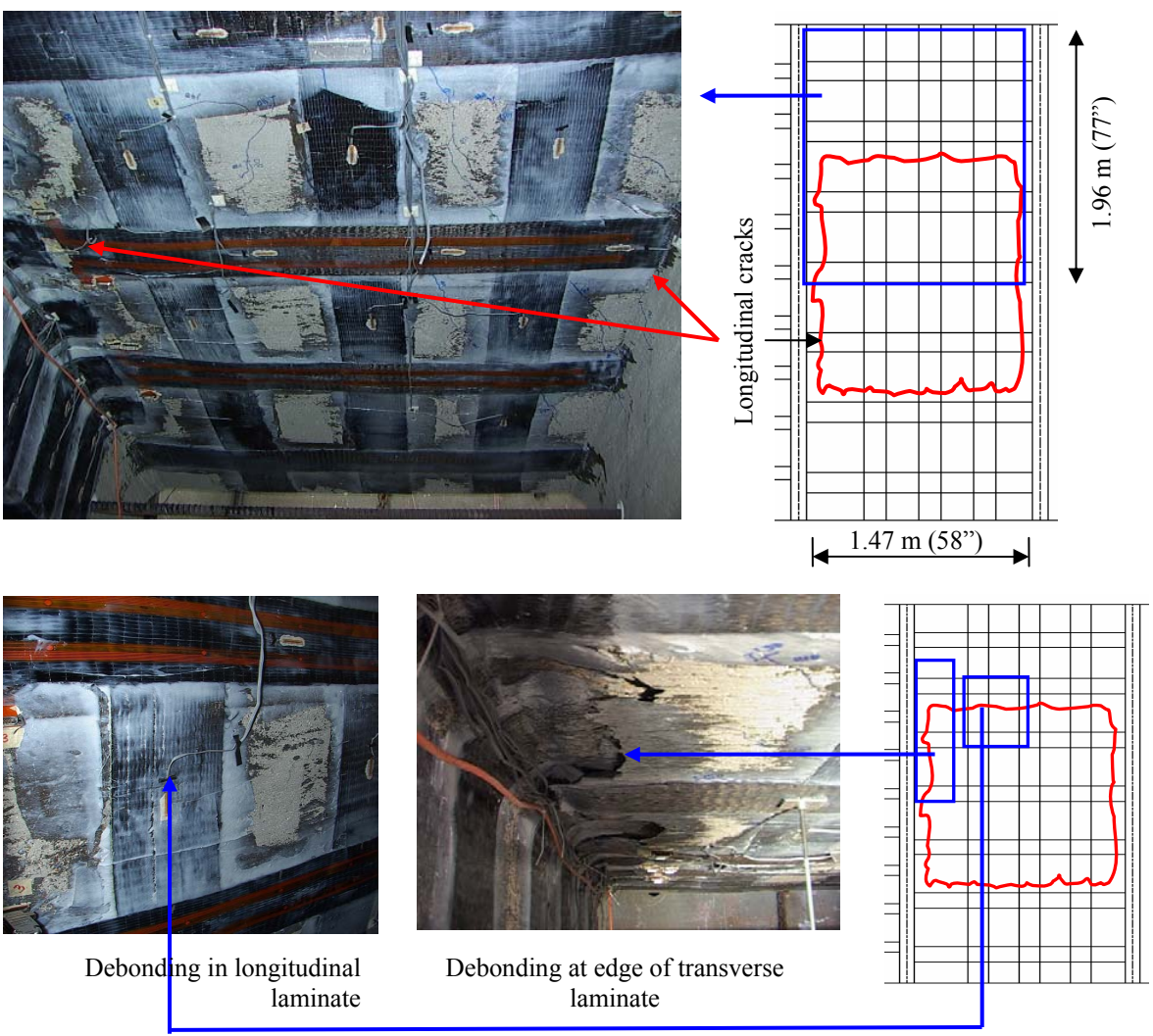


Figure 5.53 Representative damage areas in slab 2

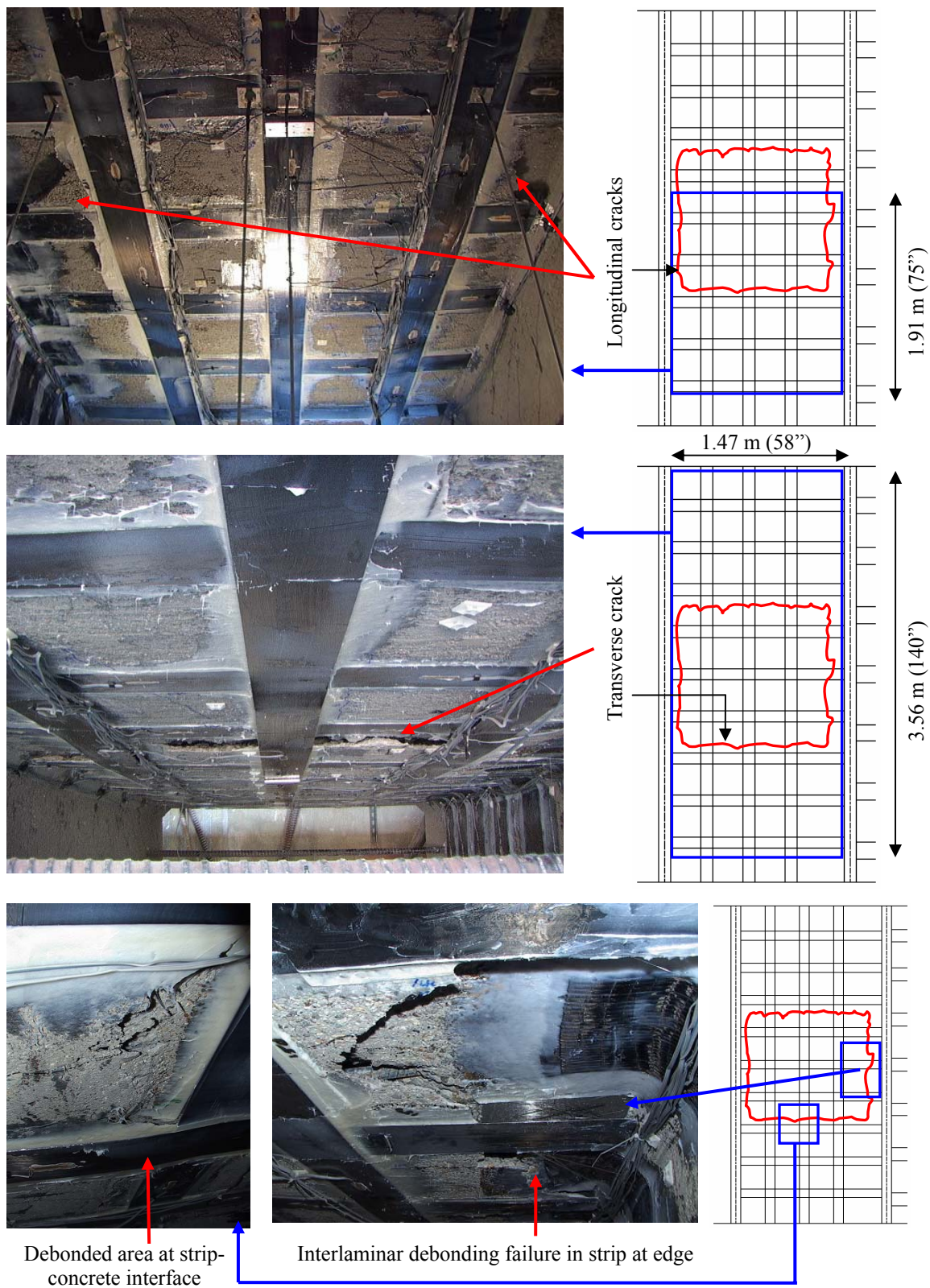


Figure 5.54 Representative damage areas in slab 1

Slab 1**Slab 2**

Figure 5.55 Punch-through of the load through concrete at top of slabs

After failure of the deck slabs, all the concrete in the damage area was removed to determine the punching shear failure planes which are presented in Figures 5.56 and 5.57.

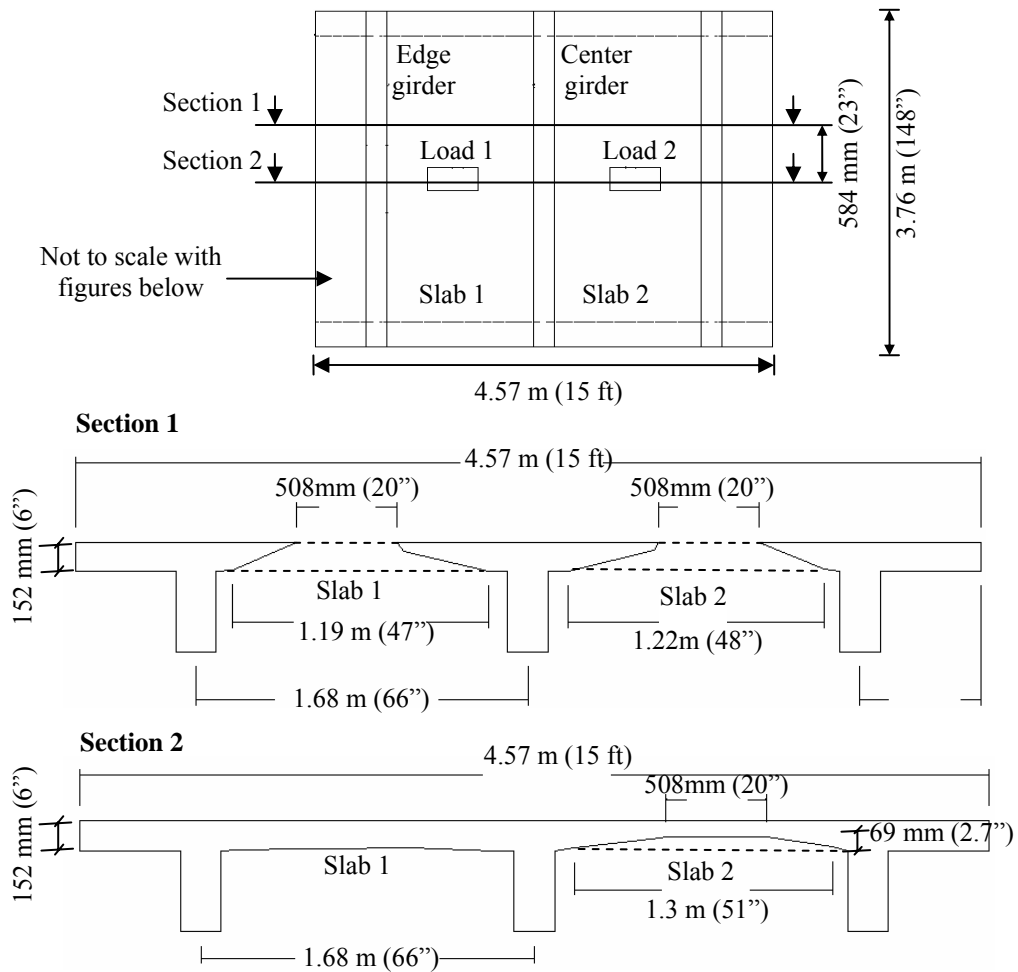
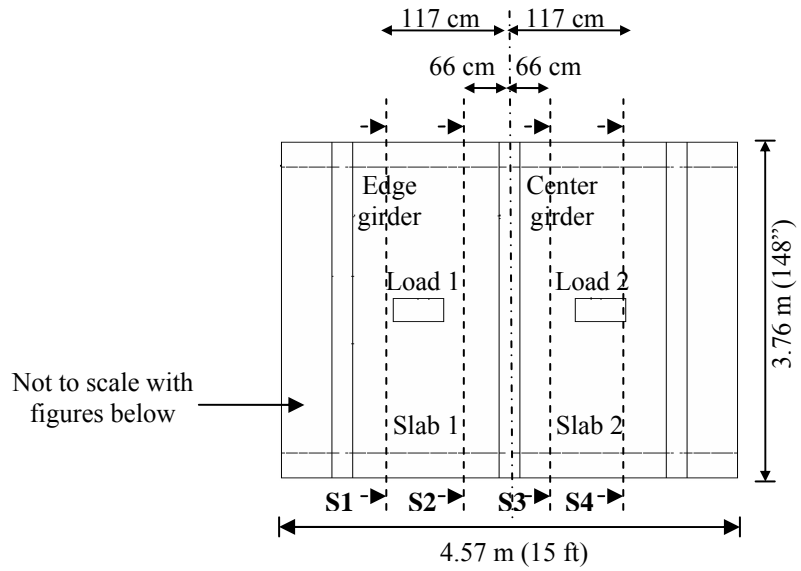
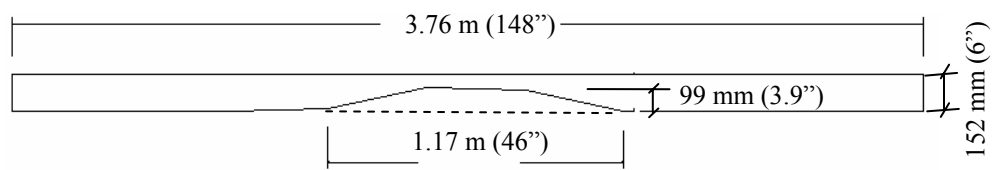


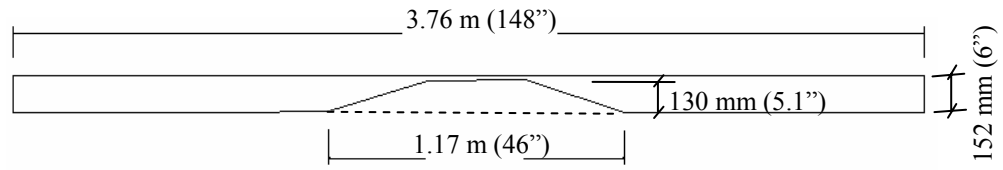
Figure 5.56 Failure planes along transverse cross section of specimen



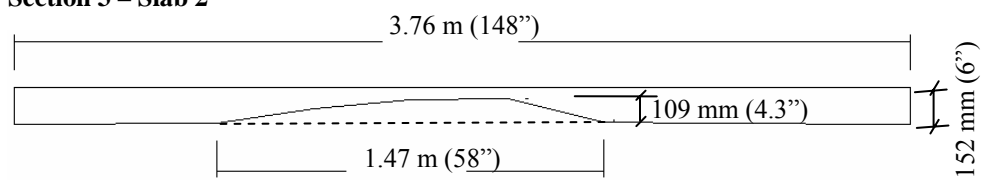
Section 1 – Slab 1



Section 2 – Slab 1



Section 3 – Slab 2



Section 4 – Slab 2

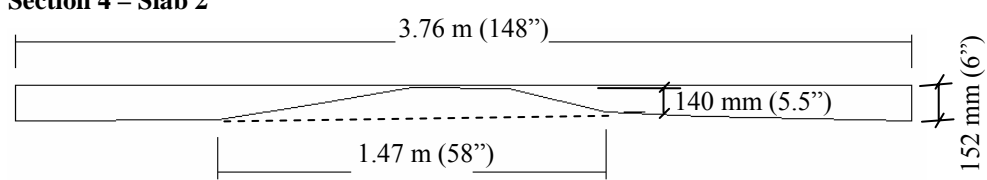


Figure 5.57 Failure planes along longitudinal cross section of specimen

No significant damage was observed in the strengthened center girder. With the onset of phase 3 loading the pre-existing shear cracks in the girder were visible (Figure 5.58), but the presence of the externally bonded composite stirrups restrained the opening of the cracks. Since the shear strengthening was designed such that the shear capacity of the girder was higher than the shear demand at the ultimate failure load of the strengthened slabs, all the damage in phase 3 loading was localized in the strengthened slabs. Through visual inspection and coin-tap tests at the end of the test, no debonded areas were found in the composite stirrups. The only exception was a region at the end of the composite stirrup in the flange area where the stirrup overlapped a fabric laminate strip of slab 2 (Figure 5.59). At failure since the punching shear crack traversing across the slab laminate caused debonding of the laminate, this resulted in pull-out and localized debonding of the composite stirrup. However the progression of the debonding was restrained by the presence of the fiber anchors at the flange-web intersection so that none of the composite stirrups had any damage in the web region of the girder at the locations of the shear cracks.

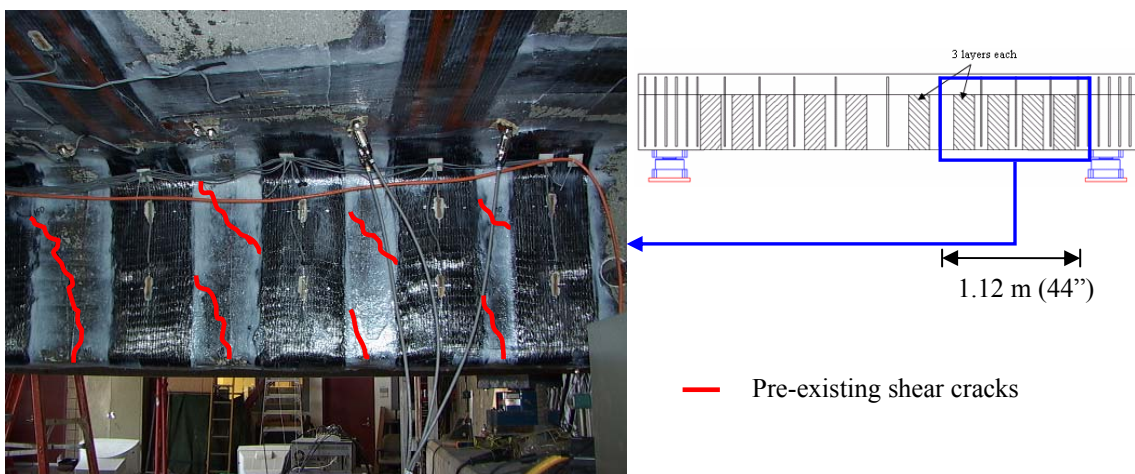


Figure 5.58 Center girder segment at the end of phase 3 loading

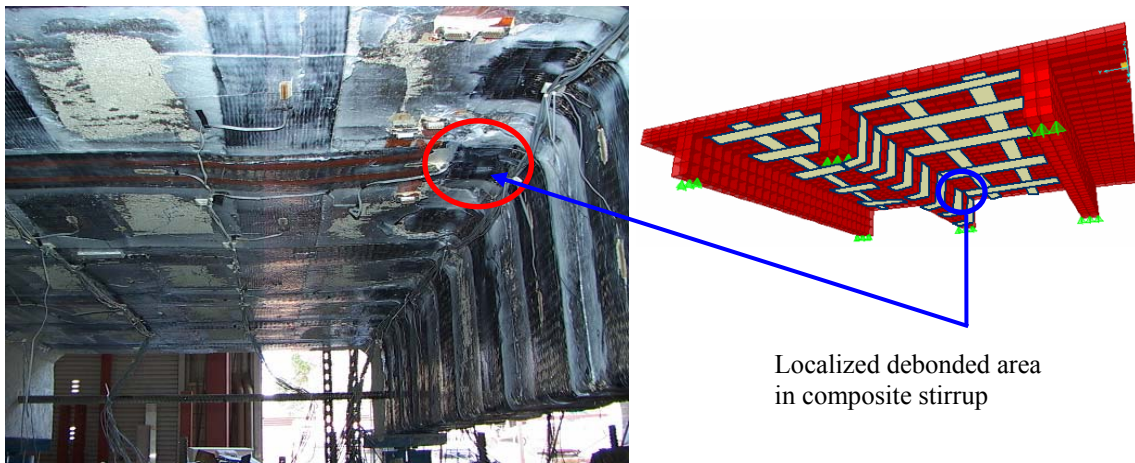


Figure 5.59 Damaged area in composite stirrup at end of test

5.3.3 Strain Profiles

The development of strain in the transverse slab reinforcement upto ultimate failure of the strengthened slabs along mid-span of the specimen is presented in Figure 5.60. The strains in the steel reinforcement below the loading areas of the actuators were almost identical in both the slabs in the 846 kN (190 kips) load cycle. However at failure, the strain profiles were different in the two slabs due to difference in the damage modes in the two slabs as discussed in the previous section. The strains near the load area were higher in the transverse steel reinforcement of slab 2 [2610 in slab 2 compare to 2205 micro-strains in slab 1 at failure below load area]. It was seen from the crack pattern that in slab 2 the failure was more gradual as compared to slab 1. Thus slab 2 could retain the load slightly longer than slab 1 resulting in slightly higher stains in the slab steel reinforcement. On the other hand in slab 1 the strains in the steel reinforcement were higher near the slab girder intersection area due to the appearance of damage in this area as was noted from the crack appearing in top of the slab in this localized area. Also

on comparing the strain profiles in the slab reinforcement at 666 kN (150 kips) load cycle, before and after strengthening of the center girder, it was seen that the strains in the slab steel reinforcement were not affected since shear strengthening of the girder had no effect on the flexural behavior of the slabs. The strain profile in the transverse slab reinforcement 508 mm (20") from mid-span is presented in Figure 5.61. The highest strains were recorded near the slab-center girder intersection area.

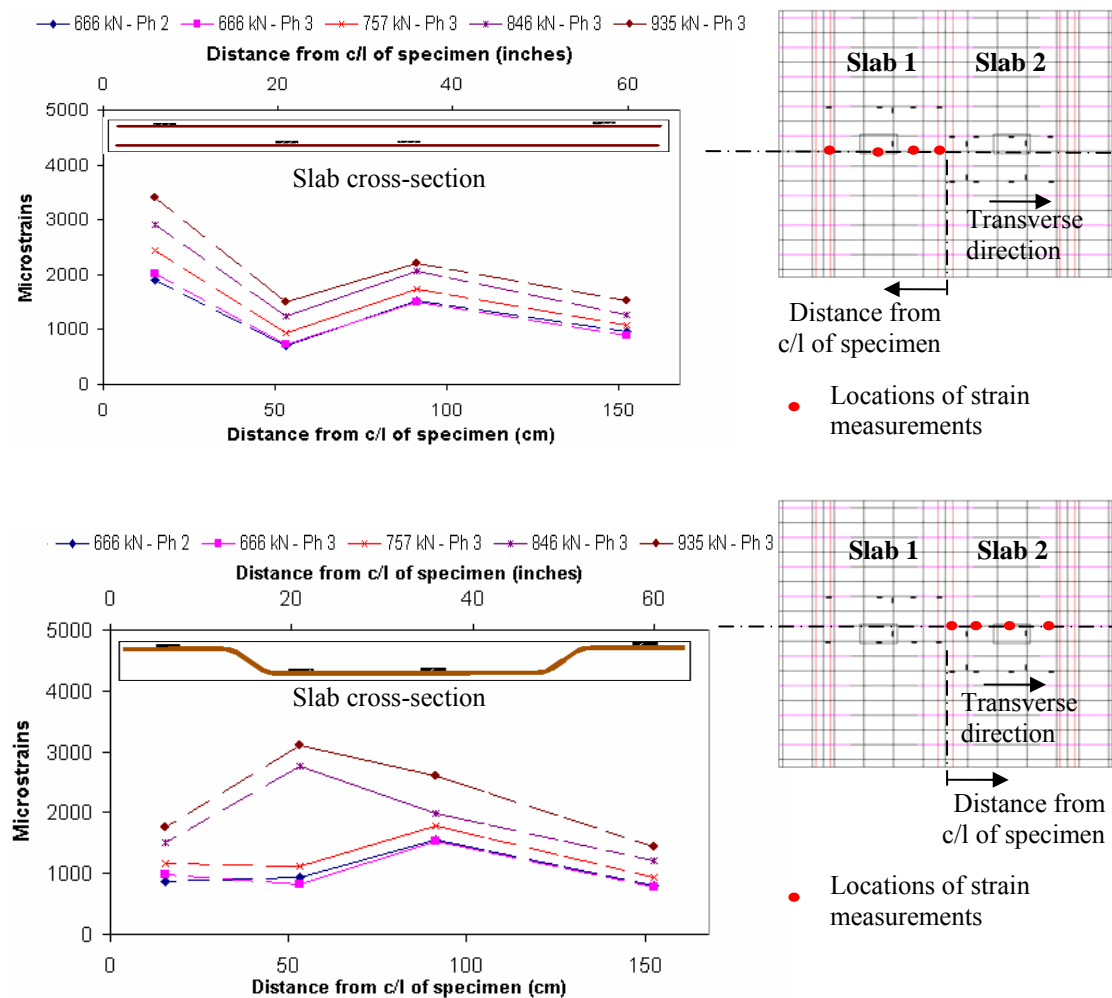


Figure 5.60 Strain profile in slab reinforcement at mid-span

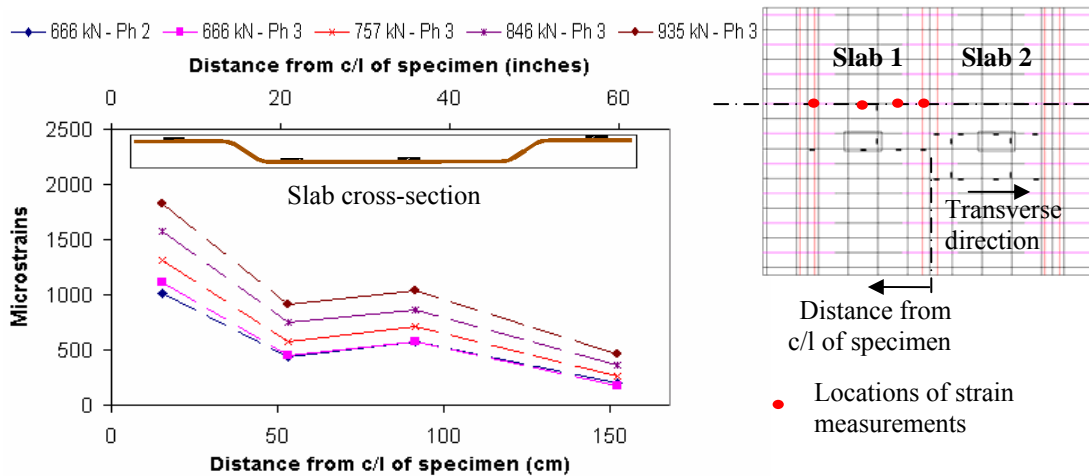


Figure 5.61 Strain profile in slab reinforcement at 508 mm (20") from mid-span

The strains in the center girder steel stirrups along the length of the girder are presented in Figure 5.62. Significant reduction of strain [from maximum strain of 1660 microstrains to 657 microstrains in the most critical steel stirrup] was observed in the steel stirrups on comparing the strain profiles at the 666 kN (150 kips) load cycles before and after strengthening of the center girder with composite stirrups. This indicated that the composite stirrups were effective in sharing the shear demand with the steel stirrups. They were able to enhance the shear capacity of the deficient girder such that even at ultimate failure of the strengthened slabs at 935 kN (210 kips), the strains in the steel stirrups were below yield strain level (2414 microstrains), with the maximum recorded strain at peak load of 935 kN (210 kips) load cycle of 2110 microstrains. This was corroborated by the visual inspections, from which the crack widths of all the pre-existing shear cracks in the girder were found to be small and no significant damage was observed in the strengthened girder.

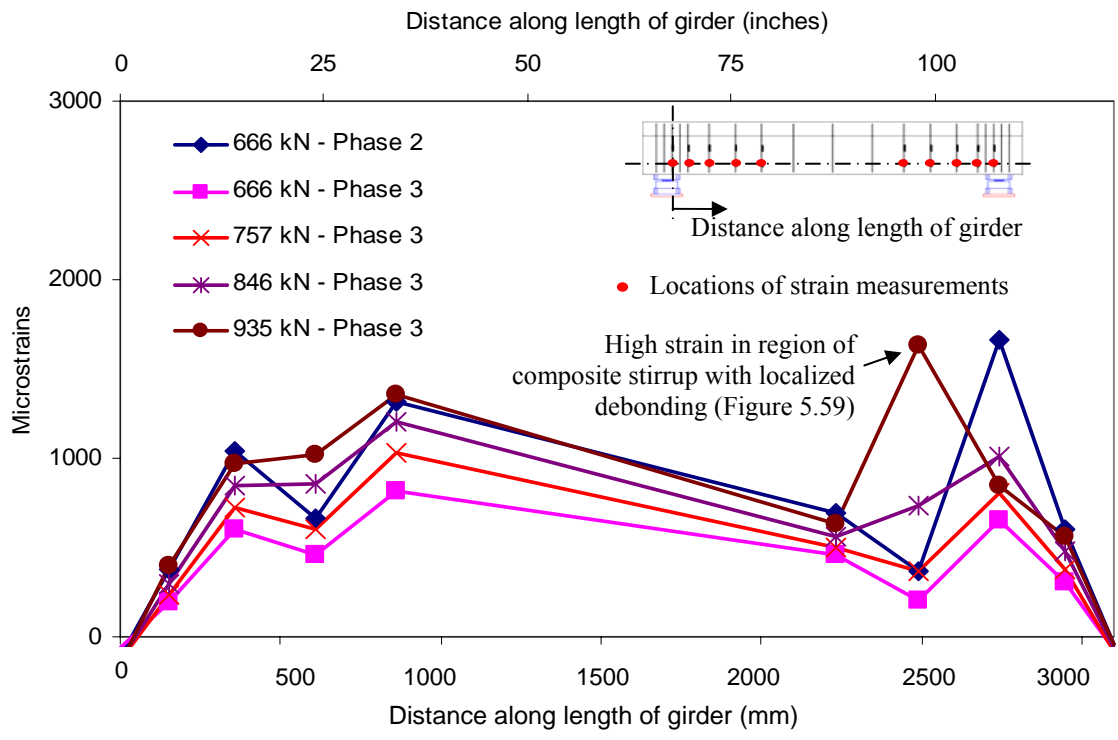


Figure 5.62a Strain profile in center girder steel stirrups along bottom line of gages

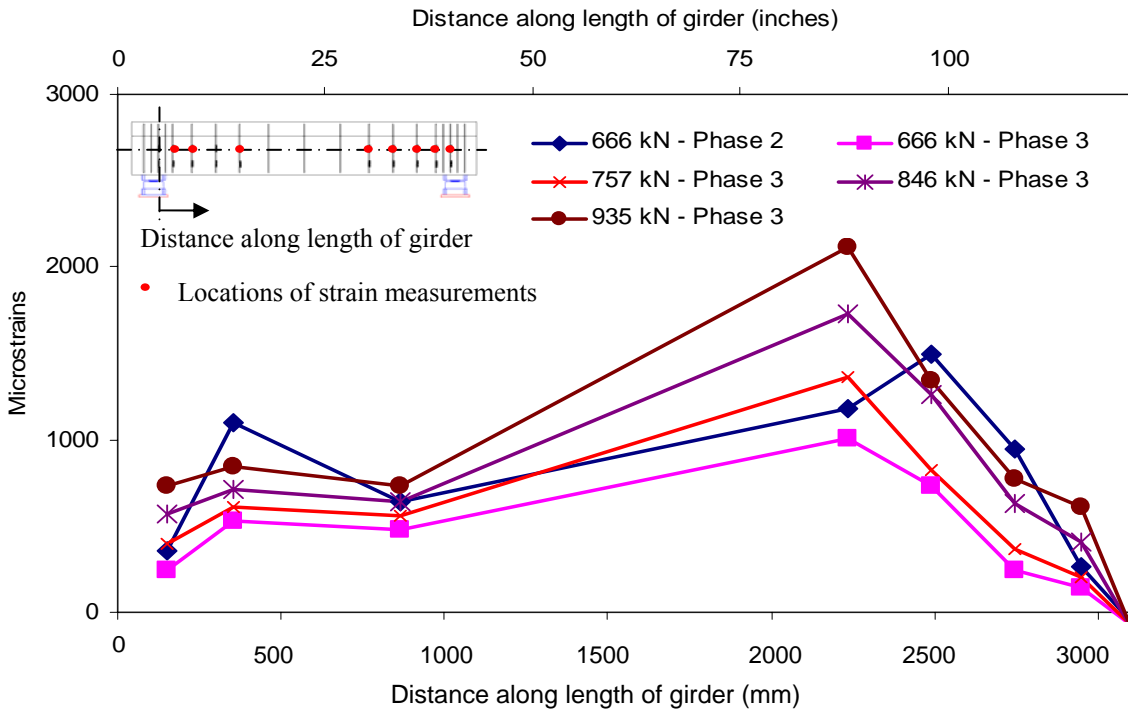


Figure 5.62b Strain profile in center girder steel stirrups along top line of gages

The strains recorded on some of the representative composite pultruded strips on the slab 1 after strengthening is presented in Figure 5.63. The highest strain of 3430 micro-strains was recorded at 933 kN (209.6 kips) in the transverse strip (T3) below the load area. This matched well with the predicted ultimate debonding strain of 3568 micro-strains (as presented in chapter 4). Also from the strain profile it was seen that the strains in the composite below the load area evened out along the length of the strip forming a plateau which was indicative of that segment of the composite not being able to take any further load since it had reached debonding. The strains in the strips away from the load area (T4, T5, T6) were lower than the debonding strain and are shown in Figure 5.63. A similar trend was observed in the fabric laminates used to strengthen slab 2 (Figure 5.64). The highest strain recorded in the transverse laminates (T8) at 933 kN (209.6 kips) was 3353 micro-strains below the load area. This matched well with the predicted ultimate debonding strain of 3262 micro-strains for the fabric laminates (as presented in chapter 4). Also as in slab 1, the strains in the transverse laminates of slab 2 away from the load area (T9, T10) were found to be lower than at mid-span of the slab at comparable load levels. The final failure in both the slabs was due to debonding of the composite at the locations of the punching shear crack perimeter away from the load area. Since these cracks were at the edge of the transverse strips/laminates it resulted in localized debonding at the intersection areas of the composite with the punching shear cracks. However this happened only after the flexural capacity of the strengthened slabs were reached in the load areas and the composite could take no further load after reaching debonding strain. This was indicated by the plateau and asymptotic nature of the strain profiles near the load area and subsequently since the slabs could no longer resist the

wheel load demand, this resulted in punching shear failure of the slabs. At similar locations of the two slabs, the strains in the laminates were lower than that in the pultruded strips. The highest debonding strains recorded in the transverse strip (T3) and laminate (T8) at 933 kN (209.6 kips) below the load area were 3430 and 3353 micro-strains, respectively. As discussed before, this was because the 2 layers of 152 mm (6") wide laminates had a larger cross-sectional area than that of 1 layer of 102 mm (4") wide pultruded strips. Thus for the same stress produced by the wheel load, the strains in the laminates were lower.

The strain profiles along the longitudinal strip and laminate below the load area are presented in Figure 5.65a and Figure 5.65b, respectively. The highest strains recorded in the longitudinal strips and laminates of the strengthened slabs at 933 kN (209.6 kips) were 3111 and 2614 micro-strains.

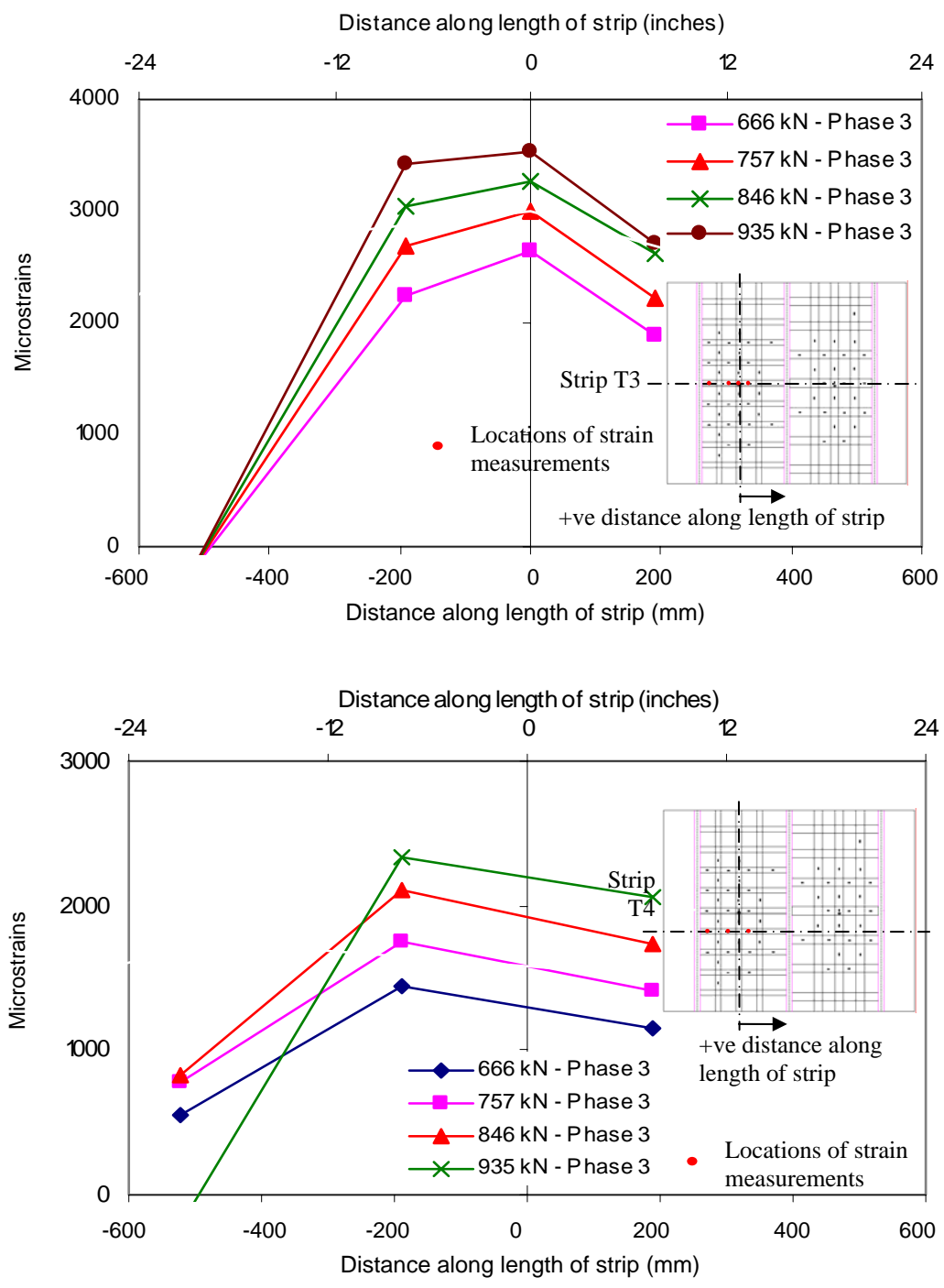


Figure 5.63a Strain profile in transverse composite strips (T3 and T4) of strengthened Slab 1 for phase 3 loading

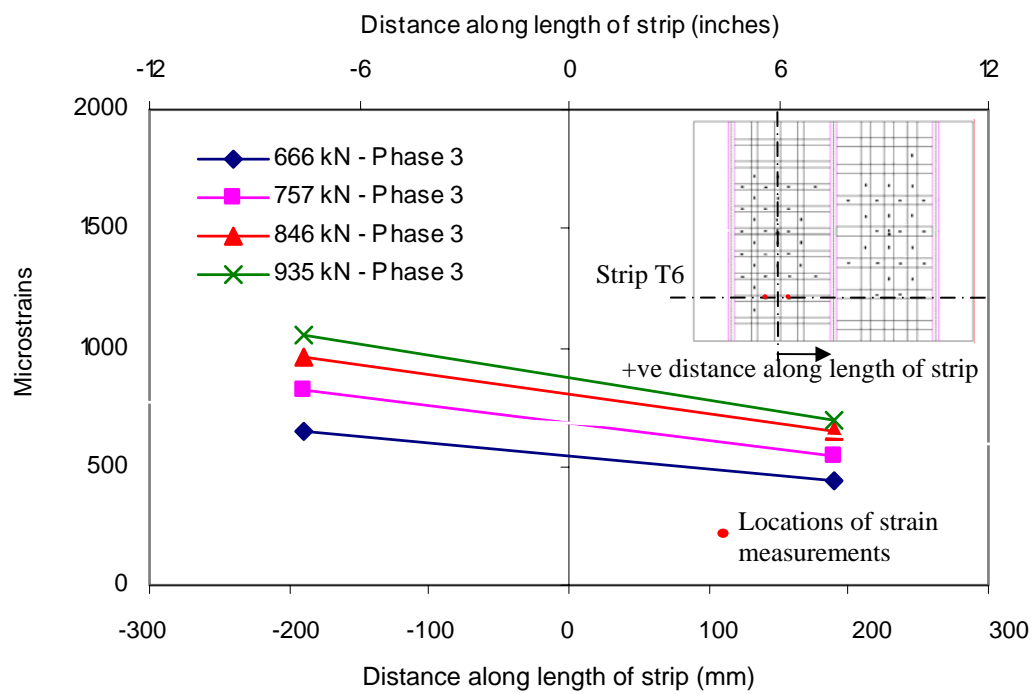
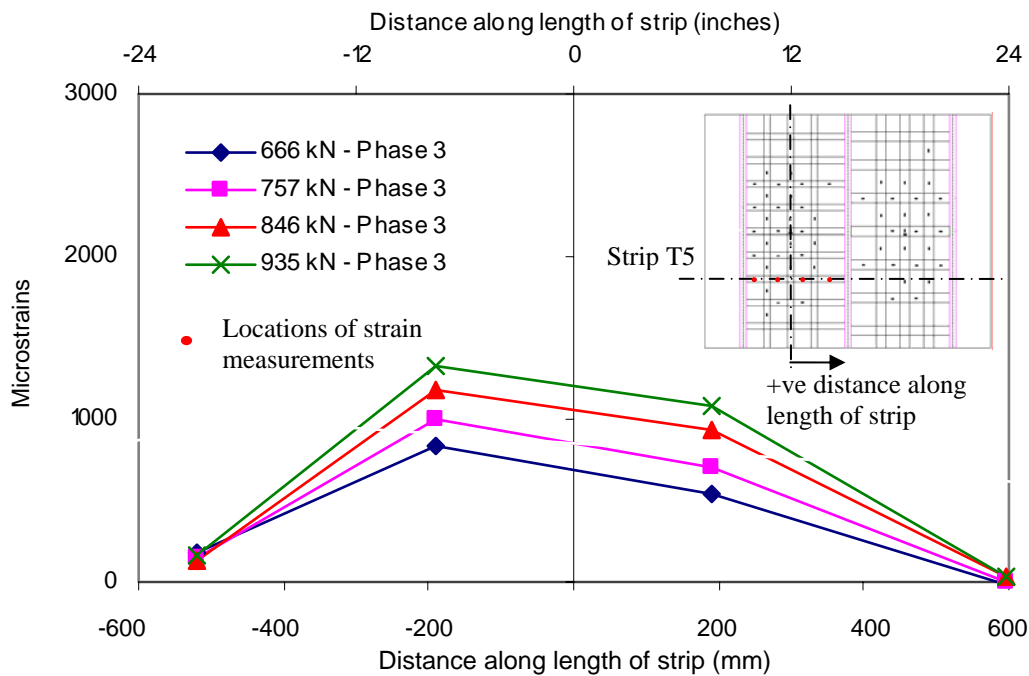


Figure 5.63b Strain profile in transverse composite strips (T5 and T6) of strengthened Slab 1 for phase 3 loading

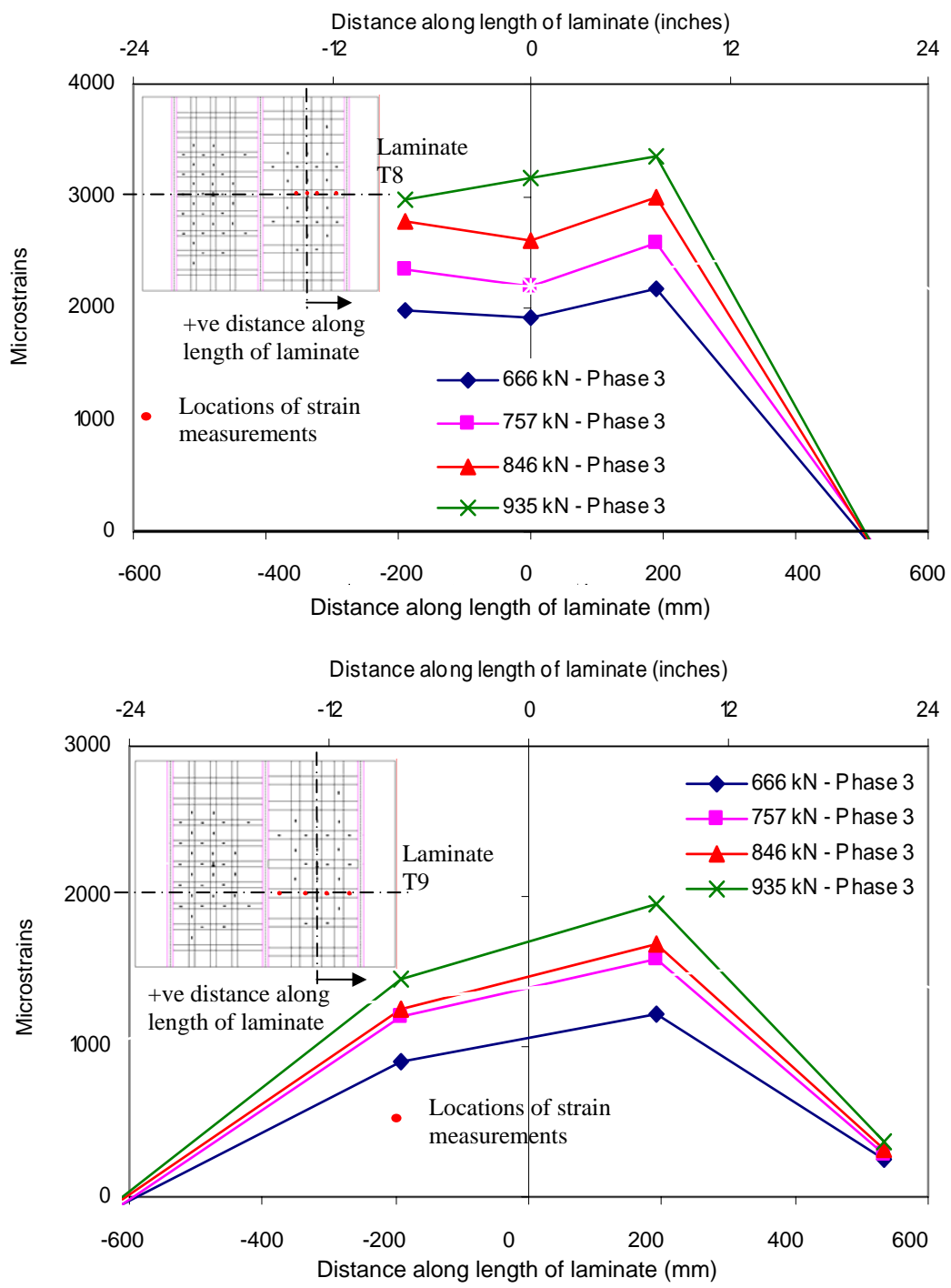


Figure 5.64a Strain profile in transverse composite laminates (T8 and T9) of strengthened Slab 2 for phase 3 loading

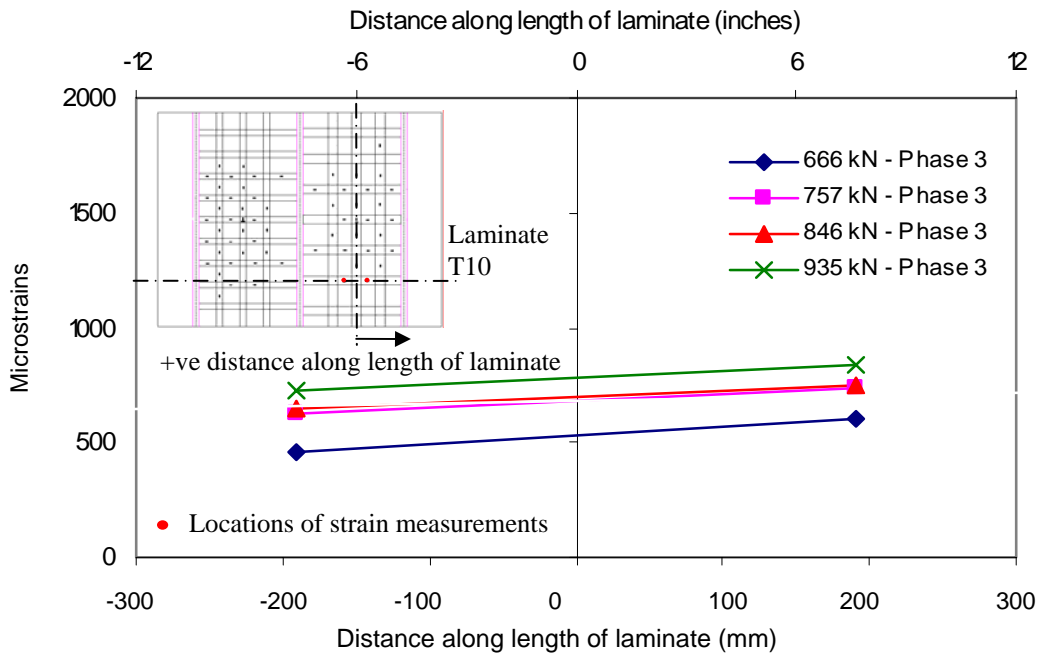


Figure 5.64b Strain profile in transverse composite laminate T10 of strengthened Slab 2 for phase 3 loading

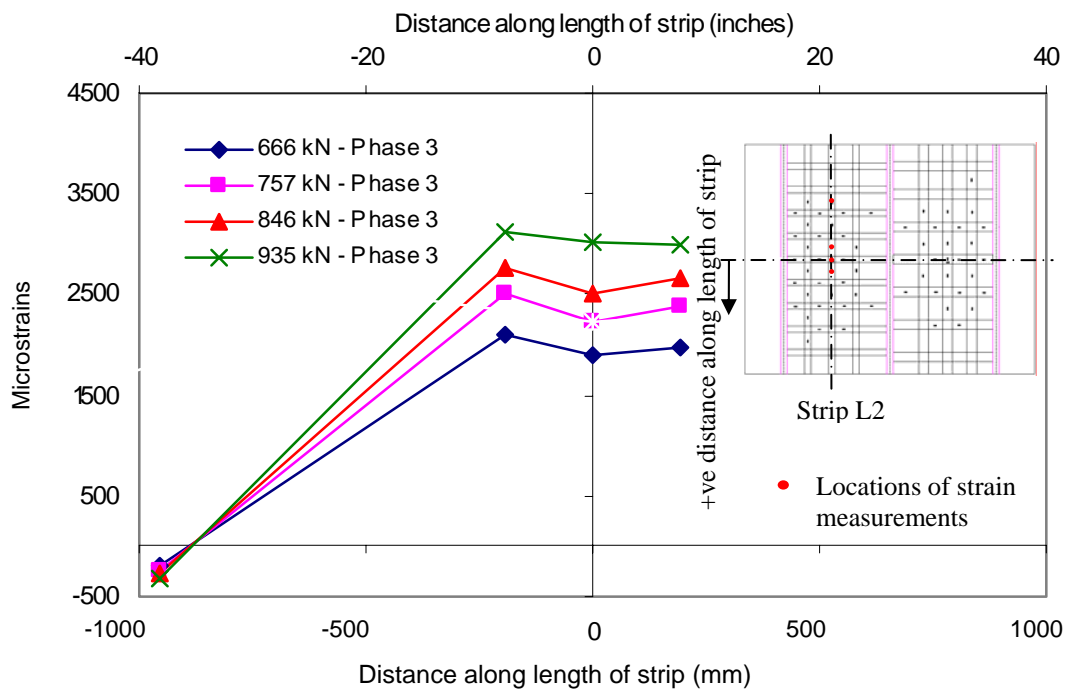


Figure 5.65a Strain profile in longitudinal composite strip of strengthened slab 1

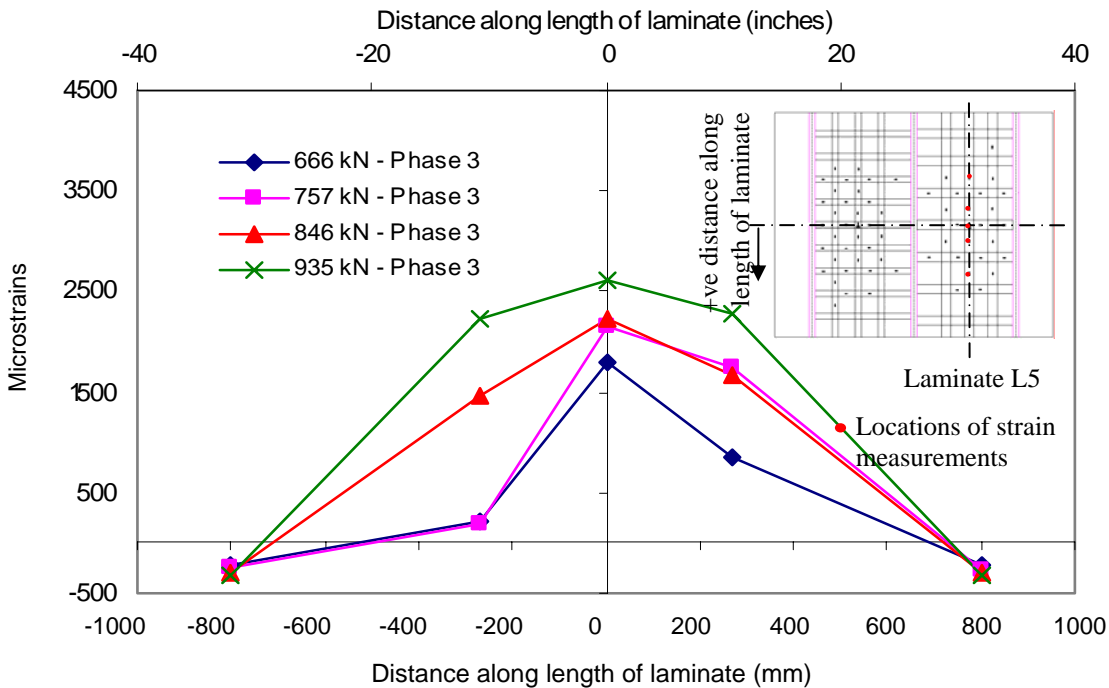


Figure 5.65b Strain profile in longitudinal composite laminates of strengthened slab 2

The strains in all the composite stirrups used for shear strengthening of the center girder were below the level predicted for the debonding strain, which corroborated the visual inspections where no debonded areas were observed. The highest strain recorded in all of the composite stirrups at 933 kN (209.6 kips) was 1386 micro-strains. The location and strain profile in this stirrup is presented in Figure 5.66.

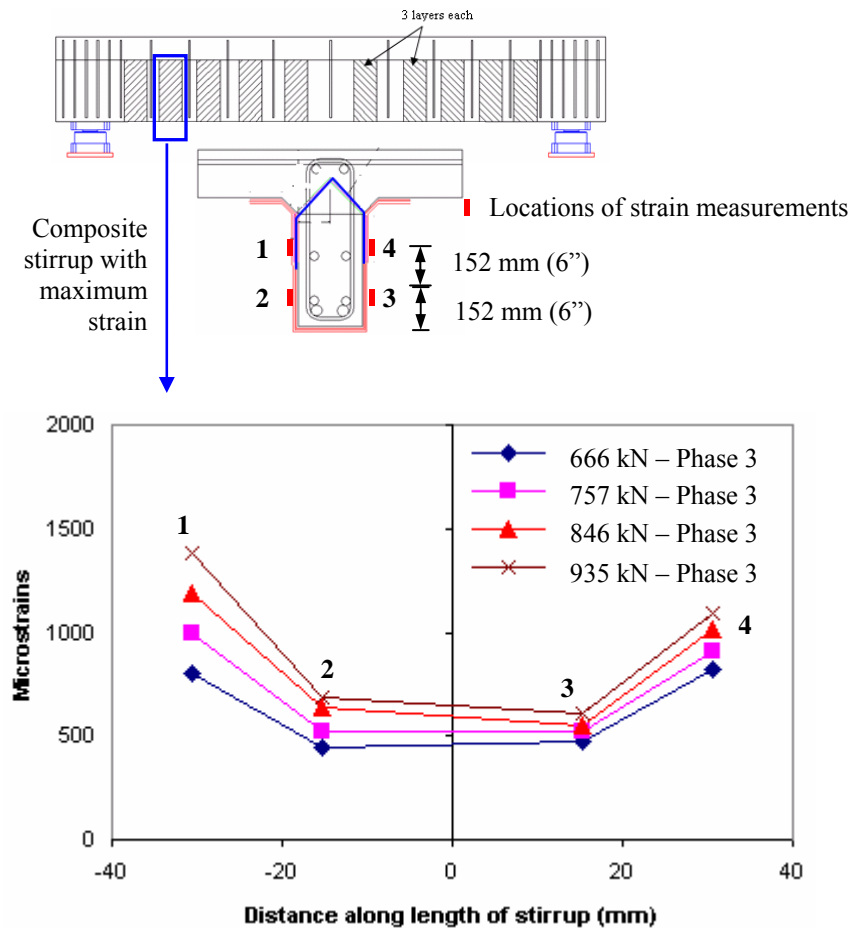


Figure 5.66 Strain profile in composite stirrup of center girder

5.3.4 Comparison of Test Results with Design Basis in Phase 3

Both the slabs reached their ultimate capacity at 933 kN (209.6 kips) which matched the predicted ultimate capacity of 935 kN (210 kips). The simultaneous failure of the two slabs also indicated that equivalent capacity was achieved using the two different composite systems. The degradation of slab stiffness was gradual over the loading stages which was representative of a flexural behavior. Thus the strengthening of the deck slabs with composite was effective in restraining the opening of existing cracks and in preventing the occurrence of punching shear failure. The slabs reached their

ultimate capacity at predicted debonding strains in the composite strips/laminates. The highest strains recorded in the transverse strips and laminates below the load area at 933 kN (209.6 kips) were 3430 and 3353 micro-strains, respectively which matched well with the predicted ultimate debonding strains of 3568 and 3262 micro-strains for the pultruded strips and fabric laminates respectively. Once the slabs had reached their flexural capacity, punching shear cracks opened up resulting in ultimate failure. The shear strengthening of the center girder with composite stirrups resulted in shear strength enhancement and control of opening of shear cracks in the girder. None of the composite stirrups reached debonding strains at failure of the deck slabs.

In this phase of test, after the slabs and the girder were strengthened with composite at the component level, the damage was localized at the slab-girder intersection region. This resulted in the formation of cracks running on top of the slab at the negative moment area near the slab-girder intersection area. Through thickness cracks running through the slab were also visible in this region at the outer edge of the specimen. This indicated that at the system level after strengthening of the slab and girder for higher load demand, it would be necessary to take into account the design of the joint to prevent localized failures that might prevent the strengthened components to reach their ultimate capacities.

6 NON DESTRUCTIVE EVALUATION (NDE) 1 – THERMOGRAPHY

6.1 IR Thermography Inspection - Objectives

The two deck slabs of the test specimen were strengthened with two different composite systems, pultruded strips in slab 1 and field impregnated fabric laminates in slab 2. This was done to enhance the capacity of the slabs and to control the crack widths thereby preventing the occurrence of abrupt punching shear failures by changing the failure mode to a flexure one. The two composite systems were externally bonded to the soffit of the two slabs using an epoxy adhesive for the strips and an epoxy resin for the laminates, as was discussed in chapter 4. The performance of the bond between the concrete and the composite is critically important to achieve the design capacity of the slabs since the force between the composite and the concrete is transferred through the composite-concrete interface. Since the presence of defects or debonded areas could have an adverse effect on the performance of the strengthened slabs, it was necessary to determine through non-destructive evaluation (NDE) using Infrared Thermography, the quality of the composite installation by locating existing defect/damage areas in the composite strips/laminates produced during installation. Also the strengthened slabs were predicted to reach their ultimate capacities when the composite below the load area reached debonding strain levels. The need to evaluate the performance of FRP composite strengthening with the increase of loading made it pertinent not only to detect and locate pre-existing defects, but also to be able to monitor and characterize the progression of defect/damage in the composite and at the composite-concrete interface with an increase in load.

6.2 Inspection Details and Post-Processing of Data

A pulsed infrared thermography technique was used in which the thermal input was provided by 2 xenon flashtubes with 5 ms flash duration, each powered by a 6.4 kJ capacitor bank to simulate a temperature differential between the composite and any potential defect. An infrared camera operating in the 2 – 5 μm spectral range was used to continuously acquire data at a 60 Hz frame rate for 10 sec after flash heating for each shot. The flash lamps and the camera were mounted inside a hood and the entire assembly was mounted on rails so that thermography inspections along the length of the composite strips and laminates could be carried out by just sliding the assembly along the rail after data acquisition at each location. The inspection setup, as presented earlier in Chapter 4, is repeated for convenience of reference in Figure 6.1. This setup helped to maintain a constant distance between the camera and the test surface. The field of view of the camera for this particular setup was 305 mm x 230 mm (12" x 9") and thus the region of inspection at the slab soffits was divided into a number of small areas which could be imaged independently. An overlap of about 51 mm (2") was maintained between adjacent shots in order to enable merging along edges.

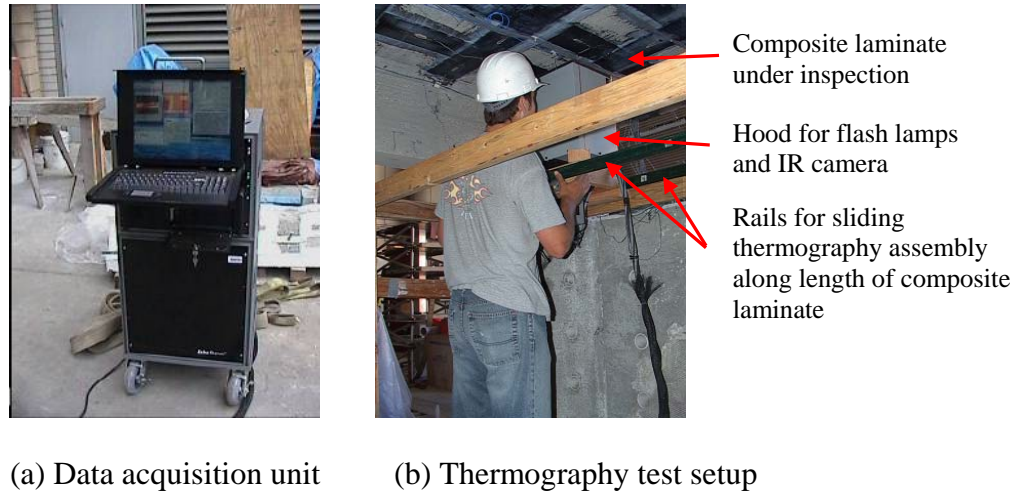


Figure 6.1 Details related to thermography data acquisition

The post-processing of the data acquired from the thermography inspections involved generating linear and 2-D thermal intensity profiles along the length of the composite for each location at each load level. The thermal intensity profiles at each load level were then compared with the baseline thermal intensity for the same location to quantitatively determine the appearance of new defects or the growth of existing defect areas. The relative difference in the intensities at different defect locations also gave quantitative information on the severity of the defects.

As mentioned earlier, for each location of inspection the data was acquired continuously for 10 seconds. Thus a series of thermograms and thermal intensity profiles were obtained over this time period. As discussed in [1], the time at which the defect would be most discernable from the time of input of heat energy would be dependent on the diffusivity of the composite material, depth of the defect, heat intensity applied, distance of the camera from the test surface and surface conditions. Thus it is necessary to calibrate the heat diffusion profile of the pultruded strips and the fabric laminates

under the test inspection conditions for typical defects, so that the time taken for the defect to reach thermal equilibrium for the specific composite used could be obtained. The temporal profiles representing the thermal intensity decay curves, obtained by taking the average of the thermal intensities at locations in the pultruded strip with and without debonded areas, are presented in Figure 6.2a. The thermal intensity difference between these two decay curves is presented in Figure 6.2b. Each data point on these plots corresponds to the thermal intensity obtained by averaging the recorded thermal intensities over a 0.5 sec time interval.

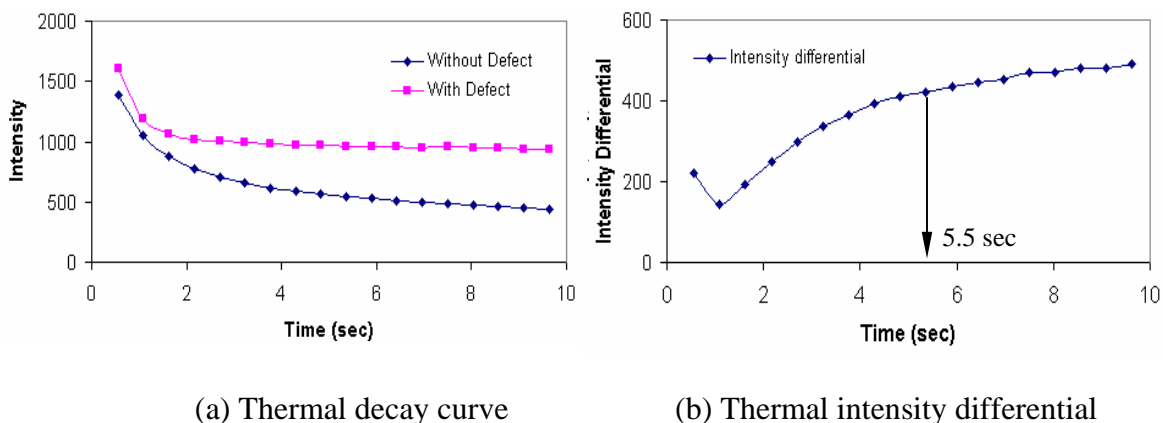


Figure 6.2 Thermal intensity profiles for pultruded strips between locations with and without defects

A typical damage area used for the determination of the thermal decay curves is presented in Figure 6.3. In the pultruded strips the most typical damage occurred due to opening of cracks traversing the strip and the gradual opening of the crack resulted in debonding of the strip at the composite-concrete interface. The thermal intensity in the area with the defect was higher, and reached thermal equilibrium much faster, than that

without the defect. The time after the heat input at which a damage/defect area in the pultruded strip could be quantitatively discerned as compared to the surrounding undamaged area was found from the thermal intensity differential curve, as the time at which the differential reached an asymptote. From Figure 6.2b, which represents the average thermal intensity differential between locations in the pultruded strip with and without debonded areas, this was computed as 5.5 seconds since beyond this point of time the thermal intensity differential between two consecutive time steps differed by less than 3%. Based on a calibration study carried out using average thermal intensities from similar defect/damage areas, all computations and comparisons between the thermal profiles obtained from the inspections after each load cycle were carried out at 5.5 seconds from the initiation of thermal input by the flash lamps.

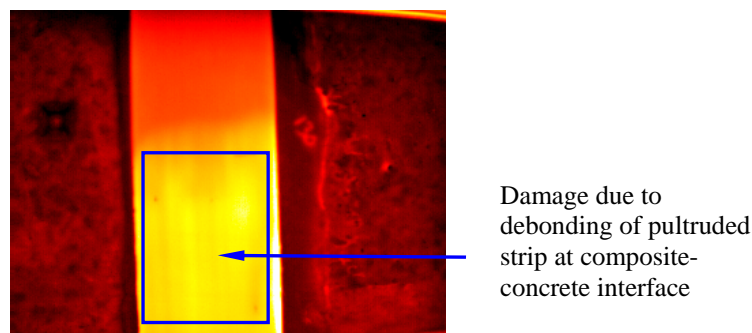


Figure 6.3 Representative damage area in pultruded strip

For the fabric laminates used for strengthening slab 2, two types of representative defects/damage areas were observed from the thermographic inspection and are shown in Figure 6.4. The first type of defect in the form of voids is generally produced during fabrication of the laminates at the concrete surface using the wet-layup process. Such

defects of varying sizes were detected through baseline thermography inspections in the fabric laminates at the composite-concrete interface and also between the fabric layers of multi-layered laminates. The second type of defect, in the form of debonded areas at the composite-concrete interface, was detected in the thermography inspections carried out towards the end of the load test in phase 3 when the high loads on the slabs applied by the actuators resulted in local debonding of the laminates at the locations of the primary punching shear cracks and these damage areas were identified by regions of high thermal intensity in the thermography data. The thermal decay and thermal intensity differential curves between locations with and without these two types of representative defect/damage areas, namely voids and debonded areas, in the fabric laminate composites are presented in Figures 6.5 and 6.6, respectively. The difference in the thermal signature between a debonded area and air void is clearly evident in Figure 6.5. The thermal signature for a debonded area reaches an equilibrium much faster as compared to that of an air void. Also although the thermal signatures at the debonded area followed similar trends for the pultruded strips and the fabric laminates, the actual intensity values (980 in the pultruded strips as compared to 1152 in the fabric laminates at 4 seconds after thermal input) were characteristic of the material and thus were different.

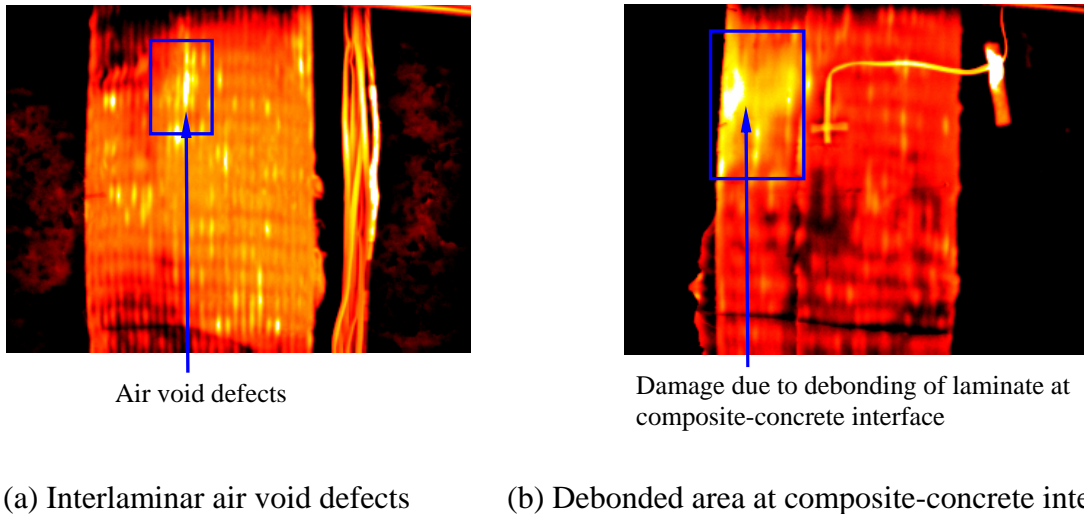


Figure 6.4 Representative defect/damage areas in fabric laminate

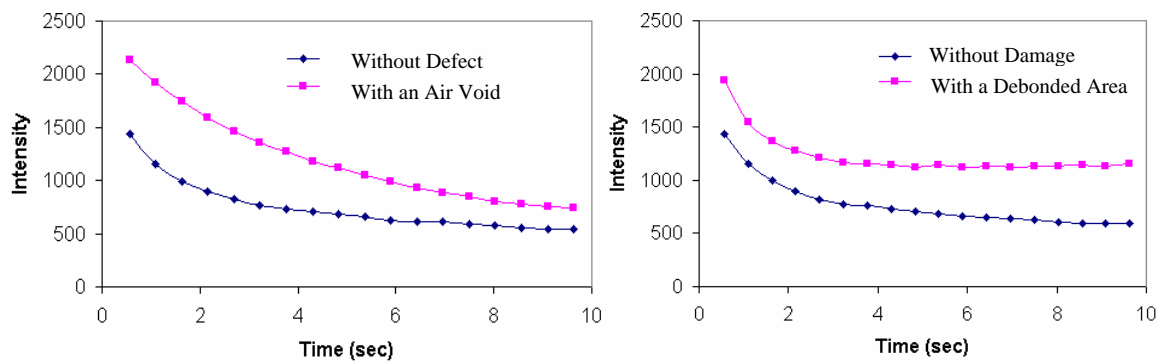


Figure 6.5 Thermal decay curves for laminates at locations with and without defects

From the thermal differential curves (Figure 6.6), it was observed that an air void, located at the composite-concrete interface or between the composite laminates, would be most discernable with respect to its surrounding defect free area around 1.75 seconds after initiation of the flash heating beyond which the thermal differential was found to decrease sharply with time. For a debonded area or for a defect located at the composite-concrete interface, the thermal differential was found to reach a steady state after around

8 seconds beyond which the change in the thermal differential was less than 2% of the previous point. This is reasonable since a defect present at a greater depth would take more time to become visible as compared to a shallow defect. Also a large debonded area would hold the heat for a longer time period as compared to a small air void, where the heat would diffuse out faster. Thus for proper identification, a small air void at the surface would have to be inspected at an earlier time frame in the time-history sequence of thermograms than a debonded area or defect at composite-concrete interface. Based on the calibration study, the computations and comparisons between the thermal profiles obtained from the inspections after each load cycle were carried out both at 1.75 seconds and 8 seconds from the initiation of thermal input by the flash lamps so that both air voids and debonded areas could be discerned.

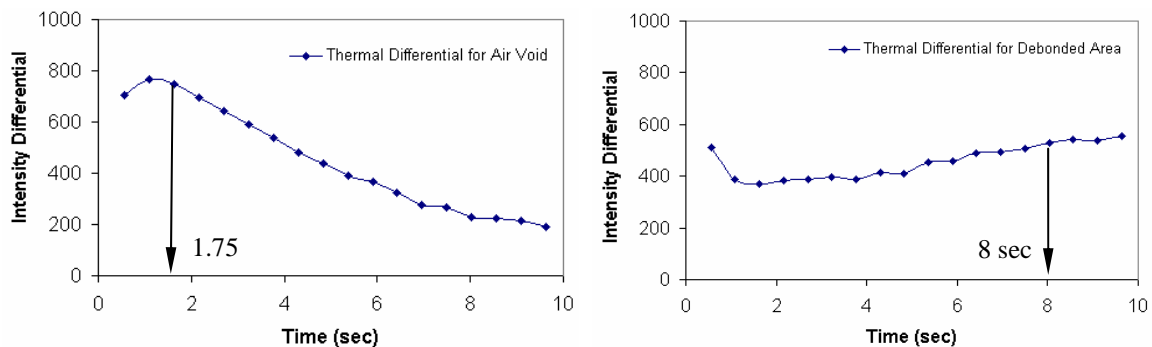


Figure 6.6 Thermal intensity differentials between areas with and without defects

6.3 Inspection Results from Pultruded Strips in Slab 1

Baseline thermography inspections were carried out after strengthening slab 1 with prefabricated pultruded strips before subjecting the specimen to the phase 2 and 3 load cycles. These inspection results were used to characterize pre-existing defect areas

in the composite strips in the form of voids at the composite-concrete interface which were produced during installation of the strips. Moreover this formed a baseline for further inspections to detect and characterize damage appearance or progression while loading the specimen. However because of the high level of quality control that can be achieved in the manufacturing of the pultruded strips no interlaminar defects were detected in the strips. Figure 6.7a shows a location at the edge of the pultruded strip where an unbonded area was visually observed. Also one of the longitudinal pultruded strips had to be peeled off after installation because it was not properly bonded to the concrete. On inspection of the surface that was bonded to the concrete, several defect areas were observed (Figure 6.7b) where the adhesive was found not to be uniformly spread out due to improper compaction of the composite system. Baseline thermography inspections were carried out in order to locate all such pre-existing sub-surface defects that could not be visually inspected.



(a) Unbonded area

(b) Defect area in strip

Figure 6.7 Typical post-installation sub-surface defects detected by visual inspection

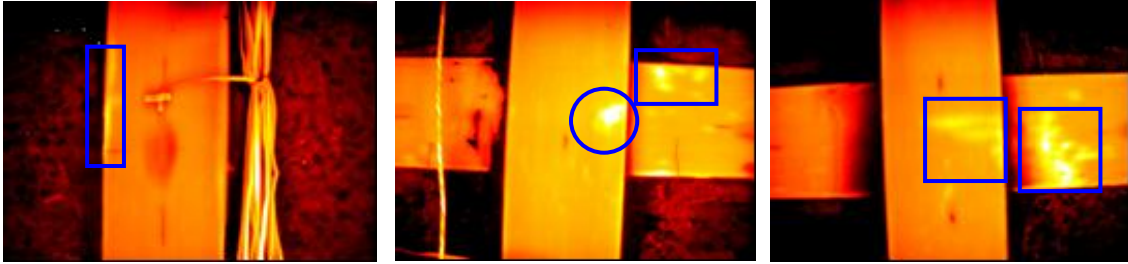


Figure 6.8 Typical sub-surface defects detected by thermography inspection

Figure 6.8 shows typical thermograms at locations where such sub-surface defects were detected from the thermography inspections. All these defect locations were checked for damage progression after loading the specimen, through subsequent thermography inspections. All these defects were easily discernable from the thermograms as regions of high thermal intensity. All the thermograms were obtained at 5.5 seconds after initiation of the flash heat input as determined by the calibration study to have the highest thermal differential between areas with and without defects for optimized detection.

Thermography inspection was then carried out at each load stage during the testing of the specimen under cyclic loading in phases 2 and 3 following the load protocol discussed in chapter 5. 2-D surface thermal contours were constructed from the thermography data obtained at 5.5 seconds after initiation of the flash thermal input to identify the defect/damage locations. Linear thermal profiles across the defect location along the length of each thermography shot were computed for each load level and these profiles from subsequent load levels were then compared to each other to determine the appearance or progression of defect areas.

The schematic of the strengthened slab 1 is presented in Figure 6.9a and the locations at which the thermography inspections were carried out in slab 1 are presented in Figure 6.9b.

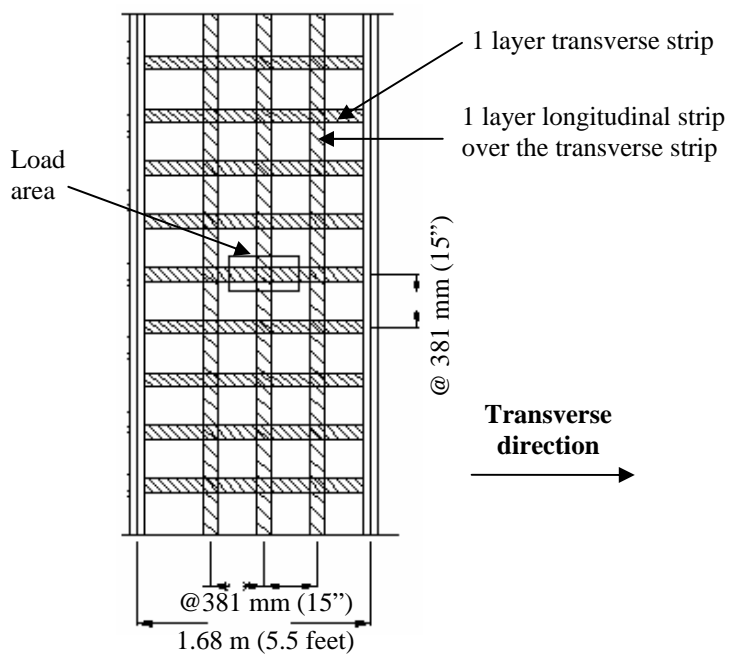


Figure 6.9a Overall schematic of slab 1 strengthened with pultruded strips

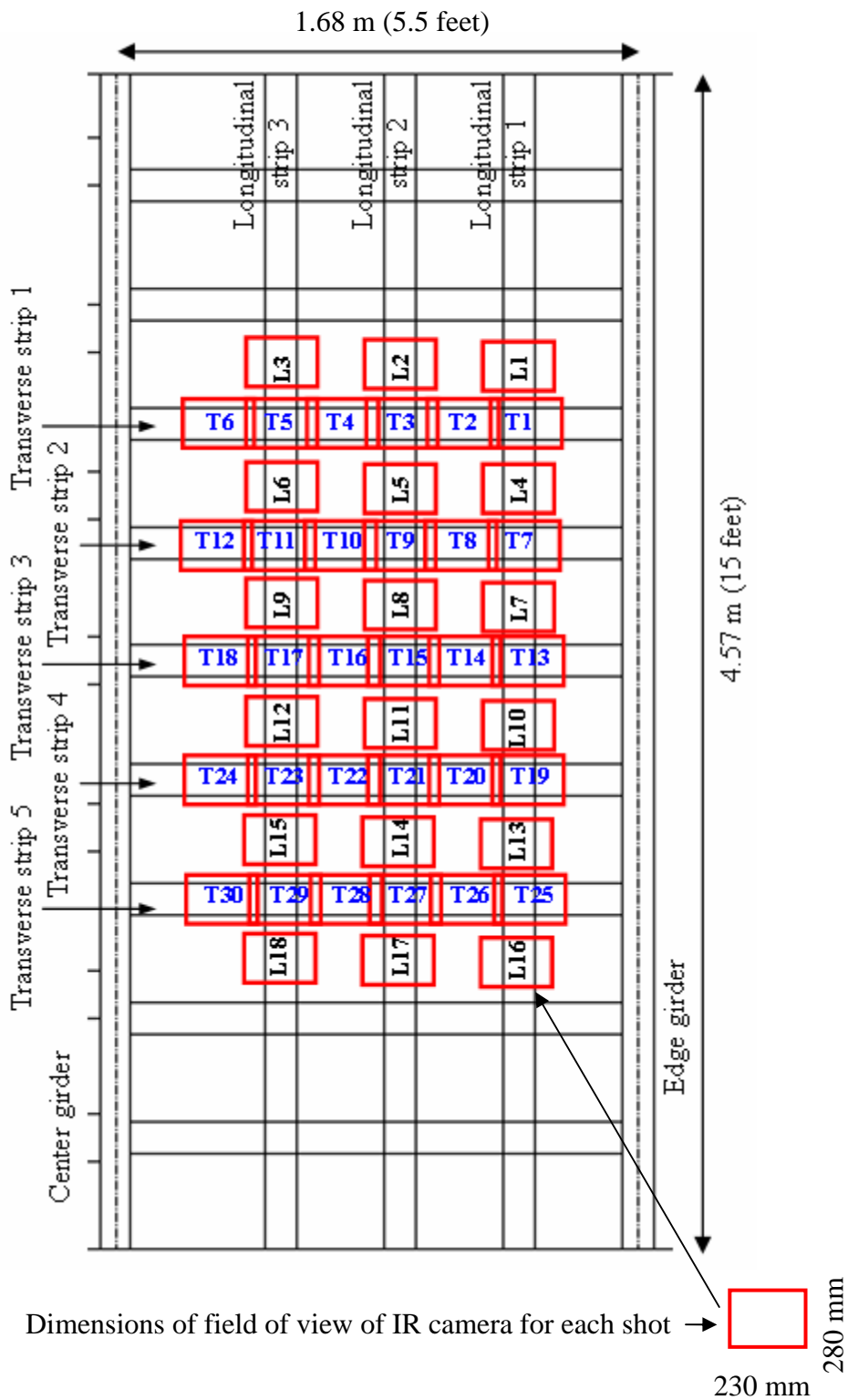
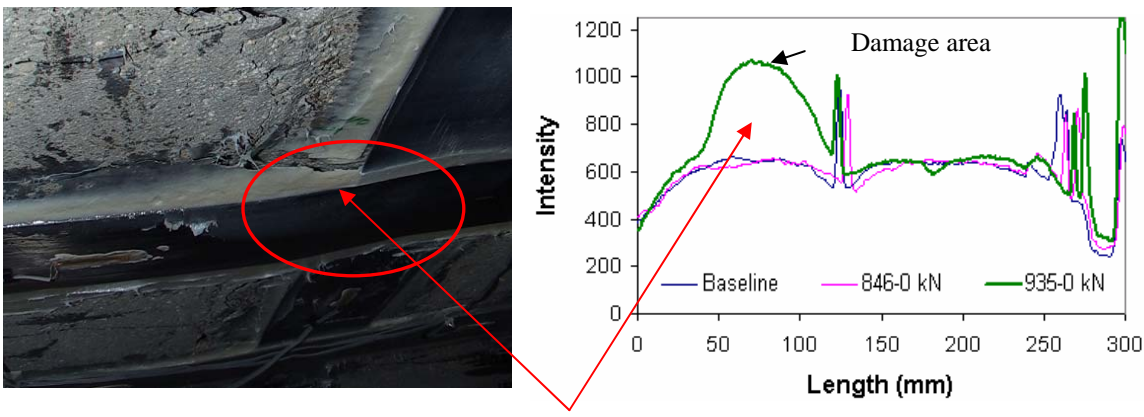


Figure 6.9b Locations of thermography inspections in Slab 1

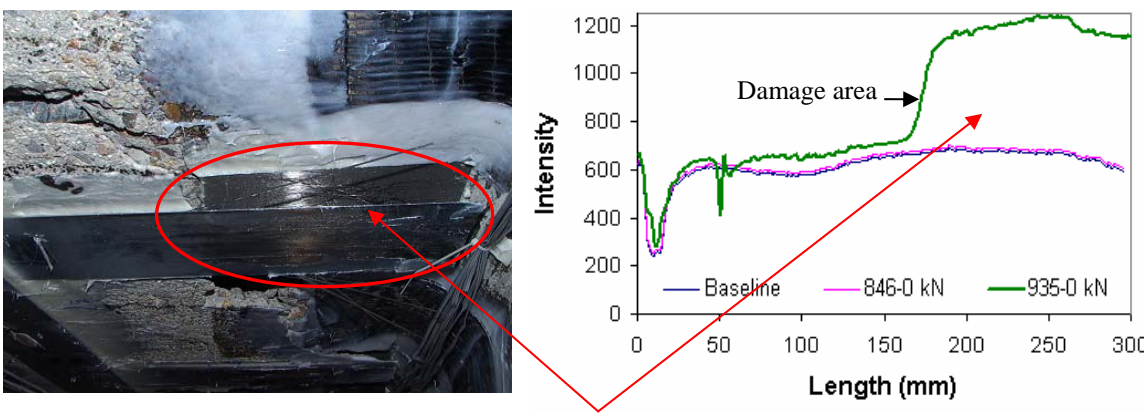
The defect/damage areas in the pultruded strips detected through thermography inspections can be categorized into four types:

- i) Areas with defects which were produced during installation of the pultruded strips and did not grow with loading
- ii) Areas showing appearance or progression of damage with the progression of loading over the load cycles at or around locations of pre-existing damage
- iii) Areas with damage produced by debonding of the composite and detected by the thermography inspections on unloading the specimen after reaching failure load. Depending on location, the type of debonding was divided into two types, namely
 - a) debonding occurring at the composite-concrete bond interface or between transverse and longitudinal composite strip bond interfaces and
 - b) interlaminar debonding occurring inside the composite strip itself, due to separation between the fibers and matrix of the pultruded strip. A different thermal intensity was obtained for the two debonding modes due to differences in depth of the damage from the composite surface and this is shown in Figure 6.10. The interlaminar debonding occurring in the composite strip was located at a shallower depth from the composite surface as compared to the debonding at the composite-concrete/composite-composite bond interface and thus a damage in the form of interlaminar debonding had a higher thermal intensity than that of debonding at composite-concrete or composite-composite interface (an intensity of 1200 compared to 1000 as shown in Figure 6.10).
- iv) Areas with no defect/damage or areas where damage could not be identified using thermography inspections.



Debonding at composite-concrete interface

(a) Debonding at composite-concrete interface



Interlaminar Debonding in composite strip

(b) Interlaminar debonding occurring in the composite strip due to separation between the fibers and matrix of the strip

Figure 6.10 Distinction between modes of debonding as observed visually and from thermography results (935-0 kN stands for thermography inspection carried out on unloading the specimen after reaching load of 935 kN)

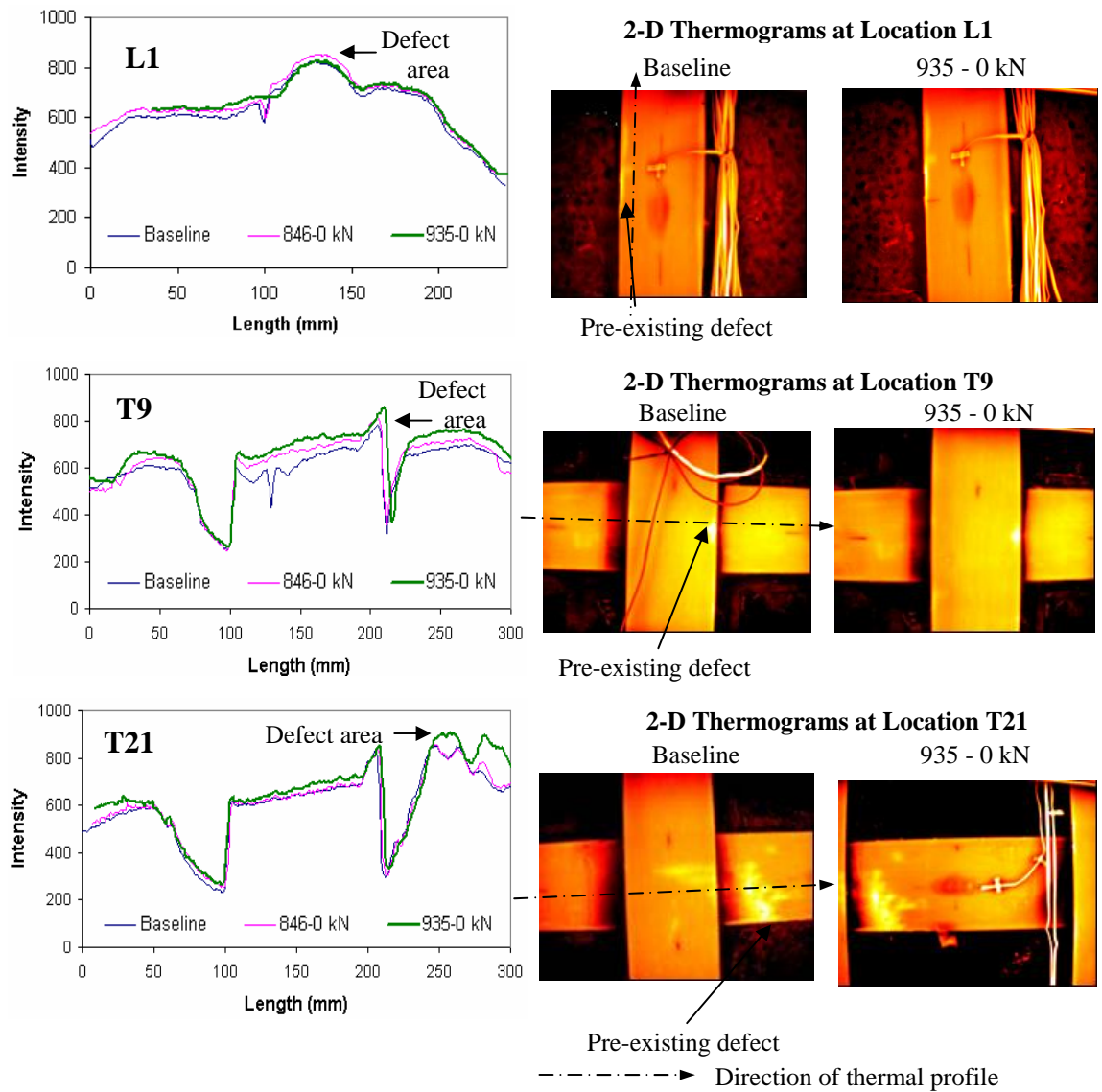
The defect categories and their locations as identified from the thermography inspections are presented in Table 6.1.

Table 6.1 Defect types and locations as identified from thermography inspections

Defect/Damage Category	Locations (as marked in Figure 6.9)	Remarks
1. Areas with defects produced during installation of the pultruded strips	L1, T3, T7, T9, T21	Pre-existing defects in the form of unbonded areas at the composite-concrete interface
2. Areas showing appearance of new defects or progression of old defects with loading	T3, T7	Appearance of new damage at locations with pre-existing damage
3. Areas with damage produced by debonding of the composite at ultimate failure	L2, L3, L4, L5, L6	Debonding at concrete – longitudinal strip interface
	T1, T3, T5, T29	Debonding within longitudinal strip – transverse strip overlap region
	T26, T27, T28	Debonding at concrete – transverse strip interface
	T7, T13, T24, T25	Debonding at composite-concrete interface at the edge of a transverse strip
	T12, T18	Interlaminar debonding inside the composite strip at the edge of a transverse strip
	T15	Damage in the transverse strip due to crack opening in concrete causing debonding at composite-concrete interface
4. Areas with no defect/damage or areas where damage could not be identified by thermography inspections	L7 to L18 T2, T4, T6, T8, T10, T11, T14, T16, T17, T19, T20, T22, T23, T30	No defects/damage identified from thermography inspections

Defect areas belonging to category 1 are presented in Figure 6.11. Most of these defects, produced during the installation of the composite, were located in non-critical areas and thus did not show any progression with increase of loading. The inspections were carried out after unloading back from a load step (for example, 846-0 kN will

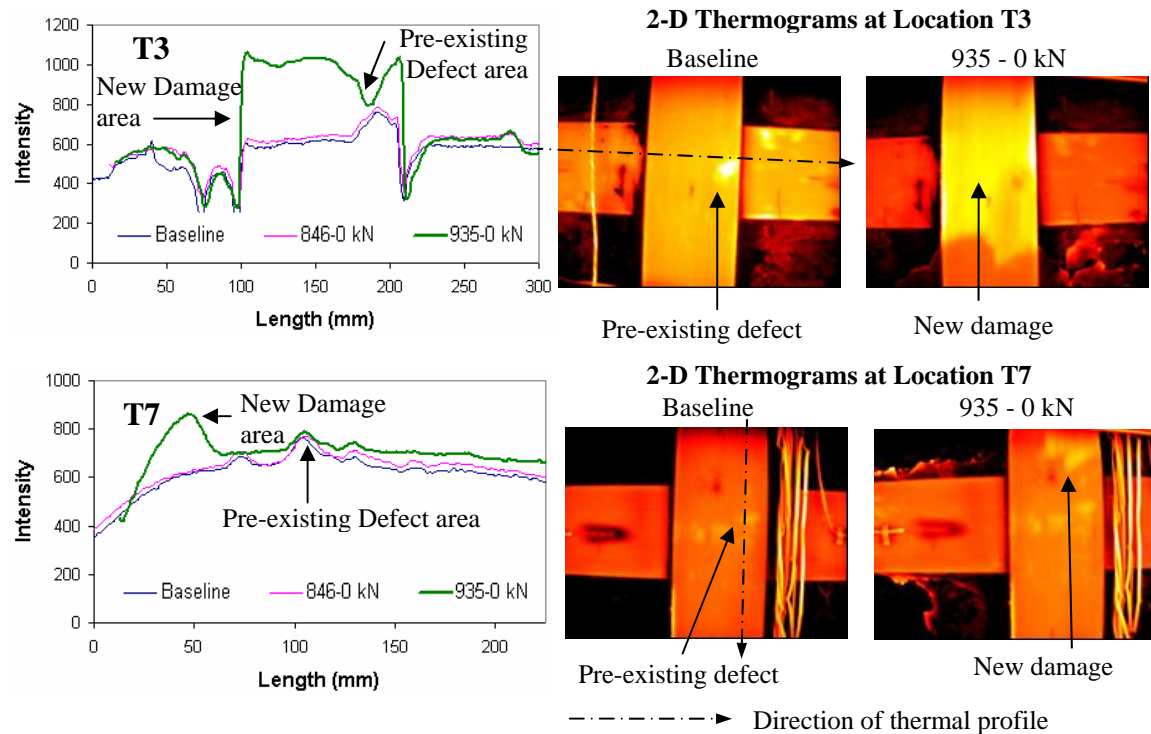
indicate that the inspection was carried out after the specimen was unloaded after loading to 846 kN load cycle).



Note : 846-0 kN indicates that the inspection was carried out after the specimen was unloaded after loading to 846 kN load cycle

Figure 6.11 Locations of defect type 1 (No progression of defects)

Defect areas of category 2 are shown in Figure 6.12. These areas had pre-existing defects with the appearance of either new defects or of growth in pre-existing defects with loading.



Note : 846-0 kN indicates that the inspection was carried out after the specimen was unloaded after loading to 846 kN load cycle

Figure 6.12 Locations of defect type 2 (With pre-existing and new defects)

The pre-existing defects in areas with defect type 2 did not increase in size till the 846 kN load cycle. However the initiation of new damage regions was observed in the surrounding areas after the specimen was unloaded after being taken to the failure load of 935 kN (210 kip). Because of safety issues, no inspection was carried out between 846 kN and 935 kN. The damage areas observed from the inspections after unloading from failure indicated that most of the damage in the strips occurred between these loads. It is of interest to observe the thermal intensities along the length of the pultruded strip at

location T3. The pre-existing defect at the edge of the strip did not grow with loading and at failure load, the longitudinal strip that overlapped the transverse strip debonded. The debonded area was indicated by a high thermal intensity (~1000) which was different from the thermal intensity (~800) at the location of the pre-existing defect. This is because each defect type has its characteristic thermal intensity depending on the type and severity of the defect, so that the debonded area was differentiable from the pre-existing defect. Also at location T7, the pre-existing defect did not grow although new damage areas were observed at failure load near the intersection of the transverse and longitudinal strips.

The damage areas of type 3 observed in the thermography inspections on unloading the specimens after reaching failure load, are presented in Figures 6.13 to 6.15. Most of these damage areas were localized in the regions where the opening of the preexisting punching shear cracks at failure load caused debonding of the composite. However this mode of damage could be divided into four categories depending on the location of damage, i) transverse strip-longitudinal strip overlap area, ii) concrete-longitudinal strip interface, iii) edge of transverse strip and iv) at concrete-transverse strip interface. Typical damage areas at the transverse strip-longitudinal strip overlap area are shown in Figure 6.13 and could be distinguished by the high thermal intensity regions along the longitudinal strips but no change in intensity in the transverse strips. Damage at the concrete-longitudinal strip interface region are shown in Figure 6.14.

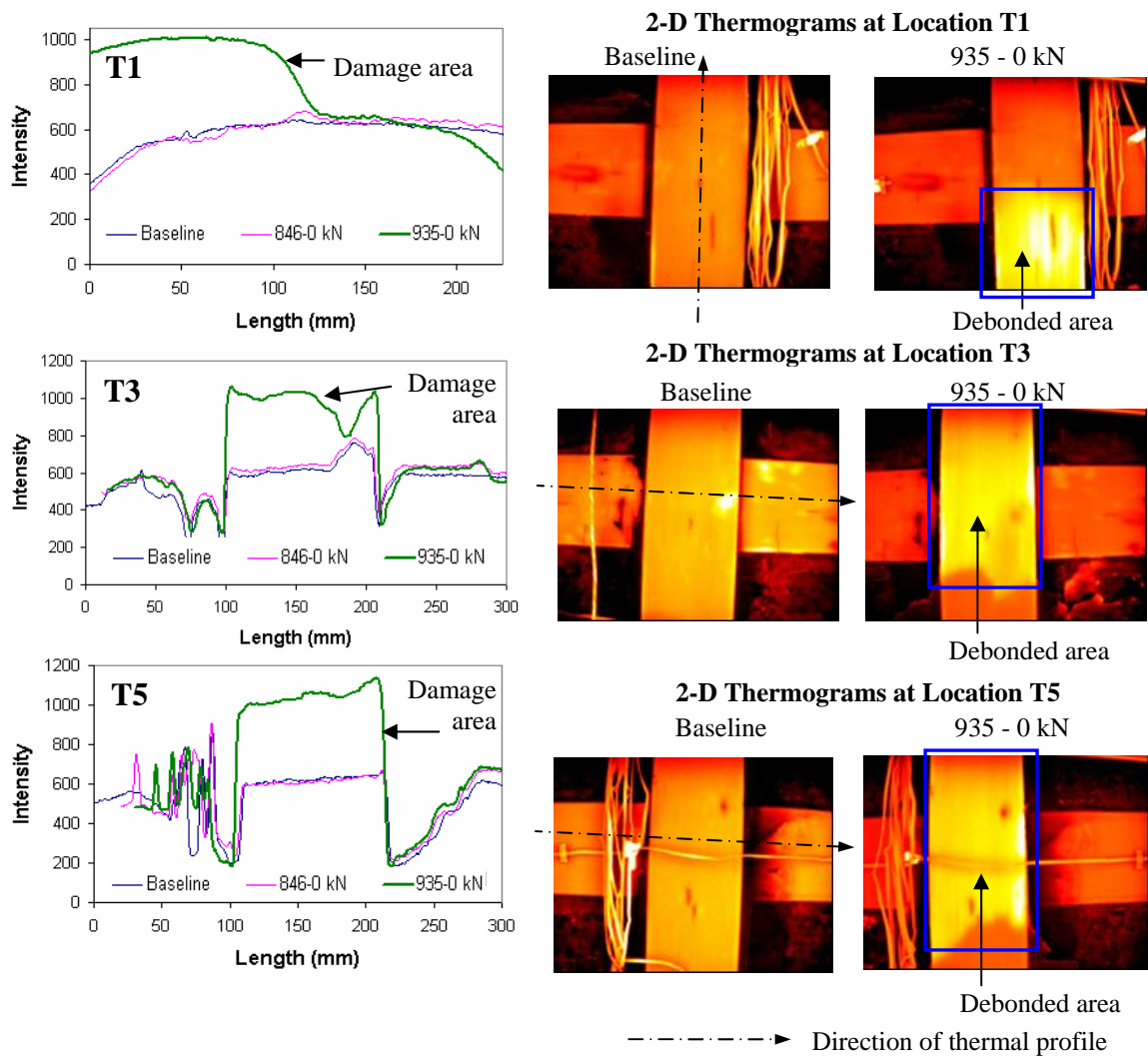


Figure 6.13 Damage at transverse strip - longitudinal strip overlap area (Defect type 3)

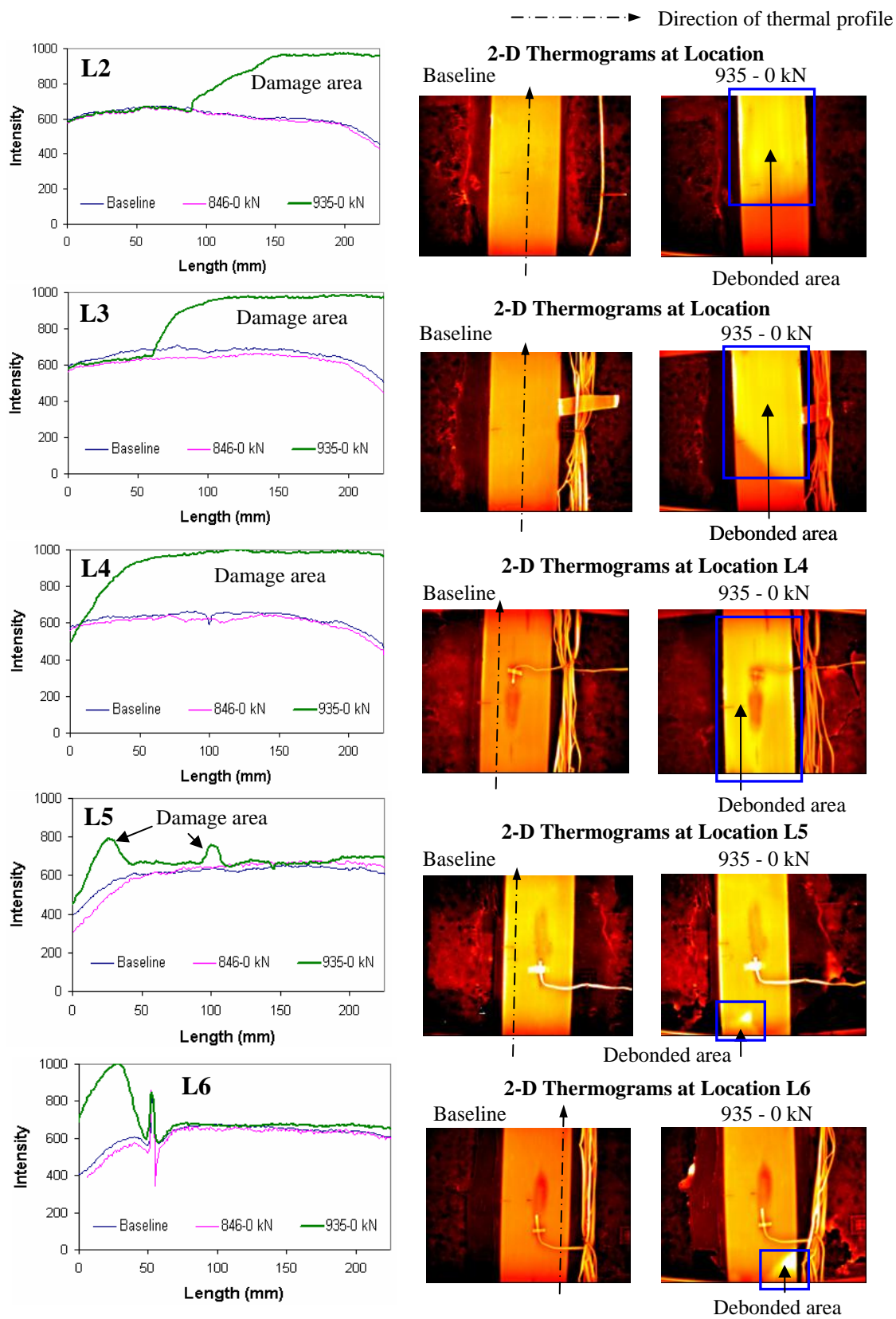


Figure 6.14 Damage at concrete-longitudinal strip interface

The debonding of the composite strips at failure load resulted in simultaneous opening of punching shear cracks, the perimeter of which ran along the longitudinal edges of the slab near the slab-girder intersection. This resulted in damage at the edges of the transverse pultruded strips and is shown in Figure 6.15. The thermography inspection results at these damage zones at the edges of the transverse pultruded strips are presented in Figure 6.16. Some of these damage regions (T12 and T18) had higher thermal intensity (~1200) as compared to the thermal intensities (~1000) at other areas (T7 and T13, T24 and T25). Visual inspection of the areas with high thermal intensity showed a correspondence to interlaminar debonding in the composite. As was shown earlier in Figure 6.10 the areas with interlaminar debonding were caused due to separation between the carbon fibers and the matrix in the pultruded strip. Since the depth of this damage from the top surface was smaller than that of the debonded areas at the composite-concrete interface, this resulted in the higher thermal intensity in damage areas with interlaminar debonding as compared to debonding at composite concrete interface or between overlapping composite strips.

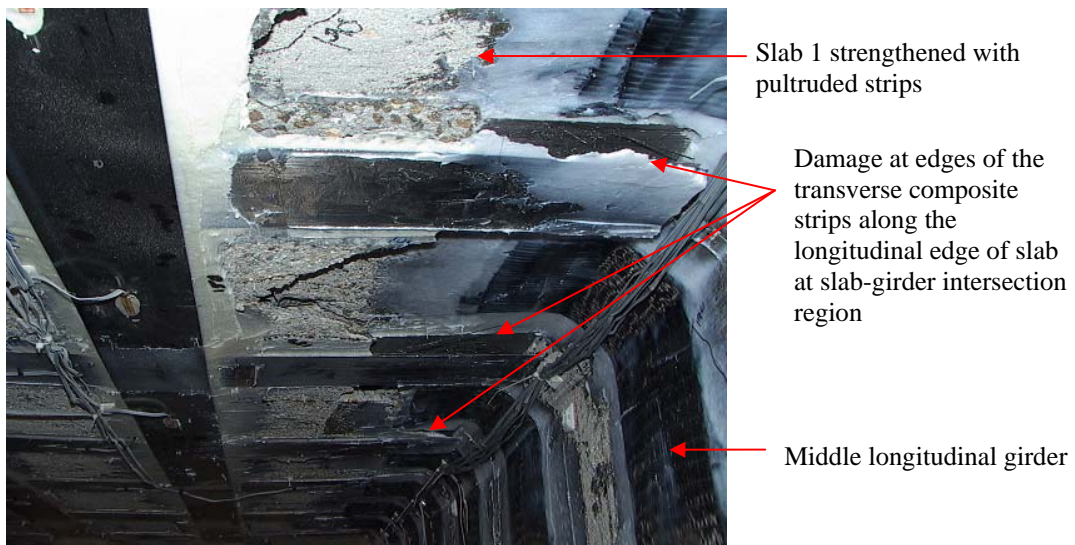


Figure 6.15 Visual observation of damage at the edges of the transverse pultruded strips on unloading specimen after reaching failure load

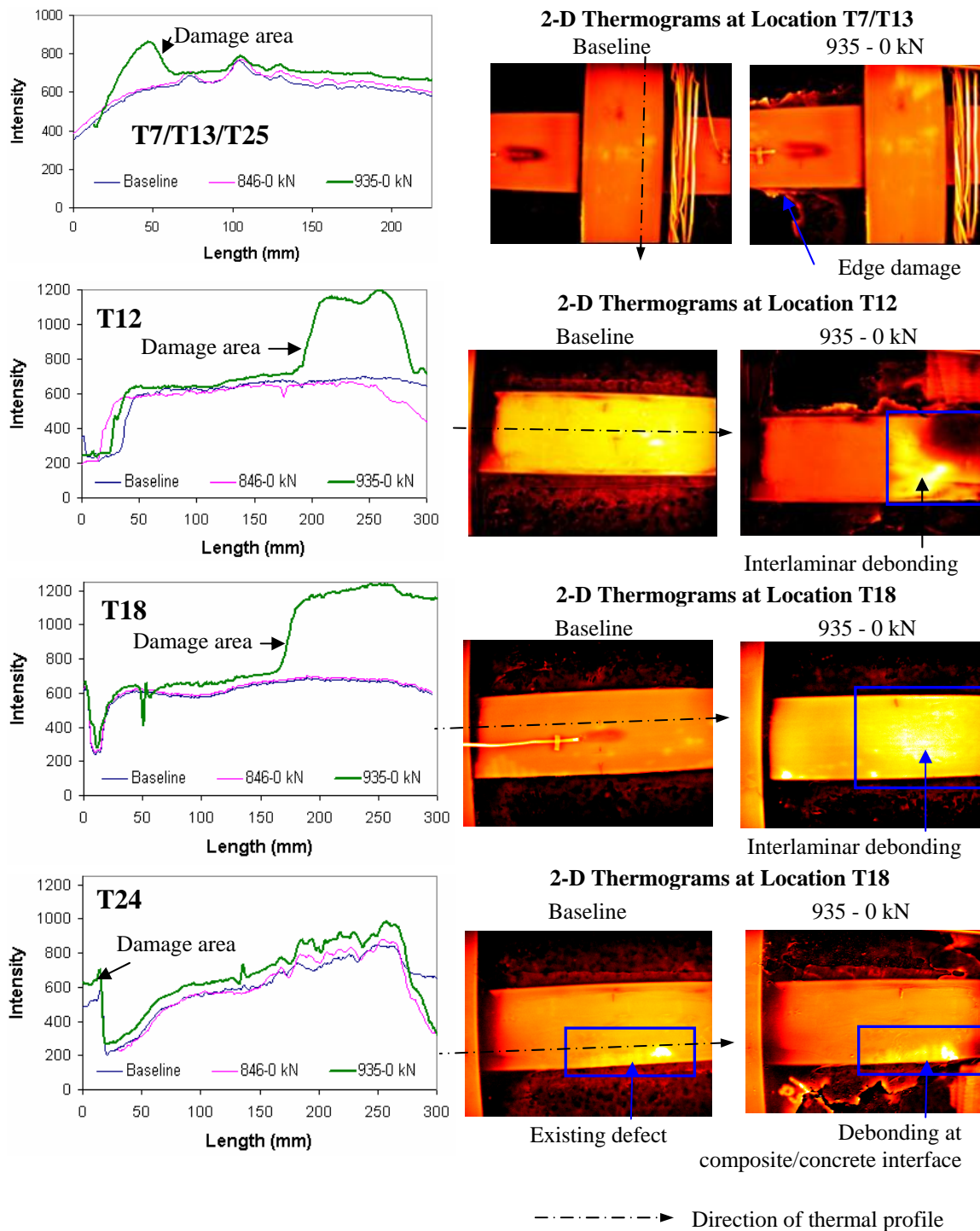


Figure 6.16 Damage at edges of transverse strips (Defect type 3)

Two types of damage areas were distinguishable at the concrete-transverse strip interface from the thermography inspections carried out after unloading the specimen after reaching failure load. The first type of damage was located in the middle transverse strip in the mid-span region of slab 1 below the load area and is presented in Figure 6.17. The damage was localized in a band along the width of the pultruded strip and had a thermal intensity (~ 900 as shown in Figure 6.17), lower than the intensity (~ 1000 as shown in Figure 6.18) at the debonded areas. On visual inspection this was found to correspond to a crack traversing the pultruded strip. Since the crack at this location was still restrained by the strip at failure it did not cause total debonding of the strip and thus the damage severity as was indicated by the lower thermal intensity was less than that of a debonded area.

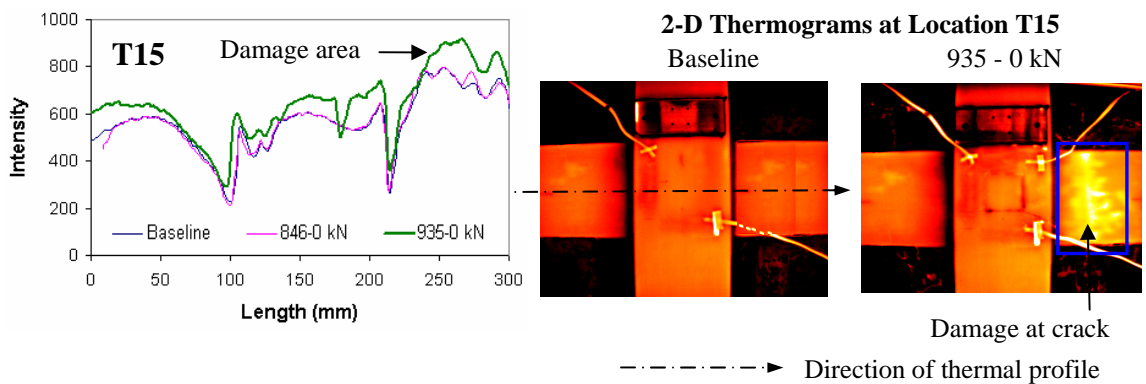


Figure 6.17 Damage at concrete-transverse strip interface (Damage after failure)

The second type of damage at the concrete-transverse strip interface, observed in the thermography inspection carried out at no-load condition on unloading the specimen after reaching failure load of 935 kN, corresponded to debonding and these damage areas

are presented in Figure 6.18. At location T27 the debonded areas were identified in the transverse strip on either side of the longitudinal strip overlap region. This indicated that the longitudinal strip was effective in restraining the debonding of the transverse strip in the overlap area so that the damage in the transverse strip was concentrated outside the edge of the longitudinal strip. On visual inspection, the perimeter punching shear crack, running in the transverse direction between the edge and middle girders, was found to propagate underneath the transverse strip at this location. However at location T29 the crack was found to propagate along the edge of the transverse strip causing damage in the longitudinal strip as well at the overlap region.

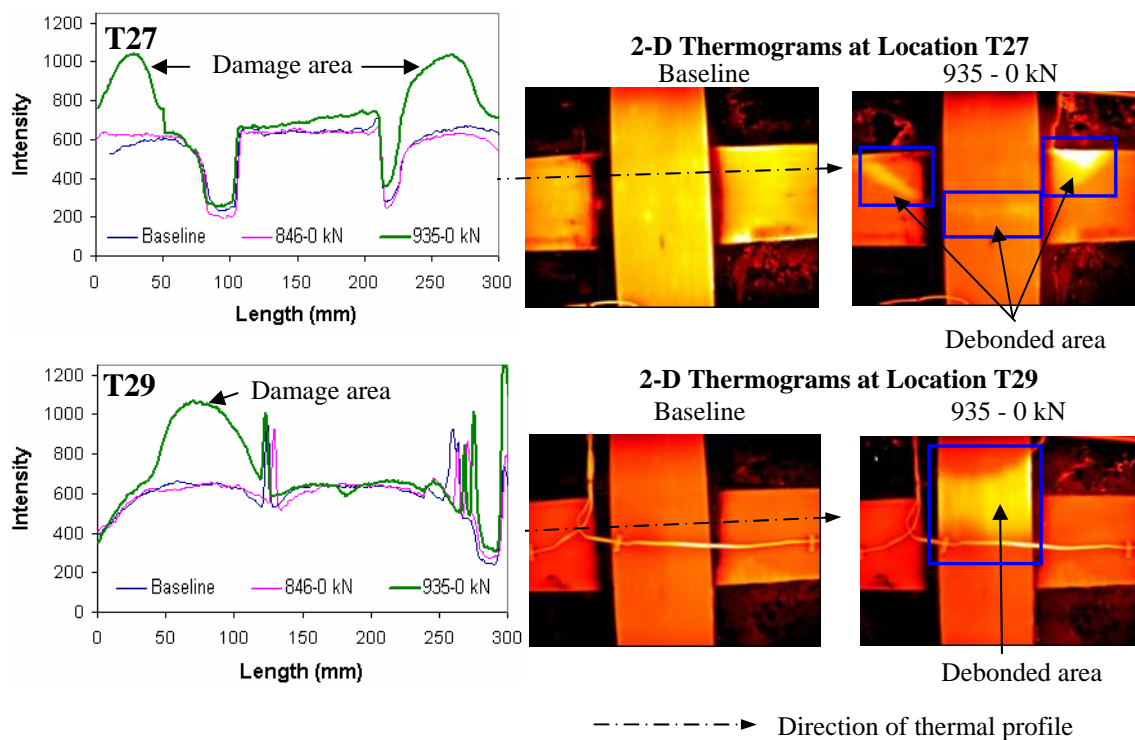


Figure 6.18 Debonded area at concrete-transverse strip interface (Damage after failure)

6.4 Comparison of Thermography Results with Crack Patterns in Slab 1

The thermography inspection results in slab 1 were compared to the crack patterns to correlate the damage types identified in terms of their thermal signature with the physical damage types identified through visual observations. The different types of damage areas identified from the thermography inspections are schematically shown in Figure 6.19. The outline of the primary damage areas, as defined by the perimeter of the punching shear crack, is shown in Figure 6.19.

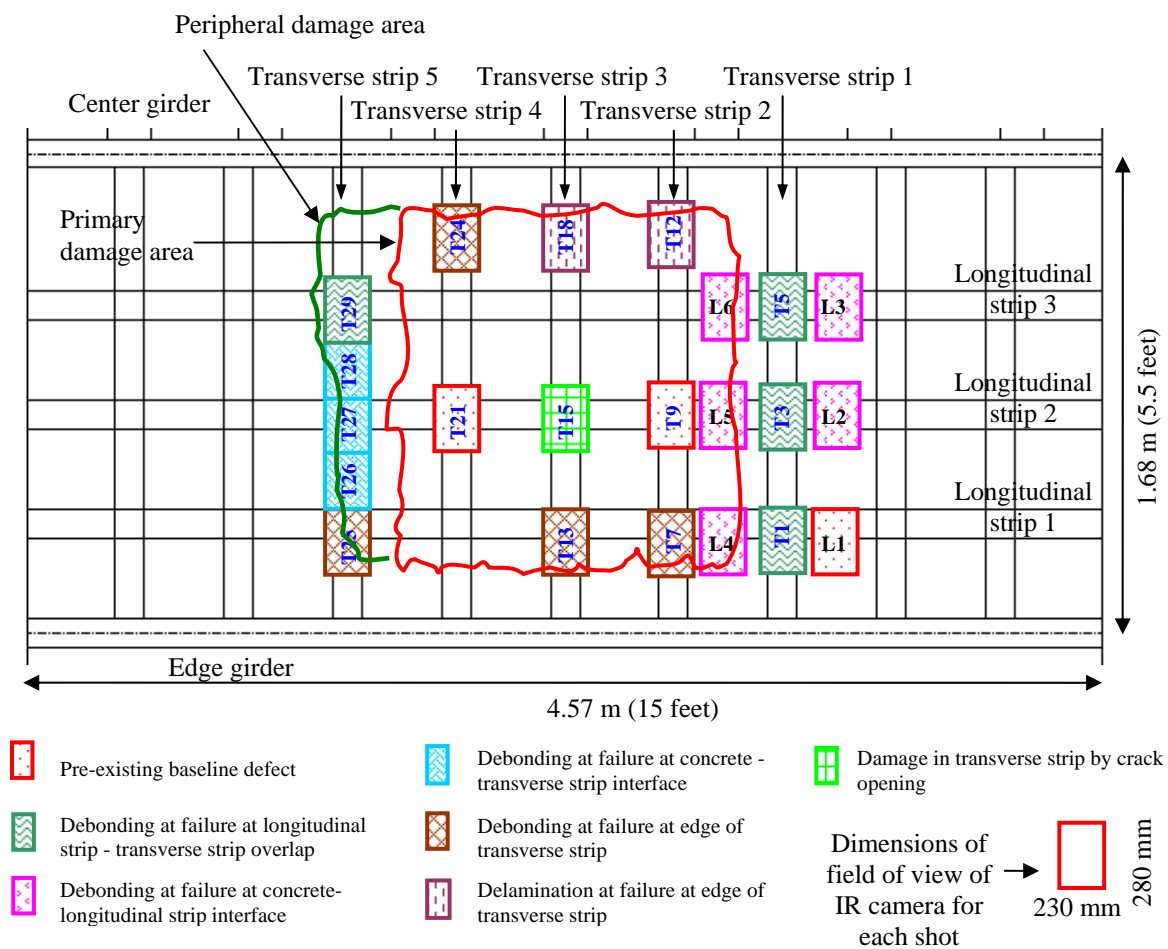


Figure 6.19 Damage areas identified through thermography inspections

The areas of the pultruded strips at the intersections of the crack perimeter with the strips matched the locations at which the high thermal intensity from the thermograms indicated damage localization. Also after the cracked concrete was taken off at the end of test, it was found that between transverse strips 4 and 5 (Figure 6.19) the primary punching shear failure plane after reaching the bottom slab transverse steel reinforcement produced a peripheral damage region in the cover concrete so that the crack at the bottom surface of the slab went along the outer boundary of transverse strip 5. The primary and peripheral damage regions are shown in Figure 6.20. The thermography inspection results along the punching shear crack perimeter are shown in Figures 6.21a, 6.21b and 6.21c. The correspondence between the thermography inspections results and the visual observation of the crack perimeter along the edge of the transverse strip 5 is shown in Figure 6.21a. The thermography inspection results as shown in Figure 6.21a indicated no damage in the longitudinal strips overlapping this transverse strip at locations T25 and T27 but damage at longitudinal and transverse strip overlap region was observed at location T29. Also the crack propagating along the strip was found to cause damage at location T27 only in the transverse strip. The correspondence between the thermography inspections results and the visual observation of the crack perimeter between transverse strips 1 and 2 is shown in Figure 6.21b. Damage was observed in the longitudinal strips at locations L4, L5 and L6 where the punching shear crack was found to traverse across the longitudinal strips. From the thermography inspections, the debonded area of the longitudinal strips was found to extend to the overlap region of these longitudinal strips with transverse strip 1 at locations T1/T2/T3, as shown in Figure 6.21b. The punching shear crack perimeter in the longitudinal direction propagated along the slab-girder

intersection regions and resulted in damage at the edges of the transverse strips. The damage detected by thermography inspections at these locations is shown in Figure 6.21c. As discussed earlier in this chapter, two types of damage in the form of debonding at the composite concrete interface (at locations T7/T13/T24) and interlaminar debonding inside the composite strip (at locations T12/T18) were identified at locations where the transverse composite strips were intersected by the crack perimeter and are shown in Figure 6.21c.

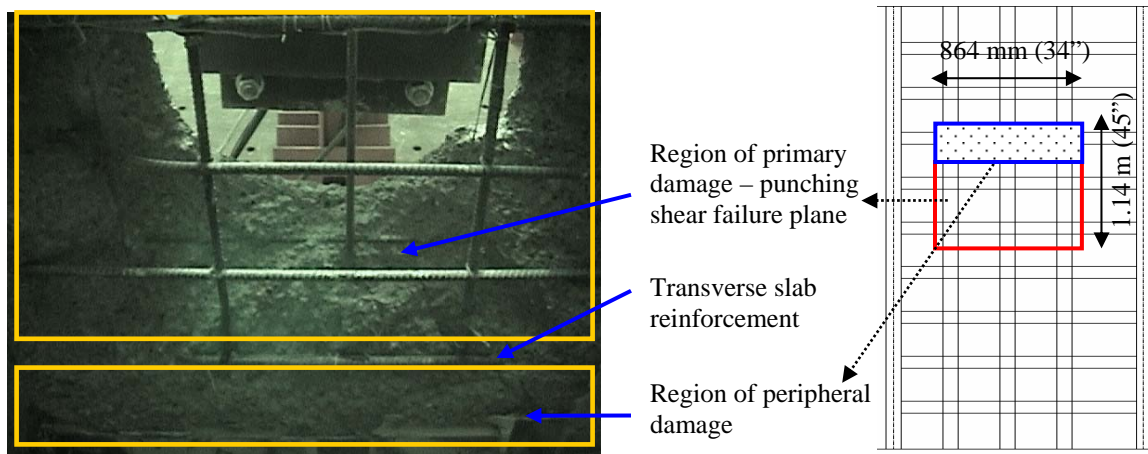


Figure 6.20 Damage regions in slab 1 after removal of cracked concrete

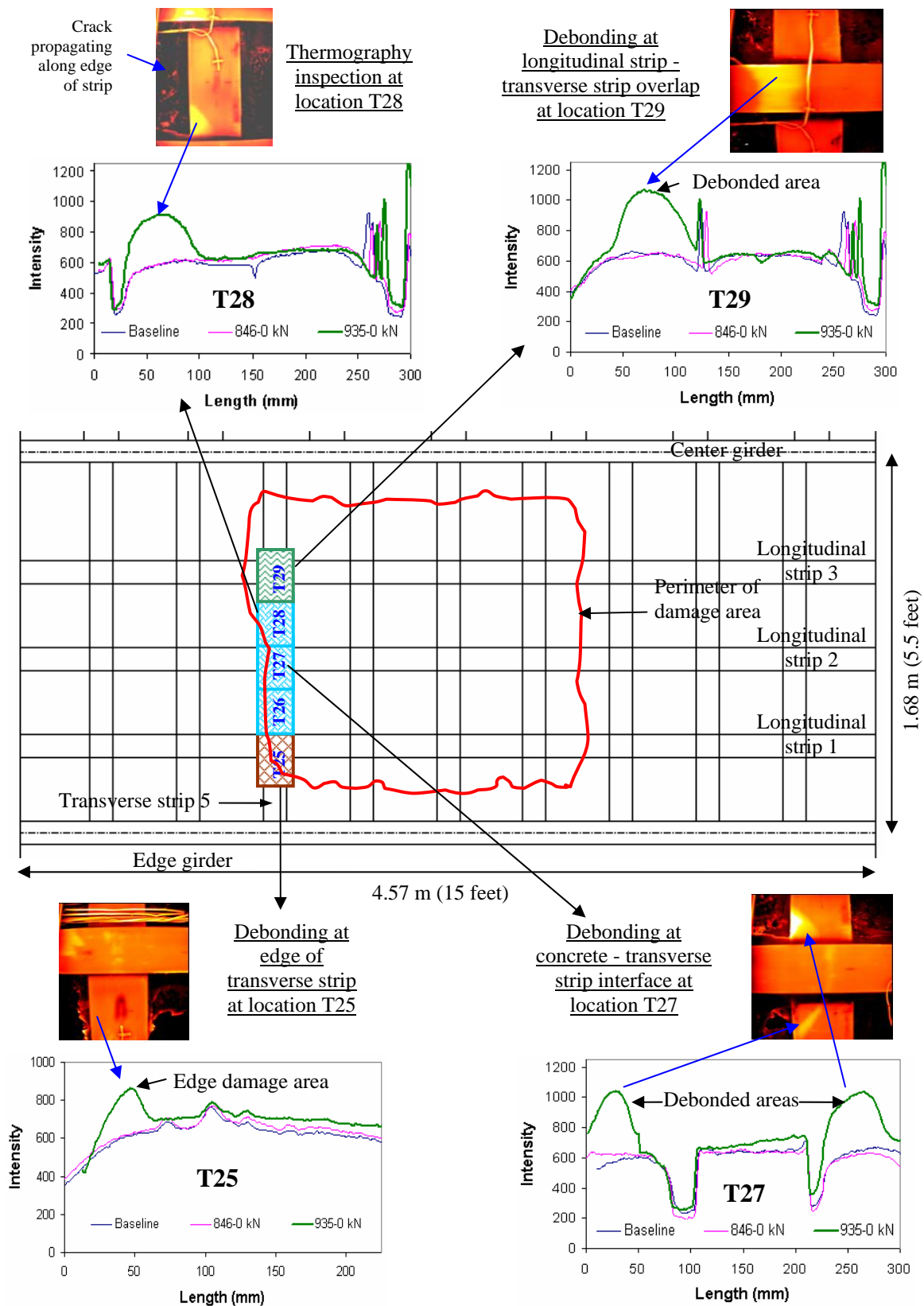


Figure 6.21a Correspondence of thermography inspections with crack pattern (Strip 5)

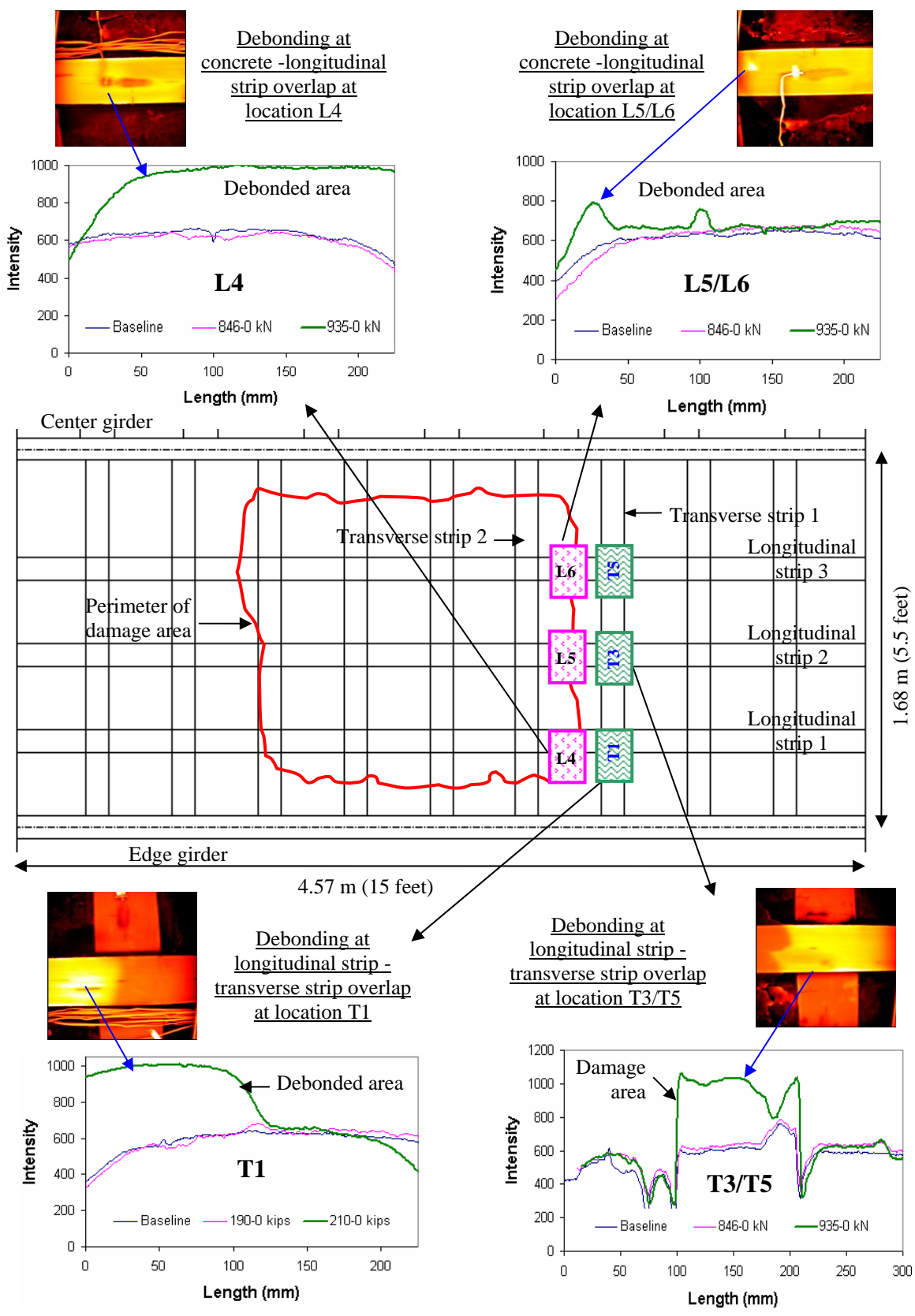


Figure 6.21b Correspondence of thermography inspections with crack pattern (Strip 1)

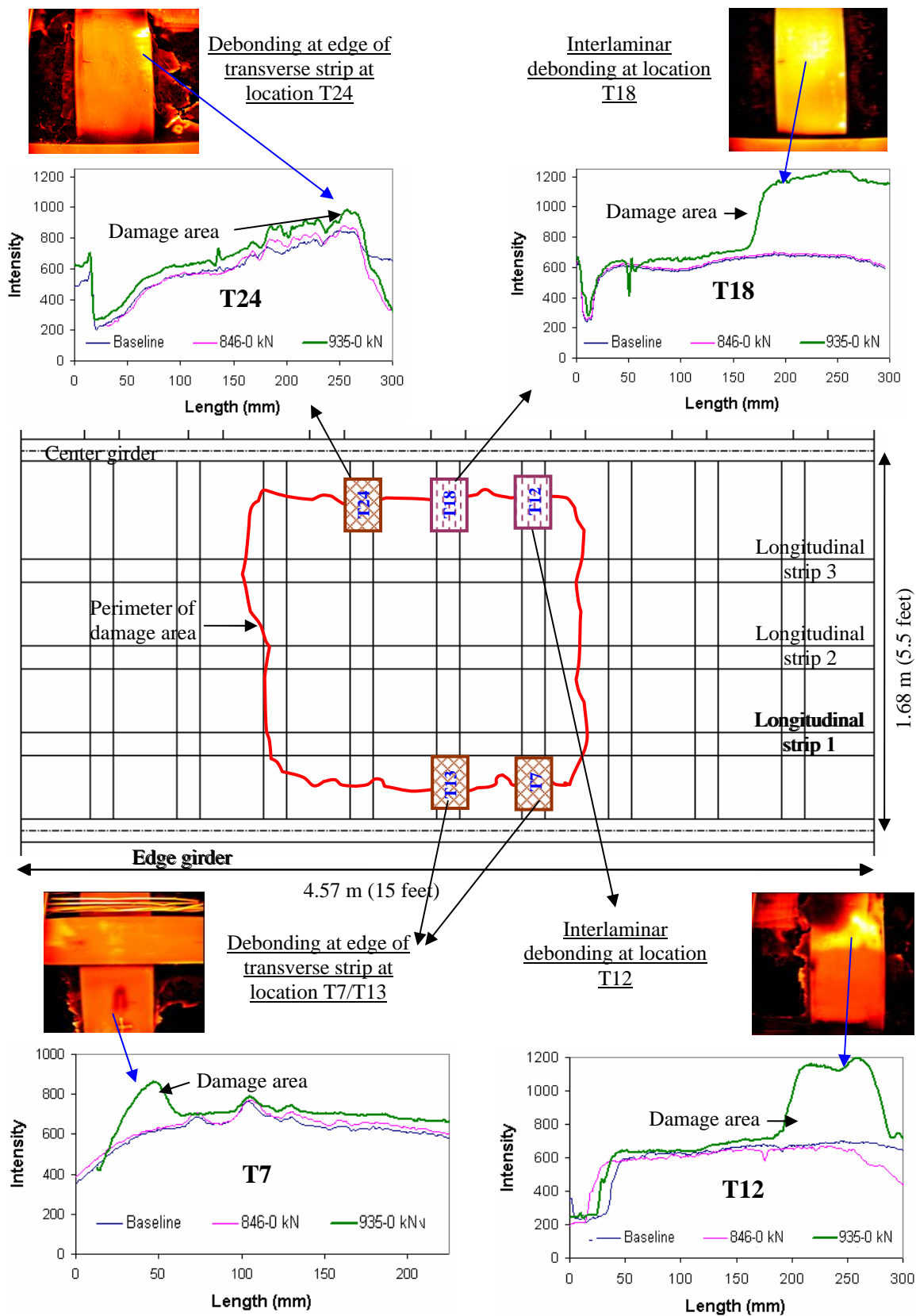


Figure 6.21c Correspondence of thermography with crack in longitudinal direction

Some comparisons of the thermography results with the visual observations of crack patterns are presented in Figure 6.22b, with the locations of these thermography inspections shown relative to the general dimensions of strengthened slab 1 being presented in Figure 6.22a. The correlation between the thermography inspection results and visual observations in terms of damage type and location indicates that based on the quantitative thermal signature, the thermography inspections can be used to identify different damage types in the pultruded strips. Also the area of subsurface damage which could not be estimated through visual inspections could be assessed using the thermograms through identification of regions with high thermal intensity. Finally since the severity of damage can be quantified in terms of thermal intensity, this technique could be used to monitor progression of damage occurring due to structural degradation.

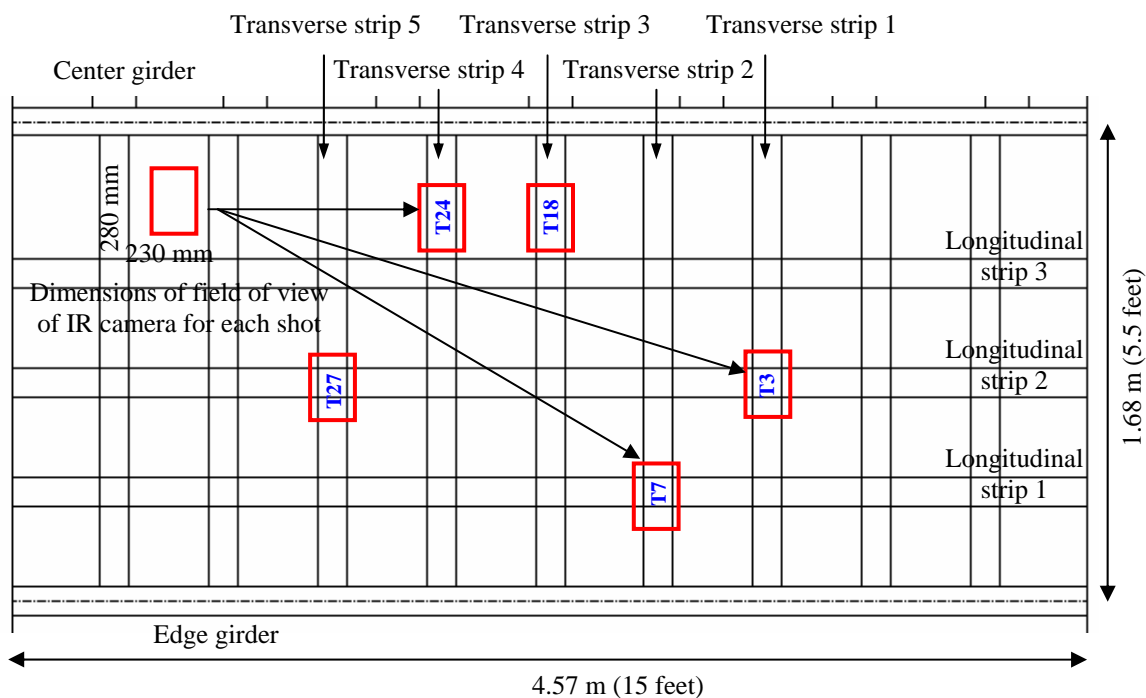
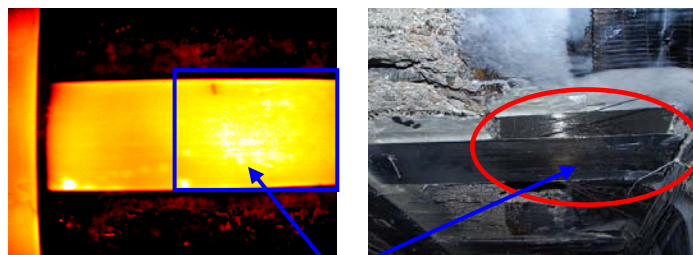


Figure 6.22a Locations of thermography inspections in Slab 1 used in Figure 6.22 (b) to show correspondence between thermography and visual observations

**T24**

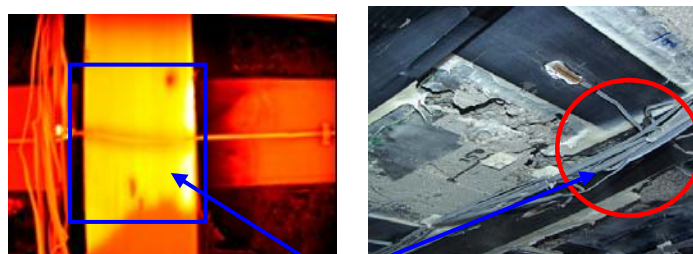
Debonded area at edge of pultruded strip at location T24

**T18**

Delaminated area at edge of pultruded strip at location T18

**T7**

Debonded area at edge of pultruded strip at location T7

**T3**

Debonded area at transverse and longitudinal strip overlap at location T3

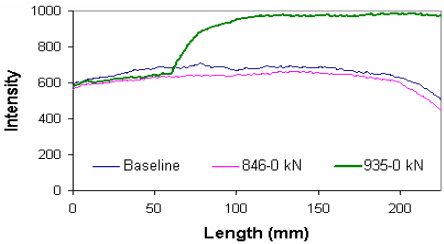
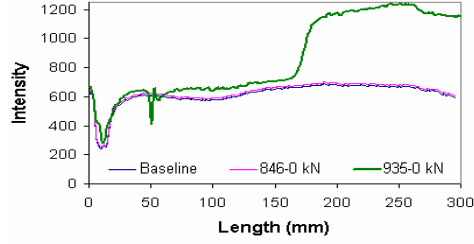
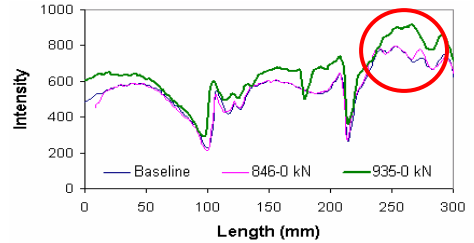
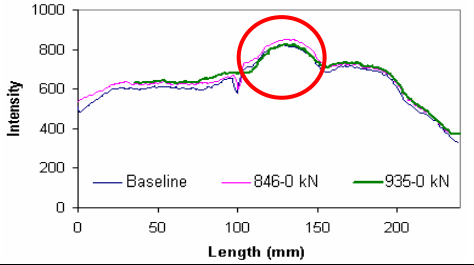
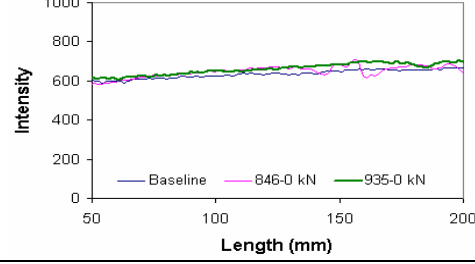
**T27**

Debonded area at concrete - transverse strip interface at location T27

Figure 6.22b Comparisons between thermography and visual inspections in slab 1

A summary of the thermal signatures for the different defect/damage types identified from the thermography inspections are presented in Table 6.2.

Table 6.2 Summary of thermal signatures for defect types

Defect type	Thermal signature	Remarks
1. Debonding of composite at pultruded strip - concrete interface		Characterized by high thermal intensity uniformly spread over area of debond. Observed at high load levels or in areas of high stress concentration (Relative thermal intensity ~ 1000)
2. Interlaminar debonding in the pultruded strip due to separation between fibers and matrix of strip		Characterized by higher thermal intensity than debonded area due to location at lesser depth and observed at failure load. (Relative thermal intensity ~ 1200)
3. Debond at pultruded strip - concrete interface due to opening of cracks		Characterized by a thermal intensity between that of air void and debonded area and also localized at the crack. Such defect can grow with crack opening. (Relative thermal intensity ~ 900)
4. Air void defects produced during installation of the pultruded strip		Characterized by a lower thermal intensity than other defect types and localized in an elliptical area around the defect. Visible in baseline inspection. (Relative thermal intensity value ~ 800).
5. No damage/defects		Characterized by a constant thermal intensity over the load cycles.

6.5 Inspection Results from Fabric Laminates in Slab 2

Baseline thermography inspections were carried out after strengthening slab 2 with site impregnated fabric laminates, bonded to the soffit of the damaged slab, before subjecting the specimen to the phase 2 and 3 load cycles. These inspection results were used to characterize pre-existing defect areas in the composite laminates (i.e. those were produced during bonding of the laminates to the concrete surface). These formed a baseline for further inspections to detect and characterize damage appearance or progression while loading the specimen. Because of the relatively poor quality associated with the manufacturing of the fabric laminates by the wet-layup process as compared to the pultruded strips, a large number of pre-existing defects were produced in the fabric laminates during their installation. Since two layers of carbon fabric were used for the transverse laminates, the defects, predominantly in the form of air voids could be present at the composite-concrete interface or between the two layers of composite. Based on its location over the depth of the composite, the defect was visible in a different time frame in the thermography inspection. Two types of defects were identified from the thermography inspections of the fabric laminates, namely shallow air voids and deeper debonds or void defects at the laminate-concrete interface. This was discussed earlier in section 6.1.2 and based on the calibration study, the computations and comparisons between the thermal profiles obtained from the inspections after each load cycle were carried out both at 1.75 seconds and 8 seconds from the initiation of thermal input by the flash lamps so that both air voids and debonded areas could be discerned. Some of the pre-existing defects were identified through visual inspections and are presented in Figure 6.23.

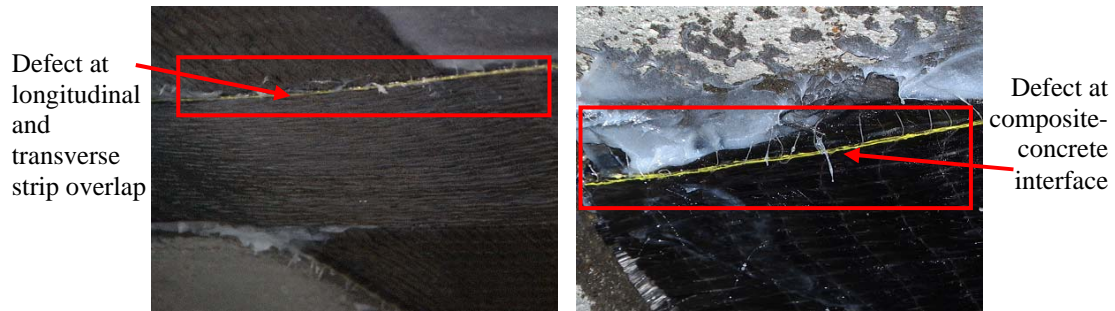


Figure 6.23 Typical post-installation sub-surface defects detected by visual inspections

The two types of pre-existing defects, namely shallow air voids and deeper debonds or defects at the laminate-concrete interface, identified from the thermograms are presented in Figures 6.24 and 6.25. The shallow air voids were innumerable in number and were observed in all the baseline thermograms. These voids are characteristic of the wet-layup process due to poor quality control. The thermal profiles of the fabric laminate composites were thus irregular and different from the uniform profile observed for the pultruded strips. Also because of the variability in the size and thickness of these voids, the thermal intensity of each such defect was different from the other. This is shown in Figure 6.24 in which the relative thermal intensity of these defects varied approximately between 1600 and 800. These thermal profiles were plotted from the thermography data at 1.75 seconds after initiation of the thermal input to discern the shallow defect best as indicated by the calibration study and presented earlier in section 6.1.2.

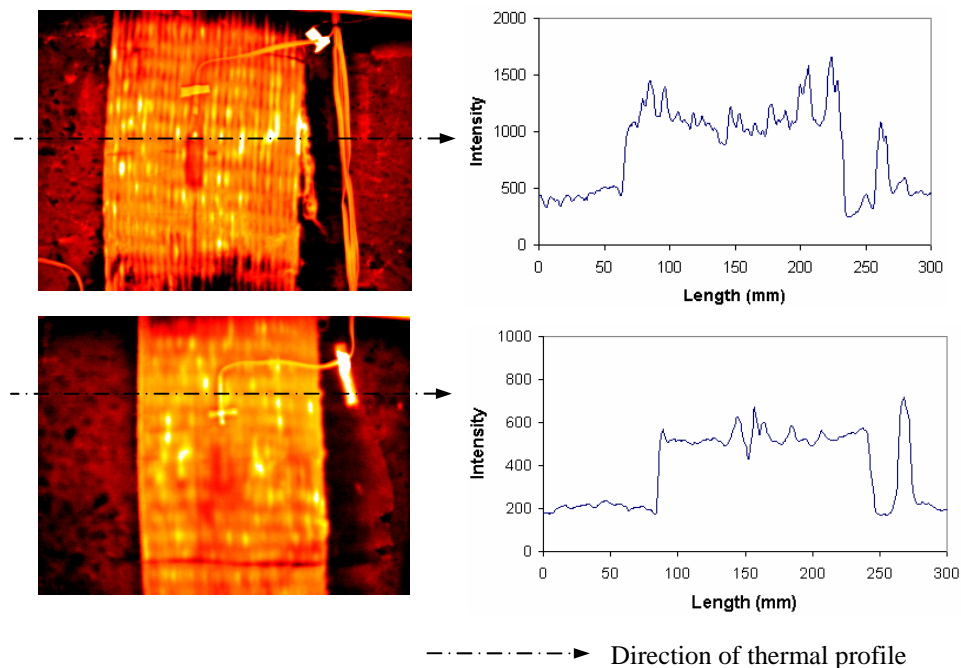


Figure 6.24 Typical shallow defects detected by baseline thermography inspections

The thermal signatures of the deeper disbonds / defects were different from those of the shallow defects and are shown in Figure 6.25. In these thermal profiles the irregularities in the intensities were not present since the profiles were drawn from the thermography data at 8 seconds after initiation of the thermal input. At this point in time, the thermal signatures of the shallow defects had disappeared and thus the locations of the deeper defects were well-defined by the localization of the high thermal intensities at those locations. Also most of these defects were located at the overlap regions of the transverse and the longitudinal laminates because of the difficulty in achieving good compaction and the probability of entrapping voids at these locations.

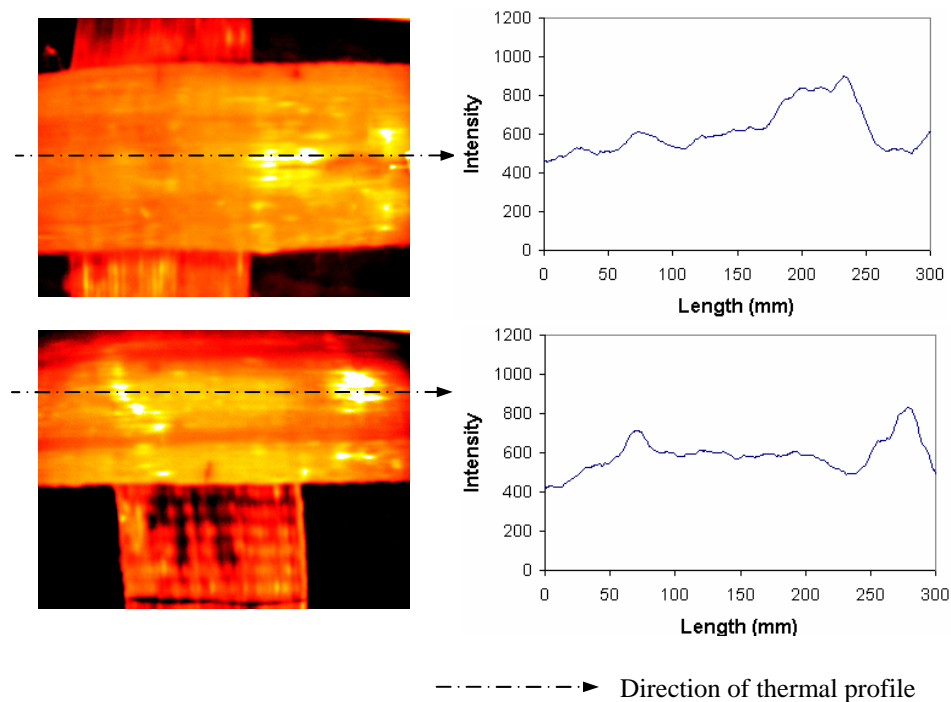


Figure 6.25 Typical debonds / deeper defects detected by baseline inspections

Thermography inspection was then carried out at each load stage during the testing of the specimen under cyclic loading in phases 2 and 3 following the load protocol as was discussed in chapter 5. Thermal profiles along the length of each thermography shot was computed for each load level and these profiles from subsequent load levels were then compared to each other to determine the appearance or progression of defect areas. The locations at which the thermography inspections were carried out in slab 2 are presented in Figure 6.26. Because of space constraints under the specimen, it was not possible to perform the thermography inspections over the entire width of transverse strips 1 and 5.

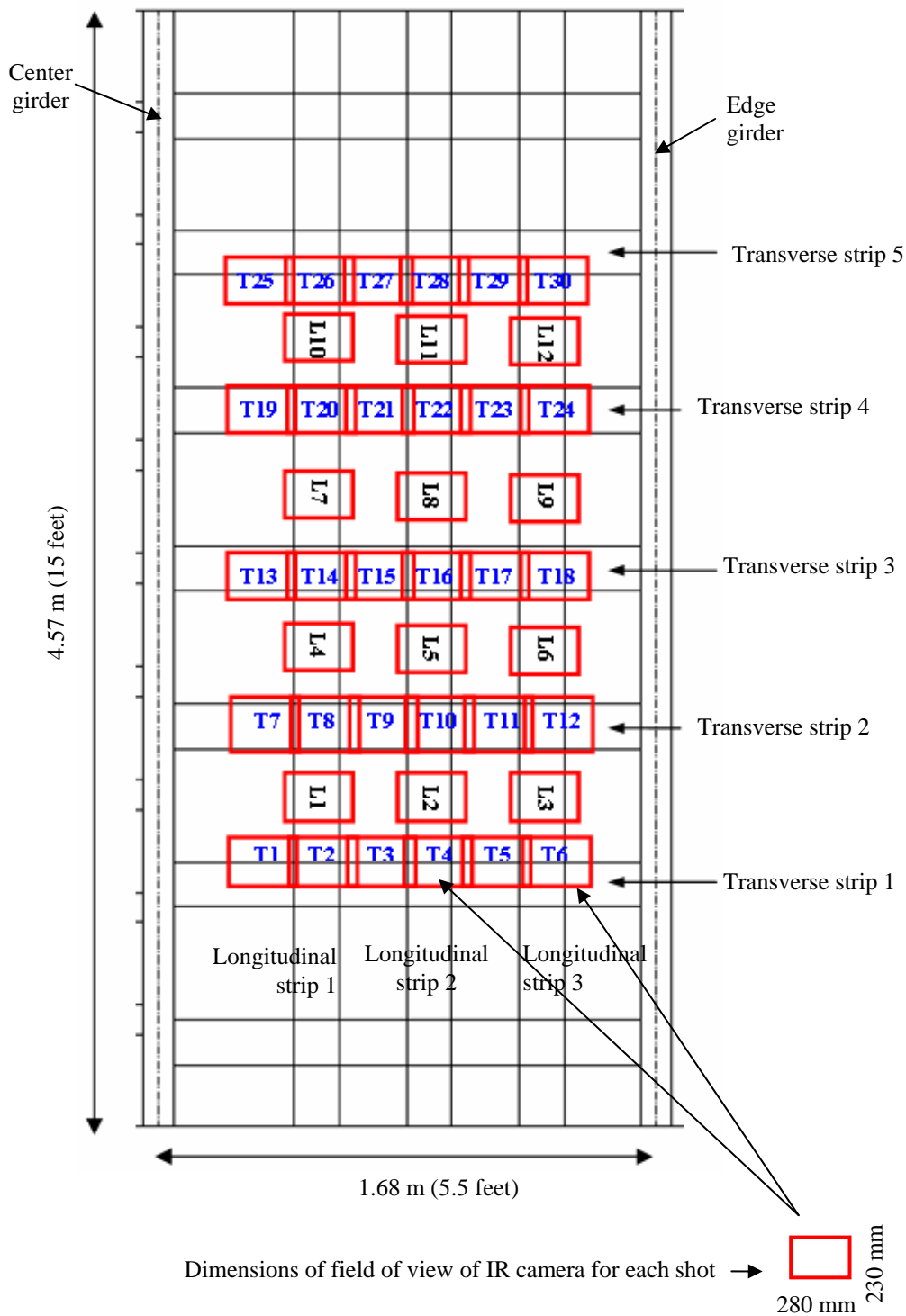
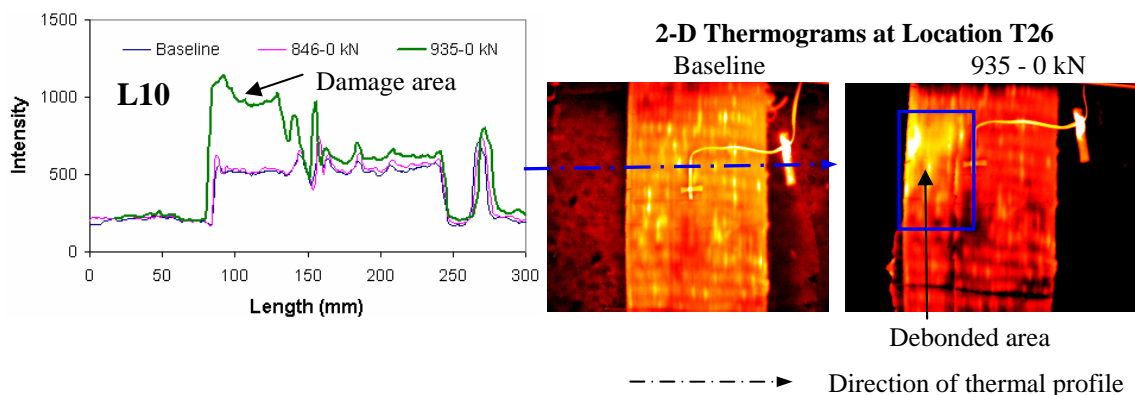


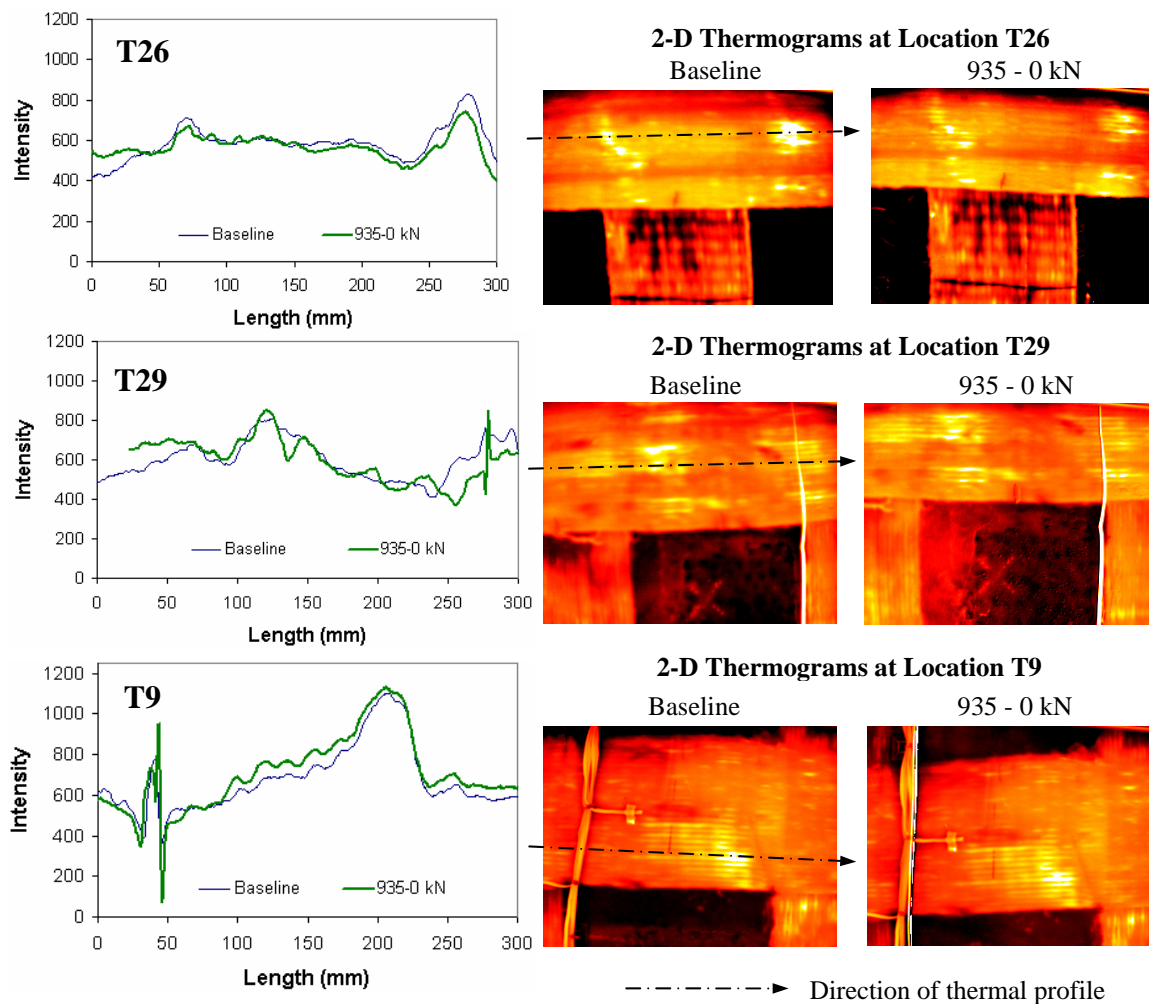
Figure 6.26 Locations of thermography inspections in Slab 2

Although a large number of defects were observed in the baseline thermography inspections almost none of these defects showed any progression with loading. The only exception was at location L10 where a high thermal intensity region indicating debonded area was observed in the inspection carried out after the specimen was unloaded back from failure load at 935 kN (210 kips). This region is presented in Figure 6.27 and was compared with the baseline inspection at the same location. However no other new damage areas were observed in the thermography inspections carried out at the end of each load cycle. The thermal profiles at the locations of the pre-existing defects were monitored and are shown in Figure 6.28. All the thermal profiles were unchanged indicating that there was no appearance of new defects or growth of the existing defects.



Note : 846-0 kN indicates that the inspection was carried out after the specimen was unloaded after loading to 846 kN load cycle

Figure 6.27 Damage area observed after failure at location L10

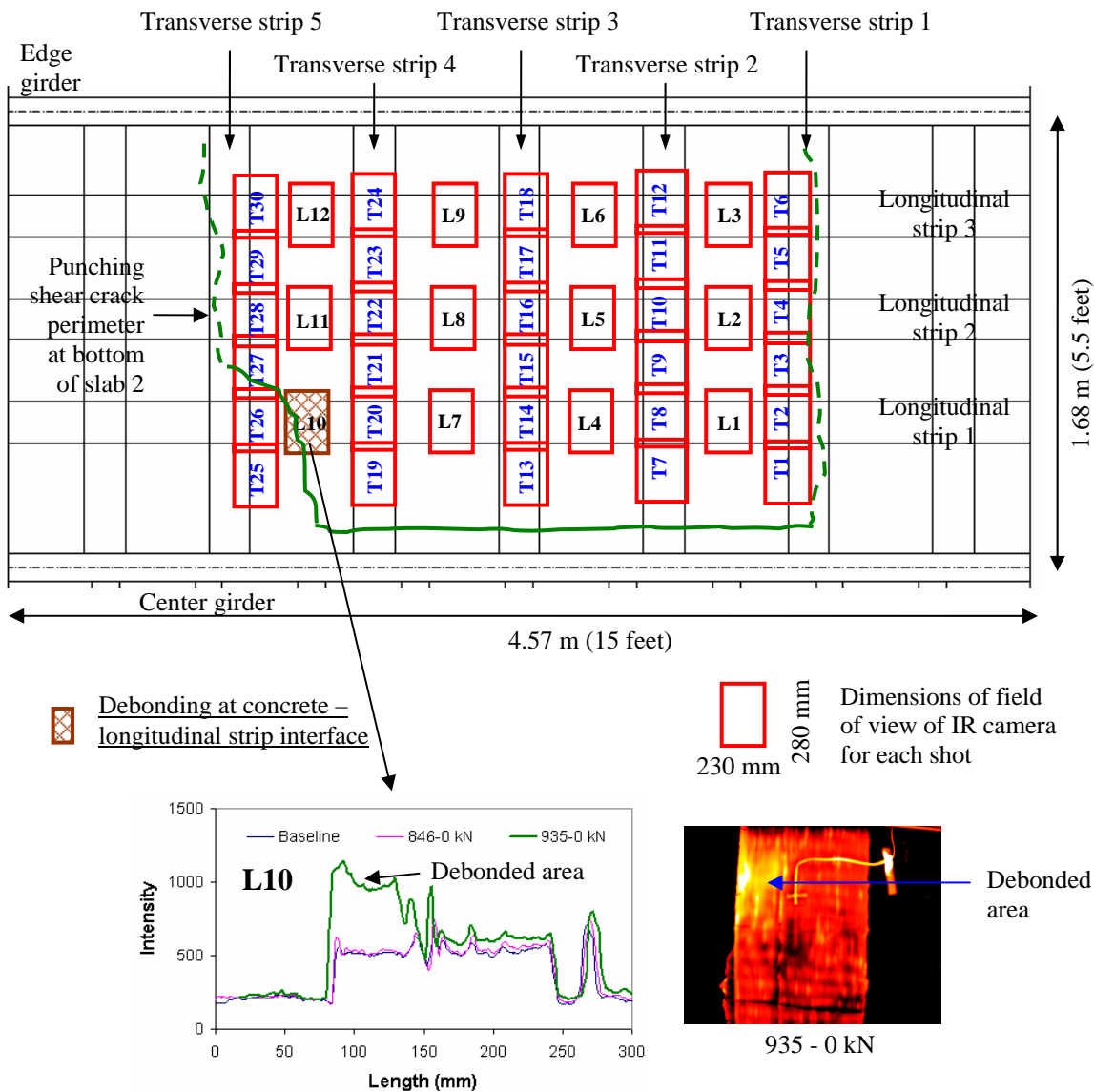


Note : 935-0 kN indicates that the inspection was carried out after the specimen was unloaded after loading to 935 kN load cycle

Figure 6.28 Comparison of inspection results at baseline and after failure

6.6 Comparison of Thermography Results with Crack Patterns in Slab 2

The crack pattern defining the punching shear failure perimeter and the relative locations of the thermography inspections is presented in Figure 6.29.



Note : 935-0 kN indicates that the inspection was carried out after the specimen was unloaded after loading to 935 kN load cycle

Figure 6.29 Comparison of failure perimeter with thermography inspection

The punching shear cracks in the longitudinal direction propagated along the edges of the center and the edge girders. It was discussed in chapter 5 that the wider and more conformable fabric laminates resulted in distribution of load over a larger area in slab 2 as compared to the pultruded strips in slab 1. This caused the punching shear

failure perimeter in the longitudinal direction to be pushed out close to the edges of the girders. The visual observations of these cracks are shown in Figure 6.30. The opening of these cracks resulted in localized debonding at the edges of the transverse composite laminates and ultimate failure of slab 2. Since the perimeter of these cracks was outside the region where the thermography inspections were carried out, insignificant progression of damage areas were observed from the thermography data. The perimeters of the punching shear failure plane at the bottom of slab 2 in the transverse direction went below transverse strips 1 and 5 and are shown by dotted lines in Figure 6.29. The cracks were confined within the laminates and there was no spalling of the cracked concrete. This is shown in Figure 6.30 and explains why no damage was observed in the laminates from the thermography inspections. The region with debonded area at location L10 of thermography inspection was confirmed from the visual observations and is shown in Figure 6.31. Thus for this test, the thermography inspections in slab 2 could not be used for monitoring the damage progression, because of the nature and location of damage associated with this test. However the baseline inspection of pre-existing damage areas showed that if the damage was to occur in the areas of inspection, then it could be used as an effective NDE technique for detection of appearance/progression of damage in composite strengthening.

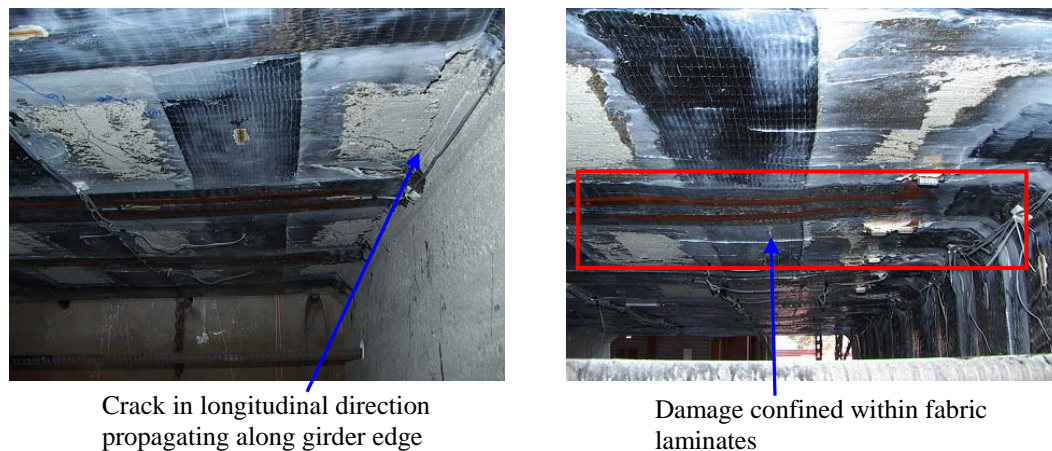


Figure 6.30 Visual inspections of damage regions in slab 2

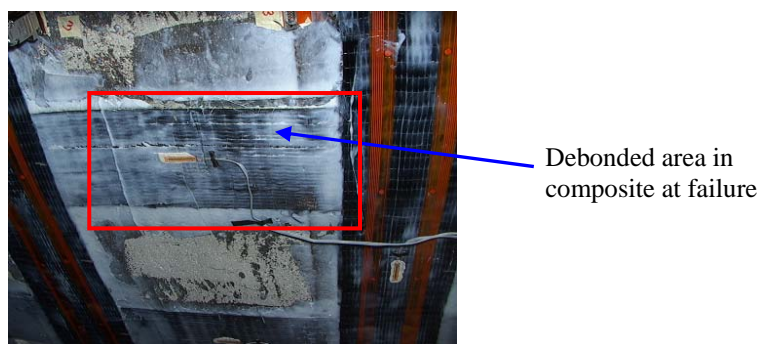


Figure 6.31 Visual inspection of damage at location L10 of thermography inspection

6.7 Conclusions

The thermography results obtained through periodic inspection of the composites in the two deck slabs established its effectiveness as a local NDE technique for detecting and identifying the type of damage as well as localizing and quantitatively monitoring any progression of the damage. Based on the thermal intensity, the damages could be classified into types such as interlaminar debonding inside the composite or composite-concrete interface debonding. Also based on the magnitude of the thermal intensity, the

severity of the damage could be monitored. Thus based on these observations it could be concluded that in a FRP composite strengthened structure once a global NDE (as will be discussed in the chapter 7) is used to identify critical components susceptible to damage, further local monitoring of the damage at the composite-concrete interface level can be carried out with a local NDE such as thermography.

The thermography inspections were most effective in identifying debonded areas and thus all pre-existing defects from the installation phase could be identified and monitored with the progression of loading. However, the failure mechanism of the composite being characterized by sudden debonding failure modes at ultimate load stages, it was not possible to obtain the final damage progression in the composites before failure through the thermography inspections. It can be concluded that thermography can be used more as an instantaneous assessment tool of a FRP composite strengthened structure and for monitoring over time existing defect areas which have the probability of progressing and leading to subsequent failure mechanisms.

7 NON-DESTRUCTIVE EVALUATION (NDE): 2 – MODAL TESTING

7.1 Introduction

Modal testing is generally used in civil engineering to obtain a signature of the dynamic or the vibration behavior of a structure when subjected to low amplitude vibrations. This signature is usually in the form of frequencies and mode shapes of the structure which can be directly related to the stiffness and mass of the structure. The deterioration of the structure under continued loading or modification of the structure in the form of performance enhancement (such as through external strengthening of a structural component with FRP composite) will result in changes in the stiffness of the structure and hence result in changes in frequencies and mode shapes. Further, the locations of the mode shapes where changes are observed will also relate to the areas of deterioration/strengthening in the structure. Thus if a structure is monitored over its life in terms of its vibration characteristics through modal tests, then it is possible to link the changes in the dynamic characteristics to changes in the performance characteristics of the structure. This forms the basis of quantitative non-destructive evaluation of a structure using modal testing. The modal information can be used to identify/estimate the structural parameters of a system. In the method of model updating a suitable baseline model of the structural system is developed using available information in terms of material properties, geometry and boundary conditions of the structure. The dynamic characteristics of this model (in terms of mode shapes and frequencies) can then be compared with the corresponding dynamic characteristics of the actual structure at the beginning of the monitoring period measured by modal testing. The discrepancies

between the results from experimental testing and the analytical model can arise due to simplifications used in developing the analytical model, uncertainties in the structural description in terms of material properties and boundary conditions and experimental errors during the modal testing. Then a least squares estimate is used to update the parameters of the model until a minimum level of discrepancy is present between the model and the structure in terms of modal characteristics. The same principle can be used to update the parameters of the model for subsequent modal testing carried out over the life of the structure with the structure going through deterioration or strengthening. Since the updated parameters represent the deterioration/enhancement of structural characteristics, the updated analytical model at each stage of system identification through non-destructive modal testing will be able to better represent the behavior of the actual structure with the current state of damage/strengthening. The principles of system identification will be discussed later in this chapter.

7.2 Current Modal Test Objectives

The test specimen was subjected to a number of monotonic load cycles defined by critical limit states that resulted in damage localization and progression in the slab and girder components over the three load stages as defined in Table 4.2 in chapter 4. The slabs and center girder were also strengthened with FRP composite at the end of phase 1 and 2 loading, respectively. Modal testing was carried out at the end of each load cycle as well as after strengthening of the individual slab and girder components. The stages at which the modal tests were carried out are shown in Table 7.1.

The objectives of the modal tests were:

- i) To determine the dynamic characteristics of the structure (frequencies and mode shapes) and to evaluate the effect of damage/strengthening on them;
- ii) To use model updating techniques to calibrate a baseline finite element model based on these dynamic characteristics obtained from the experimental modal tests carried out on the original test specimen prior to loading;
- iii) To use model updating in subsequent loading and strengthening stages to determine the changes in parameters in localized regions of the model corresponding to the changes in the frequencies and mode shapes obtained from the experimental modal test results representing damage or strength enhancement in the test specimen over the load stages;
- iv) To localize the effects of damage progression and strengthening during the test through quantification of the parameter changes over regions of the test specimen in between subsequent load stages;
- v) To compare the behavior of the test specimen in terms of stiffness degradations/enhancements over the load stages as obtained from experimentally measured data with the predicted behavior obtained from successively updated FE models over the load stages.

Table 7.1 Load stages at which modal testing was carried out

Test #	Test Phase	Load Stage	Remarks
1	Phase 1	Baseline test – Phase 1	Modal test carried out to identify parameters of the baseline model before loading of test specimen
2		214 kN (48 kips) load cycle	Modal test carried out after unloading the specimen after returning back from the 214 kN load cycle
3		289 kN (65 kips) load cycle	Modal test carried out after unloading the specimen after returning back from the 289 kN load cycle
4		400 kN (90 kips) load cycle	Modal test carried out after unloading the specimen after returning back from the 400 kN load cycle
5	Phase 2	Baseline test – Phase 2	Modal test carried out after strengthening of the slabs with FRP composite systems
6		400 kN (90 kips) load cycle	Modal test carried out after unloading the specimen after returning back from the 400 kN load cycle
7		579 kN (130 kips) load cycle	Modal test carried out after unloading the specimen after returning back from the 130 kN load cycle
8		667 kN (150 kips) load cycle	Modal test carried out after unloading the specimen after returning back from the 150 kN load cycle
9	Phase 3	Baseline test – Phase 3	Modal test carried out after strengthening of the center girder with FRP composite stirrups
10		667 kN (150 kips) load cycle	Modal test carried out after unloading the specimen after returning back from the 150 kN load cycle
11		757 kN (170 kips) load cycle	Modal test carried out after unloading the specimen after returning back from the 170 kN load cycle
12		846 kN (190 kips) load cycle	Modal test carried out after unloading the specimen after returning back from the 190 kN load cycle

7.3 Theoretical Basis of Modal Analysis

The theoretical background of modal testing can be found in [71, 72, 73] on the basis of which the modal analysis techniques can be divided into two categories: i) Frequency domain and ii) Time domain. Also the algorithms for identification of modal properties are divided into: i) Input-output excitation methods in which a forcing function is introduced to excite the structure and ii) Output only excitation methods in which ambient excitation in the form of vehicular traffic, wind, ocean waves, etc. are used to excite the structure. For the current study a frequency domain modal analysis using an input-output excitation method was used to extract the modal characteristics (frequencies and mode shapes). The basic underlying principle of frequency domain analysis used is outlined next. The equation of motion can be written as:

$$m\ddot{x} + c\dot{x} + kx = f(t) \dots\dots\dots(7.1)$$

where, m , c and k are the mass, damping co-efficient and stiffness matrices and \ddot{x} , \dot{x} , x and $f(t)$ are the acceleration, velocity, displacement and force vectors respectively. Using the Laplace domain approach, the Laplace transforms of acceleration, velocity, displacement and force can be expressed as:

$$L(\ddot{x}) = s^2 x(s) - sx_0 - \dot{x}_0 \dots\dots\dots(7.2i)$$

$$L(\dot{x}) = sx(s) - x_0 \dots\dots\dots(7.2ii)$$

$$L(x) = x(s) \dots\dots\dots(7.2iii)$$

$$L(f(t)) = f(s) \dots\dots\dots(7.2iv)$$

where, the 0 subscript denotes an initial condition.

Thus taking the Laplace transform, equation 7.1 becomes,

$$(ms^2 + cs + k)x(s) = f(s) + (ms + c)x_0 + m\dot{x}_0 \quad \dots\dots\dots(7.3)$$

Using the initial velocity and displacement conditions to be zero and letting

$(ms^2 + cs + k) = b(s)$, equation 7.3 can be written as:

$$b(s)x(s) = f(s) \quad \dots\dots\dots(7.4)$$

$$\text{or, } x(s) = h(s)f(s) \quad \dots\dots\dots(7.5)$$

$$\text{where, } h(s) = b^{-1}(s) = \frac{1}{ms^2 + cs + k} \quad \dots\dots\dots(7.6)$$

and is known as the system transfer function.

The system transfer function given by equation 7.6 is a complex valued function and produces a surface plot with σ and $j\omega$ axis, above the s - plane. The system transfer function can be expressed in a number of forms, one of them being the partial fraction form, where the expression contains contributions from the root (or pole, p) and its complex conjugate and can be written as:

$$h(s) = \frac{a_1}{s - p_1} + \frac{a_1^*}{s - p_1^*} \quad \dots\dots\dots(7.7)$$

where, p_1 is the pole and a_1 is the residue which can be obtained when the system transfer function is evaluated at p_1 . Thus a system transfer function can be obtained in terms of its pole and residue and when this function is evaluated along $s = j\omega$, it is referred to as the “Frequency Response Function” and is given by:

$$h(j\omega) = \frac{a_1}{j\omega - p_1} + \frac{a_1^*}{j\omega - p_1^*} \quad \dots\dots\dots(7.8)$$

Thus the frequency response function is equivalent to a slice taken out of the system transfer function surface. The point-to-point frequency response function which refers to the response at point i due to input at point j for m modes can then be written as:

$$h(j\omega)_{ij} = \sum_{k=1}^m \frac{a_{ijk}}{j\omega - p_k} + \frac{a_{ijk}^*}{j\omega - p_k^*} \dots\dots\dots(7.9)$$

In the current study modal testing was carried out by exciting the structure using three different point excitation sources as was discussed in section 4.8.4 of chapter 4 and the excitation signatures will be presented later in this chapter. Accelerometers distributed over the surface of the test specimen in the setup as described earlier (in section 4.8.4 of chapter 4) were used to collect acceleration time history data resulting from the vibration produced by the excitation source. The modal data was then analyzed in the frequency domain following the methodology described above to generate a mathematical function expressing the frequency response function by fitting the measured data to this relationship using curve-fitting. Thus once the point-to-point frequency response function is measured it is possible to extract the system parameters in the form of frequencies and mode shapes using modal parameter extraction techniques. In the current study the MDOF-polynomial method was used for the extraction of the modal parameters using a least squares error curve fitting algorithm to estimate the numerator and denominator polynomial coefficients of an analytical FRF model from experimental data. The numerator and denominator coefficients were then processed to obtain modal parameters. All the above analysis was performed using a commercially available software, MEScope VES [74]. The results from the modal testing will be presented in this chapter in the form of frequency response function magnitude plots which indicate the

identified frequencies of the test specimen over the load stages and mode shape plots over the load stages of modal testing as listed in Table 7.1.

7.4 Test Setup and Input-Output Data

The test setup with the locations of the accelerometers was described earlier in chapter 4 and is repeated here for reference in Figure 7.1. 25 accelerometers as numbered in Figure 7.1 were distributed over the top surface of the test specimen, with the exception of accelerometers at 8 and 18 which were at the locations of the actuator loads and thus were placed at the bottom of the slabs. The description of the accelerometers was presented in chapter 4. The location of the excitation source was chosen next to the accelerometer location at 7 so as to excite the higher order vibration modes in both the longitudinal and transverse direction of the test specimen. Three different excitation sources were chosen for comparative evaluation of the modal characteristics obtained from these sources. The three sources used were: i) A drop hammer with a mass of 22.2 kg (60 lbs) dropped from a height of 640 mm (25.5”) producing an average impact force of 7.6 kN (1.7 kips); ii) A small impact hammer with maximum impact force of 2.2 kN (500 lbs) and iii) A shaker with maximum impact force of 0.2 kN (50 lbs). The excitation sources were shown in Figure 4.36 of chapter 4. In the current study, the modal testing results using the shaker excitation will be used as the primary data for determination of the modal characteristics (frequencies and mode shapes) over all the load stages as shown in Table 7.1 due to the inherent advantages of using the shaker as a source of excitation (as will be presented next in this chapter). Thereafter the model updating will also be based on the modal parameters obtained from the data using the shaker excitation. The

modal parameters extracted from the modal testing data using the impact and drop hammer excitations will only be used for comparisons with those from the shaker excitations at the three baseline stages, namely before loading the specimen, after strengthening of the slabs and after strengthening of the center girder for comparative evaluations of the three excitation sources.

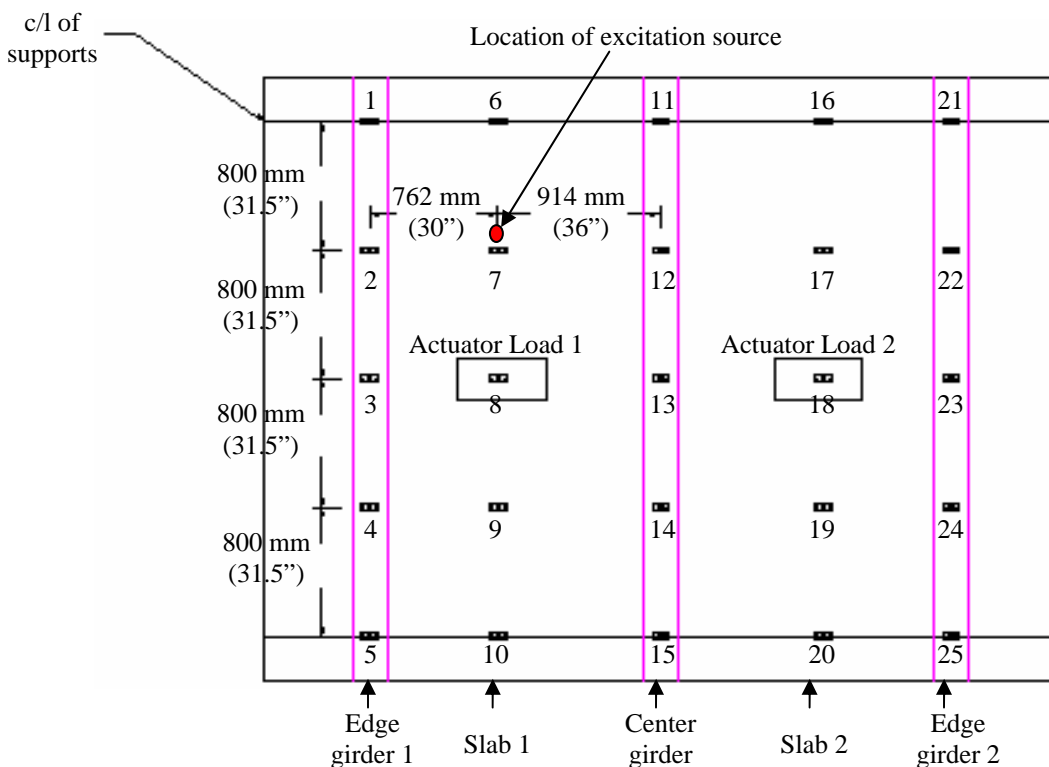
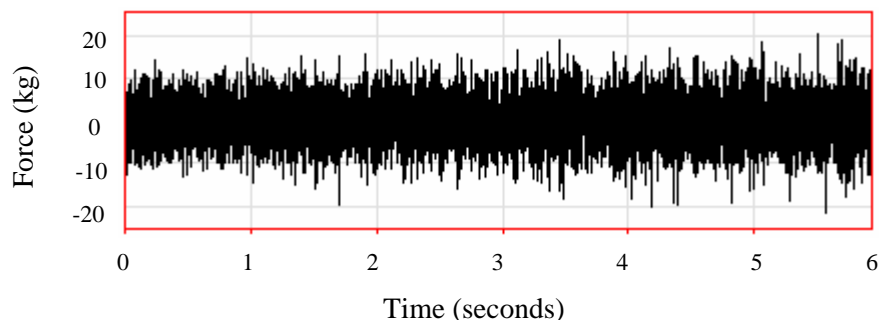


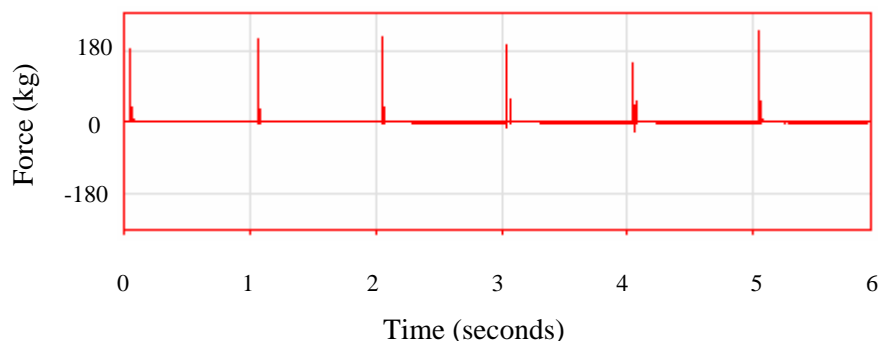
Figure 7.1 Test setup with locations of accelerometers and excitation source

Typical force inputs from the three excitation sources at location 7 are shown in Figure 7.2. The shaker force input was Gaussian random white noise over 250 seconds duration with maximum force input of 22 kg (50 lbs). The impact hammer had a maximum force input of 225 kg (500 lbs) and a sequence of 25 such impacts at about 1 second time intervals were carried out for each run so that the 25 separate acceleration

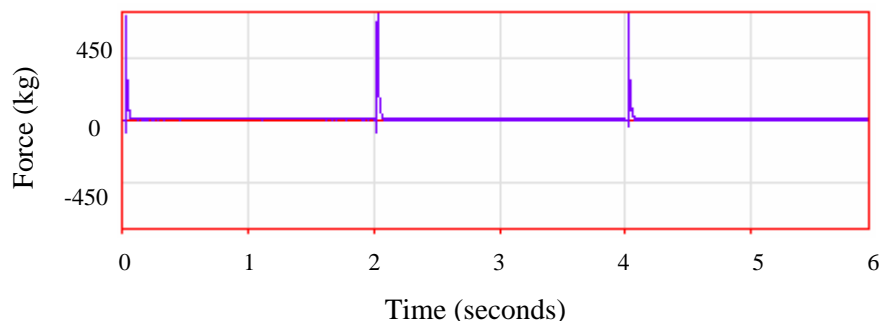
histories could be averaged. The drop hammer had an average force input of 770 kg (1700 lbs) and a sequence of 25 such impacts at about 2 second time intervals were also carried out for each run.



(a) Force input by shaker excitation



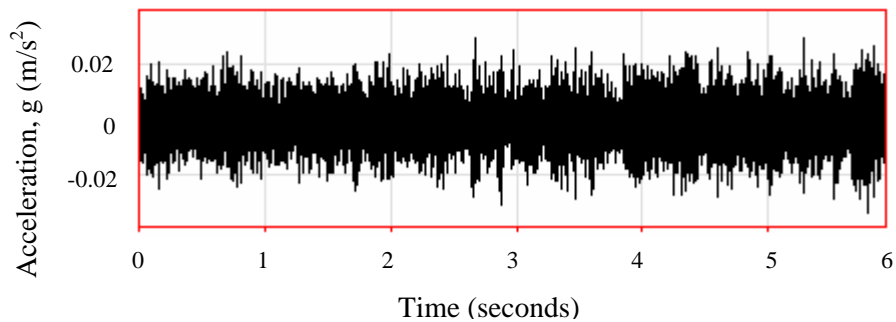
(b) Force input by impact hammer



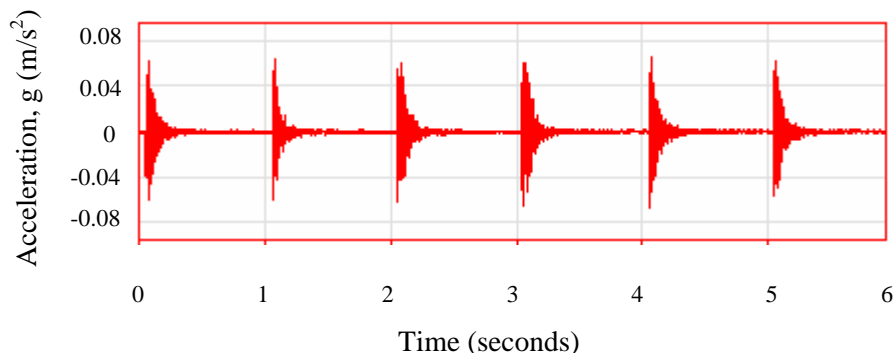
(c) Force input by drop hammer

Figure 7.2 Typical force input by the three excitation sources

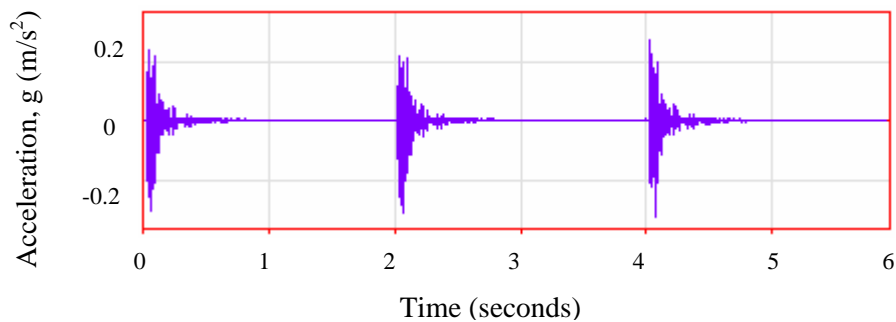
The typical acceleration time histories recorded by the accelerometers for the three excitation sources is presented in Figure 7.3.



(a) Acceleration history for shaker excitation



(b) Acceleration history for impact hammer



(c) Acceleration history for drop hammer

Figure 7.3 Typical acceleration time histories for the three excitation sources

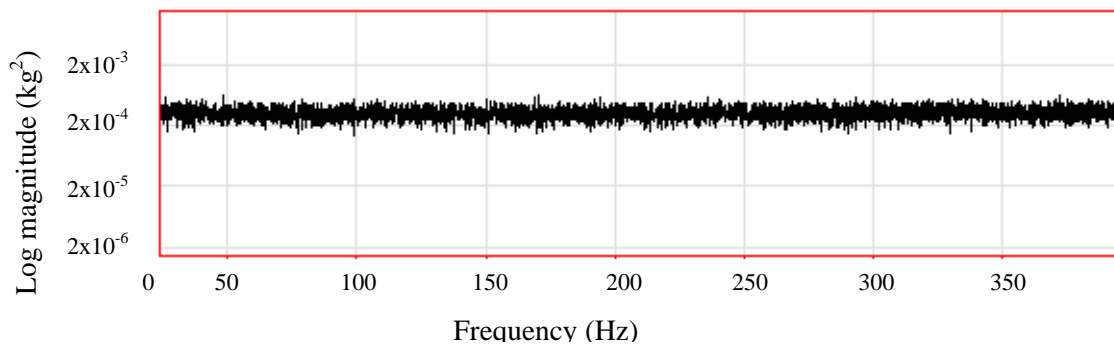
Based on the time histories and the number of samples for each excitation, the frequency resolution, Δf for each excitation can be written as:

$$\Delta f = \frac{1}{T} \quad \dots\dots\dots(7.10)$$

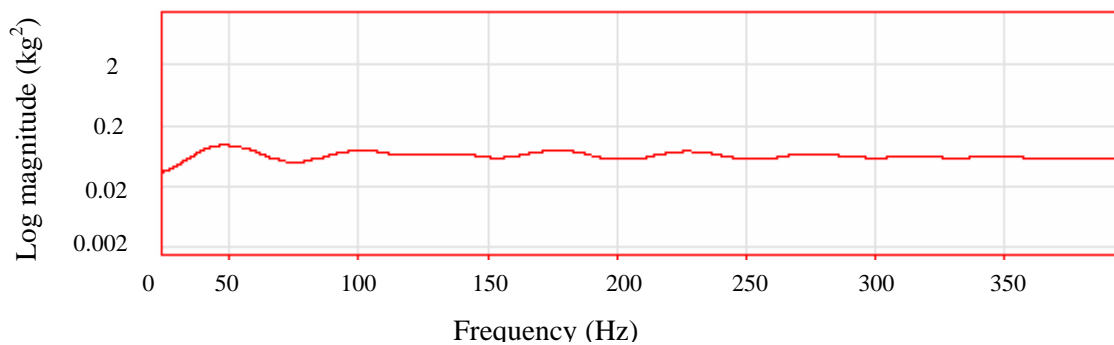
where T is the time period of excitation. The impact hammer and the drop hammer had a duration of about 1 and 2 seconds, respectively of acceleration time history for each impact resulting in a frequency resolution of the signals of 1 Hz and 0.5 Hz, respectively. The shaker excitation had acceleration time history duration of 250 seconds during which analysis was broken up into 25 data blocks each with 20 seconds duration (with about 50% overlap for each block) resulting in a frequency resolution of 0.05 Hz. This was the first advantage of using the shaker excitation over the impact hammer and drop hammer excitations. The higher frequency resolution obtained in the modal analysis of data from shaker excitations would help to better identify the changes in the frequencies of the test specimen produced by damage or strengthening over load stages as defined in Table 7.1.

The force spectrum of the three excitation sources is presented in Figure 7.4. The shaker force spectrum was found to remain constant within a wide frequency range (20 Hz to 500 Hz). In the case of the impact hammer the force spectrum was flat within a frequency range of 20 Hz to 400 Hz. However for the drop hammer the force spectrum was found to drop sharply after 100 Hz indicating that it lacks input in the high frequency region. As will be presented in the subsequent section, since the test specimen was a segment of a full-scale slab-girder bridge it was stiffer and thus the natural frequencies were higher as compared to an actual bridge. The first four primary modal frequencies as obtained from the modal analysis of the test specimen (as presented in the next section)

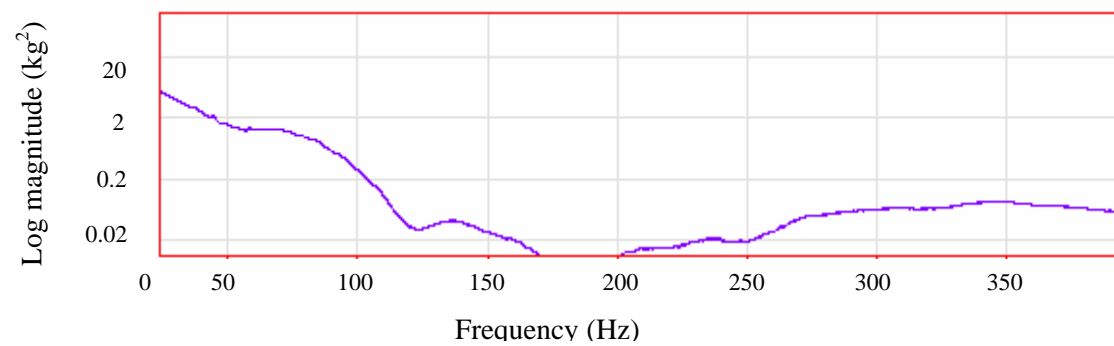
were in the range of 40 Hz to 150 Hz and thus the drop hammer was deemed to be unsuitable with the higher end of the frequency range associated with the test specimen.



(a) Force spectrum for shaker excitation



(b) Force spectrum for impact hammer



(c) Force spectrum for drop hammer

Figure 7.3 Typical force spectrum for the three excitation sources

Even though the impact hammer had a reasonably flat force spectrum between 20 Hz to 400 Hz, it was found to have a poor signal to noise ratio and being a hand-held device there was a lack of control over frequency content since it was very difficult to input an uniform impact energy. Based on all the above considerations, the shaker was chosen as the primary mode of excitation for the modal tests. However for comparative evaluations, modal tests using the impact and drop hammer excitations were also carried out.

7.5 Modal Test Results

The modal test data obtained over the load stages (as was presented in Table 7.1) as acceleration time histories and shaker force input time histories were analyzed following the principles discussed in section 7.3 to extract the modal parameters (frequencies and mode shapes). The FRF magnitude plots obtained over the three phases of loading are shown in Figures 7.4, 7.5 and 7.6. The primary natural frequencies extracted from the FRF plots over the load stages are presented in Table 7.2. In order to examine the trend of the natural frequencies with damage progression/strengthening in the test specimen, the frequency ratio was calculated for the primary identified vibration modes, defined as the ratio of the frequency obtained at a particular load stage to the baseline frequency of the structure obtained prior to loading. The trend of the frequency ratio thus provides an estimate of the change in the natural frequency of the structure as compared to the baseline frequency of the virgin structure, caused by damage/strengthening over the load stages. The trend of frequency ratio is presented in Figure 7.7.

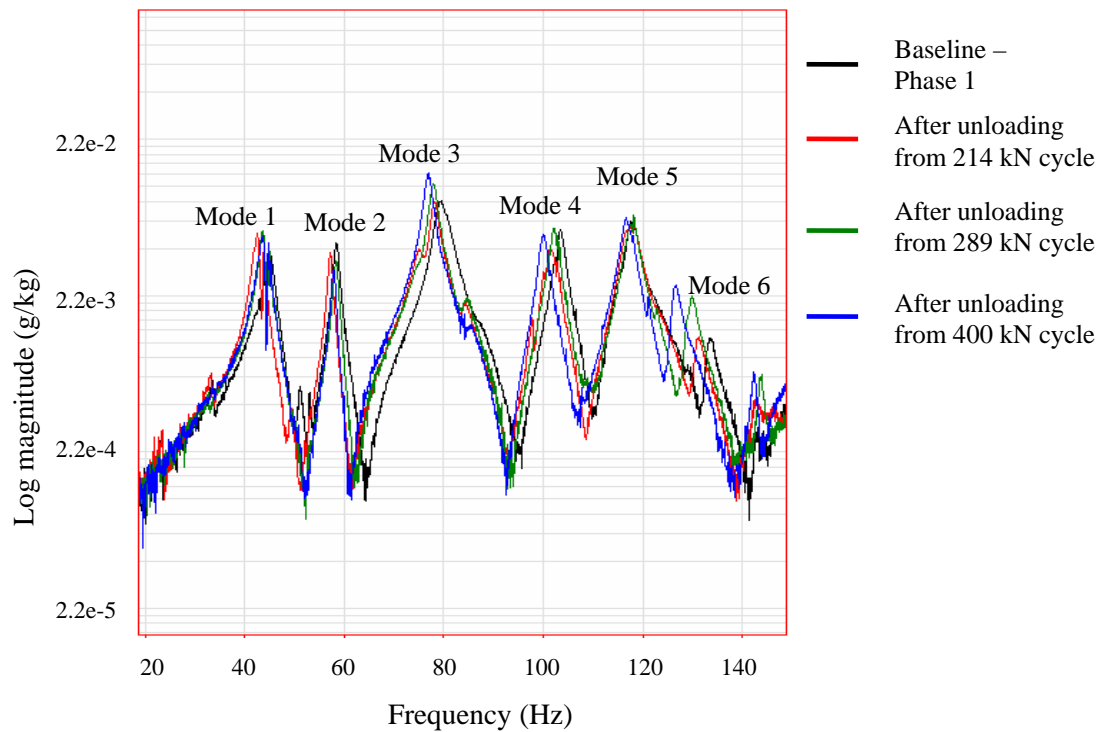


Figure 7.4 FRF magnitude plots for Phase 1 of testing

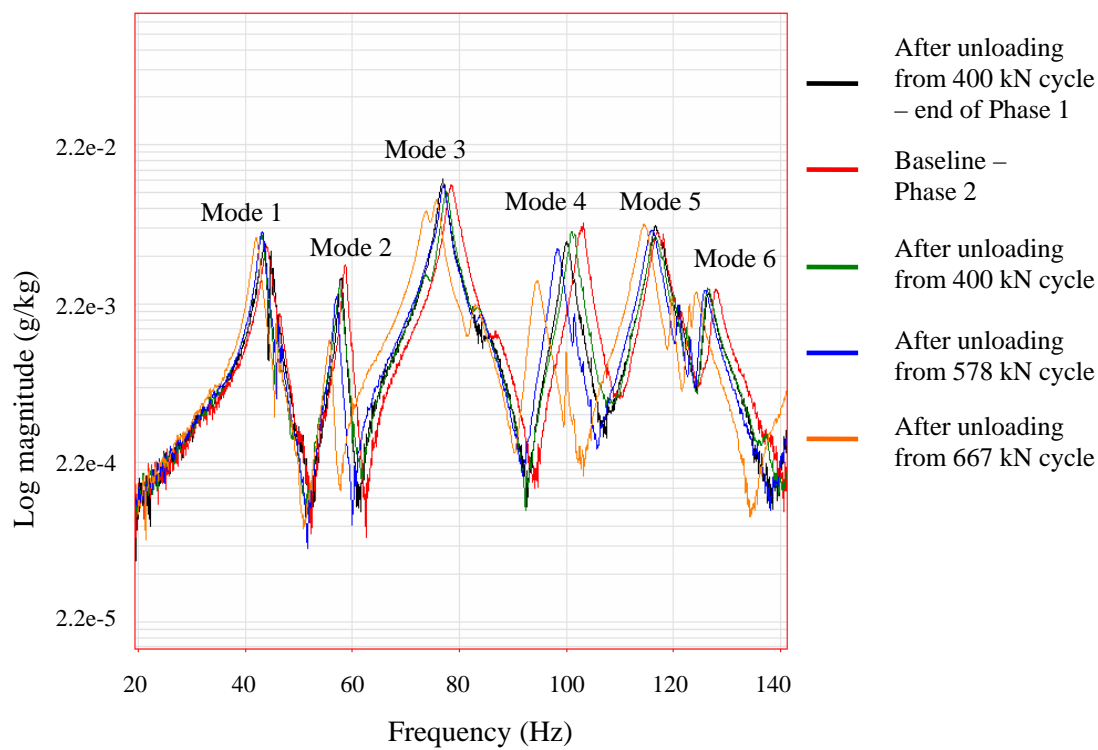


Figure 7.5 FRF magnitude plots for Phase 2 of testing

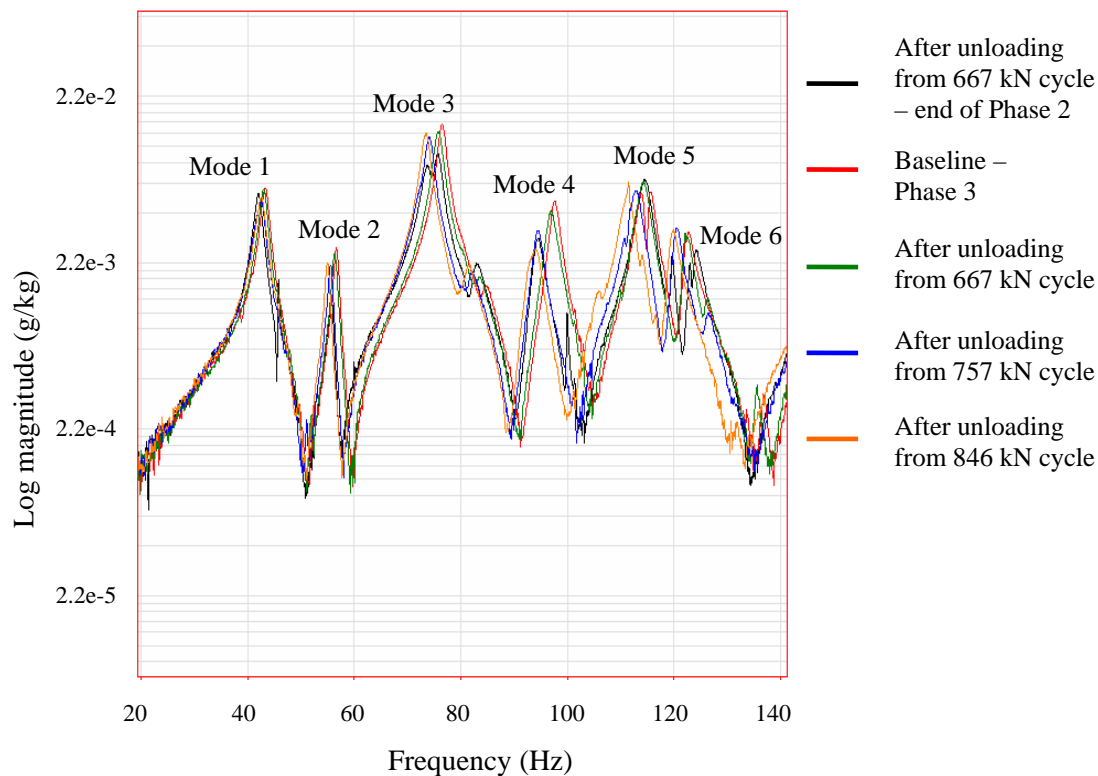


Figure 7.6 FRF magnitude plots for Phase 3 of testing

Table 7.2 Natural frequencies of the test specimen over the load stages

Load Stage	Mode 1	Mode 2	Mode 3	Mode 4	Mode 5	Mode 6
Phase I Baseline	45.048	58.434	80.056	103.43	117.54	133.1
After unloading from 214 kN	42.543	57.233	77.932	101.55	116.89	130.84
After unloading from 289 kN	43.822	58.414	77.908	102.23	117.46	130.11
After unloading from 400 kN	43.851	57.869	76.954	100.04	116.66	126.26
Phase II Baseline	43.956	58.636	78.488	103.15	116.97	127.69
After unloading from 400 kN	43.156	57.703	77.533	100.96	116.53	126.2
After unloading from 578 kN	43.203	57.025	76.977	98.301	115.95	125.62
After unloading from 667 kN	42.041	55.751	75.653	94.356	114.56	123.86
Phase III Baseline	43.38	56.682	76.451	97.513	115.36	122.53
After unloading from 667 kN	43.022	56.355	75.75	96.821	114.29	125.8
After unloading from 757 kN	42.657	55.65	74.636	94.338	112.79	123.3
After unloading from 846 kN	42.693	55.018	73.436	93.35	111.67	119.59

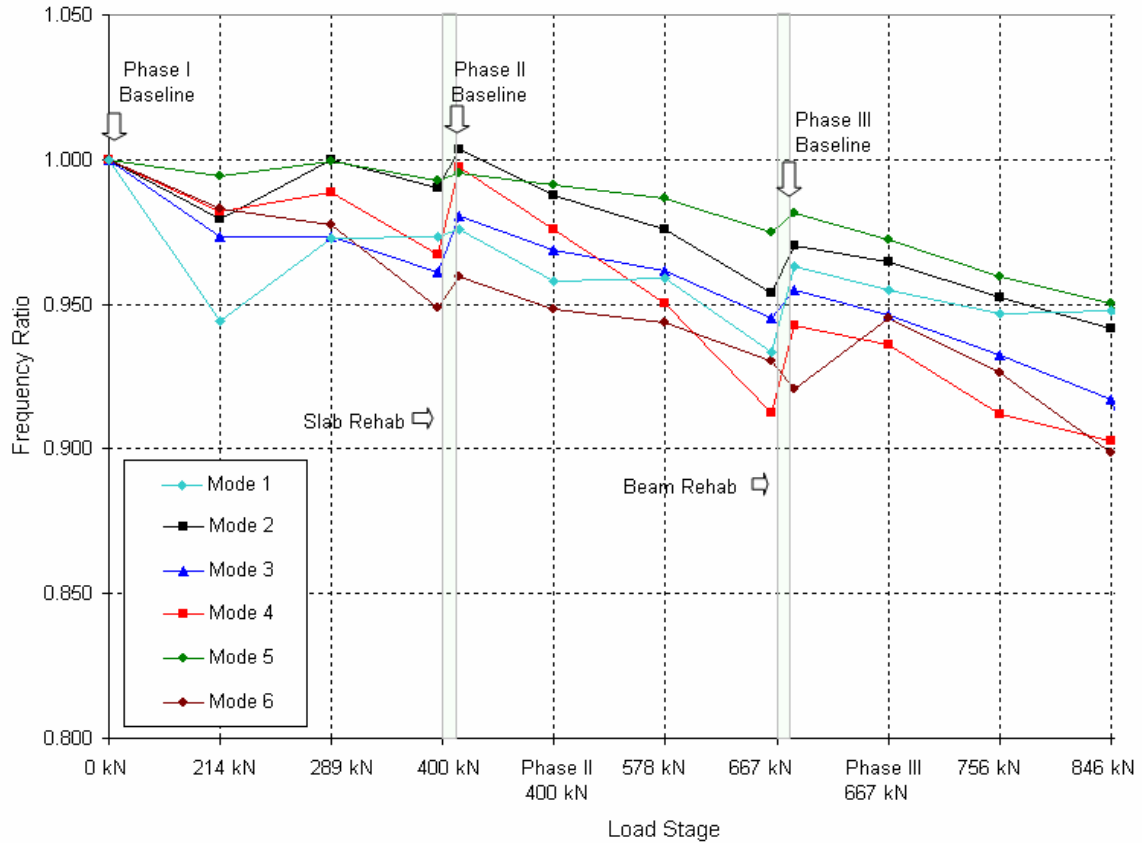


Figure 7.7 Trend of frequency ratio over the load stages

From Table 7.2 and Figure 7.7 a general trend of decrease of the natural frequency was observed over all the load stages indicative of damage progression in the test specimen since the frequency is directly related to the stiffness of the structure. Also an increase of the natural frequency was observed corresponding to results from baseline 2 and baseline 3, obtained after strengthening of the deck slabs and the center girder, respectively. The trend of the frequencies only gave an indication on the general behavior of the structure. However the stiffness degradations/enhancements in specific components of the structure due to damage/strengthening leading to such frequency

changes could only be identified through model updating as will be discussed in subsequent sections of this chapter.

As mentioned in section 7.3, three excitation sources, shaker, impact hammer and drop hammer were used and due to better suitability and accuracy, the shaker was chosen as the primary excitation source to extract the modal parameters. However a comparative evaluation of the three excitation sources was carried out from the results obtained from the three baseline inspections in terms of FRF magnitudes and are presented in Figures 7.8, 7.9 and 7.10. The FRF of the shaker and impact hammer matched relatively well in terms of general shape and peak (mode) location. However as discussed earlier, the shaker had higher frequency resolution and revealed more details around resonant peaks. FRF of drop hammer showed deviation from the other two, possibly due to the additional mass loading of the drop hammer. Comparison of FRF and modal parameters should thus be limited to the same excitation source and for the current study the shaker was chosen.

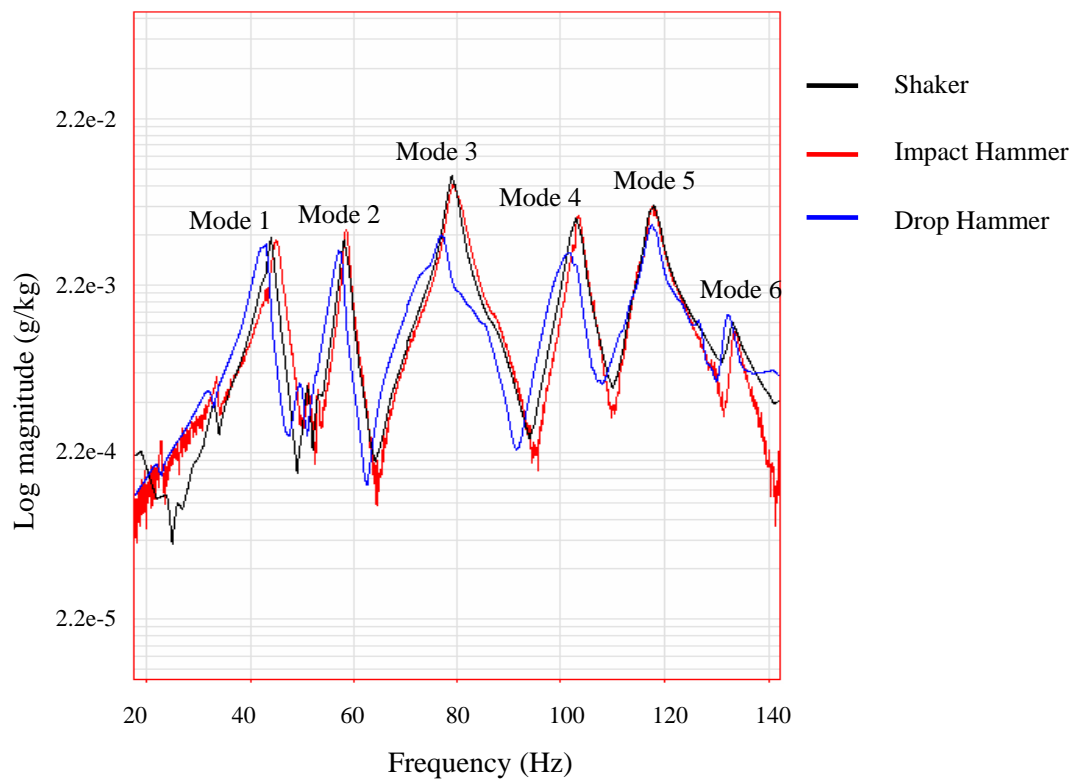


Figure 7.8 FRF comparisons from baseline 1 modal test for shaker and hammers

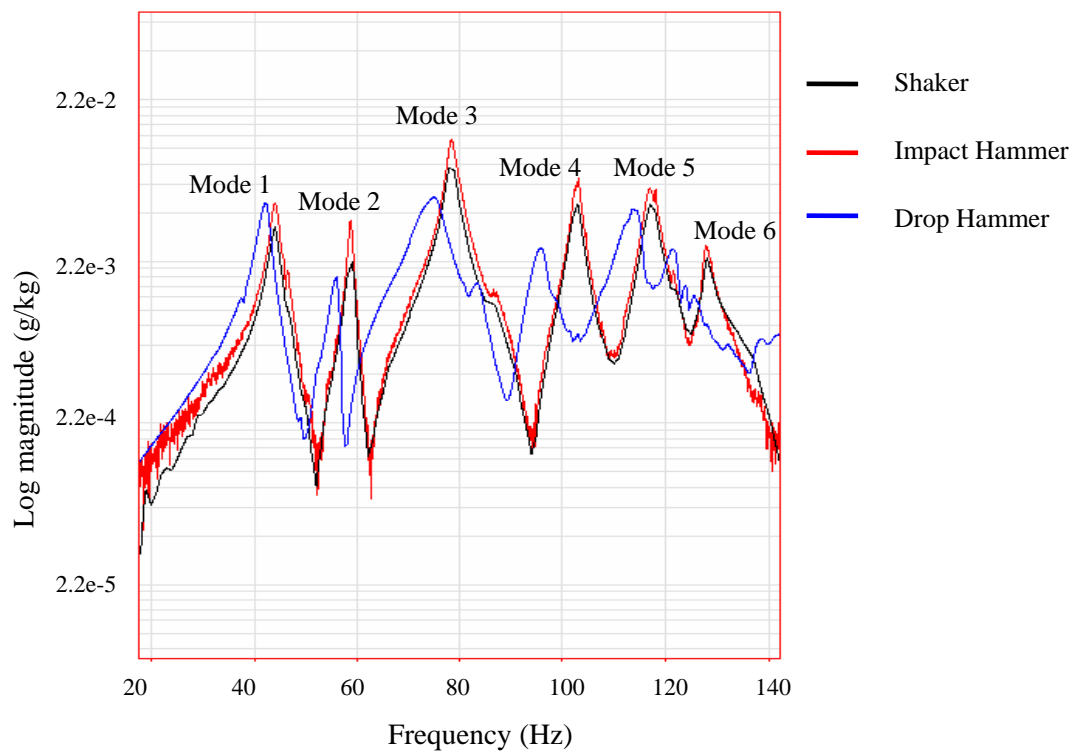


Figure 7.9 FRF comparisons from baseline 2 modal test for shaker and hammers

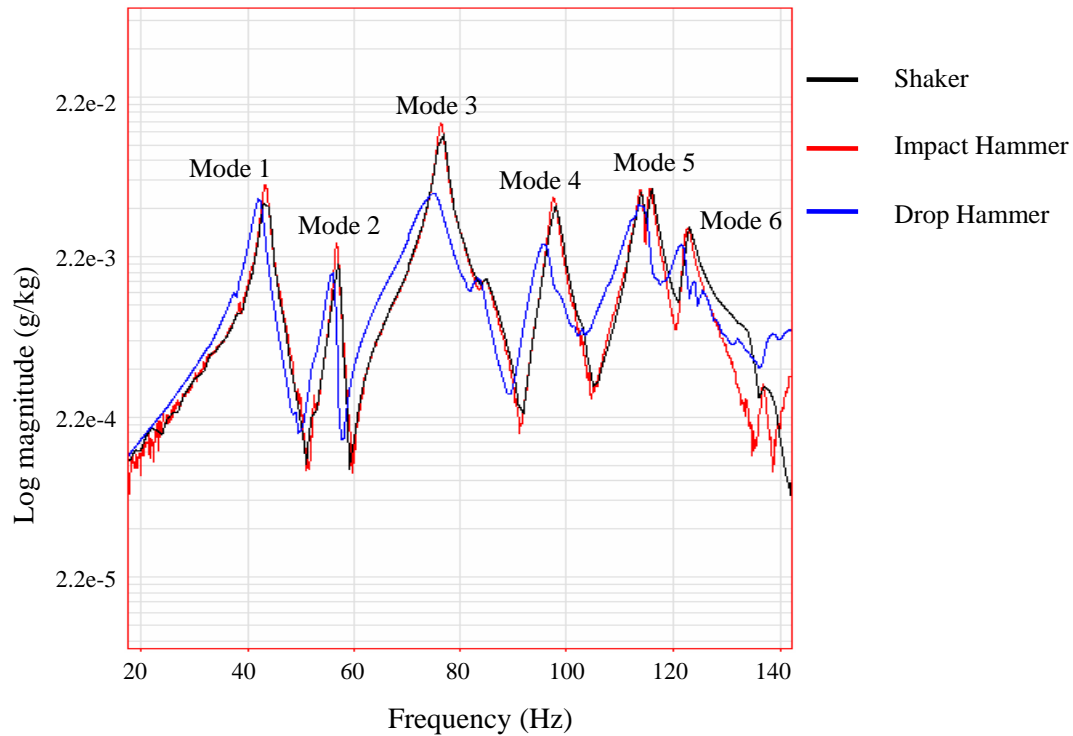


Figure 7.10 FRF comparisons from baseline 3 modal test for shaker and hammers

The mode shapes of the structure corresponding to the natural frequencies were then extracted and the mode shapes from baseline 1 test results are presented in Figure 7.11. These six primary modes identified, represented: i) Local bending mode; ii) 1st transverse bending mode; iii) 2nd transverse bending mode; iv) 1st torsion mode; v) 2nd torsion mode; and vi) 3rd transverse bending mode. For an indeterminate structure such as the test specimen it is possible to have the influence of bending on torsion or vice versa and thus it was necessary to determine if the primary modes identified were pure bending or torsion modes. This was verified from the complexity plots of the mode shapes also presented in Figure 7.11. A complexity plot displays the magnitudes and phases of the shape components of the selected mode shapes as vectors. For pure bending or torsion,

the shape will be a “normal” shape and all the shape components will have 0 or 180 degrees of phase relative to one another. However an interaction of bending and torsion or other local modes will result in a “complex” shape which will have arbitrary phases in its shape components. From Figure 7.12, modes 1, 2, 4 and 6 were found to have “normal” shapes indicating that they were purely bending or torsion modes, while modes 3 and 5 were found to have “complex” shapes. The mode shapes and the complexity plots obtained for the six primary modes from the modal tests carried out at the other load stages throughout the test are presented in Appendix A in Figures A.1 to A.11. Based on the complexity plots obtained for the six modes over all the load stages (Figures A.1 to A.11), modes 1, 2, 4 and 6 were found to be relatively “normal” modes and thus were used in model updating as will be discussed in section 7.6. The other two modes (modes 3 and 5) were found to be “complex” shapes and were excluded from model updating. It is to be noted that this decision to use modes 1, 2, 4 and 6 for model updating were based on the complexity of the model shapes observed over all the load stages and these 4 modes were judged to be relatively normal as compared to modes 3 and 5. The modal amplitudes of these 4 normal modes over all the load stages are given in Table A.1 of Appendix A.

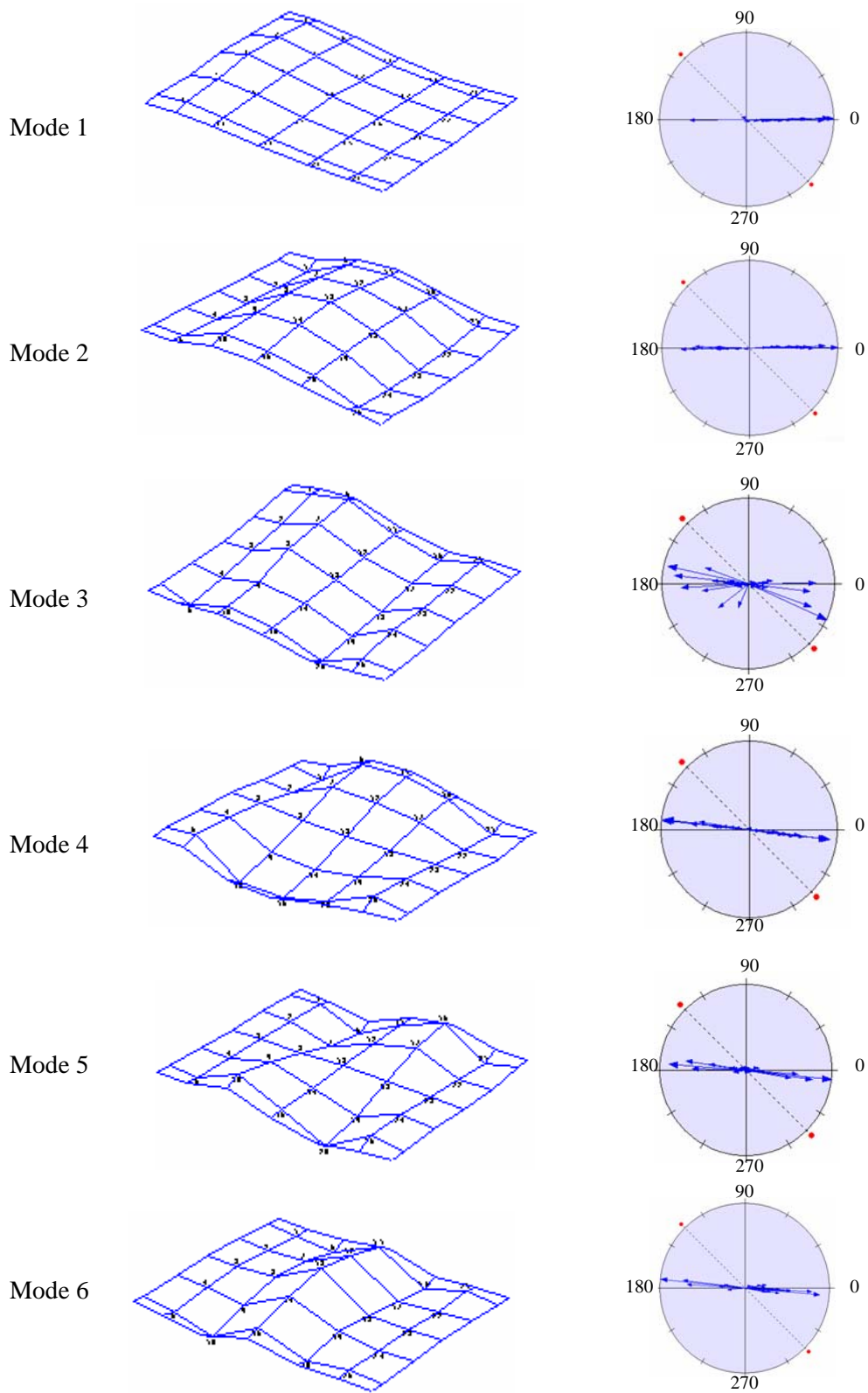


Figure 7.11 Mode shapes and complexity plots from baseline 1 modal test results

7.6 Finite Element Modeling and Initial Parameter Estimation

A three dimensional finite element model of the test specimen was created using the SAP2000 FEA program [75]. Four noded shell elements were used to model the concrete slabs and beams, the supports at the ends of the beams were modeled by linear elastic spring elements and the tie rods in the transverse direction passing through holes at the ends of the girders simulating diaphragm behavior was modeled by linear elastic link elements. The details of the material properties used for the elements will be presented next in this chapter. The model is shown in Figure 7.12 and the x, y and z axis in the model represent the transverse, longitudinal and thickness directions of the test specimen.

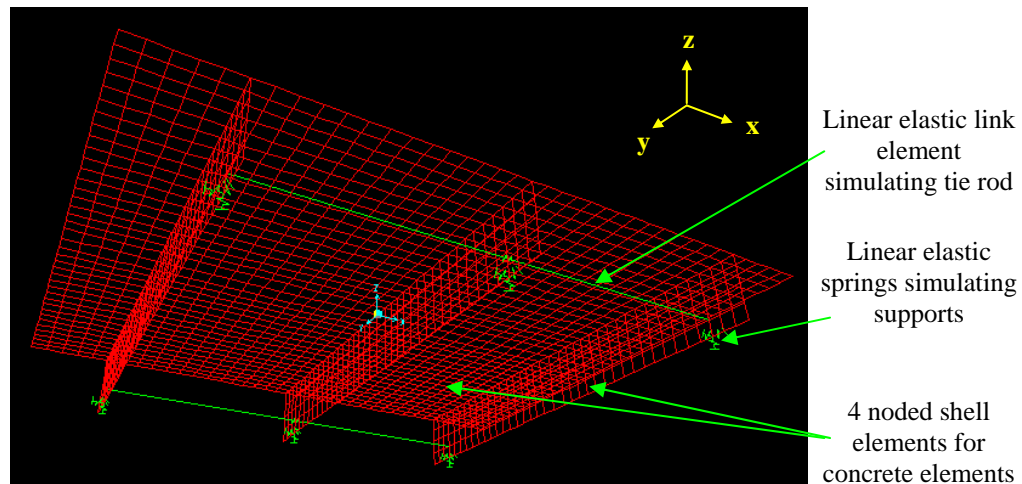


Figure 7.12 Finite element model of the test specimen

The concrete material behavior was assumed to be linear elastic, isotropic and homogeneous. The mass density of concrete was taken to be 2400 kg/m^3 (150 lb/ft^3). The initial estimate of the reinforced concrete modulus of elasticity was based on calculating a transformed modulus of elasticity for reinforced concrete based on the reinforcement

details of the slabs and the beams. The modulus of elasticity of plain concrete with an experimentally determined (as presented in Chapter 4) concrete compressive strength of 44 MPa (6390 psi) was estimated as follows:

$$E_c = 4730\sqrt{f'_c} = 31.4 \text{ GPa (4556 ksi)} \quad \dots\dots\dots(7.11)$$

The cross-sectional reinforcement details of the slabs and the beams were presented earlier in Chapter 4 and based on the elastic modulus of the steel reinforcement of 200 GPa (29000 ksi), the modular ratio, m , was defined as:

$$m = \frac{E_s}{E_c} = \frac{200}{31.3} = 6.38 \quad \dots\dots\dots(7.11)$$

The transformed elastic modulus of reinforced concrete of the slabs and the beams was then computed based on the transformed moments of inertia of the reinforced concrete sections and are presented in Table 7.3.

Table 7.3 Estimated reinforced concrete properties for slab and beam elements

Element type	Gross moment of inertia $\text{m}^4 (\text{in}^4)$	Transformed moment of inertia $\text{m}^4 (\text{in}^4)$	Elastic modulus of plain concrete GPa (ksi)	Transformed RC elastic modulus GPa (ksi)
Slab	9e-5 (216)	9.66e-5 (232.2)	31.4 (4556)	33.7 (4898)
Beam	2.95e-3 (7099)	4.24e-3 (10178)	31.4 (4556)	45.1 (6532)

This transformed elastic modulus of reinforced concrete was assigned as the elastic modulus for the slab and beam shell elements. Also the stiffness of an element, k , can be written as the product of the elastic modulus, E , and the moment of inertia, I . The progression of damage in an element or strengthening of the element with FRP composite

will result in changes in the moment of inertia, I . However since changing the moment of inertia by reducing or increasing the size of the elements becomes cumbersome and time consuming in a finite element analysis, the elastic modulus, E , was used as the variable parameter which would represent equivalent changes in the stiffness, EI , caused by changes in I . Thus the modulus was treated as an “effective” elastic modulus and would be updated during the load stages to take into account degradation or strengthening of the test specimen.

The stiffness of the link element simulating the tie rod connecting the ends of the edge girders at each end of the specimen (as shown in Figure 7.4) was determined based on the cross-sectional property and elastic modulus of the tie rod. The 38 mm (1.5”) diameter steel tie rod used had an elastic modulus of 200 GPa (29000 ksi) and length of 3.56 m (140”). Since the rod would only act in tension, the stiffness can be written as:

$$k = \frac{AE}{l} = 70.1 \text{ N/m (400 kips/inch)} \quad \dots\dots\dots(7.12)$$

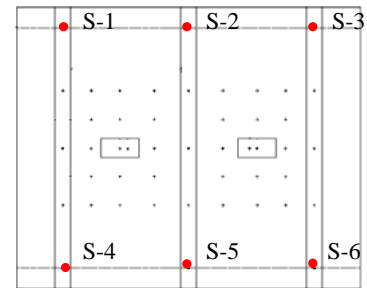
Thus the link elements in the FE model representing the tie rods were connected between the ends of the edge girders (as shown in Figure 7.4) and were assigned a linear elastic stiffness of 70.1 N/m (400 kips/inch).

The load cell supports at the ends of each girder were modeled by linear elastic spring elements. Since the spring elements would act only in compression when the specimen is loaded by the actuators, the initial stiffness of the spring elements were estimated based on the slope of the test load-deflection response recorded at the six supports in the first load cycle of 107 kN (24 kips) from the linear potentiometer and load-cell data at locations S-1 to S-6 of the six supports. The estimated stiffness at the six

supports are presented in Table 7.4 and were used as the initial stiffness values for the six linear elastic spring elements in the FE model.

Table 7.4 Initial stiffness estimates of support spring elements

Spring #	Stiffness, N/m (kips/inch)
S-1	111.4 (636)
S-2	301.9 (1723)
S-3	191.5 (1093)
S-4	218.7 (1248)
S-5	386.4 (2205)
S-6	225.5 (1287)



Note: The initial stiffness estimates of support spring elements were based on slope of the measured load deflection response at supports from linear potentiometer and load cell data.

In order to verify if the model with the initial estimated parameters was capable of predicting the general response of the test specimen, the deflections measured along the length of the specimen at mid-span during the first 107 kN (24 kip) load cycle were compared with the deflections predicted by the FE model and are presented in Figures 7.13a, 7.13b and 7.13c. It is to be noted that the initial parameters used, were only the first estimate based on the available stiffness and material property data and the model updating technique was then used (as will be discussed in subsequent sections of this chapter) to update the parameters to match the dynamic characteristics of the model and the test specimen. As was seen from the Figure 7.13 a good correspondence was obtained between the deflections predicted by the model and the test data indicating that the initial choice of parameters for the model resulted in a good match with the test behavior.

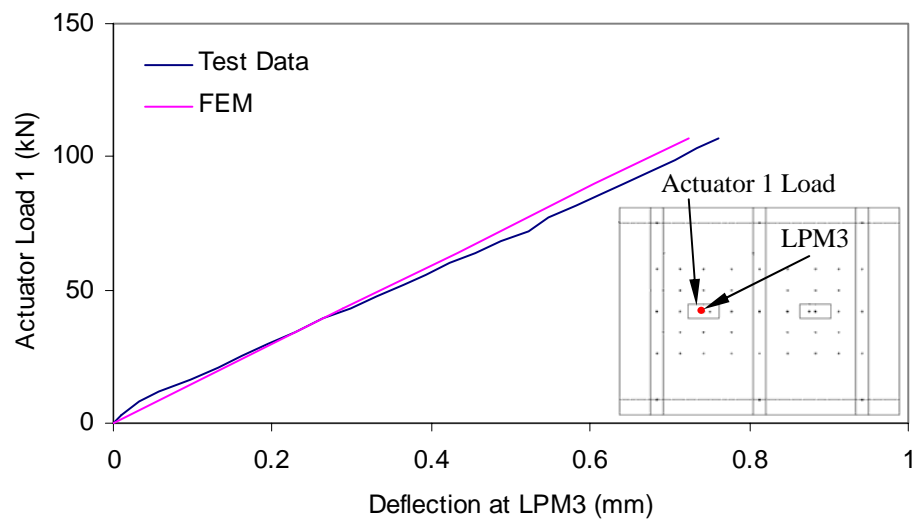


Figure 7.13a Comparison of deflections below actuator load 1 between test and model

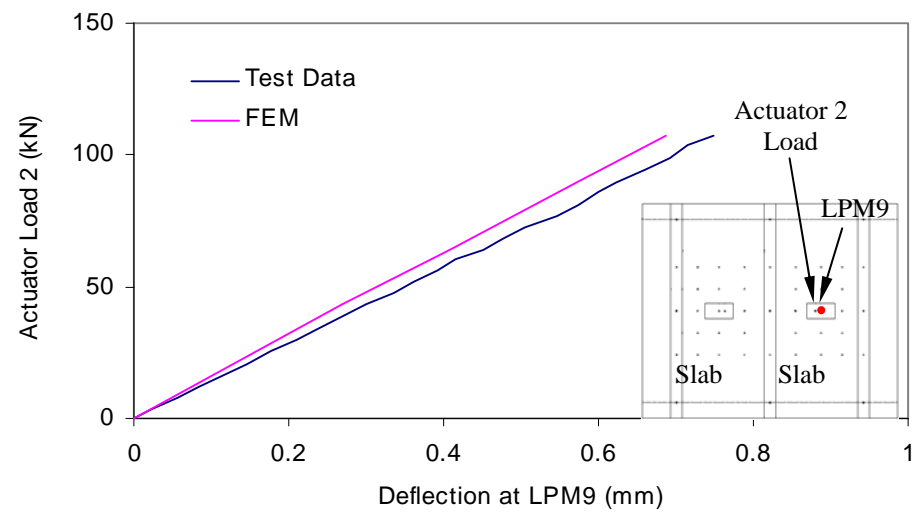


Figure 7.13b Comparison of deflections below actuator load 2 between test and model

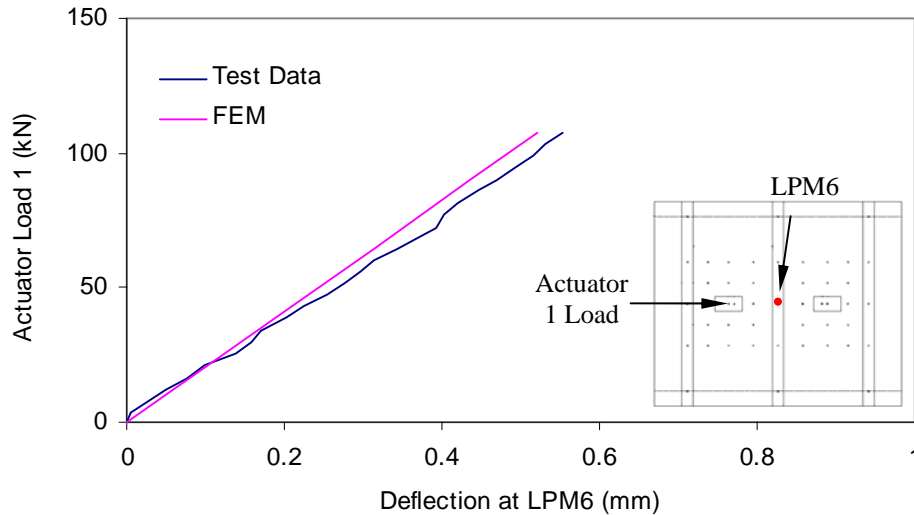


Figure 7.13c Comparison of deflection at center-girder midspan between test and model

Once the suitability of the model was established, the model updating was carried out, as discussed in the next section, based on the vibration characteristics (frequencies and mode shapes) measured from modal testing described in the previous section.

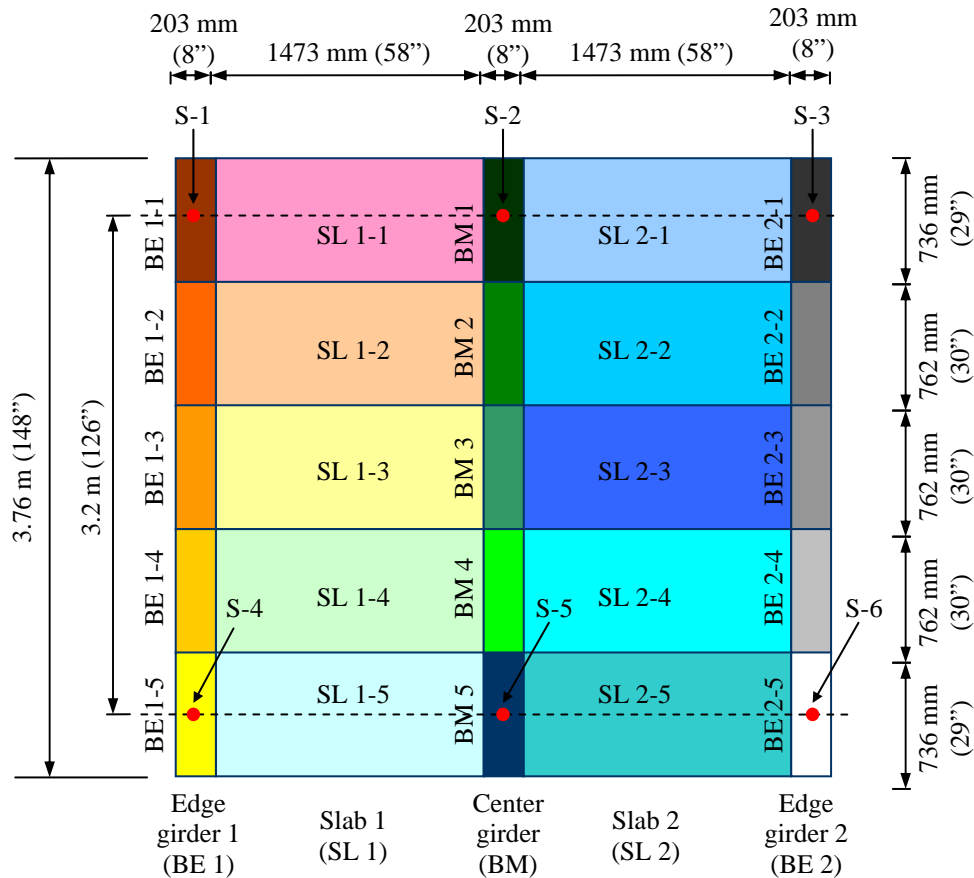
7.7 Model Updating Results

7.7.1 Segmentation of FE Model for Model Updating

As was discussed in the previous chapter, an initial estimate of the material properties for the slab and beam elements were first obtained and were used as the starting parametric values in the model for these elements. However it is to be recognized that with initiation of loading in the test specimen, different components of the structure (such as the two slabs, the two edge girders and the center girder) as well as different areas within each of those components were subjected to different amounts of damage with maximum damage occurring in the regions of highest stresses. Also since at the

systems level different components of the specimen reached their critical limit states at different load levels, depending on the stage of loading some components were subjected to more damage than others. Finally, the sequential strengthening of the specimen first for the slabs and then for the center girder resulted in changes in the damage progression. As a quantitative NDE technique at the global level, it was the objective of the model updating using the modal test results to identify the above. The slabs and the beams of the test specimen were therefore divided into a number of regions as shown in Figure 14 such that it would be possible through model updating to quantify the effects of damage progression/strengthening on each of these regions in the form of changes in the parameters caused by such damage/strengthening. Thus each of the slabs and girders was divided into 5 regions each as shown in Figure 7.14 thus resulting in 25 parameters in the model to be updated. The parameter to be identified in each of these regions, as was discussed earlier in section 7.5, was the “effective modulus”, E , of concrete, such that changes in the “effective modulus” obtained from the model updating results would be equivalent to changes in the stiffness in that region.

Also since boundary conditions can have a significant effect on the dynamic properties (frequencies and mode shapes) of the structure, the stiffness of the six supports modeled as linear elastic springs in the FE model were maintained as parameters in the model to be updated. Thus the 25 “effective modulus” parameters in the slabs and the beams and the 6 spring stiffness parameters of the supports resulted in a total of 31 parameters in the model to be updated for each stage (Table 7.1) at which modal tests were carried out.



Note: The locations of the six supports modeled as linear elastic springs in the FEM are shown as S-1 to S-6

Figure 7.14 Plan view showing regions in the specimen with parameters to be updated in the FE model

7.7.2 Model Updating

The objective of the finite element model updating over the load stages was to obtain a reasonable correlation between the experimental and numerical dynamic properties through updating of the model parameters which would be representative of the degradation/enhancement of stiffness caused by damage/strengthening. As was discussed in section 7.4, out of the 6 primary modes identified, 4 were normal modes and

2 were complex modes and for model updating only the 4 normal modes were chosen. This resulted in 4 frequencies and 100 modal amplitudes from the mode shapes (25 modal amplitudes from each of the 4 modes), i.e. a total of 104 known eigenvalues from the modal testing. However each of the mode shapes had to be normalized with respect to the maximum modal amplitude. Thus since the modal amplitude at the point of normalization would always be 1, this modal amplitude was excluded resulting in a total of 24 modal amplitudes from each of the mode shapes which could be used for model updating. This resulted in a total of 100 eigenvalues (4 frequencies and 96 modal amplitudes) from the modal testing at each stage which were matched with the corresponding 100 eigenvalues from the FE model for model updating, the principles of which are discussed next.

For the current structure with 31 elements to be updated (10 slab elements, 15 beam elements and 6 spring elements), with k_j^* as the unknown parameter (such as elastic modulus or spring stiffness in the current study) of the j^{th} element of the structure for which 100 eigenvalues (4 frequencies and 96 modal amplitudes) were known from the modal testing results and with k_j as the initial starting parameter estimate of the j^{th} element of the FE model from which the corresponding set of 100 eigenvalues could be determined, the two could be related by:

$$k_j^* = k_j(1 + \alpha_j) \quad \dots\dots\dots(7.13)$$

where, α_j was the fractional parameter change of the j^{th} element of the model required to match the eigenvalues of the structure and the model. This fractional parameter change of all the 31 elements was obtained using the model updating equation:

$$Z = F\alpha \quad \dots\dots\dots(7.14)$$

where α is a 31×1 matrix containing the fractional changes in the parameters between the FE model and the structure; Z is a 100×1 matrix containing the fractional changes in eigenvalues between the model and the structure; and F is a 100×31 sensitivity matrix relating the fractional changes in parameters to the fractional changes in eigenvalues.

Thus the model updating procedure consisted of:

- i) Determination of the sensitivity matrix, F by first generating the 100 eigenvalues of the FE model based on the initial parameter estimates, then changing each parameter by a known amount and generating the corresponding set of 100 eigenvalues for each of the perturbed parameters and finally calculating the fractional changes between the 100 eigenvalues of the initial model and the 100 eigenvalues of the modified model. Each component of the i^{th} column of the F matrix was then calculated by dividing the fractional changes in each eigenvalue caused by the change of i^{th} parameter by the magnitude of the modification of the i^{th} parameter. This resulted in the 100×31 sensitivity matrix with 31 parameter modifications.
- ii) Based on the calculated eigenvalues from the model with the initial parameter estimates and the measured eigenvalues from the structure through modal tests, the 100×1 matrix with the fractional changes in eigenvalues between the two systems, Z , was then calculated
- iii) Using equation 7.14, the fractional parameter change, α (31×1 matrix) was then calculated and thus the updated parameters were obtained using equation 7.13.

The above iterative process was followed until the difference between the subsequent updated parameters was less than 2%. The match between the frequencies obtained from

the FE model and the frequencies obtained from the modal testing on the specimen was determined in terms of the percentage difference between the two. The match between the mode shape amplitudes between the model and the structure was estimated using the Modal Assurance Criteria (MAC), defined as:

$$MAC_{jk} = \frac{(\phi_{mj}^T \phi_{ak})^2}{(\phi_{ak}^T \phi_{ak})(\phi_{mj}^T \phi_{mj})} \dots\dots\dots(7.15)$$

where, ϕ_{mj} is the measured j^{th} mode from the modal testing and ϕ_{ak} is the analytical j^{th} mode from the FE model. A value of 1 for the MAC would mean that one mode shape is a multiple of the other i.e. there is perfect match between the two. For the current study a MAC of 0.9 was used as the minimum MAC criteria for the model updating.

7.7.3 Model Updating Results

Starting with the initial estimates of the effective modulus for the beam and slab elements and the stiffness of the supports, the FE model was updated using the methodology described above using the modal testing results from baseline 1 tests to determine the updated parameters of the model which would result in match between the dynamic properties of the model and the structure before loading. These updated parameters from baseline 1 were then used as the starting parameters for the model to determine the second set of updated parameters to match the dynamic properties determined from the modal test carried out after loading the specimen to 214 kN (48 kips). The same methodology was followed over all the load stages as well as for baseline 2 and baseline 3 data corresponding to when the slabs and center girder were strengthened with composite, respectively, (as outlined in Table 7.1), in order to

determine the set of parameters in the model which would result in the best match of the dynamic properties between the model and the structure for the load stage under consideration. The values of the updated parameters for each stage of modal testing during phases 1, 2 and 3 of testing are presented in Tables A.2a, A.2b and A.2c, respectively in Appendix A.

The comparison between the frequencies obtained from the modal tests of the test specimen (for all the stages at which the modal tests were carried out) and the frequencies obtained from the FE model with the updated parameters at each of those stages is presented in Table 7.5. The correspondence of the mode shapes between the structure and the FE model as calculated by the Modal Assurance Criteria (MAC) are also presented in Table 7.5. The difference between the natural frequencies of the test specimen and the updated FE model at all the load stages were less than 5% and for the primary modes (mode 2 which was the 1st transverse bending mode and mode 4 which was the 1st torsion mode), the frequency difference was less than 2% indicating a good match between the model and the structure. In terms of mode shapes, the MAC values over all the load stages of the primary modes were over 0.9, indicating a good match between the model and the test results in terms of mode shapes.

Table 7.5 Comparison of frequencies and MAC between the test specimen and the model

		Mode	Experiment Freq. (Hz)	FE Model Freq. (Hz)	% Frequency Difference	MAC
Phase 1	Baseline 1 – No load condition	1	45.048	45.186	0.3	0.98271
		2	58.434	59.485	1.8	0.99277
		4	103.43	101.84	-1.5	0.98438
		6	133.1	127.93	-3.9	0.92409
	After unloading to 0 kN from 214 kN	1	42.543	44.871	5.5	0.97626
		2	57.233	58.915	2.9	0.98145
		4	101.55	100.9	-0.6	0.97738
		6	130.84	125.86	-3.8	0.95712
	After unloading to 0 kN from 289 kN	1	43.822	45.134	3.0	0.92755
		2	58.414	59.09	1.2	0.97305
		4	102.23	101.25	-1.0	0.9715
		6	130.11	126	-3.2	0.93456
	After unloading to 0 kN from 400 kN	1	43.851	44.995	2.6	0.90726
		2	57.869	58.285	0.7	0.96034
		4	100.04	99.87	-0.2	0.9514
		6	126.26	122.62	-2.9	0.90695
Phase 2	Baseline 2 – No load condition	1	43.956	45.138	2.7	0.94482
		2	58.636	58.847	0.4	0.97888
		4	103.15	100.63	-2.4	0.92639
		6	127.69	125.93	-1.4	0.91513
	After unloading to 0 kN from 400 kN	1	43.156	44.571	3.3	0.92385
		2	57.703	58.49	1.4	0.94683
		4	100.96	100.22	-0.7	0.95696
		6	126.2	125.03	-0.9	0.94339
	After unloading to 0 kN from 578 kN	1	43.203	44.101	2.1	0.91538
		2	57.025	57.53	0.9	0.97291
		4	98.301	98.041	-0.3	0.95508
		6	125.62	124.01	-1.3	0.92228
	After unloading to 0 kN from 667 kN	1	42.041	43.781	4.1	0.8033
		2	55.751	56.728	1.8	0.95553
		4	94.356	96.15	1.9	0.90196
		6	123.86	121.67	-1.8	0.847
Phase 3	Baseline 3 – No load condition	1	43.38	43.97	1.4	0.88403
		2	56.682	57.1	0.7	0.97081
		4	97.513	96.823	-0.7	0.96846
		6	123.53	123.48	-0.1	0.84515
	After unloading to 0 kN from 667 kN	1	43.022	44.171	2.7	0.90198
		2	56.355	56.686	0.6	0.97798
		4	96.821	96.153	-0.7	0.96868
		6	125.8	123.13	-2.1	0.95978
	After unloading to 0 kN from 756 kN	1	42.657	43.634	2.3	0.8612
		2	55.65	56.111	0.8	0.95287
		4	94.338	94.971	0.7	0.96808
		6	123.3	121.17	-1.7	0.88922
	After unloading to 0 kN from 845 kN	1	42.693	43.376	1.6	0.85951
		2	55.018	55.874	1.6	0.95613
		4	93.35	94.906	1.7	0.9612
		6	119.59	118.35	-1.0	0.92925

Based on the updated parameters of the model, the stiffness degradation/enhancement of the elements caused by damage progression and for FRP strengthening over the load stages was estimated in terms of a parameter ratio at the end of stage i of testing (shown in Table 7.1) and was defined as:

$$(\text{Parameter Ratio})_i = \frac{\text{Updated Parameter Value at Stage } i \text{ of Test}}{\text{Updated Parameter Value at Baseline 1}} \dots\dots\dots(7.16)$$

Thus an updated parameter ratio of 1.0 in an element would indicate that no damage/strength enhancement took place in that element compared to its baseline properties. A parameter ratio >1.0 would indicate strengthening or redistribution effects and a parameter ratio <1.0 would indicate damage effects on the parameter of that element with respect to its initial baseline value. Also relative values between the parameter ratios of two elements would give a quantitative estimate of the relative effects of damage/strengthening on the stiffness of the elements.

Based on the updated parameters, the effective modulus ratios of the 5 regions in each of the two slabs, the two edge girders and the center girder (as defined in Figures 7.15a and 7.15d) are shown in Figures 7.15b, 7.15c, 7.15e, 7.15f and 7.15g. Also the effective stiffness ratios of the six springs simulating the supports are shown in Figure 7.15h. For phase 1 of test, the most significant damage in terms of degradation of the effective modulus was observed in region 3 (mid-span region of specimen below load area) of slabs 1 and 2 (S1-3 and S2-3), where the effective modulus ratio fell to 0.78 and 0.81, respectively i.e. there was 22% and 19% reduction of the effective modulus of the two slabs in the regions below the load areas at the end of phase 1 loading. Regions 2 and 4 of the two slabs (S1-2, S1-4, S2-2 and S2-4) adjacent to the mid-span regions had a

slightly lower degradation with the effective modulus decreasing by approximately 14% with respect to baseline modulus in those regions. The edge regions of the slabs (S1-1, S1-5, S2-1 and S2-5) had very little degradation with the effective modulus decreasing by less than 3%. The reduction of the effective modulus in the edge girders and the center girder during phase 1 loading were also less than 4%. The only exception was region 5 of center girder (BM-5), which was the region at the support area of the girder, where the reduction of the effective modulus was about 8%. The above observations match the experimental observations discussed in Chapter 5, where in phase 1 of testing most of the damage in the specimen was concentrated in the form of punching shear cracks in the two slabs below the areas of load introduction along with the initiation of shear cracks at the support areas of the center girder at the end of phase 1 loading.

The effect of the FRP composite strengthening of the deck slabs at the end of phase 1 loading are observed from the increase in the effective modulus ratios of the slabs in the baseline 2 updating results. The effective modulus ratios of the most damaged regions of slabs 1 and 2 (S1-3 and S2-3) increased from 0.78 to 0.84 and from 0.81 to 0.86, respectively. The effective modulus ratios in regions 2 and 4 (S1-2, S1-4, S2-2 and S2-4) also increased by approximately 5%. The increase was approximately 10% in the edge regions of the slabs (S1-1, S1-5, S2-1 and S2-5). This higher increase can be explained by the fact that the edge regions were relatively undamaged during phase 1 of test and thus the effect of the composite in increasing the stiffness of these regions was maximized. The effective modulus ratios of the edge and center girders were not affected by the composite strengthening indicating that the strengthening of the slabs did not have effect on the stiffness of the girders. Thus it could be concluded that at the systems level

the strengthening of the slab components will not have any effect on the stiffness properties of the girder components. However the effect of strengthening of the slabs will be to place higher load demands on the girder components due to enhanced strength of the slab components.

Degradation of the effective modulus ratio in the center girders in the regions towards the support were observed during phase 2 loading stages. The effective modulus ratio in the support regions of the center girder (BM-1 and BM-5) fell by approximately 23% and the effective modulus ratio in regions adjacent to support of center girder (BM-2 and BM-4) fell by approximately 10%. This was congruent with the experimental observations of phase 2 loading when the center girder in the shear deficient regions near the support were found to reach shear criticality at the 667 kN (150 kips) load cycle. The degradation of the effective modulus in the most stressed regions of the strengthened slabs in line with the load areas (S1-3 and S2-3) decreased by less than 10% with respect to the modulus values of corresponding regions of the strengthened slabs. No significant reduction of the effective modulus was observed in the edge regions of the slabs. Thus the FRP composite strengthening was effective in restraining the degradation of the stiffness of the slabs. The effective modulus ratios of the edge girders with respect to initial baseline 1 properties were higher than 0.9.

The effect of strengthening of the center girder with FRP composite stirrups at the end of phase 2 loading was observed from the baseline 3 updating results. The increase of effective modulus in the most damaged regions of the girder (BM-1 and BM-5) was approximately 6% and that in the adjacent regions (BM-2 and BM-4) were approximately 10%. From Figure 7.15e, it was also seen that the effective modulus ratio of the center

girder did not degrade significantly during phase 3 load stages indicating that the composite stirrups were effective in preventing shear damage in the center girder. Over phase 3 load stages, the most significant damage in terms of decrease of the effective modulus ratio was observed to be concentrated back in the deck slabs. Over this stage the effective modulus ratio of the mid-span regions of the two slabs (S1-3 and S2-3) decreased from 0.76 to 0.64 and from 0.79 to 0.65, respectively at the end of the 845 kN (190 kips) load cycle. The changes in the adjacent regions (S1-2, S1-4, S2-2 and S2-4) were 0.82 to 0.74, 0.82 to 0.67, 0.83 to 0.65 and 0.87 to 0.71, respectively. Also it was observed that the effective modulus ratios in these regions, S1-2, S1-4, S2-2 and S2-4 (which extended from 381 mm to 1143 mm from mid-span in the FE model as shown in Figure 7.14) at the end of 845 kN load cycle were comparable to those at mid-span (S1-3 and S2-3). The experimental observations at the end of phase 2 loading, as was discussed in chapter 5, showed failure of the specimen due to debonding of the composite and opening of punching shear cracks in the slabs. These punching shear cracks in the transverse direction were formed at approximately 584 mm (23") and 736 mm (29") from mid-span of the specimen in slabs 1 and 2 respectively (as was shown in Figure 5.52 of chapter 5). Thus these punching shear cracks developed in regions S1-2, S1-4, S2-2 and S2-4 of the model and this resulted in significant drop of the effective modulus ratio (such as from 0.83 to 0.65 in region S2-2) through phase 3 loading in these regions.

The most significant change in the effective spring stiffness over the load stages was seen in spring S-5, in which the effective spring stiffness ratio fell to 0.64 at the end of 845 kN (190 kips) load cycle of phase 3. Also at location S-4 there was an increase in the spring stiffness ratio to 1.22 (i.e. 22% increase with respect to updated spring stiffness

at baseline 1) at the 757 kN (170 kips) load stage. The changes in the spring stiffness ratios at other locations were not significant. Comparison of the spring stiffness trends obtained from model updating results with the experimentally measured load-deflection responses at support locations will be discussed in the next section of this chapter.

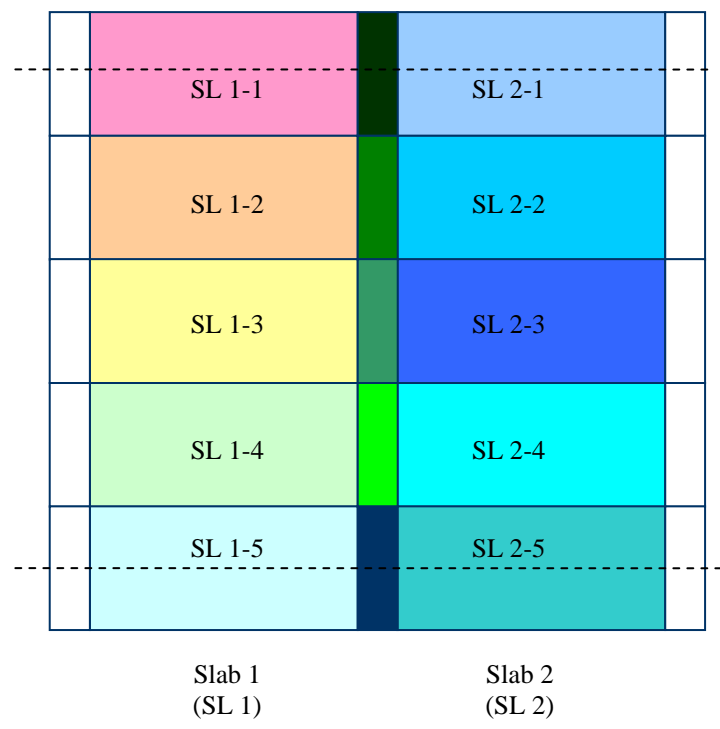


Figure 7.15a Locations of regions in the deck slabs used for model updating

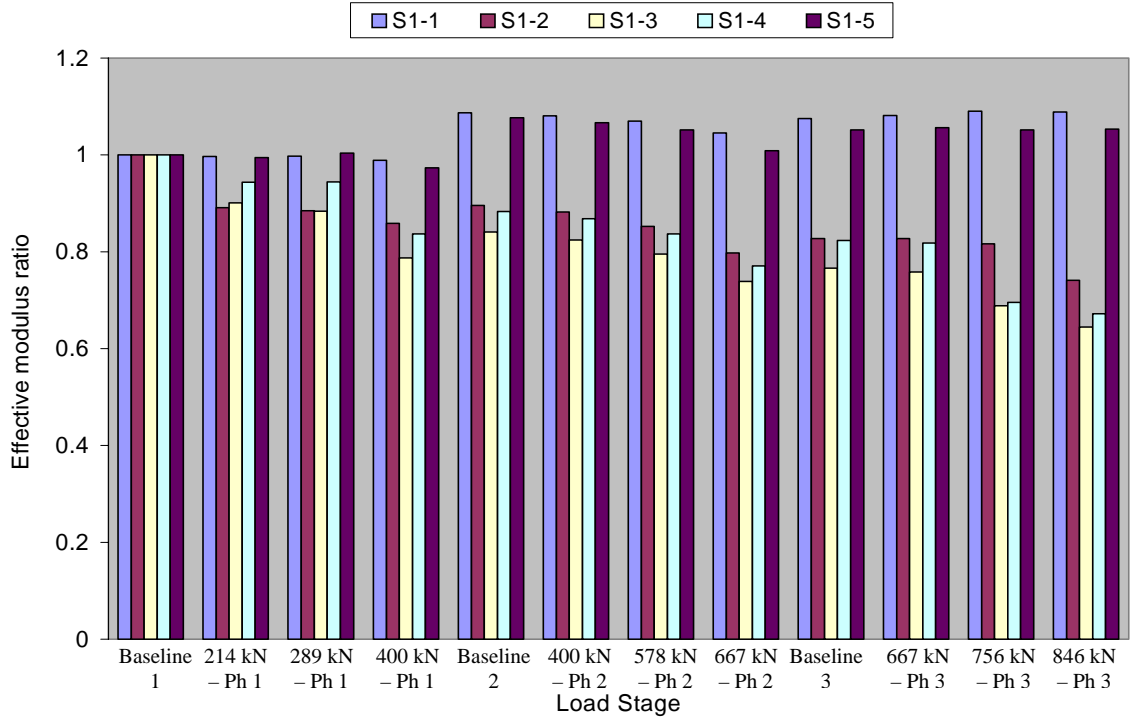


Figure 7.15b Ratio of updated effective modulus in the 5 regions of Slab 1

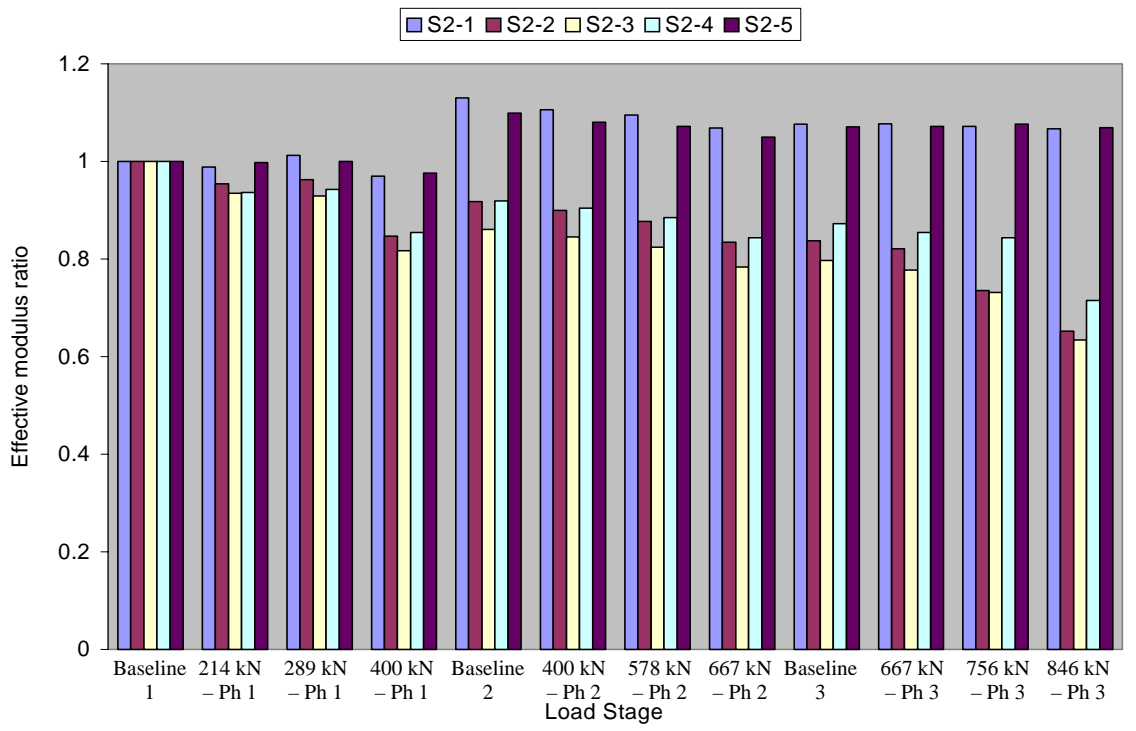
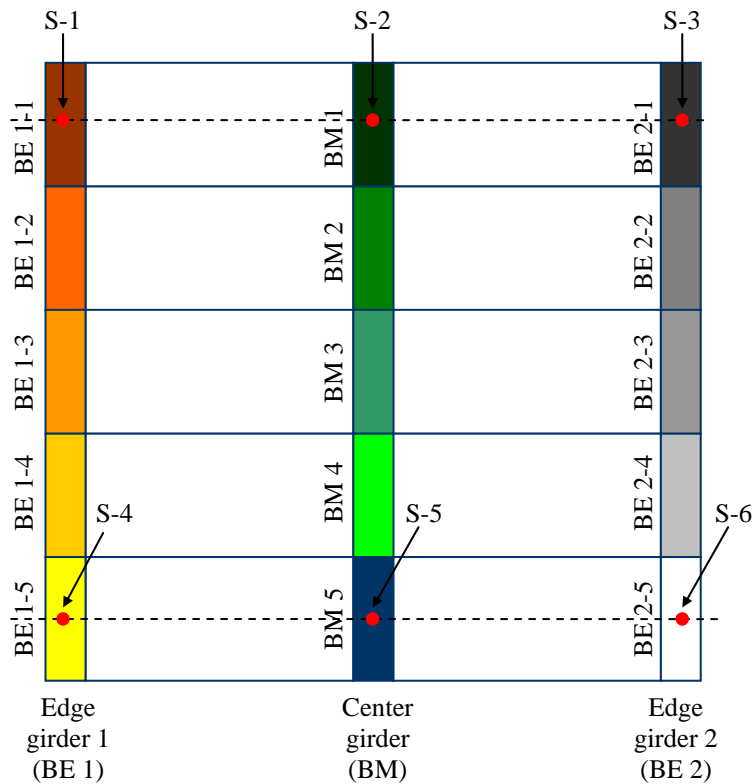


Figure 7.15c Ratio of updated effective modulus in the 5 regions of Slab 2



Note: The locations of the six supports modeled as linear elastic springs in the FEM are shown as S-1 to S-6

Figure 7.15d Locations of regions in the girders used for model updating

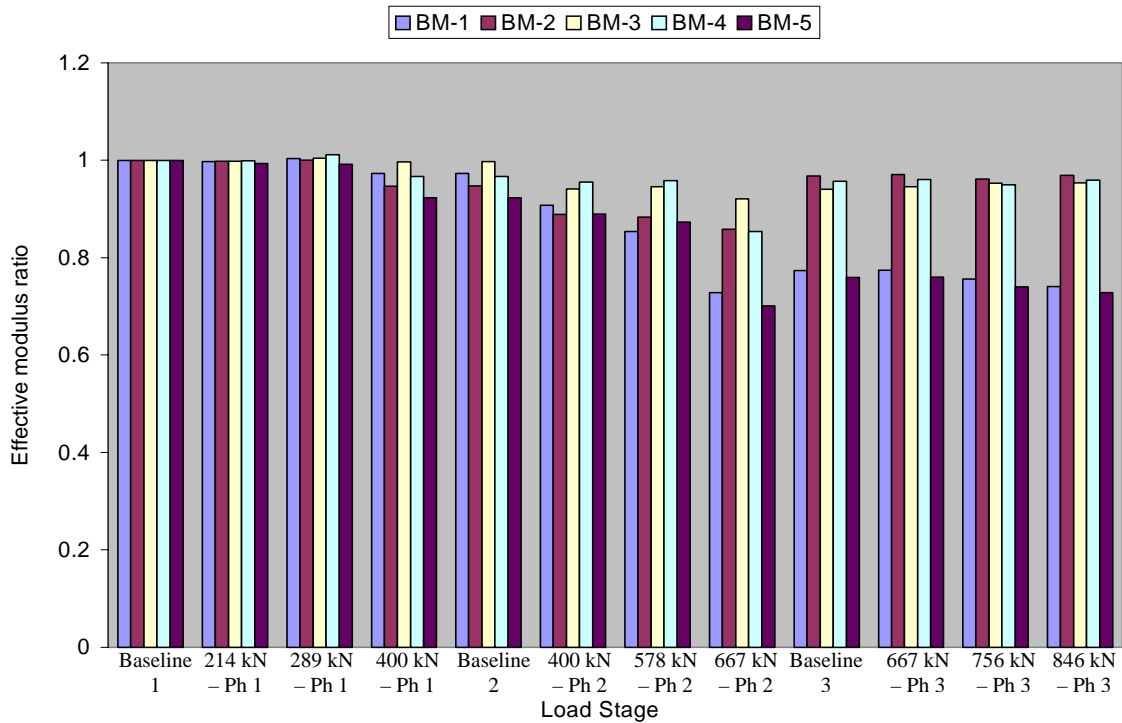


Figure 7.15e Ratio of updated effective modulus in the 5 regions of center girder

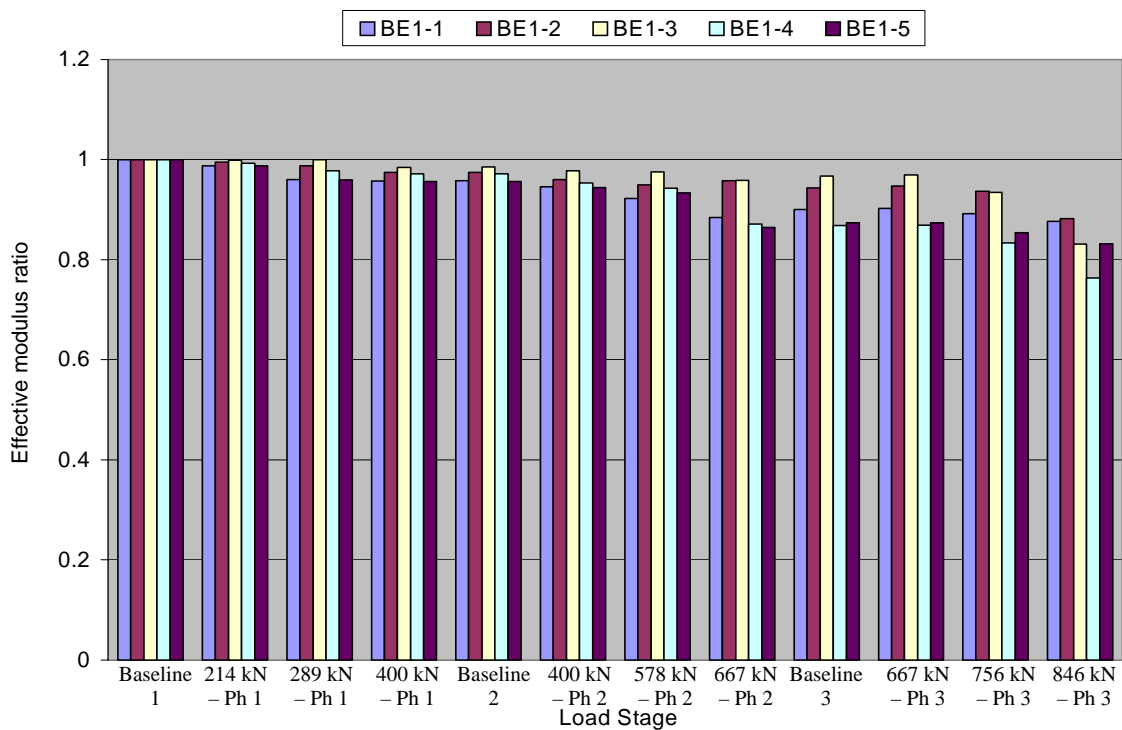


Figure 7.15f Ratio of updated effective modulus in the 5 regions of edge girder 1

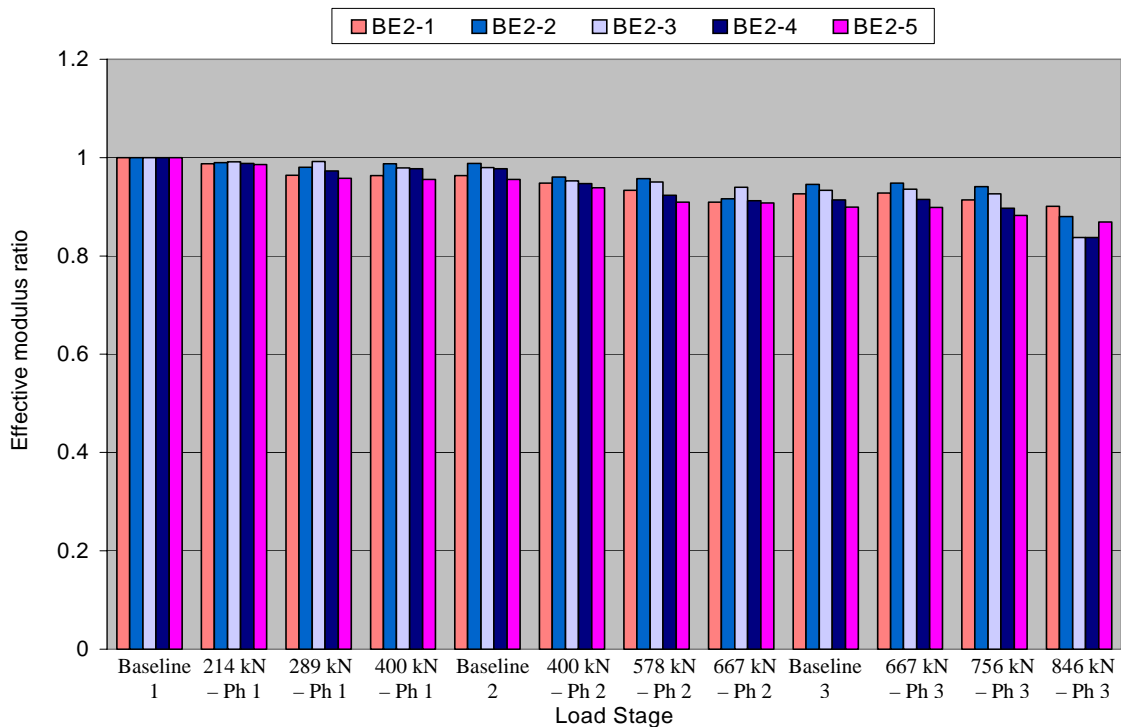


Figure 7.15g Ratio of updated effective modulus in the 5 regions of edge girder 2

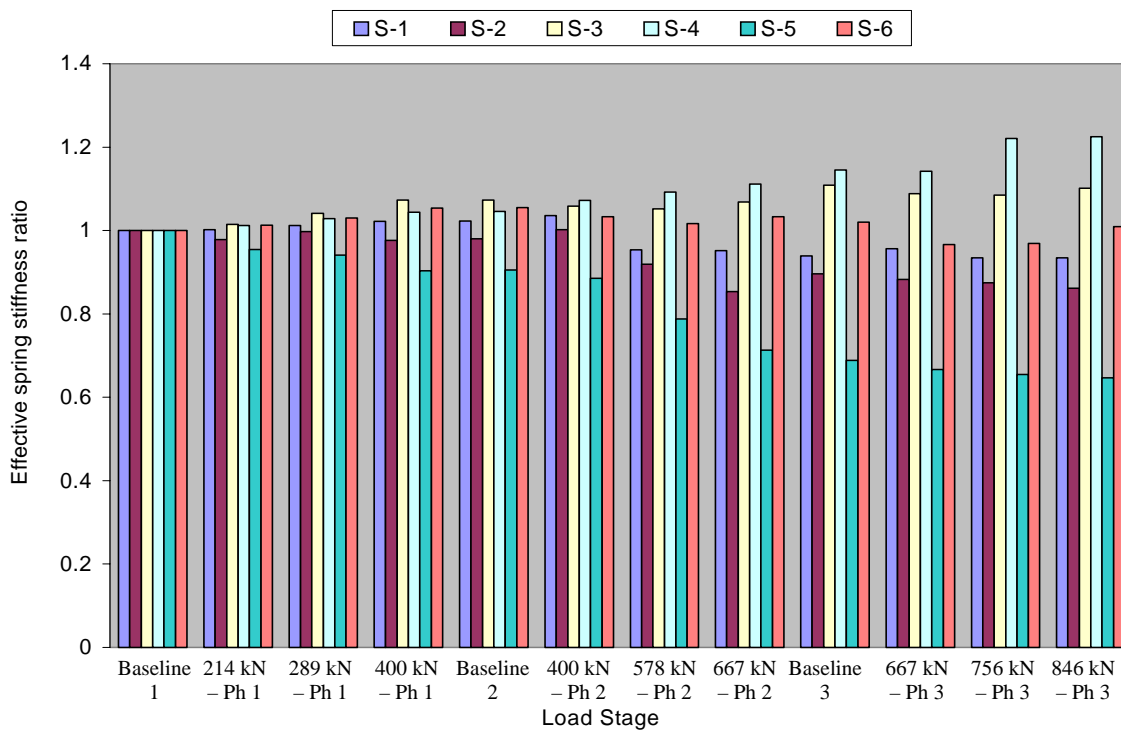


Figure 7.15h Ratio of updated effective stiffness of the 6 springs simulating supports

7.8 Comparison of Model Updating With Experimental Load-Deflection Results

The model updating was carried out based on the modal test results obtained at the end of each loading cycle and after strengthening of the slabs and girder and the modal tests were conducted with zero applied load on the specimen from the actuators. Thus the stiffness results obtained for the FE model elements based on the updated parameters (determined based on the modal test results at the end of a load cycle) would only be representative of the initial stiffness of the element for the next load cycle. In order to compare the behavior of the updated models over the load stages with the actual behavior of the test specimen obtained from experimental load-deflection data, the deflections predicted by the updated models over the load stages in the two slabs, edge girders and center girder were obtained under application of actuator load of 22.25 kN (5 kips) for each of the updated models. This load level was chosen since it represented only a small load (compared to the permit truck load of 107 kN and cracking load of the slabs at 178 kN), so that it could be assumed that no damage had occurred due to this load and that there was no change in the stiffness properties determined through model updating at the beginning of the load cycle.

The deflections below the actuator loads for the slabs and at mid-span of the edge girders and center girder calculated under applied actuator load of 22.25 kN (5 kips) are presented in Tables 7.6 and 7.7 both for experimental measurements by the linear potentiometers and predicted deflections from the updated FE models over the load stages. Also as was defined earlier in Chapter 5, the stiffness ratio was calculated to determine the effects of damage progression and strengthening. For reference the

stiffness ratio is repeated in equation 7.17 and the results for both experimental data and analytical predictions are given in Tables 7.6 and 7.7.

$$(Stiffness\ Ratio)_i = \frac{\left(\frac{\text{Load, } P_i \text{ at Stage } i}{\text{Deflection corresponding to Load, } P_i \text{ at Stage } i} \right)}{\left(\frac{\text{Load, } P_B \text{ at Baseline Load Stage}}{\text{Deflection corresponding to Load, } P_B \text{ at Baseline Load Stage}} \right)} \dots\dots\dots(7.17)$$

Since all the deflections in Tables 7.6 to 7.8 were calculated for actuator load of 22.5 kN (5 kips), (i.e. $P_B = P_i = 22.5$ kN), the stiffness ratio from Eqn. 7.17 reduces to:

$$(Stiffness\ Ratio)_i = \frac{\text{Deflection at 22.25 kN for Baseline Load Stage}}{\text{Deflection at 22.25 kN for Load Stage } i} \dots\dots\dots(7.18)$$

The stiffness ratios calculated for the slabs and the girders over the load stages (and presented in Tables 7.6 and 7.7) for the updated FE models and the experimental data are compared graphically in Figures 7.16 to 7.20. For slabs 1 and 2 the stiffness ratios obtained below the load areas from experimental data and FE model updating results over the load stages and shown in Figures 7.16 and 7.17 were found to match well. The experimental and analytical stiffness ratios at mid-span of center girder over the load stages are shown in Figure 7.18 and were also found to match well. The stiffness ratios at mid-span of the edge girders for model and experimental results are shown in Figures 7.19 and 7.20. The stiffness ratios obtained from the model updating were found to be slightly higher than the experimentally determined stiffness ratios (such as for edge beam 1 for the 935 kN load cycle the stiffness ratio from the model was 0.867 compared to 0.816 from experimental data and for edge beam 2 for the 935 kN load cycle the stiffness ratio from the model was 0.873 compared to 0.804 from experimental data),

indicating that the stiffness of the edge beams in the model were higher than the actual stiffness of the edge beams in the test specimen. However the trends of the stiffness ratio curves of the edge girders over the load stages (Figures 7.19 and 7.20) for both analytical predictions and experimental measurements were similar, indicating that the model updating methodology was able to simulate the overall behavior of the edge girders over the load stages.

Table 7.6 Deflections and stiffness ratios obtained for Slabs under 2.25 kN load

Deflections and stiffness ratios obtained for Slab 1 under 2.25 kN load				
Calculations for 2.25 kN actuator load at beginning of load cycle with peak load of:	FE Model		Experiment	
	Deflection (mm)	Stiffness ratio	Deflection (mm)	Stiffness ratio
214 kN (Baseline 1)	0.138	1.0	0.157	1.0
289 kN – Phase 1	0.144	0.958	0.169	0.929
400 kN – Phase 1	0.156	0.886	0.173	0.903
400 kN – Phase 2 (After slab rehab)	0.152	0.911	0.166	0.944
578 kN – Phase 2	0.153	0.904	0.169	0.927
667 kN – Phase 2	0.169	0.817	0.184	0.851
667 kN – Phase 3 (After girder rehab)	0.164	0.846	0.184	0.852
757 kN – Phase 3	0.165	0.836	0.190	0.825
845 kN – Phase 3	0.174	0.797	0.192	0.817
935 kN – Phase 3	0.181	0.766	0.197	0.796
Deflections and stiffness ratios obtained for Slab 2 under 2.25 kN load				
Calculations for 2.25 kN actuator load at beginning of load cycle with peak load of:	FE Model		Experiment	
	Deflection (mm)	Stiffness ratio	Deflection (mm)	Stiffness ratio
214 kN (Baseline 1)	0.126	1.0	0.159	1.0
289 kN – Phase 1	0.130	0.964	0.159	0.997
400 kN – Phase 1	0.137	0.918	0.167	0.954
400 kN – Phase 2 (After slab rehab)	0.133	0.949	0.160	0.996
578 kN – Phase 2	0.136	0.924	0.163	0.972
667 kN – Phase 2	0.147	0.858	0.170	0.934
667 kN – Phase 3 (After girder rehab)	0.144	0.874	0.172	0.926
757 kN – Phase 3	0.145	0.866	0.176	0.904
845 kN – Phase 3	0.152	0.830	0.180	0.882
935 kN – Phase 3	0.162	0.776	0.199	0.797

Table 7.7 Deflections and stiffness ratios for Girders under 2.25 kN load

Deflections and stiffness ratios for Center girder under 2.25 kN load				
Calculations for 2.25 kN actuator load at beginning of load cycle with peak load of:	FE Model		Experiment	
	Deflection (mm)	Stiffness ratio	Deflection (mm)	Stiffness ratio
214 kN (Baseline 1)	0.099	1.0	0.119	1.0
289 kN – Phase 1	0.102	0.977	0.125	0.957
400 kN – Phase 1	0.105	0.942	0.127	0.942
400 kN – Phase 2 (After slab rehab)	0.104	0.956	0.129	0.926
578 kN – Phase 2	0.106	0.937	0.129	0.927
667 kN – Phase 2	0.117	0.846	0.136	0.875
667 kN – Phase 3 (After girder rehab)	0.114	0.872	0.127	0.936
757 kN – Phase 3	0.115	0.864	0.135	0.884
845 kN – Phase 3	0.119	0.835	0.139	0.859
935 kN – Phase 3	0.120	0.826	0.144	0.826
Deflections and stiffness ratios for Edge girder 1 under 2.25 kN load				
Calculations for 2.25 kN actuator load at beginning of load cycle with peak load of:	FE Model		Experiment	
	Deflection (mm)	Stiffness ratio	Deflection (mm)	Stiffness ratio
214 kN (Baseline 1)	0.063	1.0	0.078	1.0
289 kN – Phase 1	0.064	0.983	0.083	0.940
400 kN – Phase 1	0.066	0.956	0.085	0.923
400 kN – Phase 2 (After slab rehab)	0.065	0.959	0.083	0.937
578 kN – Phase 2	0.065	0.965	0.087	0.897
667 kN – Phase 2	0.069	0.902	0.093	0.842
667 kN – Phase 3 (After girder rehab)	0.068	0.924	0.092	0.854
757 kN – Phase 3	0.068	0.921	0.092	0.852
845 kN – Phase 3	0.070	0.901	0.092	0.853
935 kN – Phase 3	0.072	0.867	0.096	0.816
Deflections and stiffness ratios for Edge girder 2 under 2.25 kN load				
Calculations for 2.25 kN actuator load at beginning of load cycle with peak load of:	FE Model		Experiment	
	Deflection (mm)	Stiffness ratio	Deflection (mm)	Stiffness ratio
214 kN (Baseline 1)	0.0530	1.0	0.064	1.0
289 kN – Phase 1	0.0534	0.993	0.067	0.963
400 kN – Phase 1	0.0527	1.006	0.068	0.948
400 kN – Phase 2 (After slab rehab)	0.0537	0.988	0.068	0.945
578 kN – Phase 2	0.0541	0.980	0.069	0.929
667 kN – Phase 2	0.0558	0.949	0.071	0.911
667 kN – Phase 3 (After girder rehab)	0.0552	0.960	0.071	0.909
757 kN – Phase 3	0.0566	0.936	0.072	0.890
845 kN – Phase 3	0.0592	0.896	0.077	0.837
935 kN – Phase 3	0.0607	0.873	0.080	0.804

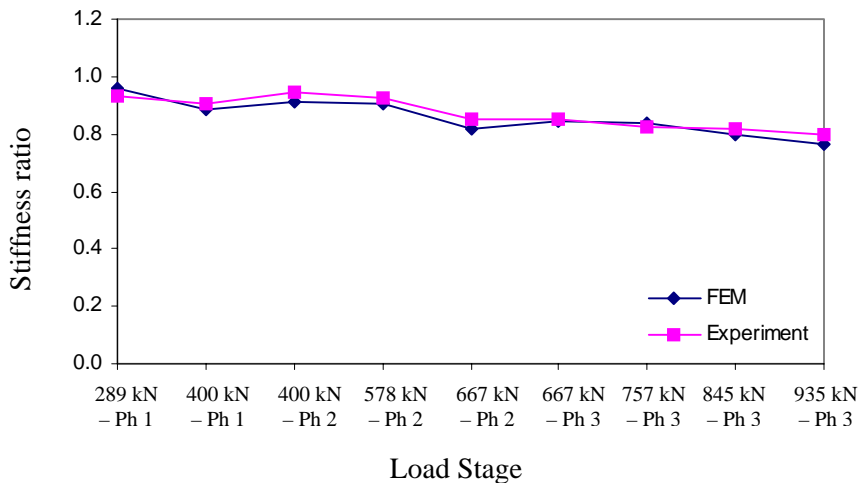


Figure 7.16 Comparison of stiffness ratio below load area of slab 1

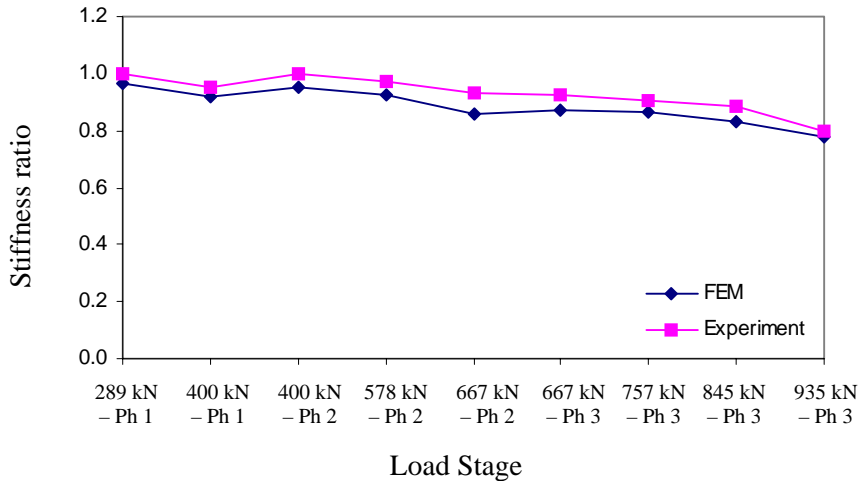


Figure 7.17 Comparison of stiffness ratio below load area of slab 2

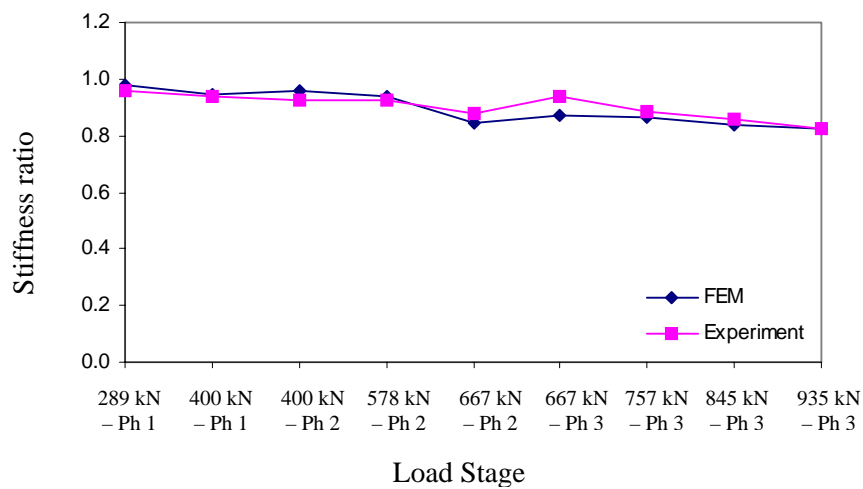


Figure 7.18 Comparison of stiffness ratio at mid-span of center girder

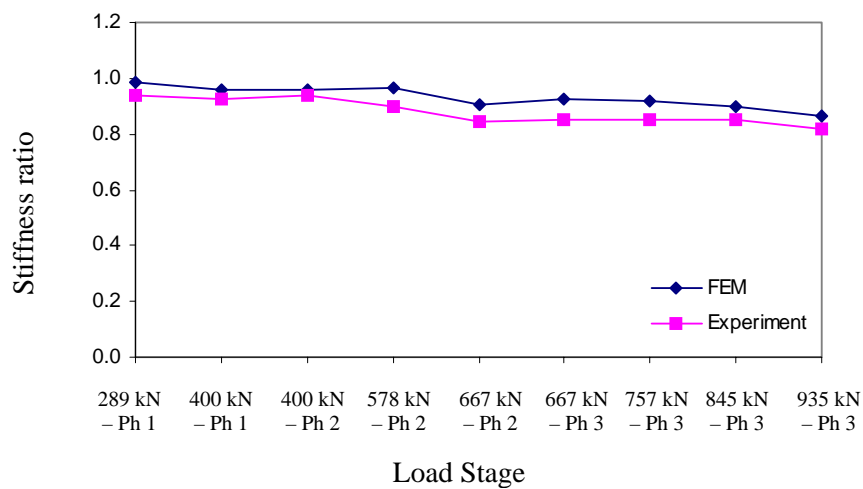


Figure 7.19 Comparison of stiffness ratio at mid-span of edge girder 1

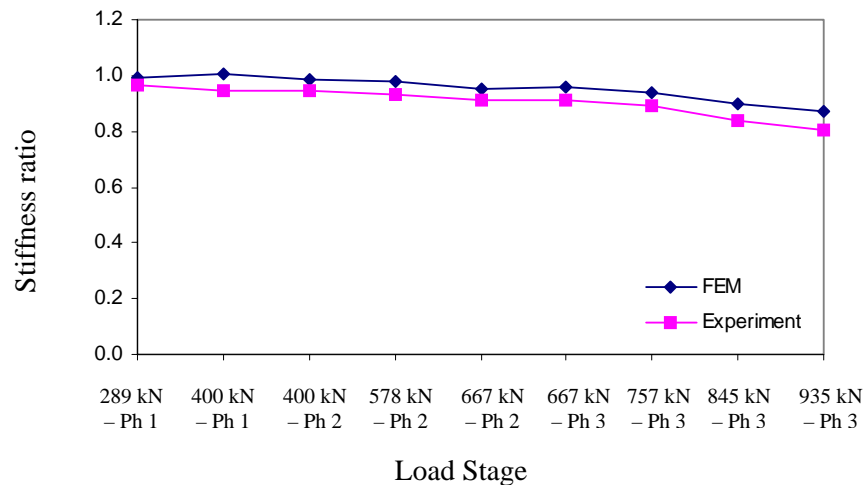


Figure 7.20 Comparison of stiffness ratio at mid-span of edge girder 2

It was discussed in the previous section of this chapter that from the model updating results, the most significant change in the effective spring stiffness over the load stages was seen in spring S-5, in which the effective spring stiffness ratio fell to 0.64 at the end of 845 kN (190 kips) load cycle of phase 3 (Figure 7.15f). To check the correspondence of the decrease of spring stiffness ratio at S-5 with the experimental observations, the initial slope of the load deflection data measured at the location of load-cell S-5 over the load stages was plotted and is shown in Figure 7.21. From the experimentally measured load deflection data, support S-5 had an initial stiffness of 386 N/m measured from the initial load-deflection slope at the 214 kN load cycle and this stiffness fell to 253.9 N/m measured from the initial load-deflection slope at the support in the 845 kN (190 kips) load cycle. Thus the experimentally measured stiffness decreased by 34% and this corresponded well with the 36% decrease (1.0 to 0.64) in the effective spring stiffness determined through model updating.

Also at location S-4 there was an increase in the spring stiffness ratio to 1.22 (i.e. 22% increase with respect to updated spring stiffness at baseline 1) at the 757 kN (170 kips) load stage. The experimentally measured load deflection response at location S-4 is shown in Figure 7.22. A change in the stiffness (initial slope) of the load-deflection response (from 218.5 N/m to 274.2 N/m, i.e. 26% increase) was observed between the initial slopes of the 214 kN (48 kips) and 757 kN (170 kips) load cycles.

The changes in the spring stiffness ratios at other locations obtained through model updating were not significant. Load-deflection response experimentally measured at support location S-6 is shown in Figure 7.23 and the support stiffness represented by the initial slopes of the load-deflection responses over the load stages were found not to change significantly. Thus the analytically updated spring element stiffness over the load stages matched well with the trends observed in the experimentally measured stiffness at the supports over the load stages.

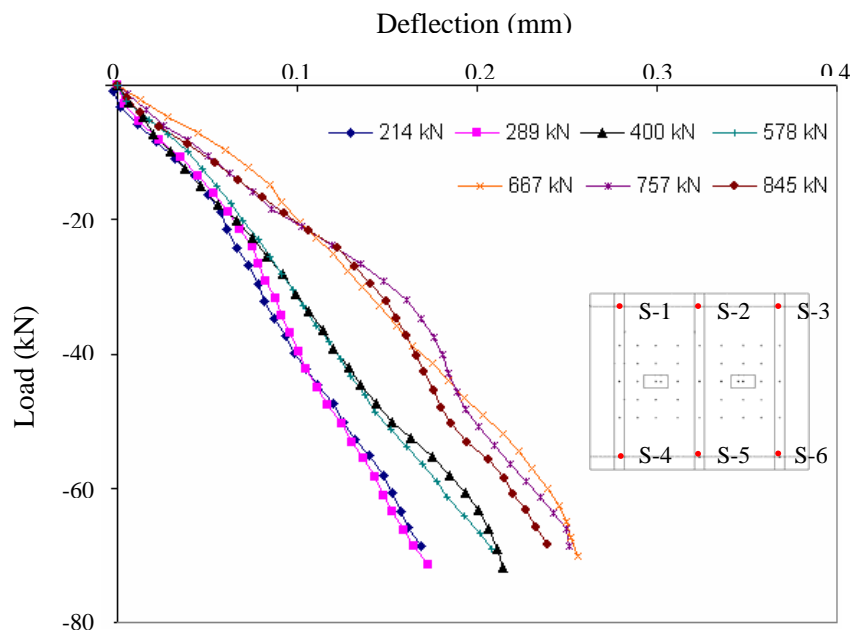


Figure 7.21 Initial load-deflection responses at S-5 over load stages

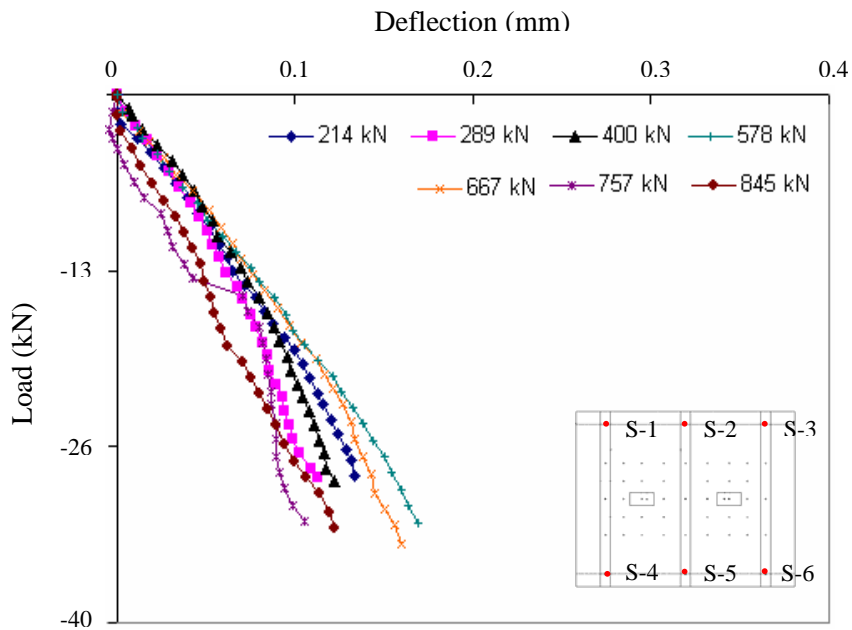


Figure 7.22 Initial load-deflection responses at S-4 over load stages

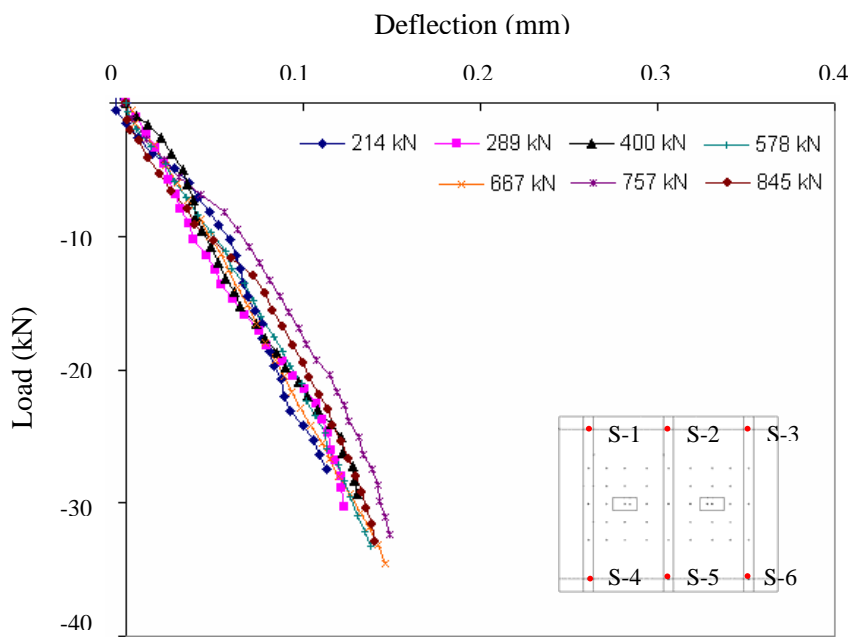


Figure 7.23 Initial load-deflection responses at S-6 over load stages

8 FINITE ELEMENT MODELING AND ANALYSIS

8.1 Introduction

Predictions of the ultimate capacities of the components of the 3-girder 2-span bridge segment were presented in Chapter 4 and comparisons of the predictions with the experimental results were presented in Chapter 5. However the previously discussed simple design models can only be used to predict the ultimate capacities corresponding to limit states, such as punching shear capacity, steel yield, composite debonding, etc. Also, all analytical models are formulated to be used at the component level and so it is not possible to look at the behavior of a system in an integrated fashion. Thus in order to correlate the progression of damage visually observed in the test specimen over the load stages with the degradation or enhancement of the stiffness characteristics of the structure caused by damage and sequential strengthening of the components, NDE using forced vibration based modal testing was carried out and the results were presented in Chapter 7. In the absence of NDE data, an alternative method to model the progression of damage will be through use of a detailed non-linear finite element analysis. In the current research program at the systems level such an analysis using the Abaqus [76] finite element program was used to simulate the behavior of the 3-girder-2-span bridge segment under simulated wheel load application with sequential strengthening of the components. The results from this analysis and comparison with the test results are presented in this chapter.

8.2 Description of the FE Model

8.2.1 Geometry and Element Types

A three dimensional finite element model using Abaqus [76] was developed to simulate the 3-girder 2-span bridge segment. The overall geometry of the baseline model matched that of the test specimen and is shown in Figure 8.1. The slabs and the girders were modeled with 4-noded shell elements (S4R) and the two steel tie rods connecting the ends of the edge girders were modeled with axial connectors (CONN3D2). The six load cells on which the test specimen was supported at the ends of the girders were modeled with grounded axial connectors (CONN3D2). The grounded connectors were tied to the specimen at the nodes which corresponded to the locations of the load cells in the test specimen. However since the load cells actually had contact over an area rather than point contact with the specimen (as was shown in Figure 4.21 in chapter 4), this region in the model at the bottom of the girders was modeled with multi-point constraints (MPC-beam) connected to the node of the grounded spring. This is shown in Figure 8.2. The properties assigned to these elements will be discussed in the next section. Modifications to this baseline model were made for Phase 2 of testing simulating the strengthening of the slabs with composite strips and laminates. The modified model for Phase 2 is shown in Figure 8.3. Both the laminates and the pultruded strips were modeled with 4-noded shell elements (S4R) and their geometry and spacing matched those of the composites in the strengthened slabs of the test specimen. The composites were connected to the slabs using tie constraints. Modifications were made to the model for Phase 3 (Figure 8.4) with 4-noded shell elements (S4R) simulating the composite stirrups used for shear strengthening, being connected to the center girder with tie constraints.

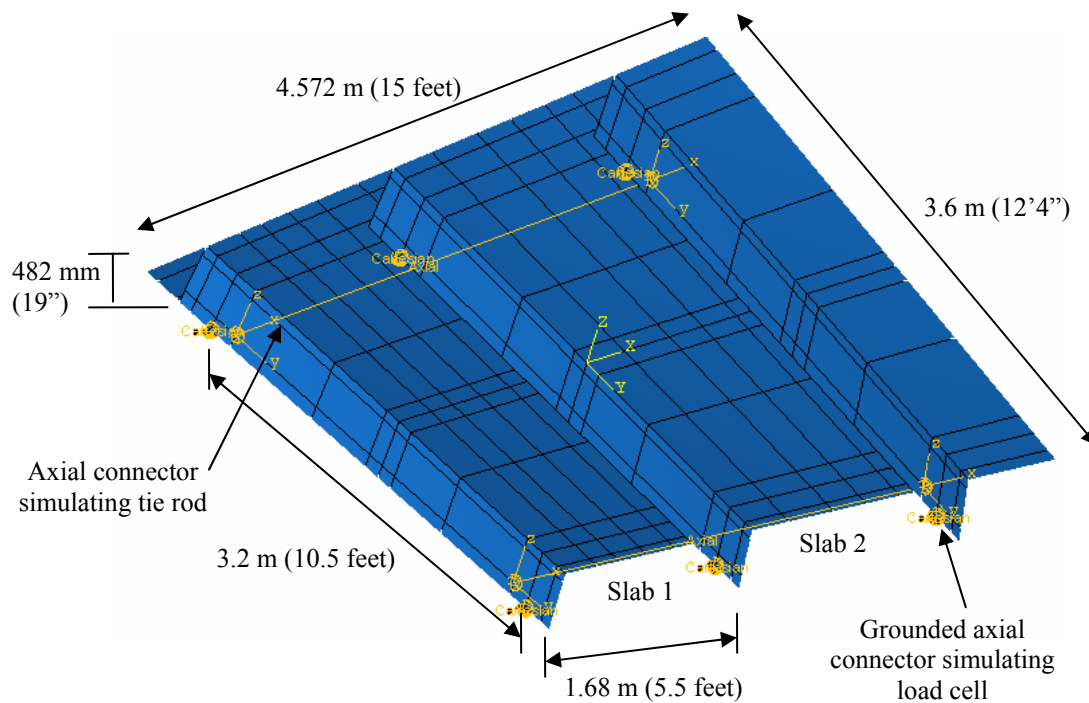


Figure 8.1 Geometry of the baseline model (Phase 1)

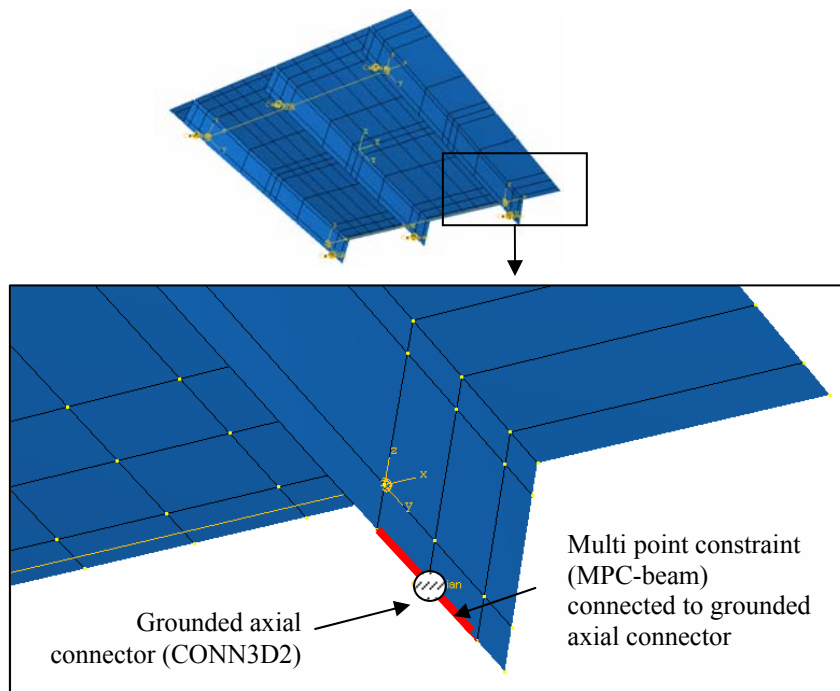


Figure 8.2 Location of multi-point constraints at locations of supports

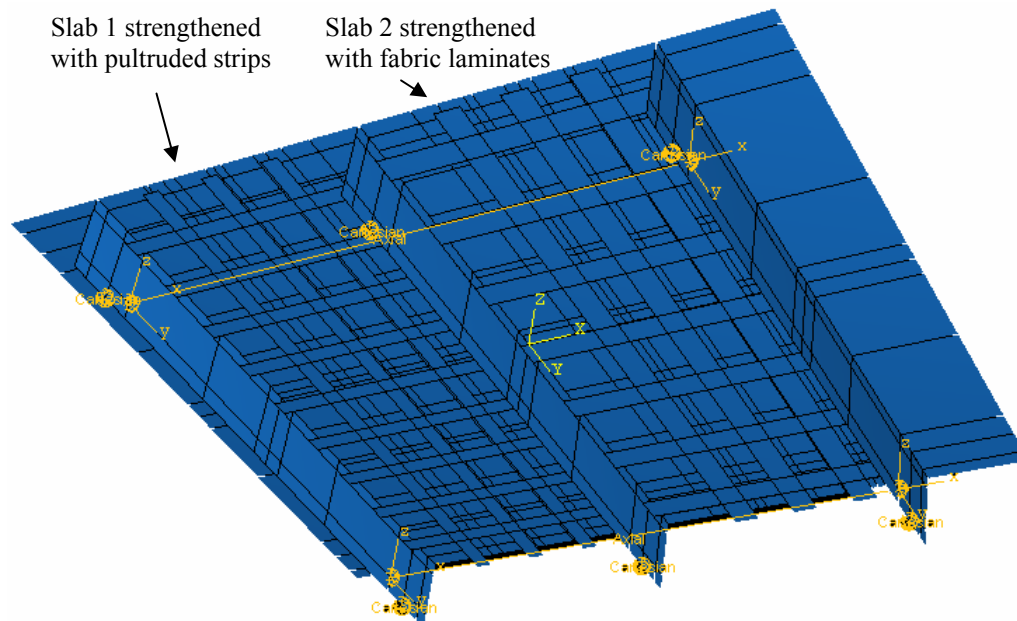


Figure 8.3 Geometry of the model with strengthening of the slabs (Phase 2)

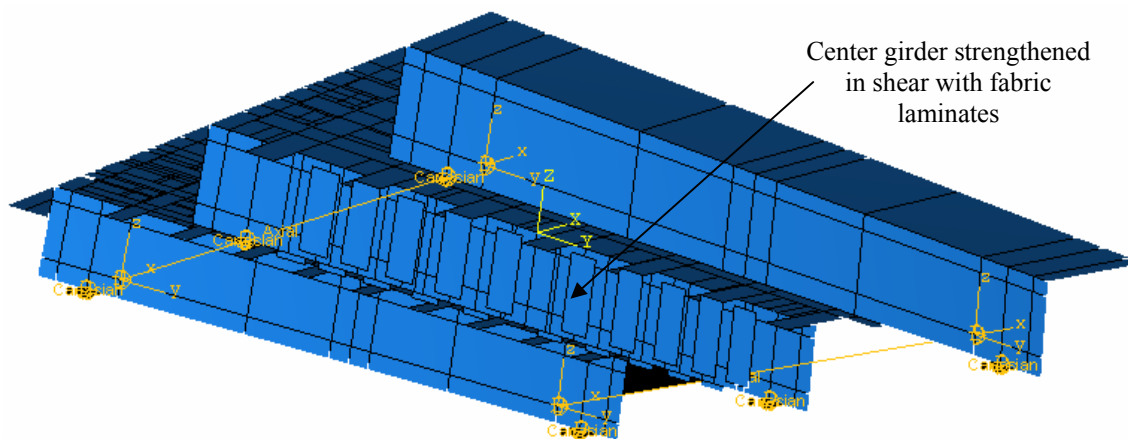


Figure 8.4 Geometry of the model with strengthening of the center girder (Phase 3)

8.2.2 Material Properties

8.2.2.1 Reinforced Concrete

The nonlinear behavior of the concrete was modeled using the Smeared Crack (SC) model [76] which takes into account the oriented-damaged elasticity (smeared cracking) and isotropic compressive plasticity in representing the non-linear behavior of concrete. Further details of the model can be found in [77]. The material properties of concrete to be used for the model were determined based on the compressive strength of 44.1 (6390 psi) as obtained from testing of the concrete used in the test specimen (further details can be found in chapter 4). A typical stress-strain curve for concrete is shown in Figure 8.5 [78].

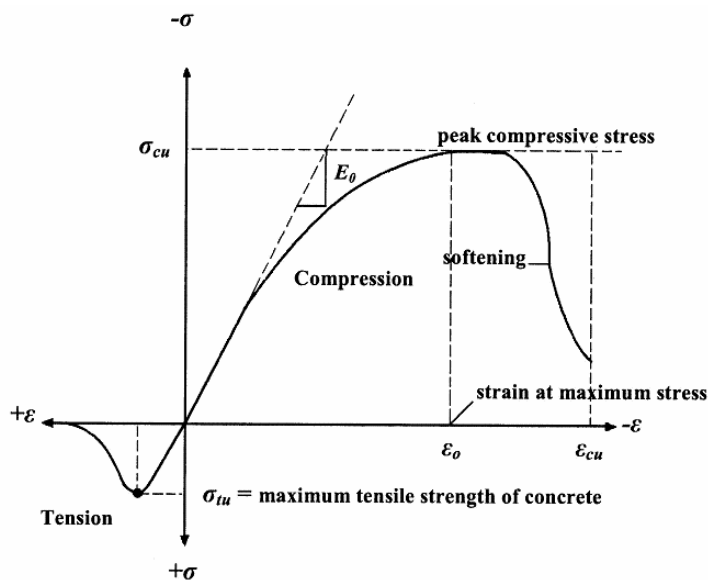


Figure 8.5 Typical stress-strain curve for concrete

In compression the stress-strain curve for concrete is found to be linear elastic upto 30% of the maximum compressive stress [78] and thereafter the stress gradually

increases upto maximum compressive stress, σ_{cu} corresponding to the strain, ε_o after which the compressive strength decreases (softens) until crushing failure occurs at ultimate compressive strain, ε_{cu} . In tension the stress-strain curve is found to be linear-elastic upto the maximum tensile strength beyond which the concrete cracks and the strength decreases to zero.

The initial tangent modulus for concrete in compression, E_o , was calculated using the following equation [69]:

$$E_o = 57000\sqrt{f'_c} = 31.4 \text{ GPa (4556 ksi)} \quad \dots\dots\dots(8.1)$$

The nonlinear portion of the stress-strain curve with stress, σ corresponding to strain, ε , was estimated using Equation 8.2 [78]. The strain in concrete, ε_o , corresponding to maximum compressive strength, σ_{cu} was assumed as 0.003 [78] and the ultimate strain of concrete, ε_{cu} was taken to be 0.004 [78].

$$\sigma = \frac{E_o \varepsilon}{1 + \frac{\varepsilon}{\varepsilon_o}} \quad \dots\dots\dots(8.2)$$

A simplified stress-strain curve for concrete in compression used for the FE model as computed from the above equation is shown in Figure 8.6. The curve was constructed by using 8 stress points at 10% increments of stress upto the ultimate compressive stress of 44.1 MPa (6390 psi), with the corresponding strains being computed using equation 8.2 and the points were connected by straight lines. Also the softening of concrete between strains of 0.003 and 0.004 was not accounted for, i.e. the

concrete compressive stress was constant between strains of 0.003 and 0.004, in the simplified curve to avoid instability and non-convergence issues in the model [78].

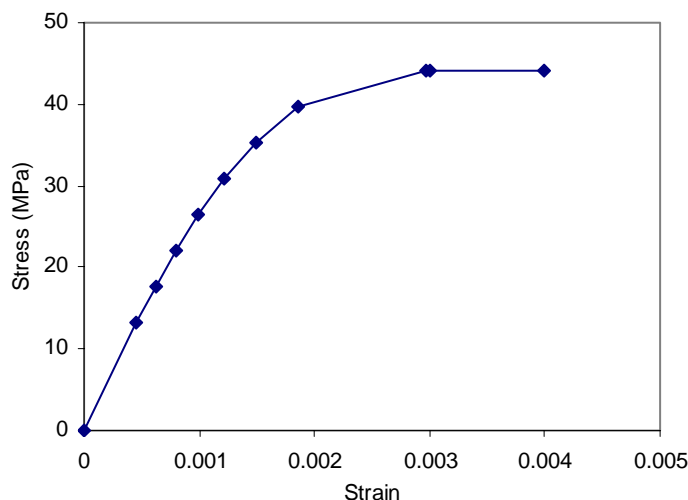


Figure 8.6 Compressive stress-strain curve of concrete used for model

The modeling of the concrete-reinforcement interaction and the energy release at cracking is of critical importance to the response of a RC structure once the concrete starts to crack. This strain-softening behavior for cracked concrete was modeled in an indirect way by adding “tension stiffening” to the concrete model by defining a linear loss of tensile strength beyond the cracking failure of the concrete. It can be assumed that the strain softening after failure reduces the stress linearly to zero at a total strain of about 10 to 20 times the strain at failure [77]. The maximum tensile strength of concrete was computed using equation 8.3 [69] and thereafter the strain at maximum tensile strength of concrete was computed using equation 8.4.

$$\sigma_t = 7.5\sqrt{f'_c} = 4.13 \text{ MPa (600 psi)} \dots\dots\dots(8.3)$$

$$\varepsilon_t = \frac{\sigma_t}{E_o} = 0.13 \times 10^{-3} \dots\dots\dots(8.4)$$

Thus the strain at which the tensile stress of concrete can be assumed to decrease to zero will be between 0.0013 and 0.0026. For the current model a strain value of 0.002 was used at which the tensile strength will be reduced to zero. The stress-strain curve in tension used for the current model taking into account tension stiffening is shown in Figure 8.7.

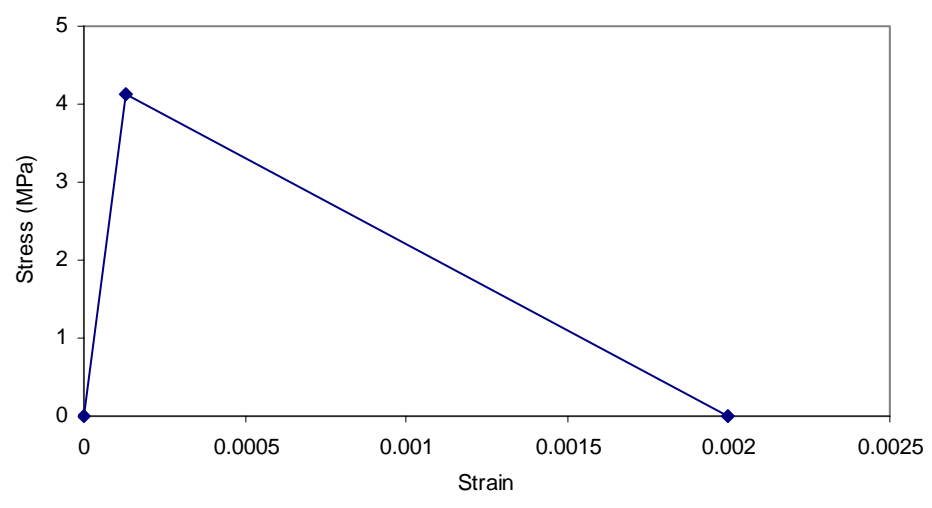


Figure 8.7 Tensile stress-strain curve of concrete used for model

The steel reinforcement in concrete was modeled using the “rebar layer” option in Abaqus [76] in which the steel reinforcement was embedded as a layer of reinforcement in the shell element. The steel reinforcement in the slabs and the girders (the reinforcement details of the test specimen were presented in chapter 4) were defined using this option and were assigned material properties which were determined through

tension tests of the steel reinforcement used for the test specimen. # 5 bars (15.8 mm or 0.625" diameter) were used for slab reinforcement and # 9 bars (28.6 mm or 1.125" diameter) were used for girder flexural reinforcement. #3 bars (9.5 or 0.375" diameter) were used as stirrup reinforcement in the girders. The tensile properties of the steel reinforcement (yield and rupture strength and strains) were presented in Table 4.1 of Chapter 4 and hence are not repeated here. Based on the stress-strain plots of the reinforcement obtained through material testing the critical points such as yield and rupture were picked along with a number of intermediate data points to define the stress-strain response of the reinforcement in the model. The representative stress-strain points of steel reinforcement used for the model are shown in Figures 8.8a to 8.8c.

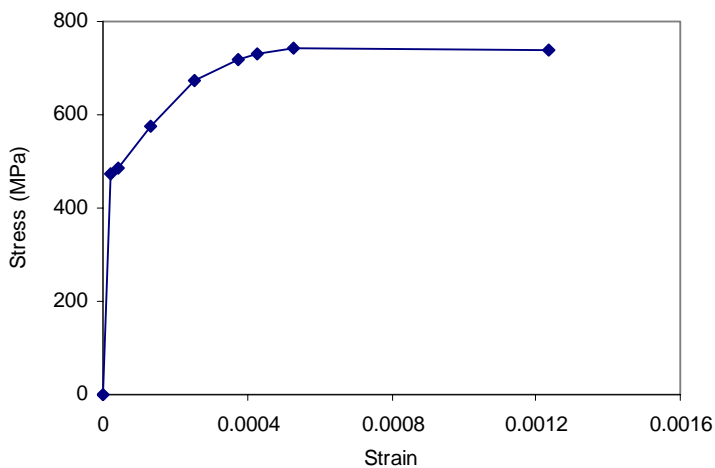


Figure 8.8a Stress-strain curve of # 3 rebars used for girder stirrups

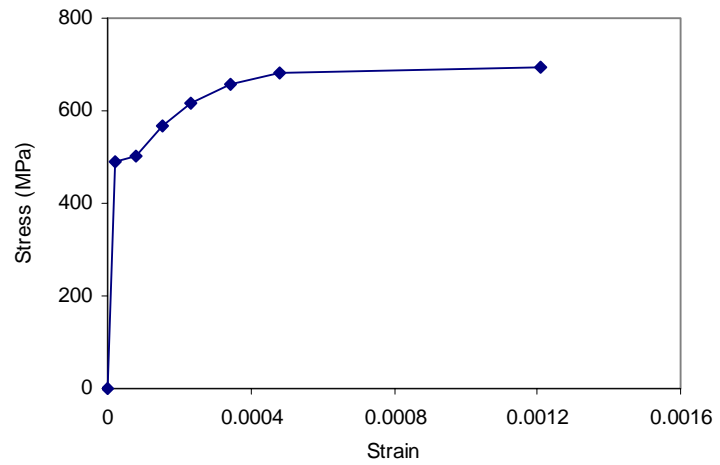


Figure 8.8b Stress-strain curve of # 9 rebar used for girder flexural reinforcement

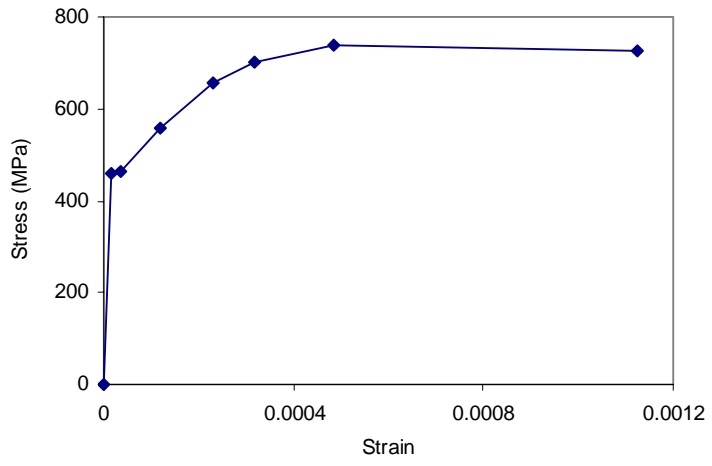


Figure 8.8c Stress-strain curve of # 5 rebar used for slab flexural reinforcement

8.2.2.2 FRP Composite

The FRP composites (fabric laminates and pultruded strips) used for Phase 2 and Phase 3 of the model (strengthening of the slabs and the center girder, respectively) were modeled with shell elements (S4R) and were assigned “composite” section option in Abaqus [76]. It is to be noted that in Phase 2 of testing, Slab 1 was strengthened with 1

layer of 102 mm (4") wide pultruded strip in both the longitudinal and transverse direction while Slab 2 was strengthened with 2 layers of 152 mm (6") wide fabric laminates as transverse reinforcement and 1 layer of 152 mm (6") wide laminate as longitudinal reinforcement. Similar geometry was used in the model. Also 3 layers of fabric laminates were used as composite stirrups for shear strengthening of the central girder in Phase 3 of testing. The corresponding thickness and the elastic modulus of the composites used in the model were based on the material test data obtained from material testing of composite samples used for the test specimen. Further details on the properties of the composites can be found in Chapter 4 and are summarized in Table 8.1.

Table 8.1 Tensile test properties of composites

Composite Type	1 layer fabric	2 layers fabric	3 layers fabric	Pultruded strip
Thickness mm (inches)	3.229 (0.127)	5.12 (0.202)	4.56 (0.18)	1.34 (0.05)
Strength MPa (ksi)	261.5 (37.92)	322.03 (46.69)	431.31 (62.54)	1944.44 (281.94)
Modulus GPa (ksi)	26.5 (3835.8)	35.94 (5211.77)	57.48 (8335.14)	140.0 (20300.1)

8.2.2.3 Connectors

Two types of connectors were used in the model, the first being the two axial connectors simulating the tie rods and the second were the grounded connectors simulating the load cell supports. Both these connectors were modeled with linear elastic properties which were determined earlier in Chapter 7 and are summarized here.

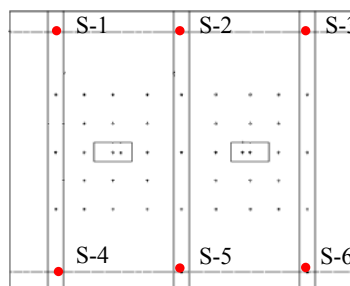
The stiffness of the axial connectors was determined based on the cross-section and elastic modulus of the tie rod used in the test. The 38 mm (1.5”) diameter steel tie rod used had an elastic modulus of 200 GPa (29000 ksi) and length of 3.56 m (140”). Since the rod would only act in tension, the stiffness was calculated as:

$$k = \frac{AE}{l} = 70.1 \text{ N/m (400 kips/inch)} \dots\dots\dots(8.5)$$

The stiffness of the grounded connectors at the supports were estimated based on the slope of the test load-deflection response recorded at the six supports in the first load cycle of 107 kN (24 kips) from the linear potentiometer and load-cell data at locations S-1 to S-6 of the six supports. The estimated stiffness at the six supports was presented in Table 7.4 of Chapter 7 and is repeated here in Table 8.2 for convenience of reference.

Table 8.2 Stiffness estimates of grounded connectors at the supports

Connector #	Stiffness, N/m (kips/inch)
S-1	111.4 (636)
S-2	301.9 (1723)
S-3	191.5 (1093)
S-4	218.7 (1248)
S-5	386.4 (2205)
S-6	225.5 (1287)



Note: The stiffness estimates of support connector elements were based on slope of the measured load deflection response at supports from linear potentiometer and load cell data

8.2.3 Loading and Solution Control

The model was loaded with pressure loads simulating the actuator loads in the test specimen. The loads were distributed over an area of 508 mm x 254 mm (20”x10”) simulating the contact area of the actuator in the test specimen.

Since considerable nonlinearity was expected in the response of the model, including the possibility of unstable regimes as the concrete cracked, the modified Riks method was used with automatic increments [77]. The essence of the method is that the solution is viewed as the discovery of a single equilibrium path in a space defined by the nodal variables and the loading parameter. Development of the solution requires that this path be traversed as far as required. Thus in this process both the load and stress components are treated as unknowns and the nonlinear equilibrium equations are solved simultaneously using Newton's method. The specified loading only acts as the upper bound of the load at which the solution will terminate. This approach can thus provide solutions regardless of whether the response is stable or unstable. Further details of the Riks algorithm can be found in [77].

8.3 Analysis Results

The analysis results from the Abaqus model were compared with the test results over the three phases of loading in terms of load-deflection response, damage progression and strain profiles in the steel and composite reinforcement and are presented next in this section.

8.3.1 Phase 1 of Test

8.3.1.1 Load-Deflection Response

Phase 1 of the test involved loading of the unstrengthened test specimen. The load-deflection responses of the two slabs, center girder and two edge girders during this phase are shown in Figures 8.9 to 8.13. A good correlation was found between the

analysis and experimental results in terms of load deflection response in Phase 1 of test. From the numerical model, the primary damage in phase 1 was localized in the slabs indicated by the high non-linearity of the load-deflection slope of the slabs and this matched test observations. The damage progression in the slabs will be discussed in the next section. From the test results, the slab deflections at 400 kN load (end of phase 1 loading) below the load areas were 4.46 mm in slab 1 and 4.23 mm in slab 2. From the numerical analysis, the corresponding deflections were 4.15 mm in slab 1 and 4.07 mm in slab 2.

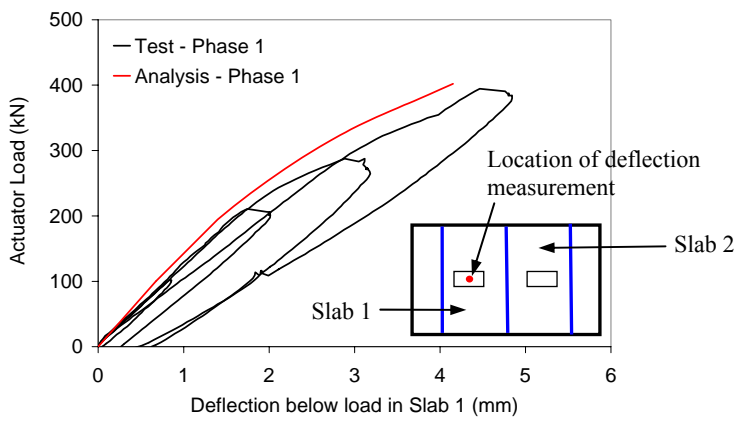


Figure 8.9 Verification of load-deflection response of slab 1 – Phase 1

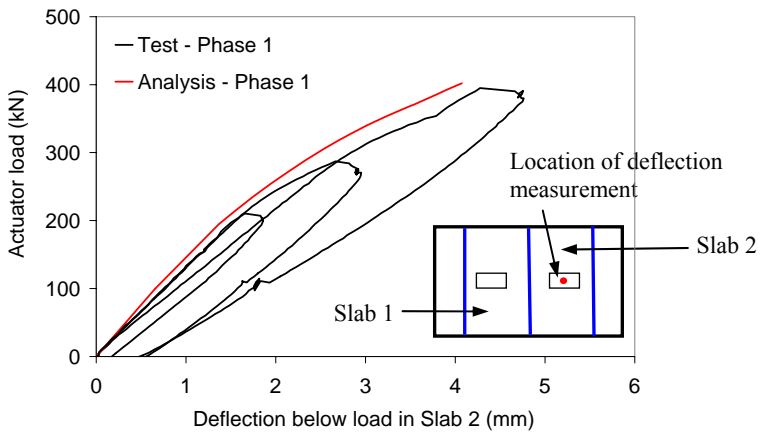


Figure 8.10 Verification of load-deflection response of slab 2 – Phase 1

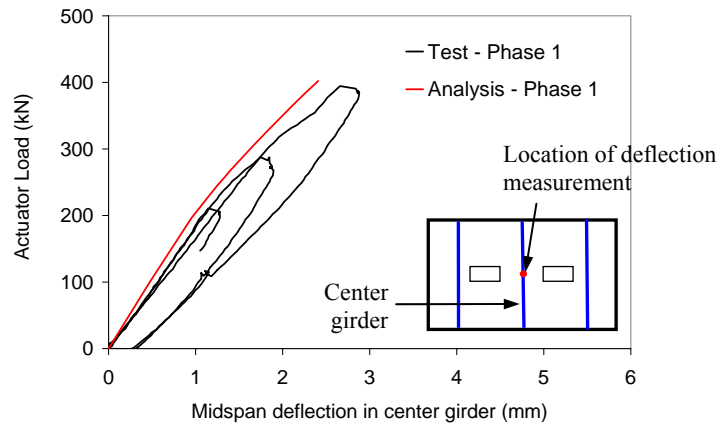


Figure 8.11 Verification of load-deflection response of center girder – Phase 1

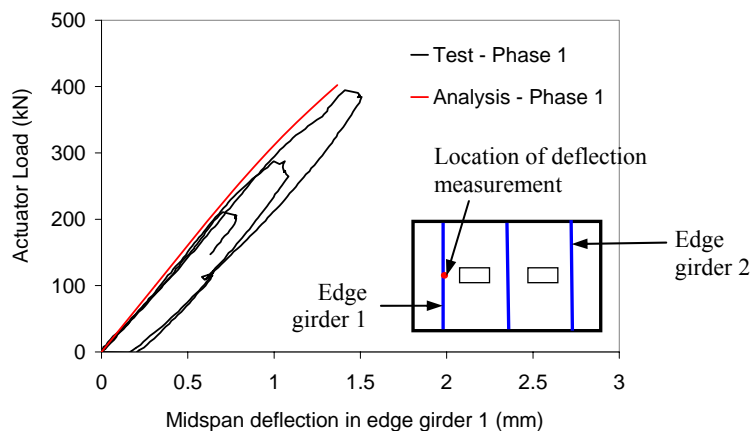


Figure 8.12 Verification of load-deflection response of edge girder 1 – Phase 1

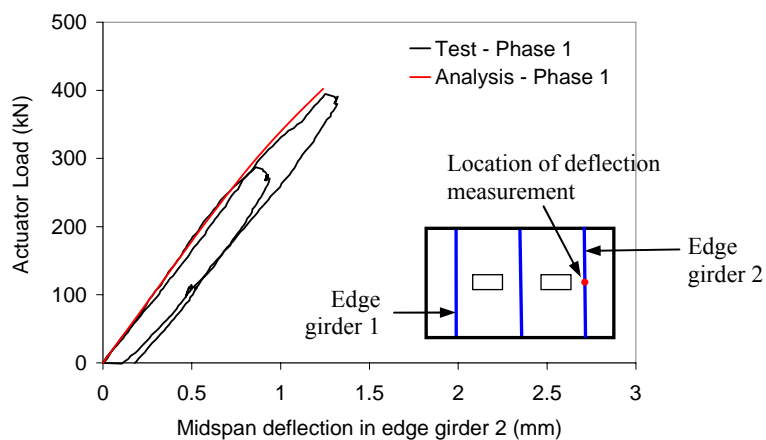


Figure 8.13 Verification of load-deflection response of edge girder 2 – Phase 1

8.3.1.2 Damage Progression and Strain Profiles

The damage progression in the numerical model was determined by monitoring the progression of cracking over the load steps in Phase 1. The progression of cracking was obtained by plotting the maximum nominal principal strain (NE-Principal) vectors in the FE model. Since the cracking strain of concrete was estimated as 0.00013 in equation 8.4, only maximum principal strain vectors with magnitudes larger than 0.0001 were plotted to determine the areas of cracked concrete. Also the direction of the crack could be estimated as the direction normal to the maximum principal strain vector. By using this concept of effective crack direction, a graphical visualization of the damage progression in the deck slabs was obtained over the load stages in Phase 1 of test and is shown in Figures 8.14 to 8.17.

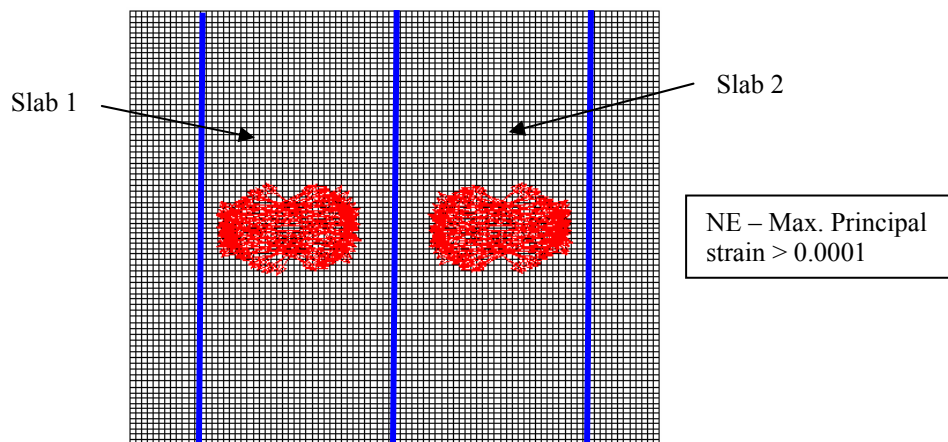


Figure 8.14 Maximum principal strain vectors in slabs at 214 kN (48 kips) – Phase 1

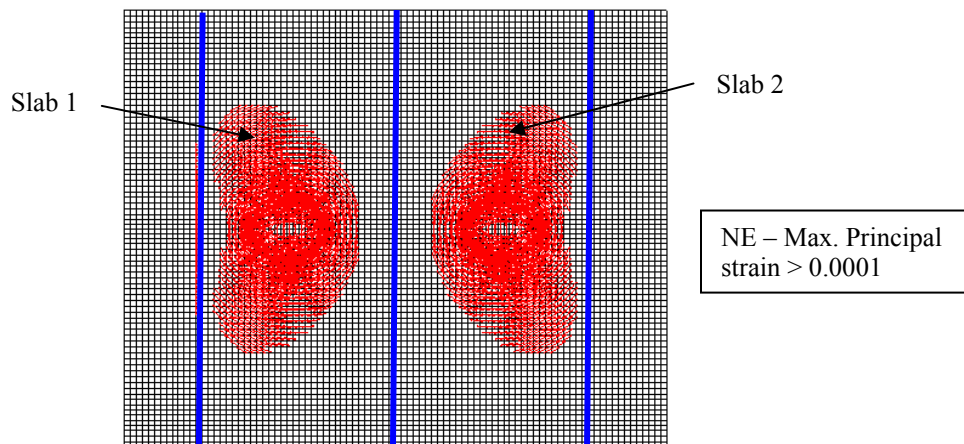


Figure 8.15 Maximum principal strain vectors in slabs at 289 kN (65 kips) – Phase 1

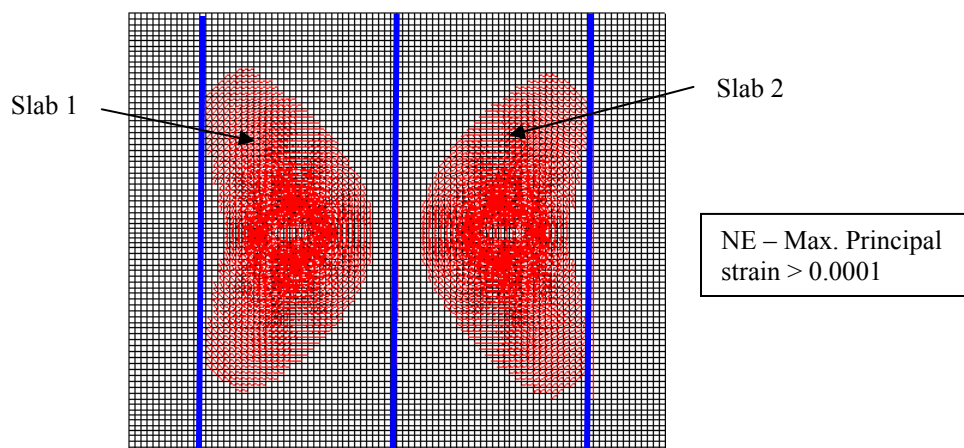


Figure 8.16 Maximum principal strain vectors in slabs at 356 kN (80 kips) – Phase 1

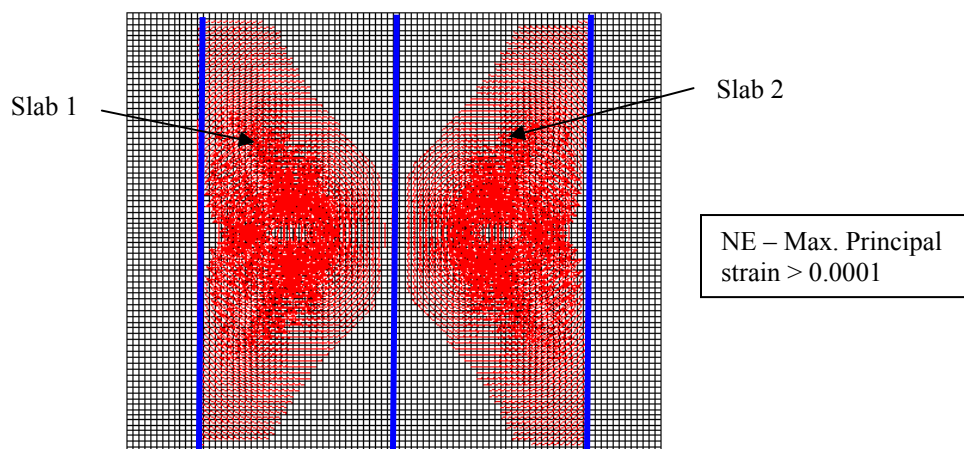


Figure 8.17 Maximum principal strain vectors in slabs at 400 kN (90 kips) – Phase 1

Also based on the concept that the direction of the crack will be normal to the direction of the maximum principal strain vector, the cracks were marked out below the load area of the slab at 400 kN load, which was the maximum load to which the slabs were loaded in Phase 1. A comparison of the crack pattern from the numerical simulation and from the visual observations of the cracks at the bottom of the slabs at this stage of loading is shown in Figures 8.18a and 8.18b. The cracks in the numerical simulation are shown as dotted lines since they represent an estimate of the crack directions. Since a smeared crack model was used, the exact locations of the cracks were not obtained from the model. A good correspondence was observed between the numerical simulation and test observations of the crack pattern.

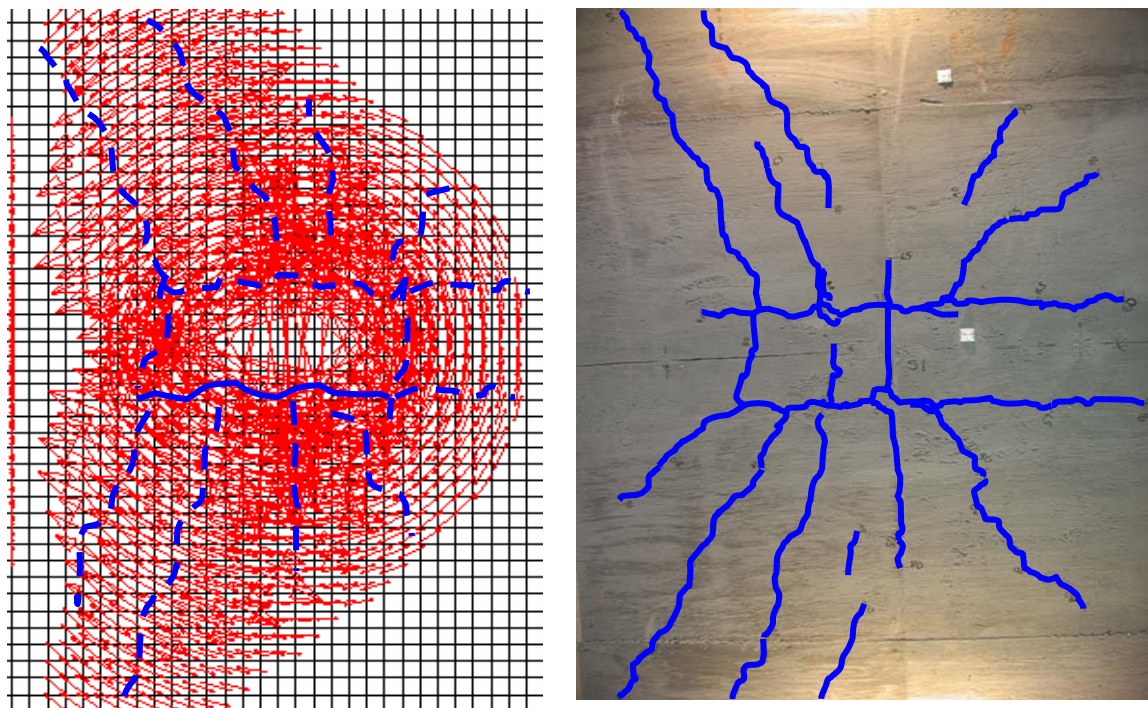


Figure 8.18a Comparison of crack patterns in slab 1 below load area from numerical model and test observations at 400 kN (90 kips) - End of Phase 1

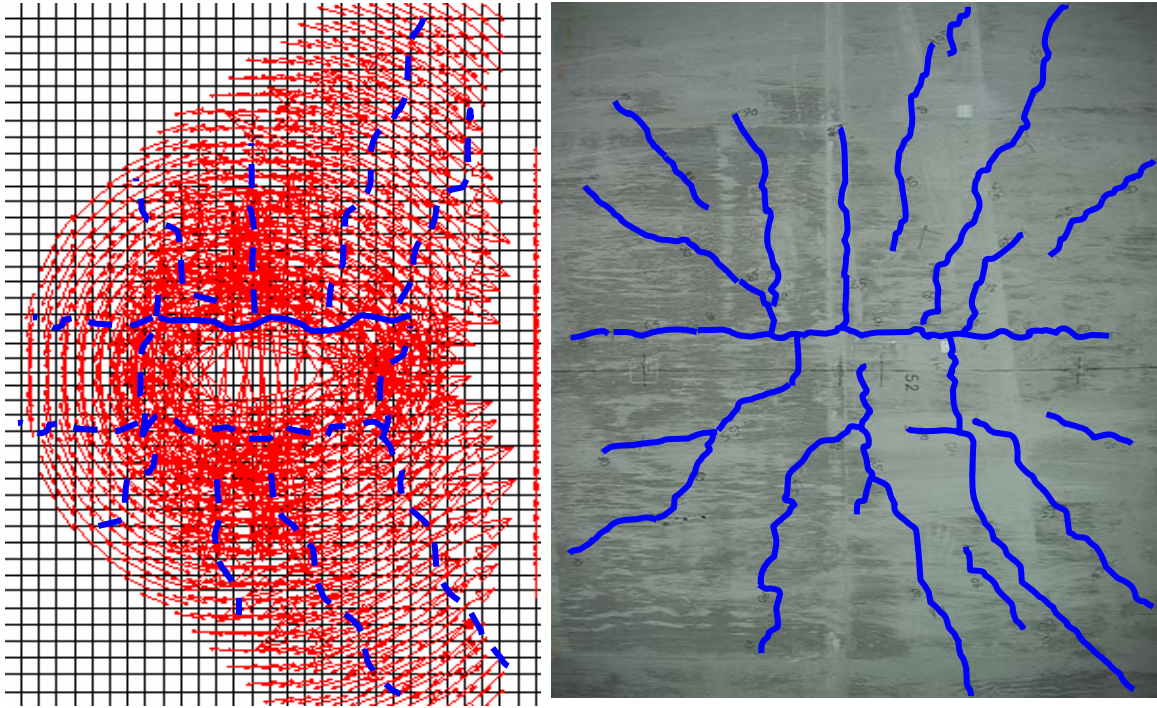


Figure 8.18b Comparison of crack patterns in slab 2 below load area from numerical model and test observations at 400 kN (90 kips) - End of Phase 1

The crack patterns and the damage progression in the numerical simulation, as shown above, were representative of punching shear deficiency in the slabs with the primary cracks initiating as longitudinal and transverse cracks below the load area and with increase of loading, new cracks were formed which propagated away from the load area towards the edge girders. Also the strain profile in the transverse steel reinforcement in the two slabs below the load areas was obtained from the numerical model and is shown in Figures 8.19a and 8.19b. The maximum strains of 945 and 938 microstrains in slabs 1 and 2, respectively matched well with the measured strains of 954 and 947 microstrains from the strain-gage data. These strain values of the steel reinforcement from the numerical simulation also showed that the slab steel reinforcement was

significantly below the yield strain of 2400 microstrains and thus punching shear rather than flexural failure was the governing limit state in the deck slabs as was observed during the actual test.

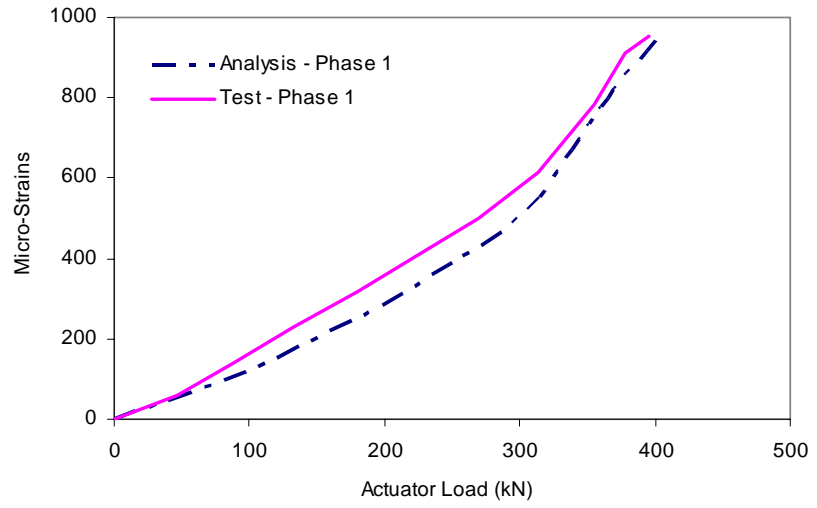


Figure 8.19a Comparison of strain profile in slab 1 transverse reinforcement below load

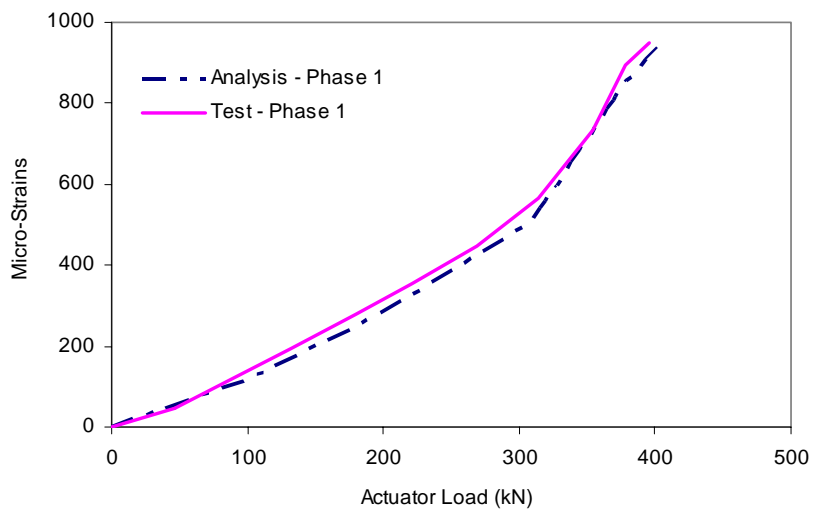


Figure 8.19b Comparison of strain profile in slab 2 transverse reinforcement below load

The numerical modeling of damage progression in the center girder during phase 1 of test is shown in Figure 8.20 by plotting the maximum principal strain vectors with strains > 0.0001 . The principal strain vectors at the 289 kN and 356 kN load stages were horizontal (i.e. direction of cracks was vertical) and confined to the mid-span of the girder indicating initiation of flexural cracks. However the principal strain vectors at the 400 kN load stage (end of phase 1 of test) were found to be diagonal in the quarter span of the girder indicating the initiation of shear cracks between the 356 kN and 400 kN load stages. These matched the test observations of development of flexural and shear cracks in the center girder during phase 1 as was presented in Chapter 5. Comparison of the crack pattern at the end of Phase 1 loading as obtained from numerical and test result is shown in Figure 8.21. As discussed earlier, the cracks in the numerical model were drawn normal to the maximum principal strain vectors and only represent estimates of their location since a smeared crack model was used in the analysis.

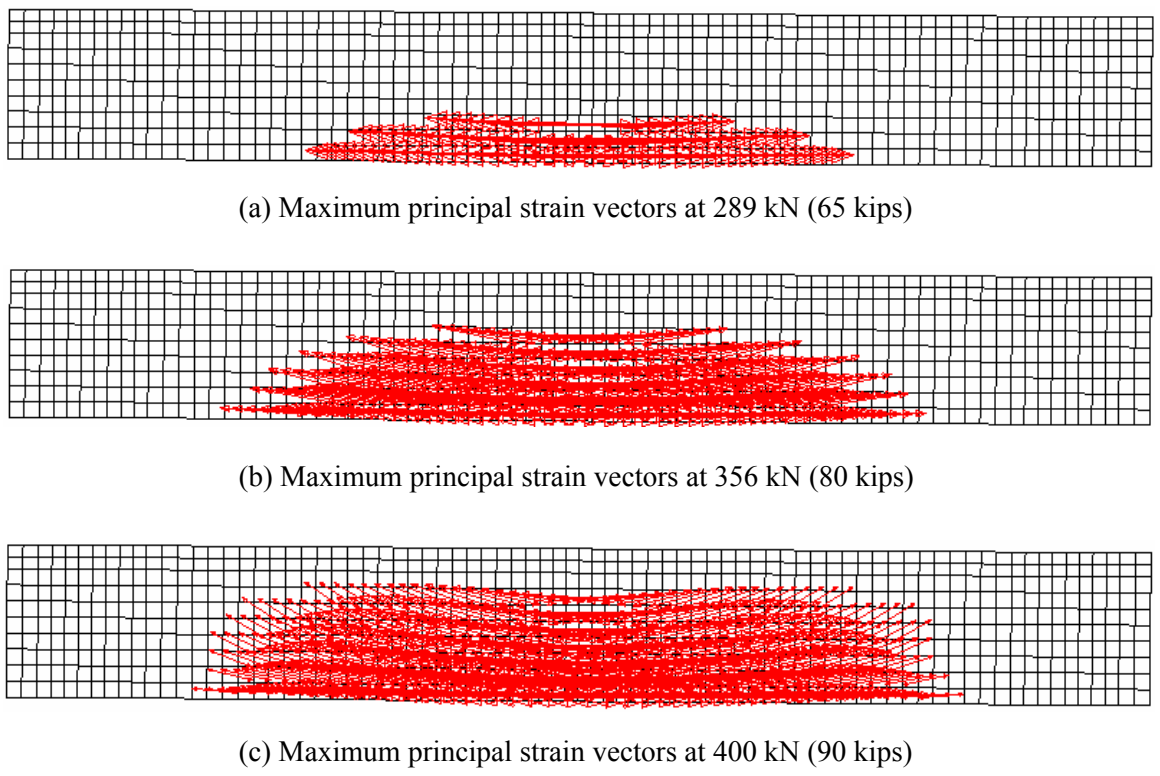


Figure 8.20 Maximum principal strain vectors ($NE > 0.0001$) in center girder – Phase 1

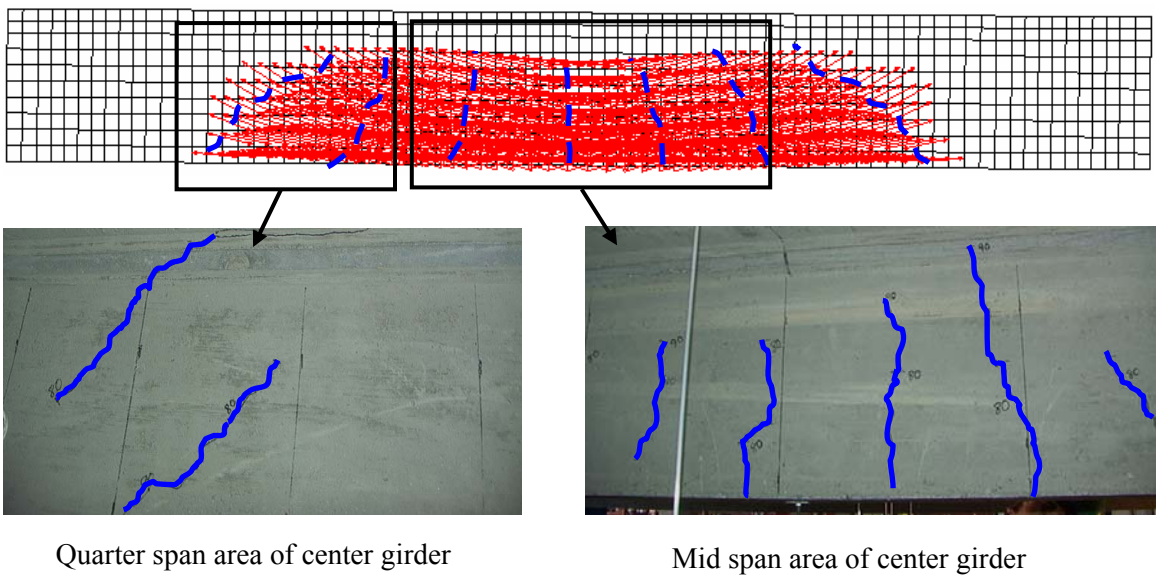


Figure 8.21 Comparison of crack patterns in center girder from numerical model and test observations at 400 kN (90 kips) - Final load cycle of Phase 1

8.3.2 Phase 2 of Test

In Phase 2 of the test, the specimen was loaded after strengthening of the slabs with FRP composites. The modeling of composite strengthening in the numerical model was discussed in section 8.2. The comparison of the test results and results of numerical analysis pertaining to this phase of test are presented next.

8.3.2.1 Load-Deflection Response

The load-deflection response of the two slabs, center girder and two edge girders during phase 2 of test are shown in Figures 8.22 to 8.26. A good correlation was found between the analysis and experimental results in terms of load deflection response in Phase 2 of test. From the load-deflection response obtained from the numerical analysis it was found that the strengthening of the slabs resulted in stiffness enhancements in the slabs, (by 24.9% in slab 1 strengthened with the pultruded strips and by 25.8% in slab 2 strengthened with the fabric laminates), but had insignificant effect on the stiffness of the girders. This was congruent with the tests results presented in Chapter 5. From the test results, the strengthening of the slabs resulted in enhancement of the slab stiffness by 20% in slab 1 strengthened with the pultruded strips and by 21% in slab 2 strengthened with the fabric laminates (as presented in Chapter 5). During phase 2 loading between the 400 kN and 667 kN the primary damage progression was observed in the center girder, as will be presented in the next section. The maximum predicted mid-span deflection in the center girder, including support settlement, at 667 kN (the final load cycle of phase 2) obtained from numerical analysis was 4.95 mm as compared to the corresponding measured deflection of 5.32 mm from test results.

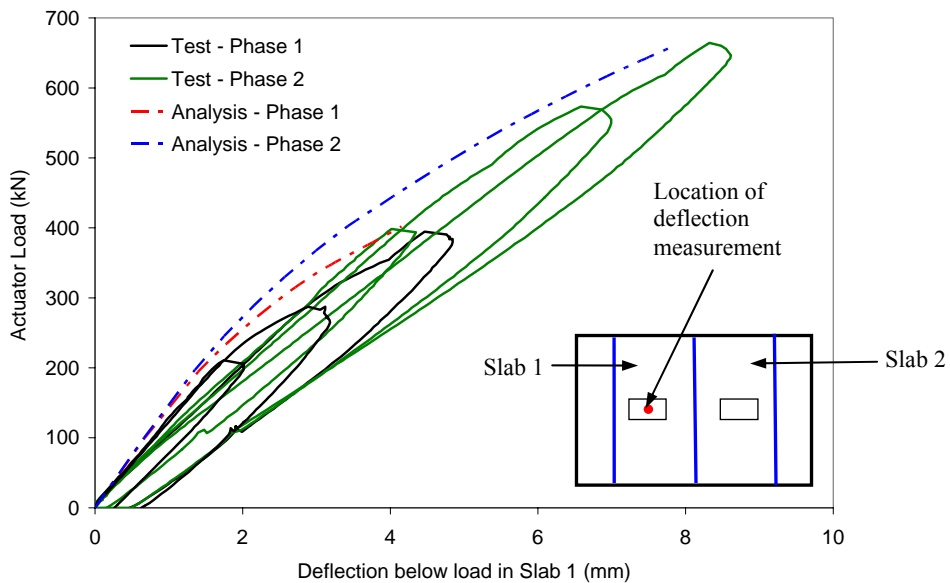


Figure 8.22 Verification of load-deflection response of slab 1 – Phase 2

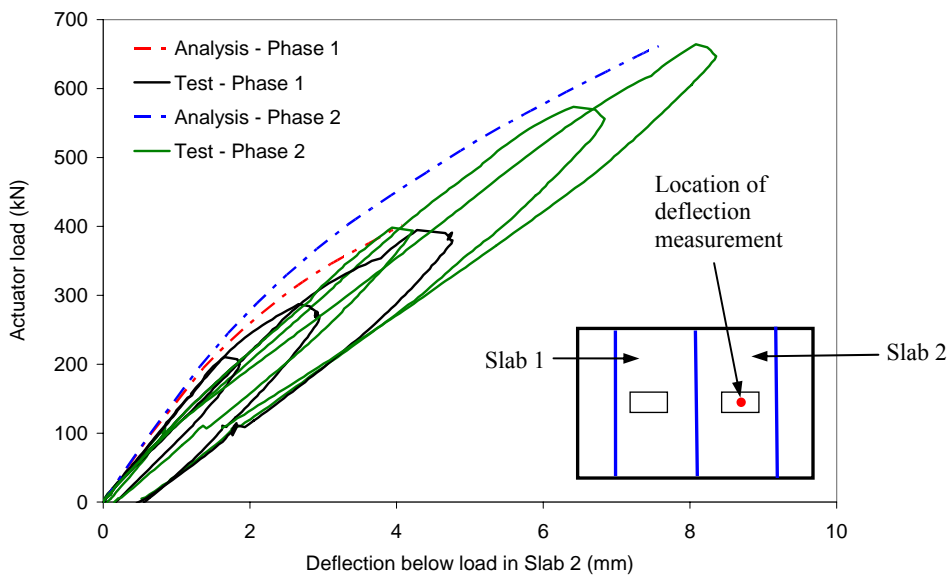


Figure 8.23 Verification of load-deflection response of slab 2 – Phase 2

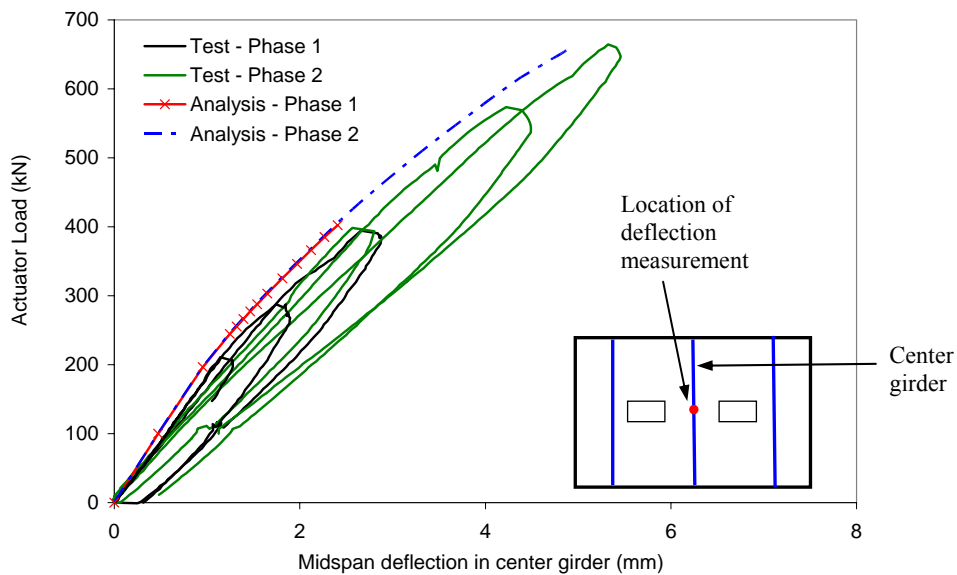


Figure 8.24 Verification of load-deflection response of center girder – Phase 2

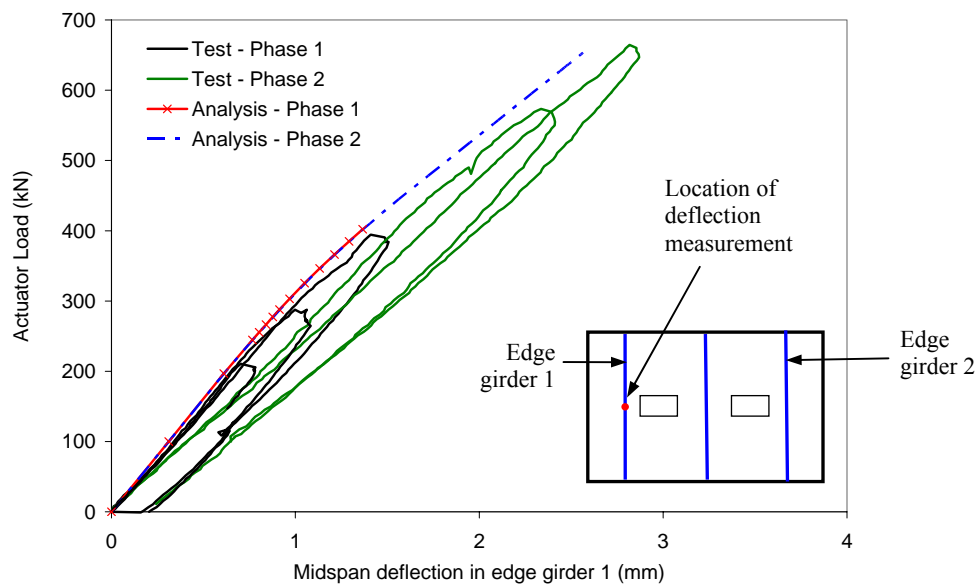


Figure 8.25 Verification of load-deflection response of edge girder 1 – Phase 2

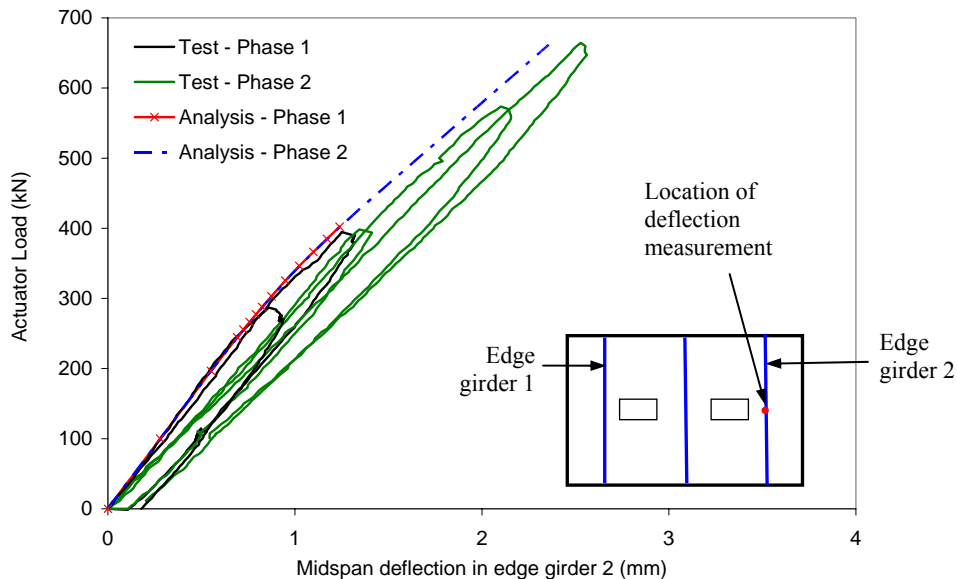


Figure 8.26 Verification of load-deflection response of edge girder 2 – Phase 2

8.3.2.2 Damage Progression and Strain Profiles

In phase 2 of loading after strengthening of the deck slabs, the center girder was subjected to shear criticality under the high load demands imposed on the shear-deficient unstrengthened girder since the strengthening of the slabs resulted in the slab-girder system being able to resist higher loads. The simulation of the damage progression in the unstrengthened center girder during phase 2 loading is shown in Figure 8.27. As mentioned earlier, the vector plot for maximum principal strains ($NE > 0.0001$) gave indication of the areas of cracked concrete (since cracking strain was estimated as 0.00013). Also the orientation of the cracks could be taken to be normal to the maximum principal strain vectors. The strain vectors in the shear critical quarter-span areas of the girder were inclined at approximately 45° indicating the development of shear cracks. Also the maximum principal strain vectors plots in Figure 8.27 are presented over the

three load cycles of phase 2 and show progression of damage in the shear critical areas of the girder. The 762 mm (30") shear critical area at quarter span represented the region of the test specimen with shear stirrups spaced at average of 254 mm (10").

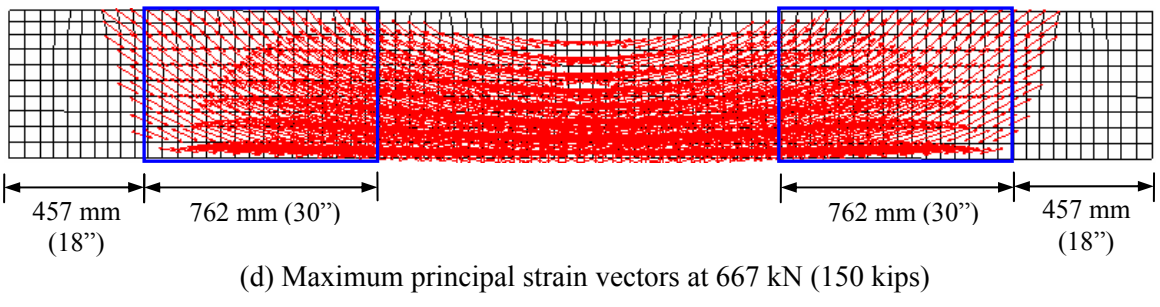
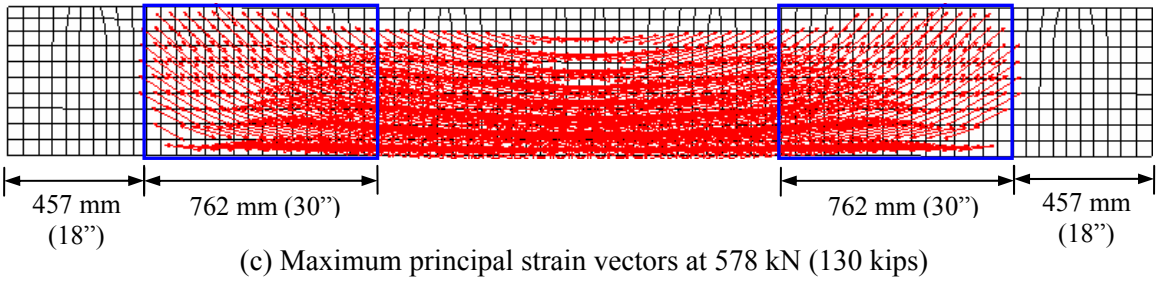
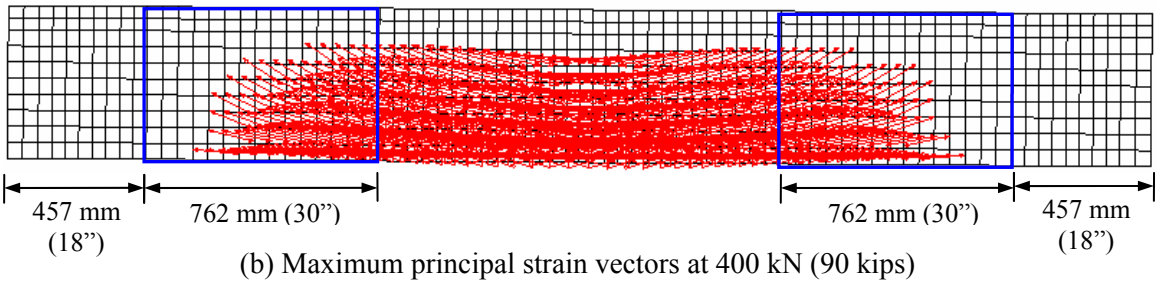
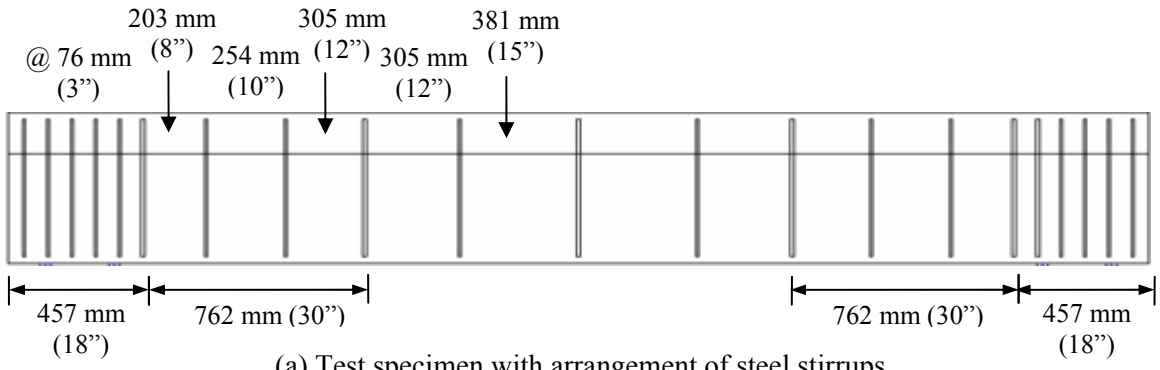


Figure 8.27 Maximum principal strain vectors (NE >0.0001) in center girder – Phase 2

The crack patterns in center girder from numerical model and test observations at 667 kN (150 kips) were compared and is shown in Figure 4.28. The estimated crack pattern from the numerical model, with the cracks drawn normal to the maximum principal strain vectors, showed good correspondence to the flexural and shear regions of the girder as observed during the test. The strains in the vertical steel stirrups of the center girder were predicted by determining the nominal strain in the vertical direction (NE11) in the stirrup reinforcement of the center girder in the model. Figure 8.29 shows the nominal strain contour in the steel stirrups located in the shear critical region at 667 kN load. The location of highest strain at 667 kN (final load cycle of phase 2 loading) in the numerical model was found to coincide well with the location of highest strain recorded in the stirrups (strain gage at location S2-72 had the highest strain reading) from the test results.

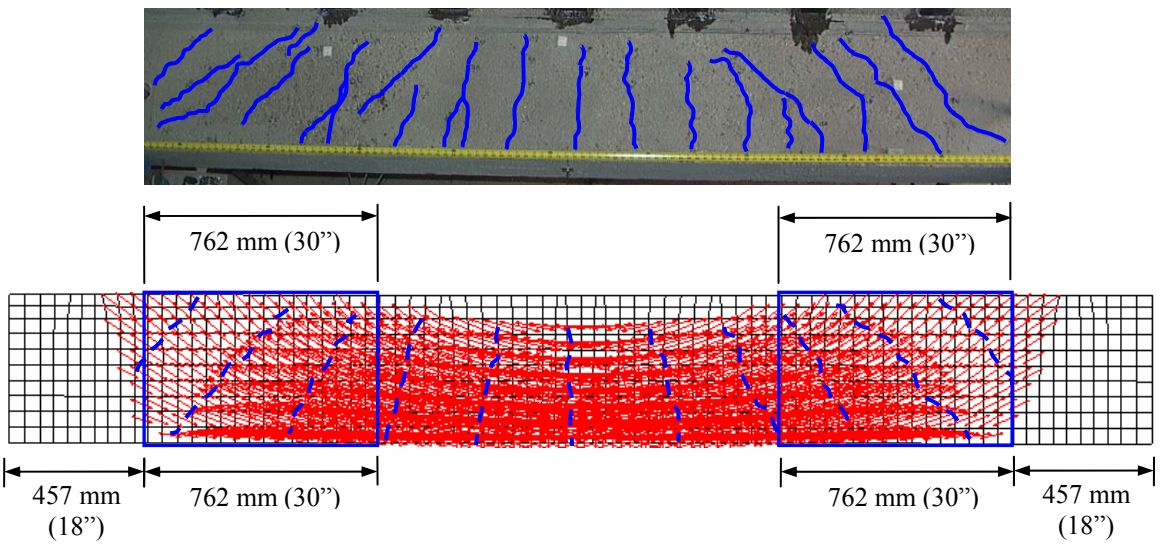


Figure 8.28 Comparison of crack patterns in center girder from numerical model and test observations at 667 kN (150 kips) – Final load cycle of Phase 2

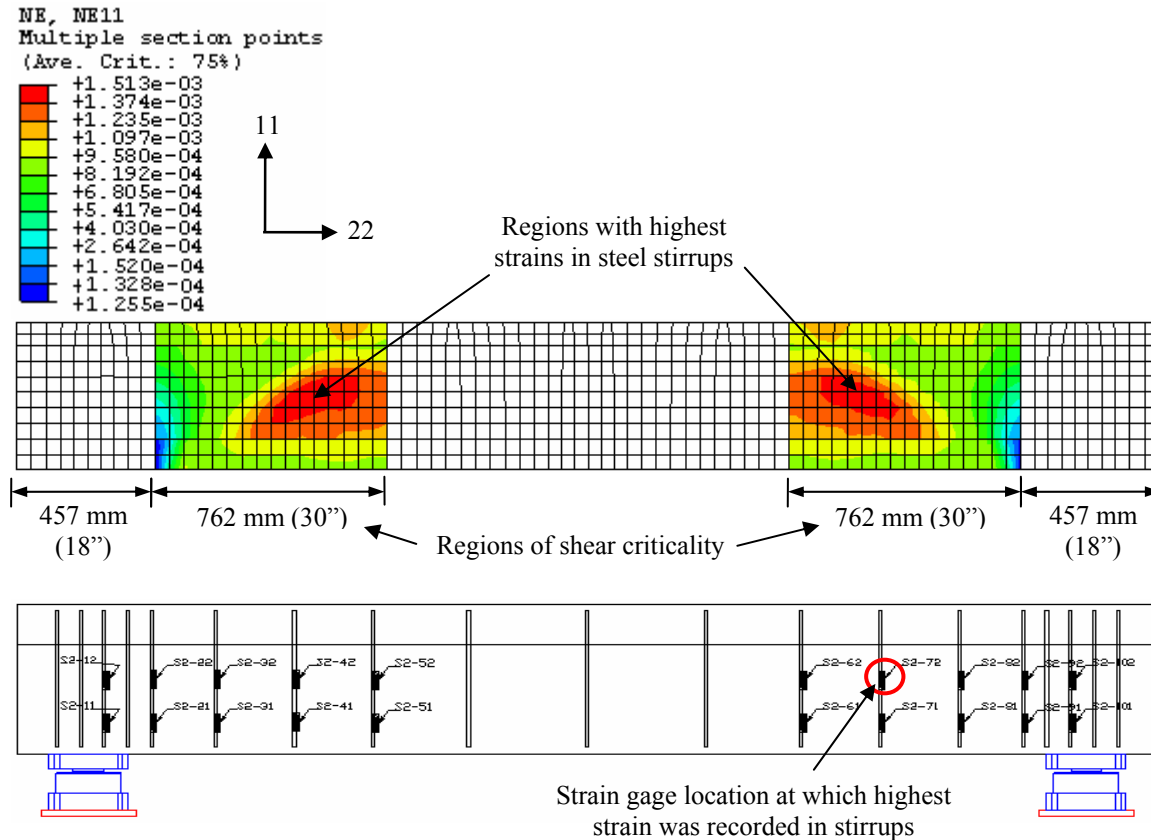


Figure 8.29 Nominal strain (N11) contours in center girder stirrups at 667 kN

The highest strain in the steel stirrups of the center girder predicted by the analytical model over phase 2 loading was compared with the strains recorded by strain gage at location S2-72 (shown in Figure 8.27) during phase 2 test and is shown in Figure 8.30. The maximum strain predicted by the analytical model at peak load of 667 kN load cycle of phase 2 loading was 1513 microstrains and this compared well with the highest strain of 1660 microstrains recorded during the test at location S2-72.

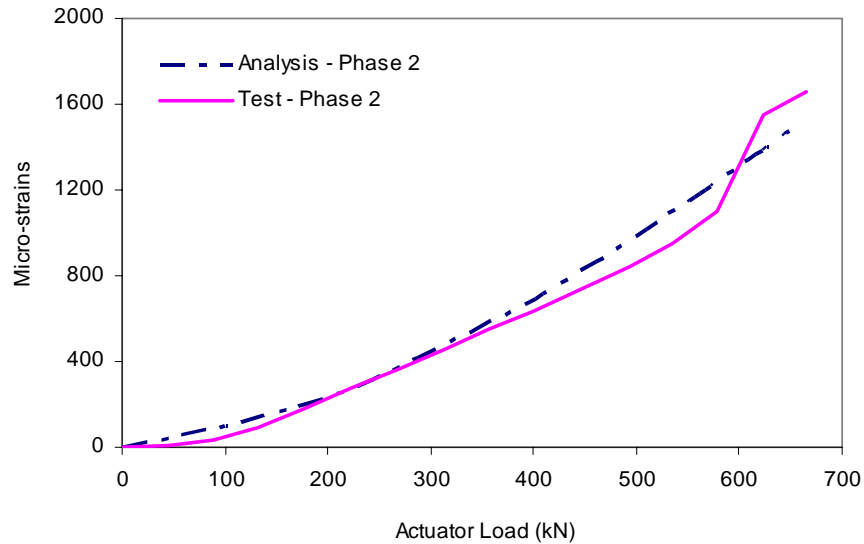


Figure 8.30 Comparison of highest strain vs. load response in center girder stirrup from analytical model and strain gage data during Phase 2

Also from the numerical model, strengthening of the deck slabs with FRP composite was found to result in reduction in the strain in the slab steel reinforcement indicating the effect of the composite strengthening. From the numerical analysis, the addition of the composite systems resulted in reduction in the strain of the slab transverse steel reinforcement below the load areas from 945 to 699 microstrains in slab 1 and from 938 to 645 microstrains in slab 2 at comparable load of 400 kN (which was the maximum load to which the specimen was subjected to at end of phase 1 before the slabs were strengthened). The corresponding reductions obtained from the strain gage data during the actual test were from 954 to 784 microstrains in slab 1 and from 947 to 716 microstrains in slab 2. The comparisons between the strain profiles of the slab transverse steel reinforcement below the load areas from analysis and test results are shown in Figure 8.31.

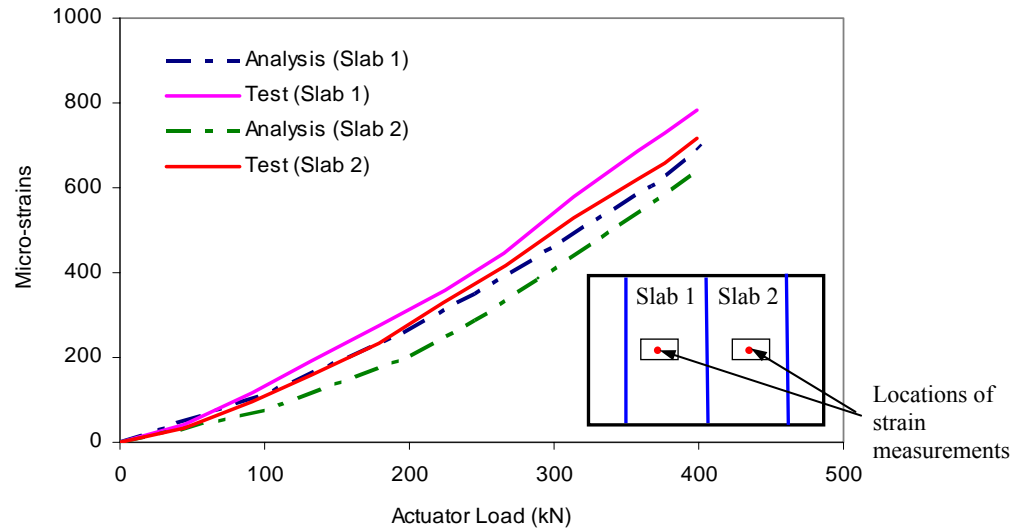


Figure 8.31 Strain profile comparison in slab transverse steel reinforcement – Phase 2

The strains in the two composite systems during phase 2 loading obtained from numerical analysis were compared with the strain gage data from the test. The maximum strains in the composite systems were observed in the transverse composite strip/laminate below the load areas of the two slabs and comparisons of the strains in the pultruded strip and the fabric laminate from analysis and test results are shown in Figure 8.32. The strain obtained in the transverse pultruded strip below the load area in slab 1 at 667 kN load (maximum load of the final load cycle of phase 2) was 2762 microstrains from numerical analysis compared to 2577 microstrains obtained from test results. The strain obtained in the transverse fabric laminate below the load area in slab 2 at 667 kN load was 2243 microstrains from numerical analysis compared to 2016 microstrains obtained from test results. Thus the numerical analysis predicted that at the end of Phase 2 loading, at which the strains in the girder stirrups indicated shear criticality of the center girder, the composite systems would be below their predicted debonding strains of 3568 and 3262

microstrains for the pultruded strips and the fabric laminates, respectively. This indicated that the numerical model was able to predict that at the systems level the shear failure of center girder would prevent the strengthened deck slabs from reaching their ultimate strength capacities.

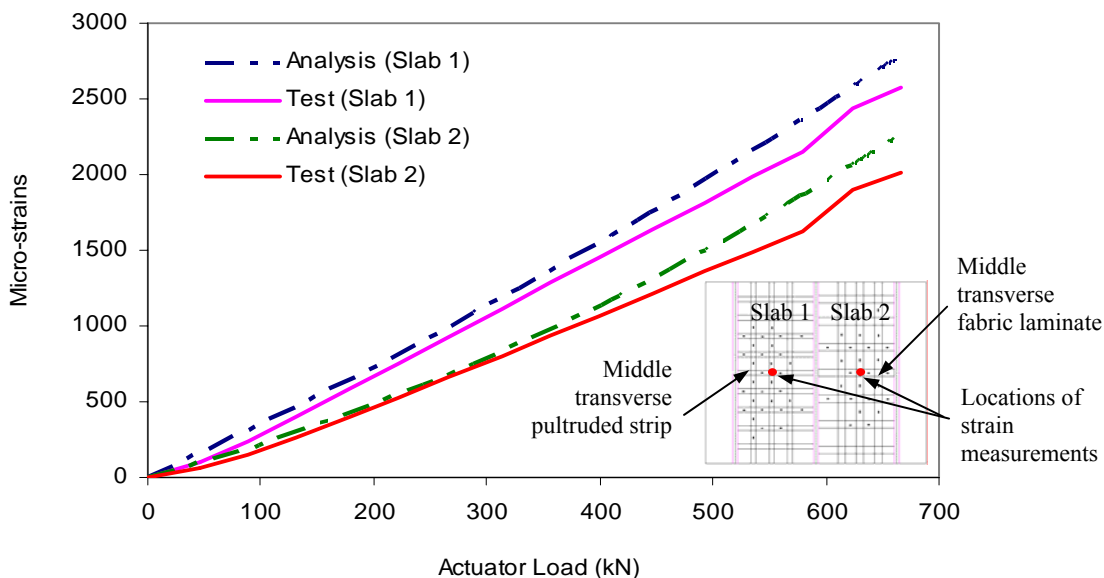


Figure 8.32 Comparison of strain profile in slab composite reinforcement – Phase 2

8.3.3 Phase 3 of Test

In Phase 3 of the test, the specimen was loaded after strengthening of the center girder with FRP composite stirrups. The modeling of composite strengthening of the center girder in the numerical model was discussed in section 8.2. The comparison of the test results and numerical analysis results during this phase of test are presented next.

8.3.3.1 Load-Deflection Response

The load-deflection responses of the two slabs, center girder and two edge girders during phase 3 of test are shown in Figures 8.33 to 8.37. Good correlation was found between the analysis and experimental results in terms of load deflection response in Phase 3 of test. From the load-deflection response obtained from the numerical analysis it was seen that the strengthening of the center girder resulted in stiffness enhancements in the center girder but had no significant effect on the stiffness of the slabs. This was congruent with the tests results presented in Chapter 5. The primary damage in this phase of loading was in the composite strengthened slabs, as is seen from the considerable nonlinearity in the load-deflection plots of the slabs, indicating decrease of stiffness in the slabs. As will be discussed in the next section, at 930 kN (209 kips), which also corresponded to experimental failure load, the maximum strain in the slab composite below the load areas exceeded both predicted and experimentally measured debonding strains and thus analysis was stopped. From the analysis results, the maximum predicted deflections in the slabs below the load areas at 930 kN were 13.32 mm in slab 1 and 12.91 mm in slab 2. From the test results, the maximum slab deflections below the load areas at failure load were 13.92 mm in slab 1 and 13.5 mm in slab 2. The maximum predicted deflections in the girders were 7.1 mm in the center girder and 3.78 mm and 3.37 mm, respectively in the two edge girders. The corresponding maximum deflections in the girders measured from the test were 7.91 mm in the center girder and 4.13 mm and 3.57 mm, respectively in the two edge girders. Thus the numerical model predicted the load deflection response of the test specimen fairly well.

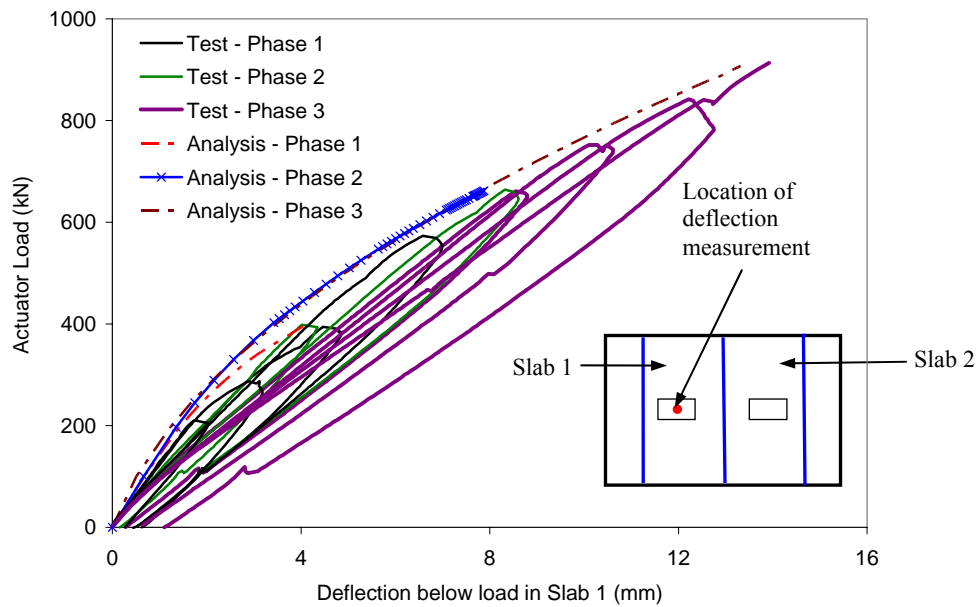


Figure 8.33 Verification of load-deflection response of slab 1 – Phase 3

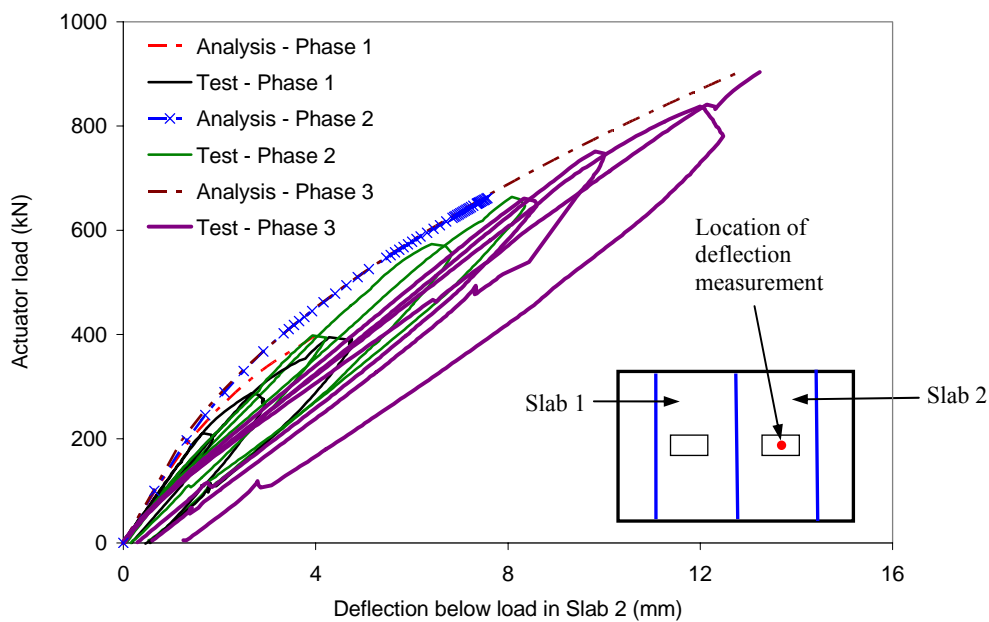


Figure 8.34 Verification of load-deflection response of slab 2 – Phase 3

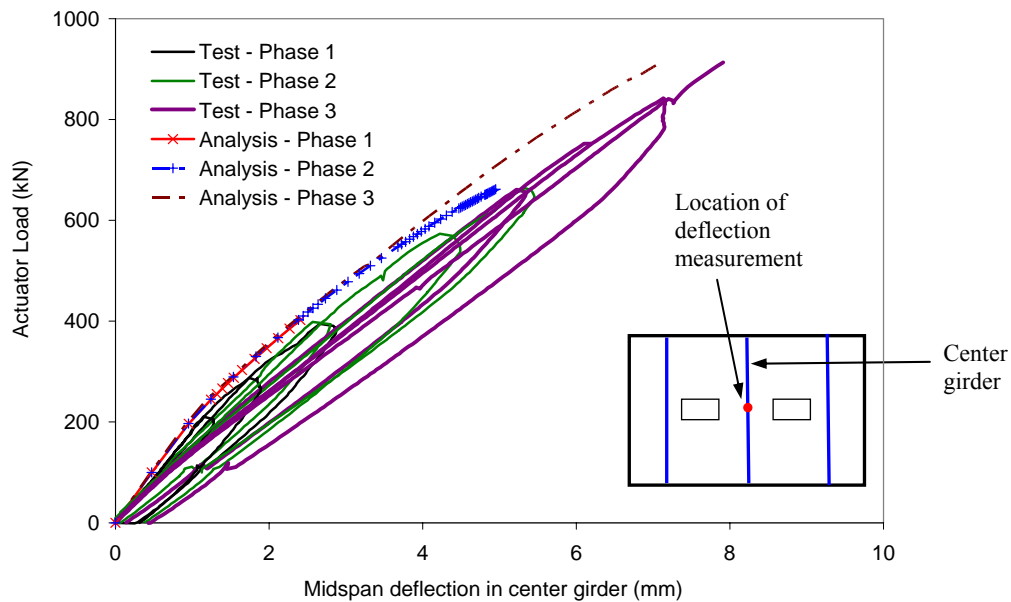


Figure 8.35 Verification of load-deflection response of center girder – Phase 3

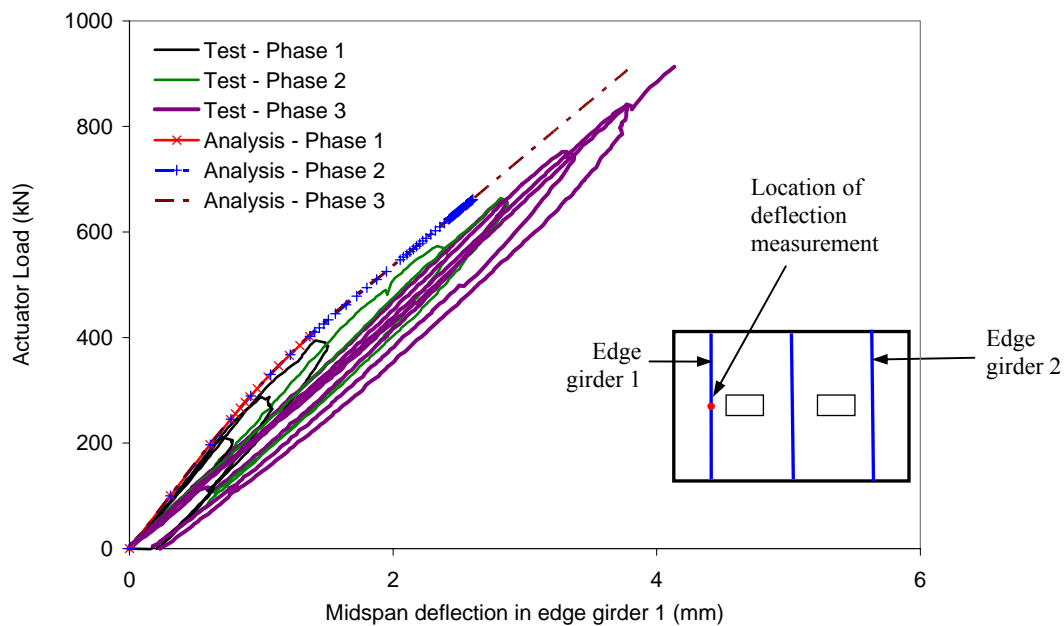


Figure 8.36 Verification of load-deflection response of edge girder 1 – Phase 3

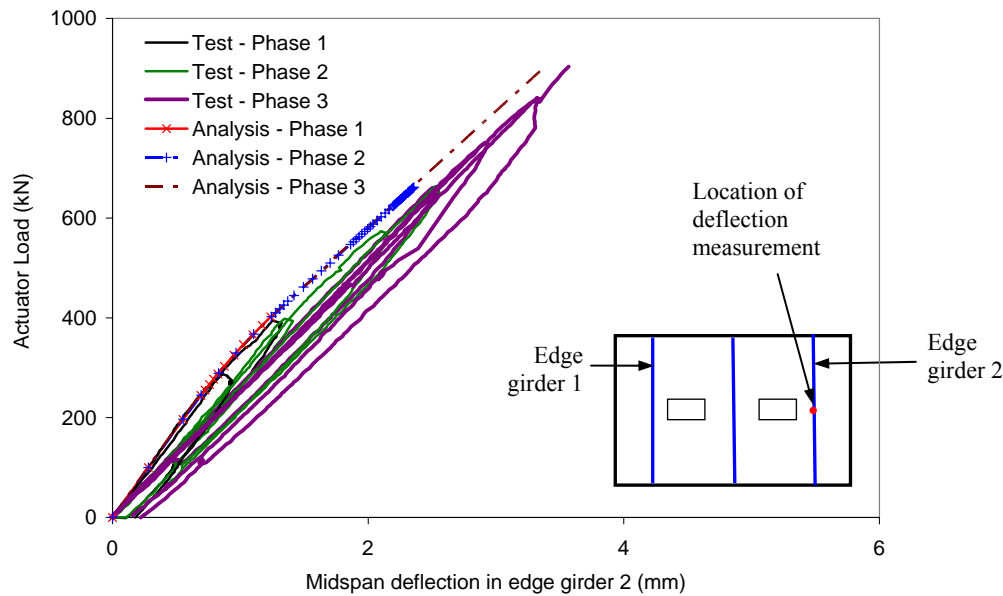


Figure 8.37 Verification of load-deflection response of edge girder 2 – Phase 3

8.3.3.2 Damage Progression and Strain Profiles

In Phase 3 loading the deck slabs were predicted to reach failure through debonding of the composite strip/laminate used to strengthen the two slabs. The debonding strains predicted from an energy based model, as discussed in chapter 4, were 3568 microstrains for the pultruded strips used in slab 1 and 3262 microstrains in the fabric laminates used in slab 2. The debonding strains in the composite systems measured from the strain gage data, as discussed in chapter 5, at failure load of 930 kN (209 kips) were 3526 microstrains in the pultruded strips and 3156 microstrains in the fabric laminates. From the numerical analysis using Abaqus [76], the maximum strains in the composite systems at 930 kN were 3767 microstrains in the pultruded strips and 3386 microstrains in the fabric laminates. The principal strain contour in the composite systems at 930 kN failure load is shown in Figure 8.38. A comparison of the maximum

recorded strains in the composite systems of the two slabs for phase 3 loading from analysis and test results is shown in Figure 8.39.

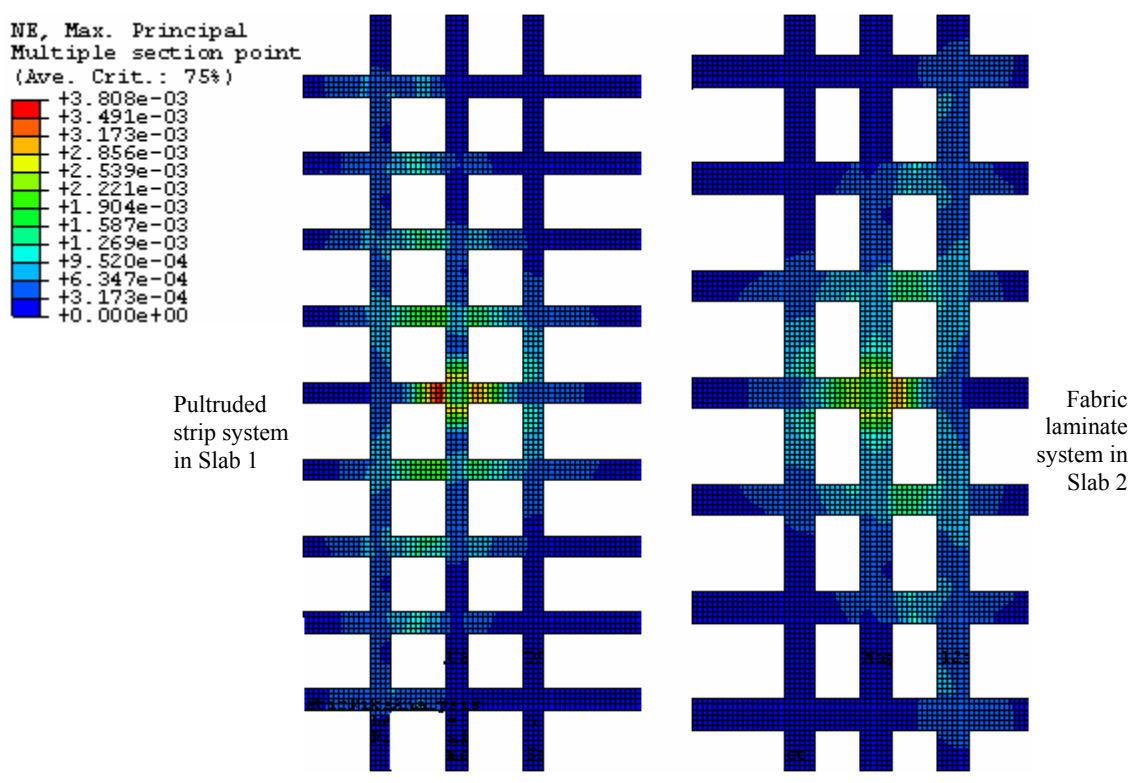


Figure 8.38 Principal strain contours in the composite systems at 930 kN – Phase 3

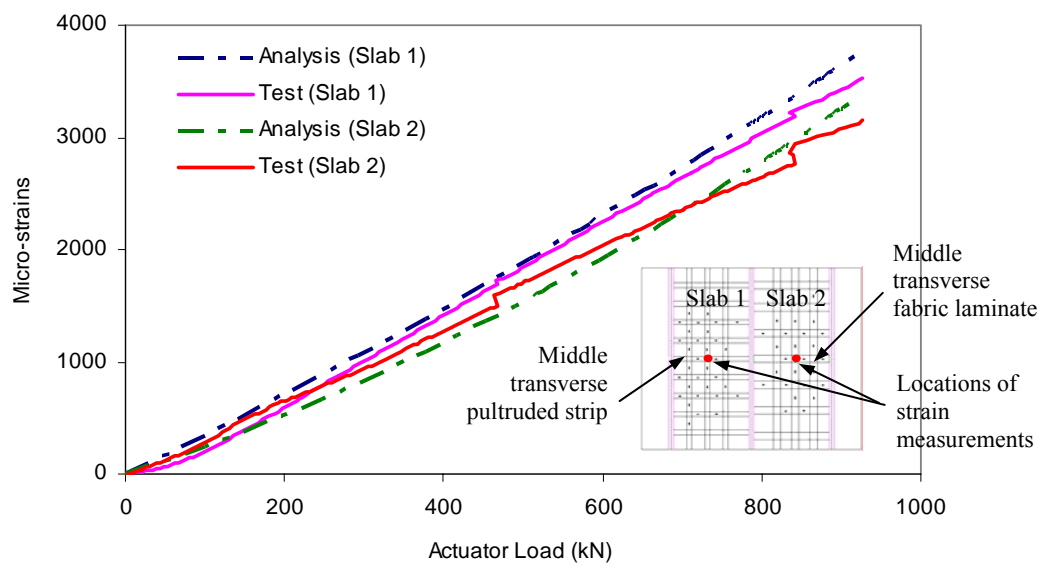


Figure 8.39 Comparison of strain profile in slab composite reinforcement – Phase 3

The damage in the slab concrete at failure load of 930 kN was estimated by plotting the maximum principal strain (tensile) contour at the bottom of the slab concrete and minimum principal strain (compressive) contour at the top of the slab concrete. These strain contours are shown in Figures 8.40 and 8.42 respectively. From the maximum principal strain (tensile) contour at the bottom of the slab concrete in Figure 8.40 it was observed that there was higher concentration of damage, indicated by the higher principal tensile strain of 0.00419 in slab 1 as compared to highest strain of 0.00349 in slab 2, below the load area at 930 kN failure load. This matched the test observations, as was presented in Chapter 5, in which it was found that the fabric laminates in slab 2 were able to distribute the load better as compared to the pultruded strips in slab 1. It was also observed these areas of highest strains in the concrete below the load areas were in the unstrengthened regions of the concrete within the composite grid. This matched the test observations of development of cracks in the unstrengthened regions of the concrete within the composite grid below the load areas. The crack pattern as seen from test observations at the bottom of the strengthened slabs below the load areas is presented in Figure 8.41 and the locations of these cracks matched the areas of high tensile strains in the concrete predicted by the numerical analysis. The high tensile strains in the concrete also indicated that the debonding of the composite would result in failure of the slabs since the concrete on its own would not be able to resist such high stresses. This matched the test observation, in which the debonding of the composite systems resulted in punching shear failure in the slabs. The numerical model was able to localize the area of damage in the concrete at failure load. However the actual locations of the punching shear cracks, which would be formed after debonding of the composite, could not be

obtained from the model. This was because the debonding of the composite, which would represent a sudden loss of resistance contributed by the composite, would make the model highly unstable and thus made it run into non-convergence problems.

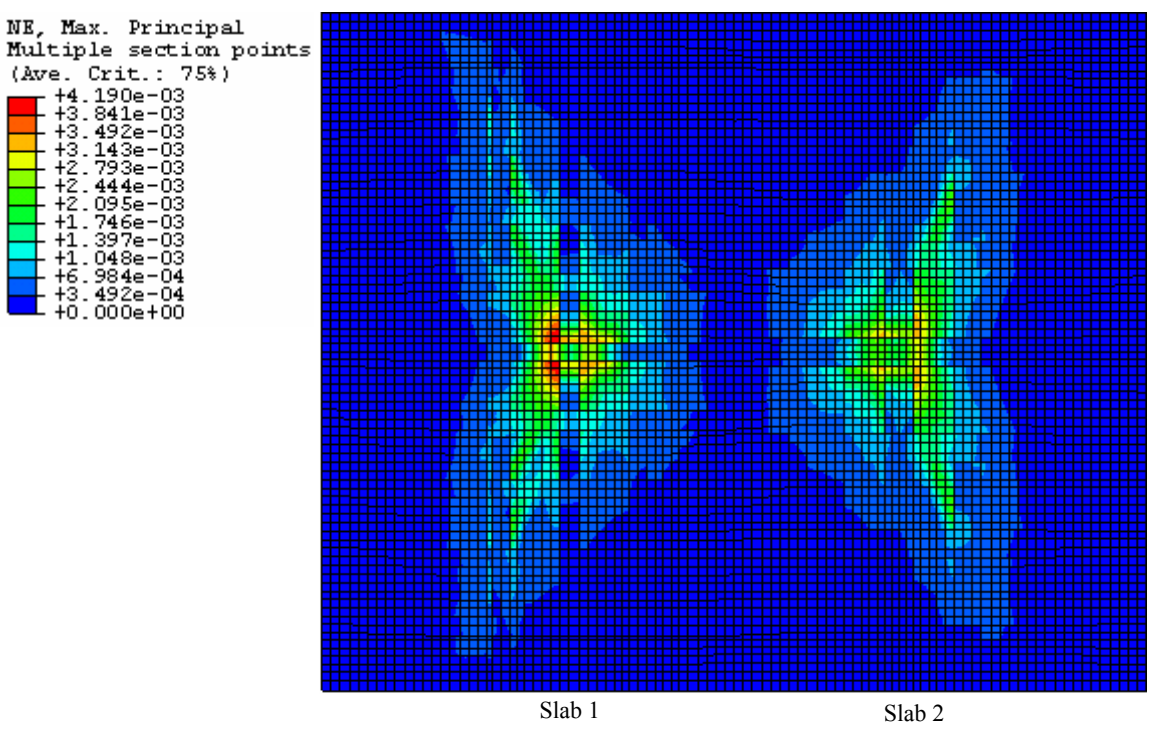
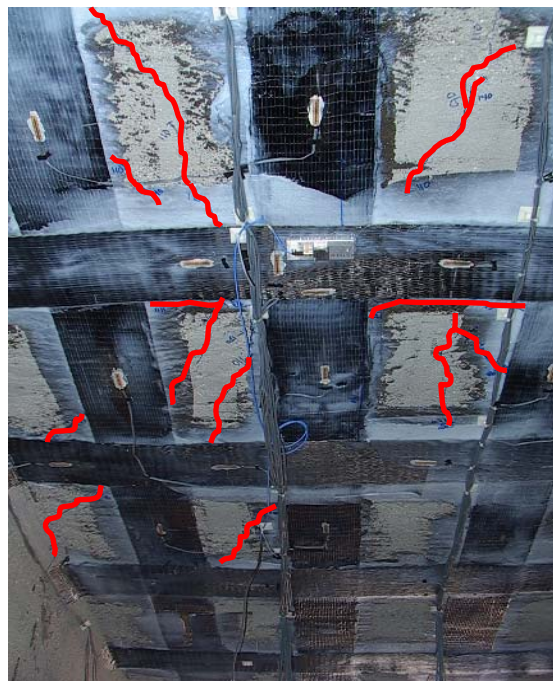


Figure 8.40 Maximum principal strain contours at slab bottom at 930 kN – Phase 3



Slab 1 with pultruded strip system



Slab 2 with fabric laminate system

Figure 8.41 Crack pattern at bottom of slabs below load areas from test observations

The compressive strains in the concrete at the top surface of the slabs were estimated by plotting the minimum (compression) principal strain contour on the top surface of the slabs at failure load of 930 kN and is shown in Figure 8.42. The maximum compressive strain predicted by the numerical analysis at 930 kN in the load areas of the slabs was 0.0028. This compared well with the estimated ultimate compressive strain in concrete of 0.003, indicating that the numerical model predicted that the debonding of the slab composite would be followed by crushing of concrete in the load areas. This matched the test observations in which the debonding of the slab composite was followed by the crushing of concrete in the load areas and is shown in Figure 8.43.

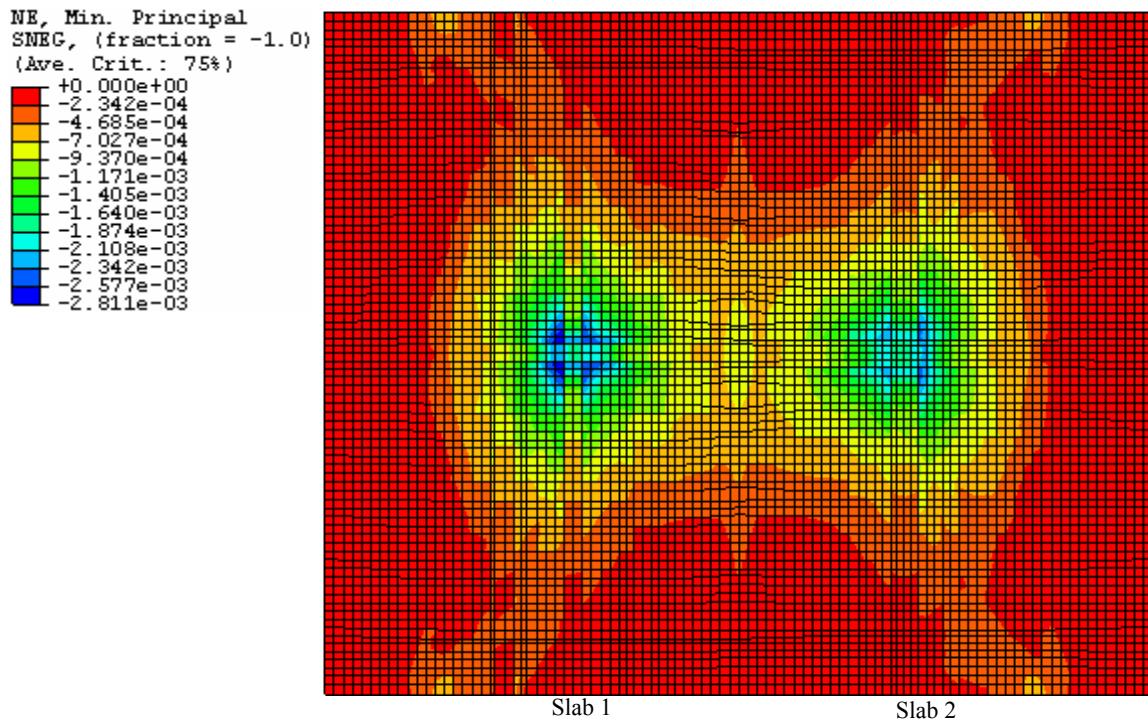


Figure 8.42 Minimum principal strain contours on slab top at 930 kN – Phase 3



Figure 8.43 Crushing of concrete on slab top below load at 930 kN – Phase 3

Also phase 3 of loading was commenced after shear strengthening of the center girder with FRP composite stirrups. The effect of the composite stirrups for shear

strengthening of the girder could be obtained from the model by determining the maximum strain in the steel stirrups of the girder before and after strengthening the girder with the composite. The highest strains developed in the steel stirrup during the 667 kN (150 kips) load cycle before and after strengthening of the girder with composite, as obtained from test data and numerical analysis were compared and is shown in Figure 8.44. The highest strain recorded from strain gage data in the steel stirrups of the center girder was reduced from 1660 microstrains to 658 microstrains at comparable load of 667 kN after strengthening of the girder with FRP composite stirrups. The corresponding reduction in the steel stirrup strain at similar location of the girder as obtained from the numerical model was from 1513 microstrains to 746 microstrains.

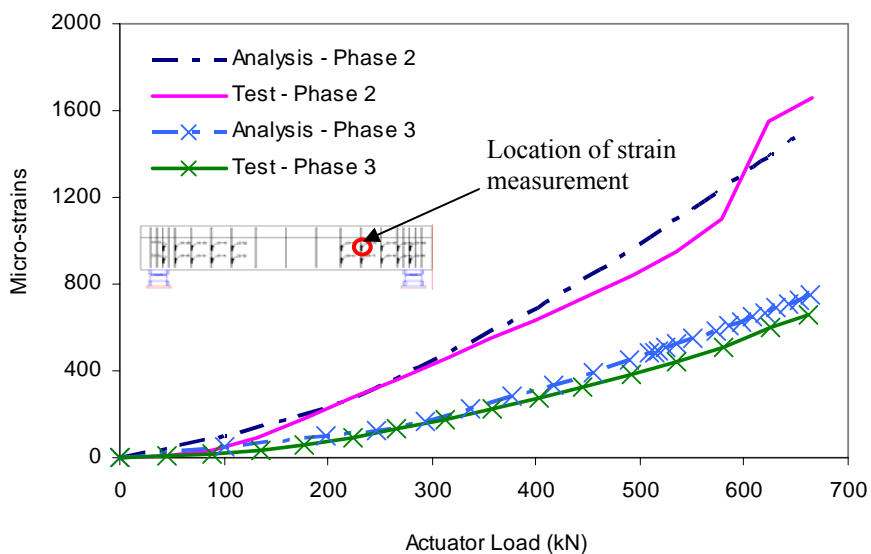


Figure 8.44 Comparison of highest strain vs. load response in center girder steel stirrup from analytical model and test data for 667 kN load cycle during Phase 2 and Phase 3

The maximum strain in the steel stirrups during phase 3 loading as obtained from numerical analysis was also compared to the maximum strain in the stirrup as obtained from the test data during the final load cycle of phase 3 upto failure load of 930 kN (209 kips). The comparison between analysis and test results is shown in Figure 8.45. The highest strain recorded in the steel stirrup of the girder from test data at failure load cycle of 930 kN was 1352 microstrains. The corresponding maximum strain predicted by the model was 1274 microstrains. This maximum predicted strain in the steel stirrup was well below the steel yield strain of 2000 microstrains indicating that the shear strengthening of the center girder with composite stirrups was effective in preventing the occurrence of shear criticality in the center girder during phase 3 loading.

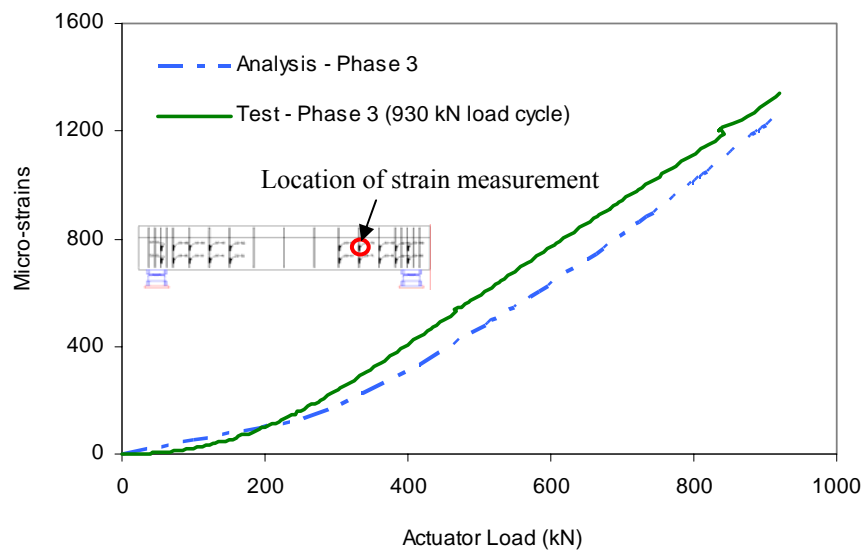


Figure 8.45 Comparison of highest strain vs. load response in center girder steel stirrup from analytical model and test data for 667 kN load cycle during Phase 2 and Phase 3

8.4 Summary

The numerical model using Abaqus [76] was able to predict the response of the test specimen over the three phases of loading, involving damage progression in the deck slabs resulting in punching shear criticality and subsequent strengthening of the slabs, damage progression in the center girder resulting in shear criticality and subsequent strengthening of the girder and finally failure of the strengthened deck slabs through debonding of the composite. Good correspondence was found between the load-deflection responses of the slabs and girders as obtained from test results and those predicted by the model. The progression of damage was predicted from the principal strain contours and vector plots and matched well with the crack patterns and damage areas observed during the testing of the specimen.

This analysis indicated the response of a system, due to progression of damage and subsequent strengthening of the components with FRP composites after they reached their corresponding limit states, can be predicted well by a FE model. However the accuracy of the model will depend on whether the material properties and the boundary conditions of the model can be well defined. For the current analysis, material tests were run for the concrete, steel and composite samples to determine the properties to be assigned to the model sections. Also the boundary conditions of the test specimen were well defined in the laboratory. However in the field it might not be possible to determine accurately the material properties and the boundary conditions of an existing structure and thus a margin for error should be accounted for in such numerical modeling.

9 DESIGN IMPLICATIONS, CONCLUSIONS AND RECOMMENDATIONS

9.1 Limitations of the Current Design Methodology

The available design guideline in the U.S. for FRP strengthened structures, ACI-440 [3] are aimed specifically at the design of concrete strengthening of building structural elements. The design recommendations are presented in Part 4 of ACI-440 [3] and are divided into flexural strengthening, shear strengthening and ductility enhancement in members under axial tension/compression. However the approach considers the treatment of each component of the structure individually based on individual component limit states and the existing state of damage in only a single component without taking into consideration the overall performance of the structure. Thus use of this design methodology results in a tendency to treat FRP strengthening as a patch repair technique resulting in the strengthening of only those components showing the most imminent signs of damage and deterioration. It was discussed in Chapter 2 that at the systems level the modification of a structure resulting from strengthening of individual components in isolation can cause changes in the load distribution and can lead other components of the structure to reach their respective limit states earlier under higher load demands. This was substantiated through the systems level test of the three girder-two span bridge segment, the results of which were presented in chapters 4 and 5. It was seen that simple strengthening of the deck slabs with FRP composite without taking into consideration the limit state of the girder can result in the girder reaching its limit state and thus producing a premature systems level failure prior to the new capacity of the strengthened deck slabs being reached. Thus it becomes necessary to develop a

design methodology that considers effects on the system as a whole to ensure that the required strength enhancement and the desired failure mechanisms in the components of the structure are achieved without violating the limit states of the other components at the systems level.

It should be noted that the provisions for flexural strengthening with FRP composites provided in ACI-440 [3] are primarily aimed at flexural strengthening of girders and thus additional provisions need to be incorporated that cater specifically to the flexural strengthening of deck slabs with composites. The deck slabs in the bridges are also often found to be deficient in punching shear. However ACI-440 [3] does not provide any provisions for this limit state and thus an appropriate methodology needs to be developed for design of FRP composite strengthening of deck slabs taking into account punching shear criticality of the slabs.

The ACI-440 [3] predictions of debonding strains governing the debonding limit state of the composites used for flexural strengthening of components have been found to be unconservative for use in predictions of ultimate capacities of FRP composite strengthened bridge slab components, as was discussed in Chapter 3. Thus an alternative design equation for more suitable prediction of debonding strains needs to be incorporated in the design methodology.

The provisions in ACI-440 [3] for shear strengthening of girders with composite stirrups do not require the use of mechanical anchors. However previous component level research [26] has shown that the use of mechanical anchors is essential for effective shear strengthening with the composite U-stirrups. This was verified through the use of the FRP anchors along with the composite stirrups for shear strengthening of a girder in a

slab-girder system in the current investigation. The design of the mechanical anchors thus needs to be included in the design methodology.

In applying the provisions of ACI-440 [3] to ridge components it must be remembered that ACI-440 [3] was developed with particular emphasis on building components and thus does not consider design issues specific to bridge components. Further it does not address the use of a load and resistance factor based design for composite strengthening of reinforced concrete components similar to the AASHTO [57] provisions for conventional reinforced concrete components which has been recommended as an alternative design approach specifically for strengthening bridge components with FRP [81].

It has been emphasized that ACI-440 [3] treats FRP composites in a manner similar to other conventional construction materials. It is recognized that the basic design principles as applied to structural components designed with conventional materials, such as concrete and steel, can remain the same. However, the use of the composite materials in civil infrastructure is a relatively new development compared to concrete and steel and thus there is limited information on their long term performance under field conditions and environmental exposures. ACI-440 [3] takes this into account by applying a somewhat arbitrarily determined environment reduction factor. Table 8.1 of ACI-440 [3] lists these reduction factors for three different exposure conditions, interior, exterior and aggressive environment exposures, respectively. However this can result in either conservative or unconservative designs depending on the application type, specific exposure condition, intended period of use and type of the composite system used. Also these factors were not formulated with particular emphasis to bridge structures. This

necessitates the incorporation of material durability data and time dependent changes in material response specific to the application type. Research data related to durability characterization of composites [55, 56, 66 and 79] need to be used for determination of more reliable environment reduction factors than those specified by ACI-440 [3].

Along with the need to develop a design methodology incorporating the above criteria, it becomes pertinent to periodically monitor the performance of FRP strengthened structures which will not only ensure public safety but also help to create a database on the long-term performance of the materials under field conditions and environmental exposures. This requires development and incorporation of a non destructive evaluation methodology, involving monitoring at both global and local levels, for periodic monitoring of the FRP strengthened structures. Also rather than just identifying and locating damage, such a NDE methodology should be able to quantitatively monitor the appearance or progression of the damage over the service life of the structure through quantitative estimation of characteristics such as degradation of stiffness and composite-concrete bond performance. The NDE methodology should also be able to quantitatively monitor the progression of damage between the components of a system and thus indicate the occurrence of any premature failure mechanisms in the FRP composite strengthened structure.

9.2 Proposed Design Methodology for FRP Composite Strengthening

The proposed methodology for designing FRP composite strengthening of deficient structural components in a system is outlined in Table 9.1. Since the primary focus of the current research was on slab-girder systems, the details pertaining to

strengthening design as relevant to slab and girder components only are outlined in the table. However the general design philosophy is applicable to any system. The notations and symbols used in Table 9.1 are described in Table 9.2.

Table 9.1 Proposed FRP composite strengthening methodology for slab-girder systems

SPECIFICATIONS	COMMENTARY
1 Nominal Strength	
<p>The strength deficiencies of each of the components of the slab-girder system shall be determined as:</p> $D_i = (N_U)_i - (\phi N_n)_i \quad \dots(9.1)$ <p>If $D_i \geq 0$ then the component i may be strengthened for the corresponding deficient limit state using externally bonded FRP composites using the design methodology as outlined in Section 2 of this recommendation for strengthening of slabs and Section 3 for strengthening of girders.</p>	<p>In the strength-design approach, the design strength of component i, based on shear, flexure or any other relevant failure modes of the component shall be required to exceed the ultimate strength of component i for the corresponding failure mode, as indicated by equation 9.1.</p> <p>The design strength $(\phi N_n)_i$ refers to the nominal strength of the component, $(N_n)_i$ multiplied by the strength reduction factor, ϕ (to be taken as 0.9 for flexure and 0.85 for shear [57]).</p> <p>The required ultimate strength, $(N_U)_i$, shall be estimated from the load effects on the component i, taking into account the load factors.</p> <p>Procedures for estimation of nominal strength of reinforced concrete slabs and girder components are outlined in section 8 (Part C) of AASHTO design standard [57] following the Allowable Stress design method or the Load Factor design method.</p> <p>Procedures for estimation of load factors and required strength of reinforced concrete slab and girder components are outlined in Section 3 of the AASHTO</p>

	design standard [57].
2 Design of FRP strengthened deck slab components	
2.1 Flexural Strengthening	C2.1 Flexural Strengthening
<p>The deficient deck slabs shall be strengthened in flexure such that:</p> $(\phi M_n) \geq (M_U) \quad \dots(9.2)$	<p>The nominal flexural strength, M_n, of a FRP composite strengthened slab component shall be determined based on strain compatibility, internal force equilibrium and the controlling mode of failure such that the design flexural strength (using $\phi = 0.9$) of the strengthened slab is higher than the ultimate strength demand M_U.</p>
2.1.1 Failure Modes	C2.1.1 Failure Modes
<p>The failure modes which should be investigated for the flexural strengthening of slab components are:</p> <ul style="list-style-type: none"> i) Crushing of concrete in compression ii) Yielding of steel in tension iii) Rupture of FRP composite iv) Debonding of FRP from concrete substrate <p>The failure mode of the strengthened slab component will be governed by one of the following strain limits:</p> <ul style="list-style-type: none"> i) Crushing of concrete: $\varepsilon_c = \varepsilon_{cu}$ ii) Yielding of steel in tension: $\varepsilon_s = \varepsilon_y$ iii) Rupture of FRP composite: $\varepsilon_f = \varepsilon_r$ iv) Debonding of FRP composite from concrete substrate: $\varepsilon_f = \varepsilon_d$ 	<p>The limiting strains for the failure modes shall be assumed to be:</p> <ul style="list-style-type: none"> i) Crushing of concrete in compression can be assumed to occur if the maximum strain in concrete, ε_{cu} reaches 0.003 ii) Yielding of steel in tension can be assumed to occur if maximum strain in tension steel, ε_y reaches 0.02 or the yield strain of steel reinforcement determined from material tests iii) The rupture strain of FRP composite reinforcement, ε_r can be determined through material tests or from manufacturer specified properties for the specific composite system used iv) Debonding of FRP composite from concrete substrate can be estimated using an energy based approach from which the debonding strain of composite can be estimated as: $\varepsilon_d = \frac{P_{\max}}{t_f b_f E_f} \quad \dots(9.3)$ <p>where $P_{\max} = b_f \sqrt{2G_f E_f t_f}$</p>

	<p>Further clarifications on the use of Equation 9.4 for estimation of debonding strains in composite can be found in Chapters 3 and 4 of this study.</p> <p>The maximum debonding strain as obtained from Equation 9.4 shall not exceed 90% of the rupture strain, i.e.</p> $\varepsilon_d \leq 0.9 \times \varepsilon_r \quad \dots(9.4)$
2.1.2 Strain Compatibility	C2.1.2 Strain Compatibility
<p>For an assumed depth of the neutral axis, c, the strain in the FRP composite shall be estimated as:</p> $\varepsilon_f = \varepsilon_{cu} \left(\frac{h-c}{c} \right) \leq \min(\varepsilon_d, \varepsilon_r) \quad \dots(9.5)$ <p>The corresponding strain in the tension steel reinforcement shall be computed as:</p> $\varepsilon_s = (\varepsilon_f) \left(\frac{d-c}{h-c} \right) \quad \dots(9.6)$	<p>The failure mode will be in concrete crushing if the first term of Equation 9.5 controls. FRP composite failure in debonding or rupture will occur if the second term of Equation 9.5 controls.</p> <p>The strain in the tension steel reinforcement (ε_s) shall be calculated as per equation 9.6. The corresponding stress in the steel reinforcement shall be calculated as follows:</p> $f_s = \begin{cases} E_s \varepsilon_s & \text{for } \varepsilon_s \leq \varepsilon_y \\ E_s \varepsilon_y & \text{for } \varepsilon_s > \varepsilon_y \end{cases} \quad \dots(9.7)$
2.1.3 Flexural Capacity	C2.1.3 Flexural Capacity
<p>With the strain compatibility determined in section 2.1.3, the new depth of the neutral axis shall be determined as:</p> $c_{new} = \frac{A_s f_s + A_f E_f \varepsilon_f}{\gamma_c' \beta_1 b} \quad \dots(9.8)$ <p>The nominal flexural strength of the composite strengthened section can be computed as:</p> $M_n = A_s f_s \left(d - \frac{\beta_1 c}{2} \right) + \psi_f A_f E_f \varepsilon_{fu} \left(h - \frac{\beta_1 c}{2} \right) \quad \dots(9.9)$	<p>The determination of the flexural strength will be based on an iterative trial and error procedure, in which for the amount of FRP reinforcement, A_f, and the strains in steel and composite reinforcement determined as per section 2.1.2, a new depth of the neutral axis will be calculated as per equation 9.8. γ and β_1 are parameters defining the rectangular stress block in concrete. Further details on use of suitable values for these factors in composite strengthening design can be found in section 9.6 of ACI-440 [3].</p>

<p>Based on nominal strength obtained in Equation 9.9, the design strength shall be calculated and checked against the required strength as given in Equation 9.2 and repeated below:</p> $(\phi M_n) \geq (M_U) \quad \dots(9.2)$ <p>If Equation 9.2 is not satisfied then the above procedure shall be followed with an increased amount of composite reinforcement, A_f.</p>	<p>The internal force equilibrium will be satisfied if the initial and new values of the neutral axis depth are equal. If not, then the new neutral axis depth will be assumed as the initial value for the neutral axis for the next trial and this iterative procedure will be followed until the equilibrium is satisfied.</p> <p>The contribution of FRP composite towards nominal strength, (M_n) shall be reduced by a factor, ψ_f. A value of 0.85 is recommended by ACI-440 [3]. However this might not be representative of all composite systems and environmental exposures. The use of available durability data of the composite system is recommended for determination of a suitable reduction factor. Further details on estimation of time dependent changes of material response and durability characterization of composites can be found in [55, 56 and 79].</p>
<p>2.2 Check for Punching Shear</p>	<p>C2.2 Check for Punching Shear</p>
<p>The maximum spacing of the composite in the longitudinal (in the traffic direction) and transverse (perpendicular to traffic direction) direction, for preventing unrestricted punching shear failure cones from forming in the unstrengthened portions of concrete inside the composite grid shall be limited by:</p> $(s_{f-\max})_{trans} = b_1 + 2h \quad \dots(9.10i)$ $(s_{f-\max})_{long} = b_2 + 2h \quad \dots(9.10ii)$	<p>The deck slabs strengthened in flexure with FRP composite might be susceptible to premature punching shear failure. Thus checks on composite spacing and strain using Equations 9.10 and 9.11 shall be done to prevent such premature failure modes.</p> <p>The punching shear failure plane can be conservatively assumed to form at 45°. Testing of FRP strengthened slab-girder systems (discussed in Chapters 3 and 5) has shown that the punching shear failure planes in FRP strengthened slabs will be formed at much shallower angles (15° to 25°). Thus the maximum composite spacing based on use of 45° failure plane will give a conservative estimate towards preventing</p>

<p>The maximum strain in the composite shall be limited by that specified in Equation 9.11 for effective control of crack widths:</p> $\left(\varepsilon_{f-\max}\right)_{Shear} = \frac{w}{s_{cr}} \quad \dots(9.11)$ <p>The spacing of the cracks to be used in Equation 9.11, for determining the limiting strains in the composite strips/laminates in the longitudinal and transverse directions of the slab can be estimated as:</p> $\left(s_{cr}\right)_{long} = b_1 + 2h \quad \dots(9.12i)$ $\left(s_{cr}\right)_{trans} = b_2 + 2h \quad \dots(9.12ii)$	<p>formation of unrestrained punching shear cracks.</p> <p>Also to prevent premature punching shear failure, the slab soffit crack widths need to be maintained within allowable limits for sufficient load transfer capability. It has been observed that high load transfer efficiency is available through aggregate interlock for crack widths upto 2.5 mm [80]. Thus it is recommended that the maximum allowable punching shear crack width, w in deck slabs be limited to 2.5 mm or less to be used in Equation 9.11.</p> <p>The spacing of the cracks, s_{cr}, as estimated by Equation 9.12 assumes the punching shear failure planes to be formed at 45°.</p>
<p>2.3 Design of Longitudinal FRP Reinforcement in One-way Slabs</p>	<p>C2.3 Design of Longitudinal FRP Reinforcement in One-way Slabs</p>
<p>The minimum composite reinforcement ratio to be used in the longitudinal direction of one-way slabs can be estimated as:</p> $\frac{\left(A_f\right)_{long}}{\left(A_f\right)_{transv}} = \frac{220}{\sqrt{S_{Span}}} \leq 67\% \quad \dots(9.13)$ <p>The maximum allowable spacing and strains in the longitudinal composite reinforcement shall also be limited by Equations 9.10ii and 9.11.</p>	<p>For one-way slabs the primary load transfer is in the transverse direction, i.e. between the supporting girders. Thus as opposed to two way slabs where the composite reinforcement is designed in both directions based on the required ultimate strength in the two directions, one way slabs shall be primarily designed for strength requirement in the transverse direction. However design of conventional reinforced concrete one-way slabs requires use of a minimum amount of longitudinal reinforcement (Cl. 3.24.10.2 of [53]) and a similar design is recommended for composite strengthened one way slabs using Equation 9.13, in the absence of further study.</p>

3 Design of FRP strengthened girders	
3.1 Flexural Strengthening	C3.1 Flexural Strengthening
<p>The flexure deficient girders shall be strengthened in flexure such that:</p> $(\phi M_n) \geq (M_U) \quad \dots(9.2)$	<p>The flexural strengthening of girders with FRP composite shall follow the same procedure as outlined for flexural strengthening of slabs in Section 2.1.</p>
3.2 Shear Strengthening	C3.2 Shear Strengthening
<p>The shear deficient girders shall be strengthened in shear such that:</p> $(\phi V_n) \geq (V_U) \quad \dots(9.14)$ <p>where,</p> $V_n = V_c + V_s + \psi_f V_f \quad \dots(9.15)$	<p>The nominal shear strength, V_n, of a FRP composite strengthened girder shall be determined by adding contributions of FRP shear reinforcement, steel stirrups and concrete and the corresponding design shear strength (using $\phi = 0.85$) of the strengthened girder shall be higher than the ultimate shear strength demand V_u.</p>
3.2.1 Contributions of steel and concrete	C3.2.1 Contributions of steel and concrete
<p>The contributions of steel and concrete towards shear strength is given by:</p> $V_c + V_s = 0.083\beta\sqrt{f_c}bd + \frac{A_v f_y d(\cot\theta + \cot\alpha)\sin\alpha}{s} \quad \dots(9.16)$	<p>The contributions of steel and concrete towards shear strength shall be estimated by Equation 9.16 similar to that for conventional reinforced concrete girders. Further details can be found in AASHTO [57] and in Chapter 4 of this report.</p>
3.2.2 Contribution of composite system	C3.2.2 Contribution of composite system
<p>The contribution of the FRP composite stirrups can be obtained as:</p> $\psi_f V_f = \psi_f \frac{A_{fv} E_f \varepsilon_{fe} d_f (\sin\alpha + \cos\alpha)}{s_f} \quad \dots(9.17)$ <p>where, $\varepsilon_{fe} = k_v \varepsilon_r \leq 0.004$ and the reduction factor for composites, ψ_f shall be determined as discussed in C2.1.3.</p>	<p>The contribution of the composite system is given by Equation 9.17. Further details can be found in Chapter 4 and in [26].</p> <p>The effective strain in the FRP composite, ε_{fe}, can be obtained as per ACI-440 [3], using a bond-reduction coefficient, k_v and limiting the maximum allowable strain in composite to 0.004. A more accurate estimate of the debonding strain can be obtained through use of a grounded spring model proposed by [26].</p>

<p>3.2.3 Design of FRP anchors</p> <p>FRP anchors for composite U-stirrups can be designed using the following equations:</p> $T_A^{Cap} \geq T_A^{Ult} \quad \dots(9.18)$ <p>The required strength of the anchors are to be estimated based on both local and global criteria:</p> <p>Local criteria:</p> $T_A^{Ult} = \frac{A_{fv} E_f (0.004)}{1 + \mu} \quad \dots(9.19)$ <p>Global criteria:</p> $T_A^{Ult} = \frac{A_{fv} E_f (0.004) \times \tan \left(\frac{4(b/2)}{\sqrt{(h)^2 + (\eta s)^2}} \right)}{2 \sin \theta} \quad \dots(9.20)$ <p>The design strength of the anchors are to be obtained as:</p> $T_A^{Cap} = \tau_{Epoxy}^{Ult} \times (2L_{Dev}^{FRP} + D_{FRP}) (t_{f-u} + t_{Anchor}) \quad \dots(9.21)$	<p>C3.2.3 Design of FRP anchors</p> <p>Previous research [26] has shown that only composite stirrups bonded to the concrete surface might not be fully effective for shear strength enhancement since some stirrups might reach debonding strains earlier and result in a drop in effective strain in the composite across the shear crack. Thus the use of ultimate debonding stress for all the composite stirrups traversing a shear crack may not be conservative. The use of FRP anchors is recommended with composite U-stirrups for shear strengthening. This will ensure that the assumption of using equal ultimate debonding stresses for all the composite stirrups traversing a shear crack will hold. The design of the anchors is dealt with in more detail in Chapter 4 and in [26].</p>
<p>4 Check for Overall Structural Performance at Systems Level</p>	
<p>The strengthening of the deficient components of the slab-girder system will result in:</p> $(\phi N_n)_i - (N_U)_i \geq 0 \quad \dots(9.22)$ <p>i.e. the design strength of the strengthened component is greater or equal to the required strength. Thus based on the strengthening ratio of each of the strengthened components, the new enhanced load demand that each of these components can resist, $[(N_U)_i]_{Strengthened}^{New}$ shall be obtained, such that:</p> $[(N_U)_i]_{Strengthened}^{New} = (\phi N_n)_i \quad \dots(9.23)$ <p>The system loads required to produce the new enhanced demands of the strengthened components shall then be obtained and the</p>	<p>After the deficient components of the slab-girder system are strengthened with FRP composite to enhance the component's capacity it becomes necessary to check if the unstrengthened components of the system can sustain the higher load demands without reaching their limit states before the full capacities of the strengthened components can be achieved. Thus these enhanced load demands on the system caused by strengthening of the deficient components need to be estimated using Equation 9.23.</p> <p>The new load that the system can resist after the strengthening of deficient components can be found by equating the</p>

<p>corresponding demands caused by these system loads on the unstrengthened components shall be estimated. The design strength of the unstrengthened components shall then be checked against the new load demand as:</p> $\left[(\phi N_n)_{Unstrengthened} \right]_i \geq \left[(N_U)_i^{New} \right]_{Unstrengthened} \dots(9.24)$ <p>If Equation 9.24 is not satisfied for a component then that component will need to be strengthened following the procedures outlined in sections 2 and 3 and the checks of section 4 shall then be repeated. The same procedure shall be repeated until the required strength enhancement and failure mechanisms in all the components of the system can be established to occur in the preferred order without violating the limit states of the other components at the systems level.</p>	<p>strength demand caused by this new load to the design strength of the strengthened components. Once this new system load is found, the strength demands on the unstrengthened components can also be estimated. This procedure is similar to that followed in Section 1 for determining the strength demands of conventional RC components. A check using Equation 9.24 should be used to ascertain if the unstrengthened components have sufficient design capacity to resist the higher load demands on the system.</p>
---	--

Table 9.2 Symbols and notations used in Table 9.1

Symbol	Description
a	Angle of inclination of steel stirrup reinforcement to longitudinal axis
β	Factor indicating ability of diagonally cracked concrete to transmit tension
β_1	Parameters defining the parameters of rectangular stress block in the concrete
γ	equivalent to the actual nonlinear distribution of stresses
ϵ_c	Strain in concrete
ϵ_{cu}	Ultimate crushing strain of concrete
ϵ_d	Debonding strain in composite reinforcement system
ϵ_f	Strain in composite reinforcement system
ϵ_{fe}	Effective strain in the composite stirrups used for shear reinforcement
$(\epsilon_{f-max})_{Shear}$	Maximum allowable strain in composite reinforcement system to restrain development of punching shear cracks
ϵ_r	Rupture strain in composite reinforcement system
ϵ_s	Strain in tension steel reinforcement

ε_y	Yield strain in tension steel reinforcement
η	Number of effective shear stirrups bridging a shear crack
θ	Angle of inclination of diagonal compressive stresses in concrete
μ	Coefficient of kinetic friction between the composite and concrete
τ_{Epoxy}^{Ult}	Ultimate shear strength of the epoxy bonding the composite to concrete
ϕ	Strength reduction factor
ψ_f	Reduction factor for composite system
A_f	Cross-sectional area of composite reinforcement system
$(A_f)_{long}$	Cross-sectional area of composite reinforcement system in longitudinal direction for slab strengthening
$(A_f)_{transv}$	Cross-sectional area of composite reinforcement system in transverse direction for slab strengthening
A_{fv}	Cross-sectional area of composite stirrups for shear reinforcement
A_s	Cross-sectional area of tension steel reinforcement
A_v	Cross-sectional area of steel stirrups for girder shear reinforcement
b	Effective width of component cross-section
b_1	Short side of the load contact area as specified in AASHTO [57]
b_2	Long side of the load contact area as specified in AASHTO [57]
b_f	Width of the composite reinforcement system
c	Depth of the neutral axis
d	Effective depth of the tension steel reinforcement
d_f	Effective depth of the composite reinforcement system
D_{FRP}	FRP fiber anchor diameter
D_i	Strength deficiency in component i of the slab-girder system
E_f	Tensile modulus of the composite reinforcement system
E_s	Tensile modulus of the tension steel reinforcement
f_s	Stress in the tension steel reinforcement
f_y	Yield stress in the tension steel reinforcement
G_f	Interfacial fracture energy at debonding of the composite system
h	Depth/thickness of the component cross-section
k_v	Bond coefficient of composite stirrups used for shear reinforcement
L_{Dev}^{FRP}	Development length of the FRP anchors
$(M_n)_i$	Nominal moment capacity in component i of the slab-girder system
$(M_U)_i$	Required ultimate moment capacity in component i of the slab-girder system
$(N_n)_i$	Nominal strength in component i of the slab-girder system
$(N_U)_i$	Required ultimate strength in component i of the slab-girder system
P_{max}	Maximum axial force in the composite system at debonding limit state

s	Spacing of steel stirrups for girder shear reinforcement
s_{cr}	Punching shear crack spacing
$(s_{cr})_{trans}$	Punching shear crack spacing in the transverse direction of slab
$(s_{cr})_{long}$	Punching shear crack spacing in the longitudinal direction of slab
s_f	Spacing of the composite reinforcement system
$(s_{f-max})_{trans}$	Maximum allowable spacing of the transverse composite strips/laminates for slab strengthening
$(s_{f-max})_{long}$	Maximum allowable spacing of the longitudinal composite strips/laminates for slab strengthening
S_{Span}	Span length of the slab in feet
t_f	Thickness of the composite reinforcement system
t_{f-u}	Thickness of the composite stirrups below the FRP anchors
t_{Anchor}	Thickness of the FRP anchor
T_A^{Cap}	Axial capacity of the FRP anchors
T_{FRP}^{Ult}	Maximum permissible FRP tensile force in the composite stirrups for shear
$(V_n)_i$	Nominal shear strength in component i of the slab-girder system
$(V_U)_i$	Required ultimate shear strength in component i of the slab-girder system
w	Punching shear crack width in deck slabs

9.3 Primary Findings

The current research focused on two primary aspects related to the strengthening of deficient reinforced concrete structures with FRP composites. The first was the assessment of the effectiveness of in-field strengthening of RC structural components with composites, through testing of deck slab components with field representative deterioration. The second aspect was to study the effect of strengthening of components on overall structural performance at the systems level and to access the progression of damage at the systems level produced by sequential strengthening of the components.

The following details the principal findings based on the component level tests of the field specimens.

- i) The unstrengthened slab specimen with reinforcement representative of existing bridge decks was susceptible to localized punching shear failure under field-representative wheel loads. While the punching shear capacity of unstrengthened deck slabs is conventionally conservatively estimated by AASHTO [57] using a failure plane angle of 45° , a theoretical formulation [58] of the punching shear capacity with a failure angle of 38° is also used. From the test results the punching shear capacity of the unstrengthened specimen was found to lie within the capacity predictions of AASHTO [57] and theoretical formulations, with the failure plane angle in the test specimen varying between 27° and 64° . This was noted to be governed by the locations of the preexisting cracks in the slab and the boundary conditions. However the total concrete failure area activated by the punching shear failure planes in the test specimen was approximately equal to the concrete failure area predicted to be activated by the theoretical formulation [58].
- ii) The specimens with field strengthening with FRP composites with two years of field representative deterioration were found to be effective in strength enhancement and in restraining the opening of punching shear cracks, thereby resulting in a flexural failure mode. The strengthening with the composite systems also resulted in better distribution of the load over the slab surface. The failure plane, at ultimate failure following debonding of the composite, was formed at an angle of 22° (as compared to theoretical failure plane angle of 38° in the unstrengthened slab).
- iii) For the composite strengthened deck slabs, the debonding strains predicted by ACI 440 [3] were found to be unconservative. The use of an energy based model

for prediction of debonding strains [11] matched the experimentally measured debonding strains to within 15% and was a conservative estimate.

- iv) Since no prior information was available on the concrete properties in the existing state of the deck slabs representing their field deterioration, forced vibration based dynamic modal tests were used to identify the baseline “effective” concrete elastic modulus of the specimens. The strength predictions of the specimens were then carried out using this effective material property and matched well with the experimental results.
- v) The presence of pre-existing defects as well as appearance and progression of new damage at the composite-concrete bondline with increase of loading was quantitatively monitored using IR Thermography. The number of pre-existing defects in the pultruded strip system was found to be much lower than that in the fabric laminates, indicating better quality control during manufacturing and installation of the strips as compared to the laminates.
- vi) Using thermography, different defect types, such as air voids, resin rich areas and substrate cracks were differentiated based on the relative thermal intensities of each defect type. The severity of each defect type could also be quantified in terms of thermal intensity and thus the progression of damage with the increase of loading could be monitored quantitatively. The locations of the defects with high thermal intensities (indicating high damage severity) were correlated with the locations of cracks and areas of initiation of debonding of the composite. It is pointed out that further research needs to be conducted as related to defect classification to enable automated assessment.

- vii) The test specimens mimicked the behavior of the bridge decks in terms of load transfer mechanism. However the non-flexible boundary conditions and smaller clear span of the test specimens as compared to the bridge decks resulted in higher stiffness. A local to global modeling methodology was used to determine the field capacity of the bridge decks from the measured capacity of the deck components tested in the laboratory. Since the behavior of both the test specimens and the bridge decks were governed by similar failure modes the equivalent capacity was achieved based on determining the load demands necessary to cause equivalent stress profiles in the potential failure zones. Using this modeling approach, the design load capacity of the unstrengthened deck slabs was found to be lower than the permit load demand indicating the susceptibility of the unstrengthened deck slabs to punching shear failures.

The following details the principal findings based on the systems level test of the three girder-two span slab-girder specimen.

- i) The concern that changes to an isolated structural component in the form of composite strengthening can result in unintended consequences to adjoining components was validated in the systems level test of a field representative slab-girder system. The progression of damage from the slabs to the center girder and then back to the strengthened slabs caused by the sequential strengthening of first the slabs and then the center girder validated the need for the development of a design methodology which would take into account the overall structural response at the systems level rather than treating composite strengthening as a patch repair

technique and designing only for the component with the most imminent signs of damage.

- ii) The initiation of damage in the deck slabs was in the form of longitudinal and transverse cracks. However with the increase of loading diagonal cracks were found to develop and propagate away from the load area indicative of punching shear criticality. At 75% of the predicted punching shear capacity of the slabs there was approximately 40% reduction of stiffness in the slabs. The corresponding stiffness reductions in the center girder and edge girder were approximately 15% and 5% respectively. Thus in the first phase of loading the damage was primarily localized in the slabs and thus with the current strengthening design methodology only the deck slabs would be strengthened.
- iii) The two deck slabs were strengthened with two different composite systems, fabric laminates and pultruded strips to evaluate their comparative effectiveness. The composite strengthening was designed based on use of debonding strains predicted by an energy based model [11] rather than using the debonding strain predictions by ACI-440 [3]. Also the strengthening was designed by taking into account the susceptibility of the slabs to premature punching shear type failures to ensure that the slabs will fail in flexure through debonding of the composite.
- iv) The objective of the strengthening design for the two composite systems was to achieve equivalent capacities for the two strengthened slabs. However for equivalent capacity, the weight of carbon fibers used for strengthening the slabs in the transverse direction (primary direction of load transfer) with the fabric laminate system was 4.5 lbs as compared to 4.9 lbs for the pultruded strip system,

i.e. weight of carbon fibers used in the fabric laminates was approximately 9% lower than that used in the pultruded strip system.

- v) The strengthening of the slabs resulted in about 20% increase in stiffness of both the slabs. However the corresponding stiffness changes were insignificant in the girders. The composite strengthening was effective in restraining the opening of the pre-existing punching shear cracks in the slabs.
- vi) The behavior of the two slabs with the two strengthening systems was similar in terms of deflections and strain profiles. However in slab 1, strengthened with pultruded strips, a number of short minor cracks were found to develop under the load area, while fewer cracks developed in slab 2, strengthened with fabric laminates. This indicated that the wider laminates in slab 2 resulted in better distribution of stress away from the load area while the stiffer and thinner pultruded strips attracted more stress and this resulted in localized cracking below the load area in slab 1.
- vii) Loading of the system after strengthening of the slabs caused the center girder to reach shear criticality at a load equivalent to 71% of ultimate load capacity of the strengthened slabs. At this load level the strain in the center girder steel stirrups exceeded 75% of yield strain and there was 33% reduction of stiffness of the girder. Considerable shear cracking was observed in the support regions of the girder in the areas of highest shear demands. This indicated that systems level failure would occur in the girder before the full capacity of the strengthened slabs could be reached if a design methodology based on only component design is used.

- viii) The center girder was strengthened in shear with U-shaped composite stirrups and GFRP anchors designed as per recommendations of previous research [26]. This resulted in a stiffness enhancement in the center girder by about 6%. Also the strain in the most critical shear stirrup was reduced from 1660 to 657 microstrains, at equivalent loads before and after strengthening, indicating the effectiveness of the composite stirrup-anchor system for shear strengthening.
- ix) With the strengthening of the girder, further damage progression in the slab-girder system with increase of loading switched to the strengthened slabs as the next critical component in the system. The failure in the slabs occurred due to debonding of the composite systems followed by punching shear failure. The failure load was 1.75 times the predicted punching shear capacity of the unstrengthened slabs. Also the failure in the two slabs occurred simultaneously indicating that the design approach used to determine the equivalent capacity of the two composite systems was able to simulate the test behavior.
- x) The measured debonding strains in the composite systems compared well with the corresponding predictions using the energy based model [11].
- xi) Comparison of the punching shear failure perimeters of the two slabs indicated that slab 1 strengthened with the pultruded strips, had a smaller damage area of 1.39 sq.m (15 sq.ft) as compared to damage area of 1.79 sq.m (19.3 sq.ft) in slab 2 which was strengthened with the fabric laminates. This indicated that the fabric laminates were able to distribute the load over a larger area as compared to the pultruded strips.

- xii) In the slab strengthened with the fabric laminates, the failure was characterized by gradual and smaller opening of the punching shear cracks. There were very few severely debonded areas and most of the debonding was localized at intersections with the punching shear cracks. In contrast, for the pultruded strips, large areas of the strip in the vicinity of the punching shear cracks were debonded. Also at many locations of the debonded composite, the failure was within the composite strip itself, caused by separation between the fibers and matrix, rather than at the composite-concrete interface. This resulted in a more abrupt mode of debonding with large opening of the punching shear cracks as compared to the failure in the slab strengthened with the fabric laminates.
- xiii) IR Thermography was used for local non-destructive evaluation of bond performance between the composite and concrete. No significant damage progression was observed in the composite systems before failure load indicating that the composite systems were effective in carrying the load without any premature debonding.
- xiv) In the final loading stage damage areas in the composites could be quantified in terms of their corresponding thermal intensities. Based on the thermal intensities two types of damage areas could be identified, namely, debonding at composite-concrete interface and debonding inside the composite due to separation between the fibers and matrix of the pultruded strips. The damage areas identified from the thermography inspections were correlated to the crack patterns.
- xv) Modal testing using three different excitation sources, impact hammer, drop hammer and shaker, were used to monitor changes in dynamic characteristics of

the structure. The shaker was best suited for this application because of its higher frequency resolution, relatively constant force spectrum within a wide frequency range and good signal to noise ratio.

- xvi) The stiffness changes as obtained from model updating results over the load stages were expressed in terms of a stiffness ratio in which the stiffness predicted at different segments of the model were compared to the corresponding baseline stiffness. The trend of stiffness degradations and enhancements in terms of stiffness ratio as obtained from the model updating compared well with the corresponding trend from experimental measurements.
- xvii) A detailed non-linear FE model was used to predict the behavior of the test specimen and the progression of damage due to sequential strengthening of the components. All the failure mechanisms, namely punching shear criticality of the unstrengthened slabs, shear criticality of the center girder and the ultimate failure of the strengthened slabs due to debonding of the composite were predicted well by the model in terms of deflections, stress/strain profiles and damage pattern. The progression of damage between the components and the effect of composite strengthening of individual components on the other components of the system were also simulated well by the model. Thus in the absence of NDE data or load tests such a numerical simulation can be used to obtain a fairly good representation of the performance of a structure strengthened with FRP composites.

9.4 Conclusions

Based on the overall study the following primary conclusions can be drawn:

- i) It is essential that design of FRP strengthening of concrete be considered at the systems level rather than through isolated consideration of individual members;
- ii) The use of FRP results in the ultimate formation of a larger punching shear envelope due to better redistribution of forces with a significantly shallow set of angles. However in specific cases this envelope can extend to the girder edges resulting in failure planes along slab-girder intersections;
- iii) The use of fabric impregnated in the field, while having greater field variability and need for a higher degree of quality control attention, results in a higher efficiency of use of the fiber reinforcement and better redistribution of forces as a result of rehabilitation;
- iv) ACI 440 [3] based debonding strains are unconservative and need to be replaced by use of a fracture based approach;
- v) Separate provisions for strengthening of deck slabs taking into consideration punching shear criticality of the slabs and design of longitudinal reinforcement in one-way slabs need to be incorporated in ACI-440 [3];
- vi) The use of appropriately designed anchors is critical for shear strengthening of girders with FRP composite U-stirrups;

9.5 Recommendations for Future Research

The following are proposed for future research:

- i) The existing design guideline for composite strengthening (ACI-440) should be updated with provisions as proposed in this research and outlined in Table 9.1.
- ii) There is need for further research towards analytical modeling of development of the punching shear failure envelope and for prediction of the ultimate punching shear capacity of composite strengthened slabs. Of particular relevance will be future research towards prediction of punching shear behavior of deck slabs with existing in-field damage before being strengthened with composites
- iii) Further study needs to be carried out to optimize the composite strengthening in the longitudinal direction of one-way slabs and to check if the criteria developed for providing a minimum longitudinal reinforcement ratio, similar to conventional reinforced concrete slabs, also holds for composite strengthened slabs
- iv) As different composite systems become available for strengthening of civil structures it is necessary to develop a methodology for optimized use of these systems, such as comparing the amount of the reinforcing fibers in for each of the prospective systems to achieve equivalent strengthening and failure mechanisms
- v) Further research is recommended for the development of more reliable environmental reduction factors for the composite systems based on analysis of time dependent changes in material response in realistic field conditions
- vi) Since the degradation of the composite system itself might be different from the degradation of the composite-concrete interfacial properties, further research on the study of time dependent bond strength degradation under different

environmental exposures is recommended and should be incorporated in the models for prediction of debonding strains

- vii) A more realistic estimate of strength reduction factors for composite strengthened structures needs to be obtained based on reliability analysis of these structures
- viii) For further use of IR thermography as a NDE tool for locally monitoring the progression of damage at the composite-concrete bondline, there is a need for further research in terms of automation of the data analysis process through characterization of the defect types depending on type and location of the defect and incorporating this into a data processing algorithm. It will also be relevant to study the effectiveness of thermography for quantitative monitoring of damage in the field where the effects of environment, distance from the object and surface conditions of the composite strengthened component will have a significant influence on the quantitative process
- ix) Further study has to be carried out towards incorporating quantified stiffness degradation (due to damage) or enhancement (such as caused by composite strengthening) at localized areas of the structural components, as obtained through periodic monitoring using a global non-destructive technique such as modal testing, into models for prediction of strength and estimation of remaining service life of the structure

APPENDIX A

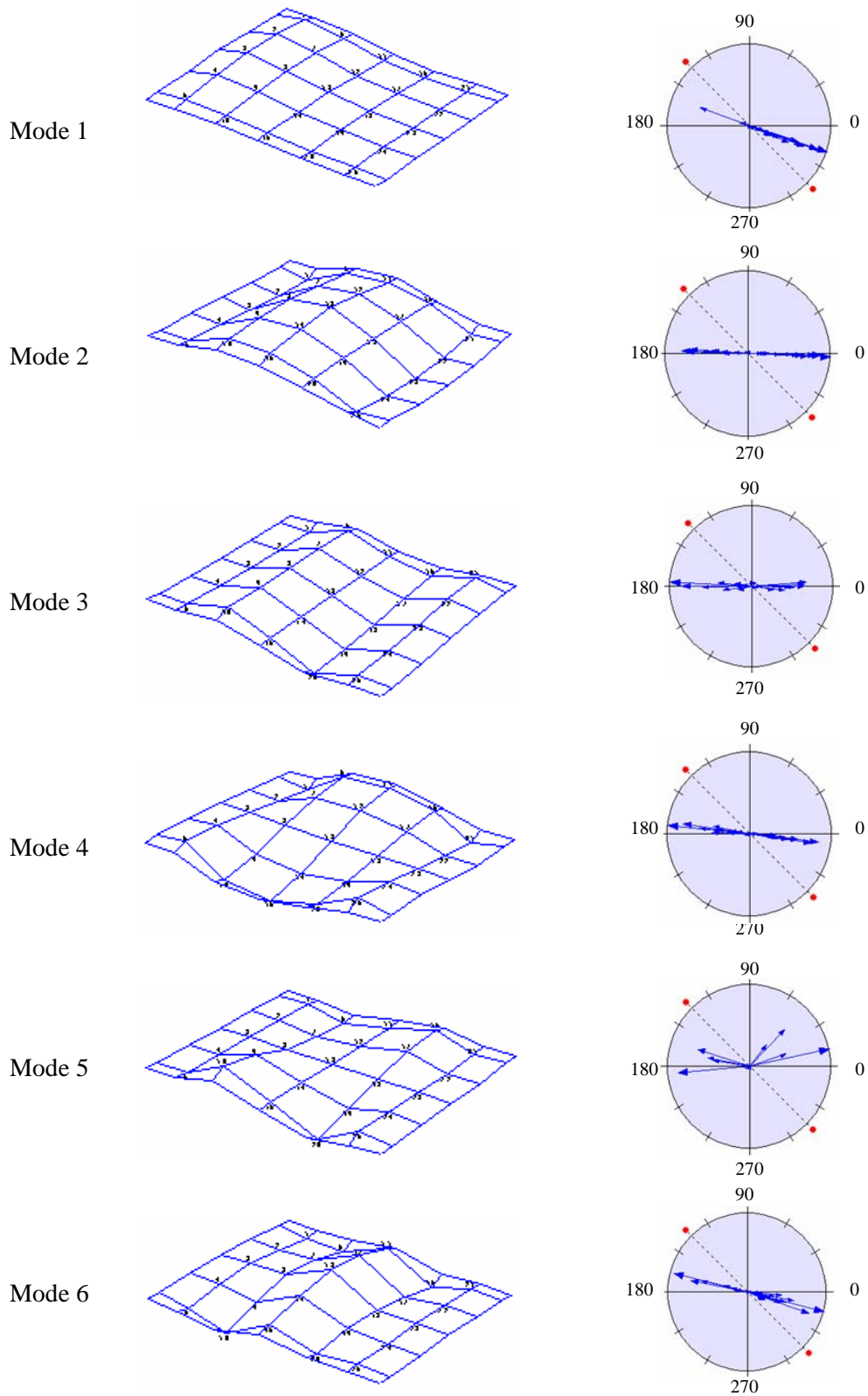


Figure A.1 Mode shapes and complexity plots after unloading from 214 kN – Phase 1

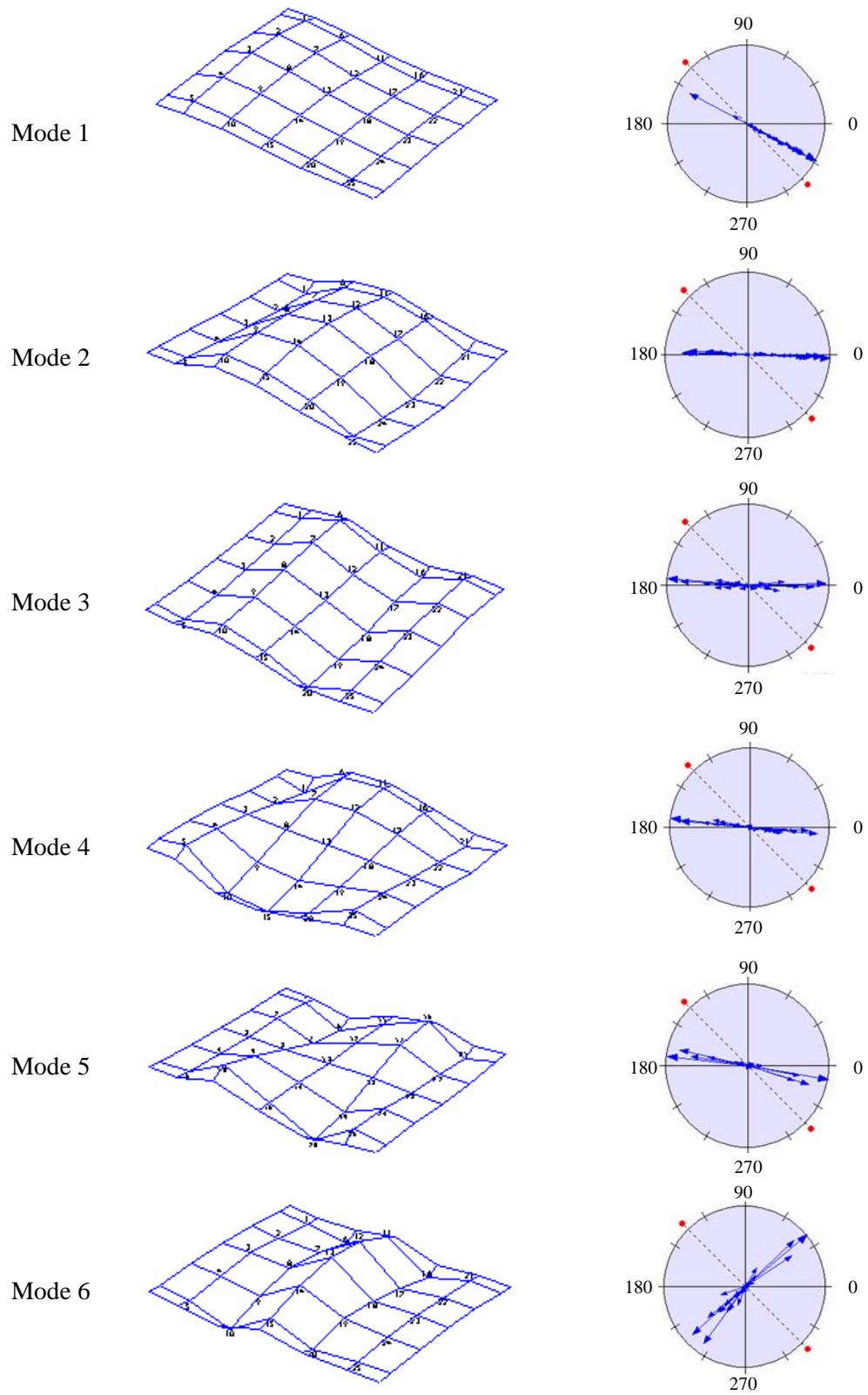


Figure A.2 Mode shapes and complexity plots after unloading from 289 kN – Phase 1

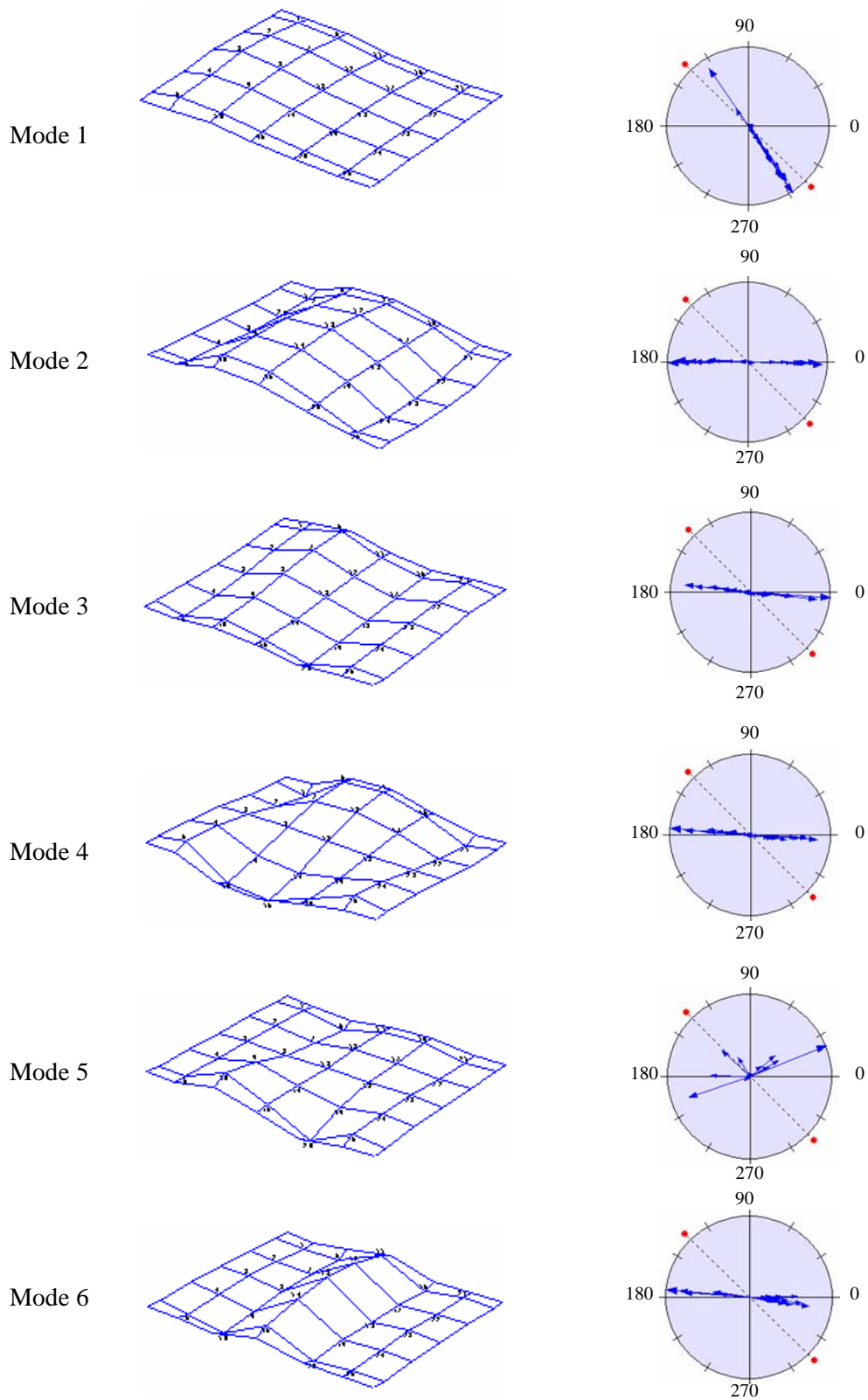


Figure A.3 Mode shapes and complexity plots after unloading from 400 kN – Phase 1

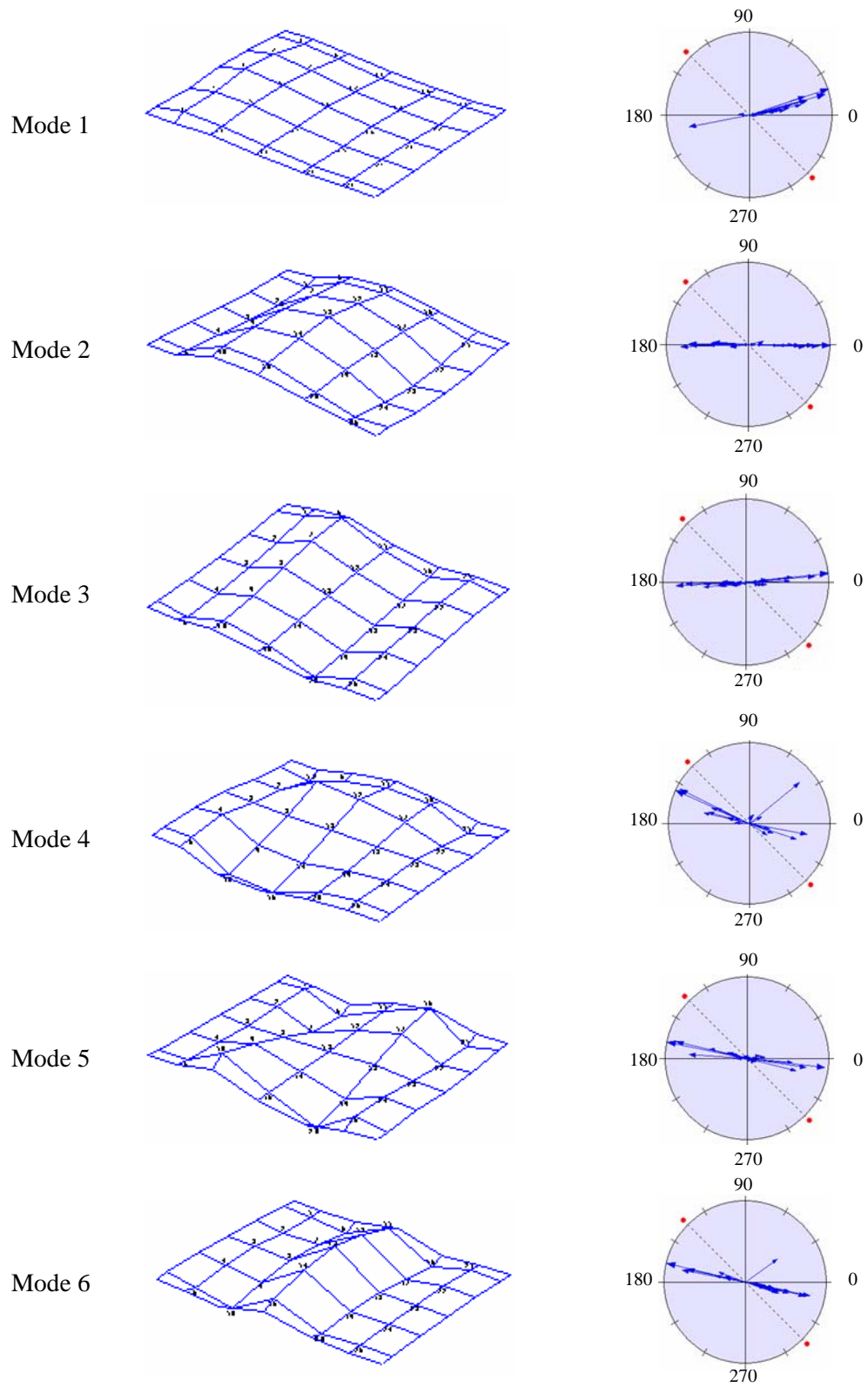


Figure A.4 Mode shapes and complexity plots from Baseline 2 modal test – Phase 2

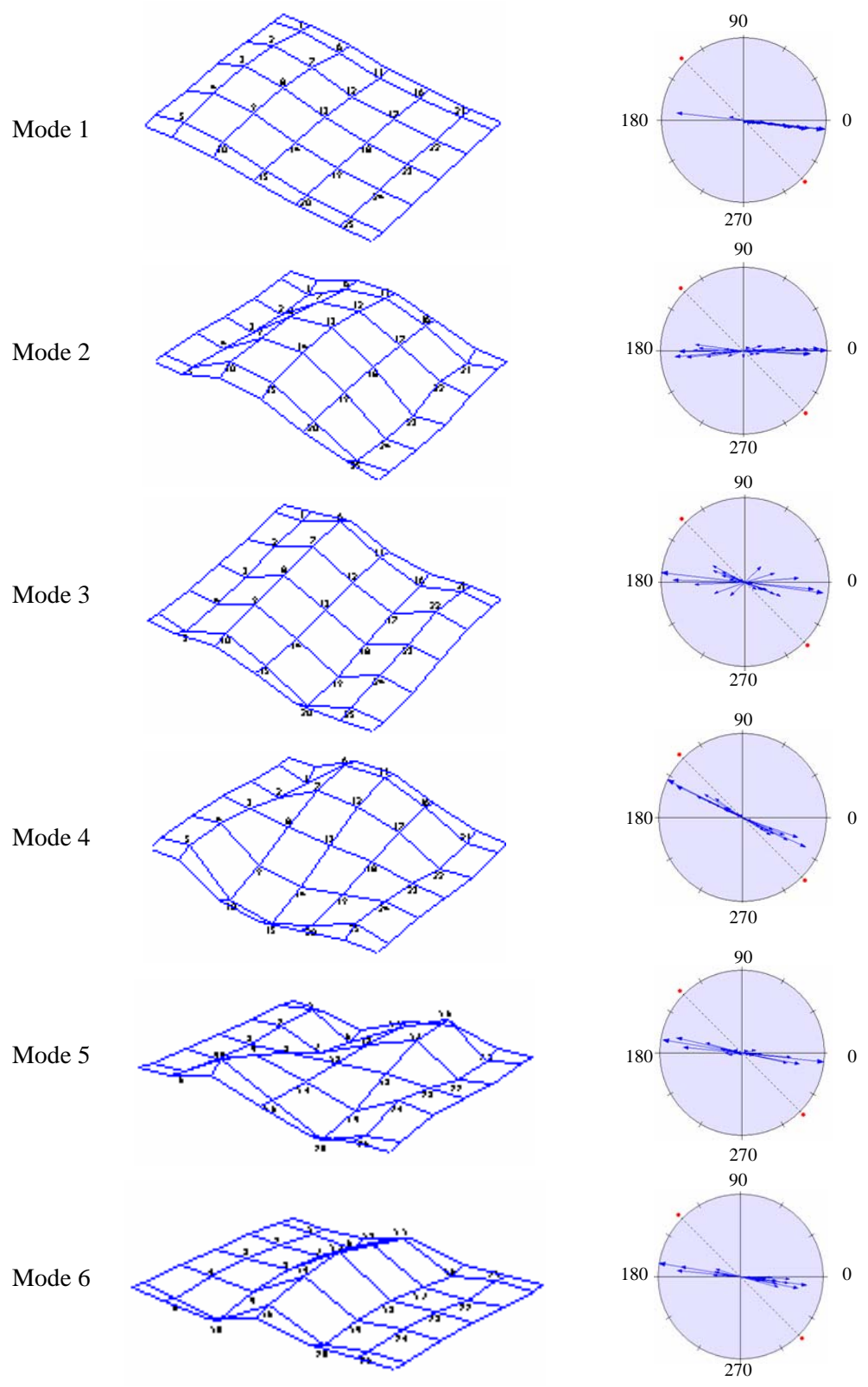


Figure A.5 Mode shapes and complexity plots after unloading from 400 kN -Phase 2

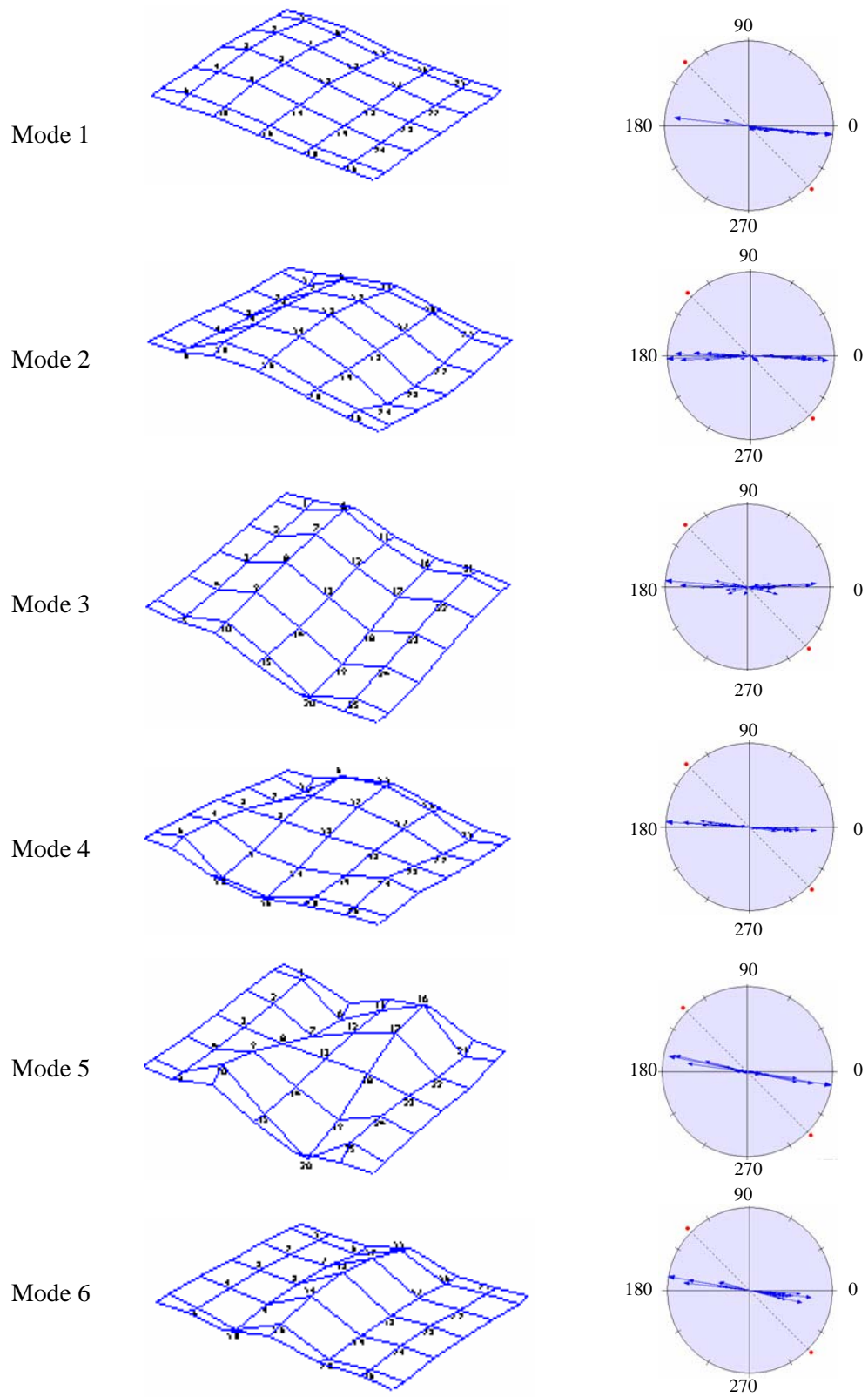


Figure A.6 Mode shapes and complexity plots after unloading from 578 kN -Phase 2

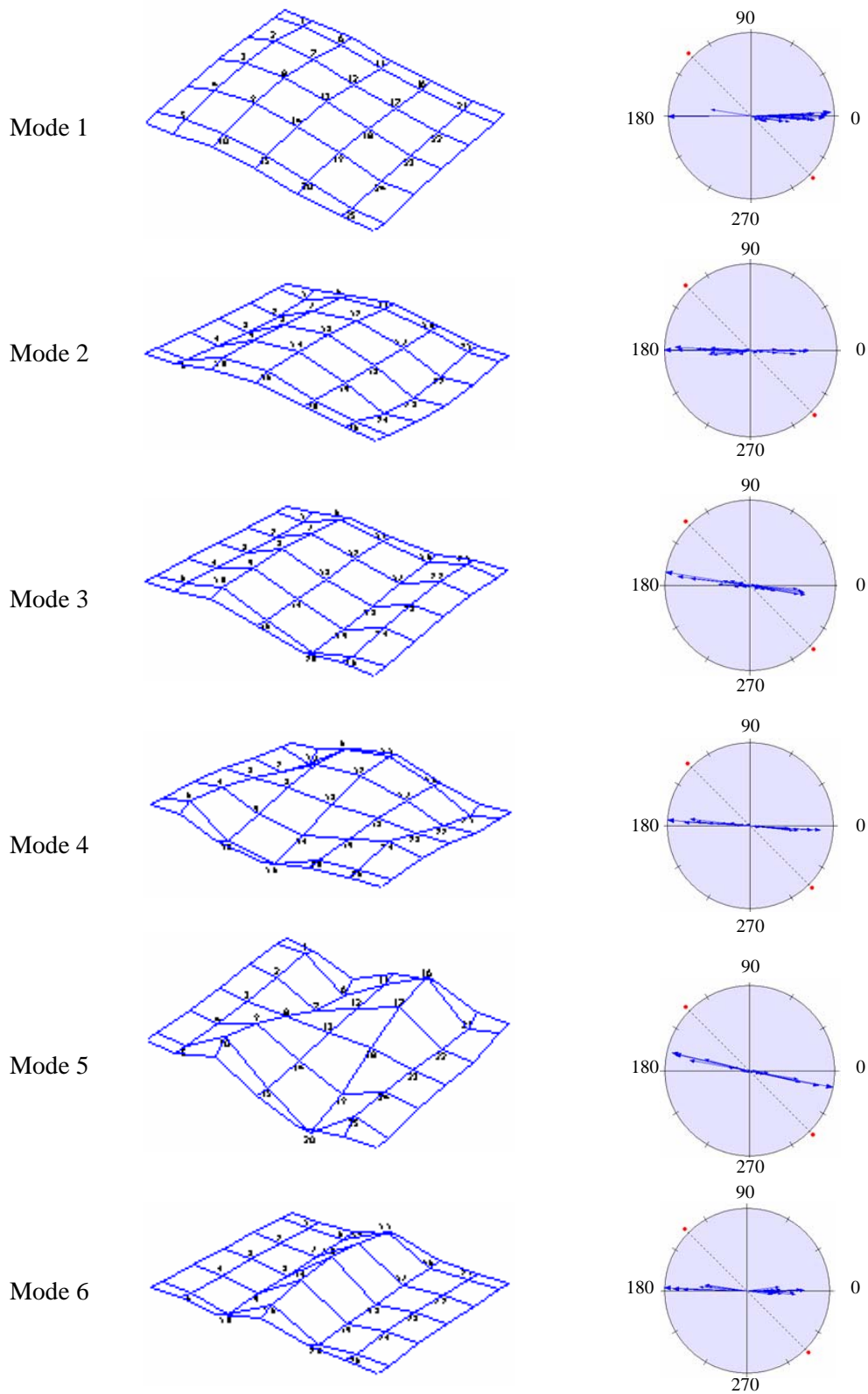


Figure A.7 Mode shapes and complexity plots after unloading from 668 kN -Phase 2

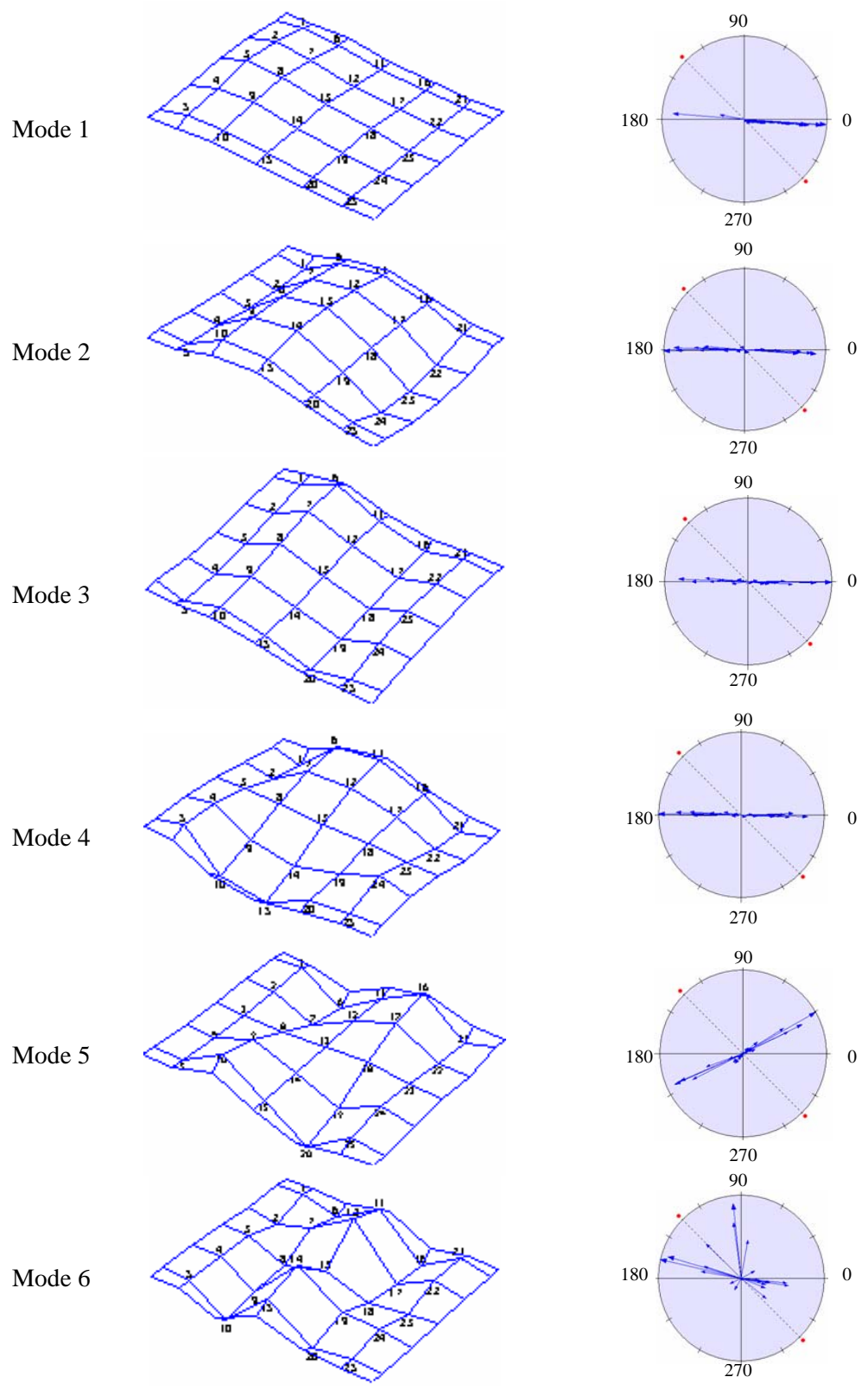


Figure A.8 Mode shapes and complexity plots from baseline 3 modal tests – Phase 3

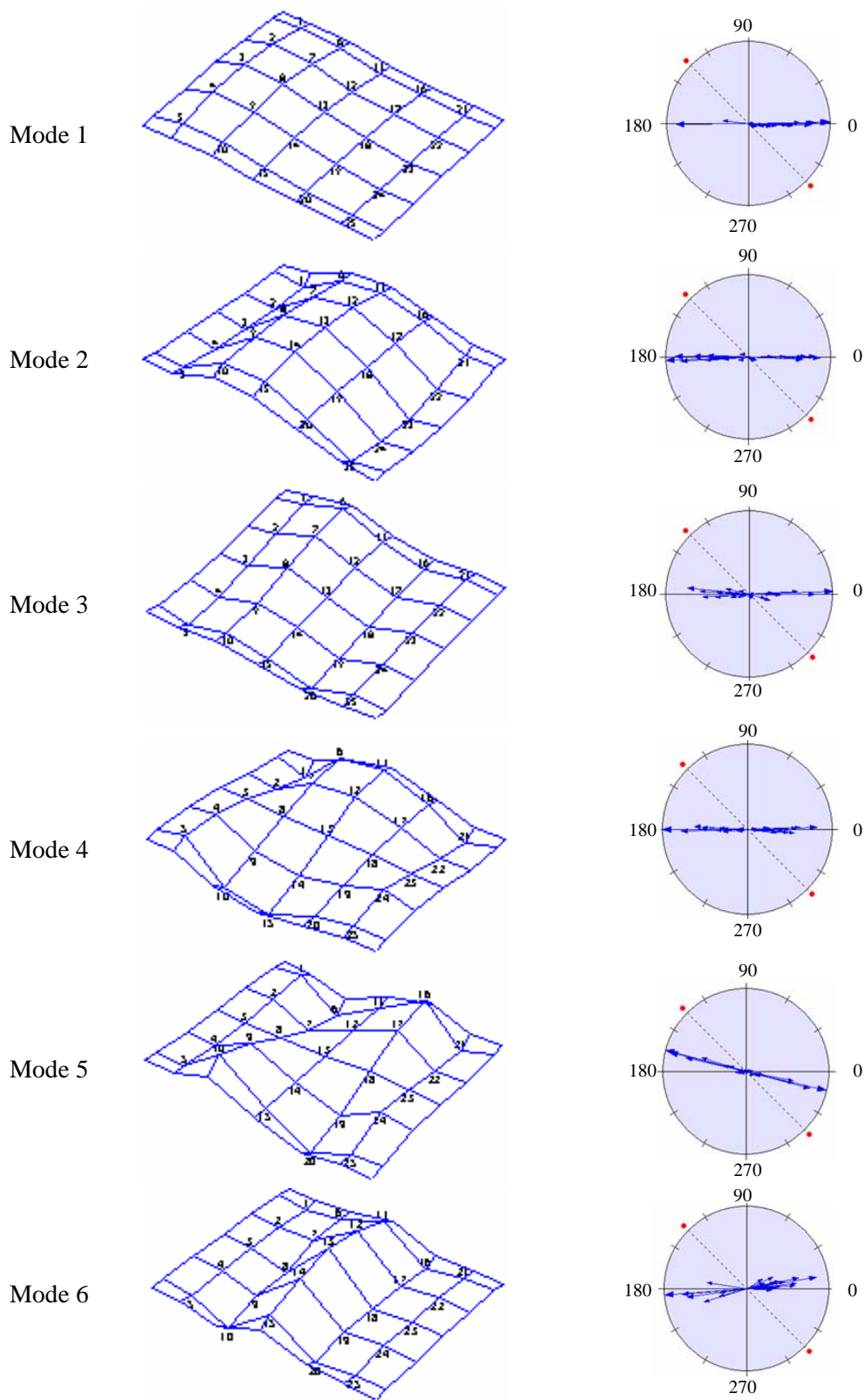


Figure A.9 Mode shapes and complexity plots after unloading from 668 kN -Phase 3

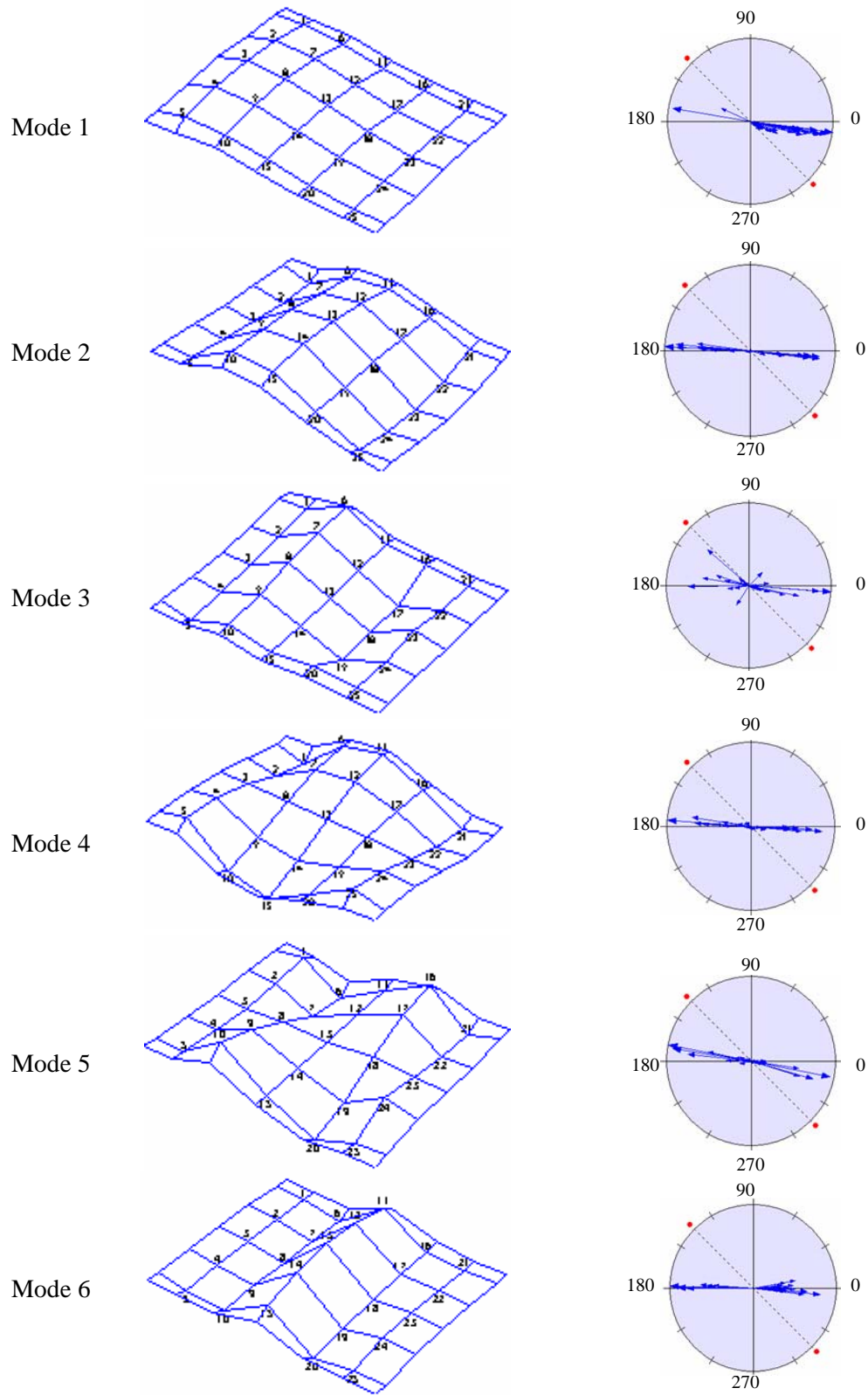


Figure A.10 Mode shapes and complexity plots after unloading from 756 kN -Phase 3

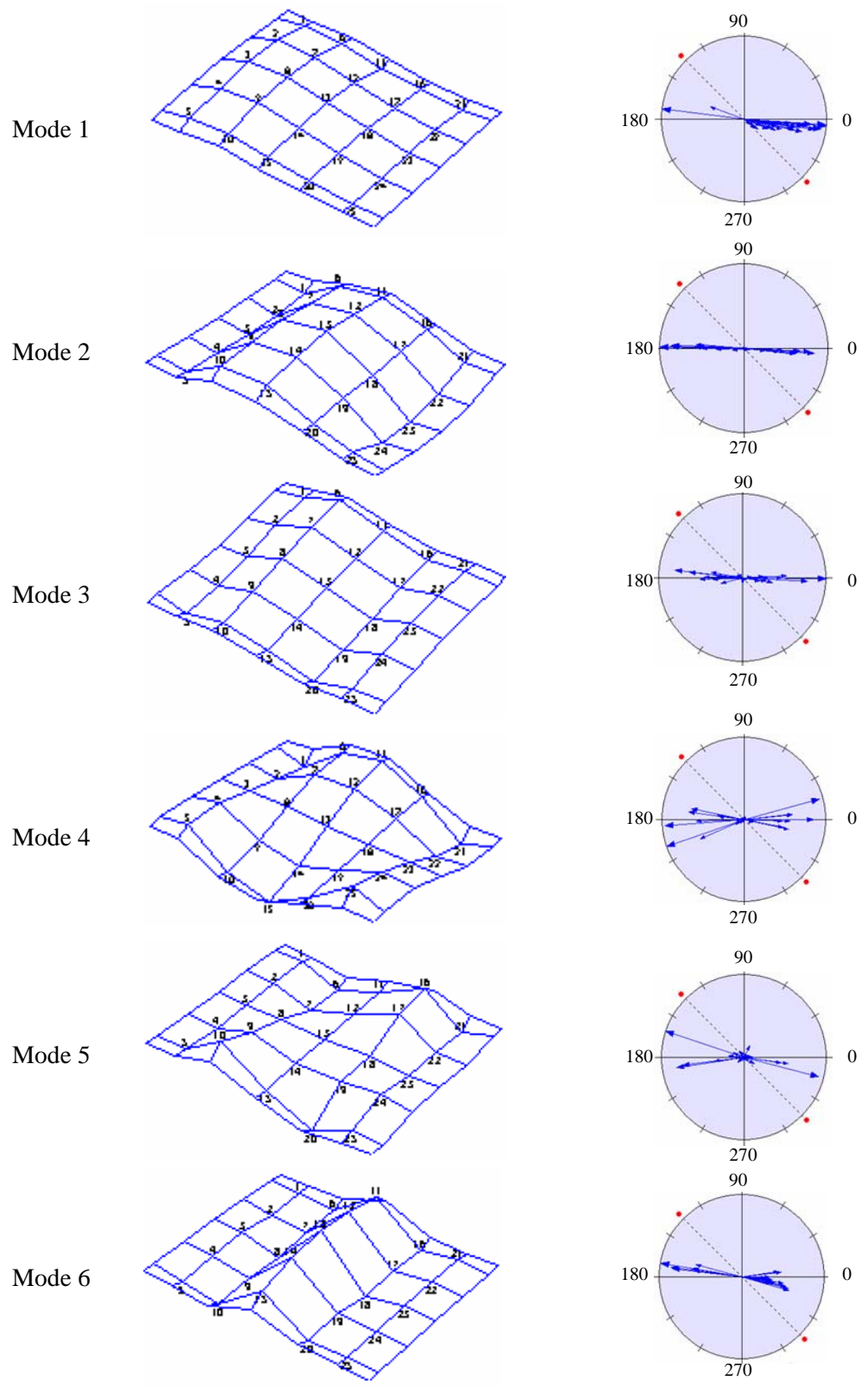


Figure A.11 Mode shapes and complexity plots after unloading from 846 kN -Phase 3

Table A.1a Mode 1 normalized modal amplitudes over the load stages

Node #	Phase 1				Phase 2				Phase 3			
	B1	214-0 kN	289-0 kN	400-0 kN	B2	400-0 kN	578-0 kN	667-0 kN	B3	667-0 kN	757-0 kN	845-0 kN
1	0.890	0.892	0.843	0.825	0.756	0.790	0.808	0.788	0.771	0.798	0.775	0.781
2	1.000	1.000	1.000	1.000	1.000	1.000	1.000	1.000	1.000	1.000	1.000	1.000
3	0.943	0.884	0.977	1.001	1.056	1.029	0.988	1.024	1.061	1.027	1.055	0.990
4	0.699	0.676	0.756	0.780	0.735	0.840	0.792	0.809	0.793	0.833	0.855	0.819
5	0.410	0.382	0.533	0.534	0.533	0.607	0.536	0.558	0.563	0.541	0.605	0.563
6	0.570	0.600	0.630	0.652	0.507	0.559	0.632	0.716	0.609	0.646	0.675	0.709
7	0.671	0.704	0.788	0.836	0.740	0.765	0.834	0.973	0.840	0.853	0.912	0.937
8	0.645	0.640	0.815	0.874	0.779	0.841	0.888	1.064	0.918	0.906	1.004	1.003
9	0.506	0.510	0.686	0.743	0.667	0.738	0.756	0.947	0.800	0.779	0.891	0.871
10	0.303	0.296	0.481	0.521	0.453	0.542	0.530	0.718	0.574	0.553	0.667	0.628
11	0.159	0.191	0.249	0.293	0.178	0.221	0.293	0.406	0.296	0.302	0.363	0.404
12	0.238	0.276	0.388	0.436	0.336	0.364	0.462	0.657	0.479	0.469	0.562	0.599
13	0.273	0.347	0.455	0.525	0.397	0.443	0.552	0.824	0.588	0.561	0.684	0.710
14	0.221	0.279	0.383	0.452	0.311	0.384	0.481	0.782	0.525	0.493	0.621	0.630
15	0.132	0.186	0.257	0.314	0.211	0.259	0.337	0.638	0.385	0.355	0.471	0.465
16	-0.017	0.027	0.105	0.116	0.039	0.100	0.157	0.242	0.150	0.187	0.199	0.225
17	0.045	0.093	0.169	0.209	0.105	0.161	0.247	0.406	0.254	0.278	0.324	0.355
18	0.064	0.128	0.203	0.258	0.144	0.182	0.291	0.520	0.312	0.328	0.408	0.437
19	0.049	0.146	0.173	0.222	0.094	0.135	0.243	0.499	0.277	0.282	0.374	0.400
20	-0.027	0.049	0.107	0.155	0.013	0.061	0.159	0.410	0.196	0.196	0.285	0.304
21	-0.031	-0.002	-0.038	0.039	-0.004	0.051	0.064	0.103	0.052	0.084	0.092	0.098
22	-0.035	0.005	0.057	0.060	-0.012	0.047	0.089	0.177	0.089	0.109	0.150	0.163
23	-0.042	0.006	0.056	0.074	0.026	0.040	0.093	0.217	0.104	0.112	0.179	0.200
24	-0.037	0.010	-0.052	0.068	-0.016	-0.022	0.069	0.200	0.088	0.086	0.159	0.185
25	-0.031	0.005	-0.030	0.041	-0.006	-0.027	-0.037	0.145	-0.053	-0.054	0.113	0.134

Table A.1b Mode 2 normalized modal amplitudes over the load stages

Node #	Phase 1				Phase 2				Phase 3			
	B1	214-0 kN	289-0 kN	400-0 kN	B2	400-0 kN	578-0 kN	667-0 kN	B3	667-0 kN	757-0 kN	845-0 kN
1	-0.379	-0.456	-0.497	-0.525	-0.409	-0.584	-0.548	-0.696	-0.558	-0.559	-0.712	-0.649
2	-0.362	-0.425	-0.49	-0.547	-0.441	-0.534	-0.558	-0.736	-0.578	-0.595	-0.704	-0.707
3	-0.283	-0.32	-0.389	-0.468	-0.405	-0.385	-0.458	-0.652	-0.496	-0.522	-0.565	-0.6
4	-0.17	-0.18	-0.221	-0.291	-0.227	-0.192	-0.296	-0.426	-0.286	-0.343	-0.309	-0.399
5	-0.061	-0.046	-0.063	-0.115	-0.08	-0.09	-0.136	-0.211	-0.115	-0.147	-0.07	-0.173
6	0.4815	0.3896	0.3535	0.3716	0.3699	0.231	0.2964	0.234	0.2783	0.3385	0.2218	0.3025
7	0.6672	0.5994	0.5759	0.5914	0.541	0.5058	0.533	0.4605	0.5063	0.5574	0.4888	0.4988
8	0.7782	0.7547	0.7684	0.7947	0.7068	0.7581	0.7264	0.6869	0.7054	0.742	0.7605	0.6819
9	0.7261	0.7283	0.7639	0.7888	0.6872	0.8041	0.735	0.7596	0.7418	0.7594	0.8495	0.7196
10	0.6204	0.65	0.7121	0.7506	0.6247	0.7796	0.7026	0.8055	0.7358	0.741	0.9001	0.7319
11	0.5781	0.5308	0.5001	0.5159	0.4748	0.4453	0.4893	0.4554	0.4808	0.5095	0.457	0.5369
12	0.8601	0.8267	0.8077	0.8107	0.8033	0.7824	0.8038	0.7624	0.7894	0.8056	0.7681	0.8138
13	1	1	1	1	1	1	1	1	1	1	1	1
14	0.8481	0.889	0.9025	0.917	0.86	0.9134	0.9271	1.0276	0.9465	0.9369	0.9966	0.9452
15	0.5751	0.6541	0.6683	0.7036	0.6154	0.6837	0.7212	0.9276	0.7636	0.7514	0.8555	0.7795
16	0.2842	0.1826	0.1384	0.0758	0.0897	0.1351	0.1077	-0.092	0.0422	0.1135	-0.043	0.0214
17	0.3488	0.2509	0.2119	0.0915	0.1908	0.197	0.126	-0.125	0.0625	0.1236	-0.045	0.0331
18	0.3724	0.3021	0.2672	0.1079	0.2145	0.2268	0.1286	-0.122	0.078	0.1345	-0.036	0.0666
19	0.297	0.2693	0.2222	0.0753	0.1847	0.1585	0.0818	-0.057	0.0727	0.1	-0.036	0.077
20	0.1978	0.2176	0.1536	0.0464	0.0286	0.0815	0.0436	0.0359	0.0657	0.0795	-0.046	0.0981
21	-0.404	-0.554	-0.494	-0.599	-0.466	-0.684	-0.583	-0.851	-0.62	-0.6	-0.713	-0.712
22	-0.576	-0.735	-0.705	-0.912	-0.714	-0.447	-0.899	-1.286	-0.955	-0.95	-1.061	-1.048
23	-0.669	-0.809	-0.807	-1.075	-0.824	-0.825	-1.069	-1.502	-1.129	-1.146	-1.225	-1.197
24	-0.612	-0.696	-0.718	-0.967	-0.725	-0.766	-0.959	-1.316	-0.991	-1.026	-1.067	-1.02
25	-0.466	-0.491	-0.533	-0.715	-0.476	-0.604	-0.715	-0.936	-0.653	-0.751	-0.752	-0.694

Note: 214-0 kN denotes that the modal test was carried out after retracting the actuators (unloading the specimen) after returning from the 214 kN load cycle

Table A.1c Mode 4 normalized modal amplitudes over the load stages

Node #	Phase 1				Phase 2				Phase 3			
	B1	214-0 kN	289-0 kN	400-0 kN	B2	400-0 kN	578-0 kN	667-0 kN	B3	667-0 kN	757-0 kN	845-0 kN
1	0.42	0.4066	0.4734	0.5341	0.5082	0.5287	0.5856	0.7268	0.6138	0.6253	0.6704	0.6723
2	0.1792	0.1767	0.2129	0.2496	0.1801	0.2494	0.2738	0.347	0.2925	0.2951	0.3318	0.3238
3	-0.137	-0.114	-0.118	-0.124	-0.076	-0.12	-0.129	-0.146	-0.14	-0.135	-0.122	-0.128
4	-0.336	-0.299	-0.314	-0.361	-0.311	-0.348	-0.378	-0.457	-0.389	-0.414	-0.43	-0.498
5	-0.385	-0.35	-0.382	-0.444	-0.173	-0.42	-0.458	-0.582	-0.49	-0.483	-0.559	-0.568
6	-0.895	-0.754	-0.74	-0.698	-0.1	-0.698	-0.587	-0.47	-0.627	-0.579	-0.553	-0.577
7	-0.624	-0.572	-0.576	-0.558	-0.726	-0.539	-0.497	-0.465	-0.525	-0.492	-0.463	-0.476
8	-0.01	-0.074	-0.078	-0.103	-0.002	-0.051	-0.101	-0.186	-0.118	-0.106	-0.088	-0.098
9	0.5813	0.4527	0.4716	0.4234	0.5211	0.4663	0.3782	0.2455	0.3724	0.3743	0.3449	0.338
10	0.9746	0.8272	0.8787	0.8254	0.9637	0.8729	0.7846	0.6516	0.7853	0.7885	0.7085	0.6989
11	-0.921	-0.84	-0.845	-0.826	-0.798	-0.83	-0.801	-0.752	-0.805	-0.819	-0.844	-0.876
12	-0.58	-0.577	-0.606	-0.593	-0.609	-0.604	-0.599	-0.585	-0.586	-0.622	-0.597	-0.605
13	0.0501	-0.015	-0.048	-0.051	-0.029	-0.051	-0.081	-0.121	-0.065	-0.106	-0.068	-0.032
14	0.6739	0.6201	0.5978	0.5876	0.5761	0.5963	0.5635	0.5167	0.5769	0.55	0.569	0.598
15	1	1	1	1	1	1	1	1	1	1	1	1
16	-0.517	-0.439	-0.404	-0.275	-0.258	-0.391	-0.285	-0.026	-0.195	-0.257	-0.18	-0.119
17	-0.32	-0.324	-0.313	-0.229	-0.263	-0.305	-0.261	-0.111	-0.182	-0.242	-0.174	-0.126
18	0.0328	-0.033	-0.057	-0.064	-0.008	-0.088	-0.123	-0.131	-0.083	-0.112	-0.093	-0.051
19	0.3229	0.2734	0.2228	0.1376	0.1965	0.2158	0.1244	-0.04	0.0943	0.1292	0.0703	0.0598
20	0.4576	0.4617	0.4015	0.2652	0.2717	0.3983	0.2883	0.0528	0.2102	0.2963	0.1686	0.1184
21	0.3896	0.4431	0.3802	0.515	0.4436	0.2338	0.4984	0.7991	0.6032	0.5369	0.6672	1.026
22	0.2429	0.245	0.2375	0.3334	0.2739	0.361	0.3161	0.4943	0.388	0.3352	0.4236	0.5981
23	-0.008	-0.046	-0.006	0.012	0.0001	0.0093	-0.007	-0.01	-0.009	-0.006	-0.004	-0.001
24	-0.27	-0.309	-0.256	-0.337	0.0154	-0.233	-0.323	-0.521	-0.401	-0.346	-0.443	-0.598
25	-0.44	-0.459	-0.421	-0.569	-0.12	-0.391	-0.519	-0.852	-0.562	-0.554	-0.731	-0.979

Note: 214-0 kN denotes that the modal test was carried out after retracting the actuators (unloading the specimen) after returning from the 214 kN load cycle

Table A.1d Mode 6 normalized modal amplitudes over the load stages

Node #	Phase 1				Phase 2				Phase 3			
	B1	214-0 kN	289-0 kN	400-0 kN	B2	400-0 kN	578-0 kN	667-0 kN	B3	667-0 kN	757-0 kN	845-0 kN
1	-0.339	-0.456	-0.353	-0.416	-0.404	-0.448	-0.407	-0.37	-0.051	-0.406	-0.386	-0.371
2	-0.237	-0.219	-0.188	-0.308	-0.48	-0.267	-0.298	-0.347	-0.307	-0.298	-0.337	-0.404
3	-0.123	-0.064	0.0095	-0.215	-0.158	-0.148	-0.21	-0.297	-0.254	-0.21	-0.299	-0.284
4	-0.254	-0.215	-0.179	-0.267	-0.203	-0.251	-0.267	-0.292	-0.225	-0.267	-0.34	-0.291
5	-0.404	-0.472	-0.44	-0.367	-0.404	-0.474	-0.4	-0.333	-0.351	-0.4	-0.418	-0.363
6	-0.532	-0.62	-0.598	-0.45	-0.552	-0.587	-0.529	-0.393	-0.252	-0.527	-0.648	-0.48
7	-0.128	-0.16	-0.244	-0.363	-0.34	-0.305	-0.344	-0.388	-0.577	-0.343	-0.605	-0.51
8	-0.021	-0.012	-0.052	-0.359	-0.244	-0.214	-0.327	-0.519	-0.487	-0.327	-0.564	-0.577
9	-0.399	-0.444	-0.394	-0.512	-0.43	-0.435	-0.485	-0.592	-0.187	-0.486	-0.477	-0.534
10	-0.878	-1.051	-0.887	-0.718	-0.754	-0.812	-0.752	-0.699	-0.903	-0.752	-0.512	-0.589
11	0.3114	0.3247	0.2752	0.4423	0.2609	0.3311	0.3987	0.5807	0.4654	0.3968	0.6392	0.6265
12	0.7336	0.77	0.8294	0.8508	0.7276	0.7695	0.802	0.8909	0.9205	0.8	0.9126	0.8674
13	1	1	1	1	1	1	1	1	1	1	1	1
14	0.6805	0.6292	0.6877	0.7953	0.7891	0.7348	0.7551	0.7762	0.5844	0.7556	0.803	0.845
15	0.2105	0.1731	0.1881	0.4285	0.3738	0.3133	0.3729	0.4739	0.1491	0.3714	0.5189	0.593
16	-0.785	-0.863	-0.868	-0.624	-0.808	-0.711	-0.653	-0.469	-0.68	-0.651	-0.393	-0.582
17	-0.532	-0.521	-0.46	-0.465	-0.544	-0.454	-0.456	-0.427	-0.469	-0.454	-0.344	-0.541
18	-0.254	-0.233	-0.123	-0.437	-0.349	-0.319	-0.383	-0.509	-0.159	-0.384	-0.474	-0.579
19	-0.079	-0.195	-0.018	-0.385	-0.313	-0.385	-0.438	-0.569	-0.386	-0.438	-0.639	-0.331
20	-0.419	-0.461	-0.344	-0.57	-0.435	-0.598	-0.619	-0.654	-0.554	-0.619	-0.803	-0.444
21	-0.311	-0.362	-0.321	-0.383	-0.346	-0.32	-0.442	-0.406	-0.314	-0.441	-0.498	-0.369
22	-0.335	-0.303	-0.192	-0.343	-0.28	-0.441	-0.347	-0.375	-0.341	-0.346	-0.4	-0.343
23	-0.237	-0.257	-0.093	-0.247	-0.263	-0.221	-0.254	-0.325	0.017	-0.254	-0.287	-0.335
24	-0.255	-0.257	-0.072	-0.275	-0.256	-0.241	-0.255	-0.305	-0.055	-0.255	-0.284	-0.35
25	-0.191	-0.237	-0.18	-0.288	-0.308	-0.312	-0.302	-0.288	-0.052	-0.302	-0.32	-0.33

Note: 214-0 kN denotes that the modal test was carried out after retracting the actuators (unloading the specimen) after returning from the 214 kN load cycle

Table A.2a Updated parameters for Phase 1 of testing

		Initial	Baseline 1	214-1	289-1	400-1
S1	Springs (N/m)	111.38	125.40	125.68	126.91	128.20
S2		301.74	272.16	266.26	271.39	265.70
S3		191.41	257.28	261.03	267.91	275.95
S4		218.56	277.44	280.76	285.30	289.59
S5		386.15	329.64	314.79	310.25	297.72
S6		225.39	285.77	289.47	294.49	301.27
SL1-1	Slab 1 (MPa)	33094.83	33536.10	33434.06	33465.08	33166.54
SL1-2		33094.83	29560.58	26326.94	26152.50	25376.84
SL1-3		33094.83	31815.86	28660.13	28116.13	25063.13
SL1-4		33094.83	32879.03	31014.69	31049.16	27527.32
SL1-5		33094.83	38738.19	38528.59	38875.40	37706.05
SL2-1	Slab 2 (MPa)	33094.83	40687.34	40225.39	41189.97	39451.80
SL2-2		33094.83	37437.84	35712.77	36051.31	31700.71
SL2-3		33094.83	36282.28	33914.62	33700.88	29642.63
SL2-4		33094.83	36771.81	34428.28	34663.39	31414.58
SL2-5		33094.83	39207.04	39111.89	39218.07	38252.80
BE1-1	Edge girder 1 (MPa)	45505.40	45746.02	45173.07	43914.30	43800.32
BE1-2		45505.40	50897.10	50663.36	50250.85	49588.47
BE1-3		45505.40	54820.21	54778.15	54807.35	53972.16
BE1-4		45505.40	49623.63	49263.73	48500.64	48208.83
BE1-5		45505.40	46102.48	45523.32	44225.89	44097.49
BE2-1	Edge girder 2 (MPa)	45505.40	46136.27	45545.39	44484.44	44462.22
BE2-2		45505.40	49833.92	49317.51	48869.24	49221.67
BE2-3		45505.40	52934.50	52493.92	52502.91	51816.86
BE2-4		45505.40	49013.45	48424.64	47696.47	47908.22
BE2-5		45505.40	45719.82	45093.09	43810.21	43687.25
BM-1	Center girder (MPa)	45505.40	44273.30	44137.48	44419.47	43072.24
BM-2		45505.40	47051.20	46946.40	47085.67	44555.99
BM-3		45505.40	48456.35	48364.65	48649.41	48299.84
BM-4		45505.40	46942.95	46900.21	47488.33	45373.71
BM-5		45505.40	44034.06	43741.03	43670.70	40655.62

Note: As shown in Figure 7.14, S-i denotes stiffness of spring i, SL1- i denotes effective modulus in region i of slab 1, SL2-i denotes effective modulus in region i of slab 2, BE1-i denotes effective modulus in region i of edge girder 1, BE2-i denotes effective modulus in region i of edge girder 2 and BM-i denotes effective modulus in region i of center girder. Also, load stage (214-1) stands for model updating based on modal test results obtained after unloading the specimen at the end of the 214 kN load cycle of phase 1 of test.

Table A.2b Updated parameters for Phase 2 of testing

		Baseline 1	Baseline 2	400-2	578-2	668-2
S1	Springs (N/m)	125.40	128.31	129.83	119.56	119.38
S2		272.16	266.75	272.64	250.12	232.18
S3		257.28	276.16	272.27	270.57	274.88
S4		277.44	290.05	297.54	302.95	308.33
S5		329.64	298.50	291.88	259.64	235.18
S6		285.77	301.43	295.26	290.55	295.21
SL1-1	Slab 1 (MPa)	33536.10	36460.16	36238.84	35874.11	35072.94
SL1-2		29560.58	26486.21	26092.52	25205.85	23585.58
SL1-3		31815.86	26756.48	26238.69	25290.66	23503.54
SL1-4		32879.03	29037.27	28554.64	27521.11	25350.64
SL1-5		38738.19	41716.73	41318.21	40734.91	39077.41
SL2-1	Slab 2 (MPa)	40687.34	45978.38	44982.08	44537.37	43485.23
SL2-2		37437.84	34344.16	33676.75	32844.55	31233.25
SL2-3		36282.28	31220.15	30665.81	29912.90	28435.36
SL2-4		36771.81	33804.30	33242.38	32523.95	31027.10
SL2-5		39207.04	43077.06	42350.36	42019.41	41145.84
BE1-1	Edge girder 1 (MPa)	45746.02	43807.22	43252.88	42180.74	40466.02
BE1-2		50897.10	49613.29	48862.45	48315.01	48764.55
BE1-3		54820.21	54008.01	53595.70	53488.15	52547.70
BE1-4		49623.63	48225.38	47320.10	46772.65	43232.19
BE1-5		46102.48	44104.38	43538.32	43041.90	39845.49
BE2-1	Edge girder 2 (MPa)	46136.27	44470.49	43748.61	43061.89	41963.56
BE2-2		49833.92	49245.11	47875.81	47699.31	45658.46
BE2-3		52934.50	51849.26	50444.80	50307.59	49731.19
BE2-4		49013.45	47926.15	46450.67	45247.53	44721.46
BE2-5		45719.82	43693.45	42911.59	41571.94	41516.78
BM-1	Center girder (MPa)	44273.30	43085.34	40174.37	37797.06	32235.75
BM-2		47051.20	44573.23	41826.35	41578.83	40393.62
BM-3		48456.35	48330.87	45600.54	45839.10	44614.59
BM-4		46942.95	45398.53	44842.81	44995.87	40082.67
BM-5		44034.06	40667.35	39171.87	38468.61	30876.79

Note: As shown in Figure 7.14, S-i denotes stiffness of spring i, SL1- i denotes effective modulus in region i of slab 1, SL2-i denotes effective modulus in region i of slab 2, BE1-i denotes effective modulus in region i of edge girder 1, BE2-i denotes effective modulus in region i of edge girder 2 and BM-i denotes effective modulus in region i of center girder. Also, load stage (400-2) stands for model updating based on modal test results obtained after unloading the specimen at the end of the 400 kN load cycle of phase 2 of test.

Table A.2c Updated parameters for Phase 3 of testing

		Baseline 1	Baseline 3	668-3	757-3	846-3
S1	Springs (N/m)	125.40	117.77	119.96	117.24	117.21
S2		272.16	243.99	240.34	238.05	234.46
S3		257.28	285.32	280.08	279.08	283.37
S4		277.44	317.70	317.00	338.73	339.99
S5		329.64	227.05	219.82	215.97	213.23
S6		285.77	291.60	276.26	277.03	288.47
SL1-1	Slab 1 (MPa)	33536.10	36054.75	36269.18	36556.00	36504.29
SL1-2		29560.58	24463.29	24461.91	24137.17	21920.50
SL1-3		31815.86	24375.03	24138.54	21897.06	20509.83
SL1-4		32879.03	27071.57	26887.48	22871.29	22099.76
SL1-5		38738.19	40746.63	40933.48	40743.19	40818.34
SL2-1	Slab 2 (MPa)	40687.34	43783.78	43829.28	43612.10	43399.74
SL2-2		37437.84	31349.77	30730.62	27529.39	24428.81
SL2-3		36282.28	28909.03	28220.93	26552.40	23010.56
SL2-4		36771.81	32065.45	31420.10	31011.93	26304.19
SL2-5		39207.04	41998.03	42015.27	42200.74	41935.29
BE1-1	Edge girder 1 (MPa)	45746.02	41192.04	41267.88	40795.59	40101.98
BE1-2		50897.10	48021.98	48197.80	47656.56	44880.04
BE1-3		54820.21	53029.64	53146.86	51209.43	45559.86
BE1-4		49623.63	43100.50	43108.78	41340.27	37908.06
BE1-5		46102.48	40286.07	40291.58	39373.89	38347.26
BE2-1	Edge girder 2 (MPa)	46136.27	42753.70	42805.41	42176.61	41578.14
BE2-2		49833.92	47127.04	47249.08	46906.41	43843.07
BE2-3		52934.50	49391.97	49528.49	49034.13	44347.08
BE2-4		49013.45	44810.40	44840.74	43958.21	41061.73
BE2-5		45719.82	41112.06	41099.65	40354.32	39738.62
BM-1	Center girder (MPa)	44273.30	34257.98	34263.49	33490.59	32786.64
BM-2		47051.20	45520.56	45681.90	45237.19	45590.20
BM-3		48456.35	45566.76	45812.21	46180.39	46209.35
BM-4		46942.95	44902.10	45096.54	44595.98	45006.91
BM-5		44034.06	33453.36	33460.95	32590.14	32064.76

Note: As shown in Figure 7.14, S-i denotes stiffness of spring i, SL1- i denotes effective modulus in region i of slab 1, SL2-i denotes effective modulus in region i of slab 2, BE1-i denotes effective modulus in region i of edge girder 1, BE2-i denotes effective modulus in region i of edge girder 2 and BM-i denotes effective modulus in region i of center girder. Also, load stage (668-3) stands for model updating based on modal test results obtained after unloading the specimen at the end of the 668 kN load cycle of phase 3 of test.

REFERENCES

- 1 Bonacci, J.F. and Maalej, M., "Externally Bonded FRP for Service Life Extension of RC Infrastructure." ASCE Journal of Infrastructure Systems, Vol. 6, No. 41, March 2000, pp 41-51.
- 2 Bakis, C. E., Bank, L. C., Brown, V. L., Cosenza, E., Davalos, J. F., Lesko, J. J., Machida, A., Rizkalla, S. H. and Triantafillou, T. C., "Fiber- Reinforced Polymer Composites for Construction - State-of-the-Art Review," ASCE Journal of Composites for Construction, V. 6, No. 2, 2002, pp. 73-87.
- 3 ACI Committee 440 (2002), "Guide for the Design and Construction of Externally Bonded FRP Systems for Strengthening Concrete Structures (ACI 440.2R-02)," American Concrete Institute, Farmington Hills, Michigan, 44 pp.
- 4 Saadatmanesh, H. and Ehsani, M., "RC Beams Strengthened with GFRP Plates – I: Experimental Study," ASCE Journal of Structural Engineering, V117, No. 11, 1991, pp 3417-3433.
- 5 Ritchie, P. A., Thomas, D. A., Lu, L.-W. and Connelly, G. M., "External Reinforcement of Concrete Beams Using Fiber Reinforced Plastics," ACI Structural Journal, V. 88, No. 4, July-Aug., 1991, pp. 490-500.
- 6 Al-Sulaimani, G. J., Sherif, A., Basunbul, I. A., Balunch, M. H., and Ghalib, B. N., "Shear Repair for Reinforced Concrete by Fiberglass Plate Bonding," ACI Structural Journal, V. 91, No. 4, July-Aug., 1994, pp. 458-464.
- 7 Chaallal, O., Nollet, M. and Perraton, D., "Strengthening of Reinforced Concrete Beams with Externally Bonded Reinforced Plastic Plates: Design Guidelines for Shear and Flexure," Canadian Journal for Civil Engineering, V. 25, 1998 pp. 692-704.
- 8 GangaRao, H. V. S. and Vijay, P. V., "Bending Behavior of Concrete Beams Wrapped with Carbon Fabric," ASCE Journal of Structural Engineering, V. 124, No. 1, 1998, pp. 3-10.
- 9 Malek, M. A., Saadatmanesh, H. and Ehsani, M. R., "Prediction of Failure Load of R/C Beams Strengthened with FRP Plate Due to Stress Concentration at the Plate End," ACI Structural Journal, V. 95, No. 2, Mar.-Apr., 1998, pp. 142-152.
- 10 Eng, C., "The Use of Mechanical Anchorage in FRP Strengthening of Reinforced Concrete Beams," M.S. Thesis - University of California, San Diego, 2004, 369 pp.

- 11 Niu, H. and Wu, Z., "Prediction of Debonding Failure Load Due to Flexural Cracks in Concrete for FRP Strengthened Structures," Proceedings of FRPRCS-5, Cambridge, July 2001, pp. 361-370.
- 12 Niu, H. and Wu, Z., "Numerical Analysis of Debonding Mechanisms in FRP Strengthened RC Beams," Computer-Aided Civil and Infrastructure Engineering, V. 20, 2005, pp. 354-368.
- 13 Cao, L.C. and Shing, P. B., "Simplified Analysis Method for Slab-on-Girder Highway Bridge Decks," ASCE Journal of Structural Engineering, V. 125, No. 1, January, 1999, pp. 49-59.
- 14 Arduini, M., Nanni, A. and Romagnolo, M., "Performance of One-Way Reinforced Concrete Slabs with Externally Bonded Fiber-Reinforced Polymer Strengthening," ACI Structural Journal, V. 101, No. 2, March-April 2004, pp. 193-201.
- 15 Seim, W., Horman, M., Karbhari, V. and Seible, F., "External FRP Post-strengthening of Scaled Concrete Slabs," ASCE Journal of Composites for Construction, V. 5, No. 2, May, 2001, pp. 67-75.
- 16 Kikukawa, K., Mutoh, K., Ohya, H., Ohyama, Y. and Tanaka, H., "Flexural Reinforcement of Concrete Floor Slabs by Carbon Fiber Textiles," Composite Interfaces, V. 5, No. 5, 1998, pp. 469-478.
- 17 Lam, L., and Teng, J. G., "Strength of RC Cantilever Slabs Bonded with GFRP Strips," ASCE Journal of Composites for Construction, V. 5, No. 4, Nov., 2001, pp. 221-227.
- 18 Ebead, U. and Marzouk, H., "Fiber-Reinforced Polymer Strengthening of Two-Way Slabs," ACI Structural Journal, V. 101, No. 5, September-October 2004, pp. 650-659.
- 19 Marzouk, H., and Hussein, A., "Experimental Investigation on the Behavior of High-Strength Concrete Slabs," ACI Structural Journal, V. 88, No. 6, Nov.-Dec., 1991, pp. 701-713.
- 20 Triantafillou, T. C., "Shear Strengthening of Reinforced Concrete Beams Using Epoxy-Bonded FRP Composites," ACI Structural Journal, V. 95, No. 2, Mar.-Apr., 1998, pp. 107-115.
- 21 Saadatmanesh, H., Norris, T. and Ehsani, M., "Shear and Flexural Strengthening of R/C Beams with Carbon Fiber Sheets," ASCE Journal of Structural Engineering, V. 123, No. 7, July, 1997, pp. 903-911.
- 22 Challal, O., Nollet, M.J. and Perraton, D., "Shear Strengthening of RC Beams by Externally Bonded Side CFRP Strips," ASCE Journal of Composites for Construction, V. 2, No. 2, 1998, pp. 111-113.

- 23 Chaallal, O., Shahawy, M. and Hassan, M., "Performance of Reinforced Concrete T-Girders Strengthened in Shear with Carbon Fiber-Reinforced Polymer Fabric," *ACI Structural Journal*, V. 99, No. 3, May-June 2002, pp. 335-343.
- 24 Taljsten, B., "FRP Strengthening of Existing Concrete Structures : Design Guidelines," Lulea University of Technology, 2002, pp. 59-72.
- 25 Schuman, P., "Investigation on Mechanical Anchorage for Shear Rehabilitation of Continuous Reinforced Concrete T-Beams with CFRP Externally Bonded Stirrups," Masters Thesis, Dept. of Structural Engineering., University of California, San Diego, 2002, pp. 415.
- 26 Schuman, P., "Mechanical Anchorage for Shear Rehabilitation of Reinforced Concrete Structures with FRP: An Appropriate Design," Ph.D. Thesis, Dept. of Structural Engineering, University of California, San Diego, 2004, pp. 528.
- 27 Oh, H., Sim, J. and Meyer, C., "Experimental Assessment of Bridge Deck Panels Strengthened With Carbon Fiber Sheets," *Composites Part B: Engineering*, Vol. 34, No. 6, September 2003, pp. 527-538.
- 28 Oh, B., Kim, K.S. and Lew, Y., "Ultimate Load Behavior of Post-Tensioned Prestressed Concrete Girder Bridge through In-Place Failure Test," *ACI Structural Journal*, V. 99, No. 2, March-April 2002, pp. 172-180.
- 29 Shahrooz, B.M., Saraf, V., Godbole, B. and Miller, R., "Response of Slab Bridges Before, During and After Repair," *ASCE Journal of Bridge Engineering*, V. 7, No. 5, Sept. 2002, pp. 267-275.
- 30 Issa, M., Yousif, A. and Issa, M.A., "Experimental Behavior of Full-Depth Precast Concrete Panels for Bridge Rehabilitation," *ACI Structural Journal*, V. 97, No. 3, May-June 2000, pp. 397-407.
- 31 Priestley, M.J.N., Seible, F. and Calvi, G.M., "Seismic Design and Retrofit of Bridges," Wiley Interscience, New York, 1996.
- 32 Bracci, J., Reinhorn, A. and Mander, J., "Seismic Resistance of Reinforced Concrete Frame Structures Designed For Gravity Loads: Performance of Structural System," *ACI Structural Journal*, V. 92, No. 5, Sept.-Oct. 1995, pp. 597-609.
- 33 Calvi, G. M.; Magenes, G.; and Pampanin, S., "Relevance of Beam-Column Joint Damage and Collapse in RC Frame Assessment," *Journal of Earthquake Engineering*, V. 6, No. 1, 2002, pp. 75-100.
- 34 Prota, A., Nanni, A., Manfredi, G. and Cosenza, E., "Selective Upgrade of Underdesigned Reinforced Concrete Beam-Column Joints Using Carbon Fiber-Reinforced Polymers," *ACI Structural Journal*, V. 101, No. 5, September-October 2004, pp. 699-707.

- 35 Priestley, M.J.N., Seible, F. and Anderson, D.L., "Proof Test of a Retrofit Concept for the San Francisco Double Deck Viaducts: Part 1 – Design Concepts, Details and Model," *ACI Structural Journal*, V. 90, No. 5, September-October 1993, pp. 467-479.
- 36 Griezic, A., Cook, W.D. and Mitchell, D., "Seismic Behavior and Retrofit of Outrigger Beam-Column Frames," *ASCE Journal of Bridge Engineering*, Vol. 6, No. 5, September-October, 2001, pp. 340-348.
- 37 Lowes, L. and Moehle, J.P., "Evaluation and Retrofit of Beam-Column T-Joints in Older Reinforced Concrete Bridge Structures," *ACI Structural Journal*, V. 96, No. 4, July-August 1999, pp. 519-533.
- 38 Miller, T.C., Chajes, M.J., Mertz, D.R. and Hastings, J.N., "Strengthening of a Steel Bridge Girder Using CFRP Plates," *ASCE Journal of Bridge Engineering*, Vol. 6, No. 6, November-December, 2001, pp. 514-522.
- 39 Cardinale, G. and Orlando, M., "Structural Evaluation and Strengthening of a Reinforced Concrete Bridge," *ASCE Journal of Bridge Engineering*, Vol. 9, No. 1, 2004, pp. 35-42.
- 40 Hag-Elsafi, O., Alampalli, S. and Kunin, J., "Application of FRP Laminates For Strengthening of a Reinforced Concrete T-beam Bridge Structure," *Journal of Composite Structures*, Vol. 52, No. 3-4, May-June 2001, pp. 453-466.
- 41 Hutchinson, R., Tadros, G., Kroman, J. and Rizkalla, S., "Use of Externally Bonded FRP Systems for Rehabilitation of Bridges in Western Canada," *Field Applications of FRP Reinforcement: Case Studies*, ACI SP-215, 2003, pp. 239-248.
- 42 Stallings, J.M., Tadesco, J.W., El-Mihilmy, M. and McCauley, M., "Field Performance of FRP Bridge Repairs," *ASCE Journal of Bridge Engineering*, Vol. 5, No. 2, 2000, pp. 107-113.
- 43 Schuman, P., Karbhari, V. and Seible, F., "Rehabilitation of A Multi-Span Bridge Using FRP Composite Materials," *High performance materials in bridges: proceedings of the international conference, July 29-August 3, Kona, Hawaii, ASCE, 2001*, pp. 374 -385.
- 44 Lee, L., Karbhari, V. and Sikorsky, C., "Integrity and Effectiveness of Watson Wash Bridge Deck Rehabilitation Using CFRP Composites," *Proceedings of Caltrans Bridge Research Conference, Sacramento, California, Oct. 31-Nov. 1, 2005*.
- 45 Oh, H. and Sim, J. "Punching Shear Strength of Strengthened Deck Panels with Externally Bonded Plates," *Composites Part B: Engineering*, v 35, 2004, pp 313-321,
- 46 Stubbs, N. and Kim, J. T., "Damage Localization in Structures without Baseline Modal Parameters," *AIAA Journal*, Vol. 34, No. 8, 1996, pp. 1644-1649.

- 47 Kaiser, H. and Karbhari, V.M., "Non-Destructive Testing Techniques for FRP Rehabilitated Concrete: I – A Critical Review," *International Journal of Materials and Product Technology*, Vol. 21, No. 5, 2004, pp. 349-384.
- 48 Kaiser, H., Karbhari, V.M. and Sikorsky, C., "Non-Destructive Testing Techniques for FRP Rehabilitated Concrete: II – Assessment," *International Journal of Materials and Product Technology*, Vol. 21, No. 5, 2004, pp. 385-401.
- 49 Jackson, D.R., Islam, M., Hurley, F.J. and Alvarez, F.J., "Feasibility of Evaluating Fiber Reinforced Plastic (FRP) Wrapped Reinforced Concrete Columns Using Ground Penetrating Radar (GPR) and Infrared (IR) Thermography," *Demonstration Project No. 84-2, US Department of Transportation, Federal Highway Administration, Washington, D.C., 1999.*
- 50 Levar, J.M. and Hamilton, H.R., III, "Non-Destructive Evaluation of Carbon Fiber-Reinforced Polymer-Concrete Bond Using Infrared Thermography," *ACI Materials Journal*, Vol. 100, No. 1, 2003, pp. 63-72.
- 51 Starner, M.A., Carino, N.J. and Kausel, E.A., "Preliminary Thermography Studies for Quality Control of Concrete Structures Strengthened With Fiber-Reinforced Polymer Composites," *ASCE Journal of Materials in Civil Engineering*, Vol. 15, No. 3, 2003, pp. 266-273.
- 52 Lee, L., Karbhari, V.M. and Sikorsky, C., "Comprehensive Evaluation and Monitoring of Strengthening Using FRP Composites," *Proceedings of the International Symposium of the Japan Concrete Institute on Latest Achievement of Technology and Research on Retrofitting Concrete Structures, Kyoto, Japan, July 2003*, pp. 9-16.
- 53 California Bridge Design Standard, Engineering Services – Bridge Manuals, California Department of Transportation (CalTrans), 2005, available on web at <http://www.dot.ca.gov/manuals.htm>.
- 54 Karbhari, V.M., Sikorsky, C. and Lee, L.S., "Field Monitoring and Degradation Assessment of FRP Bridge Rehabilitation Using Level IV NDE Techniques," *Proceedings of the Structural Health Monitoring Workshop, SHM/ISIS, Winnipeg, Canada, September 2002*, pp. 319-328.
- 55 Lee, L.S., Sikorsky, C. and Karbhari, V.M., "Remaining Service Life of FRP Rehabilitated Structures," *Proceedings of the 60th SAMPE Technical Conference, May 2004, Long Beach, California.*
- 56 Lee, L., "Monitoring and Service Life Estimation of Reinforced Concrete Bridge Decks Rehabilitated with Externally Bonded Carbon Fiber Reinforced Polymer (CFRP) Composites," *Ph.D. Thesis, Dept. of Structural Engineering, University of California, San Diego, 2005*, pp. 275.

- 57 AASHTO LRFD Bridge Design Specifications, American Association of State Highway and Transportation Officials, Third Edition, 2004.
- 58 Graddy, J.C., Kim, J., Whitt, J.H., Burns, N.H. and Klingner, R.E., "Punching Shear Behavior of Bridge Decks under Fatigue Loading," *ACI Structural Journal*, Vol. 99 No. 3, 2002, pp. 257-266.
- 59 Nevada, R., "An Experimental Assessment of Defect Criticality in FRP Rehabilitated Concrete using a Fracture Mechanics Approach," M.S. Thesis, Department of Structural Engineering, University of California, San Diego, 2004.
- 60 Niu, H., Vasquez, A. and Karbhari, V.M. "Effect of Materials Configuration on Strengthening of Concrete Slabs by CFRP Composites," *Composites Part B: Engineering*, Vol. 37, No. 2-3, April 2005-March 2006, pp. 213-226.
- 61 Ghosh, K. and Karbhari, V., "A Critical Review of Infrared Thermography as a Method for Non-Destructive Evaluation of FRP Rehabilitated Structures," *International Journal of Materials and Product Technology*, Vol. 25, No. 4, 2006, pp. 241-266.
- 62 Ghosh, K. and Karbhari, V. "Progressive Damage and Capacity Evaluation of FRP Rehabilitated Bridge Decks Under Simulated Wheel Loads," *International SAMPE Technical Conference*, May 2004, Long Beach, California.
- 63 Meier, U. and Kaiser, H. "Strengthening of Structures with CFRP Laminates," *Advanced Composite Materials in Civil Engineering Structures*, ASCE Specialty Conference, 1991, pp. 224-232.
- 64 Sharif, A., Al-Sulaimani, G., Basunbul, I., Baluch, M. and Ghaleb, B. "Strengthening of Initially Loaded Reinforced Concrete Beams Using FRP Plates," *ACI Structural Journal*, Vol. 91, No. 2, March-April, 1994, pp. 160-168.
- 65 Collins, M.P. and Mitchell, D. "Prestressed Concrete Structures," Prentice Hall, Englewood Cliffs, NJ, 1991, 766 pp.
- 66 Ghosh, K. and Karbhari, V. "Evaluation of Environmental Effect on FRP/Concrete Bond," *International SAMPE Technical Conference*, May 2004, Long Beach, CA.
- 67 Schuman, P.M. and Karbhari, V., "Development of Appropriate Design Limits For Externally Bonded FRP For Shear Strengthening," *Proceedings of the 4th International Conference on Advanced Composite Materials in Bridges and Structures Conference*, July 20-30, 2004, Calgary, Canada.
- 68 Burgueno, R., Karbhari, V.M., Seible, F. and Kolozs, R. "Experimental Dynamic Characterization of an FRP Composite Bridge Superstructure Assembly," *Journal of Composite Structures*, Vol. 54, No. 4, 2001, pp. 427-444.

- 69 ACI Committee 318, "Building Code Requirements for Reinforced Concrete (ACI 318-99) and Commentary (ACI 318 R-99)," American Concrete Institute, Detroit, Michigan, 1999, 391 pp.
- 70 Joints in Concrete Construction (ACI 224.3R), "ACI Manual of Concrete Practice – Part 2," American Concrete Institute, Farmington Hills, MI, 2004.
- 71 Maia, N.M. and Silva, J.M. editors, "Theoretical and Experimental Modal Analysis," Research Studies Press, Ltd., 1997.
- 72 Ewins, D.J., "Modal Testing: Theory, Practice and Application," Research Studies Press, Ltd., Second Edition, 2000.
- 73 Chopra, A.K., "Dynamics of Structures," Prentice Hall, Second Edition, 2000.
- 74 MEScope VES, 5.0, Visual Engineering Series, Vibrant Technology, Inc.
- 75 SAP 2000, Version 10, Three Dimensional Static and Dynamic Finite Element Analysis and Design of Structures, Computers and Structures Inc., 2006.
- 76 Abaqus, Version 6.5, ABAQUS Inc., 2004.
- 77 Abaqus/Standard User's Manual, Version 6.5, ABAQUS Inc., 2004.
- 78 Bangash, M.Y.H., "Concrete and Concrete Structures: Numerical Modeling and Applications," Elsevier Science Publishers Ltd., London, England, 1989.
- 79 Abanilla, M.A., Li, Y. and Karbhari, V.M., "Durability Characterization of Wet Layup Graphite/Epoxy Composites used in External Strengthening," Composites Part B: Engineering, Vol. 37, No. 2-3, April 2005/March 2006, pp 200-212.
- 80 Jensen, E.A. and Hansen, W., "A New Model for Predicting Aggregate Interlock Shear Transfer in Jointed Concrete Pavements," Proc. 16th ASCE Engineering Mechanics Conference, University of Washington, Seattle, July 16-18, 2003.
- 81 Atadero, R. "Development of Load and Resistance Factor Design for FRP Strengthening of Reinforced Concrete Structures," Ph.D. Thesis, Dept. of Structural Engineering, University of California, San Diego, 2006, pp. 392.